Faculty of Engineering, Computer and Mathematical Sciences

School of Mechanical Engineering

The Aeroacoustics of Finite Wall-Mounted Cylinders

Ric Porteous

A thesis submitted in fulfilment of
the requirements for the degree of
Doctor of Philosophy in engineering.

September 2016

Supervisors: *Prof. Ben Cazzolato*
Assoc. Prof. Anthony Zander
Assoc. Prof. Con Doolan
Dr. Danielle Moreau

Submission date: May 13, 2016
Amendment date: September 10, 2016

School of Mechanical Engineering
The University of Adelaide, 5005
SA, Australia

Typeset by the author using LaTeX.
Printed in Australia.

Abstract

Community noise is one of the most poorly controlled environmental pollutants. Controlling the noise generated by bluff-body flow can alleviate community noise generated by transportation systems such as aircraft, automobiles and highspeed rail. A foundational example of bluff-body flow is the flow around a square Finite Wall-Mounted Cylinder (FWMC). An FWMC models the major noise producing components of transportation systems, such as landing gear and pantographs, but is also relevant to many facets of engineering including flow around chimney stacks, wind turbine masts, heat exchangers and mountains.

This thesis studies the flow-induced noise generated by square FWMCs with aspect ratios ranging from $0 < L/W < 23$ immersed in boundary layers of thickness $\delta/W = 1.3$ and $\delta/W = 3.7$ at a Reynolds number based on the side width, W, of $Re_W = 1.45 \times 10^4$. The flow-induced noise is measured using single microphone, directivity and phased microphone array measurements. The measured noise is related to the flow around the FWMC with fluctuating wake velocity measurements using a single hot-wire. Surface pressure measurements and oil-film flow visualisation are also conducted to further investigate the flow physics.

The flow-induced noise of FWMCs is characterised in terms of the frequency, magnitude and directivity of the low frequency acoustic tones generated through periodic vortex shedding and the magnitude of the high frequency broadband component. It is found that as the aspect ratio increases, the FWMC transitions through four vortex shedding regimes based on the number of tones in their acoustic spectra. The aspect ratio where the FWMC transitions from one regime to another is dependent on the boundary layer thickness. Within each shedding regime, the noise producing vortex filaments are observed to have different topological structures, corresponding to either a single or multi-cellular wake.

Measurements of the mean and fluctuating aerodynamics using wake velocity and surface pressure measurements provide explanations for the observed acoustic phenomena. In particular, it is discovered that maximum three-dimensional interaction of the free-end downwash with spanwise vortices can disrupt the wake and reduce the flow-induced noise to near background levels, even for aspect ratios as large as $L/W = 7$.

Several numerical models are also developed to aid the analysis. These include a modified version of Curle's Aeolian tone theory suitable for FWMCs and a wake model of higher aspect ratio FWMCs used to study cellular wake vortex topologies.

Finally, phased array source localisation shows that the magnitude of the high frequency broadband noise is closely related to dynamics of the large-scale vortex structures that generate tonal noise. Because of this, broadband noise can be reduced by approximately 30% when the boundary layer is thickened, even when the free-end of the FWMC lies well outside the edge of the boundary layer.

Declaration

I certify that this work contains no material which has been accepted for the award of any other degree or diploma in my name, in any university or other tertiary institution and, to the best of my knowledge and belief, contains no material previously published or written by another person, except where due reference has been made in the text. In addition, I certify that no part of this work will, in the future, be used in a submission in my name, for any other degree or diploma in any university or other tertiary institution without the prior approval of the University of Adelaide and where applicable, any partner institution responsible for the joint-award of this degree. I give consent to this copy of my thesis when deposited in the University Library, being made available for loan and photocopying, subject to the provisions of the Copyright Act 1968.

The author acknowledges that copyright of published works contained within this thesis resides with the copyright holder(s) of those works.

I also give permission for the digital version of my thesis to be made available on the web, via the University's digital research repository, the Library Search and also through web search engines, unless permission has been granted

Ric Porteous

Acknowledgements

Thank you to Associate Professor Con Doolan, Dr. Danielle Moreau, Professor Ben Cazzolato and Associate Professor Anthony Zander for all their guidance and inspiration during this journey.

I would also like to extend my gratitude to Associate Professor Vincent Valeau, Dr. Akhilesh Mimani, Dr. Thomas Geyer, Dr. Mohamed Sukri Mat Ali and the University of New South Wales for affording me the opportunity for collaboration.

Finally, to Dr. Zebb Prime - I couldn't have done it with you mate.

My sincerest thanks to all of you.

Contents

List of Figures

List of Tables

Nomenclature

The majority of the mathematical symbols and abbreviations used in this dissertation are outlined below. In some cases, the same symbol has been used for multiple purposes. These should be unambiguous based on the context of the work in which they appear.

Greek symbols

Γ	Circulation
Π	Boundary layer pressure gradient parameter
α	Temperature coefficient of resistance
β	Base suction coefficient
γ	Ratio of specific heats of air
δ	Boundary layer thickness
δ^*	Displacement thickness
ϵ	Expanded uncertainty, Strength of the van der Pol oscillator
η	Non-dimensional fluid packet dynamics
θ^*	Momentum thickness
κ	von Kármán constant, Non-dimensional viscous coupling constant
λ	Wavelength
μ	Dynamic viscosity of air
ν	Kinematic viscosity
ρ	Density
$\rho(\tau)$	Cross correlation coefficient function
σ	Standard deviation
σ^2	Variance
ϕ	Phase angle
ω	Frequency

Roman symbols

A	The DAMAS A-matrix
B	Number of averaging blocks
B_W	The array beamwidth
C_d	Drag coefficient
C_l	Lift coefficient
C_p	Pressure coefficient

D	Diameter
E	Voltage
F	Force
G	Cross spectral matrix
$G_{xy}(f)$	Cross spectral density
H	Number of data points in each averaging block when performing Welch's method, Hermetian transpose, Boundary layer shape factor
L	Cylinder span
L/W	Aspect ratio
L_p	Overall sound pressure level
M_∞	Free-stream Mach Number
M_0	Number of microphones in the array
N	Number of time record samples
$\mathbf{P}$	Pressure Vector
P	Total pressure
$R_{12}(\Delta z)$	Axial correlation function
Re_W	Reynolds number based on cylinder width, W
St	Strouhal number
$T.I.$	Turbulence intensity
T	Temperature
T_I	Integral time scale
V_∞	Free-stream mean velocity
$\mathbf{W}$	Shading matrix
W	Cylinder width
Y_t	Classical beamforming output at the t^{th} point in the scanning grid
Z	The CLEAN-SC output
a_{it}	Transfer function relating pressure at the i^{th} microphone to the amplitude of the t^{th} source
c_0	Speed of sound
f	Frequency
$\mathbf{h}$	Steering vector
$h_{1/2}$	Half thickness
h_{damp}	Damping ratio
i	Microphone index
j	Imaginary number, $\sqrt{-1}$
k	Wave number
l_f	Formation length
p	Inflation factor of spanwise coupling due to spanwise flow
p_d	Dynamic pressure
q	Fan speed
q_t	Ampltiude of the t^{th} source in a beamforming map
R	Specific gas constant of air
r	Distance
s	Spanwise correlation length parameter
t	Scanning grid index, Time

t_p	Ray propagation time
u	Streamwise velocity
u^+	Velocity in wall units
u_c	Convection velocity
v	Cross-stream velocity
$\mathbf{x}_{Ic}$	Intersection point of the acoustic ray with the velocity shear layer
$\mathbf{x}_t$	Spatial location of the t^{th} position in the scaning grid
x	Streamwise direction (unless otherwise stated)
y	Cross-stream direction (unless otherwise stated)
z	Spanwise direction (unless otherwise stated)
z^+	Spanwise distance in wall units
z_t	Array gain factor at the t^{th} point in the scanning grid

Abbreviations

18WT	18 inch Wind Tunnel
2D	Two-dimensional
3D	Three-dimensional
AWT	Anechoic Wind Tunnel
DAS	Delay-and-Sum
DR	Diagonal removal
FWMC	Finite wall mounted cylinder
HSV	Horseshoe vortex
MDF	Medium density fibreboard
NAH	Near-field acoustic holography
OASPL	Overall sound pressure level
PDF	Probability distribution function
PIV	Particle image velocimetry
POD	Proper orthogonal decomposition
PSD	Power spectral density
PSF	Point Spread Function
R0	Shedding Regime 0
RI	Shedding Regime 1
RII	Shedding Regime 2
RIII	Shedding Regime 3
SPL	Sound pressure level

Operators

$\hat{(.)}$	Estimator
$\overline{(.)}$	Mean operator
bias(.)	Bias operator
Exp(.)	Expectation operator
Prob(.)	Probability distribution function

var(.)	Variance operator
*	Conjugate operator

Chapter 1

Introduction

Every day, millions of people are exposed to unwanted, harmful environmental noise known as 'community noise'. Community noise includes a range of noise sources from high-speed rail and air traffic to noise generated by computer cooling systems. According to the World Health Organisation, community noise is poorly controlled when compared with other man-made pollutants, particularly in developing nations (*Guidelines for community noise* 1999). Repetitive exposure to excessive levels of community noise can have damaging effects on human health including loss of sleep, lower productivity, psychological discomfort and annoyance (Levinson et al. 1997).

An important source of community noise is that generated by high speed transportation systems, e.g., aircraft or high-speed rail. Meeting the acceptable standards for noise levels in the areas surrounding an airport or railway is a challenging problem. In some cases, strict community noise expectations can be the main barrier for technological improvement.

In the aircraft industry, the advent of high by-pass-ratio engines has allowed a significant reduction in aircraft noise during take-off and landing over the last 40 years. Unfortunately, the current rate of noise reduction based on today's understanding of aircraft noise sources may be not enough to achieve globally set future targets. For example, in their 2011 technical report, 'FLIGHTPATH2050' (European Commission 2011), the European Commission set a target of a 65% reduction in aircraft noise by 2050 (compared with the year 2000 reference levels). According to Astley (2014), this target will not be achieved at today's rate of improvement in aircraft noise reduction.

With the reduction in engine noise, one of the most dominant sources of aircraft noise has become the airframe (known as 'aerodynamic noise'), especially during the approach (Guo et al. 2006) and landing phases of an aircraft's trajectory, when the engines are throttled back. Of the airframe, the landing gear generates noise at tonal frequencies where the human ear is most sensitive (Dobrzynski 2010) ($f \approx 1 - 2\,\mathrm{kHz}$). Figure 1.1 shows a sound map (or beamforming image) at the 1 kHz $1/3^{\mathrm{rd}}$ octave band highlighting the dominance of landing gear noise. Similarly, aerodynamic noise generated by high-speed rail pantographs has become the main technological barrier to increasing rail speed (Kurita et al. 2010). This is important as improvements in rail speed may eventually provide a cheap transportation alternative to aircraft.

The commonality between these two examples is that a *finite bluff-body* generates noise. A finite bluff-body is defined as one that terminates after a finite length, i.e., it

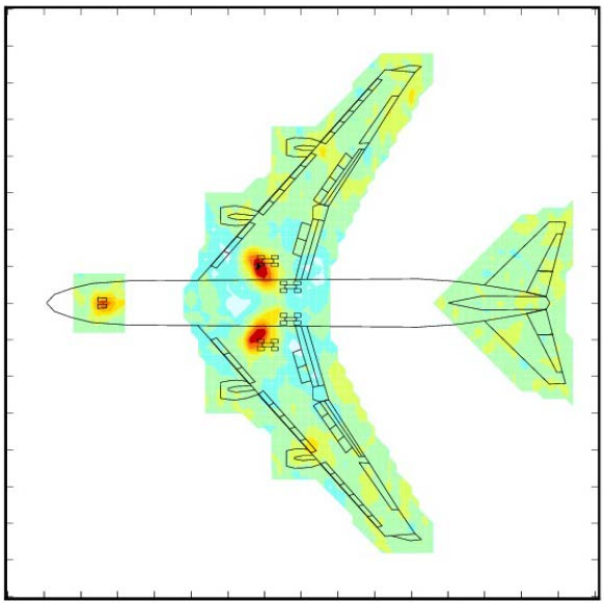

Figure 1.1: A beamforming image of the 1 kHz $1/3^{\text{rd}}$ octave band of an aircraft during approach with its landing gear deployed, reprinted from Siller et al. (2010).

is 'three-dimensional'. In fact, there are several other examples where finite bluff-body aerodynamic noise is a major source of community noise. These include computer cooling systems, car radio antenna, and car side mirrors. Traditional approaches of investigating bluff-body noise, such as those by Schlinker and Fink (1976), Gerrard (1955), Ali et al. (2011), and Iglesias et al. (2016) have concentrated on infinitely long, 'two-dimensional' cylinders, which do not account for this three-dimensionality. According to Moreau et al. (2014), finite length three-dimensionality can significantly augment the noise characteristics of a bluff-body compared with their two-dimensional counterparts. In fact, aeroacoustic studies that account for finite length three-dimensionality are rare, despite the fact that most real-world applications use finite length bluff-bodies. As such, a greater understanding of the noise generated by finite bluff-bodies is required and is crucial to mitigating real-world bluff-body noise.

Finite bluff-body aerodynamic noise is actually a subset of the larger problem of finite bluff-body flow. Finite bluff-body flow is of interest in many facets of engineering including the flow around chimney stacks, wind turbine masts, commercial buildings, heat exchangers, bridge piers and mountains. However, similar to finite bluff-body noise, finite bluff-body flow is not completely understood. Therefore, understanding the flow-induced noise mechanisms of finite bluff-bodies will also lead to improvements in other branches of engineering including wind and civil engineering.

To facilitate a basic understanding of finite bluff-body flow, there is first a requirement to understand the flow around a foundational example of a finite body with which the dynamics of more complicated geometries may be compared. The finite wall-mounted cylinder (FWMC) is a perfect candidate.

An FWMC is shown in Figure 1.2. The cylinder has one end that terminates in the Figure (referred to as the 'free-end') and the other end fixed to a flat surface (referred to as the cylinder-wall 'junction' , 'plate', 'wall', 'surface' or 'ground plate') so that it is immersed in a boundary layer of height δ, that is fully developed when it reaches the

cylinder. The cylinder is geometrically characterised by its span, L, and its diameter D (or width, W, when referring to a cylinder of square cross-section).

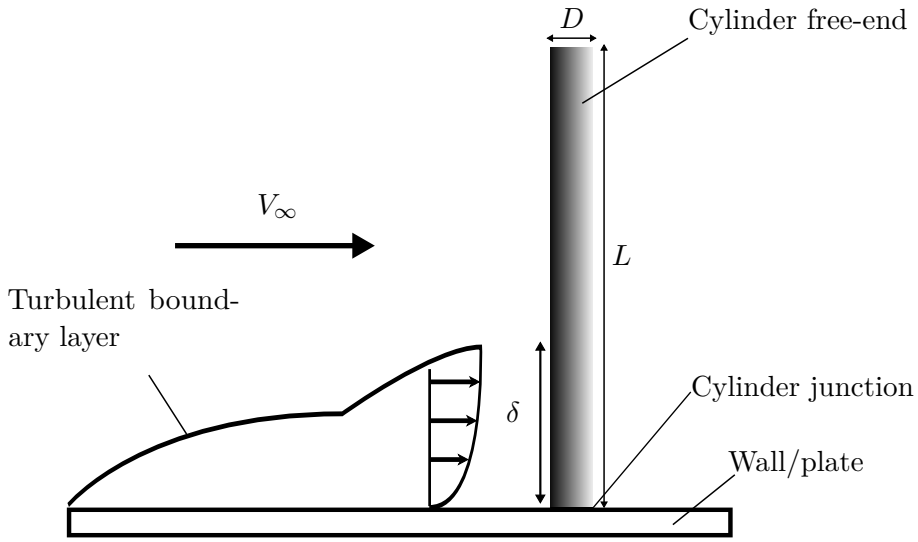

Figure 1.2: An FWMC mounted to a flat plate with a diameter, D and span, L subject to a flow with free-stream velocity, V_∞ and an incoming boundary layer with height δ.

The geometric simplicity of the FWMC allows the effects of the free-end and junction to be relatively isolated. Flow at the mid-span of the cylinder should be nominally two-dimensional if sufficiently far from the free-end and junction. Two-dimensional unsteady flow around cylinders has been studied for over 130 years and is reasonably well understood (e.g., Roshko (1993), Williamson (1996) and Norberg (2003)). Similarly, the tonal noise generated by this two-dimensional cylinder flow has been comprehensively studied (e.g., Curle (1955), Schlinker and Fink (1976), Casalino and Jacob (2003) and Brooks and Humphreys (2006)). Only flow around the junction and flow around the free-end will perturb the flow at the mid-span from its 'two-dimensional' state. This is not true for more complicated geometries such as real-life landing gear or pantographs, that contain additional features that can interact with the flow.

Furthermore, assuming *ceteris paribus* of the inflow conditions, the 'amount' of three-dimensionality can be controlled by changing only two parameters: the FWMC aspect ratio, L/W, or the wall boundary layer thickness, δ. By comparing the aeroacoustic noise characteristics of FWMCs with the known characteristics of a two-dimensional cylinder for a range of aspect ratios and boundary layer conditions, one can understand how three-dimensionality from the free-end and junction impact the wake dynamics of the FWMC and thus the flow-induced noise. Similar parameter sweeps for more complicated geometries may not be possible due to the large amount of parameters included.

This work presents a comprehensive study of the flow-induced noise produced by FWMCs. The focus will be on the influence of the aspect ratio and boundary layer thickness on the magnitude and spectral content of the flow-induced noise. The objective of the study is to examine the physical mechanisms by which aerodynamic sound is generated for this class of bodies. In doing so, further insight into the properties of the turbulent flow in the wake of the cylinder will be gained.

1.1 Thesis aims and objectives

The overall aim of this research is to develop a comprehensive understanding of the flow-induced noise characteristics and mechanisms of a square FWMC. This includes an understanding of the role that a) aspect ratio and b) wall boundary layer thickness have on the wake dynamics and flow-induced noise of FMWCs.

The specific aims of this research are:

1. To characterise the various components of noise (tonal and broadband) from square FWMCs;
2. To determine how these components change with aspect ratio and boundary layer thickness;
3. To understand the dynamic flow structures responsible for tonal and broadband noise; and
4. To understand why these dynamic flow structures change with aspect ratio and boundary layer thickness.

The objectives of this research are:

1. To measure the tonal and broadband noise sources for FWMCs with a range of aspect ratios in different boundary layers;
2. Determine the flow patterns associated with FWMC wakes for different aspect ratios and boundary layers;
3. Measure the salient flow parameters around the FWMC for differing aspect ratios and boundary layers; and
4. Relate these patterns and features to the flow-induced noise.

1.2 Thesis overview

The aforementioned aims fill a well-defined gap in the literature that is based on a thorough evaluation of the current state of knowledge of the problem. This evaluation is provided in Chapter 2. The methodology used to achieve the research objectives is given in Chapter 3. Here the flow measurement techniques used in this study are described, including the principle of operation, calibration methods as well as quantifying the error associated with each method. This study utilises microphone array beamforming and makes novel contributions to the field. Consequently, Chapter 4 is dedicated towards phased microphone array measurements. In this chapter, the mathematics behind the beamforming methodology are developed, the specific array properties are defined and calibration and error analysis is performed.

Chapter 5 describes measurements of the flow-induced noise characteristics of square FWMCs in a thin boundary layer while parametrically changing the aspect ratio. Chapter 5 then relates the measured noise to the wake flow-dynamics using hot-wire wake measurements, oil-flow surface visualisations and surface pressure measurements. In

Chapter 6, the impact of thickening the boundary layer on aerodynamic noise production is investigated. These findings are again related back to the wake dynamics using hot-wire anemometry.

The dissertation is concluded in Chapter 7 with a synopsis of the major contributions of the work as well as recommendations for future experimental direction.

1.3 Publications arising from this thesis

Sections of the work presented in this thesis have been previously published. The work in Chapter 2 led to the publication

- **Porteous, R., Moreau, D. J., and Doolan, C. J. (2014a). "A review of flow-induced noise from finite wall-mounted cylinders". In: *Journal of Fluids and Structures* 51, pp. 240–254. DOI:** 10.1016/j.jfluidstructs.2014.08.012,

and the work presented in Chapter 4 and Appendix C resulted in the publication

- **Porteous, R., Prime, Z., Valeau, V., Doolan, C., and Moreau, D. (2015). "Three-dimensional beamforming of dipolar aeroacoustic sources". In: *Journal of Sound and Vibration* 355, pp. 117–134. DOI:** 10.1016/j.jsv.2015.06.030.

Additionally, portions of Chapter 5 have been published in the following conference article

- **Porteous, R., Moreau, D., Doolan, C., and Prime, Z. (2014b). "The flow-induced noise of square finite wall-mounted cylinders in different boundary layers." In: *Proceedings of INTERNOISE, November 16-19, 2014, Melbourne, Australia*.**

The oil-film visualisation technique developed in Chapter 3 was used in the following publication

- **Moreau, D. J., Prime, Z., Porteous, R., Doolan, C. J., and Valeau, V. (2014). "Flow-induced noise of a wall-mounted finite airfoil at low-to-moderate Reynolds number". In: *Journal of Sound and Vibration* 333, pp. 6924–6941. DOI:** 10.1016/j.jsv.2014.08.005.

Chapter 2

Literature review

2.1 Introduction

Most research on the flow-induced noise of FWMCs has focused on the flow aspects of the problem. Recently there have been a few studies which have characterised various aspects of the noise produced by FMWCs (Becker et al. 2008; Moreau and Doolan 2013). However, there has been little effort to relate the flow dynamics around the cylinder to the acoustics and consequently the aeroacoustic mechanisms responsible for noise generation remain unclear.

Research into the flow dynamics of FWMCs has been disjointed. Differing experimental conditions between studies, which span over 30 years, make direct comparisons of results difficult. As such, questions still remain about the nature of the flow around an FWMC. For example, the effect of the relative height of the incoming boundary layer, that is the ratio δ/L, on the vortex shedding characteristics is still unresolved. This question makes it difficult to understand the relationship between the flow dynamics and the flow-induced noise.

The chapter will first briefly outline the flow behind and flow-induced noise generated by infinitely long cylinders, a topic that has been studied for over 130 years. Next, the flow features of the FWMC periodic wake are discussed. The chapter will finish with a review of studies that have focused on noise from FWMCs and conclude with several specific research questions on which the remainder of the thesis is based.

The discussions on FWMCs are restricted to incompressible (low Mach number) subsonic flows over square FWMCs with $(L/W) > 1$ (circular FWMCs are the topic of a supplementary discussion) at 0° angle of attack (the front face completely perpendicular to the flow). For FWMCs with L/D (or L/W)< 1, the reader is directed to the work of Hajimirzaie et al. (2012) and Mason and Morton (1987). Additionally, this discussion focuses mostly on experimental investigations, although some pioneering numerical studies (e.g., Krajnovic (2011)) have been included. For additional numerical studies on FWMCs, the reader is referred to Afgan et al. (2007), Palau-Salvador et al. (2010), Saha (2013), Uffinger et al. (2013), Javadi and Kinai (2014), Saeedi et al. (2014), Vinuesa et al. (2015) and Joubert et al. (2015).

2.2 Wakes and flow-induced noise generated by infinitely long cylinders

A cylinder that does not include a junction or free-end is known as an 'infinite' cylinder. It should be noted that the term 'infinite' is often incorrectly replaced with the term 'two-dimensional'. The two cases are subtly different and it is important to understand the distinction between them. A two-dimensional cylinder is what is realised in low Reynolds number experiments ($Re_W = \rho_\infty V_\infty W/\mu_\infty =< 190$ where ρ_∞ is the density of the free-stream, V_∞ is the velocity of the free-stream and μ_∞ is the dynamic viscosity of the free-stream), numerical simulations and theoretical analysis, where there is no spanwise variation in the wake dynamics. Conversely, for an infinitely long cylinder at Re_W>190, there will always be a degree of spanwise variation in the wake. This spanwise variation is also known as 'quasi three-dimensionality' and the degree of three-dimensionality is dependent on the Reynolds number of the flow. Both two-dimensional and infinitely long cases have been investigated from a flow and aeroacoustic perspective. The key concepts of such flows are briefly reviewed below.

For truly two-dimensional cylinders, the wake dynamics are dominated by the periodic wake instability known as von Kármán vortex shedding. Gerrard (1966) describes this flow phenomena as when the vorticity in the separated shear layer on one side of the cylinder accumulates ('rolls up') some distance behind cylinder trailing face (referred to as 'base'). This action draws in the shear layer from the opposite side which eventually restricts vorticity accumulation. The final vorticity concentration is subsequently shed and convected downstream and the process is continued on the opposite side of the cylinder. The process is illustrated in Figure 2.1.

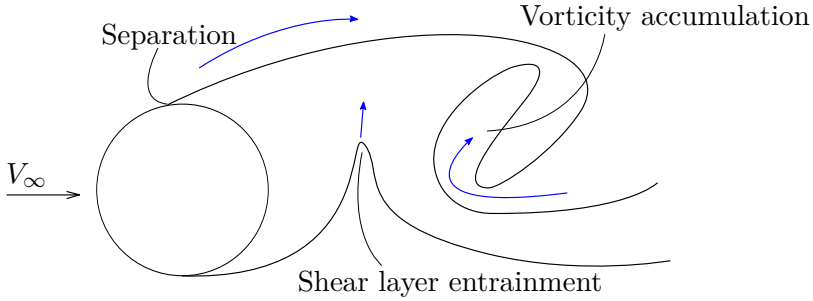

Figure 2.1: An illustration of the vortex formation mechanics behind a circular cylinder, adapted from Gerrard (1966).

Roshko (1954) found that the frequency of vortex shedding varies with the Reynolds number (based on cylinder diameter) of the flow. The frequency, f_s, is often represented in non-dimensional form by the Strouhal number based on cylinder diameter, $St = f_s D/V_\infty$ where V_∞ is the free-stream velocity.

Along with the Strouhal number of vortex shedding, other aerodynamic parameters in the cylinder wake also vary with Reynolds number. These wake parameters include the vortex formation length, L_f, the wake Reynolds stress, $\tau = \rho\overline{u'v'}$ and the sectional drag coefficient, C_d. Williamson (1996) discusses that the variations of these parameters are completely driven by variations in the cylinder base suction, P_{base} (again note that cylinder 'base' refers to the cylinder trailing face and not the cylinder-wall interface as in an FWMC) that, in turn, also varies with Reynolds number.

To understand the relationship between these wake parameters and cylinder base pressure, Roshko (1993) modelled the mean wake behind a cylinder (without vortex shedding) as a region of zero velocity ($V = 0$) fluid with an infinitesimally thin shear layer separating it with the free-stream. Such a model is shown in Figure 2.2. By considering that Reynolds stress (τ), free-stream pressure (P_∞) and cylinder base pressure (P_{base}) all act on the shear layer and balance to equilibrium, Roshko (1993) derived a relationship between the three parameters as

$$\frac{L_f}{D} = \frac{1}{4}\beta\frac{\overline{u'v'}}{V_\infty^2} \tag{2.1}$$

where $\beta = -C_{pb} = -P_{base}/1/2\rho V_\infty^2$. Roshko (1993) also used a 'free-streamline' model based on potential flow methods (for example see Vallentine (1967)) to relate the formation length and base pressure as

$$-C_{pb} \approx \frac{9}{2}\left(\frac{L_f}{D}\right)^{-5/3} \tag{2.2}$$

Therefore, according to Roshko's method, as base suction increases (base pressure reduces), vortex formation length reduces, two-dimensional wake Reynolds stress increase and sectional drag increases. Strictly speaking, the analysis of Roshko (1993) is only applicable for the case of a static cylinder wake with no vortex shedding. However, even with vortex shedding present, the relationships derived above have still been observed experimentally (Williamson 1996) over a wide range of Reynolds number extending from $Re_D = 10^3$ to $Re_D = 2 \times 10^5$ and can even be used to explain the observed variation in vortex shedding frequency with Reynolds number. As base pressure increases, the vortex formation length increases. This increase in vortex formation length effectively inflates the time scale over which a single vortex is formed (Ali et al. 2011), reducing the vortex shedding frequency. However, as base pressure increase, the opposite process occurs and vortex shedding frequency increases.

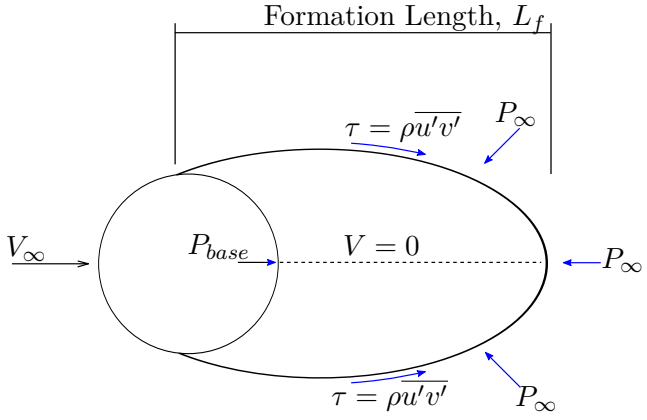

Figure 2.2: A time averaged representation of the fluctuating wake, adapted from Roshko (1993).

The previous discussion concentrated on the dynamics of a completely two-dimensional cylinder wake. Quasi three-dimensional effects start as the Reynolds number (based on cylinder diameter) increases above 190 (Roshko 1993). From $190 < Re_D \leq 260$, the initially straight vortices experience large scale spanwise deformation into a series of vortex loops (known as Mode A shedding). Between $260 < Re_D \leq 10^3$ finer scale oscillations

(Mode B shedding) are introduced into the wake (see Williamson (1996) and Bailey et al. (2002) for a discussion of Mode A and Mode B shedding). For higher Reynolds numbers between $10^3 < Re_D \leq 2 \times 10^5$ (known as the 'shear layer transition regime'), which is the Reynolds number range for most practical applications, the main three-dimensional feature is an aperiodic 'bursting' of the fluctuating lift and drag (Roshko 1993) caused by large scale 'vortex dislocations' occurring sporadically over the span of the cylinder. Prasad and Williamson (1997) suggest that this is a result of an oblique vortex shedding mode. For even higher Reynolds numbers, the boundary layer developing on the side of the cylinder transitions to turbulence before separating. This results in a reduced base pressure, a reduced wake width and a fluctuating signal at $St = 0.4$, although it is unclear whether this signal is related to the roll up of conventional von Kármán vortices (Roshko 1993).

Three-dimensionality is often represented mathematically in aerodynamic or aeroacousitc analysis by the spanwise correlation length (Norberg 2003). This is essentially an average spanwise length over which a vortex filament is assumed to shed with the same phase (Blake 1986). Two-point wake velocity measurements or surface pressure measurements made along the span, where the measurement positions are at a spanwise distance that is greater than the correlation length, will show reduced coherence. With this interpretation of vortex shedding, vortices are shed in small spanwise packets, the phase of which varies stochastically in time and space. Such an interpretation is quite appropriate for cylinder flows with $Re_D > 10^3$ as can be seen from the smoke flow visualisations by Williamson (1996). Stochastic phase variations can also model the bursting phenomenon described previously for $Re_D > 10^3$. This is due to the statistical equivalence of a harmonic signal with either random phase or random amplitude variations (Casalino and Jacob 2003).

It has been argued that stochastic phase variations can account for other types of three-dimensionality (Casalino and Jacob 2003) which may include oblique shedding, chevron patterns, vortex dislocations and phase shocks, since these phenomena all result in spanwise phase and amplitude variations. In fact, these phenomena have all been linked to the same phenomenological process (Prasad and Williamson 1997), so it seems natural that they may be described by the same statistical technique. On the other hand, some types of three-dimensional vortex shedding cannot be completely described by the stochastic phase method. For example, *cellular* shedding is a phenomena where the frequency of vortex shedding varies in a step-wise manner across the cylinder span. Oblique shedding, vortex dislocations and severe amplitude modulation at points near the cell boundaries may be observed (Szepessy and Bearman 1992). Although the phase variation method may account for the variations of amplitude and phase observed within each cell, it will not account for the stepwise differences in vortex shedding frequency. To model this, further information relating the period of instability at the cell boundary to the aerodynamics are required. The phenomenon of cellular shedding is discussed later in Section 2.5.

Regardless of their spanwise behaviour, periodic von Kármán vortices induce a fluctuating pressure on the surface of the cylinder, causing tonal noise to be generated at the vortex shedding frequency, known as an 'Aeolian' tone. Phillips (1956) applied Curle's theory (Curle 1955) to flow over an infinite circular cylinder to predict the Aeolian tone

level generated by von Kármán vortex shedding. In his formulation, the contribution of the noise from the quadrupole wake sources was neglected. This assumption is valid for subsonic low Mach number flows since the ratio of quadrupole to dipole sound pressure level scales with the square of the Mach number (Blake 1986). As such, this assumption has been widely adopted in many experimental (Keefe 1961; Amiet 1975; Schlinker and Fink 1976; Hutcheson and Brooks 2006; Fujita 2010; Leclercq and Doolan 2009; Oguma et al. 2013; Iglesias et al. 2016) and numerical (Cox 1998; Casalino and Jacob 2003; Cheong et al. 2008; Doolan 2010; Ali et al. 2011; Ali et al. 2013) investigations on Aeolian tone generation with a high degree of consistency between experimental, numerical and theoretical values. For these flow-induced noise studies, three-dimensionality in the wake is generally accounted for using the spanwise correlation length technique because it is easily incorporated into the derivation of Phillip's equation (Phillips 1956) directly from the statistical treatment of Lighthill's equation (Lighthill 1952).

A common feature amongst experimental studies on flow-induced noise of infinitely long cylinders is spectral broadening of the acoustic peak at the Aeolian tone shedding frequency. Casalino and Jacob (2003) showed that the amplitude modulation of the vortex shedding signal due to the inherent quasi three-dimensionality of vortex shedding directly contributes to this spectral broadening. Ross et al. (2008) showed that Aeolian tone spectral broadening could also be caused by severe frequency modulation induced by a variable approach speed in, for example, highly turbulent approach flows. It was also hypothesised by Ross et al. (2008) that cylinder broadband noise (noise at frequencies above the vortex shedding frequency) could be increased via unsteady lift generated by a gust component of velocity, in a similar manner to an aerofoil reacting to ingested turbulence. This hypothesis was tested by Ross et al. (2008) and the mechanism was not found to contribute significantly to the flow-induced sound. It must be said, however, that there have been very few studies concentrating on the broadband sound generated by infinite cylinders.

2.3 The general features of the FWMC wake

The flow around an FWMC (be it square or circular in cross-section) is more complex than that of its two-dimensional counterpart. The general mean flow structure around a generic (in this case circular) FWMC is shown in Figure 2.3 and consists of four different mean vortex systems (Lee 1997; Heseltine 2003; Wang et al. 2004; Bourgeois et al. 2011); a free-end vortex system, a spanwise von Kármán vortex system (similar to that found in an infinite cylinder wake), a junction vortex system and a horseshoe vortex system.

The free-end region is characterised by separated flow that penetrates into the wake (known as 'downwash'). This culminates in complicated three-dimensional flow structures near the free-end trailing edge. Generally, the mean flow pattern in this region is characterised by a pair of streamwise counter-rotating vortices which induce downwash into the wake. The junction vortex system also often feature a pair of counter-rotating vortices, opposite in rotation to the free-end vortices, that induce upwash into the near wake. The junction and free-end vortices interact with the mid-span von Kármán vortex system to partially or completely alter the flow field around the body. The last vortex system is the horseshoe vortex, which is generated by the separation and roll-up of

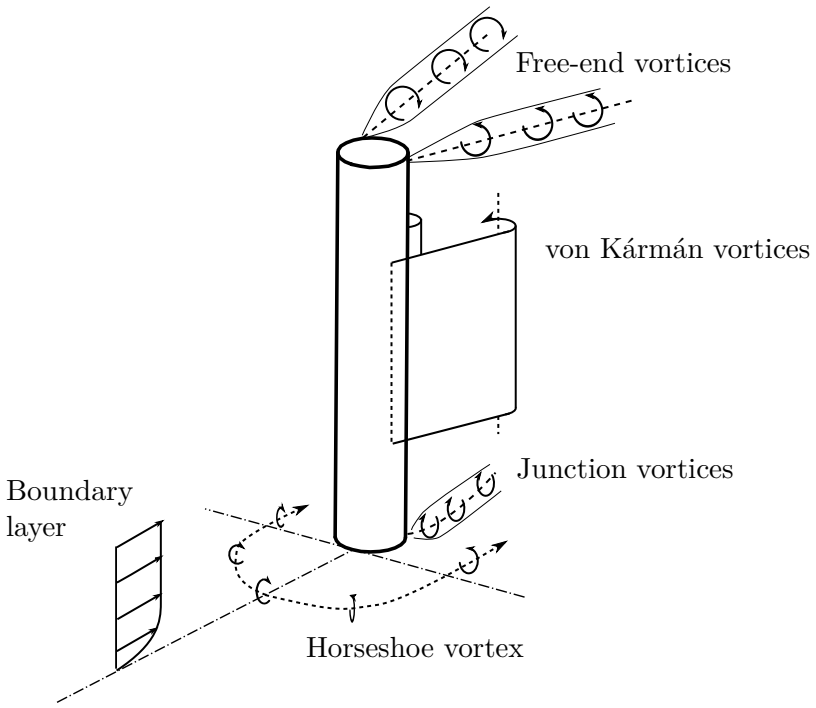

Figure 2.3: The near wake flow features present around an FWMC, adapted from Heseltine (2003). They consist of free-end vortices near the free-end, von Kármán vortices at the mid-span, junction vortices at the junction and a horseshoe vortex at the front of the cylinder that wraps around the cylinder to form a U-shape.

boundary layer vorticity in front of the cylinder. This vorticity is diverted around the cylinder to form a U-shaped vortex due to cross-stream velocity gradients induced by the presence of the cylinder (Baker 1980). For turbulent boundary layers, the horseshoe vortex exhibits bimodal switching behaviour; the vortex system will switch between a 'backflow mode', where the horseshoe vortex sits upstream up the cylinder, and a 'zeroflow mode', where the horseshoe vortex core is situated close to the leading edge (Moreau et al. 2014). The switching from one state to another is aperiodic with the probability density function assumed to be Markovian in nature and has no relationship with the frequency of von Kármán vortex shedding in the wake (Simpson 2001). Because of this, it has been proposed that the influence of the horseshoe vortex on the near wake structure is considerably milder than the influence of the other vortex systems (Bourgeois et al. 2011; Uffinger et al. 2013). Recently it has been found by El Hassan et al. (2015) that the backflow mode of the horseshoe vortex has an indirect contribution to the mechanisms of streamwise vorticity generation at the junction.

The general flow structure around an FWMC will be altered by the geometry of the FWMC relative to the impinging flow. Aspect ratio, defined as the ratio of the span, L, to the width, W (or diameter, D), is the main geometric characteristic which influences the flow round the FWMC. For example, a cylinder of lower aspect ratio ($L/W \leq 3$) may experience no mid-span vortex shedding, with the effect of downwash over the free-end extending towards the base. The height of the impinging boundary layer relative to the length of the cylinder also has an important influence on the flow structure (Sumner et al. 2015). For example, unlike the free-end vortices, the presence of the junction vortices are not always measured and seem to be intricately related to the boundary layer thickness

(Hosseini et al. 2013; Bourgeois et al. 2011; Krajnovic 2011). Both Wang et al. (2006) and Porteous et al. (2014c) found that boundary layer thickness can impact the fluctuating statistics of the wake well beyond the height of the boundary layer for both square and circular geometries, respectively. Furthermore, Bourgeois et al. (2011) has stated that the boundary layer thickness has a greater influence on the general flow structure than the Reynolds number and the turbulence intensity of the flow.

Experimental flow studies that have investigated how geometric and flow parameters affect the general flow structure of square and circular FWMCs are summarised in Table 1. The studies are ordered chronologically and show the variation in aspect ratio, L/W (or L/D), Reynolds number (Re either based on diameter or width) and relative boundary layer height δ/D (or δ/W) that were investigated in each study. From Table 1, it can be seen that, although a large amount of data exist, studies that systematically vary parameters other than aspect ratio are rare. For example, only one study (Sakamoto and Arie 1983) has investigated the impact of varying the relative height of the incoming boundary layer on the flow over circular FWMCs. This is despite the fact that the boundary layer had been identified as a primary flow parameter than governs the structure of the near wake as early as 1984 (Kawamura et al. 1984).

Table 1 also indicates that within the last 10 years, focus has shifted towards the study of square FMWCs. In fact, although fewer studies have been conducted on square FWMCs, the recent surge of detailed experimental work by Wang et al. (2004) and (2006), Bourgeois et al. (2011), Sattari et al. (2012), Hosseini et al. (2013), and El Hassan et al. (2015) using phase averaged Particle Image Velocimetry (PIV) and Proper Orthogonal Decomposition (POD) have all resulted in a relatively congruent interpretation of the flow structure in the near wake and downstream of the body. As a result, there is a generally consistent understanding of the periodic near wake flow structure of square FWMCs, which is summerised below.

2.4 Square FWMCs

The ideas presented in the landmark studies of Wang and Zhou (2009), Bourgeois et al. (2011) and Hosseini et al. (2013) have set a precedent in the current understanding of the dynamics of the large scale coherent structures in the wake of square FWMCs for $L/W \leq 8$. For cylinders of sufficiently high aspect ratio ($L/W > 4$), the wake will take the form of an 'alternatively shed full-loop structure'. For low aspect ratio cylinders ($L/W \leq 4$), the wake will take a 'half-loop shedding' structure. The boundary layer thickness, δ, however, has been found to influence whether the wake is half-loop or full-loop, even for aspect ratios as high as 8.

2.4.1 High aspect ratio cylinders ($L/W > 4$)

In the literature, 'high aspect ratio' refers to cylinders with aspect ratios greater than about 4. The full-loop shedding structure of high aspect ratio cylinders was postulated by Bourgeois et al. (2011) and Hosseini et al. (2013). However, Wang and Zhou (2009) were first to describe the wake structure in terms of the deformation of vortex filaments near the free-end and junction for a square FWMC and because of this, the full-loop shedding model will be herein known as the 'Wang model'. In the Wang model, the free-steam

Table 2.1: Summary of previous methods and conditions for experimental studies on square and circular FWMCs.

	Quantitative Flow Measurements						Flow Visualisation				Acoustic Data		Geometric Parameters			Flow Parameters	
Author(s)	P[i]	HW[ii]	FP/FC[iii]	7PP/CP[iv]	LDA[v]	PIV[vi]	WD[vii]	OF[viii]	S[ix]	WP[x]	SM[xi]	MA[xii]	Sq.[xiii]	Circ.[xiv]	AR[xv]	Re($\times 10^4$)[xvi]	δ/D[xvii]
Baker (1980)	✓							✓	✓					✓	4.75		Not given
Farivar (1981)	✓	✓	✓											✓	2.78 → 15	7	Not given
Ayoub and Karamcheti (1982)	✓	✓												✓	12	8.5 → 77	N/A
Gerich and Eckelmann (1982)		✓												✓	N/A	N/A	N/A
Sakamoto and Arie (1983)		✓											✓	✓	1 → 8	N/A	
Kawamura et al. (1984)	✓	✓						✓	✓					✓	1 → 8	3.2	0 → 1
Sakamoto and Oiwake (1984)	✓	✓	✓										✓	✓	1 → 6		
Uematsu et al. (1990)	✓	✓						✓						✓	1 → 4	4 → 15	Not given
Budair et al. (1991)		✓												✓	37		
Baban and So (1991)	✓	✓	✓											✓	1 → 2	4.6	0.2
Okamoto and Sunabashiri (1992)	✓	✓					✓	✓						✓	0.5 → 7	2.5 → 4.7	Not given
Agui and Andreopoulos (1992)	✓							✓	✓					✓	2	10, 22	0.09
Szepessy and Bearman (1992)	✓	✓												✓	0.25 → 12	8 → 15	N/A
Fox and West (1993a)(1993b)	✓	✓	✓					✓						✓	4 → 30	4.4	Not given
Fox and Apelt (1993)	✓		✓											✓	4 → 30	4.4	Not given
Uematsu and Yamada (1994)	✓													✓	1 → 4	3.8→140	N/A
Lee (1997)														✓	N/A	N/A	N/A
Park and Lee (2000)	✓	✓								✓				✓	6	2	6
Park and Lee (2002)	✓	✓								✓				✓	6	2	6
Becker et al. (2002)					✓			✓	✓				✓		N/A		
Roh and Park (2003)								✓	✓					✓	1.25, 4.25	0.6, 15	0
Sumner et al. (2004)		✓	✓	✓										✓	3 → 9	6	
Wang et al. (2004)		✓				✓							✓		3 → 7		
Pattenden et al. (2005)	✓					✓		✓						✓	1	20	0.1
Wang et al. (2006)					✓	✓							✓		3 → 7	1.2	0.5 → 2
Sahin et al. (2007)						✓								✓	N/A	N/A	N/A
Hain et al. (2008)						✓								✓	2.2	10	0.25
Becker et al. (2008)	✓	✓			✓				✓		✓		✓		6	N/A	N/A
King and Pfizenmaier (2009)											✓		✓	✓	2 → 35 (c) 16.7,25 (s)	N/A	N/A
Wang and Zhou (2009)		✓			✓	✓	✓						✓		3 → 11	0.93	1.35
Bourgeois et al. (2011)	✓					✓							✓		4	1.2	0.72
Hajimirzaie et al. (2012)					✓	✓							✓		0.7,0.9	20,26	0.125, 0.1
Sattari et al. (2012)	✓	✓				✓							✓		4	1.2	0.72
Moreau and Doolan (2013)		✓									✓		✓	✓	1.6→ 22.6(c) 1→14(s)	1→1.4(c), 1.6 → 2.4	1.6
Rostamy et al. (2013)						✓							✓	✓	3 → 9	4.2	1.6
Uffinger et al. (2013)					✓				✓				✓		4	1.3	0.1
Hosseini et al. (2013)	✓					✓							✓		8	1.2	0.72, 2.56
Wang et al. (2014)						✓							✓		7	0.93	1.35
El Hassan et al. (2015)	✓					✓		✓					✓		6	1.2	0.72, 2.56
Sumner et al. (2015)						✓								✓	3 → 9	4.2	1.7
Ogunremi and Sumner (2015)		✓	✓	✓	✓								✓		3 → 9	7.4	1.5

[i] P=Pressure tap [ii] HW=Hot-wire [iii] FP/FC=Force plate/cell [iv] 7PP/CP=7 point hole pressure probe or Cobra probe [v] LDA=Laser Doppler Anemometry [vi] PIV=Particle Image Velocimetry [vii] WD=Water-Dye method [viii] OF=Oil-film method [ix] S=Smoke method [x] WP=Water Particle method [xi] SM=Single microphone [xii] MA=Microphone array [xiii] Sq.=Square cross-section [xiv] Circ.=Circular cross-section [xv] AR=Aspect ratio [xvi] Re=Reynolds number [xvii] δ/D=Boundary layer height to diameter (or width) ratio

impinges on the upsteam surface of the cylinder and is redirected either around the side or over the free-end where it separates at the sharp leading edge. Flow around the cylinder sides enters into a regular alternating von Kármán vortex street. The pressure difference between the lee-side and the free-stream induces downwash into the wake. The PIV results of Rostamy et al. (2013) show that the separated shear layer does not reattach over the top of the cylinder due to the high degree of bluffness of the square profile. The vorticity generated by the separated free-shear feeds a nascent vortex filament that penetrates through the plane of symmetry and connects the spanwise vortex filament from one side of the cylinder to the opposing side as the vortices are shed. This filament is commonly referred to as a cross stream 'connector strand'.

Under the action of Biot-Savart induction, the spanwise vortex filament is 'bent' upstream. This can be visualised as a spanwise phase lag in two-point hot-wire measurements made across the span of the cylinder (Kawamura et al. 1984; Hosseini et al. 2013). The same behaviour is also found near the junction of the cylinder. It was assumed by Wang and Zhou (2009) and Bourgeois (2012) that the velocity gradient in the boundary layer causes the streamwise rotation of the vortex filaments near the junction. Recently, El Hassan et al. (2015) has suggested that this rotation is actually caused by the interaction of the legs of the turbulent horseshoe vortex with the lower portion of the spanwise vortex filament (discussed in Section 2.4.4). Regardless of the mechanism, the resulting structure is such that the now deformed, initially vertical, vortex filaments project a system of four counter rotating vortices in the cross-steam plane, known as a quadrupole distribution. An illustration of full-loop shedding that gives rise to a quadrupole wake distribution is given in Figure 2.4. The projection at the base of the cylinder are known as junction vortices and the projection at the free-end are known as the free-end vortices. Downstream, the strength (total wake circulation) of the junction vortices decays significantly under viscous action. It has also been found that the cross-stream connector strands significantly increase the magnitude of total fluctuating kinetic energy (both coherent and unresolved components of the phase average) near the free-end and the junction regions.

The most important finding made in the Wang model is that the free-end, junction and mid-span vortices are one of the same coherent structure. Prior to the study of Wang and Zhou (2009), it was assumed that these vortex components were generated separately (Wang et al. 2004; Lee 1997; Kawamura et al. 1984), although Sumner et al. (2004) had previously suggested that junction vortices were due to inclined von Kármán vortices on circular cylinders. Dye flow visualisation from Wang and Zhou (2009) corroborates the structure from each portion of the cylinder are the same entity, at least for cylinders $L/W < 8$, which is the aspect ratio range over which the studies were performed. It should be noted that the independence of free-end and junction vortices may still be true for cross-sections other than square. In fact, for circular cylinders there is compelling evidence that the free-end vortex pair is topologically separated from the other vortex structures. Circular cylinders are discussed in Section 2.5.

2.4.2 Aspect ratio effects

The effect of aspect ratio on the flow structure around the square FWMC has been investigated by Sakamoto and Arie (1983), Wang et al. (2004) and Wang and Zhou

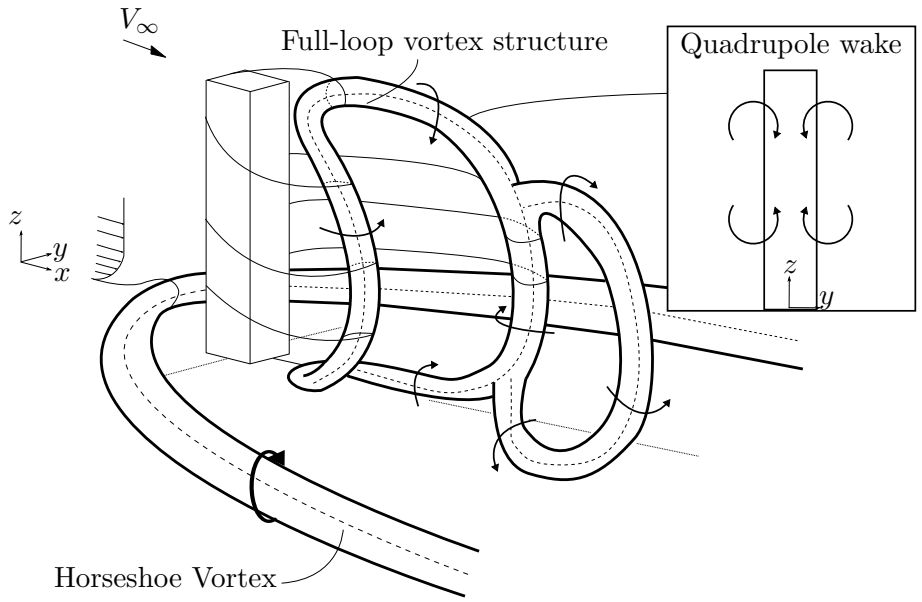

Figure 2.4: Illustration of the development of a full-loop shedding structure in the wake of a square FWMC, adapted from Bourgeois et al. (2011).

(2009), although these studies predate current understanding of the wake structure. Sakamoto and Arie (1983) have shown that the vortex shedding frequency is reduced below that of the two-dimensional case as the aspect ratio is lowered. For example, the vortex shedding frequency of the two-dimensional case was measured as $St = 0.13$ (Lyn et al. 1995), while Bourgeois et al. (2011) measured the dominant Strouhal number as $St = 0.1$ for an $L/W = 4$ square FWMC. This is attributed to the large influence that downwash has across the entire cylinder span at lower aspect ratio. According to Moreau and Doolan (2013), the downwash flow elongates the vortex formation region, lowering the vortex shedding frequency. This mechanism seems plausible. In a recent study by Wang et al. (2014), a positive correlation between downwash from the free-end and recirculation length in the mid-span of the cylinder for an $L/W = 6$ square FWMC was demonstrated. Furthermore, this inverse relationship between vortex formation length and vortex shedding frequency (i.e., as the formation length increases the vortex shedding frequency reduces) in the wake of circular cylinders has been observed and studied for over 50 years (see Roshko (1954), Blake (1986) or Williamson (1996) for detailed summaries). Ali et al. (2013) puts forth that the increase in formation length increases the time scale over which the vortex rolls up and subsequently reduces the period of oscillation in the wake.

As the aspect ratio is lowered from a high aspect ratio ($L/W = 8$), a 'critical aspect ratio' is encountered, as noted by several authors (Wang et al. 2004; Moreau et al. 2014; Sattari et al. 2012). The critical aspect ratio is usually described as when the downwash from the free-end dominates the near wake. While this is a vague description of critical aspect ratio, Bourgeois et al. (2011) provides a more robust definition. In this study, the critical aspect ratio is encountered when the wake changes from a quadrupole distribution to a dipole distribution. A dipole wake structure is illustrated in Figure 2.5. In a dipole wake, only a single pair of counter rotating vortices inducing downwash exists in the wake and the wake changes to a 'half-loop shedding structure'. This is where columnar vortices,

that are shed parallel to the span of the cylinder near the base, are connected across the wake through vorticity generated by the separation and roll up of the free-shear layer at the free-end (in a similar manner to the quadrupole wake). The inductive effect of the cross stream vorticity acts to deform the structure in such a manner as to project two sets of counter rotating vortices near the free-end. The difference to the Wang model is that no such deformation occurs near the junction and hence no 'junction vortices' are formed. Instead the vorticity in the spanwise vortex filaments is proposed to interact with the very near wall vorticity field. Another pertinent difference between half-loop shedding and full-loop shedding is that the legs of the half loop penetrate deep into the wall layer, while the legs of the full loop vortex reconnect to the anteceding structure on the opposite side. This causes a loss of strong spectral periodicity in velocity fluctuations at the junction region in quadrupole wakes (Hosseini et al. 2013).

When half-loop shedding occurs, the deformation of the structures near the free-end tends to dominate the flow. Two-dimensional-like shedding is not observed up to half a span length away from the free-end. Wang et al. (2004) also show that below the critical aspect ratio (during half-loop shedding) the downwash dominated wake tends to increase random turbulence and broaden the spectral peak of the vortex shedding signal measured in the wake. It should be noted that below the critical aspect ratio, for square FWMCs, a spectral peak in the velocity wake signal is always present. Only for very short aspect ratios ($L/W < 1$) does the sharp peak disappear and vortex shedding is said to be suppressed.

2.4.3 Symmetric shedding

It has been proposed by Sakamoto and Arie (1983) that for $L/W \leq 2.5$ alternating von Kármán vortices cease to exist and are instead replaced with less coherent symmetric vortices, which shed, as their name suggests, simultaneously from either side of the body. This conclusion was based on low Reynolds number smoke flow visualisation images of symmetrically arranged vortices in the near wake. Sakamoto and Arie (1983) also found that, for $L/W < 2.5$, a change in the slope of the shedding frequency with aspect ratio occurs. For $L/W > 2.5$, the shedding frequency decreases at approximately $(L/W)^{-0.84}$ while for $L/W < 2.5$, the frequency decreases more rapidly at $(L/W)^{-0.89}$.

The concept of symmetric shedding has enjoyed a substantial amount of popularity prior to the study of Bourgeois et al. (2011). As recently as 2009, Wang and Zhou (2009) argued that even for $L/W > 2.5$, although the shed structure is connected across the plane of symmetry, the different principle cores of the opposing columnar vortices are shed either 'anti-symmetrically' or 'symmetrically' based on a certain probability. The classification of symmetry was based on a geometric inspection of the relative location of vortex cores of select PIV images (i.e., the cores were in either a staggered arrangement or symmetrical about the centreline). The probability of symmetric shedding was found to be higher near the free-end of the cylinder, where three-dimensional effects occur. Here downwash was found to promote symmetric shedding. Near the junction, however, where three-dimensional affects are comparatively small, anti-symmetric shedding dominates. Presumably, for low enough aspect ratios (even lower than the critical aspect ratio, i.e., $L/W < 2.5$), downwash over the free-end dominates the entire wake promoting a purely

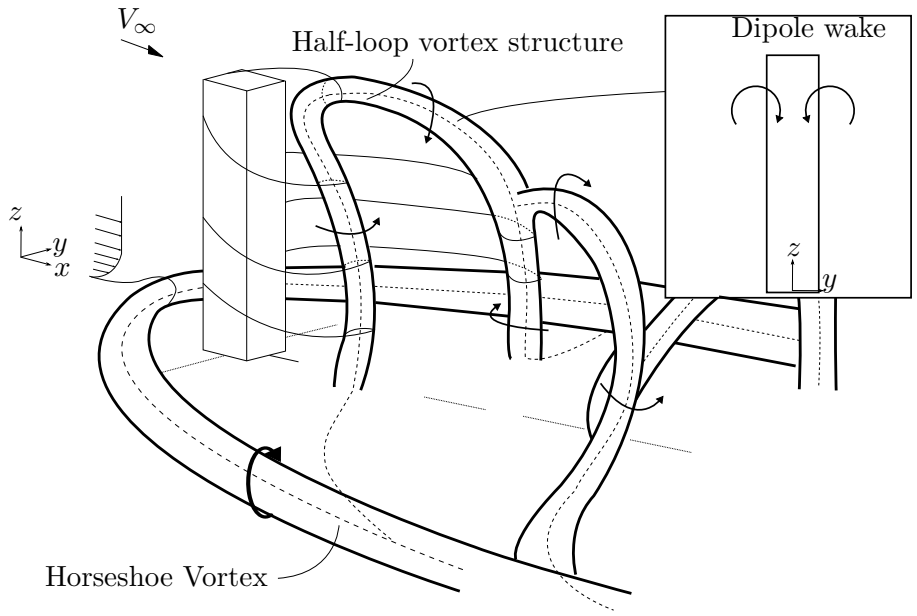

Figure 2.5: The dipole near wake flow features present around an FWMC, adapted from Hosseini et al. (2013).

symmetrically shed structure. This symmetrically shed structure has different vortex shedding characteristics to the anti-symmetric structure and thus corroborates the earlier finding of Sakamoto and Arie (1983).

Additionally, Wang and Zhou (2009) found that the two modes of shedding (symmetric or anti-symmetric) had vastly different vortex formation characteristics and therefore different sectional aerodynamic characteristics and effects on Reynolds stress production in the wake. In general, it was found that symmetric type shedding was associated with larger recirculation zones (in the mid-span), longer formation lengths, lower Reynolds stress and therefore 'weaker' vortex shedding when compared with anti-symmetric shedding. As a result, periods of symmetric shedding were found to reduce sectional drag and fluctuating lift coefficients near the mid-span of the cylinder, in accordance with Roshko's theory (Roshko 1954). It was hypothesised, however, that this relationship was not necessarily true at the extremities of the cylinder where the severe upwash and downwash create highly three-dimensional conditions for which Roshko's theory is invalid. This hypothesis was confirmed in a later study by Wang et al. (2014). Here, low dimensional reconstructions of the square FWMC wake employing Proper Orthonormal Decomposition (POD) showed that near the extremities of the cylinder, the length of the reverse flow region was related to the amount of downwash and upwash near the free-end and junction. In this case, higher downwash and upwash reduced the size of the recirculation zone and promoted symmetric shedding. At the same time, higher downwash from the free-end was correlated with an increase in reverse flow region near the mid-span of the cylinder. Downwash and upwash were also found to weaken the vortex shedding strength near the mid-span and the junction through the lateral stretching of vorticity of the anti-symmetric mode. Additionally, although not explicitly stated, the presented PIV snapshots clearly showed that a smaller reverse flow region near the free-end was associated with lower total wake circulation of the symmetric shedding mode.

On the other hand, Sattari et al. (2012) provides evidence, via simultaneous surface pressure phase analysis, that symmetrically shed vortices shed in an $L/W = 4$ square FWMC wake do not exist at high Reynolds numbers. Instead, shedding is always anti-symmetric (out of phase) but associated with either high amplitude surface pressure fluctuations (HAF) or low amplitude surface pressure fluctuations (LAF). LAF is associated with the existence of two co-existing counter rotating vortices that appear to be symmetrically arranged (but are still shed out of phase) while HAF is associated with a staggered vortex arrangement, akin to regular von Kármán vortex shedding. LAF instances were rare but increased in probability near the free-end. During LAF intervals, the wake was found to be relaxed, with lower vorticity production, higher amplitude modulation, and a longer recirculation region. These results corroborate the previous findings of Wang and Zhou (2009). It was also hypothesised that instances of LAF were consistent with a vortex dislocation and wake reorganisation mechanism, similar to that in a two-dimensional circular cylinder wake (Williamson 1996).

From the preceding discussion, the shedding behaviour in the wake of the FWMC shows a strong spanwise dependence. As in studies concerning the wake structure, there is general consistency between various authors about the behaviour of 'symmetric' and 'anti-symmetric' modes of shedding. It appears that the symmetric mode is the main feature of the FWMC three-dimensionality and seems to be enhanced by increasing levels of upwash and downwash. As such, this mode dominates the free-end and to a lesser extent the junction of the cylinder. Perhaps unsurprisingly, the symmetric mode is associated with weaker circulation, lower fluctuating pressure and lower wake Reynolds stress. Rather paradoxically however, it is also associated with smaller reverse flow regions, a wake feature generally found in strong vortex shedding zones. On the other hand, the anti-symmetric mode is present near the mid-span, but tends to be disrupted by the downwash and upwash in a more predictable manner (in accordance with Roshko's theory). Specifically, the downwash and upwash reduce the vortex circulation and consequently, because the mid-span shows more two-dimensional traits, the wake relaxes and the reverse flow regions increase. This discovery is perhaps more relevant to sound production than knowledge of the specific wake structure downstream of the cylinder (half-loop or full-loop). If the relative occurrence of symmetric vortex shedding in the mid-span is altered with changes in aspect ratio (and evidently it is based on the early results of Sakamoto and Arie (1983)) then total circulation production in the wake of the cylinder must also change. Based on Powell's theory of sound (Powell 1964), if the circulation magnitude changes, the magnitude of flow-induced sound production will also change.

2.4.4 Boundary layer effects

The effect of the relative height of the boundary layer to cylinder length has been investigated by Sakamoto and Oiwake (1984), Wang et al. (2006) and more recently by Bourgeois (2012), Hosseini et al. (2013) and El Hassan et al. (2015). Sakamoto and Arie (1983) found that increasing the boundary layer height suppresses vortex shedding at the mid-span of the cylinder. Wang et al. (2006) found that increasing the boundary layer increases the strength of the upwash flow in the plane of symmetry of the wake near the junction. This, in turn, has a profound effect well beyond the near wall region. The

increased upwash near the junction region was accompanied by decreased downwash near the free-end. Simultaneously, the probability of occurrence of anti-symmetric shedding (or HAF shedding) increases at locations near the free-end, while the junction region experiences decreased vorticity production and an increased probability of symmetric shedding (LAF shedding). This was observed by an increase in Reynolds stresses near the free-end and confirmed using a similar procedure to their 2009 study (Wang and Zhou 2009). From these results, it was reasoned that the boundary layer thickness enhances the strength of 'junction vortices' and reduced the strength of 'free-end vortices', making way for more two-dimensional shedding near the free-end.

Having understood that junction, free-end and spanwise vortices are the same component of a much larger coherent structure in the wake, Hosseini et al. (2013) rationalised the findings of Wang et al. (2006) to be caused by a streamwise rotation of the initially columnar vortices near the junction by the larger boundary layer. It is hypothesised by Bourgeois (2012) that δ/D must be greater than 1 for this rotation to occur, since the boundary layer must be of the order of magnitude of the spanwise vortex core to significantly interfere. However, the actual boundary layer thickness required to induce a quadrupole wake may be higher than this. Recently, Ogunremi and Sumner (2015) showed that the wake of a square FWMC with $L/W = 9$ with boundary layer thickness $\delta/W = 1.5$ was still dipole in nature.

With this understanding, a thicker boundary layer tends to cause the early transition from a dipole to a quadrupole wake. Bourgeois (2012) reasons that for low aspect ratios in thick boundary layers, the limitation of the vertical length-scale of the columnar vortices results in a dipole wake structure because a full-loop structure cannot 'fit' into the wake, and the number of possible vortex topologies are limited. When the aspect ratio increases, this restriction is released, and a full-loop structure is allowed to form. In contrast, a thinner boundary layer allows the FWMC to retain a dipole wake from low ($L/W = 4$) to high ($L/W = 9$) aspect ratios because there is no mechanism by which large scale streamwise deformation of the vortex structures occurs.

Having now a rotated vortex core, it stands to reason that upwash is induced in the plane of symmetry and increases with increasing streamwise rotation (or increasing boundary layer thickness). By extension the induced velocity caused by this rotated core diminishes the downwash near the free-end, even though the free-end may lie beyond the boundary layer height. Thus the mechanism of the apparent reduction in free-end vortex strength observed by Wang et al. (2006) is explained by the full-loop shedding model. What is also pertinent is that the length scale δ/W appears to be a more important parameter than δ/L for FWMCs with $L/W > 4$.

Additionally, the Reynolds stress distribution near the free-end changes with the increase in boundary layer height. Wang et al. (2006) explains that the reduced downwash from the free-end promotes anti-symmetric, or 'two-dimensional' like shedding that replaces what would otherwise be symmetric type shedding. Because the wake is more two-dimensional, downstream Reynolds stresses are higher, a result that is internally consistent with the findings of Wang et al. (2014). The recirculation length near the free-end also increases, because the downwash is reduced. Bourgeois (2012), finds that the magnitude of the $\overline{u'}^2$ and $\overline{v'}^2$ Reynolds stresses are similar in the wakes of two boundary layers, but that the effect of the boundary layer is to move the concentrations

of Reynolds stress closer to the cylinder, presumably caused by the change from dipole to quadrupole and the additional connector strand that occurs. Additionally, it is found that the connector strand increases the magnitude of incoherent velocity fluctuations (those fluctuations not associated with the half or full loop).

Another interesting discussion point regarding the effect of the boundary layer is the method by which streamwise vorticity is generated near the junction, i.e., the mechanism through which stream rotation of the columnar vortex filament occurs. Bourgeois (2012) stipulates that the filament is bent upstream through the spanwise velocity gradient occurring in the high boundary layer which causes a convection velocity deficit close to the junction. This is coupled with streamwise vorticity generated in the sidewall boundary layer of the square cylinder caused by the downwash induced by the horseshoe vortex.

El Hassan et al. (2015) presents supporting evidence that streamwise bending of the vortex filament near the junction is enhanced when the boundary layer is significantly increased above $\delta/W = 1$. However, contrary to previous assumptions, these authors show that it is in fact the horseshoe vortex that causes this streamwise reorientation. Surface flow visualisation and POD analysis show that a 'backflow mode' exists in the boundary layer where high-momentum irrotational fluid in front of the cylinder is advected toward the junction (at the front of the cylinder) and ejected upstream. The energy of this mode is enhanced for thicker boundary layers. The wall jet is responsible for reorientation of the horseshoe vortex legs which act to bend to shed vortices towards the cylinder base.

2.5 Circular FWMCs

Unlike the square FWMC, a single consistent flow model of circular FWMCs that encompasses the full range of aspect ratios tested (up to $L/D = 30$) which explains all of the near wake flow phenomena has not yet been formulated. This is despite the fact that most studies on FWMCs have concentrated on those with circular cross-section. The reason why circular FWMC wakes are of interest in this literature review is that no studies on square FWMCs have concentrated on aspect ratios above 11 (although some studies (McClean and Sumner 2014; Wang and Zhou 2009) have investigated square FWMC flow at $L/W = 11$). Alternatively, there are many experimental flow studies on the wakes of circular FWMCs for aspect ratios up to 30. Given that square cylinders and circular cylinders display similar noise characteristics at high aspect ratios (Moreau et al. 2014), the intention of this discussion is to amalgamate the current state of knowledge on circular FWMCs with high aspect ratios to supplement the lack of understanding of the wakes of their square counterparts.

2.5.1 Proposed near wake models

The most important wake models for circular FWMCs are those put forward by Sakamoto and Arie (1983), Kawamura et al. (1984), Lee (1997), Pattenden et al. (2005), Frederich et al. (2008) and Krajnovic (2011). Figures 2.6 to 2.9 give an overview of these competing wake models.

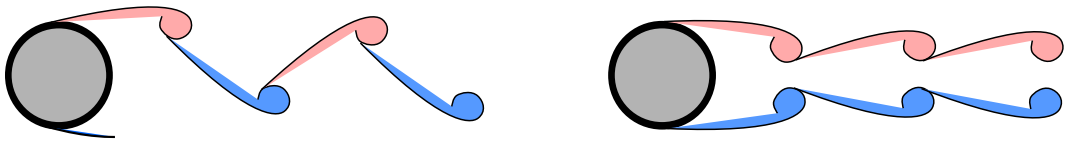

Alternate Kármán Shedding Symmetric Arch type shedding

Figure 2.6: The near wake flow model proposed by Sakamoto and Arie (1983). The vortices are shed either anti-symmetrically (left) or symmetrically (right) in an arch structure that is connected through the plane of symmetry.

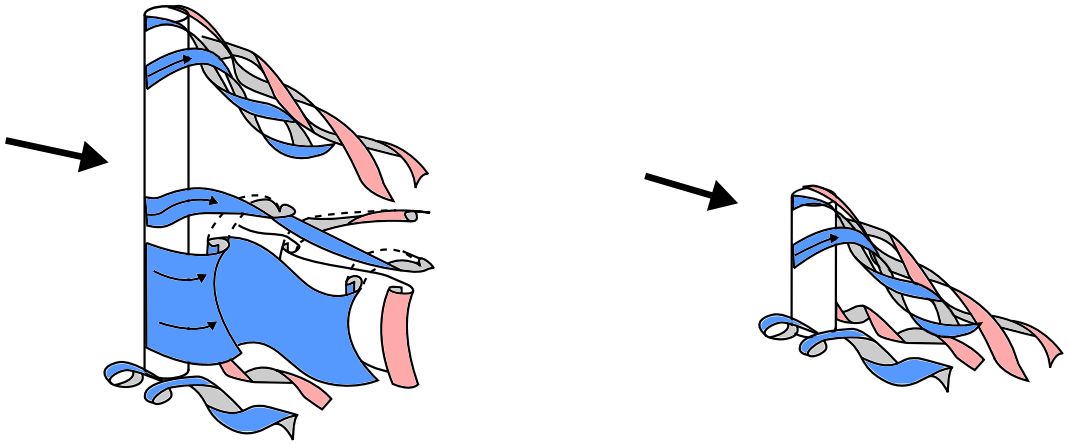

L/D >critical L/D <critical

Figure 2.7: Near wake flow model proposed by Kawamura et al. (1984).

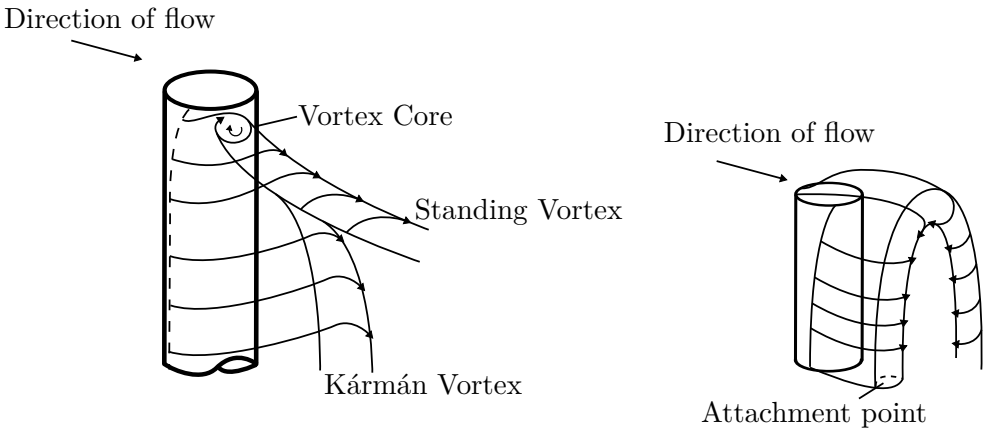

$L/D > 3$ $L/D < 3$

Figure 2.8: Near wake flow model proposed by Lee (1997).

The model of Sakamoto and Arie (1983) is shown in Figure 2.6. This model suggests that at aspect ratios above the critical (in this case $L/D_{crit} = 2.5$), circular cylinders shed von Kármán alternating vortices across the entire cylinder span. As the aspect ratio is decreased below the critical aspect ratio, the shedding changes from the von Kármán type to *symmetrically shed* arch structures. An arch structure is one where periodically shed vortices are connected across the plane of symmetry to form an arch or hairpin like structure. The arch structure differs from a half-loop because vortices are always shed symmetrically. The model is two-dimensional in nature and lacks important details

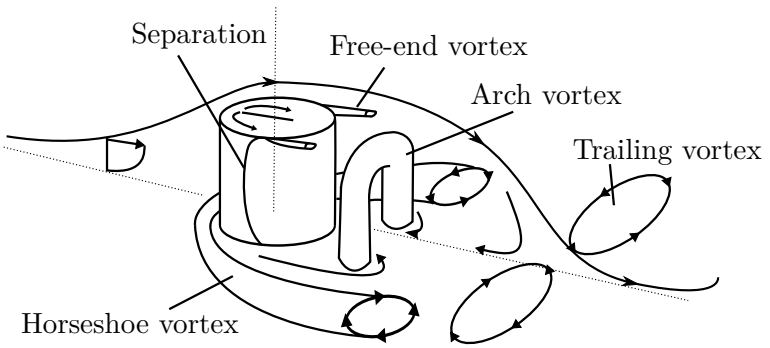

$L/D < critical$

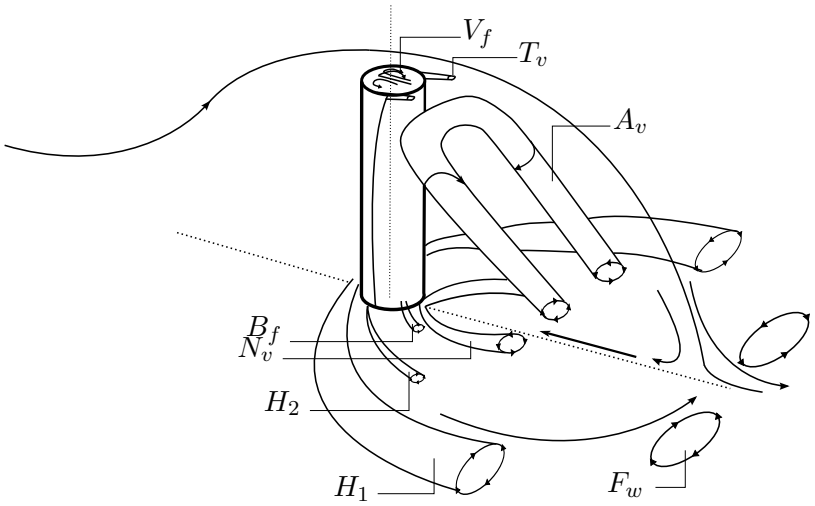

Legend

V_f	Mushroom vortex
T_v	Free-end vortex
F_w	Far wake vortex
A_v	Connected Kármán vortex
H_1	Primary horseshoe vortex
H_2	Secondary horseshoe vortex
N_v	Near wake junction vortex
B_f	Junction Vortex

$L/D > critical$

Figure 2.9: Near wake flow model as proposed by Pattenden et al. (2005), Frederich et al. (2008) and Krajnovic (2011).

concerning the three-dimensionality of the flow; junction vortices and free-end vortices are not accounted for and no interaction between the free-end and base flow is considered. Nevertheless, the model is important as it was one of the first to propose a change of wake structure from anti-symmetric to symmetric shedding behind circular cylinders when the aspect ratio is lowered below a critical value. As discussed, the concept of anti-symmetric and symmetric shedding is frequently used in many wake models.

The 'Kawamura model', proposed by Kawamura et al. (1984), shown in Figure 2.7, does account for counter rotating free-end vortices and, unlike the Wang or Bourgeois models, treats these structures as independent of the mid-span von Kármán vortices. Near the cylinder free-end, the mid-span vortices are inclined downstream by the downwash, where they are annihilated by the stronger, oppositely rotating free-end vortices. Kawamura et al. (1984) reports a critical aspect ratio of $L/D_{crit} = 6$. The definition of the critical aspect ratio is slightly different to that of Sakamoto and Arie (1983); instead of being

based on a change from symmetric to anti-symmetric shedding, the critical aspect ratio is defined as the point where free-end vortices dominate the flow and *suppress* alternate von Kármán vortex shedding. Kawamura et al. (1984) also suggest that the difference in critical aspect ratio when compared with the model of Sakamoto and Arie (1983) is due to the relative height of the incoming boundary layer to span of the cylinder. This is because increasing the relative boundary layer height increases the critical aspect ratio. Importantly this model has no arch vortices or junction vortices present at any aspect ratio. Kawamura et al. (1984) argues that the existence of free-end vortices at all aspect ratios preclude the existence of any closed structure forming from the rear of the cylinder.

The 'Lee model', proposed by Lee (1997), shown in Figure 2.8, indicates that four changes occur in the cylinder wake depending on aspect ratio. Below $L/D = 3$, arch shedding occurs, with the vortex filaments rooted to the ground plane in the recirculation region. With an increase in aspect ratio ($3 < L/D < 7$), von Kármán vortex shedding occurs along the midspan of the cylinder. For $L/D > 7$, two spanwise cellular regions occur; one produced by the alternating von Kármán vortex and the other produced by a 'standing free-end vortex', which is anchored just below the free-end and induces downwash into the wake. At even higher aspect ratios ($L/D > 12$), another pair of standing vortices appear, this time rooted near the junction of the cylinder, with the opposite sense of rotation to the free-end vortices, creating a triple cellular spanwise structure. Lee (1997) proposes that the von Kármán vortex is *entrained* into the standing free-end vortex cell, and has the same rotational direction as the free-end vortex structure. This is a different mechanism to that proposed by Kawamura et al. (1984), and implies that the von Kármán vortex filament is bent upstream, much in the same way as described in the Wang model.

The last class of flow models are those for which a connected spanwise structure coexists with a pair of counter rotating free-end vortices and are shown in Figure 2.9. These models are described by Pattenden et al. (2005) and Frederich et al. (2008), for cylinders with $L/D = 1$ and $L/D = 2$ respectively, and by Krajnovic (2011) for cylinders with $L/D = 6$. Additionally, the results of Sumner et al. (2004) agree with this class of flow models. The investigation of Pattenden et al. (2005) was performed for cylinders below the critical aspect ratio, while the investigations of Frederich et al. (2008) and Krajnovic (2011) were for cylinders above the critical aspect ratio. Here, the critical aspect ratio follows the definition of Kawamura et al. (1984), where there is a suppression of vortex shedding in the near wake of the cylinder. Unlike square FWMCs, the aspect ratio where this occurs does not correspond to a change from a quadrupole wake structure to a dipole wake structure. These type of flow models are referred to here as the 'Krajnovic model'.

The Krajnovic model indicates that at low aspect ratio, an arch structure is shed from the cylinder, much like that described by Sakamoto and Arie (1983), with the important difference being that a free-end vortex, denoted as the 'T_v' vortex system in Figure 2.9, simultaneously sheds independently of the arch structure. The free-end vortex system and arch structure are shed with a much lower central frequency than the two-dimensional case. Over the cylinder free-end, two counter rotating foci are present and are attributed to the end filaments of a 'mushroom' like vortex, denoted as the 'V_f' vortex system, which is produced by the separation and roll up of the free shear layer over the free-end. At

aspect ratios above the critical, alternating von Kármán vortex filaments on either side of the cylinder, denoted as the 'A_b' vortex system, are connected by a vortex forming just underneath the cylinder free-end, and are inclined so as to produce downwash in the wake. Similar to aspect ratios below the critical, a free-end vortex system is also developed around the curved free-end of the high aspect ratio cylinders due to the swirling up of free-end and von Kármán flow (Krajnovic 2011). Sumner et al. (2004) provides evidence that free-end vortices are indeed present for cylinders with aspect ratios above and below the critical, regardless of whether alternate vortex shedding is suppressed or not. The free-end vortex system is merged into the recirculation zone as explained by Frederich et al. (2008). Instantaneous realisations of the flow indicate that the free-end region is in fact comprised of two pairs of counter rotating vortices, similar to that shown in the smoke visualisations of Roh and Park (2003), which again appear intermittently (Hain et al. 2008) and have weak coherency (Sumner 2013). In contrast to the findings of Bourgeois et al. (2011) for square FWMCs, the legs of the inclined von Kármán vortex do not incline upstream near the wall and terminate inside the recirculation zone of the wake. Instead, reverse flow creates two pairs of counter rotating junction vortices, denoted 'B_f' and 'N_v' respectively, which induce upwash into the wake and rise downstream, while being restricted to the recirculation region. The 'B_f' vortex system is anchored near the junction of the cylinder and resembles the 'standing junction vortex' described in the Lee model. Hence, in the Krajnovic model, free-end, junction and von Kármán vortices are all independent structures and von Kármán vortex filaments are connected through the symmetry plane by a cross stream vortex.

The aforementioned flow models are different to the Wang flow model for square cylinders. In particular, there is an overriding similarity between the models for circular FWMCs in that free-end, junction and spanwise vortices are formed as independent structures. This contrasts to the Wang and Bourgeois flow models, where the occurrence of counter rotating vortices at the free-end and junction regions in mean flow reconstructions are explained by the periodic downstream convection of interconnected coherent spanwise flow structures.

2.5.2 Cellular shedding

One commonly observed feature of circular FWMC flow is discrete spanwise variation of vortex shedding frequency for cylinders with $L/D > 7$. This phenomenon is often referred to as *cellular* shedding because the vortices are said to be shed in cells or physical regions of different frequency. Cellular shedding is often observed for very long cylinders with suitable end conditions (Williamson 1989; Eisenlohr and Eckelmann 1989) at low Reynolds numbers ($Re_D = O(10^2)$). Instances of cellular shedding at high Reynolds numbers for infinitely long cylinders are rare, although according to Prasad and Williamson (1997), there does not appear to be a physical reason as to why it should not occur. Cellular shedding is usually *induced* by setting non-uniform inflow or geometric conditions. These may include placing the cylinder in a shear flow (Griffin 1985), tapering the cylinder (Noack et al. 1991) or having a dual step cylinder (Morton and Yarusevych 2014). An FWMC is an example of where the cylinder itself causes non-uniform spanwise variation of the wake aerodynamics that renders cellular shedding possible.

A cellular variation in wake frequency along the span indicates that the spanwise vortex system is not a single connected structure. The Lee model accounts for such a phenomenon but it does not account for the variation of wake frequencies for FWMCs with $L/D > 15$. The existence of cellular shedding is the main reason why a complete wake model for either circular or square FWMCs cylinders has not yet been realised.

Figure 2.10 is a compilation of data showing how the dominant wake frequency of a circular FWMC varies along the span for different aspect ratio cylinders. The data have been taken from Farivar (1981), Kawamura et al. (1984), Fox and Apelt (1993), Kitagawa et al. (1999), Lee (1997) and Sumner et al. (2004). Cylinder aspect ratio (L/D) is denoted by colour while normalised vortex shedding frequency, f_s (expressed as the Strouhal number, $St = f_s D/V_\infty$ where D is the diameter and V_∞ is the mean free-stream velocity) and spanwise location (y/D) are on the ordinate and abscissa axis respectively. Different studies are represented by different symbols.

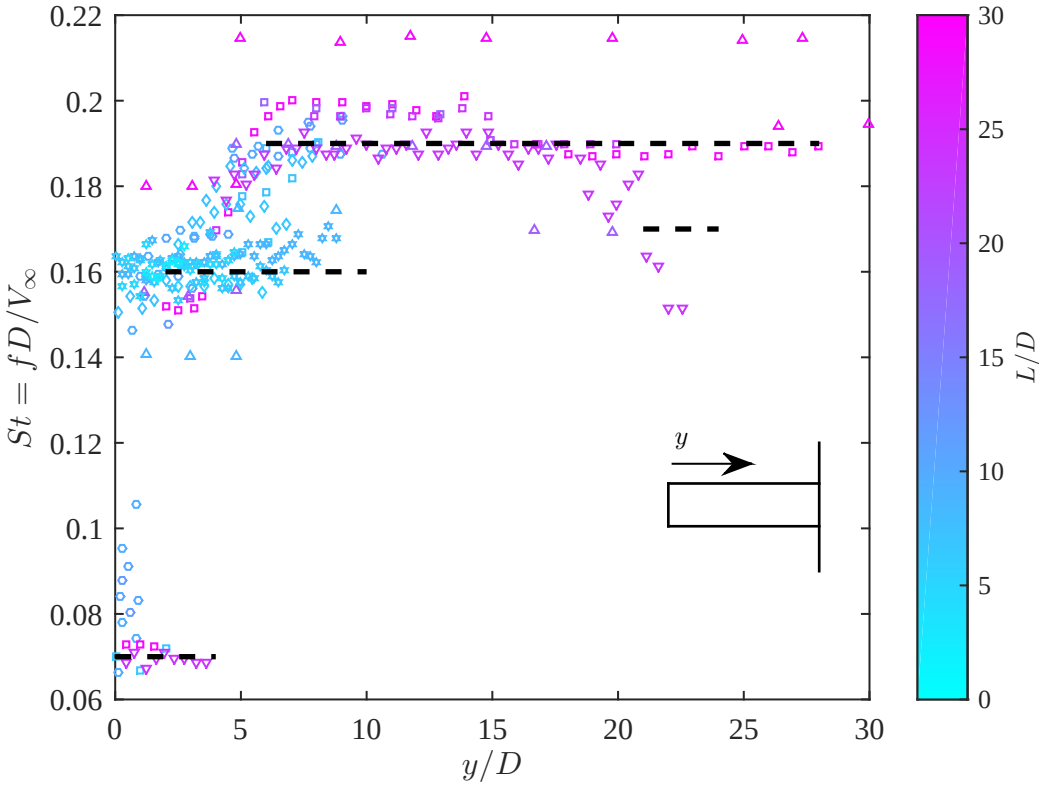

Figure 2.10: The variation of measured wake Strouhal number ($St = fD/V$) data of a circular cylinder with distance from the free-end of a circular cylinder, coloured according to aspect ratio (L/D). Dashed black lines indicate regions where cells possibly occur. ◯, Farivar (1981), $L/D = 2.78 - 15$, $Re = 7 \times 10^4$, $\delta/D =$ Unknown; □, Fox and Apelt (1993), $L/D = 4 - 30$, $Re = 4.4 \times 10^4$, $\delta/D =$ Unknown; ◇, Kawamura et al. (1984), $L/D = 1 - 8$, $Re = 3.2 \times 10^4$, $\delta/D = 0 - 1$; ▽, Kitagawa et al. (1999), $L/D = 25$, $Re = 3.3 \times 10^4$, $\delta/D =$ Unknown; △, Lee (1997), $L/D = 9 - 30$, $Re = 0.3 \times 10^4 - 1.5 \times 10^4$, $\delta/D =$ Unknown; ✡, Sumner et al. (2004), $L/D = 3 - 9$, $Re = 0.6 \times 10^4 - 1.5 \times 10^4$, $\delta/D = 2.6$.

Although there is considerable variation in the experimental conditions between each study (the experimental conditions of each study can be found in Table 2.1), Figure 2.10 shows that the frequency of shedding generally falls into 'cells' near the free-end, indicated by the black dotted lines at $St = 0.07$, $St = 0.16$ and $St = 0.19$. For $L/D < 10$,

there seems to be a relatively consistent collapse of data around $St = 0.16$ for about 90% of the span. Within one diameter of the free-end, the Strouhal number is greatly reduced to a mean value of approximately $St = 0.07$. The fluctuating velocity signal within this region has a much wider bandwidth than the signals found in other cells (Park and Lee 2000). For $L/D > 10$, more cells are apparent at distances father away from the free-end. Between 5 and 10 diameters from the free-end, the Strouhal number returns to the two-dimensional value of $St = 0.2 \pm 0.01$. In some cases, the Strouhal number decreases again when in close proximity to the wall while in other cases it does not. This is attributed to differences in the incoming boundary layer thickness and the experimental conditions. Nevertheless, the fact that the data over a wide range of Reynolds numbers, and experimental conditions (turbulence intensity, boundary layer thickness etc.) can neatly collapse into identifiable cells indicates that the production mechanism for cells in the wake of FWMCs is strongly dependent on the aspect ratio of the cylinder. Therefore, in the absence of any geometric variation across the cylinder span, there must be an aerodynamic wake parameter governing the vortex shedding frequency, that shows strong variation as the aspect ratio varies.

This wake parameter may be the cylinder base pressure (here the word 'base' refers to the cylinder back wall). Similar mechanisms have been proposed for cylinders exhibiting cellular shedding in low Reynolds numbers by Williamson (1989). According to Roshko's two-dimensional wake theory discussed previously, cylinder base pressure drives the wake parameters including formation length, Reynolds stress and vortex shedding frequency. It is well understood that at the free-end of the cylinder, the flow is 'short circuited' over the top of the cylinder (Williamson 1989), a process that causes significant pressure recovery near the free-end (Sakamoto and Oiwake 1984). A similar process can be envisioned near the junction region where upwash is indicative of pressure recovery (in an analogous manner to downwash flow near the free-end). Since the base suction is lower (base pressure is higher) near the extremities of the cylinder than in the mid-span region, there is a mechanism that forces a lower frequency vortex shedding cell to occur. This is also the reason why cells are always observed near the extremities of the cylinder. An important note is that while the base pressure may vary linearly in the spanwise direction, the frequency of vortex shedding will be constant within a particular cell. This is due to the well known 'lock-in' effect (Gerich and Eckelmann 1982) where the response of a forced non-linear oscillatory system locks into the forcing frequency if the forcing is near (but not equal to) the natural frequency of the system. The above hypothesis is well supported by the discussion of Griffin (1985) on tapered cylinders and cylinders in shear flow. Here it is demonstrated that cellular shedding is always accompanied by a near linear change in cylinder base pressure, which, in these cases, is caused by non-uniform geometric or inflow conditions.

In the literature, several other mechanisms have been proposed to explain the generation of cellular variation in wake frequency. Near the junction region, Gerich and Eckelmann (1982) conjecture that the low Strouhal number vortex shedding cell near the junction is caused by the velocity deficit in the plate boundary layer. They explain that if the velocity gradient in the boundary layer is sufficiently high, then cells with lower frequency will naturally form. This would mean that higher boundary layers will form lower frequency cells and low boundary layers will conceivably form no cells, a result

that seems to be consistent within the literature. The Lee near wake model (Lee 1997) conjectures that the presence of a standing vortex anchored at the base of the cylinder is responsible for the single cell in the junction region. From these two explanations, it appears that streamwise junction vorticity and the junction cell of lower frequency shedding are related, which is consistent with the explanation that the velocity deficit in the boundary layer acts to rotate the columnar vortices to create streamwise vorticity near the junction. On the other hand, there are several competing results in the literature regarding the role that the boundary layer has on cellular shedding near the junction region. Both Sakamoto and Arie (1983) and Sumner et al. (2004) measured constant spanwise Strouhal numbers behind a circular cylinder of aspect ratios ranging from 1.5 to 9 in relatively high boundary layers ($\delta/L > 0.3$, $\delta/D > 2$) and concluded that the large height of the incoming boundary layer may suppress spanwise cellular variation in shedding frequency. Although this claim has yet to be validated by any study, the results of Sakamoto and Arie (1983) and Sumner et al. (2004) may be misleading since the aspect ratio ranges of their respective studies appear to be too low for cellular shedding to occur (see Figure 2.10).

Williamson (1989) shows that the existence of spanwise cells near the free-end is related to an *oblique* mode of von Kármán vortex along the span of very long cylinders. Each cell has its own frequency that is related to the angle of shedding by $f_\theta = f_0 \cos\theta$, where f_0 is the frequency of two-dimensional shedding and θ is the angle of shedding. The models proposed by both Lee (1997) and Kawamura et al. (1984) and the numerical results of Krajnovic (2011) indicate that flow near the free-end is obliquely shed, thus potentially giving rise to several cells of vortex shedding in that region.

One important point to make is that for very long cylinders ($L/D > 45$), the frequencies in the end cell vortex shedding at Reynolds numbers above 180 are generally measured at $St = 0.14$ or higher and have a narrow bandwidth (Williamson 1989). This is in contrast with the cell of shedding observed at the free-end in Figure 2.10 at $St = 0.07$, which is at a much lower frequency. Examples of the latter signal can be found in Fox and West (1993b), Kitagawa et al. (1999), Park and Lee (2000), Park and Lee (2002) and Moreau and Doolan (2013). Given this evidence, Kitagawa et al. (1999) proposes that this low frequency signal is related to the generation of independent streamwise vorticity near the free-end, i.e., independent 'free-end-vortices' or 'free-end-associated' vortices. In fact, Lee (1997) states specifically that the counter rotating vortices generated at the free-end are responsible for the low frequency cell, which is in accordance with his near wake model (Figure 2.8). Porteous et al. (2013) used flow-induced noise measurements to show that the strength of the tone supposedly generated by these free-end vortices remained constant for a wide range of aspect ratios between $8 \leq L/D \leq 22$, providing further evidence that a structure independent of the aspect ratio forms near the free-end. This interpretation seems to be consistent with the Krajnovic class of flow models, where independent free-end vortices, T_v, shed alongside larger spanwise obliquely shed structures, A_v (see Figure 2.9). Following from this interpretation, it could be that trailing free-end vortices cause the end cell at $St = 0.07$ and locally oblique shedding of the connected structure is responsible for the additional cells of vortex shedding at $St \geq 0.14$ observed near the free-end of circular FWMCs with $L/D > 20$ (see Figure 2.10).

2.6 FWMC flow-induced noise

Only three experimental studies exist that specifically address the noise produced by FWMCs; Becker et al. (2008), Moreau and Doolan (2013) and Porteous et al. (2013). Additionally, King and Pfizenmaier (2009) have investigated the flow-induced noise of a finite cylinder in a free jet rather than a developing boundary layer. In their study, the interaction of the cylinder junction with the plate boundary layer was removed. Lastly, Kaltenbacher et al. (2010) used Computational Aeroacoustics (CAA) to briefly study the noise directionality of a square FWMC of $L/W = 6$. Despite the limited studies available, a number of common features can be identified between these studies. These relate to the relationship between the main Aeolian tone and aspect ratio, the existence of multiple peaks in far-field acoustic spectra and the directivity of the acoustic tones. When combined with the proposed flow structures described in Sections 2.4 and 2.5, these provide insight into the possible connection between the flow-induced noise and quasi-periodic flow features, which are discussed in Section 2.6.2.[1]

2.6.1 Flow-induced noise characteristics

When regular spanwise vortex shedding exists, an FWMC will produce an Aeolian tone, similar to that of an infinitely long cylinder. The bandwidth of this tone is generally wider than that of a two-dimensional cylinder indicating severe three-dimensional effects (amplitude or phase modulation) are occurring across the span. The frequency and strength of this tone change with the aspect ratio of the cylinder.

The frequency of the Aeolian tone of FWMCs is generally lower than that measured for the two-dimensional equivalent. Becker et al. (2008) found the Strouhal number of the Aeolian tone of a square FWMC of aspect ratio of 6 to be approximately 20% below that measured for two-dimensional square cylinders. Both King and Pfizenmaier (2009) and Moreau and Doolan (2013) also reported Aeolian tone Strouhal numbers lower than the expected two-dimensional value for both circular and square FWMCs. Both authors reported that this Strouhal number increased asymptotically towards the two-dimensional value as the aspect ratio of the FWMC increased.

The strength of the Aeolian tone is related to the aspect ratio and also to the spanwise coherency of the shed vortices, which varies with the cross section of the cylinder. King and Pfizenmaier (2009) and Moreau and Doolan (2013) both reported an increase in Aeolian tone level with increasing aspect ratio, which is to be expected, given that higher integrated acoustic pressure fluctuations occur for longer FWMCs.

In general, square FWMCs were found to have a much stronger fundamental Aeolian tone which occurs over a narrower frequency band when compared with circular cylinders (King and Pfizenmaier 2009; Moreau and Doolan 2013). King and Pfizenmaier (2009) attributed this to higher spanwise coherence of vortex shedding in square cylinders due to the predetermined separation point of a square cross-section. Becker et al. (2008) studied

[1] It is important here to mention that the above studies have only studied noise produced by structures in the near wake of cylinder. Noise produced by flow interaction at the front of the cylinder by, for example, free-stream turbulence or horseshoe vortices, have not been investigated in any published study. Therefore this noise cannot be characterised or related to any previously discussed flow-mechanisms and consequently it is not discussed here.

the effect of attaching fore- and aft- bodies and end plates to a square FWMC on the flow-induced sound. It was found that upstream instabilities generated by forebodies reduced the coherence of vortex shedding and decreased the wake turbulent kinetic energy, thereby reducing the Aeolian tone level. In contrast, adding an aft-body did not disturb the flow upstream of the separation point and limited downwash flow from the free-end from entering the wake. This caused the Aeolian tone level to increase by allowing coherent development of vortex shedding across the span. The acoustic spectrum of the aft-body cylinder was also compared with that of a finite cylinder fitted with an end plate. The end plate effectively limited downwash from the free-end (it inhibited the existence of a 'roof-vortex') in a similar manner to the aft-body, which promoted two-dimensional development of the cylinder wake as evidenced by a stronger Aeolian tone at a higher shedding frequency. The acoustic spectrum of both the end-plated cylinder and FWMC with an aftbody were very similar, confirming the proposed mechanism.

Apart from the fundamental Aeolian tone, King and Pfizenmaier (2009), Moreau and Doolan (2013) and Porteous et al. (2013) have detected lower frequency tones in the acoustic spectra of both square and circular FWMCs. King and Pfizenmaier (2009) also found evidence of a single secondary tone at a frequency just below that of the fundamental for circular cylinders at $L/D = 35$ and for square cylinders at $L/D = 16.7$, both at Reynolds numbers of $O(10^4)$. King and Pfizenmaier (2009) attribute the secondary tone to either cylinder end effects in the case of circular cylinders, or a separation and reattachment process in the case of square cylinders. However, the investigation by King and Pfizenmaier (2009) was not accompanied by simultaneous flow measurements. Furthermore, the peaks found by King and Pfizenmaier (2009) may not be due to developing free-end structures, but interactions of the cylinder with the impinging shear layer of the wind tunnel jet, which has been known to produce vortex shedding cells (Griffin 1985).

Moreau and Doolan (2013) are the only authors to simultaneously use single microphone and hot-wire measurements to specifically investigate the lower frequency tones generated by FWMCs at subcritical Reynolds numbers. In addition to the main Aeolian tone generated by regular vortex shedding, several other secondary peaks were also found by Moreau and Doolan (2013) in the velocity and acoustic spectra of select aspect ratio cylinders. For circular FWMCs with $L/D > 17$, a low frequency, broad peak corresponding to flow around the free-end and a narrow peak, close to the vortex shedding frequency, corresponding to flow around the junction were found. For square FWMCs with sufficiently high aspect ratio ($L/W > 8$), a single secondary peak was measured corresponding to flow structures near the free-end. Figure 2.11 gives examples of acoustic spectra for flow over square and circular FWMCs of $L/W = 14$ and $L/D = 22.7$ respectively. The data presented in these figures were obtained with a microphone located directly above the cylinder approximately $r/W = 50$ and $r/D = 83$ from the cylinder axis respectively (where r is the distance from the cylinder axis to the microphone) . The spectra are compared with that obtained for full-span (infinite) cylinders taken in the same facility.

The acoustic spectrum of the square FWMC (Figure 2.11a) shows two peaks straddling $St = 0.1$ corresponding to structures near the free end and structures near the junction. As found by Moreau and Doolan (2013), these tones only occur for $L/W > 9$. Below

$L/W = 9$, only one peak is reported and below $L/W = 2$ no peaks are reported. The acoustic spectrum for the circular FWMC shows all three peaks corresponding to free-end, junction and mid-span flow respectively while the two-dimensional cylinder only displays one peak corresponding to von Kármán vortex shedding. The occurrence of these peaks also depended on the aspect ratio of the cylinder. For circular cylinders of $L/D > 19$ all three peaks exist (Moreau and Doolan 2013). Below this aspect ratio, only one peak corresponding to the Aeolian tone and one peak corresponding to the free-end flow exist. Below $L/D = 8.1$, no peaks are present (except for $L/D = 3.2$ which is discussed in the next section).

Becker et al. (2008), Moreau and Doolan (2013), King and Pfizenmaier (2009), Porteous et al. (2013) and Kaltenbacher et al. (2010) all show that the Aeolian tones are dipoles around the cylinder. Phase measurements between pressure fluctuations on opposite surfaces of a square cylinder show a 180 degrees phase separation at the vortex shedding frequency and single microphone directivity measurements at this shedding frequency show dipole-like lobes around the periphery (Becker et al. 2008). Measurements at different flow speeds performed by both King and Pfizenmaier (2009) and Moreau and Doolan (2013) show a 6^{th} power velocity collapse which is to be expected for dipole sources. Porteous et al. (2013) directly measured the directivity pattern of the main Aeolian tone and the tones associated with free-end and junction structures and confirmed that all three components had dipolar directivity. Lastly, three-dimensional directivity patterns from the numerical simulations of Kaltenbacher et al. (2010) also show distinct dipole-like directionality of the acoustic pressure fluctuations at the vortex shedding frequency.

2.6.2 Noise generation mechanisms

The fundamental tone evident in the acoustic spectra of both circular and square FWMCs can be attributed to mid-span von Kármán vortex shedding. As the aspect ratio is increased, both the strength and frequency of the Aeolian tone will increase towards a two-dimensional level. This is to be expected as the longer the cylinder, the weaker the influence of the free-end and junction on the mid-span (Fox and West 1993a), allowing the flow in the mid-span to develop with an increasing level of two-dimensionality. As the aspect ratio is lowered, the frequency and strength of the tone will be similarly lowered as the influence of the free-end downwash engulfs the entire span of the cylinder, prohibiting the development of alternate von Kármán shedding. As has been discussed, it is hypothesised that the frequency of the Aeolian tone is reduced because the base suction is reduced following greater influence of the downwash and upwash at the mid-span of the cylinder. This is well supported by the end plate experiment of Becker et al. (2008). When the end plate is fitted onto a square FWMC, the frequency of vortex shedding increases because the downwash into the wake reduces, increasing the base suction, increasing Reynolds stress production and decreasing the formation length.

Following this, it has been suggested by Moreau and Doolan (2013) that the aspect ratio where an Aeolian tone is not measured corresponds to the critical aspect ratio of the cylinder. For a circular FWMC, the critical aspect ratio is the aspect ratio where the vortex shedding is suppressed. This is certainly true for circular FWMCs. The

results of Moreau and Doolan (2013) indicate that the Aeolian tone is suppressed for $L/D < 8.1$, which approximately corresponds to the critical aspect ratio of a circular FWMC measured by Kawamura et al. (1984). However, for square cylinders, the critical aspect ratio is defined as when the wake changes from dipole to quadrupole, as the vortex filaments bend upstream near the junction. As was noted in Section 2.4, a strong vortex shedding peak (and hence Aeolian tone) is still expected for both quadrupole and dipole wake structures for square FWMCs. Further investigation is required to relate the far-field acoustic spectrum to the critical aspect ratio of the cylinder.

One very interesting aerodynamic noise characteristic of FWMCs is that the relationship between overall sound pressure level (OASPL) and aspect ratio is not monotonic. Local maxima in the OASPL occur at $L/D = 3.2$ for circular FWMCs and $L/W = 4$ for square FWMCs. Interestingly, Moreau and Doolan (2013) measured the reappearance of an Aeolian tone at $L/D = 3.2$. The reappearance of the Aeolian tone at $L/D = 3.2$ found by Moreau and Doolan (2013) for circular FWMCs may be related to boundary layer effects. In the study of Moreau and Doolan (2013), at $L/W = 3.2$, the relative height of the boundary layer was $\delta/L = 0.5$. Based on the results of Sakamoto and Arie (1983) and Sumner et al. (2004) for circular FWMCs, a relative boundary layer height of $\delta/L > 0.33$ is enough to influence flow structures across the entire span of the cylinder. Kawamura et al. (1984) found that if the aspect ratio of a circular FWMC is small enough so that the height is comparable with the height of the boundary layer, flow reattachment on the surface of the free-end will occur. A recent review by Sumner (2013) of free-end flow over circular FWMCs indicates that increasing δ/L will move this reattachment point towards the leading edge of the free-end and when the boundary layer height exceeds the length of the cylinder, the mushroom vortex over the free-end is suppressed. The shift in reattachment point is also related to the downwash entering the wake of the FWMC. Wang et al. (2006) showed that increasing the relative boundary layer height reduced the downwash from the free-end of a square cylinder and in doing so, promoted greater coherent von Kármán shedding along the span. Based on these results, it is suggested that when the boundary layer height is sufficiently high, downwash from the free-end is reduced. This will promote the development of von Kármán vortices at aspect ratios below the critical aspect ratio, which results in the production of an Aeolian tone. A similar mechanism may also be present for square cylinders. However, because of the sharp leading edge and the tendency for square cylinders to exhibit vortex shedding below the critical aspect ratio, the spanwise coherency of the Aeolian tone is only enhanced by the boundary layer, rather than completely reappearing.

Moreau and Doolan (2013) found that the lower frequency acoustic tones observed for circular cylinders of $L/D > 13$ are related to the cellular variation in Strouhal number along the cylinder span. From the discussion in Section 2.5.2, the spanwise variation in Strouhal number may be caused by the development of independent structures at the free-end, base and mid-span of the FWMC which shed at different frequencies. This causes multiple peaks in the acoustic spectrum of the flow-induced noise. Certainly there is agreement in the frequencies found across the span of the circular FWMC shown in Figure 2.10 and the frequencies of the acoustic tones found by Moreau and Doolan (2013) at similar aspect ratios.

Like circular FWMCs, square FWMCs also produce lower frequency tones for $L/W >$

9 (Moreau and Doolan 2013) in addition to the Aeolian tone. This suggests that vortex splitting and cellular shedding also occurs in the wake of square cylinders as it does in the wake of circular cylinders. To the author's knowledge, this is the only published work which has reported evidence of a cellular variation in vortex shedding frequency for square FWMCs using flow measurements (double peaked velocity spectra have been reported by Bailey et al. (2002) for semi-infinite cylinders near a plane wall). The models developed by Wang and Zhou (2009) and Bourgeois et al. (2011) cannot explain this phenomena because they are based on the premise that the sharp leading edge of the square cylinder produces a single interconnected coherent structure along the entire span. It should be noted though that these models were only developed by investigating square cylinders of $L/D < 9$ so direct applications of this model to the results of Moreau and Doolan (2013) may not be justified. Some aspects of the acoustic data by Moreau and Doolan (2013) do, however, support the Wang or Bourgeois flow models. In particular, no evidence of a peak at $St = 0.07$ in either velocity or acoustic spectra associated with the free-end was found by Moreau and Doolan (2013). This gives further evidence that no independent free-end vortex structures are created in the wake of square FWMCs but may occur for circular FWMCs. One question that remains unclear, however, is what happens to the spanwise behaviour of vortex shedding from a square FWMC with $L/W > 14$. There have been virtually no studies that have examined square FWMCs beyond this range. Circular FWMCs above this aspect ratio tend to develop an additional cell of shedding near the junction region, as discussed in Section 2.5.2. No such phenomena has ever been observed in square FWMCs below $L/W < 14$. If such a phenomena were to exist, this would provide further evidence that the flow behaviour of square FWMCs becomes increasingly like circular FWMCs as the aspect ratio is increased, especially near the junction.

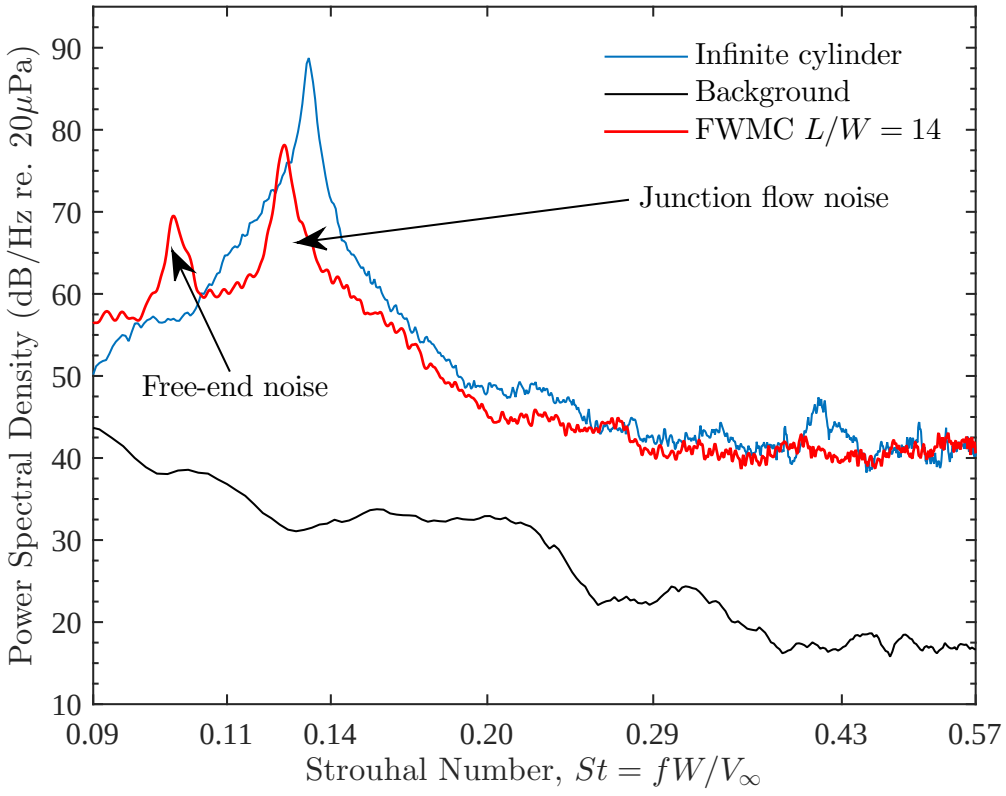

(a) Square FWMCs

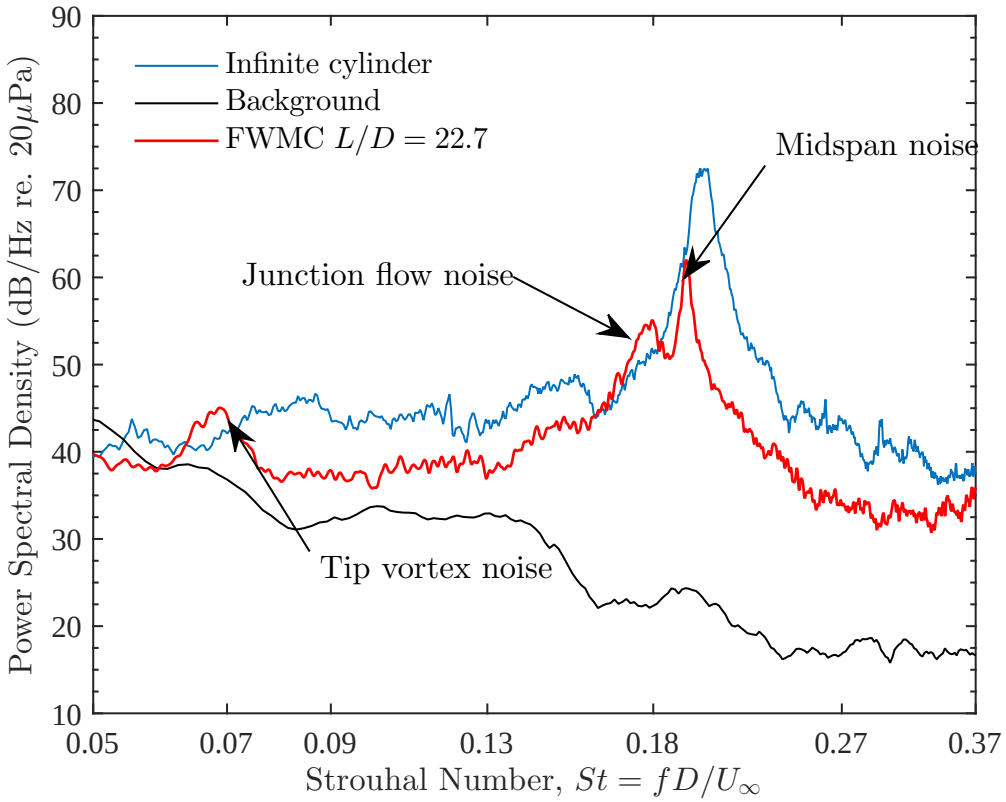

(b) Circular FWMCs

Figure 2.11: Example of an acoustic spectrum from (a) a square and (b) a circular FWMC of $L/W = 14$ and $L/W = 22.7$ respectively obtained by Moreau and Doolan (2013). The Reynolds number of the experiments were $Re_W = 2.3 \times 10^4$ and $Re_D = 1.2 \times 10^4$. The spectra are compared with that obtained for full-span (infinite) cylinders taken in the same facility.

2.7 Summary and research questions

The state of knowledge on the both the quasi-periodic flow structures and resulting flow-induced noise of a square and circular FWMC has been reviewed. The discussion has shown that the wake structure behind finite-length cylinders is very different when compared with its two-dimensional counterpart due to three-dimensional flow interactions introduced by the presence of a free-end and junction. Along with regular von Kármán shedding, a pair of counter rotating free-end vortices, junction vortices and horseshoe vortices may also be present in the wake depending on the aspect ratio and the height of the incoming boundary layer. These features, however, are only present in time-averaged realisations of the wake and generally do not represent the true nature of the quasi-periodic flow structures. To explain the true nature, several wake models have been proposed in the literature. The wake structure of a square FWMC was found to consist of a fully interconnected series of vortex loops that are shed periodically and deform under the action of three-dimensionality, named the 'Wang' flow model. This deformation causes interesting modifications to the shedding behaviour, particularly with respect to the modes of shedding (symmetric or anti-symmetric) near the free-end, mid-span and junction of the FWMC.

At low aspect ratios, circular cylinders display subtly different wake characteristics that appear to invalidate the proposed interconnected vortex loop model for square FWMCs. This is due to the presence of a pair of independent free-end vortices generated at the curved free-end that leave the signature of low frequency broadband periodicity in both near wake velocity and noise spectra. Nevertheless, several characteristics of the wakes of circular FWMCs at higher aspect ratios can be used to study high aspect ratio square FWMCs, which have not received as much attention in the literature. Of relevance is the spanwise cellular nature of vortex shedding that has been reported for circular cylinders of $L/D > 7$. Based on the aeroacoustic results of Moreau and Doolan (2013) and King and Pfizenmaier (2009), cellular vortex shedding is proposed to also occur in the wakes of square FWMCs for $L/W \geq 8$. It is unclear how cellular shedding is incorporated into the Wang wake flow model. Likewise, the shedding behaviour for square FWMCs with $L/W > 14$ is also unknown, since this range has never been investigated.

The flow-induced noise of FWMCs has several characteristics that are different to that of two-dimensional cylinders. These include lower frequency Aeolian tones with wider bandwidths, multiple Aeolian tones, changes in the Aeolian tone magnitude with aspect ratio and boundary layer height and increased noise generation at frequencies much higher than the Aeolian tone (called 'broadband' noise). Previous studies on the aeroacoustics of FWMCs that have identified these noise characteristics have not related these characteristics back to the known behaviour of the near wake flow. This is possibly due to the disjointed nature of the research on FWMCs in the past leading to an inconsistent understanding of the flow aspects of the problem. However, with the present amalgamation of literature concerning the flow over FWMCs, it is now possible to formulate several specific research questions, for which the remainder of the thesis is based, that will help to establish a link between the aerodynamic noise and the flow. These are

1. How does the Aeolian tone(s) alter with changes in aspect ratio and boundary layer

thickness for square FWMCs? How are these alterations related to the difference in wake structures behind square FWMCs?

2. What are the major causes of broadband noise generation? Is this type of noise also related to the boundary layer height and aspect ratio?

3. Do square FWMCs exhibit the same spanwise cellular shedding behaviour of circular FWMCs for $L/W>14$? What role does the boundary layer have, if any, in the formation of spanwise cellular shedding?

Chapter 3

Experimental facilities, anemometry and methods

3.1 Introduction

This chapter details the facilities, technology and methodology used in the experimental campaign undertaken in this thesis.

The experimental campaign can be divided into two separate experiments, each conducted in a different facility, and is summarised in Table 3.1. The first, Experiment 1, conducted in an Anechoic Wind Tunnel (AWT), measured the flow-induced noise generated by a number of aspect ratio square FWMCs models in two different boundary layers using single microphone measurements, directivity measurements and phased microphone array measurements. Wake velocity data for select aspect ratio FWMCs, using a single hot-wire, were measured concurrent with the flow noise.

The second experiment, Experiment 2, conducted in a closed test section open circuit wind tunnel (known as the '18 Inch Wind Tunnel' or '18WT'), measured the mean and fluctuating surface pressure of different aspect ratio square FMWCs models. Similar flow conditions (Reynolds number and relative boundary layer thickness) to that of Experiment 1 were achieved. Oil-film visualisation of the FWMC models was also conducted.

These experimental techniques were chosen to achieve the thesis aims and objectives specified in Chapter 1 and answer the research questions provided in Chapter 2. How each experimental technique relates to these aims and objectives is summarised in Table 3.2. Single microphone, directivity and microphone array measurements in Experiment 1 are used to measure and characterise the magnitude and various spectral components of flow noise associate with FWMCs of various aspect ratio with different incoming boundary layer thicknesses. The link between the flow induced noise and the dynamic FWMC wake flow is found by conducting simultaneous microphone and hot-wire wake

Table 3.1: Summary of the experimental measurements taken in this thesis.

Experiment name	Facility	Measurements
Experiment 1	AWT	Single microphone noise spectra characterisation, noise directivity, microphone array source localisation, hot-wire wake velocity
Experiment 2	18WT	Surface pressure, oil-film visualisation

velocity measurements in Experiment 1 and performing surface pressure measurement and oil-film visualisations in Experiment 2. Various hypotheses on why certain flow and noise phenomena are observed are made based on a holistic analysis of all of the results from both Experiments 1 and 2.

The structure of this Chapter is as follows: first the Anechoic Wind Tunnel facility used in Experiment 1 (and its associated equipment) is described and characterised. This includes the design and calibration of a custom built 'cylinder rig', which was capable of automatically changing the FWMC aspect ratio. Importantly, the rig provided the ability to perform an aeroacoustic experiment on FWMC models *with the highest number of different aspect ratios ever conducted in a single experiment.* Next, the transducers and anemometry used in Experiment 1 are discussed, including single microphones and hot-wire anemometry. In particular, a comprehensive overview of the possible sources of hot-wire error is provided. Several novel techniques are used to accurately quantify the experimental hot-wire uncertainty, which ultimately reduces the uncertainty in each hot-wire measurement. Afterwards, the facilities and experimental techniques for Experiment 2, including surface pressure measurements and an oil-film flow visualisation method are discussed. The oil-film method used in this study is validated against similar results in the literature. Finally, the experimental conditions that the FWMC models were tested in, such as the Reynolds number and boundary layers, are characterised for both Experiments 1 and 2.

Table 3.2: How each thesis aim and objective is achieved through the experimental campaign.

Experimental techniques	Objective	Aim
Single microphone, directivity, microphone array measurements	Measure the tonal and broadband noise from FWMCs	Characterise the FWMC flow noise and determine its relationship with boundary layer thickness and aspect ratio.
Simultaneous microphone and hot-wire measurements, oil-film visualisation, surface pressure measurements	Determine the vortex flow patterns and measure the salient flow parameters in the wake of FWMCs	Understand the dynamic flow structures responsible for tonal and broadband noise generation from FWMCs.
Holistic analysis noise-flow data	Relate flow patterns and wake measurements to the flow induced noise	Understand why flow and noise change with aspect ratio and boundary layer thickness.

3.2 Experiment 1

3.2.1 Facility description

Experiment 1 was conducted inside the University of Adelaide's Anechoic Wind Tunnel (AWT). A three-dimensional schematic of the AWT is shown in Figure 3.1.

In this wind tunnel, air is supplied via a 3-kW centrifugal fan (Fantech model no. 27B B1) located above the test chamber. The fan is controlled with a Vacon NXL-series speed controller connected to a PC located outside of the main chamber. The air is passed through an 8-m-long silencer. The silencer has five 90° corners (each with turning vanes installed to minimise pressure loss) and is lined with 200-mm-thick acoustic foam (BaryNal). The flow then enters a circular settling chamber where it first passes through a fine wire mesh gauze screen, then through a honeycomb section made from drinking straws and, finally, through another mesh. After exiting the settling chamber, the air flows through a rectangular contraction with a contraction ratio of 3.67 and an outlet with a height of 75 mm and a width of 275 mm. The outlet is flanged to allow models to be mounted against the contraction via 12 mounting holes drilled around the perimeter. A diagram of the contraction outlet is shown in Figure 3.2.

The flow is exhausted into an anechoic chamber with internal dimensions of 1.4 m × 1.4 m × 1.6 m. The chamber is isolated from the laboratory floor with isolation mounts. The walls of this chamber are lined with pyramid shaped foam wedges (with a height of 295 mm and a base width of 100×100 mm^2) which provide a near anechoic environment above 250 Hz (see Section 3.2.2). A funnel-shaped collector is located approximately 800 mm from the exit plane of the contraction outlet to eliminate air recirculation within the chamber, making the area outside of the jet flow near quiescent. In this study, the coordinate system origin of the contraction outlet is located at the right hand edge of the contraction, as shown in Figure 3.2: x is the aligned with the streamwise direction of the flow, going out of the page, y is the cross-stream direction, pointing to the wind tunnel floor and z is the span-wise direction, going to the left.

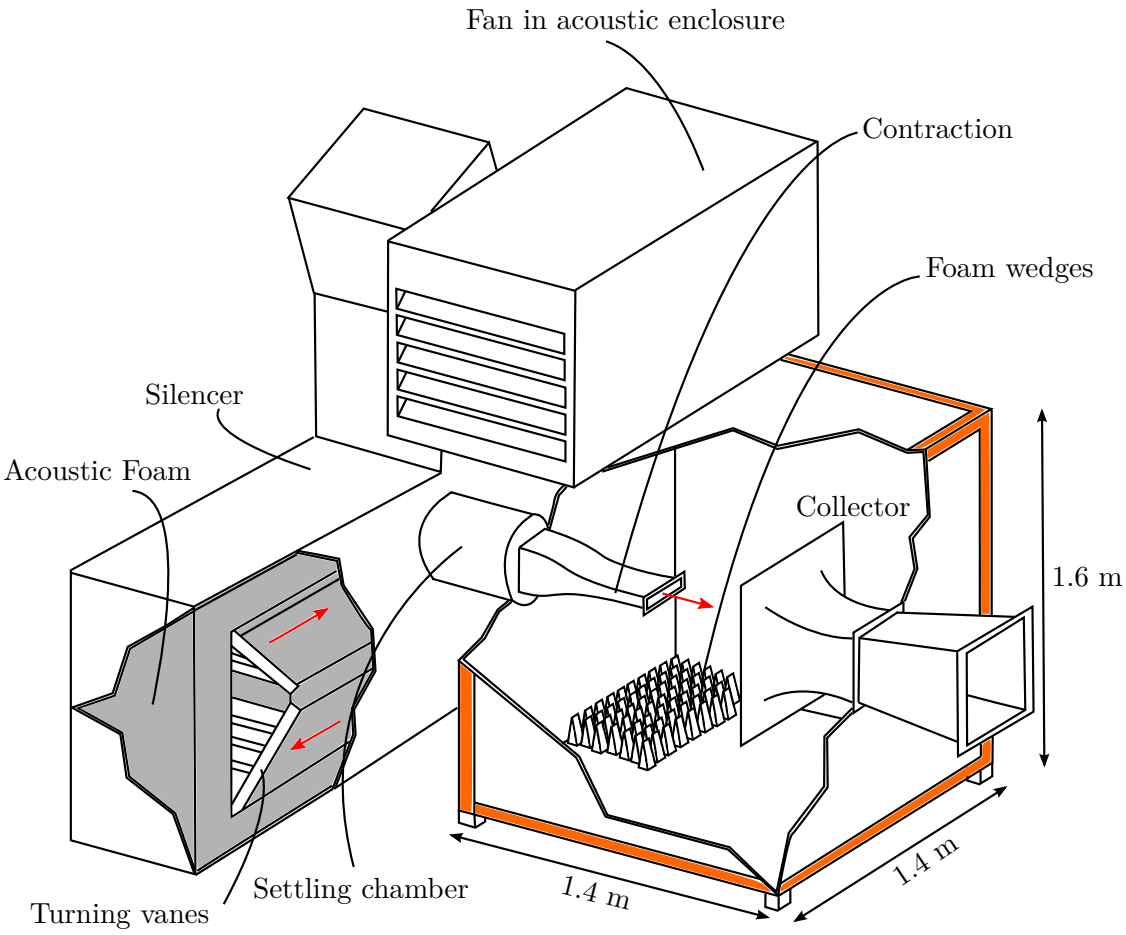

Figure 3.1: A three dimensional schematic of the Anechoic Wind Tunnel used for aeroacoustic measurements. Air flow is produced by a fan, passed through a silencer and exhausted through a rectangular contraction into an anechoic chamber. The chamber is lined with foam wedges to provide an anechoic environment above 250 Hz.

3.2.2 The Anechoic Wind Tunnel aeroacoustic characterisation

Aerodynamic characteristics

The aerodynamic characteristics of the AWT were analysed using (1) a Pitot-static tube connected to a 10-Torr differential Baratron via 5-mm-I.D plastic tubing (length ≈ 5 m) and (2) a TSI 1210-T1.5 single-wire probe with a wire length of 1.27 mm and a diameter of 3.81 μm. The hot-wire probe was controlled with a TSI IFA300 constant temperature anemometer and connected to a three-dimensional Dantec Dynamics robotic traverse with a 6.25 μm positional accuracy. A detailed discussion of constant temperature hot-wire anemometry is given in Section 3.2.5. The hot-wire was calibrated outside of the wind tunnel in a TSI manual velocity calibrator (Model 1128). After calibration, the experimental error of the mean velocity was around 2.3%.

Figure 3.3 shows the variation of mean velocity and turbulence intensity ($T.I. = \sigma_u/V_\infty$ where σ_u is the standard deviation of the velocity signal) measured at the centre of the contraction outlet ($(x, y, z) = (0, 0, 0)$). The mean velocity increases linearly with fan speed. Based on a least squares fit, the tunnel mean velocity, V_∞, can be approximated

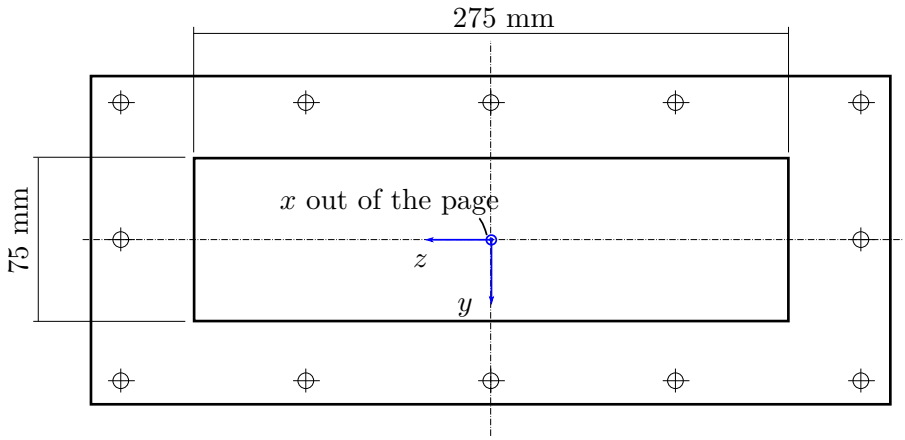

Figure 3.2: A close up view of the rectangular contraction outlet which has a height of 75 mm and a width of 275 mm. In this study, the coordinate system origin of the contraction is located at the centre of the contraction, as shown.

as $V_\infty = 0.74q$ where q is the fan speed in Hz. The maximum contraction outlet velocity of 38 m/s is achieved when the fan is driven at 51 Hz. The turbulence intensity decreases exponentially with increasing tunnel velocity. A minimum turbulence intensity of 0.4% occurs when the fan is driven between 40 and 51 Hz. These measurements were conducted at a lab temperature of 20 degrees Celsius and an atmospheric pressure of 1.024 Bar (measured using a thermometer and a mercury barometer located in the lab). Day-to-day changes in these lab conditions would result in slightly different wind tunnel mean velocity and turbulence intensity properties, however the changes are not expected to alter the main results significantly.

Figure 3.4 shows the profiles of the mean velocity and the turbulence intensity across the exit plane of the contraction outlet in the y and z directions at $V_\infty = 38$ m/s. The results are repeated for various downstream stations, starting from $x = 0$ and repeating every 75 mm (a legend is shown in Figure 3.5). The profiles show that the outlet flow is highly uniform at locations up to 150 mm away from the exit plane in both the y and z directions.

Figure 3.5 shows the profile of turbulence intensity across the exit plane of the contraction outlet measured at the same streamwise locations. As expected, the turbulence intensity inside the potential core of the jet increases as the distance downstream from the contraction outlet increases. The maximum turbulence intensity is observed near the edges of the contraction outlet which indicate the presence of the turbulent shear layer around the potential core of the jet. The increasing turbulence intensity in the mid-span is a result of the shear layer descending into the mid-plane of the jet as the potential core reduces in size. The profiles indicate that at $x = 75$ mm, the turbulence intensity is approximately equal to that at $x = 0$ mm ($T.I. = 0.4\%$). Along with the mean velocity profiles, these results show that near optimal testing conditions (highly uniform flow, $T.I. = 0.4\%$) exist up to 75 mm from the contraction exit plane and that good testing conditions (highly uniform flow, $T.I. \approx 1\%$) are still available at 150 mm from the exit plane.

Similar properties were also observed at 15 m/s. Although these results are not presented here, they indicate that similar testing conditions can be expected for flow speeds between 15 to 38 m/s, although with a higher turbulence intensity at the outlet.

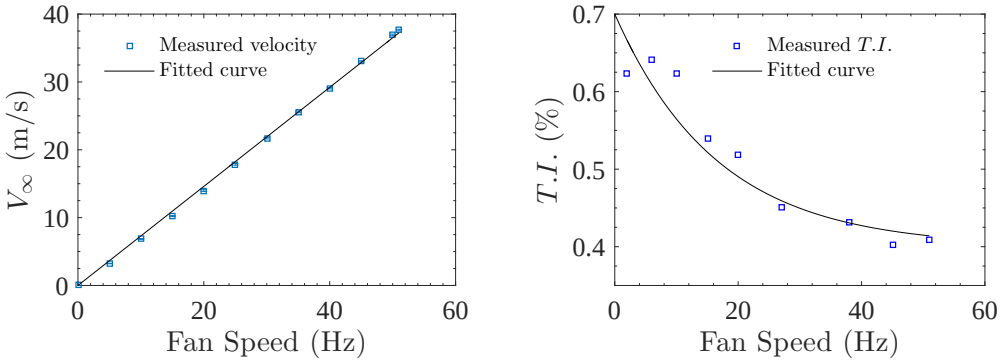

(a) V_∞ (m/s) (b) $T.I.$ (%)

Figure 3.3: The variation of mean velocity and turbulence intensity with fan speed at the centre of the AWT contraction outlet.

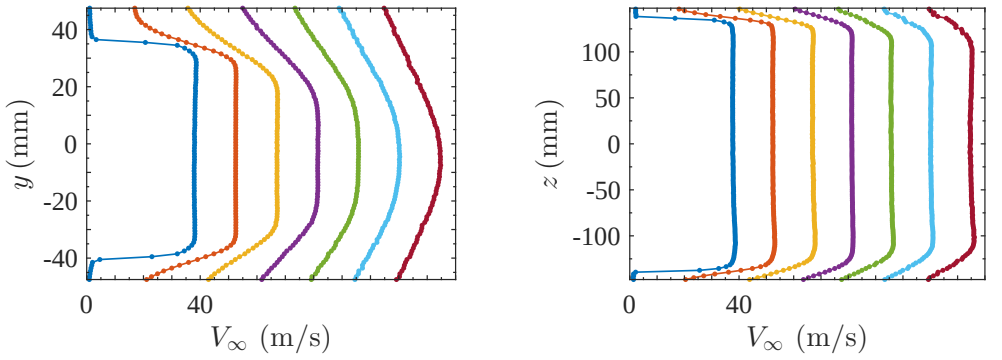

(a) y-direction (b) z-direction

Figure 3.4: The mean velocity profiles across the mid-plane of the contraction outlet at various downstream stations in (a) the z-direction and (b) the y-direction at $V_\infty = 38\,\mathrm{m/s}$. Each profile is displaced by 15 m/s from the previous profile.

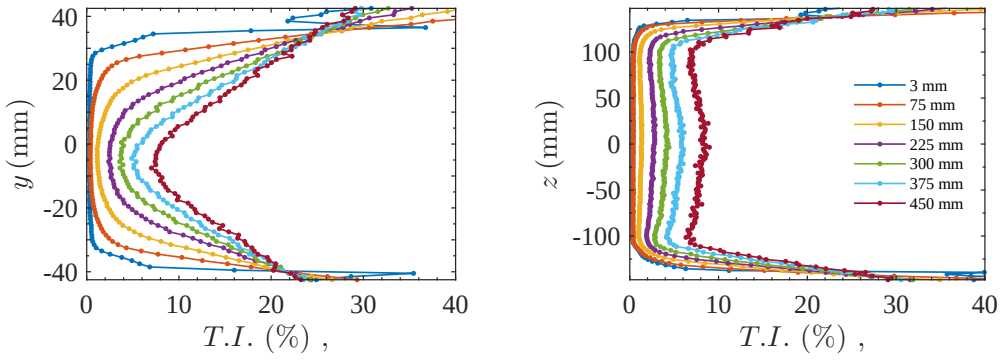

(a) y-direction (b) z-direction

Figure 3.5: The turbulence intensity ($T.I.$) profiles across the mid-plane of the contraction outlet at various downstream stations in (a) the y-direction and (b) the z-direction at $V_\infty = 38\,\mathrm{m/s}$.

Acoustic characteristics

To simulate an anechoic environment, the sound radiated by a monopole source must follow the inverse square law, i.e., the sound pressure level must reduce by 6 dB for a doubling of the distance. To test the free-field approximation of the acoustic chamber, a 6.5” loud

speaker was placed on the chamber floor and driven with white noise. Acoustic pressure fluctuations were recorded using a B&K 1/2" omni-directional condenser microphone (Model No. 4190) that was traversed in 50 mm increments along a vertical path from the centre of the speaker. Data were collected at 5×10^4 Hz for 8 s at each measurement location.

Figure 3.6 shows the variation of the sound pressure level in select $1/3^{\text{rd}}$ octave bands (denoted by their centre frequencies) with distance from the centre of the speaker. The black straight line indicates the theoretical free-field reduction of sound pressure level of 20 dB per decade. At 200 Hz there is deviation from the theoretical curve. However, the measured sound pressure level follows the free-field theory at 250 Hz and above, indicating that a suitable anechoic test environment is achieved above 250 Hz.

An important characteristic of the anechoic tunnel is the nature and level of the background noise in the tunnel when the flow is on. Background noise is mainly generated by the interaction of the contraction lip with the turbulent boundary layer generated on the contraction wall, fan noise or jet noise.

To measure the nature of the background noise, a 4190 1/2" B&K microphone was placed 500 mm directly underneath the centre of the contraction at $(x, y, z) = (0, 560, 0)$ so that the microphone position and flow direction made a 90° angle. Figure 3.7 shows the variation in overall sound pressure level, L_p, with contraction outlet velocity measured by this microphone. The overall sound pressure level scales proportionately with $V_\infty^{5.2}$. This suggests that the dominant source of background noise is trailing edge noise produced by the interaction of the turbulent boundary layer on the contraction walls with the outlet edges. This mechanism is similar to the noise generated by a semi-infinite flat plate of zero-thickness. Ffowcs-Williams and Hall (1970) showed that this noise scales proportionately with V_∞^5 to V_∞^6.

Figure 3.8 shows the background Power Spectral Density (PSD) measured by the same microphone for three different velocities. The background noise increases with increasing velocity, but is below 20 dB/Hz re. 20μPa[1] at 38 m/s for frequencies greater than 2 kHz. Additionally, there is evidence of low amplitude oscillations in the spectra for all velocities. These oscillations are caused by weak reflections off the acoustically untreated surfaces in the chamber (including the traverse and collector). This was determined by taking acoustic measurements with all untreated hard surfaces inside the chamber covered with additional sound absorption foam, which eliminated the oscillations. The oscillations do not appear to influence the acoustic measurements presented in this thesis.

3.2.3 Experimental equipment

AWT cylinder rig

A rig (called the 'cylinder rig') was used to test square FMWC models. The rig was designed to automatically change the aspect ratio of the cylinder in small increments so

[1]The Power Spectral Density (PSD) is a measurement of the rate of change of mean-square pressure with frequency, and hence its units are Pa^2/Hz. When presenting as a log-scale, the $\text{PSD}_{\text{dB}}(f)$ is defined as $\text{PSD}_{\text{dB}}(f) = 10 \log 10(\text{PSD}(f)/P_{ref}^2)$. Hence the units are 'dB/Hz'. Strictly speaking then, the reference value of $\text{PSD}_{\text{dB}}(f)$ is $4 \times 10^{-10} \mu\text{Pa.}^2$/Hz. However, there is a widely adopted convention to quote the units as 'dB/Hz' and the reference value as 20μPa. This thesis will follow this convention.

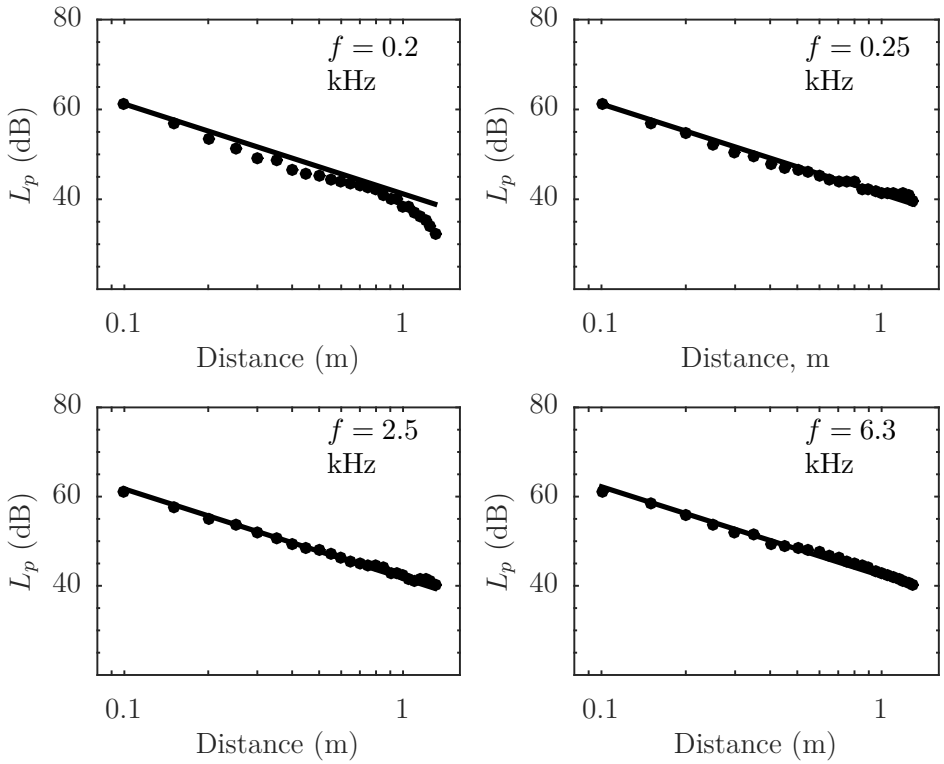

Figure 3.6: The decay of overall sound pressure level, L_p in dB re. 20μPa, of white noise driven through a speaker with distance from the microphone, which is placed directly above the speaker.

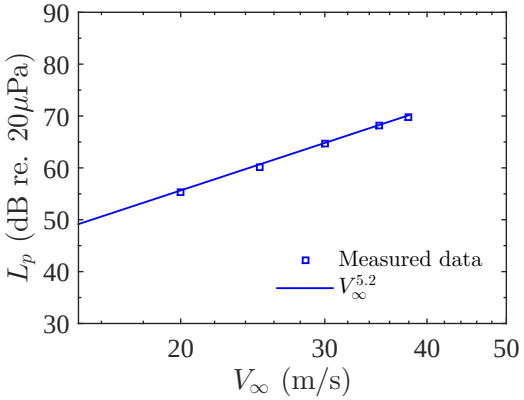

Figure 3.7: The variation of overall sound pressure level, L_p, in dB re. 20μPa, with contraction outlet velocity, measured by a 4190 B&K microphone located at $(x, y, z) = (0, 560, 0)$).

that a large amount of data could be taken efficiently. A schematic diagram of the rig is shown in Figures 3.9 and 3.10. A stepper motor is used to rotate a 300-mm threaded rod with an 8-mm pitch via a helical shaft coupling. As the threaded shaft rotates, a lead screw transfers the rotational motion into linear motion. The lead screw is fastened onto a small acrylic plate, where a 300-mm-long square cylinder with a width of 7 mm is mounted at one end. The cylinder is driven linearly through a square hole in a flat plate made from 10-mm-thick aluminium. The aluminium plate measures 150 mm in the

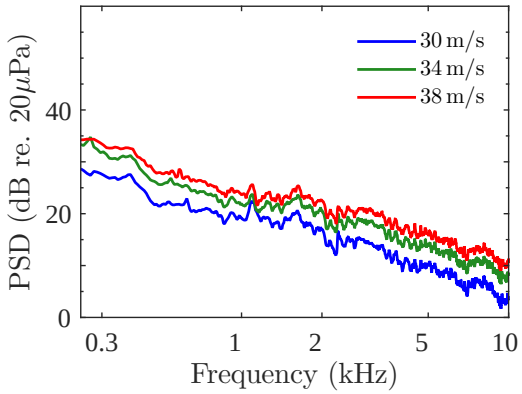

Figure 3.8: Background PSD in dB/Hz re. 20 μPa as measured by the B&K 1/2" microphone located at $(x, y, z) = (0, 560, 0)$.

downstream ('x') direction and 300 mm in the cross-stream ('y') direction while the hole is located in the centre of the plate, 43 mm downstream from where the plate bolts to the contraction. The maximum wetted length of the cylinder is 160 mm. The flat plate has a 90-degree elbow and is mounted onto the contraction outlet flanges such that the surface of the flat plate is flush with the inner sidewall of the contraction outlet. The acrylic plate that holds the lead screw and the cylinder is also connected to a linear bearing mounted on an additional aluminium shaft to ensure the cylinder tracks smoothly.

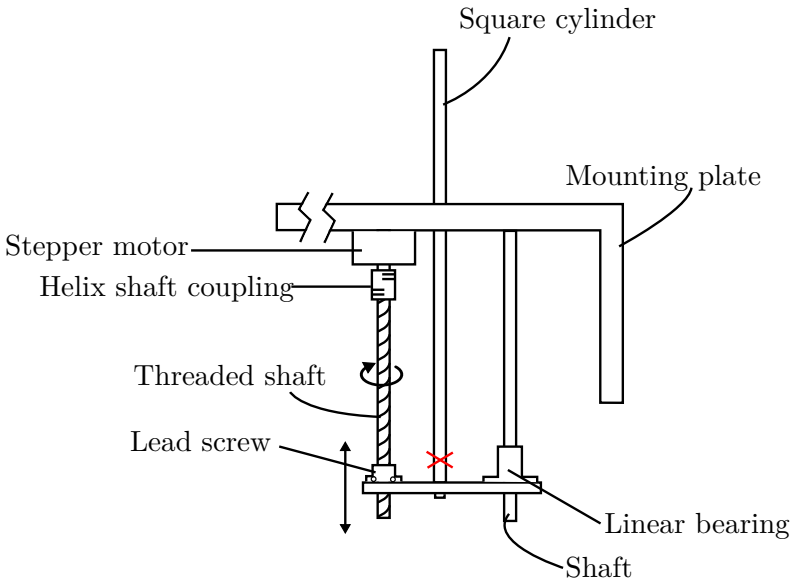

Figure 3.9: A schematic of the rig constructed to automatically change the aspect ratio of the cylinder. The red cross indicates the location of the accelerometer.

The stepper motor was controlled via an Arduino Uno microcontroller with an Adafruit Motor Shield. Tethered communication with the microcontroller was facilitated using the MathWorks Arduino I/O package.

The rig needed to be calibrated to quantify the lead i.e., the unit displacement of the cylinder per revolution of the stepper motor. To do this, the rig was mounted in position inside the AWT. A common off-the-shelf laser range-finder (Bunnings type Model Number 446000060L) was placed on a tripod outside of the AWT approximately 1.7 m away from the cylinder rig. The range-finder estimates a distance to an object by sending a laser

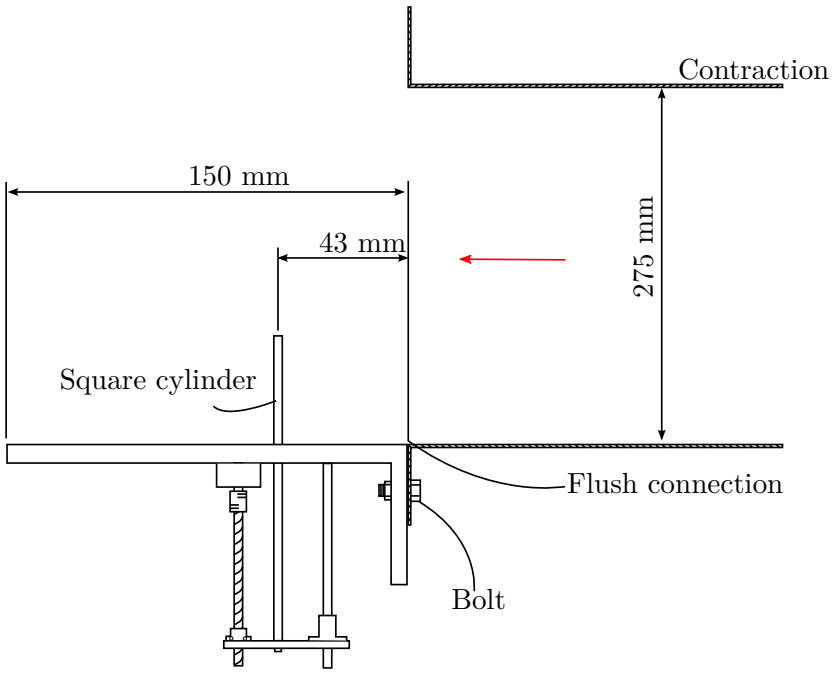

Figure 3.10: An illustration of how the cylinder rig is flush mounted to the contraction outlet via a bolted connection.

pulse toward the object and measuring the time taken for the pulse to be reflected off the target with a reported precision of ±0.05 mm. The stepper motor was then rotated by 200, 100 and 50 steps. For each rotation, the change in distance was recorded by the range finder. To reduce random error caused by the range finder, the calibration was repeated four times with each position being measured five times in each trial.

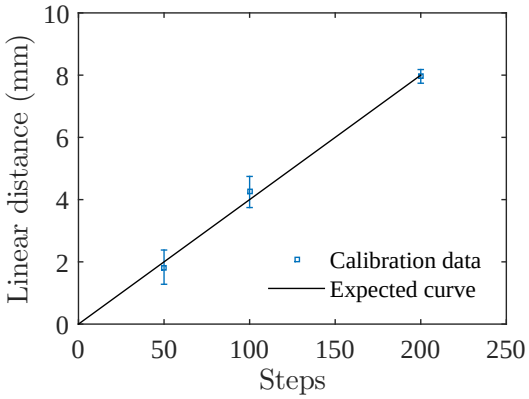

Figure 3.11: The cylinder rig calibration curve measured with a laser range-finder. The measured points (in blue) coincide well with the expected relationship (in black) based on the pitch of the lead screw.

Figure 3.11 shows the variation of the average linear distance travelled with the number of steps rotated. The error bars denote the 95% confidence interval of $2\sigma_p$ where σ_p is the standard error of the mean across the four trials (see Section 3.4 for details of how the uncertainty in the mean was calculated). The curve compares favourably with the expected relationship of 8 mm per revolution (200 steps) based on the pitch of the lead screw, thus demonstrating the good performance of the system. However, from the magnitude of the error bars shown, it could be concluded that the possible random error

of the system is in the order of 0.5 mm for a 90-degree rotation (50 steps of the stepper motor). An error of this magnitude is unacceptable since the errors may compound with each successive movement of the cylinder. For example, if 80 movements were used to reach a cylinder length of 160 mm, the error would be of the order of 40 mm if each movement had a random error of 0.5 mm. In order to test whether the random error in Figure 3.11 was actually due to random errors in the system or merely random errors in the measurement device (i.e., the rangefinder), 80 quarter rotations (nominal linear displacement of 2 mm per quarter rotation) were used to reach a nominal cylinder length of 160 mm. After the 80 quarter rotations were completed, the length of the cylinder was measured using a ruler with 1-mm increments (hence a precision of 0.5 mm). The process was repeated 10 times. Each time, a length of 160 ± 0.5 mm was recorded by the ruler, demonstrating that the error bars in Figure 3.11 are caused by random errors in the measuring device and not in the actuation process. The actual uncertainty in the movement of the system is estimated to be $\pm 0.5/80 = \pm 6.25 \times 10^{-3}$ mm for every 2 mm of linear motion.

An FWMC in cross-flow is subject to vortex induced vibration through the periodic forcing of the structure by vortex shedding (Kitagawa et al. 1999). According to Bearman (1984), the wake formation process will be altered when the cylinder experiences resonance due to vortex induced vibration. This would consequently impact the flow-induced noise mechanisms.

To measure vortex induced vibration effects, the cylinder rig vibration spectrum was recorded for a range of aspect ratios at several different tunnel velocities using a 5 mm diameter accelerometer. The accelerometer was located on the quiescent side of the cylinder, at the position marked 'x' in Figure 3.9. This allowed measurement of the vibration spectrum while not altering the vortex formation process on the part of the cylinder immersed in the flow. Velocities where the root-mean-square of the vibration dramatically increased were those for which resonance occurred, i.e., the frequency of vortex shedding was close enough to the natural frequency of the rig to significantly increase the vibration and potentially alter the far-field flow induced noise.

Figure 3.12 shows the variation in the magnitude of the accelerometer root-mean-square output voltage with cylinder length and tunnel velocity. Since the accelerometer was not amplitude calibrated, all measurements are normalised by the maximum level detected (so that all values lie between 0 and 1). Resonance only occurred below 30 m/s as evidenced by the appearance of large amplitude vibration between 80 and 120 mm.

This resonance was confirmed to be caused by the vortex shedding frequency coinciding with the cylinder rig natural frequency, as shown in Figure 3.13a. Here, the natural frequency of vibration and its harmonics are displayed against the cylinder length for a flow speed of 25 m/s (in dB/Hz re. 20μV) where the highest amplitude vibration occurs at a cylinder length of approximately 90 mm. The frequencies where tonal noise is generated (and hence vortex shedding occurs) is also displayed, shown as the black dotted lines and labelled 'FWMC acoustic tones'. The acoustic tonal frequencies coincide with the natural frequency of the structure at a cylinder length of 90 mm, causing excitation of all of the higher frequency modes and consequently a large amplitude vibration.

Conversely, at speeds above 30 m/s, only low amplitude vibration is detected. At this speed the vortex shedding frequency has increased (because the free stream velocity has

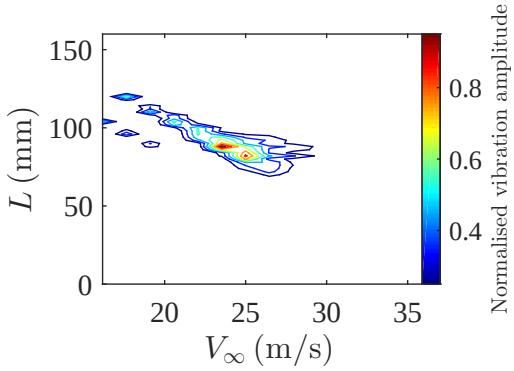

Figure 3.12: The cylinder rig vibrational characteristics.

increased) so that it lies between the fundamental and second harmonic. This is shown Figure 3.13b at a tunnel velocity of 37 m/s. Here the aeroacoustic tones do not coincide with the natural frequency of the structure. Williamson (1989) demonstrates that placing the vortex shedding frequency between the fundamental and the second harmonic of the vibration spectrum will minimise the influence of vibration on the vortex shedding process. Hence at tunnel velocities above 30 m/s, vortex induced vibration of the cylinder does not influence the acoustic or aerodynamic results.

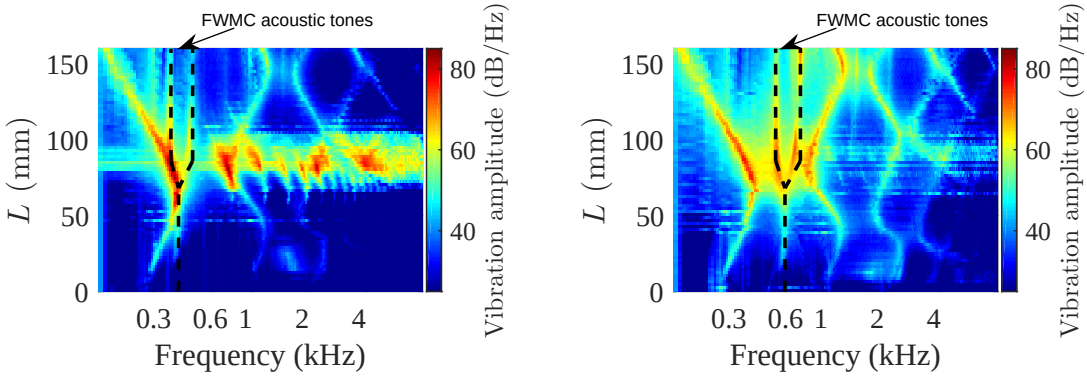

(a) $V_\infty = 25\,\mathrm{m/s}$ (b) $V_\infty = 37\,\mathrm{m/s}$

Figure 3.13: A spectral map of the vibration spectrum at (a) $V_\infty = 25\,\mathrm{m/s}$ and (b) $V_\infty = 37\,\mathrm{m/s}$. The results are expressed in dB/Hz re. 20μV.

The Anechoic Wind Tunnel traverse

A Dantec Dynamics 3-axis robotic traverse (model 41T33), sketched in Figure 3.14, is located inside the AWT test chamber. The traverse was used to automatically move both the microphone, during directivity measurements (discussed in Section 3.2.4), and the hot-wire, during wake velocity measurements (discussed in Section 3.2.5).

The traverse is controlled with an 'isel' Microstep controller (model C142-4.1) located outside of the chamber. Commands are sent from a PC to the controller via an RS232 serial connection. With this controller, the mounting plate on the traverse can be independently moved in three-orthogonal directions as shown, with a range of 610 mm in each direction. According to the documentation, the traverse has a positional accuracy of 6.25 μm. The x-axis of the traverse is aligned parallel to the streamwise direction of the flow.

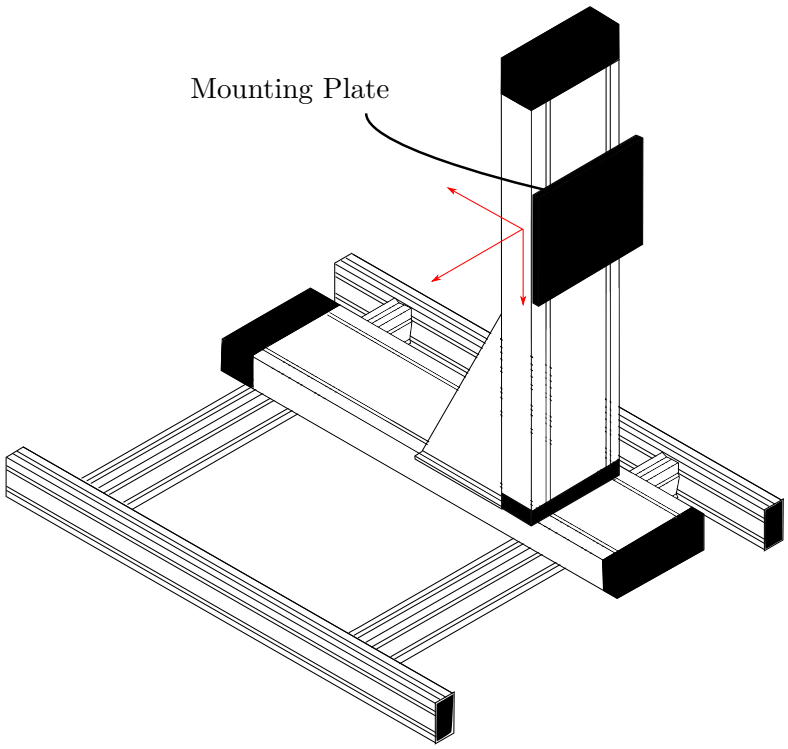

Figure 3.14: An illustration of the traverse used to mount the B&K microphones for directivity measurements and the hot-wire for wake measurements.

The Anechoic Wind Tunnel data acquisition system

The AWT data acquisition system (DAQ) is used to collect data from both microphones and hot-wires and thus gathered data from all sensor types used for the experiments in the AWT (Experiment 1).

The DAQ has an 8-slot National Instruments PXI Express Chassis (Model PXIe-1082) housing five PXIe-4499 simultaneous sample and hold ADC cards for data acquisition. Each card is DC coupled, has inbuilt automatic anti-aliasing filters, 24-bit quantisation resolution and a maximum input range of $\pm 10\,\mathrm{V}$. Since each card can accept 16 analogue inputs, the system can sample a maximum of 80 channels simultaneously at full bandwidth. This means that single microphone, microphone array and hot-wire data can be collected simultaneously.

3.2.4 Microphone measurements

Microphone models and experimental details

Microphone measurements were made using two types of microphones; (1) a B&K 1/2" type 4190 condenser microphone for directivity measurements and (2) several G.R.A.S. 40PH array microphones for single microphone and array measurements. Details of the microphone array are given in Chapter 4.

The B&K 1/2" type 4190 microphone was powered using a B&K 4 channel microphone power supply (Type 2829). The voltage signals were transmitted via coaxial cables to the data acquisition system described in Section 3.2.3. According to the transducer documentation, B&K 1/2" 4190 microphones have a frequency response that is flat (to

within ±0.4 dB) at frequencies from 20 Hz to 20 kHz, covering the frequency range of interest in this thesis (300 Hz to 10 kHz).

The G.R.A.S. 1/4" 40PH microphones were powered using an excitation current provided by the DAQ system. According to the transducer documentation, G.R.A.S. 1/4" 40PH microphones have a frequency response that is flat (to within ±1 dB) for frequencies from 20 to 10 kHz.

A schematic diagram of the experimental set up for all the microphone measurements is shown in Figure 3.15. Single microphone measurements were taken using one of the G.R.A.S. microphones in the array. The plane of the array was 0.5 m above the cylinder. The microphone that was chosen to take single microphone measurements was a microphone that lay directly above the cylinder face, in the middle of the contraction i.e., at location $(x, y, z) = (43, -500, 0)$ in the contraction coordinate system. In total, single microphone measurements were taken for 80 different aspect ratio cylinders for each boundary layer (yielding a total of 160 different single microphone measurements). Each measurement was sampled at 2^{15} Hz for 30 seconds. The array was covered 25 mm thick sound absorbent foam (EchoSorb 25 with a sound absorption coefficient of 0.8 at 500 Hz) to prevent spurious reflections from the fibreboard layer underneath from reaching the G.R.A.S. microphones.

For the directivity measurements, the B&K microphone was attached to an aluminium rod that was attached to the traverse. The traverse was programmed to move the microphone in a circular arc around the cylinder. This centre of this arc was at the cylinder position, had a radius of 510 mm, commenced at an angle of 40° from the horizontal and ended at 110° from the horizontal. Eight measurements were taken within this arc for each cylinder that was measured. Each measurement was sampled at 2^{15} Hz for 30 seconds. In total, 8 different aspect ratio cylinders were measured for two boundary layer conditions, yielding a total of 16 different directivity measurements. More details on the aspect ratio and boundary layers used in the experiments are given in Section 3.6.

Calibration

To provide end-to-end mechanical calibration of the microphone and measurement chain, a piston phone calibrator (B&K Type, serial number 723888) was used to provide a sinusoidal input with an amplitude of 95.4 dB re. 20μ.Pa at 1000 Hz. The sensitivity was calculated by first filtering the signal between 300 and 2000 Hz using a 6^{th}-order Butterworth filter, calculating the root-mean-square value of the filtered time signal and comparing it with the theoretical amplitude of 95.4 dB re. 20μ.Pa. The resulting sensitivity of the B&K microphone was measured at 43.1 mV/Pa. This sensitivity was calculated at lab conditions of 21 degrees Celsius and 1.024 Bar. According to the transducer documentation, the response of B&K 4190 microphones vary by -.007 dB/°C and -0.01 dB/kPa. The lab conditions during the experiment varied by less than 1 °C and 1 kPa so no change microphone sensitivity was expected during the experiment.

End-to-end mechanical calibration of the array microphones (G.R.A.S) was not performed because it was too difficult to accurately calibrate the microphones *in-situ* using a piston phone calibrator. Instead, each microphone's nominal sensitivity based on the information given in their data sheet was used to convert the measured voltage

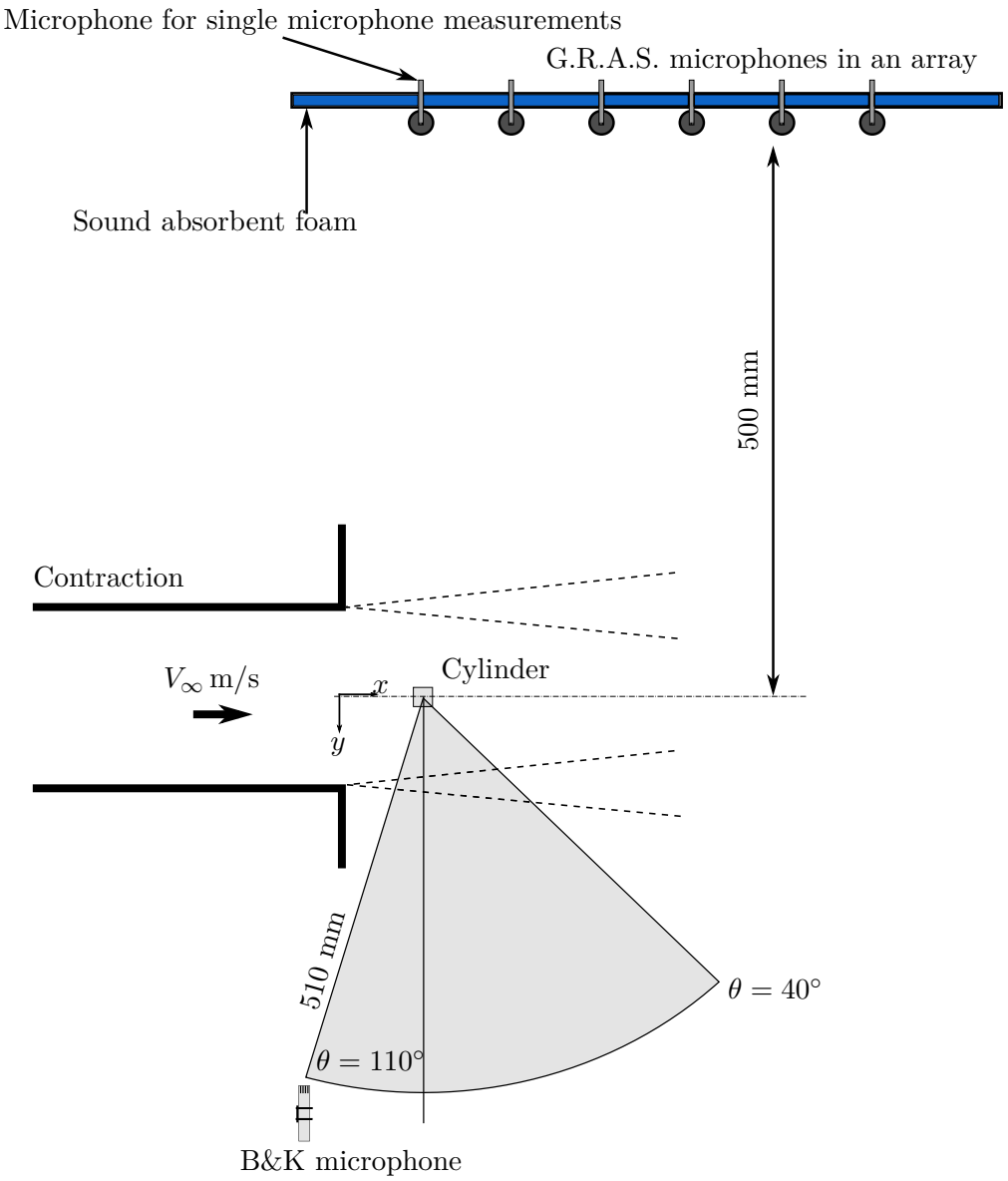

Figure 3.15: A schematic diagram of the experimental set-up used for the acoustic measurements.

to pressure (the nominal sensitivity was approximately 50 mV/Pa depending on the particular microphone). A Monte-Carlo analysis was then performed to understand how errors in the assumed properties of the microphones then propagated to errors in the amplitude and location estimates of source in the resulting beamforming maps. A similar analysis was performed for phase variations between each of the microphones. The details and results of this Monte-Carlo analysis is outlined in Section 4.

3.2.5 Hot-wire anemometry

Hot-wire anemometry was used to perform a wake survey of the streamwise velocity downstream of the FWMCs. A hot-wire is a thin cylindrical wire made from tungsten or platinum (or platinum alloys) that is kept at a constant temperature by placing it in one arm of a Wheatstone bridge. When air flows over the wire, heat transfer from the wire will act to reduce the wire's temperature and unbalance the bridge. By simultaneously powering the wire and supplying it with current at the same rate at which heat is lost,

the bridge can re-balance itself at a rate much faster than the smallest eddies in the flow and the temperature of the wire can be kept virtually constant in time. The heat loss from the wire (which is directly proportional to the bridge voltage) is then monotonically related to the velocity of the flow through simple thermodynamics.

Hot-wire properties and experiment details

A Dantec Dynamics single miniature hot-wire (model 55P16) was used for the wake survey. These hot-wires are made from platinum plated tungsten, have a diameter of $5\,\mu$m and a wire length of 1.25 mm. The hot-wire was held in an aerodynamic probe support constructed from a 3-mm-diameter aluminium rod with a 90-degree bend. This rod was secured to a 20×20-mm solid steel square bar that was bolted to the Dantec traverse, allowing the hot-wire to move in all three directions. The set-up is illustrated in Figure 3.16.

The hot-wire was used to survey the wake behind 8 different aspect ratio cylinders for two different boundary layers, yielding a total of 16 different wake surveys. More details on the aspect ratios and boundary layers used can be found in Section 3.6. The measuring plane behind each aspect ratio cylinder was a grid of points that measured 50 mm in the streamwise (x) direction and the spanned of the cylinder in the span-wise (z) direction. The measuring plane began at approximately 0.2 mm from the trailing edge of the cylinder and 2 mm above surface of the plate (see Figure 3.16). Additionally, the measurement plane was located at $y/W = 0.6$ to avoid entering the reverse flow region. The grid increments were $\Delta x = \Delta z = 2$ mm. A hot-wire velocity record was taken at each node in the grid. Each velocity record was sampled at 2^{15} Hz for 15 seconds.

Anemometer system

An IFA300 Constant Temperature Anemometer system was used to control the hot-wire. The IFA300 contains the Wheatstone bridge circuit and a signal conditioner that automatically low-pass filters the analogue signal to avoid spectral fold-back. An important feature of the IFA300 is that it automatically optimises the frequency response of the of the bridge and prevents current oscillations that may damage the sensor. It does this by constantly monitoring the bridge voltage and feeding the signal back to the amplifier circuit to maintain an optimum response. Consequently, the system does not require manual tuning via conventional methods such as a square wave test using the method of Bruun (1995).

Calibration

The hot-wire was calibrated inside of the AWT instead of a dedicated calibrator. This type of *in-situ* calibration was preferred because the orientation of the hot-wire could be kept constant throughout the wind tunnel experiment. A hot-wire is weakly sensitive to yaw and pitch components of velocity (Perry 1982). Therefore, if a hot-wire is calibrated in a nominal orientation, any deviation of the hot-wire position from this nominal orientation will be reflected in the relationship between the bridge voltage and the free-stream velocity (the calibration function). Hence, *in-situ* calibration can eliminate probe misalignment error.

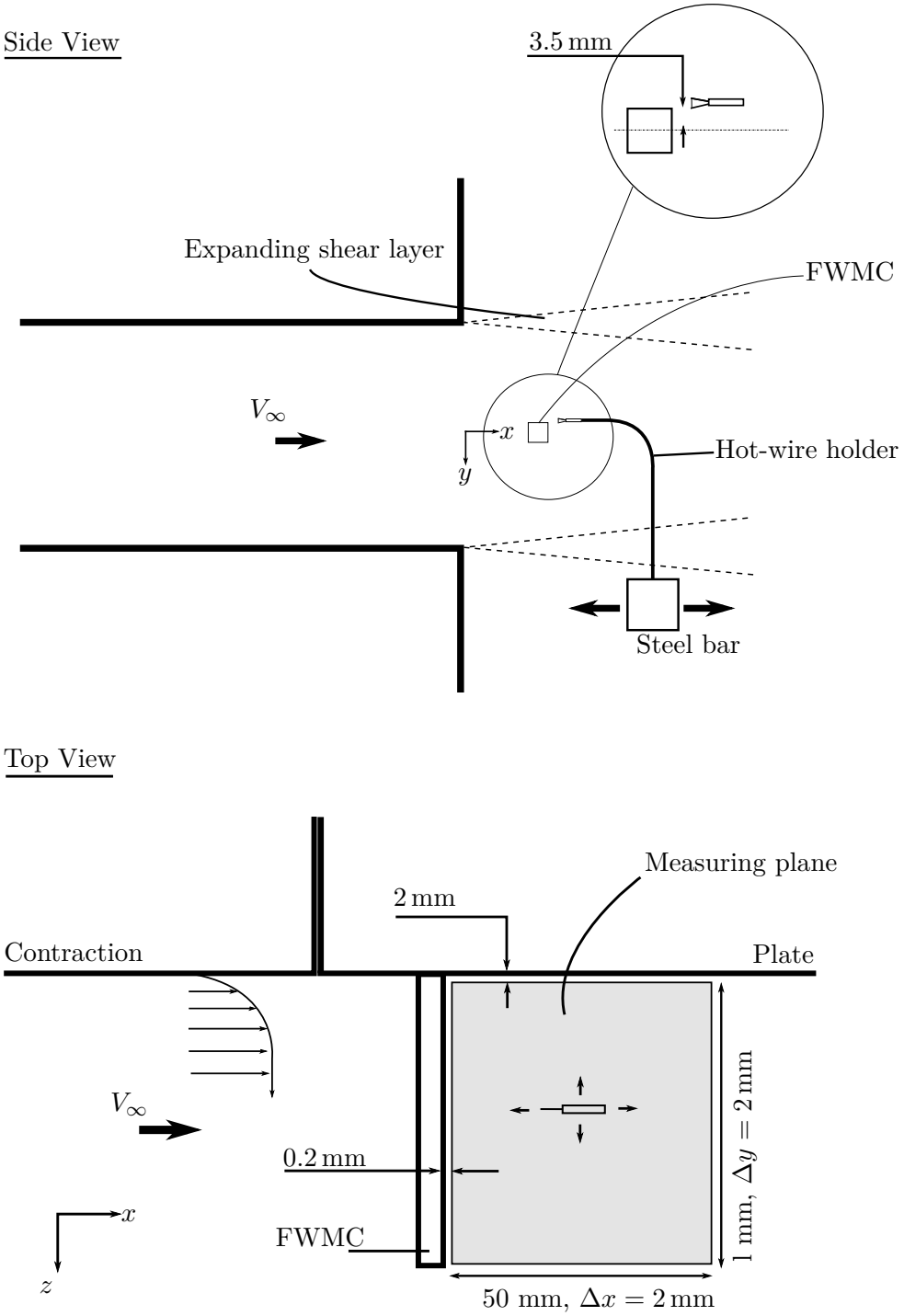

Figure 3.16: A schematic diagram of the experimental set up for the hot-wire wake survey measurements.

To create the calibration function, the hot-wire was placed on the traverse arm and positioned in the potential core of the wind tunnel (approximately 10 mm away from the contraction exit plane). The wind tunnel was then run at 11 different velocities ranging from zero to 38 m/s. The velocity of the tunnel was monitored using a Pitot tube connected to a 10-Torr MSK Baratron pressure transducer via 5-m-long plastic tubing with an outer diameter of 5 mm. A 5^{th}-degree polynomial was then fitted through the points to obtain the calibration function, $u = f(E)$, relating the air velocity normal to the hot-wire (in this case the streamwise velocity), u, to the bridge voltage, E. A 5^{th} order polynomial data reduction was used because it minimises linearisation[2] errors over other functional forms such as King's Law, cubic spline interpolation or lower order polynomials (Perry 1982). Two calibration curves were generated for every cylinder wake that was surveyed - one curve before the survey and one directly after. These two calibration curves were averaged to obtain the final calibration curve for each cylinder wake survey.

Bruun (1995) suggests that the maximum velocity used in the calibration routine be as high as 1.5 times the maximum velocity used for experiments. Since the experimental free stream velocity was set at 32 m/s, the *in-situ* calibration process described above did not provide an adequate calibration velocity range because the maximum speed of the tunnel was only 38 m/s. To overcome this, velocities that lay beyond the calibration range were extrapolated from the calibration function. Extrapolation is not usually recommended for hot-wire measurements because large linearisation errors can occur. However, in this study a customised technique, known as the 'modified extrapolation method', was developed to minimise the linearisation errors for velocities beyond the calibration range and is outlined below.

Suppose a polynomial calibration curve, $u = f(E)$, has been created between bridge voltages E_{min} and E_{max} giving corresponding velocities of u_{min} and u_{max}. A voltage $E_1 > E_{max}$ is converted to a velocity by first using the original transfer function, $u_a = f(E_1)$. A second data reduction is then performed by calculating the derivative of the transfer function, $B = \partial f(E)/\partial E|_{E=E_{max}}$ at $E = E_{max}$. The second velocity, u_b, is calculated as $u_b = B(E_1 - E_{max}) + u_{max}$. The final reduced velocity is given as the average of u_a and u_b.

This procedure was tested outside of the wind tunnel in a TSI manual velocity calibrator (Model 1128). A calibration was performed between velocities of 0 to 60 m/s. The calibration curve, however, was only generated using points between 2 and 38 m/s, simulating an AWT calibration. Velocities that lay outside of this range were reduced using the extrapolation procedure described above. The extrapolated relative linearisation error, ϵ_{lin}, calculated as the difference between the extrapolated values and the true values normalised by their velocity, are shown in Figure 3.17. This figure also shows the relative linearisation error for velocities that lie in the calibration range. By using the extrapolation technique described above, the linearisation errors are reduced to levels that are comparable with velocities that lie inside the calibration range. The errors associated with conventional extrapolation techniques, i.e., simply using the original transfer function in an extended domain, are also shown. By comparison the linearisation errors associated with the conventional extrapolation technique are much higher than

[2]The term 'linearisation' is often used to refer to data conversion even though the calibration function is not linear.

the modified extrapolation technique used in this study.

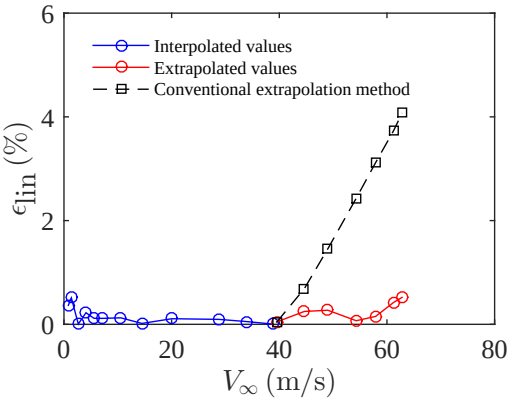

Figure 3.17: The linearisation error of the hot-wire using the modified extrapolation technique.

Sources of experimental error in hot-wire velocity measurements and corrections

Experimental error in hot-wire velocity measurements is the uncertainty of an individual velocity measurement after it has been converted from a voltage reading. This is different to the uncertainty of statistical quantities, such as mean, variance, autospectra etc., which are discussed in Section 3.4.

There were several sources of experimental error during the FWMC hot-wire measurements. These included error associated with hot-wire drift, temperature variations, linearisation, digital quantisation, probe alignment and calibration error. In the following discussion, the uncertainty of each contribution is expressed as a *relative variance* (the relative standard deviation squared) based on an assumed probability distribution of each error. The total experimental error of a hot-wire velocity measurement is then calculated using the Law of Propagation of Errors.

Hot-wire drift Hot-wire drift is the unquantifiable change of the metallurgic properties of the hot-wire during an experiment. This can be caused by many factors including build-up of particulate matter on the hot-wire probe. There is no known way to counter hot-wire drift. In Experiment 1, the drift error was reduced by calibrating the hot-wire before and after every wake survey (yielding 16 pairs of calibration curves) and averaging the result. The velocity uncertainty due to hot-wire drift was calculated using the technique described below.

Suppose the hot-wire is calibrated before a measurement time t_1 and calibrated after at t_2. In between these two times, at time $t_1 < t < t_2$, a hot-wire measurement is made. When converting the recorded voltage into a velocity, u_1 is obtained using the calibration function created at t_1 and u_2 is obtained when using the calibration function created at t_2. The goal is to calculate the velocity, u_3, at time t based on the values of u_1 and u_2.

Intuitively, u_3 must lie between u_1 and u_2 if the drift is linear (which is the only sensible assumption). Thus, a simple way to calculate u_3 is to take the average of u_1 and u_2 using

$$u_3 = \frac{u_1 + u_2}{2}. \tag{3.1}$$

Furthermore, u_3 is unlikely to take the value of either u_1 or u_2 (since the hot-wire calibration function has drifted). To capture this, it is assumed that the velocity at time t has a triangular probability density function between u_1 and u_2, and u_3 is the velocity at the apex of this distribution, as shown in Figure 3.18. A triangular distribution implies that the probability that the velocity is u_1 or u_2 is zero and is maximum at u_3.

For a triangular probability distribution, the expected value of velocity, $\mathrm{Exp}(u)$, is

$$\mathrm{Exp}(u) = \int_{-\infty}^{\infty} up(u).du = \frac{u_1 + u_2 + u_3}{3} \tag{3.2}$$

and the variance, $\mathrm{var}_{drift}(u)$, is given by

$$\mathrm{var}_{drift}(u) = \int_{-\infty}^{\infty} [u - \mathrm{Exp}(u)]^2 p(u).du = \frac{u_1^2 + u_2^2 + u_3^2 - u_1u_2 - u_1u_3 - u_2u_3}{18}. \tag{3.3}$$

When $u_3 = (u_1 + u_2)/2$ (as in Equation 3.1) is substituted into Equation 3.3, the variance is

$$\mathrm{var}_{drift}(u) = \frac{-6u_1u_2 + 3(u_1^2 + u_2^2)}{72}. \tag{3.4}$$

In other words, for any given pair of calibration curves, if the velocity at any time between when the calibration curves were measured using Equation 3.1, the variance due to drift is calculated by Equation 3.4.

It should be noted that Equation 3.3 is a quadratic with respect to u_3. It is trivial to show that the velocity at the vertex of this quadratic is in fact $u_3 = (u_1 + u_2)/2$. Therefore, Equation 3.4 actually represents the *maximum possible* variance of the velocity due to hot-wire drift (given the assumptions regarding the probability density). If u_3 were chosen based on different rule, say a linearly weighted average of u_1 and u_2 based on the time that has elapsed from t_1, then u_3 would be different to Equation 3.1. According to Equation 3.3 the variance of u_3 would be lower and so too the relative uncertainty at that particular measurement point. In this study Equation 3.1 was used because the time elapsed between calibrations was not recorded.

Figure 3.19 shows Equation 3.4 (normalised by the square of the velocity) for the 16 different pairs of calibration curves at select velocities between 10 to 45 m/s. For all curves except two, the maximum relative variance of the velocity due to drift was less than 0.0001 over all velocities concerned. For the remaining two curves, indicated in the Figure, the relative variance tends towards 0.0015 and 0.005 respectively, which are an order of magnitude larger than their counterparts. These curves correspond to measuring FWMCs with aspect ratios of $L/W = 21.4$ in a high boundary layer (HTB) and $L/W = 10$ in a low boundary layer (LTB) respectively. While these errors are high, it should be noted that these represent the maximum possible uncertainty in the velocity measurements due to drift and most of the measurements for these cylinders will have errors significantly less than these values.

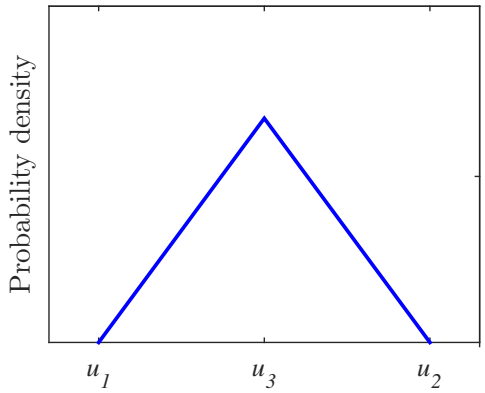

Figure 3.18: The assumed probability density function of a hot-wire velocity measurement, u_3, given by Equation 3.1, that lies between u_1 and u_2.

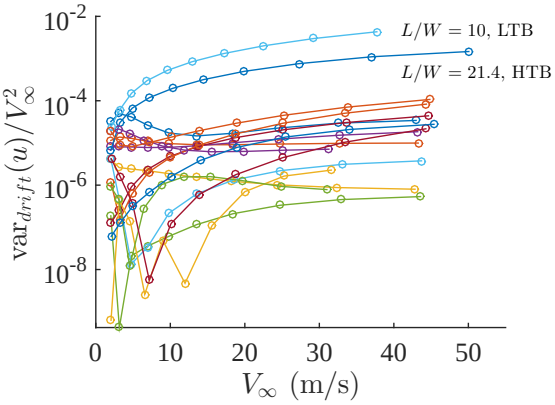

Figure 3.19: The magnitude of the maximum possible relative variance due to hot-wire drift using Equation 3.4 as a function of velocity.

Linearisation error Linearisation error has already been discussed. The maximum relative difference between the linearised values and the true values is approximately 0.25% for $5 < V_\infty < 60$. Therefore, it is assumed that a linearised velocity value may take, with equal probability, a quantity that is ±0.25% within that of the true value, i.e., the value has a rectangular probability distribution with a half width of 0.25%. Hence the relative variance of linearisation error is $\mathrm{Var}_{Linearisation}(u)/V_\infty^2 = 0.0025^2/3 = 0.0000021$.

Probe misalignment Similar to linearisation error, probe misalignment error must be addressed. Probe misalignment error is the error caused by using the hot-wire in a slightly different orientation to when it was calibrated. In Experiment 1, by calibrating the hot-wire *in-situ*, the orientation of the hot-wire was exactly the same as that for calibration. Hence, the probe misalignment error is $\mathrm{var}_{Alignment}(u)/V_\infty^2 = 0$.

Quantisation errors Quantisation errors are associated with the resolution of the ADC board. The uncertainty due to the finite resolution is stochastic with a rectangular distribution, the half width of which is equal to $b/2$ where b is the bit width. The bit width, $b = E_{AD}/(2^n - 1)$ where n is the resolution of the ADC and $E_{AD} = 10\,\mathrm{V}$ is its voltage input range. The relative variance of the velocity value due to this uncertainty

type is

$$\frac{\mathrm{var}_{ADC}(u)}{V_\infty^2} = \frac{1}{V_\infty^2}\frac{E_{AD}^2}{(2^n-1)^2}\left(\frac{\partial u}{\partial E}\right)^2. \tag{3.5}$$

In Experiment 1, a 24-bit data acquisition system was used. As such, the relative variance is of the order of $\mathrm{O}(10^{-14})$, regardless of what speed the hot-wire senses. Hence, the quantisation error can be ignored.

Temperature The temperature of the free-stream air during the experiment was not constant, and varied by a maximum of 4 degrees Celsius. Changes in the ambient temperature affects the rate of heat transfer from the wire and if the ambient temperature changes from calibration to experimental conditions then errors can be introduced. These errors were corrected following the procedure of Jørgensen (2002). For each voltage, the free-stream temperature was simultaneously measured using a k-type thermocouple located several 100 diameters downstream of the model. The original voltage, E, was then corrected to E_{corr} by applying a correction factor,

$$E_{corr} = \frac{a/\alpha}{a/\alpha + T_{ref} - T_{flow}}E, \tag{3.6}$$

where a is the overheat ratio of the hot-wire bridge ($a = 1.6$ in this study), α is the temperature coefficient of resistance ($\alpha = 3.6 \times 10^{-3}\,\mathrm{K}^{-1}$ in this study), T_{ref} is the temperature at calibration (21°C) and T_{flow} is the temperature when the voltage was measured. By applying this correction, the estimated uncertainty due to temperature variation is reduced to negligible levels, i.e., $\mathrm{var}_T(u)/V_\infty^2 \approx 0$.

Calibration error Calibration error is the uncertainty of the final reduced velocity measurement caused by the uncertainty of the input calibration points. That is, the velocity measured with a Pitot-static tube that the hot-wire references also has an uncertainty associated with it, which causes uncertainty in the calibration curve. This uncertainty is caused by higher than desired random turbulent fluctuations in the potential core of the jet and uncertainties in the free-stream reference values. Calibration errors are generally the largest contributor to hot-wire experimental relative variance and are typically assumed to be about 0.0001 for Pitot-static tube calibration (Jørgensen 2002). In this study, a more rigorous and novel approach to quantifying calibration uncertainty is undertaken in order to reduce it. This approach is based on the ISO/IEC Guide 98-1:2009 standard for evaluating the measurement uncertainty for multi-input, single output functions (Lira 2002).

Consider the functional form of the velocity calibration curve,

$$u = f(E, c_i) = c_0 + \sum_{i=1}^{i=5} c_i E^i, \tag{3.7}$$

where c_i are scalar coefficients and E is the input voltage. Classically, the coefficients c_i are found by a least squares adjustment using a $1 \times n$ vector of measured mean voltages, $\overline{\mathbf{E}}$, and mean Pitot tube velocities, $\overline{\mathbf{u}}_{pitot}$, where n is the number of measurements used for the curve fit. However, both $\overline{\mathbf{E}}$ and $\overline{\mathbf{u}}_{pitot}$ will have an uncertainty (variance) associated with their measurement. These are denoted $\mathrm{var}(\mathbf{E})$ and $\mathrm{var}(\mathbf{u}_{pitot})$ respectively and are

both $n \times n$ diagonal matrices. Hence each c_i will also have an uncertainty, var($\mathbf{c}$). This uncertainty is expressed as a 6×6 matrix with the off diagonal components corresponding to the covariance of each coefficient pairing and a diagonal corresponding to the variance of each coefficient. According to the ISO/IEC Guide 98-1:2009, the uncertainty matrix associated with the coefficients can be calculated as

$$\text{var}(\mathbf{c}) = [\mathbf{F}^T[\mathbf{D}\text{var}(\mathbf{E})\mathbf{D} + \text{var}(\mathbf{u}_{pitot})]^{-1}\mathbf{F}]^{-1}, \tag{3.8}$$

where

$$\mathbf{F} = \begin{bmatrix} 1 & E_1 & E_1^2 & \dots & E_1^5 \\ 1 & E_2 & \dots & \dots & E_1^5 \\ \vdots & \vdots & \ddots & ... & \vdots \\ 1 & E_n & \dots & \dots & E_n^5 \end{bmatrix},$$

for the n calibration voltage inputs and $\mathbf{D}$ is an $n \times n$ diagonal matrix with the i^{th} diagonal elements D_{ii} given by

$$D_{ii} = \sum_{j=0}^{5} j c_j E_i^{j-1}, \tag{3.9}$$

where E_i is the i^{th} element of the vector $\overline{\mathbf{E}}$. Using this procedure, the calibration error can be correctly quantified. As discussed, the bit error associated with ADC can be ignored. Hence the diagonal terms of the input variance, var($\mathbf{E}$), are simply the sample variances of the bridge voltage when the hot-wire is placed inside the flow. That is, the j^{th} diagonal element of var($\mathbf{E}$) is

$$\text{var}(\mathbf{E})_{jj} = \frac{1}{N-1} \sum_{k=1}^{N} E_{kj} - \overline{E_j}, \tag{3.10}$$

where $k = 1...N$ are the individual samples of the j^{th} voltage record. The output variance, var($\mathbf{u}_{pitot}$), has several sources since the velocity measured by the Pitot-static reference tube is a derived quantity based on measurements of the dynamic pressure, Δp, temperature, T_{flow}, the specific gas constant for air, $R = 287.058\,\text{J.kg}^{-1}\text{K}^{-1}$, and ambient pressure, P_{amb} according to

$$u_{pitot} = \sqrt{\frac{2\Delta p}{P_{amb}} R T_{flow}}, \tag{3.11}$$

which can be derived from Bernoulli's Equation. The General Error Propagation Formula (Lira 2002) states that the total uncertainty of a function with mutually uncorrelated inputs, z_i, is the sum of the individual uncertainty of the inputs multiplied by the square of the *condition number*, k_i^2, for each input, which is the square of the rate of change of the function with the i^{th} input. Mathematically, for the velocity based on the dynamic pressure, the j^{th} ($j = 1...n$) diagonal element of var($\mathbf{u}_{pitot}$) is

$$\mathrm{var}(\mathbf{u}_{pitot})_{jj} = \sum \mathrm{var}(z_i)k_i^2 = \Big(\frac{\partial u}{\Delta p}\Big)^2 \mathrm{var}(\Delta p)_j + \Big(\frac{\partial u}{T_{flow}}\Big)^2 \mathrm{var}(T_{flow})_j + \Big(\frac{\partial u}{P_{amb}}\Big)^2 \mathrm{var}(P_{amb})_j. \quad (3.12)$$

The uncertainty in j^{th} measurement of dynamic pressure, $\mathrm{var}(\Delta p)_j$, is the variance of the measured dynamic pressure, calculated using an equation similar to Equation 3.10. The temperature during calibration was measured using a thermometer which had a resolution of 0.5 degree Celsius and a rectangular probability distribution. Hence the variance of temperature was $\mathrm{var}(T_{flow})_j = 0.5^2/12\,\mathrm{C}^2$. Similarly, the ambient pressure was measured using a mercury gauge with increments of 5×10^{-4} mm.Hg and a rectangular probability distribution. Hence the variance in ambient pressure was $\mathrm{var}(P_{amb})_j = 5 \times 10^{-2}/12\,\mathrm{mm}^2.\mathrm{Hg}^2$.

Now reconsider the functional form of the velocity calibration equation, Equation 3.7. The data reduction process can be thought of as taking a perfectly known voltage, E (because the bit error is negligible), and 6 calibration coefficients with an uncertainty matrix $\mathrm{var}(\mathbf{c})$ and passing them through Equation 3.7 to calculate a velocity, u. The uncertainty in this velocity, $\mathrm{var}_{calibration}(u)$ (which is not the same as the variance of the reference velocities, $\mathrm{var}(\mathbf{u}_{pitot})$, used to calculate the calibration function), can be derived from the General Law of Error Propagation for correlated inputs (Lira 2002) as

$$\mathrm{var}_{calibration}(u) = \sum_{i=0}^{5} \Big(\frac{\partial u}{\partial c_i}\Big)^2 \mathrm{var}(c)_{ii} + 2\sum_{i=0}^{4}\sum_{j=i+1}^{5} \frac{\partial u}{\partial c_i}\frac{\partial u}{\partial c_j}\mathrm{var}(c)_{ij}. \quad (3.13)$$

Since Equation 3.7 is a polynomial, the condition numbers $\dfrac{\partial u}{\partial c_i} = E^i$. Hence, Equation 3.14 reduces to

$$\mathrm{var}_{calibration}(u) = \sum_{i=0}^{5} E^{2i}\mathrm{var}(c)_{ii} + 2\sum_{i=0}^{4}\sum_{j=i+1}^{5} E^{(i+j)}\mathrm{var}(c)_{ij} = \mathbf{E}^{\mathbf{T}}\mathrm{var}(\mathbf{c})\mathbf{E}, \quad (3.14)$$

where $\mathbf{E} = [1\ E^1\ E^2\ E^3\ E^5\ E^5]^T$.

The relative variance for several sets of calibration data, $\mathrm{var}_{calibration}(u)/V_\infty^2$, is plotted in Figure 3.20 as a function of velocity. This shows that the calibration variance is approximately 0.00003 for all velocities investigated, which is approximately 3 times less than what is conventionally assumed for Pitot-tube calibrations.

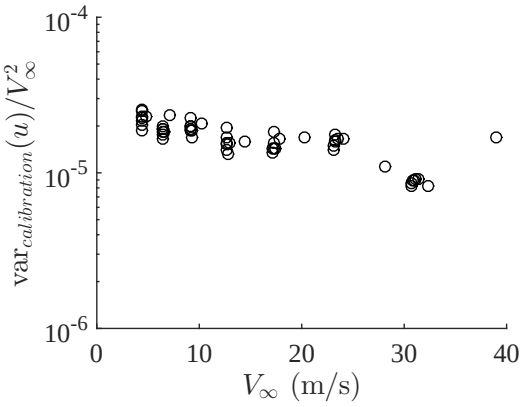

Figure 3.20: Calibration error of the hot-wire using the total expanded uncertainty method.

Total expanded uncertainty According to Lira (2002), by assuming that all sources of error are uncorrelated the total experimental uncertainty of the single hot-wire measurement can be calculated using

$$\epsilon_{total} = 2\sqrt{\sum \frac{\mathrm{var}_i(u)}{V_\infty^2}}. \tag{3.15}$$

where $\mathrm{var}_i(u)/V_\infty^2$ is the relative variance of the i^{th} source of error.

Table 3.3 summarises the magnitude experimental sources of error discussed previously. Note that temperature error, bit error and probe misalignment error were assumed to be 0%. The total relative uncertainty when a voltage is reduced into a velocity is approximately 2.3%.

Table 3.3: A summary of the major contributors to hot-wire measurement error.

Error source	Relative variance
Drift	0.0001
Linearisation	0.0000021
Calibration	0.00003
Temperature	0
Probe misalignment	0
Quantisation	0
Total expanded uncertainty	$\approx 2.3\%$

There are two exceptions to the estimated error quoted above. For $L/W = 10$ in the thin boundary layer, the larger drift error causes the velocity uncertainty to increase to a maximum of 14%. For the $L/W = 21.4$ case in the thick boundary layer, the experimental error is approximately 8%.

A comment on measuring velocity fluctuations in highly turbulent flows with a hot-wire

The final hot-wire-specific error type that will be discussed is the error caused when the hot-wire measures in regions where the turbulence intensity, $T.I. = \sigma/V_\infty > 0.3$. This

error is different to those described above because it is a source that causes averaging errors in statistical estimates rather than an uncertainty at any one individual data point. It is not, however, included in the next section (which deals with the uncertainty in statistical estimates of data record in general) because it is exclusive to only hot-wire measurements and not data records in general.

When a hot-wire is placed in highly turbulent regions, a combination of heat transfer non-linearities and quadratic non-linearities occur due to transverse components of velocity (Perry 1982). As well as the streamwise component of velocity, transverse components of velocity will also add to the heat transfer from the wire, essentially raising the effective cooling velocity. Bradbury (1976) models the effect of transverse components of velocity. In his analysis, the effective cooling velocity, V_e, is given by the Pythagorean sum of two velocity components, u (in the streamwise direction) and v (in the transverse direction), that are normal to the wire,

$$V_e = (u^2 + v^2)^{0.5}. \tag{3.16}$$

The probability density function of the turbulence, $p(u, v)$, is assumed to be Gaussian with a streamwise mean velocity and variance of V_∞ and σ^2 respectively and a transverse mean velocity and variance of 0 and $K^2\sigma^2$ respectively, where K is a scalar constant. Then, according to Bradbury (1976), the apparent mean velocity, V_a, sensed by the wire immersed in turbulent velocity field is given by

$$V_a = \int\int V_e p(u,v) du dv = \frac{1}{2\pi K\sigma^2} \int\int (u^2+v^2)^{0.5} e^{-(u-V_\infty)^2/2\sigma^2} e^{-v^2/2K^2\sigma^2} du dv. \tag{3.17}$$

Figure 3.21a and 3.21b presents the ratio of the actual streamwise velocity to the apparent mean velocity, V_∞/V_a, and the ratio of actual streamwise turbulence to apparent streamwise turbulence σ/σ_a, sensed by a hot-wire as a function of the apparent turbulence intensity of the velocity field, σ_a/V_a, using Equation 3.17. It is observed that as the apparent turbulence intensity increases, the apparent velocity deviates significantly from the true velocity. Similarly, for the apparent turbulence intensity, there is more deviation the higher the turbulence, although, surprisingly, the effect is less severe. For the orientation of the hot-wire in the current experiments (shown in Figure 3.16), the most important components of velocity are the streamwise components and the span-wise components that act parallel to the span of the cylinder. Wang and Zhou (2009) and Rostamy et al. (2013) show that the streamwise and span-wise components of fluctuating velocity in the free-end and junction of the square FWMC wake have approximately the same order of magnitude. This corresponds to a value of $K = 1$ in Equation 3.17. From the turbulence model, the error in the measured mean velocity would be approximately 8% at a longitudinal turbulence level of $\sigma = 0.35$. The error in the measured turbulence intensity would be approximately 5% at the same turbulence level.

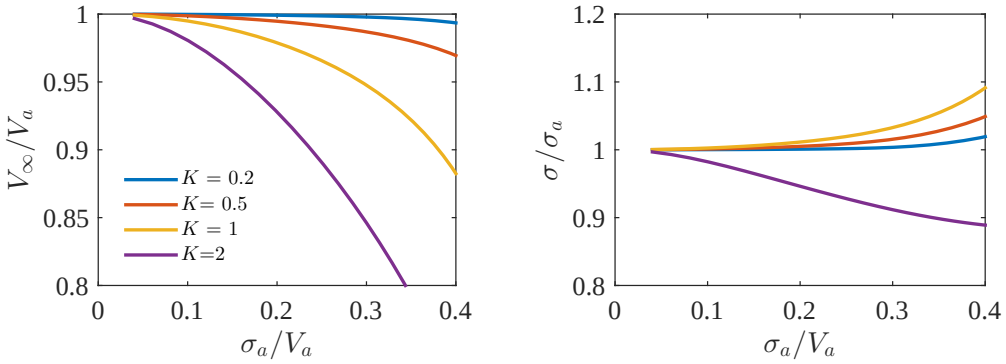

(a) Mean velocity (b) Turbulence intensity

Figure 3.21: (a) The ratio of true mean velocity to apparent mean velocity, V_∞/V_a, and (b) true velocity turbulence to apparent velocity turbulence, σ/σ_a, both as a function of the apparent turbulence intensity, σ_a/V_a, and degree of homogeneity of that turbulence that the hot-wire is immersed in, K.

3.3 Experiment 2

Experiment 2 was conducted in a second wind tunnel facility at the University of New South Wales (UNSW), known as the '18-inch Wind Tunnel' (18WT). The specifications 18WT are given in Section 3.3.1. The experiments conducted in the 18WT included surface pressure measurements (described in Section 3.3.2) and surface flow visualisation (described in Section 3.3.3).

3.3.1 Facility description

The 18WT is an open-circuit, suction-type, closed-test-section wind tunnel with a working section that measures 460×460 mm and a maximum velocity of 29 m/s. Air first passes through a four flow smoothing screens before entering a contraction with a contraction ratio of 5.5 and subsequently passing through the test section. The air is drawn through the wind tunnel by an 8-blade, 5.5-kW axial fan located downstream of the test section. Afterwards, the air is ejected through a vertical diffuser. The longitudinal turbulence intensity the air at 15 m/s (the speed for which the surface pressure and flow visualisation experiments were conducted) is approximately 0.5%, which is comparable to the turbulence intensity measured in the AWT at 32 m/s. A schematic diagram of the wind tunnel is provided in Figure 3.22.

3.3.2 Surface pressure measurements

Cylinder models

The FWMC models used for surface pressure measurements were 3D printed out of ABS plastic using an 'Ultimaker^2' 3D printer. Two models were printed: (1) a model that had an aspect ratio of $L/W = 4$ and (2) a model that had an aspect ratio of $L/W = 12.5$. The widths of the FWMCs were 12 mm. Each model was printed with a series of internal vanes that ran from the base of the cylinder to a number of pressure taps located on one of the cylinder side faces. The pressure taps each had a diameter of 1 mm and the vanes had an inner diameter of 1.5 mm. The $L/W = 4$ cylinder has 8 pressure taps while the

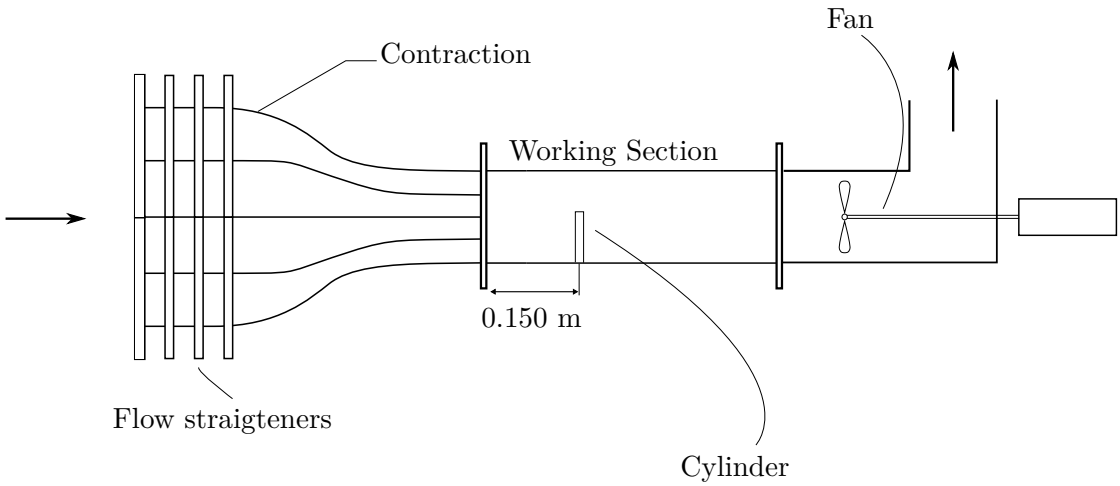

Figure 3.22: A schematic diagram of the 18WT.

$L/W = 12.5$ FWMC has 7 pressure taps. The pressure taps were evenly spaced in the spanwise direction of the cylinders and located directly in the centre of the side face.

The FWMCs were printed such that they could be pressed through a 12×12 mm hole located in the floor of the working section. The square hole was such that the cylinder and the hole made an interference fit. The hole was located 150 mm from the end of the contraction. The aspect ratio of each FWMC could be lowered by reducing the length of the cylinder exposed to the flow. Once an aspect ratio had been chosen, the cylinder was clamped outside of the wind tunnel to prevent any movement. It should be noted that because each of the two printed FWMC models had a fixed number of pressure taps, the number of pressure taps exposed to the flow changed when the aspect ratio was changed.

Pressure sensor

Static and fluctuating pressure was measured using a Scanivalve Digital Sensor Array (DSA), model number 3217/16 Px (Serial No. 10136). The DSA has 16 transducer channels. Each channel has a temperature compensated piezoresistive pressure sensor and measures differential pressure relative to a common reference pressure port. The module also contains a 16-bit ADC and interfaces with a computer through TCP/IP communication protocol. Pressures are recorded at a maximum rate of 500 samples/second/channel. The differential input pressure range of the DSA is ± 2.5 kPa.

In this study, each pressure port in the FWMC was connected to a channel of the DSA via PVC tubing, with an inner diameter of 1.53 mm. The PVC tubing was carefully cut so that the total length from the pressure tap to each channel of the DSA was 600 mm. The reference pressure port was connected to a static wall pressure tap on the roof of the 18WT test section.

According to the DSA calibration sheet, static readings of each channel of the DSA is accurate to within $\pm 0.09\%$ of the output. In this study, the dynamic response of the pressure tubing system was estimated using the approach of (Holman 2012). Here, the pressure amplitude ratio, P/P_0, of the tubing system is estimate using

$$\frac{P}{P_0} = \frac{1}{[(1-(\omega/\omega_n)^2)^2 + 4h_{damp}^2(\omega/\omega_n)^2)]^{0.5}}, \tag{3.18}$$

where ω_n is the natural frequency of the tubing system, h_{damp}, is the damping ratio of the tubing system and ω is the frequency of the signal. The natural frequency of the system, ω_n, is given by

$$\omega_n = \sqrt{\frac{3\pi r_{tube}^2 c_0^2}{4 L_{tube} V_{chamber}}}, \tag{3.19}$$

where r_{tube} is the radius of the tubing, L_{tube} is the length of the tubing, c_0 is the speed of sound and $V_{chamber}$ is the volume of the chamber just before the connection to the pressure transducer. The damping ratio, h_{damp}, is the given by

$$h_{damp} = \frac{2\mu}{\rho c_0 r_{tube}^3} \sqrt{\frac{3 L_{tube} V_{chamber}}{\pi}}, \tag{3.20}$$

where $\mu = 1.91 \times 10^{-5}\,\mathrm{kg/m.s}$ is the dynamic viscosity of air at 20 degrees Celsius and $\rho = 1.2\,\mathrm{kg/m^3}$ is the density of air at 20 degrees Celsius. Additionally, the phase, $\phi_{pressure}$, of the pressure signal is given by

$$\phi_{pressure} = \tan^{-1} \frac{-2h(\omega/\omega_n)}{1 - (\omega/\omega_n)^2}. \tag{3.21}$$

According to the transducer documentation, $V_{chamber} = 1.64 \times 10^{-7}\,\mathrm{m^3}$. Using $L_{tube} = 0.6\,\mathrm{m}$, $r_{tube} = 0.75 \times 10^{-3}\,\mathrm{m}$, the pressure and phase of the tubing system are calculated using Equations 3.18 and 3.21 and are shown in Figure 3.23.

In Figure 3.23 the natural frequency of the system is calculated to be approximately ω_n =1300 Hz while the damping ratio is approximately $h_{damp} = 0.063$. Bendat and Piersol (2010) recommend that for systems with low damping, the frequencies of interest must be less than 20% of the natural frequency. For the current system, this corresponds to a usable frequency range of less than 260 Hz. For the surface pressure experiments conducted in this study, the frequencies of interest where vortex shedding occurs, lie between 120 to 240 Hz depending on the aspect ratio. Thus, the system is suitable for dynamic pressure measurements in this case.

Furthermore, at the frequencies of interest, Figure 3.23 shows the amplitude distortion is less than 3.5% while the phase distortion remains less than 2 degrees and is close to

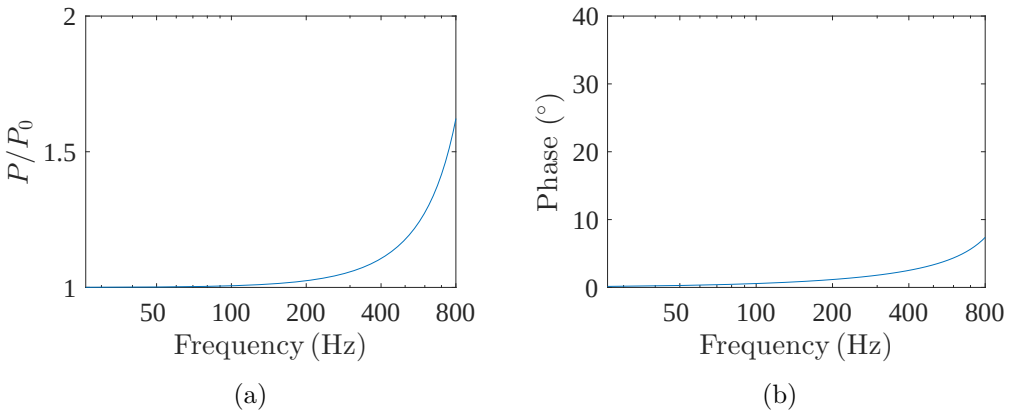

Figure 3.23: The amplitude (a) and phase (b) response of the pressure tubing system estimated using Equations 3.18 and 3.21.

linear (when plotted on a linear frequency scale). Thus, without correcting for these effects, the experimental error of the amplitude of the pressure measured by the Scannivalve is approximately ±3.5% across all frequencies.

3.3.3 Oil-film flow visualisation

Visualisation of surface flow topology over three-dimensional obstacles, i.e., visualising the location and nature of separation, reattachment and vortex cores on the body surface, is important to the overall understanding of the dynamics of the flow around the surface. Surface oil-flow visualisation (SOFV) is a technique that has been used extensively in the last 50 years to give a qualitative summary of the surface flow topology of various objects in cross flow (Lu 2010). With regards to FWMCs, Table 2.1 indicates that the technique has been used by a number of authors including Okamoto and Sunabashiri (1992), Kawamura et al. (1984), Lee (1997), Agui and Andreopoulos (1992), Uematsu et al. (1990) and Becker et al. (2002). Its popularity stems from the fact that SOFV is inexpensive, easy to use and gives consistent results which is advantageous when studying complicated three-dimensional flow. Table 2.1 also indicates that while the method is popular when used for examining the flow features of circular FWMCs, there are few studies that have applied the method to square FWMCs. This may be due to the recent shift to study square FWMCs with more elaborate quantitative diagnostic methods such as PIV (Bourgeois 2012; Wang et al. 2014). The drawback with high fidelity methods is that it is difficult and time consuming to investigate a higher number of L/W-δ/W combinations. To this end, SOFV is a very appropriate technique to visualise the impact that aspect ratio has on square FWMC flow to complement the hot-wire, surface pressure, microphone array and single microphone results.

The principle behind SOFV is that skin-friction lines will generally follow the surface streamlines (Lu 2010), except perhaps in the immediate region of separation (Maltby 1962). This means that the skin-friction topology is largely indicative of the behaviour of the flow streamlines close to the wall and therefore the flow around the body. Consequently, a thin fluid (a paint or 'oil-suspension') that is applied to the surface of the body will, in-principle, approximately follow the local streamlines before evaporating. The residual pattern left by the pigment resembles the surface flow pattern.

The challenge with SOFV is to prepare a paint that (1) has the correct consistency to follow the flow, (2) dries quickly enough so that experiments do not take a long time, (3) leaves streaks that are bold enough to be photographed, (4) does not run until the desired wind speed has been reached and (5) is largely unaffected by gravity (Maltby 1962). There is no one oil-suspension mixture that satisfies all these requirements and many different 'recipes' exist. As noted by Lu (2010), a trial-and-error process often occurs to educe a suitable mixture of pigment and oil. This was extensively carried out for the present investigation using a variety of oils, alcohols and pigments. It was found that the best paint was obtained by saturating ethanol with hydrated magnesium silicate (Talcum power). To achieve the best photographic conditions, the models and base of the test section were covered in black adhesive paper. The best photographic results were obtained by placing a light tent around the model (after the tunnel was switched off) and taking the photograph with the model *in-situ*.

Experimental set-up

For the SOFV experiments, the floor of the working section was covered in a thin layer of black plastic film to enhance the visibility of the oil-film pigment. A square cylinder made from ABS plastic that measured 12 mm×12 mm was pushed through the same square hole used for the pressure measurements to create the FWMC. The cylinder was allowed to move in and out of the hole to change the aspect ratio of the FWMC. Once an aspect ratio had been chosen, the junction of the cylinder was clamped on the outside of the wind tunnel to prevent any movement of the FWMC. The maximum aspect ratio that could be achieved was $L/W = 12.5$.

Prior to wind tunnel operation, the oil-suspension mixture was applied to the surface of the cylinder model and to the test section floor upstream and downstream of the FWMC. The wind tunnel speed was then quickly ramped up to 15 m/s. Once the solution had settled the wind tunnel was stopped. The light tent was then placed around the FWMC and still photographs were then taken with a Nikon D70s DSLR camera located directly above the FWMC.

Oil-film methodology validation

A qualitative and quantitative validation of the oil-film mixture and methodology was conducted to ensure that the selected oil-pigment suspension gave results comparable with those found in the literature. Here, SOFV was carried out on a $L/W = 1$ square cylinder (a cube) at a Reynolds number of 3.6×10^4. The boundary layer thickness for this case was $\delta/W \approx 0.5$. The resulting streak patterns, shown in Figure 3.24c are compared with that of a similar experiment conducted by Martinuzzi and Tropea (1993) at similar experimental conditions and the result of a DNS computation by Yakhot et al. (2006) at a lower Reynolds number.

It is evident that the current methodology gives qualitatively similar results to the validation cases. There are several features that consistently occur in all three of the images. The first is two lines of separation upstream of the cylinder, denoted 'A' and 'B' in the validation case (Figure 3.24c), that wrap around the base of the cylinder in the classical 'horseshoe' shape. The second is two pairs of counter rotating foci, labelled N_1 and N_2 in the validation case, that occur in the wake of the cylinder and on top of the free-end of the cylinder respectively. The third is back-flow over the free-end of the cylinder that begins at the trailing edge of the free-end and ends near N_2.

A quantitative validation was also conducted. This was done by comparing the magnitude of three parameters in each of the images. These were the distance between the first and second separation point in the plane of symmetry, denoted D_1, the distance from the leading edge to the point where the wake reaches maximum contraction, denoted D_2 and finally the minimum distance of the two opposing shear layers in the wake of the cylinder, denoted D_3. These three parameters are compared in Table 3.4. Excellent agreement is achieved between the results of Martinuzzi and Tropea (1993) and the present study. Good agreement between the results of Yakhot et al. (2006) and the present study are achieved for D_2 and D_3, however, the agreement is poor for D_1. This is attributed to the much lower Reynolds number and much higher relative boundary layer in the simulated results of Yakhot et al. (2006).

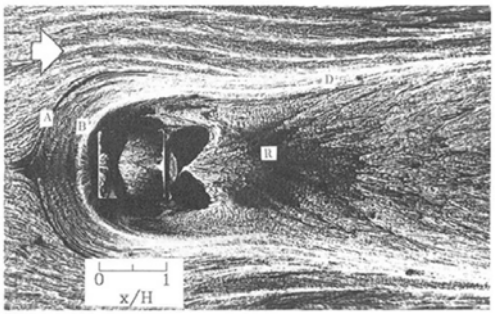

(a) Martinuzzi and Tropea (1993)

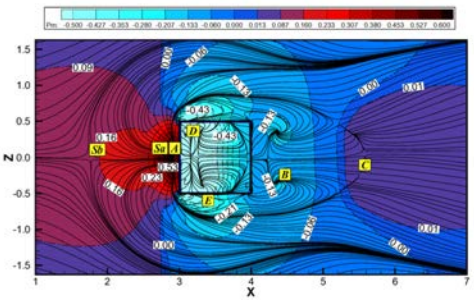

(b) Yakhot et al. (2006)

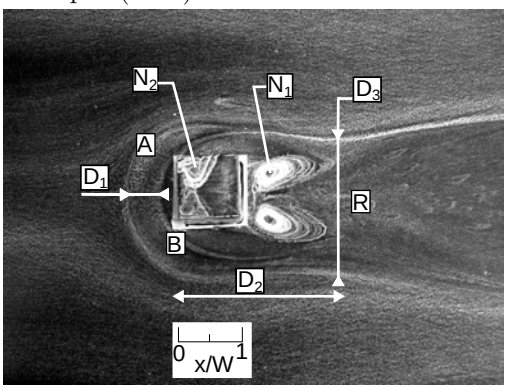

(c) Present study, $\delta/W = 0.5$

Figure 3.24: A comparison of the surface streak-lines of a square FWMC with $L/W = 1$ between this study ($L/W = 1$, $\delta/W = 0.5$, $Re_W = 3.6 \times 10^4$) and the results of Martinuzzi and Tropea (1993) ($L/W = 1$, $\delta/W = 1$, $Re_W = 4 \times 10^4$) using an oil-film method and Yakhot et al. (2006) ($L/W = 1$, $\delta/W = 1.5$, $Re_W = 0.2 \times 10^4$) using DNS.

Table 3.4: A comparison of several wake length scales for an FWMC of $L/W = 1$ between the present study and two different studies by Martinuzzi and Tropea (1993) and Yakhot et al. (2006).

	$Re_W(\times 10^4)$	δ/W	D_1/W	D_2/W	D_3/W
Martinuzzi and Tropea (1993)	4	1	0.6	2.6	2.2
Yakhot et al. (2006)	0.2	1.5	1	2.6	2.5
Validation case	3.6	0.5	0.6	2.6	2.3

3.4 The uncertainty of statistical quantities

Several statistical quantities will be used to describe the stochastic data sets obtained with the hot-wire, microphone and surface pressure data records, presented in Chapters 5 and 6. These quantities include mean, variance, cross-correlation, probability distribution, cross-spectral density, coherence and phase.

Because data records are sampled discretely, taken over a finite time, T_{acq}, and sometimes contain data that are correlated with itself, the true statistical quantity of a random process that generates the data, x, labelled $\Phi(x)$, can only be *estimated* within an interval with a certain level of confidence using an 'estimator', $\hat{\Phi}(x)$. The interval width depends on the mean square error (MSE) of $\hat{\Phi}$. The MSE of an estimator is equal its variance, var($\hat{\Phi}$), plus a biasing factor. In most of the cases described (with a few exceptions), the estimates are *unbiased* for all practical considerations meaning that the MSE is the variance of each estimator.

The following will outline the equations used to calculate the MSE of each of the aforementioned statistical quantities. The actual numerical value of the error of an individual data point will depend on a number of parameters specific to that measurement (e.g., the time integral scale, the variance, the sampling time, etc.) that may not be universal over all data points presented. Thus, the numerical error of individual data points (that use the aforementioned statistical quantities) are quoted as they are presented in Chapters 5 and 6 and reference the equations outlined here.

3.4.1 Mean estimator, $\hat{\bar{x}}$

According to Bendat and Piersol (2010), an unbiased estimate of the mean of a process x, discretely sampled with N samples is given as

$$\hat{\bar{x}} = \frac{1}{N}\sum_{i=1}^{N} x_i, \tag{3.22}$$

where x_i are the sampled data points, also known as the 'data set' (this convention will be used herein). Generally, the samples used to estimate the mean will be correlated. The variance of the mean of correlated data is given by (Loucks et al. 2005)

$$\mathrm{var}(\hat{\bar{x}}) = \frac{\sigma_x^2}{N}(1 + 2f_s\int_0^\infty \rho_x(\tau).d\tau) = \frac{\sigma_x^2}{N}(1 + 2f_s T_I), \tag{3.23}$$

where $\rho_x(\tau)$ is the correlation coefficient function, f_s is the sampling frequency and σ_x^2 is the true variance of the data set. The integral of $\rho_x(\tau)$ with time is called the integral time scale, T_I. Equation 3.23 shows that correlation of the data with itself will increase the uncertainty of the mean. Intuitively this makes sense because a faster sampling time does not reduce the error in the mean estimate unless the sampling time is simultaneously increased to allow more uncorrelated data points to be part of the estimate. In Equation 3.23, the variance of the data set, σ_x^2, must be estimated from the data set using the estimator, described below.

3.4.2 Variance estimator, $\hat{\sigma_x^2}$

According to Bendat and Piersol (2010), an estimate of the true variance, σ_x^2, of a set of data is given by

$$\hat{\sigma_x^2} = \frac{1}{N-1}\sum_{i=1}^{N}(x_i - \hat{\bar{x}})^2. \tag{3.24}$$

When the signal is correlated with itself, this estimate is unbiased for large N. As mentioned, it is practical to use the estimate $\hat{\sigma_x^2}$ to calculate the variance of the mean estimator. However, it should be noted that $\hat{\sigma_x^2}$ is itself an estimate and is also subject to uncertainty. For large N and correlated samples, Loucks et al. (2005) derives that the variance of the $\hat{\sigma_x^2}$ is given by

$$\mathrm{var}(\hat{\sigma_x^2}) = 2\frac{\sigma_x^4}{N}(1 + 2f_s\int_0^\infty \rho_x^2(\tau).d\tau). \tag{3.25}$$

Indeed, this equation uses the true value of the data variance in its formulation, as do

most of the expressions for estimated variance. Hence it is important to remember that the quoted uncertainties for the statistical quantities presented here are only educated approximations of the order of magnitude of the error.

3.4.3 Correlation function estimates, $\hat{Z}_{xy}(\tau)$

An unbiased estimate of the cross-correlation between two jointly stationary random processes x and y is (Bendat and Piersol 2010)

$$\hat{Z}_{xy}(m\Delta t) = \frac{1}{N-m}\sum_{n=1}^{N-m} x_{n+m}y_n, \tag{3.26}$$

for the time lag of $m\Delta t$ and $m = 0, 1, 2, 3, 4.....r$, where $r < N$ and $\Delta t = 1/f_s$ where f_s is the sampling frequency. The cross-correlation coefficient used to calculate the integral time scale is estimated as (Bendat and Piersol 2010)

$$\hat{\rho}_{xy}(m) = \frac{\hat{Z}_{xy}(m)}{\frac{1}{N}\sqrt{\sum_{i=1}^{N}(x_i)^2\sum_{i=1}^{N}(y_i)^2}}. \tag{3.27}$$

The autocorrelation is found when $y = x$. For bandlimited Gaussian white noise, the normalised variance of the cross-correlation is (Bendat and Piersol 2010)

$$\frac{\mathrm{var}(\hat{Z}_{xy}(m))}{Z^2_{xy}(m)} = \frac{1}{N_I}[1 + \rho^{-2}_{xy}(m)], \tag{3.28}$$

where $N_I = \dfrac{T_{acq}}{2T_I}$ and T_{acq} is the total aquisition time of the record. Finally, because $\mathrm{var}(bx) = b^2\mathrm{var}(x)$ for any scalar b, it can be shown that

$$\frac{\mathrm{var}(\hat{\rho}_{xy}(m))}{\rho^2_{xy}(m)} = \frac{1}{N_I}[1 + \rho^{-2}_{xy}(m)], \tag{3.29}$$

i.e., the autocorrelation and correlation coefficient have the same relative error.

3.4.4 Probability distribution function estimates, $\hat{\mathrm{Prob}}(x)$

An estimate of the Probability Distribution Function (PDF) of a data set is (Bendat and Piersol 2010)

$$\hat{\mathrm{Prob}}(x, W_b) = \frac{N_x}{f_s T_{acq}}, \tag{3.30}$$

where T_{acq} is the total sampling time, W_b is the width of the bin where data are to fall into, N_x is the number of accumulated data points x_i that fall between $x - W_b/2$ and $x + W_b/2$, and f_s is the sampling frequency. The PDF is a measure of how likely the value of x is to fall between $x - W_b/2$ and $x + W_b/2$. The estimate is unbiased and the variance of $\hat{\mathrm{Prob}}(x, W)$ is (Bendat and Piersol 2010)

$$\mathrm{var}(\hat{\mathrm{Prob}}(x, W_b)) = \frac{\mathrm{Prob}(x, W_b)(1 - \mathrm{Prob}(x, W_b))}{N_I}. \tag{3.31}$$

3.4.5 Cross-spectra estimates, $\hat{G}_{xy}(f)$

In this study, auto and cross-spectra are estimated using Welch's averaged modified periodogram method (Welch 1967). The time records are split into a number of overlapping blocks (or 'sub-records'), B, and a window function, $w(t)$, is applied to each individual sub-record to avoid spectra leakage due to truncation. The cross-spectral density at frequency discrete f_k is estimated using

$$\overline{G}_{xy}(f_k) = \frac{2}{\omega_0 BH} \sum_{i=1}^{B} X(f_k) Y^*(f_k), \tag{3.32}$$

where

$$X(f_k) = \sum_{n=0}^{H-1} w_n x_n e^{-j2\pi f_s^{-1} f_k n} \tag{3.33}$$

is the H-point discrete Fourier transform of the data set $x(t)w(t)$, $Y(f_k)$ is the discrete Fourier transform of the data set $y(t)w(t)$, the superscript * denotes complex conjugation, f_s is the sampling frequency, H is the number of data points in each block and ω_0 is a weighting constant that depends on the window function. The frequency resolution, Δf, obtained using this method is given by

$$\Delta f = \frac{f_s}{H}. \tag{3.34}$$

The number of averaging blocks can be calculated with (Yardibi et al. 2010),

$$B = 1 + \frac{T_{acq} f_s / H - 1}{1 - v/100}, \tag{3.35}$$

where is the T_{acq} is the acquisition time and v is the percentage overlap of each block. When the data sets x and y are equal, then Equation 3.32 gives the autospectral density. The relative variance of the autospectral density is given by (Bendat and Piersol 2010),

$$\mathrm{var}(G_{xx}(f)) = \frac{1}{\omega_0 B}. \tag{3.36}$$

The variance of the magnitude of the cross-spectral density is given as (Bendat and Piersol 2010),

$$\mathrm{var}(|G_{xy}(f)|) = \frac{1}{\gamma_{xy}^2(f) \omega_0 B}, \tag{3.37}$$

where $\gamma_{xy}^2(f)$ is the magnitude squared coherence function, defined below.

Magnitude squared coherence estimates, $\hat{\gamma}_{xy}^2(f)$

According to Bendat and Piersol (2010), an unbiased estimate of the magnitude squared coherence is,

$$\hat{\gamma}_{xy}^2(f) = \frac{|\hat{G}_{xy}(f)|^2}{\hat{G}_{xx}(f)\hat{G}_{yy}(f)}. \tag{3.38}$$

The variance of $\hat{\gamma}_{xy}^2(f)$ is (Bendat and Piersol 2010),

$$\mathrm{var}(\hat{\gamma}^2_{xy}(f)) = \frac{2\gamma^2_{xy}(f)(1-\gamma^2_{xy}(f))^2}{\omega_0 B}. \tag{3.39}$$

A bias in the estimated γ^2_{xy} may occur due to the finite propagation time, τ, between signals x and y. For this case, the multiplicative bias factor is calculated as

$$\hat{\gamma}^2_{xy}(f) = \left(1 - \frac{f_s \tau}{H}\right)^2 \gamma^2_{xy}. \tag{3.40}$$

3.4.6 Phase angle estimates, $\hat{\phi}_{xy}(f)$

According to Bendat and Piersol (2010), an unbiased estimate of the phase angle between two random processes at a particular frequency is

$$\hat{\phi}_{xy}(f) = \tan^{-1} \frac{\mathrm{Im}(\hat{G}_{xy}(f))}{\mathrm{Re}(\hat{G}_{xy}(f))}. \tag{3.41}$$

The variance of the phase estimate is (Bendat and Piersol 2010)

$$\mathrm{var}(\hat{\phi}_{xy}(f)) = \frac{(1-\gamma^2_{xy}(f))}{\gamma^2_{xy}(f) 2\omega_0 B}. \tag{3.42}$$

3.5 Coordinate system when presenting results

Unless otherwise stated, the formal coordinate system used in this thesis is fixed to the FWMC as shown in Figure 3.25. The origin is taken at the junction of the FWMC, centred on the FWMC axis. The x-direction runs parallel with the free-stream flow, the z-direction runs parallel with the span of the FWMC and the y-direction runs orthogonal to both, in the cross-stream direction. Figure 3.25 illustrates the coordinate system used.

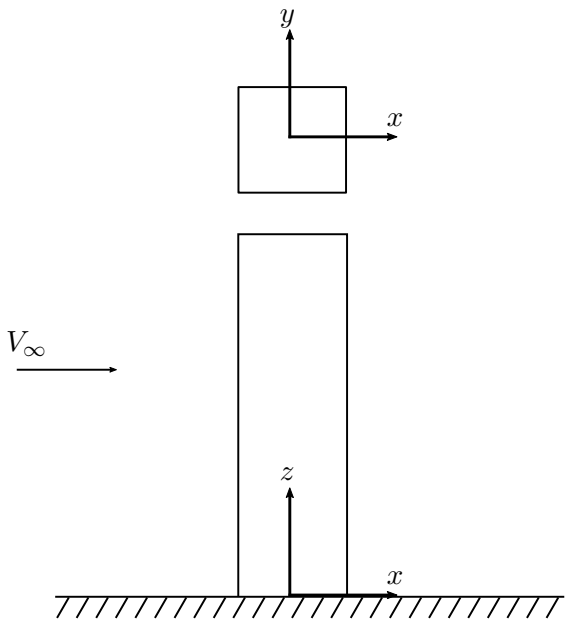

Figure 3.25: The coordinate system used in this thesis unless otherwise stated. The coordinate system is fixed to the FWMC junction.

There are some situations where it becomes convenient to use a coordinate system

different to that above, for example, when discussing the aerodynamic performance of the AWT (in Section 3.2.1) or presenting beamforming images (in Section 6.4.2). These alternative coordinate systems are described when required.

3.6 A comparison of the experimental conditions

In this section, the experimental measurement conditions in both the AWT (Experiment 1) and the 18WT (Experiment 2) are compared. These measurement conditions include the Reynolds number, the free-stream turbulence intensity, the solid blockage ratio, the aspect ratio range of the FWMCs and the plate boundary layers.

3.6.1 Reynolds number

The experiments conducted in the AWT were performed at a free-stream velocity of $V_\infty = 32\,\text{m/s}$. Since the width of the FWMCs in the AWT was 7 mm, the Reynolds number $Re_W = V_\infty W/\nu = 1.4 \times 10^4$. The Reynolds number for experiments in the 18WT was slightly lower at $Re_W = 1.1 \times 10^4$ owing to a slightly lower velocity ($V_\infty = 32\,\text{m/s}$) and slightly higher cylinder width ($W = 12\,\text{mm}$). According to Bourgeois et al. (2011), the fixed separation point on a 2D square cylinder makes the wake dynamics of the ensuing vortex street largely independent of Reynolds number. Bourgeois et al. (2011) also shows that the Strouhal number of vortex shedding for square FWMCs with $L/W = 4$ remains constant between $Re_W = 0.5 \times 10^4$ to 2×10^4. It is thus reasonable to assume that the vortex shedding process at $Re_W = 1.1 \times 10^4$ and $Re_W = 1.4 \times 10^4$ will be similar for the test cases studied here. Hence, the surface pressure measurements and oil-film flow visualisation performed in the 18WT at a lower Reynolds number should be indicative of the processes occurring in the AWT at higher Reynolds numbers.

3.6.2 Turbulence intensity

The turbulence intensity of the AWT at $V_\infty = 32\,\text{m/s}$ was approximately 0.4 to 0.5%. Norberg (2003) suggests that such a level of free-stream turbulence is slightly higher than most experimental studies on the fluctuating lift on circular cylinders. However, according to Blackburn and Melbourne (1996), this level of free-stream turbulence is not expected to alter the vortex formation process from what is expected for a 2D cylinder in low turbulence intensity studies ($T.I. < 0.1\%$). The 18WT has similar levels of turbulence intensity at 0.5%.

3.6.3 Aspect ratios

In the AWT single microphone measurements in Experiment 1, the cylinder rig was used to incrementally change the aspect ratio in the range from $L/W = 0$ to $L/W = 22.9$. The size of each increment was $\Delta L/W = 0.29$ (2 mm in length), which yielded a total of 80 different aspect ratios cylinders. The same measurements were taken for two different boundary layer heights (these boundary layers are discussed below). For the hot-wire wake surveys, directivity and beamforming measurements, only 8 different aspect ratio FWMCs were used in each boundary layer. These aspect ratios were $L/W = 1.4$, 4.3, 7.1, 10.0, 12.9, 15.7, 18.6 and 21.4. In the 18WT surface pressure and oil-film measurements

in Experiment 2, the aspect ratios that were studied were $L/W = 0.75$, 1.5, 4, 6.2, 6.9, 7.7, 8.4, 9.2 9.9 and 12.5.

3.6.4 Solid blockage

The maximum solid blockage ratio of FWMCs in the AWT was 5% for the FWMC with $L/W = 22.9$. The maximum blockage ratio of FWMCs in the 18WT was 0.9% for the FWMC with $L/W = 12.5$. In both situations, the maximum solid blockage ratio is low (Norberg 2003; Becker et al. 2002) and consequently this study has not employed any schemes to correct for solid blockage effects.

3.6.5 Boundary layers

AWT boundary layers

In Experiment 1 in the AWT, two different plate boundary layers were used for each aspect ratio to investigate the influence of the height of the plate boundary layer on the flow-induced noise of the FWMCs. The first was a boundary layer that was allowed to develop naturally on the side of the contraction, referred to as the low turbulent boundary layer or 'LTB'. The second was a boundary layer that was tripped with a 4-mm circular rod placed 20 cylinder widths (210 mm) upstream of the position of the cylinder, referred to as the high turbulent boundary layer, or 'HTB'.

Figures 3.26a and 3.26b compare the boundary layer mean velocity normalised by the free-stream, $\overline{u(z)}/V_\infty$ for the LTB and HTB respectively. These were measured using a hot-wire, as outlined in Section 3.2.5. It should be noted that when the hot-wire was measuring close to the wall, heat transfer from the aluminium plate raised the temperature of the sensing element, which reduced the measured velocity. By observing the change in hot-wire bridge voltage when the flow was off as the hot-wire moved closer to the wall, the heat affected region was found to extend to $z/W \leq 0.3$. Measurements beyond this region were free from heat-transfer effects.

From Figure 3.26 it is evident that the LTB has a significantly lower boundary layer height than the HTB. The 'boundary layer thickness', δ, is defined as that point above the plate where the velocity reaches 99% of the free-stream velocity. Table 3.5 quantifies the boundary layer thickness for the LTB and HTB and shows that the LTB has $\delta = 1.3W$, compared with the HTB which has $\delta = 3.7W$.

Figure 3.26 also compares the mean velocity profiles with the laminar Blasius solution (Pope 2000) of equivalent boundary layer thickness. It is observed that both the LTB and HTB have higher velocities closer to the wall ($z/W = 0$) indicating that the profiles resemble that of a turbulent boundary layer.

Figure 3.27 plots the mean velocity profiles of the HTB and LTB in wall units. In these figures, $z^+ = zu_\tau/\nu$ and $u^+ = \overline{u(z)}/u_\tau$, where u_τ is the friction velocity and ν is the kinematic viscosity of air. The friction velocity, u_τ, was found by fitting the boundary layer mean velocity profiles to the Law of the Wake for turbulent boundary layers (Coles 1956), described by

$$u^+ = \frac{1}{\kappa}\log(z^+) + C + \frac{2\Pi}{\kappa}\sin^2(\frac{y\pi}{2\delta}), \tag{3.43}$$

where $\kappa = 0.41$ and $C = 5.0$. In this equation, both the friction velocity, u_τ, and the parameter Π (which describes the boundary layer's streamwise pressure gradient) were found by varying them independently until the total variance between Equation 3.43 and the measured data was minimised. Figures 3.27a and 3.27b compare the measured data to the fitted equation and good agreement is observed for both the LTB and HTB cases. Figures 3.27a and 3.27b also compare the boundary layers with measurements made by Spalart (1988) and Klebanoff (1954) at similar Reynolds numbers for the LTB and HTB respectively. Good agreement is achieved which further confirms the boundary layers' turbulent nature. For completeness, the near wall solution of van Driest (1956) is also given for $z^+ < 30$.

Finally Figure 3.28 shows the wall normal turbulent intensity profiles of the LTB and HTB. For the LTB, the maximum turbulence intensity close to the wall is approximately $T.I. = 8\%$ which quickly reduces to the free stream value of $T.I. = 0.5\%$ by $z/W = 4$. Conversely, the trip used to artificially thicken the boundary layer to the HTB also increases the turbulence to $T.I. = 10\%$ close to the wall. In the HTB, this high turbulence continues to approximately $z/W = 2$ where it slowly reduces to $T.I. = 0.5\%$ by $z/W \approx 6$.

Table 3.5 compares the measured boundary layer integral properties, normalised by the appropriate scale. These include the boundary layer thickness, δ/W, the friction velocity, u_τ/V_∞, the parameter Π, the displacement thickness, δ^*/W, the momentum thickness, θ^*/W, the shape factor, $H = \delta^*/\theta^*$ and the Reynolds number based on momentum thickness, $Re_\theta = V_\infty\theta/\nu$. In this table, the displacement thickness is defined as

$$\delta^* = \frac{1}{V_\infty}\int_0^\infty (V_\infty - \overline{u(z)})dz, \tag{3.44}$$

while the momentum thickness is defined as

$$\theta = \frac{1}{V_\infty^2}\int_0^\infty \overline{u(z)}(V_\infty - \overline{u(z)})dz, \tag{3.45}$$

where V_∞ is the free-stream velocity and $\overline{u(z)}$ is the mean streamwise velocity at position z above the plate. According to Wilcox (2006), a Π value between 0 and 0.6, which is what was measured for both boundary layer cases, indicates a near zero streamwise pressure gradient. Also shown in Table 3.5 is that the LTB has a shape factor of $H = 1.6$ while the HTB has a shape factor of $H = 1.4$. According to Pope (2000), a fully developed turbulent boundary layer has a shape factor of 1.3 while a laminar boundary layer has a shape factor of $H = 2.6$. This indicates that both the LTB and the HTB are in a turbulent and nearly fully developed state.

Table 3.5: A comparison of key characteristics of the boundary layers used in this thesis.

	δ/W	Π	u_τ/V_∞	δ^*/W	θ/W	H	Re_θ
LTB	1.3	0.28	0.04	0.2	0.14	1.6	2023
HTB	3.7	0.37	0.04	0.5	0.36	1.4	5398
18WT	0.9	0	0.05	0.11	0.07	1.4	930

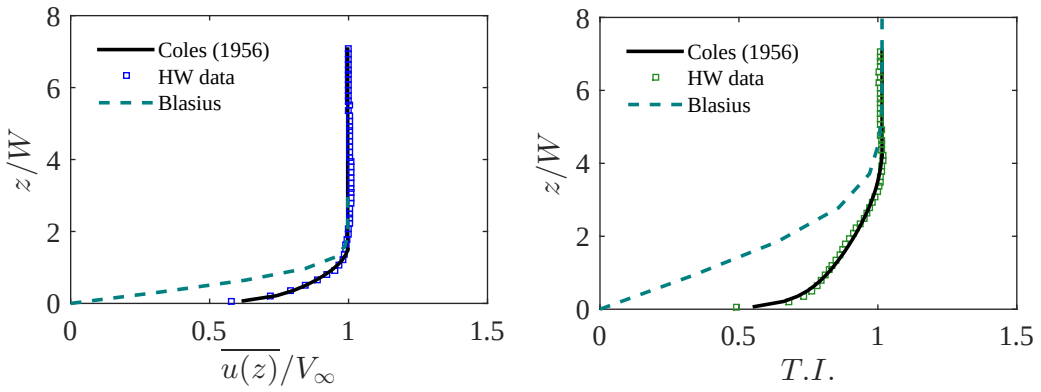

(a) LTB (b) HTB

Figure 3.26: Mean velocity profiles of the LTB (a) and HTB (b) in the AWT. The profiles are compared with Coles Law of the Wake (Coles 1956) and the Blasius boundary layer.

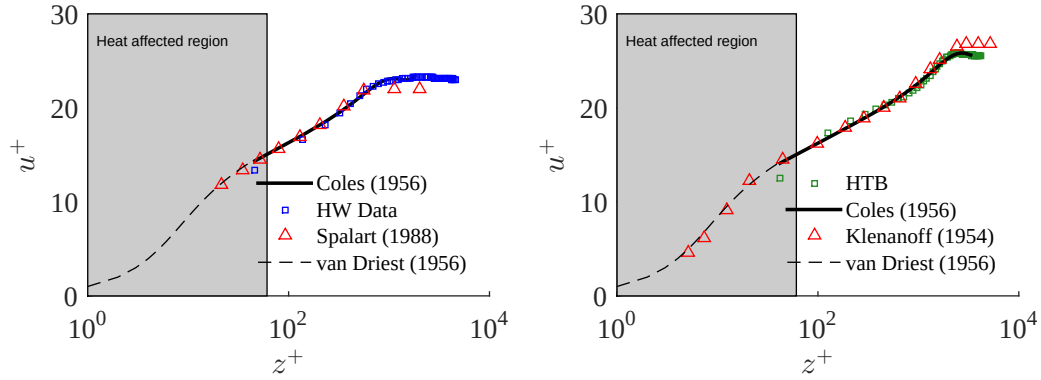

(a) LTB (b) HTB

Figure 3.27: Mean velocity profiles of the LTB (a) and HTB (b) in the AWT plotted in wall-units. The profiles are compared with Coles Law of the Wake, van Driest's near wall solution (van Driest 1956) and results by Spalart (1988) and Klebanoff (1954) for the LTB and HTB respectively.

The 18WT boundary layer

Only one boundary layer was used for the surface pressure and oil-film experiments conducted in the 18WT. This boundary layer developed naturally out of the contraction, similar to the LTB in the AWT. Figures 3.29, 3.30 and 3.31 show the mean velocity profile, the mean velocity profile in wall units and the turbulence intensity profile respectively of the 18WT boundary layer. The last line of Table 3.5 shows this boundary layer's integral properties.

The boundary layer's shape factor of $H = 1.4$ indicates the 18WT boundary layer is turbulent and near fully developed. Comparison with a Blasius boundary layer of equal height in Figure 3.29 demonstrates that higher velocity is measured closer to the wall, again consistent with the boundary layer's turbulent nature. The mean velocity profiles are not compared with the Law of the Wake given in Equation 3.43. This is because the 18WT boundary layer cannot be fitted well to Cole's Law of the Wake since the 'log region' of the 18WT boundary layer is small. The 'log region' is that region of the boundary layer where the quantity du^+/dz^+ is constant (Wilcox 2006), and is observed in Figure 3.30 only between $30 < z^+ < 100$. In contrast, for the boundary layers in the

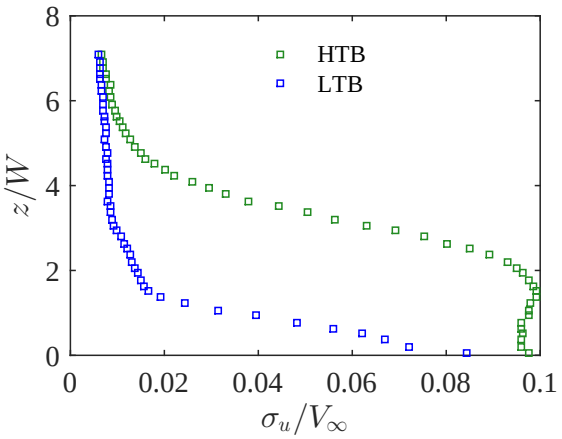

Figure 3.28: Comparison of the LTB and HTB turbulence intensity σ_u/V_∞.

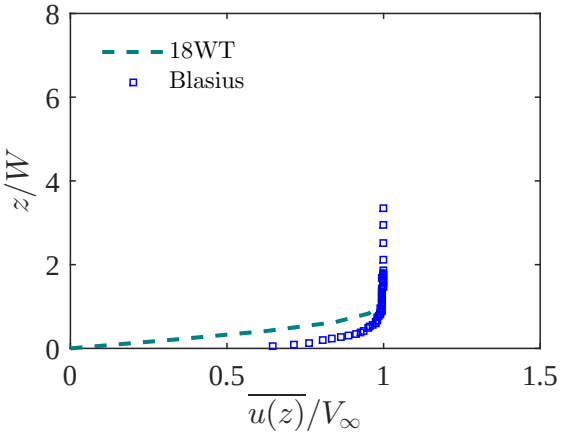

Figure 3.29: Mean velocity profile of the 18WT boundary layer, compared with the Blasius laminar boundary layer of equal thickness.

AWT, the log region extends between $30 < z^+ < 600$. According to Spalart (1988), a small log region occurs in the 18WT boundary layer because the momentum thickness Reynolds number of the 18WT boundary layer is low at $Re_\theta = 930$. Based on the results of Spalart (1988), Cole's Law of the Wake becomes a better boundary layer model as the Reynolds number increases. This is the reason why good agreement is achieved with the AWT boundary layers which have Reynolds numbers of $Re_\theta = 2023$ and $Re_\theta = 5398$ respectively.

Because the Law of the Wake could not be used to estimate the friction velocity, the traditional 'Clauser Chart' method (Clauser 1954) was used. In this method, the value of Π in Equation 3.43 is assumed to be 0. When $\Pi = 0$ in Equation 3.43, the resulting equation is known as the 'Law of the Wall'. The friction velocity is then chosen to minimise the difference between the Law of the Wall and the data points that lie in the 'log region' in Figure 3.30. Figure 3.30 compares the measured velocity with the Law of the Wall equation and good agreement is achieved for $30 < z^+ < 100$. The 18WT boundary layer is also compared to the near fully developed turbulent boundary layer of El Hassan et al. (2015). In the study of El Hassan et al. (2015), the boundary layer momentum thickness Reynolds number was very similar to that of the 18WT at $Re_\theta = 1000$. Excellent agreement is achieved for regions beyond the log region, further corroborating that the 18WT boundary layer is turbulent and near fully developed.

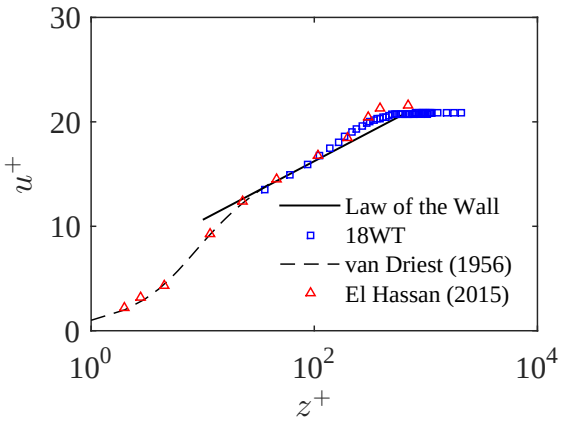

Figure 3.30: Mean velocity profile of the 18WT boundary layer, plotted in wall-units. The data are compared with the boundary layer of El Hassan et al. (2015), the 'Law of the Wall' and the near wall solution of van Driest (1956) for completeness.

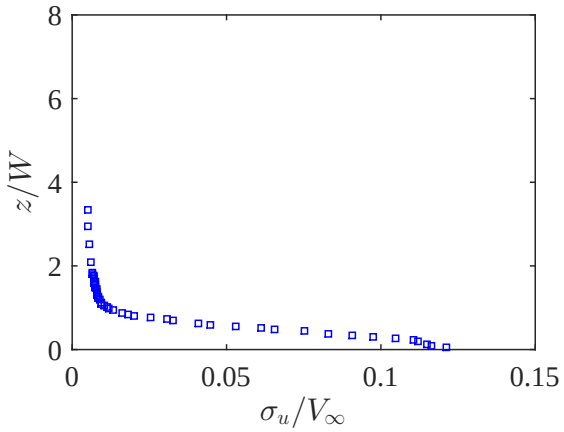

Figure 3.31: The turbulence intensity profile of the 18WT boundary layer.

Figure 3.31 shows a similar profile to that of the LTB in the AWT. While the turbulence intensity very close to the wall is higher than that of the AWT ($T.I. = 12\%$ compared with $T.I. = 8\%$), the turbulence intensity decays to $T.I. = 0.5\%$ by $z/W = 2$.

3.7 Summary and the final test matrix

The final test matrix is given in Table 3.6. This matrix has a similar format to Table 2.1 so that a direct comparison with other previous studies can be made. In particular, this experimental campaign is the first to study square FWMCs with a phased microphone array. Another important feature of this experimental campaign is that it investigates the widest range of aspect ratio cylinders in the finest detail. No other study has investigated square FWMCs with an aspect ratio increment as small as $\Delta L/W = 0.28$. Furthermore, no other studies on square FWMCs have measured aspect ratios beyond $L/W = 14$.

Table 3.6: Test matrix of the experimental campaign undertaken in this study. This matrix can be compared with Table 2.1 for a comparison with other experimental studies in the literature on FWMCs.

		Acoustic Data		Geometric Parameters			Flow Parameters	
Facility	Flow measurement method	SM[i]	MA[ii]	Sq.[iii]	Circ.[iv]	AR[v]	Re($\times 10^4$)[vi]	δ/D[vii]
AWT	Hot-wire anemometry	✓	✓	✓		$1 \rightarrow 23$	1.45	1.3, 3.7
18WT	Surface pressure, Oil-film visualisation			✓		$1 \rightarrow 12.5$	1.1	0.9

[i] SM=Single microphone [ii] MA=Microphone Array [iii] Sq.=Square cross section [iv] Circ.=Circular cross section [v] AR=Aspect Ratio [vi] Re=Reynolds Number [vii] δ/D=Boundary layer height to diameter (or width) ratio

Chapter 4

Source localisation using a microphone array

4.1 Introduction

Phased microphone arrays are a popular method for aeroacoustic source localisation (Johnson and Dudgeon 1993; Mueller 2002) because they can be used without mechanical movement to obtain directional (positional) information of the source (Brooks and Humphreys 1999) and therefore are suitable for use inside wind tunnels (Moreau et al. 2014; Geyer et al. 2012; Brooks and Humphreys 2003).

There are three common sound source localisation techniques using phased microphone arrays (Prime et al. 2014b); (1) Near-field Acoustic Holography (NAH), (2) aeroacoustic beamforming and (3) aeroacoustic Time-Reversal (TR). Out of the three methods, time reversal is the least well established and has not yet been employed in many experimental applications (Prime et al. 2014b; Mimani et al. 2016). In contrast, NAH and beamforming are well established and have been utilised in wind tunnel experiments of various aeroacoustic sources (Faszer et al. 2006; Moreau et al. 2014; Brooks and Humphreys 2006; Suzuki 2006), field measurements of wind turbine noise (Oerlemanns et al. 2009) and aircraft jet noise (Siller et al. 2010). NAH is only suitable for measurements when the array is in the acoustic near-field, approximately 1-2 wavelengths (λ) from the source. This corresponds to lower frequency (generally less than 1-2k Hz (Lanslots et al. 2010)) source localisation when the array is at a fixed distance from the source, as in wind tunnel testing. In contrast, beamforming is suitable for far-field noise measurements at distances greater than 2λ from the source, generally corresponding to a higher frequency range (approximately greater than 2 kHz) when used in wind tunnel testing.

Noise generated by FWMCs is categorised into low frequency tonal noise and high frequency broadband noise. In this study, tonal noise occurs between 400 and 600 Hz depending on the FWMC aspect ratio, while broadband noise is generated above 2 kHz. The plane of the microphone array in the AWT is located at a fixed distance from the plane of the FWMC at 0.5 m. This means that for tonal noise generation, the array lies at approximately 0.6 to 0.8λ, satisfying the near-field condition. Alternatively, for broadband noise, the array lies over 4λ from the cylinder, in the far-field.

While NAH is a suitable technique to study tonal noise generation from FWMCs for the present experimental configuration, it is not employed in this study. Instead, lower fre-

quency (between 300 to 600 Hz) tonal noise generation is studied using single-microphone measurements, hot-wire wake measurements and surface pressure measurements, as discussed in Chapter 3. On the other hand, this investigation will employ beamforming to study broadband, higher frequency (greater than 2 kHz) noise generated by FWMCs.

Sound source localisation of FWMC broadband noise using a microphone array is a significant scientific contribution because there are no studies that have characterised such noise. However, the lack of studies on FWMC broadband noise makes it difficult to benchmark the results against previous research. Therefore, a detailed mathematical overview of beamforming is provided in this chapter to understand the limitations of the technology, quantify any errors and outline any corrections that can be used to improve the confidence of the results.

This chapter will first describe conventional cross-spectral beamforming theory. Next, two popular 'deconvolution' techniques called DAMAS (Brooks and Humphreys 2006) and CLEAN-SC (Sijtsma 2007) will be presented. Deconvolution techniques are used to enhance the resolution of the conventional cross-spectral sound map. In particular, this chapter will generalise the DAMAS procedure to accommodate different propagation vectors outlined by Sarradj (2012). As it turns out, this generalisation is important to quantify the limitations of DAMAS, which is used extensively in Chapter 6 to quantify the broadband noise. The chapter will then proceed with a discussion of the sources of error in the conventional and deconvolved beamforming output and quantify this error. The chapter will conclude with a variety of correction methods to either eliminate the aforementioned errors and improve and quantify the confidence of the results.

4.2 Background theory of beamforming

Phased microphone arrays (or 'beamformers') consist of a number of microphones in a fixed spatial arrangement. The majority of beamformer arrangements in aeroacoustic applications are planar (Brooks and Humphreys 2003; Geyer et al. 2012; Sarradj 2012), although non-planar arrangements exist (Hileman et al. 2004; Dougherty 2010; Padois et al. 2013a). Each microphone simultaneously records a pressure signal. The records are then delayed and summed coherently to enhance the signal from a focal position and minimise the signal from an out-of-focus location (Johnson and Dudgeon 1993). Ideally, the beamformer response should be maximum when the focal position coincides with the location of the source. Therefore, the source location can be determined by scanning over a grid of focal points (known as the scanning grid) and selecting the location of the maximum. The scanning grid can be a one-dimensional (1D) line, a two-dimensional (2D) planar grid, or a three-dimensional (3D) volume.

Beamforming algorithms can be split into two categories: (1) conventional delay-and-sum (DAS) beamforming and (2) deconvolution (although the second category is reliant on the first). Conventional beamforming is known classically as 'delay-and-sum', because originally the signal delays were performed in the time domain. Modern versions of the DAS algorithms are performed in the frequency domain, where time delays in the cross-correlation are transformed into phase shifts of the cross-spectrum. Hence, an alternative designation of DAS beamforming is 'cross-spectral beamforming'. 'Deconvolution' is a post processing step that removes the array characteristics from the DAS sound map to

reveal the theoretically true source distribution and power.

In this study, deconvolution methods are used to investigate FWMC broadband noise. As such, both the cross-spectral beamforming and the deconvolution approaches will be rigorously formulated and analysed in the proceeding sections.

4.2.1 Conventional cross-spectral beamforming

Consider an array of M_0 microphones where the position of the i^{th} microphone in 3D space is given by $\mathbf{x}_i = (x_i, y_i, z_i)$, as in Figure 4.1.

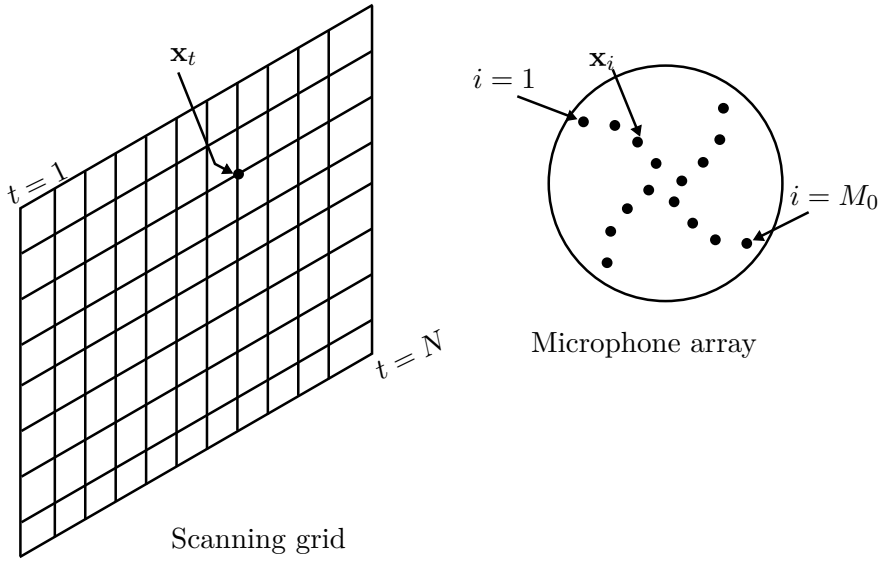

Figure 4.1: An illustration of the microphone array and scanning grid configuration. An array output, Equation 4.1, is generated at each point, $\mathbf{x}_t$ $(t = 1...N)$, in the scanning grid.

These microphones simultaneously record a complex-valued vector of sound pressures in frequency space denoted $\mathbf{P}(\omega) = [p_1, ..., p_{M_0}]^T$. The array is then electronically 'steered' to a grid of N locations in three-dimensional space, denoted $\mathbf{x}_t = (x_t, y_t, z_t)$ for $(t = 1...N)$. The real-valued output (or 'Power Spectral Density') of the array steered to each scanning grid location is given by

$$Y_t = Y(\mathbf{x}_t, \omega) = \mathbf{h}(\mathbf{x}_t, \omega)^{\mathrm{H}} \mathrm{W}(\omega) \overline{\mathbf{P}(\omega)\mathbf{P}(\omega)^{\mathrm{H}}} \mathrm{W}(\omega)^{\mathrm{H}} \mathbf{h}(\mathbf{x}_t, \omega). \tag{4.1}$$

The source location can be estimated by mapping the array output on a predetermined grid of spatial points (scanning grid) and finding the maximum. In Equation 4.1, the outer product $\mathrm{G} = \overline{\mathbf{P}(\omega)\mathbf{P}(\omega)^{\mathrm{H}}}$ is known as the Cross-Spectral Matrix (CSM). The overbar denotes the averaging over the Fourier transforms in a number of discrete time blocks while the superscript 'H' refers to the Hermitian transpose.

In the CSM, the diagonal terms are commonly removed in a step known as 'diagonal removal' (DR). The removal of the diagonal terms improves the ability of the array to identify sources by 'subtracting' the high amplitude autospectral terms that can be dominated by phenomena that are correlated with their own signal, i.e., turbulent boundary layer noise/flow noise, electrical self noise, rather than an acoustic source in the far-field (Oerlemanns et al. 2007). Since cross-spectral beamforming relies only on phase differences from one microphone to another, the subtraction of the diagonal of

the CSM will not influence the source localisation capability of the array (although, as will be discussed, DR will change the estimated source amplitude if not accounted for properly). Hence, this step is generally required when the microphones are exposed to flow as in a closed wind tunnel or an open jet wind tunnel with low level recirculation.

The term $\mathbf{h}(\mathbf{x}_t, \omega)$ is known as the 'steering vector' and is dependent on the $M_0 \times 1$ transfer vector, $\mathbf{a}(\mathbf{x}_t, \omega)$ that relates the pressure recorded at each microphone to a theoretical source at the scanning grid location, $\mathbf{x}_t$, with strength (pressure amplitude) $q(\mathbf{x}_t)$. That is

$$\mathbf{a}_t(\omega) q_t = \mathbf{a}(\mathbf{x}_t, \omega) q(\mathbf{x}_t) = \mathbf{P}(\omega). \tag{4.2}$$

The transfer vector is typically the three-dimensional Green's function of the Helmholtz equation with the Sommerfield (anechoic) radiation condition applied (Sijtsma and Stoker 2004), i.e.,

$$a_i(\mathbf{x}_t, \omega) = a_{it} = c_t \frac{e^{-jk(r_{it})}}{r_{it}}, \tag{4.3}$$

where $k = \omega / c_0$ is the wave number, r_{it} is the distance from the t^{th} point to the i^{th} microphone and c_i is a normalisation parameter. For most practical applications of planar beamforming, monopole transfer vectors (as given by Equation 4.4) are used but for some specialised applications, the transfer vector may also take the form of a dipole (Liu et al. 2008) or a multi-pole (Susuki 2011) source.

The choice of normalisation parameter, c_t, does not affect the localisation results but does affect the interpretation of the magnitude of the peaks in the beamforming map (Dougherty et al. 2013). Commonly, the normalisation factor is chosen to reference the levels back to that measured by a reference microphone located at $\mathbf{x}_{ref}$ (Brooks and Humphreys 2006; Sarradj 2010; Yardibi et al. 2010), by setting

$$c_t = r_{reft} e^{jk(r_{reft})}, \tag{4.4}$$

where r_{reft} is the distance from the t^{th} point in the scanning grid to the reference microphone. The level that would be obtained by incoherently ('pressure-squared') summing the source levels would then be the level measured by the reference microphone.

It is also common to set $c_t = 1/4\pi$ so that the steering vector represents the Green's function of a monopole radiating spherically with far-field wave propagation characteristics (Liu et al. 2008). The magnitude of the source map could then be interpreted as that which would be measured by a listener located exactly at the t^{th} scan grid point. In this case, spatial integration of the source powers may not have physical meaning. However, the differences in relative integrated magnitudes between different source maps will be identical regardless of the reference location. This implies that even though the power of an integrated source map may not perfectly match the power spectrum obtained using the reference microphone, the source map will still give an indication of the relative contributions of each source in the integration region.

In the literature, there are four choices of steering vectors that relate $\mathbf{a}(\mathbf{x}_t, \omega)$ to $\mathbf{h}(\mathbf{x}_t, \omega)$ (Sarradj 2012). These are known as sv1, sv2, sv3 and sv4, respectively, and are summarised in Table 4.1. In this table, h_{it} refers to the steering vector element from the i^{th} microphone to the t^{th} point in the scanning grid and * refers to the complex

conjugate.

Table 4.1: Summary of the four different steering vector formulations commonly used in beamforming where h_{it} refers to the steering vector element from the i^{th} microphone to the t^{th} point in the scanning grid.

	h_{it}
sv1	$\frac{1}{M_0}\frac{a_{it}}{\sqrt{a_{it}a_{it}^*}}$
sv2	$\frac{1}{M_0}\frac{a_{it}}{a_{it}a_{it}^*}$
sv3	$\frac{a_{it}}{\mathbf{a}_t^{\mathrm{H}}\mathbf{a}_t}$
sv4	$\frac{1}{\sqrt{M_0}}\frac{a_{it}}{\sqrt{\mathbf{a}_t^{\mathrm{H}}\mathbf{a}_t}}$

The choice of steering vector will determine the properties of the beamforming map. For a single point source, it can be shown that using sv1 and sv4 will guarantee a local maximum in the beamforming map at the exact source location, i.e., $Y(\mathbf{x}_t, \omega)$ will be stationary at $\mathbf{x}_t = \mathbf{x}_s$ where the subscript s denotes the location of the source. No guarantee can be made for sv2 or sv3 (Sarradj 2012). On the other hand, using sv1 and sv4 will result in erroneous source strength estimation (referenced levels or otherwise) due to a spatially dependent multiplication factor known as the 'array gain field'. The array gain field is essentially an artificial amplification of a source's strength based on its location. For example, sources located near to the array centre will be amplified above those located further from the array centre. This trait is undesirable as it could result in inaccurate relative source strength estimation. Fortunately, the array gain field can be calculated (in the next section) and source levels adjusted accordingly.

Finally, in Equation 4.1, $\mathrm{W}(\omega)$ is an $M_0 \times M_0$ diagonal matrix known as the 'shading matrix'. Each diagonal element of W, W_{ii}, is a frequency dependent real valued coefficient that weights the effect of the i^{th} microphone. If W is the identity matrix, then all microphones are active in the array. Brooks and Humphreys (2003) formulate special values of W_{ii} to keep the beamwidth (resolution) of the array constant over the desired frequency range.

4.2.2 Deconvolution

A microphone array is a multi-dimensional spatial filter that separates signals according to their direction of propagation and frequency content (Johnson and Dudgeon 1993). The output of the microphone array (the 'source map') will therefore be *convolved* with the spatial filter characteristics, known as the Point Spread Function (PSF). The PSF is the response of the beamformer to a pure harmonic signal at a particular point in the scanning grid. 'Deconvolution' techniques attempt to remove the PSF from the calculated source map to educe the true source map. Several methods of deconvolution exist; DAMAS, CLEAN-SC, DAMAS2, DAMAS-C, MUSIC, TIDY and several eigenvalue decomposition approaches. In the literature, the most widely used deconvolution methods are DAMAS and CLEAN-SC.

DAMAS

A popular deconvolution scheme is the 'Deconvolution Approach for the Mapping of Acoustic Sources', abbreviated as 'DAMAS', developed by Brooks and Humphreys (2006). The DAMAS method assumes a theoretical PSF for each point in the scanning grid and subsequently formulates an inverse problem, the solution of which is the theoretically true source map. In the original paper by Brooks and Humphreys (2006), DAMAS was formulated based on sv2 only. In the following, a *generalised* DAMAS method is developed to account for the other three steering vectors, with and without diagonal removal. The generalisation of the DAMAS methodology presented in this thesis has never been published and is a new contribution to the field.

The sound pressure level at the microphones is a linear combination of the pressures due to each individual source in the map, q($\mathbf{x}_{t'}$) for $t' = 1...N$. That is to say,

$$\mathbf{P} = \sum_{t'}^{N} \mathbf{a}_{t'} q_{t'}. \tag{4.5}$$

Therefore, the CSM can be recast as,

$$\mathrm{G} = \overline{\mathbf{P}\mathbf{P}^{\mathrm{H}}} = \overline{\sum_{t'=1}^{N} \mathbf{a}_{t'} q_{t'} \left[\sum_{t'=1}^{N} \mathbf{a}_{t'} q_{t'} \right]^{\mathrm{H}}}, \tag{4.6}$$

where H denotes the Hermitian transpose.

If it is then assumed that the sources are spatially incoherent with one another (statistically independent), the cross terms in Equations 4.6 equate to 0 and the only contributing terms are the source autopowers. The CSM simplifies to

$$\mathrm{G} = \sum_{t'=1}^{N} \mathbf{a}_{t'} \mathbf{a}_{t'}^{\mathrm{H}} X_{t'}, \tag{4.7}$$

where $X_{t'} = \overline{q_{t'} q_{t'}^*}$ and * denotes complex conjugation. Substituting this theoretical CSM into Equation 4.1 yields,

$$Y_t = \sum_{t'=1}^{N} \mathbf{h}_t^{\mathrm{H}} \mathrm{W} \mathbf{a}_{t'} \mathbf{a}_{t'}^{\mathrm{H}} \mathrm{W}^{\mathrm{H}} \mathbf{h}_t X_{t'}. \tag{4.8}$$

The output can be rewritten as a linear system

$$\mathbf{b} = \mathrm{A}\mathbf{x}, \tag{4.9}$$

where the vectors $\mathbf{b}$ and $\mathbf{x}$ have components Y_t and $X_{t'}$ respectively ($t, t' = 1...N$) and the matrix A is $N \times N$. The elements of matrix A (denoted the 'A- matrix') can be written as

$$\mathrm{A}_{tt'} = \mathbf{h}(\mathbf{x_t})^{\mathbf{H}} \mathbf{h}_t^{\mathrm{H}} \mathrm{W} \mathbf{a}_{t'} \mathbf{a}_{t'}^{\mathrm{H}} \mathrm{W}^{\mathrm{H}} \mathbf{h}_t = \sum_{q=1}^{M_0} \sum_{p=1}^{M_0} \mathrm{W}_{qq} \mathrm{W}_{pp} h_{qt}^* h_{pt} a_{qt'} a_{pt'}^*, \tag{4.10}$$

where h_{qt} denotes the q^{th} element ($q = 1...M_0$) of the steering vector $\mathbf{h}_t$. The steering vector, $\mathbf{h}_t$, can be one of the four listed in Table 4.1. It can be proven that the A-matrix is symmetric and real (not shown here).

If diagonal removal is used, then the diagonal elements of the theoretical CSM in Equation 4.7 are removed and Equation 4.10 is modified to

$$\mathrm{A}_{tt'DR} = \sum_{q=1}^{M_0} \sum_{p=1, p\neq q}^{M_0} \mathrm{W}_{qq}\mathrm{W}_{pp} h^*_{qt} h_{pt} a_{qt'} a^*_{pt'}. \tag{4.11}$$

The final step of the DAMAS methodology involves solving Equation 4.9 for $\mathbf{x}$. Gauss-Seidel iteration (Brooks and Humphreys 2006), linear programming (Dougherty et al. 2013) or co-variance matrix fitting approaches (Yardibi et al. 2008) can be used to solve the system.

CLEAN-SC

CLEAN-SC (Sijtsma 2007) is another deconvolution algorithm which removes the PSF from the main lobe. Unlike DAMAS, CLEAN-SC calculates the PSF based on the recorded data of the microphones and, in doing so, the method removes side-lobes that are coherent with the main lobe. The CLEAN-SC algorithm is described in the following steps;

1. A source map is obtained from conventional beamforming (also known as the 'dirty map'). The CSM for such a map is denoted as D^0.
2. Set $i = 1$.
3. While $||\mathrm{D}^{(i)}|| \leq ||\mathrm{D}^{(i-1)}||$
   (a) The peak location from the dirty map is obtained, i.e., $\mathbf{x}_{max}$ is found such that $Y^{(i-1)}_{max} = \mathbf{h}^{\mathrm{H}}_{max}\mathrm{D}^{(i-1)}\mathbf{h}_{max}$ is a maximum, where $\mathbf{h}$ is the steering vector defined in Section 4.2.1.
   (b) A scaled version of the PSF associated with the maximum is subtracted from the dirty map to create the next dirty map, i.e., $\mathrm{D}^i = \mathrm{D}^{(i-1)} - \xi Y^{(i-1)}_{max}\mathbf{s}\mathbf{s}^{\mathrm{H}}$. The outer product $\mathbf{s}\mathbf{s}^{\mathrm{H}}$ is the calculated PSF based on the recorded data. It is found by iteratively solving

   $$\mathrm{D}^{(i-1)}\mathbf{h}_{max} = Y^{i-1}_{max}(\mathbf{s}\mathbf{s}^{\mathrm{H}} - \mathrm{diag}(\mathbf{s}\mathbf{s}^{\mathrm{H}}))\mathbf{h}_{max} \tag{4.12}$$

   by using Newton's method. The term $0 < \xi \leq 1$ is known as the loop gain and is necessary to ensure proper convergence. It is typically set at $\xi = 0.99$.
   (c) A 'clean map' contribution, $Q^{(i)}$, is created by scaling a user defined clean beam, $\Phi(\mathbf{x})$, i.e., $Q^{(i)} = Y^{i-1}_{max}\Phi(\mathbf{x})$. $\Phi(\mathbf{x})$ is usually a two-dimensional Gaussian surface with a variance parameter related to the beamwidth of the beam.
4. The completed clean map, Z_{clean}, is generated summing Q^i over all iterations, i.e., $Z_{clean} = \sum Q^i$.

CLEAN-SC iteratively removes PSFs of only the dominant noise sources and unlike DAMAS does not consider the PSF at every point in the scanning grid. Additionally, the PSFs used in CLEAN-SC are derived directly from the recorded noise data. This means that coherence loss at the outer microphones due to non-uniform directivity of

the sources and shear layer interference are inherently taken into account (Sijtsma 2007). Another benefit of this is that the computational time of CLEAN-SC scales linearly with the number of points in the grid, making it much faster than DAMAS: DAMAS typically takes 500 times longer to calculate than CLEAN-SC.

4.3 Characterisation of the AWT microphone array

Having discussed the mathematics governing microphone array acoustic source localisation for a general microphone layout, the specific microphone array layout used in this dissertation is discussed. This discussion precedes an error analysis of the beamformer in Section 4.5.

4.3.1 Microphone arrangement

The planar microphone array used in this study is part of a larger, non-planar array located inside the AWT. A schematic of the non-planar array is shown in Figure 4.2. The non-planar array consists of 62 microphones arranged in two Underbrink spiral pattern sub-arrays (Mueller 2002) of 31 receivers each. An Underbrink pattern was chosen because it has superior performance metrics (beamwidth and resolution, discussed in the next section) over other spiral array designs (Prime and Doolan 2013) such as the B&K spiral design, multi-spiral design, Dougherty spiral design and Archimedian spiral design.

The two sub-arrays comprising the full array are known as the 'top array' and the 'side array' respectively. The focus of this chapter is the top array because only the top array was used to measure the noise from FWMCs (in Experiment 1). A schematic of the top array (herein known as just the 'array') is shown in Figure 4.3. The coordinate system of the array is such that the centre microphone lies at the origin, 360 mm from the edge of the contraction. The scanning grid of the beamforming maps taken with the array is at the mid-plane of the contraction, 500 mm from the plane of the array. The array has an aperture (diameter) of approximately 1 m. The microphone with the black circle around it in Figure 4.3 (microphone number 13) was used for single microphone measurements, as discussed in Section 3.2.4.

The microphones themselves are G.R.A.S. 40PH 1/4" microphones that are phased-matched to within 10 degrees up to 10 kHz (according to the transducer documentation) and have a frequency response that is flat to within ± 1 dB up to 10 kHz. The microphones are press fit into a 12 mm medium-density fibreboard sheet with an EchoSorb 25 sound absorption layer (with a sound absorption coefficient of 0.85 for frequencies above 1 kHz) covering the top. During the experiments, each microphone head was covered with a windsock to isolate it from low level recirculation inside the wind tunnel chamber.

To record experimental data, each of the microphones in the array are connected to a National Instruments PXI-8106 data acquisition system with 4 PXIe-4499 simultaneous sample and hold ADC cards. Each card has a 24-bit resolution with 114 dB dynamic range and inbuilt automatic anti-aliasing filters. The data acquisition system was described in detail in Section 3.2.3.

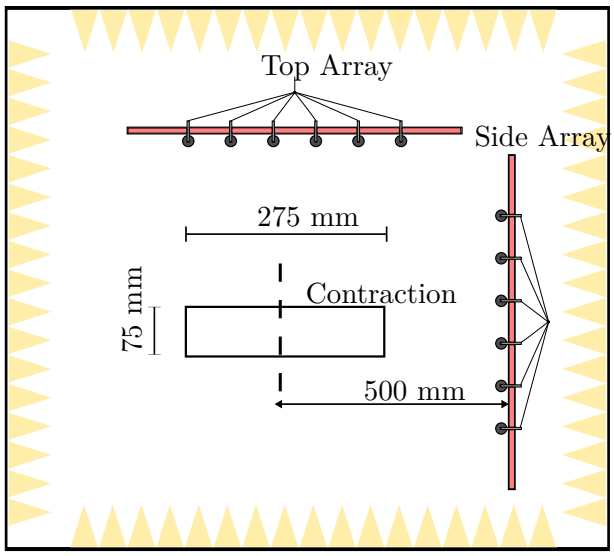

a) Front View

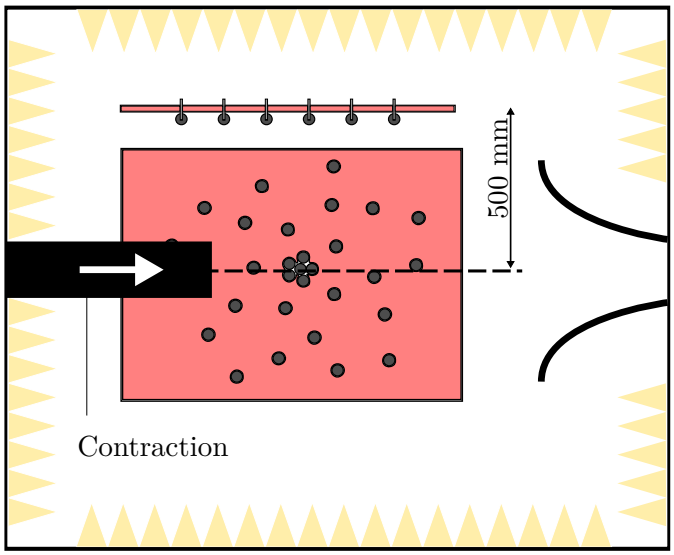

b) Side View

Figure 4.2: A schematic of the 62-channel dual spiral microphone array inside the AWT. From the 'front view' the flow is coming out of the page.

4.3.2 The array beamwidth and Maximum Side-lobe Level

Two quantities are used to characterise the array's performance. The first is the beamwidth, B_W, which is a measure of the array's spatial resolution. The second is the Maximum Side-lobe Level (MSL) which is the maximum level of ghost images in the array's PSF. It can be interpreted as a measure of the array's spatial dynamic range (Christensen and Hald 2004).

Beamwidth, B_W

The resolution of an array is defined as the distance that two individual sources can be spaced apart and still individually localised. A good measure of an array's resolution is the

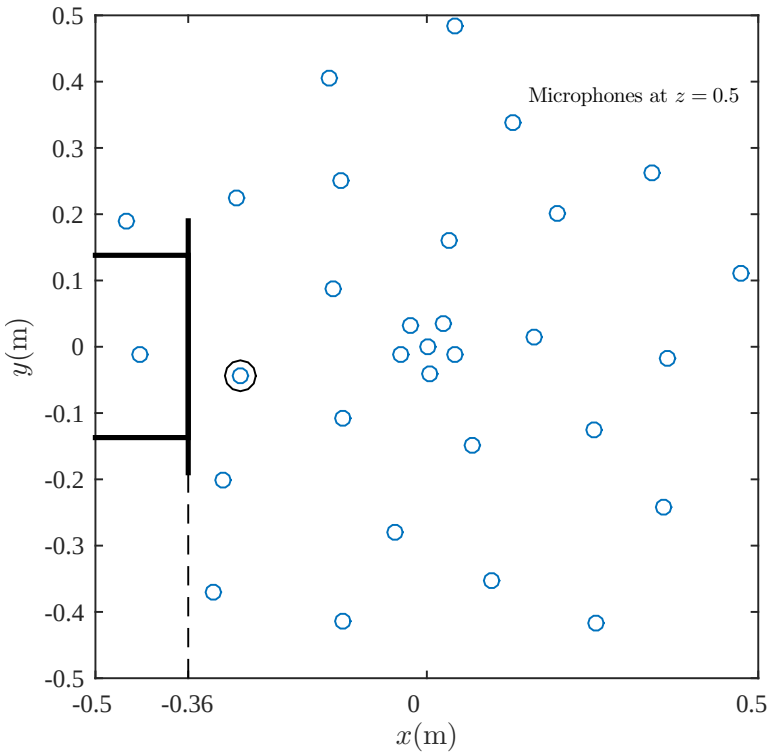

Figure 4.3: Schematic diagram of the top array microphone locations. The microphone with the black circle around it (microphone number 13) was used for single microphone measurements.

3 dB down beamwidth, B_W, of the main lobe. Consider the case of two sources, 'Source 1' and 'Source 2', spaced close together, as shown in Figure 4.4. The beamforming output for each source individually is modelled as a Gaussian curve with a half-width (equivalent to the 3 dB down beamwidth) of 50 mm. In Figure 4.4a, the separation distance of the two sources is just over 50 mm. The output of the beamformer is the sum of the beamforming maps for the two sources individually. Although between the sources, the amplitude will be increased, two distinct peaks will still be recognisable, as the sum in the centre will not be greater than the sum at the source locations. Now consider the case where the distance between the two sources is just less than the beamwidth, as in Figure 4.4b. The total output will be a single peak corresponding to the merger of the two single peaks, meaning the beamformer has not resolved the correct locations of each source. Hence, the smaller the beamwidth, the 'better' the resolution because the minimum required source separation decreases.

Dougherty (2010) gives an expression for the theoretical resolution of a microphone array based purely on its aperture. This resolution is also known as the Sparrow Limit. The Sparrow Limit, d_s, can be expressed as

$$d_s = 0.96\frac{\lambda}{\sin(\theta)}, \tag{4.13}$$

where λ is the wavelength of sound and θ is the half angle subtended by the phased array. For a source located 0.5 m away from the centre of the array, $\sin(\theta) \approx 1/\sqrt{2}$ for the AWT array. Hence the theoretical resolution of the AWT array is given by $d_s = 0.66\lambda$.

To measure the beamwidth, B_W, of the AWT array, a synthetic CSM for a monopole

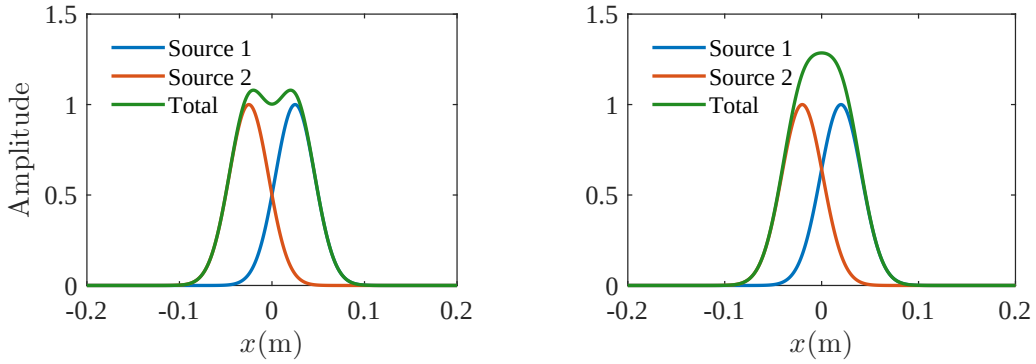

(a) Separation $> B_W$ (b) Separation $< B_W$

Figure 4.4: An illustration of the influence of beamwidth on the beamforming output.

source located at $x_s = (-0.3, 0, 0)$ (in array coordinates) was generated. This source location was chosen because it approximates the location of the sources in the FWMC experiments. Synthetic acoustic data from an ideal point monopole source was generated using

$$p_i = p_i(\mathbf{x}_s, \omega) = q(\omega)\frac{e^{-jkr}}{4\pi r_{is}}, \tag{4.14}$$

where $p_i(r, \omega)$ is the pressure recorded by the i^{th} microphone, $r_{is} = |\mathbf{x}_i - \mathbf{x}_s|$ is the distance from the source location to the i^{th} microphone, $\mathbf{x}_s$ is the location of the source, $\mathbf{x}_i$ is the location of the i^{th} microphone, $j = \sqrt{-1}$ and k is the wavenumber. Equation 4.14 is the transfer function used in Section 4.2.1. The frequency dependent constant $q(\omega)$ represents the strength of the source at a frequency ω. When steered to the source location, the beamforming output, Y_s, is exactly $q(\omega)^2$.

Once the synthetic CSM was calculated, four sound maps were generated corresponding to the four steering vector formulations, sv1, sv2, sv3 and sv4. For each map, the 3 dB down beamwdith was measured by searching for the -3 dB point in the radial direction from the global maxima. The process was repeated for frequencies ranging from 1 to 7 kHz.

The results of the analysis are shown in Figure 4.5. Here the beamwidth is measured in metres. The results are also compared with the Sparrow Limit defined in Equation 4.13 and a beamwidth of 1λ for reference. Figure 4.5 shows that for all four steering vectors used, the beamwidth is larger than the Sparrow Limit over all frequencies concerned. This is caused by the non-central location of the source. As the lateral position of the source is moved further from the array centre (in either the x or z-direction), the main lobe is stretched into an ellipse, with the major axis pointing toward the centre of the array. This increases the effective beamwidth of the array. At frequencies greater than 2 kHz, which are the frequencies of practical interest, there is negligible difference between each steering vector formulation and the beamwidths fall between the wavelength of sound and the Sparrow Limit.

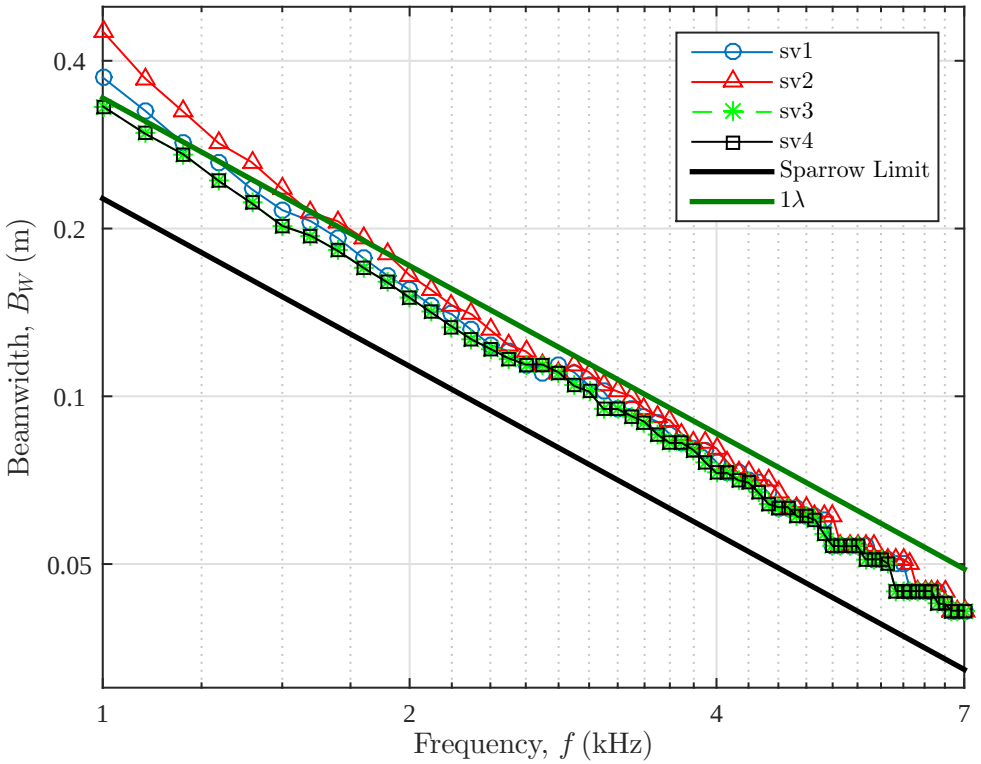

Figure 4.5: Comparison of the beamwidth, B_w, of the AWT array measured at $\mathbf{x}_s = (-0.3, 0, 0)$ using the four different steering vector formulations. The results are compared with the theoretical beamwidth of the array given by the Sparrow Limit, Equation 4.13.

Maximum Side-lobe Level, MSL

Good phased array designs are also characterised by having low Maximum Side-lobe Levels (MSL). At some spatial points in the array map, signals from non-source points will constructively interfere, causing ghost images to occur. For spiral, non-regular or random arrays, these ghost images have amplitudes lower than the main lobe (Christensen and Hald 2004). The ghost images are referred to as 'side-lobes' because they are unwanted consequences of the array processing as it acts as a spatial filter. An example of the maximum side-lobe in a source map is shown in Figure 4.6.

The MSL can be thought of as the dynamic range of the array. Consider two sources separated at a distance greater than the beamwidth of the array. If the second source has an amplitude lower than the first by more than the MSL, it may be hidden as part of the first source's PSF. If it is higher than the MSL, it will not be hidden.

The MSL behaviour for the top array was calculated for each steering vector formulation in a similar manner to the beamwidth. The sound map for the synthetic monopole at $\mathbf{x}_s = (-0.3, 0, 0)$ was generated for frequencies ranging from 1 to 7 kHz. The MSL was then measured by finding the locations of the local maxima and selecting the location of the second largest (the largest belonging to the main lobe). The results are shown in Figure 4.7. Here there is a more significant difference between steering vector formulations when compared with the beamwidth characteristics.

For frequencies lower than 2 kHz, sv2 has higher MSLs than the other formulations by up to 1 dB/Hz. Conversely, at frequencies above 2 kHz, sv2 outperforms the other

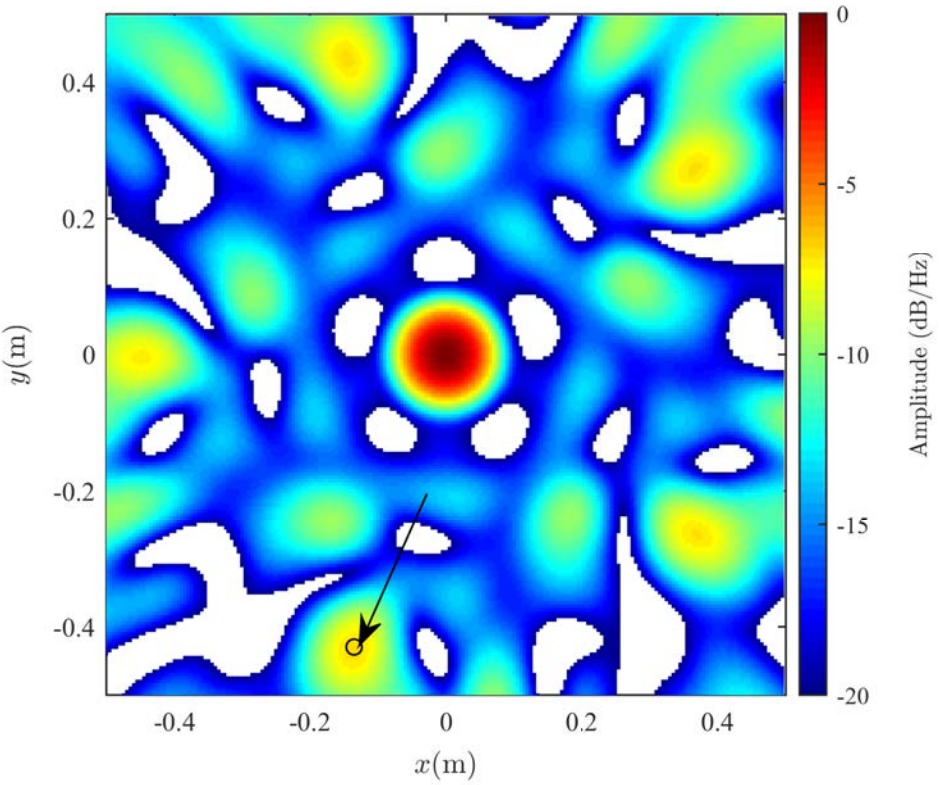

Figure 4.6: An illustration of the concept of the Maximum Side-lobe Level (MSL) for a general beamforming source map with the source located at $\mathbf{x}_s = (0, 0, 0)$.

steering vector formulations. Steering vectors sv3 and sv4 have the highest MSLs in this frequency band.

At the position of the FWMC models relative to the array ($x_s \approx (-0.3, 0, 0)$) above 2 kHz, the aforementioned analysis predicts that steering vector 2 will have the best dynamic range (lowest MSL) with no compromise in resolution (beamwidth) compared with the other steering vector formulations. Therefore, based on these results, steering vector 2 (sv2) was used as the steering vector in the FWMC experiments.

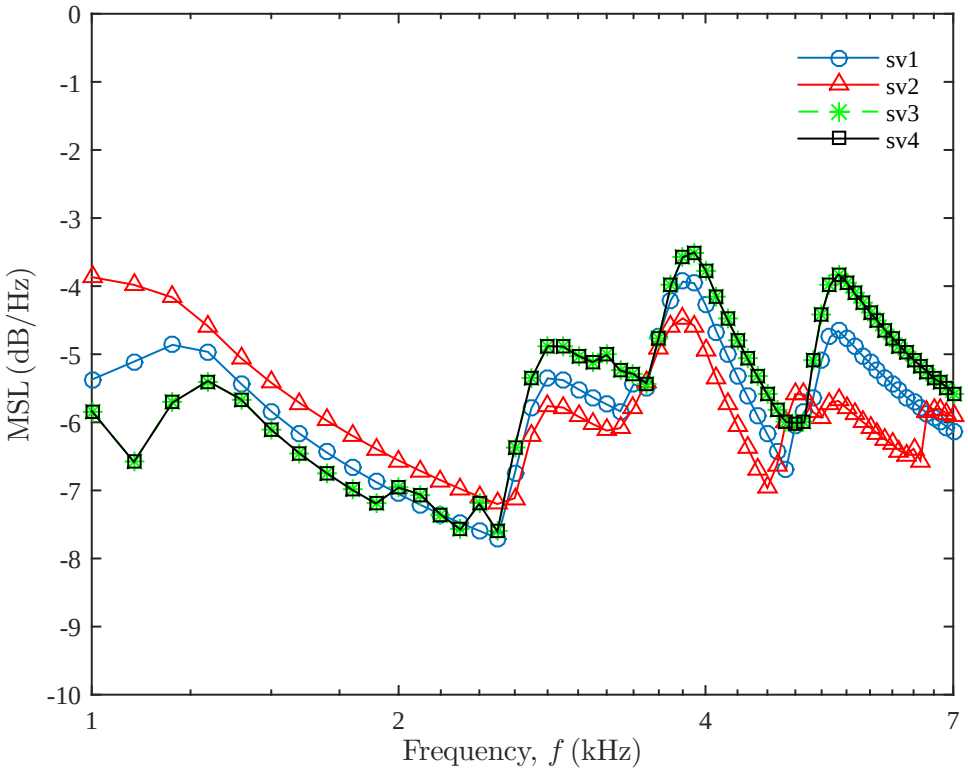

Figure 4.7: The variation of the MSL of the AWT array with frequency measured using a synthetic source at $\mathbf{x}_s = (-0.3, 0, 0)$ with four different steering vectors.

4.4 Algorithmic limitations of beamforming

Algorithmic limitations of beamforming are those limitations that are associated with the mathematics of beamforming, and not necessarily those that are associated with the layout of the array, as the beamwidth and the MSL are. The discussion in this section will focus on two aspects of algorithmic limitations associated with conventional beamforming and deconvolution. The first is the ability of conventional beamforming to correctly estimate the amplitude of the source. The second is the resolution improvements that are gained by using deconvolution.

4.4.1 Beamforming amplitude estimation and the array gain field

Equation 4.8 shows that the conventional beamforming output at any point in the grid is a linear combination of the columns of the A-matrix, where the multiplication coefficients are the source autopowers of all the points in the grid. The t^{th} column of the A-matrix represents the PSF of the array for a single source at position $\mathbf{x}_t$. Therefore, the conventional beamforming output is a convolution of the true output and the array properties.

Because each column of the A-matrix represents the response of the microphone array due to a unit input at a particular position, the diagonal elements of the A-matrix must be exactly 1. *Depending on the steering vector formulation* and whether diagonal removal is used, this condition is not always satisfied using Equation 4.10 or 4.11. To meet this condition, each PSF (or column of A) must be divided by a normalisation factor, z_t. This

normalisation factor (denoted the 'spatial correction factor') is the value of the A-matrix at each diagonal. That is, the correction factor of the t^{th} column is

$$z_t = \mathrm{A}_{tt} = \sum_{q=1}^{M_0} \sum_{p=1}^{M_0} \mathrm{W}_{qq} \mathrm{W}_{pp} h_{qt}^* h_{pt} a_{qt} a_{pt}^*, \tag{4.15}$$

and in the case of diagonal removal

$$z_{tDR} = \mathrm{A}_{tt} = \sum_{q=1}^{M_0} \sum_{p=1, p\neq q}^{M_0} \mathrm{W}_{qq} \mathrm{W}_{pp} h_{qt}^* h_{pt} a_{qt} a_{pt}^*. \tag{4.16}$$

Table 4.2 gives the derived spatial correction factors using the four different steering vector formulations with and without diagonal removal. Table 4.3 gives the correction factors when the weighting matrix, W is the identity matrix. The results show that the corrections when using sv2 or sv3 reduce to simple expressions independent of the column number (i.e., independent of the spatial position in the scanning grid, $\mathbf{x}_t$). In the original formulation of DAMAS, sv2 was used and the results of Table 4.2 exactly match those presented by Brooks and Humphreys (2006).

One might question the utility of deriving analytical expressions for the A-matrix correction factors when it is valid to simply divide each column of the A-matrix by the value of the diagonal to achieve the same result. It is also valid to solve Equation 4.9 without considering the correction factors at all, since $\mathbf{x}$ is independent of any scaling applied to A and $\mathbf{b}$. Actually, this is an important feature of the generalised DAMAS methodology: it will inherently account for spatial correction because it is calculated as part of the A-matrix.

The reason why analytical expressions for the correction factors are useful is that this correction factor is exactly the 'array gain field' discussed in the previous section. Every correction factor, z_t, can be mapped to the t^{th} point in the scanning grid, creating a correction 'field'. To reiterate, the array gain field is the amplification of the source strength when performing conventional beamforming as the signal from that source is passed through the beamformer as it acts as a spatial filter. Derivation of the correction factors therefore gives further insight into the properties of the beamforming array.

Table 4.2: The array gain fields for the different steering vector formulations. z_t denotes the correction factor applied to the t^{th} point in the scanning grid.

	z_t	z_{tDR}
sv1	$\left[\frac{1}{M_0}\sum_{p=1}^{M_0} \mathrm{W}_{pp}\lvert a_{pt}\rvert\right]^2$	$\frac{1}{M_0}\left[\left(\sum_{p=1}^{M_0} \mathrm{W}_{pp}\lvert a_{pt}\rvert\right)^2 - \sum_{p=1}^{M_0} \mathrm{W}_{pp}^2\lvert a_{pt}\rvert^2\right]$
sv2	$\left[\frac{1}{M_0}\sum_{p=1}^{M_0} \mathrm{W}_{pp}\right]^2$	$\frac{1}{M_0^2}\left[\left(\sum_{p=1}^{M_0} \mathrm{W}_{pp}\right)^2 - \sum_{p=1}^{M_0} \mathrm{W}_{pp}^2\right]$
sv3	$\left[\frac{1}{\lvert\mathbf{a}_t\rvert^2}\sum_{p=1}^{M_0} \mathrm{W}_{pp}\lvert a_{pt}\rvert^2\right]^2$	$\frac{1}{\lvert\mathbf{a}_t\rvert^4}\left[\left(\sum_{p=1}^{M_0} \mathrm{W}_{pp}\lvert a_{pt}\rvert^2\right)^2 - \sum_{p=1}^{M_0} \mathrm{W}_{pp}^2\lvert a_{pt}\rvert^4\right]$
sv4	$\frac{1}{M_0\lvert\mathbf{a}_t\rvert^2}\left[\sum_{p=1}^{M_0} \mathrm{W}_{pp}\lvert a_{pt}\rvert^2\right]^2$	$\frac{1}{M_0\lvert\mathbf{a}_t\rvert^2}\left[\left(\sum_{p=1}^{M_0} \mathrm{W}_{pp}\lvert a_{pt}\rvert^2\right)^2 - \sum_{p=1}^{M_0} \mathrm{W}_{pp}^2\lvert a_{pt}\rvert^4\right]$

Table 4.3: The array gain fields for the different steering vector formulations when the weighting matrix is the identity matrix.

	z_t	z_{tDR}
sv1	$\left[\frac{1}{M_0}\sum_{p=1}^{M_0}\lvert a_{pt}\rvert\right]^2$	$\left[\frac{1}{M_0}\sum_{p=1}^{M_0}\lvert a_{pt}\rvert\right]^2 - \sum_{p=1}^{M_0}\left[\frac{\lvert a_{pt}\rvert}{M_0}\right]^2$
sv2	1	$\frac{M_0-1}{M_0}$
sv3	1	$1 - \frac{1}{\lvert\mathbf{a}_t\rvert^4}\sum_{p=1}^{M_0}\lvert a_{pt}\rvert^4 \approx \frac{M_0-1}{M_0}$
sv4	$\frac{\lvert\mathbf{a}_t\rvert^2}{M_0}$	$\frac{1}{M_0\lvert\mathbf{a}_t\rvert^2}\sum_{p=1}^{M_0}\lvert a_{pt}\rvert^2[\lvert\mathbf{a}_t\rvert^2 - \lvert a_{pt}\rvert^2]$

Consider, for example, a single source located at $\mathbf{x}_t$ with amplitude q_t. The beamforming output using sv1 and unity weighting is

$$Y(\mathbf{x}_t) = \mathbf{h}(\mathbf{x}_t)^{\mathrm{H}}\mathbf{a}_t\mathbf{a}_t^{\mathrm{H}}\mathbf{h}(\mathbf{x}_t) = \left[\frac{1}{M_0}\sum_{p=1}^{M_0}\lvert a_{pt}\rvert\right]^2 E(qq^*) = z_t X_t \tag{4.17}$$

which is the correction factor, z_t, in Table 4.3 multiplied by the source autopower, X_t.

Conventional beamforming maps (without deconvolution) can then be scaled by the array gain field presented in Table 4.2 to educe the true source power (relative to a reference microphone or otherwise). This is useful when diagonal removal is used, since the removal of the microphone self noise means that the array gain is never unity for any steering vector (see column 2 of Table 4.3).

As an example, consider a synthetic monopole source located at $\mathbf{x}_s = (0, 0, 0)$ with X_t=100 dB/Hz re. 20μPa (Figure 4.8) using the microphone array presented in Figure 4.3. Using sv4 with diagonal removal and setting the reference location to be the source position ($c_t = 1/4\pi$), conventional beamforming yields the maximum as 83 dB/Hz re. 20μPa (Figure 4.8a). When the array gain correction is applied, the maximum is increased to 100 dB/Hz re. 20μPa (Figure 4.8b). When DAMAS is used without considering the array gain (Figure 4.8c), the 100 dB/Hz re. 20μPa source amplitude is recovered. It is also observed that DAMAS improves the source map by reducing the resolution to effectively one pixel (the DAMAS 'resolution' is discussed in Section 5.3.2) and reducing the side-lobe level to negligible levels (at least 20 dB/Hz below the maximum value).

In the current FWMC results (presented in Chapter 6) a combination of CLEAN-SC deconvolution (which relies on the conventional beamforming map) and DAMAS is used to present the source maps and quantify the noise level respectively. While DAMAS will inherently account for the array gain correction, CLEAN-SC does not. In CLEAN-SC, the 'clean map' is built from scaled versions of the dirty conventional beamforming map. This means that, unlike DAMAS, there is no capability for the true source powers to be recovered without appropriately scaling the dirty map. The spatial corrections presented in Table 4.2 can be used to approximately correct the clean map. Figure 4.9 shows a comparison between beamforming maps that have been taken using CLEAN-SC, using sv4, with and without array gain correction. The sources are three synthetic monopole sources located at $\mathbf{x}_1 = (-0.1, 0, 0)$, $\mathbf{x}_2 = (0, 0.1, 0)$ and $\mathbf{x}_3 = (0.1, 0, 0)$ with strengths

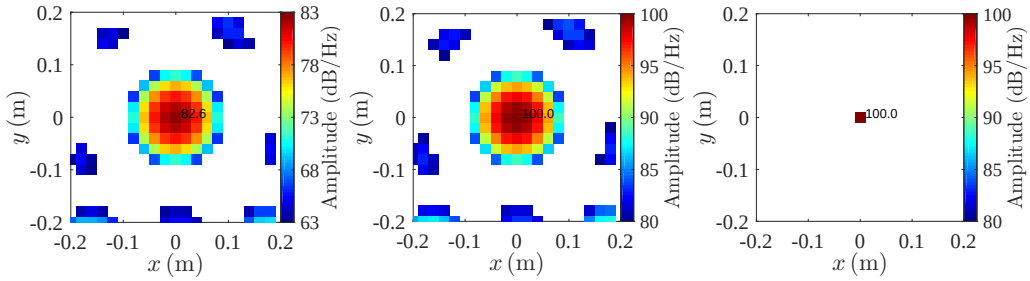

(a) No array gain correction (b) Array gain correction (c) DAMAS

Figure 4.8: An illustration of array gain correction and DAMAS output for a single monopole source at $\mathbf{x}_s = (0, 0, 0)$ with a nominal source strength of $X_t = 100\,\text{dB/Hz}$ re. $20\mu\text{Pa}$. a) Conventional beamforming using sv4 and no array gain correction. b) Conventional beamforming using sv4 with array gain correction. c) Conventional beamforming using sv4 with no array gain correction and DAMAS deconvolution.

$X_1^* = 100$, $X_2^* = 95$ and $X_3^* = 90\,\text{dB/Hz}$ re. $20\mu\text{Pa}$ respectively. Unlike DAMAS, without spatial correction CLEAN-SC does not recover the true source powers. After spatial correction has been applied, the true source powers are approximately recovered.

An important consideration when using the array gain field is that the correction is applied *after* CLEAN-SC has been performed. Application before CLEAN-SC could lead to amplification of an erroneous source, for example, a side-lobe. This may cause the side-lobe to appear larger than the main lobe after correction. CLEAN-SC would then identify the side-lobe as the dominant noise source, leading to an erroneously deconvolved map.

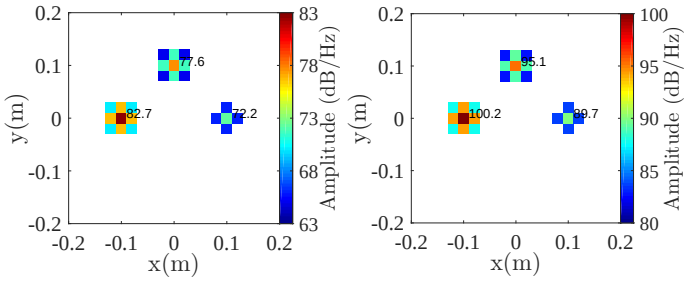

(a) No array gain correction (b) Array gain correction

Figure 4.9: An illustration of the use of CLEAN-SC on three monopole sources without (a) and with (b) the array gain field. The sources are located at $\mathbf{x}_1 = (-0.1, 0, 0)$, $\mathbf{x}_2 = (0, 0.1, 0)$ and $\mathbf{x}_3 = (0.1, 0, 0)$ with strengths $X_1^* = 100$, $X_2^* = 95$ and $X_3^* = 90\,\text{dB/Hz}$ re. $20\mu\text{Pa}$ respectively.

4.4.2 Resolution of DAMAS and CLEAN-SC

The 'resolution' that can be obtained using DAMAS is not well defined. As seen in Figure 4.8, the DAMAS output for a single monopole source is a single pixel with the correct amplitude. The same is true for multiple sources. On this evidence it would seem that the 'beamwidth' of DAMAS is only limited by the pixel size. However, this is not the case. Brooks and Humphreys (2006) notes that if the pixel size is too large, ghost images in the DAMAS output can appear. They also demonstrated that because of these ghost images, the main lobe 'leaks' power, meaning that the total power from a region

integrated around the source is lower than expected. This phenomenon is referred to as 'spatial aliasing' due to its analogies with FFT sampling rates. It is suggested that to avoid this, pixel sizes should be below $0.2B_w$, where B_w is the beamwidth of the array at a particular frequency.

On the other hand, there is no lower bound on the DAMAS pixel size. Brooks and Humphreys (2006) commented that the pixel size must be large enough to allow for mutual influence between grid points, although they did not qualify what size is necessary. The lower bound of the DAMAS pixel size is therefore normally based on minimising computational expense.

As it stands, the current definition of DAMAS 'resolution' is unsatisfactory. In this thesis, a more robust approach is taken to select the DAMAS pixel size. The approach is based on the beamformer's ability to resolve multiple sources. First, the CSM corresponding to two monopole sources of strength 100 dB/Hz re.20μPa are synthetically generated. The two sources are separated by a distance d_q and are located at $\mathbf{x}_1 = (-d_q/2, 0, 0)$ and $\mathbf{x}_2 = (d_q/2, 0, 0)$. Then beamforming using the top array microphone layout is performed along a single dimension (the x-axis) using DAMAS. The DAMAS pixel size is chosen to be 1 mm, far smaller than the recommended size of $0.2B_w$ for frequencies less that 7 kHz. This pixel size can be used because only one dimension is used, lowering the computational expense. The algorithm is repeated for incrementally decreasing values of separation distance. The point where only one maxima occurs in the DAMAS output then corresponds to the minimum separation of two point sources that can theoretically be resolved using DAMAS (and the top array microphone lay-out). This effectively defines the DAMAS 'beamwidth' and is therefore a suitable choice for pixel size. The routine is repeated for several frequencies between 1 and 7 kHz.

The result of this procedure is shown in Figure 4.10. The limiting beamwidth of DAMAS is $0.4B_w$, which lies between the Sparrow Limit (0.66λ) and $0.2B_w$. This means that 'super-resolution' is achieved because the algorithm is able to resolve sources spaced closer than the Sparrow Limit. The results are in general agreement with the super-resolution calculated for DAMAS2 by Dougherty (2010). In that study, DAMAS2 was measured to have a beamwidth that was 21% smaller than the Sparrow Limit (compared with 40% smaller than the Sparrow Limit in this study).

According to these results, the DAMAS resolution is lower than the recommended value by Brooks and Humphreys (2006) to avoid spatial aliasing. However, in the study by Brooks and Humphreys (2006), only a low level of spatial aliasing was observed even at a pixel size of $0.5B_w$. Therefore, it appears appropriate to choose the DAMAS pixel size of $0.4B_w$ and expect low spatial aliasing. It should be noted that choosing a pixel size lower than $0.4B_w$ will still result in a correct map, but at unnecessary computational expense and yield no new information.

With the above analysis, the DAMAS pixel size can now be chosen for the FWMC experiments. Broadband noise from FWMCs (which beamforming is employed to study) falls between 3 kHz and 10 kHz. Previously it was found that $B_w = 0.9\lambda$. Therefore, for 3 kHz, the maximum pixel width is 3 cm (using a nominal speed of sound of 343 m/s) and for 10 kHz the maximum pixel width is 1 cm. When performing DAMAS, it is convenient to choose a universal pixel width across all frequencies to ensure that spatial integration regions cover the same area (spatial integration is discussed in Section 4.5). Thus the

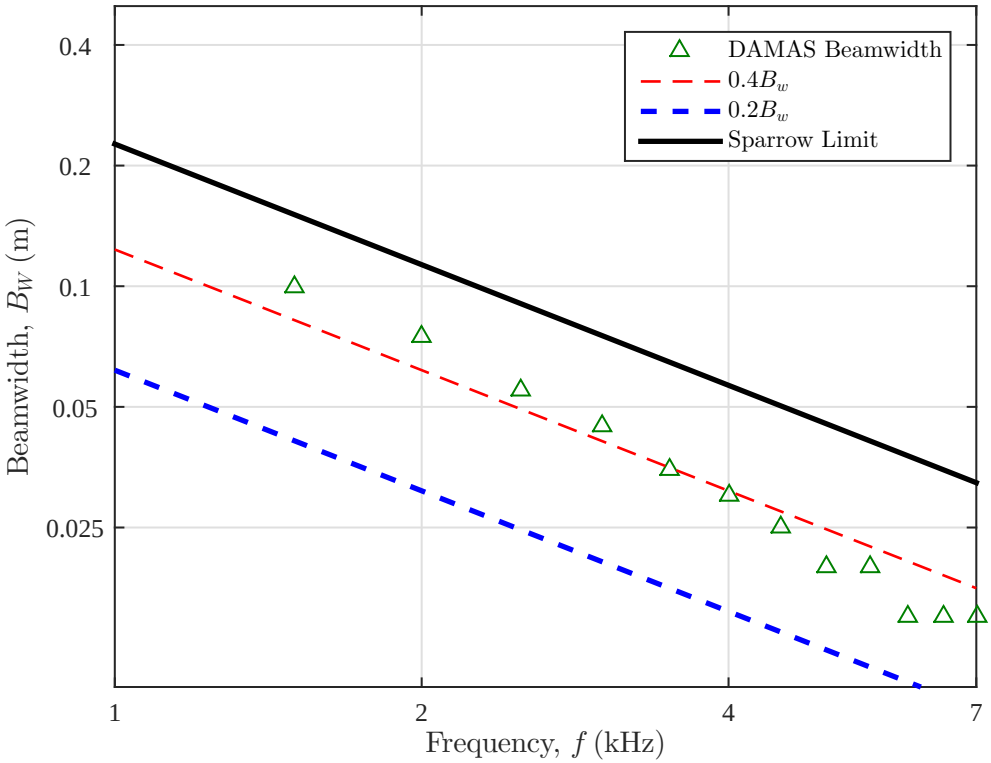

Figure 4.10: The variation of the resolution, measured as beamwidth, B_w, of the DAMAS algorithm using the top array microphone layout.

chosen pixel width for the present investigation is 1 cm.

The main reason why this study uses DAMAS deconvolution to quantify FWMC broadband noise over CLEAN-SC is that CLEAN-SC has lower resolution. This is because the CLEAN-SC algorithm requires the maximum of the conventional beamforming source map to represent the location of the source. If, for example, the maximum in the beamforming map was a merged peak from two noise sources that were close together, i.e., the two sources were within the beamwidth of the array, then CLEAN-SC will not be able to separate the sources. Comparatively, because of its super-resolution, DAMAS would be able to separate the sources.

To illustrate this discrepancy, Figure 4.11 shows a situation where there are two monopole noise sources at 3 kHz, both with strengths of 100 dB/Hz re. 20μPa, side-by-side, as visualised using the top array. The sources are spaced 120 mm apart, which is above the beamwidth of the array at that frequency, meaning conventional beamforming can resolve two peaks. CLEAN-SC and DAMAS manage to deconvolve the map and separate the two peaks independently. In Figure 4.12, the sources are now 80 mm apart, which is slightly narrower than the beamwidth of the array at that frequency, meaning that conventional beamforming yields one elongated maxima. Although DAMAS is able to separate the two sources, CLEAN-SC calculates an erroneous source map signifying that the sources lie within the resolution limit of CLEAN-SC.

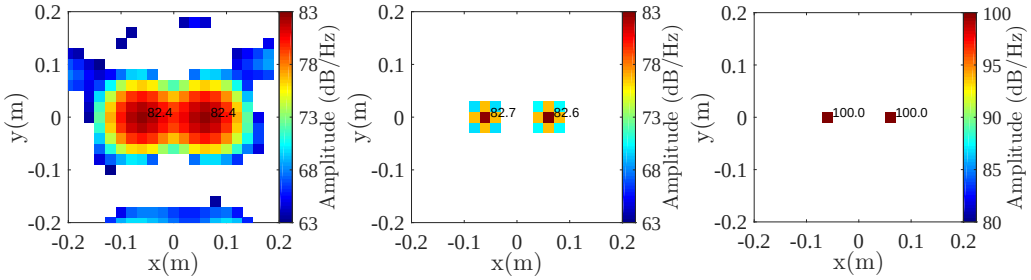

(a) Conv. beamforming (b) CLEAN-SC (c) DAMAS

Figure 4.11: A comparison of beamforming map using (a) conventional beamforming, (b) CLEAN-SC and (c) DAMAS for two point sources spaced 120 mm apart, each with a source strength of 100 dB/Hz re. 20μPa .

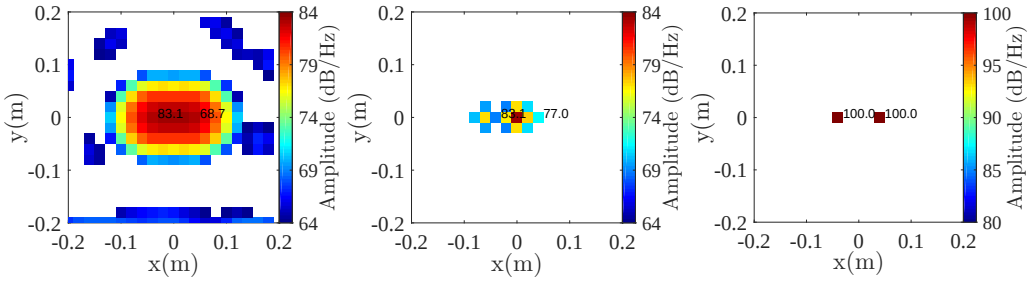

(a) Conv. Beamforming (b) CLEAN-SC (c) DAMAS

Figure 4.12: A comparison of the source visualisation using (a) conventional beamforming, (b) CLEAN-SC and (c) DAMAS for two point sources spaced 80 mm apart, each with a source strength of 100 dB/Hz re. 20μPa .

4.5 Identification, quantification and correction of experimental sources of error in beamforming

Experimental beamforming error can be categorised into two types - systematic errors that can theoretically be corrected and random errors that cannot be corrected but whose probability level can be quantified so confidence intervals can be established. In this study, systematic errors include coherence loss between microphone signals due to turbulent scattering of sound by the shear layer, errors caused by reflections in the test chamber and errors caused by shear layer refraction. Random error includes uncertainty in the assumed microphone locations, random microphone phase errors, the statistical errors due to the finite length of the microphone records and random errors in the assumed speed of sound. All of these sources of error will be discussed by using an experimental test case. The final uncertainty bounds of the beamforming analysis incorporating all of the above sources of error and appropriate corrections will then be estimated for the experimental test case using a Monte-Carlo based approach.

4.5.1 Experimental test case

The test case was a cylinder that spanned the length of the contraction. The cylinder had a diameter of 4 mm and the axis of the cylinder was located 110 mm downstream from the nozzle exit plane. The length of the cylinder was 400 mm so that it exceeded the width of the nozzle and was mounted so that no boundary layer was developed at the

mounting point. For the test case, the free-stream velocity was 38.75 m/s, so that cylinder was expected to shed anti-symmetric von Kármán vortices at 2 kHz. According to Phillips (1956), anti-symmetric von Kármán vortex shedding at 2 kHz will produce dipolar sound radiation at 2 kHz (the fundamental 'Aeolian tone') and 6 kHz (the second harmonic) with the lobes of the dipole pointing toward the top array. For this length cylinder, the shedding frequency was approximately 10 times more than the natural frequency of the cylinder, so structural vibration was not expected to influence the acoustic results. The test case is a good indicator of the experimental performance of the array and the applicability of the systematic error correction schemes outlined in the following sections because the cylinder is small enough to not perturb the shear layer significantly (so common shear layer correction schemes are applicable) but is long enough to produce high frequency tonal noise with a good signal-to-noise ratio. Reflections may occur due to the cylinder's proximity with the contraction nozzle exit and coherence loss may also occur due to the turbulent scattering of the flow-induced noise, particularly at the edges of the shear layers. An illustration of the experimental set up of the test case is shown in Figure 4.13.

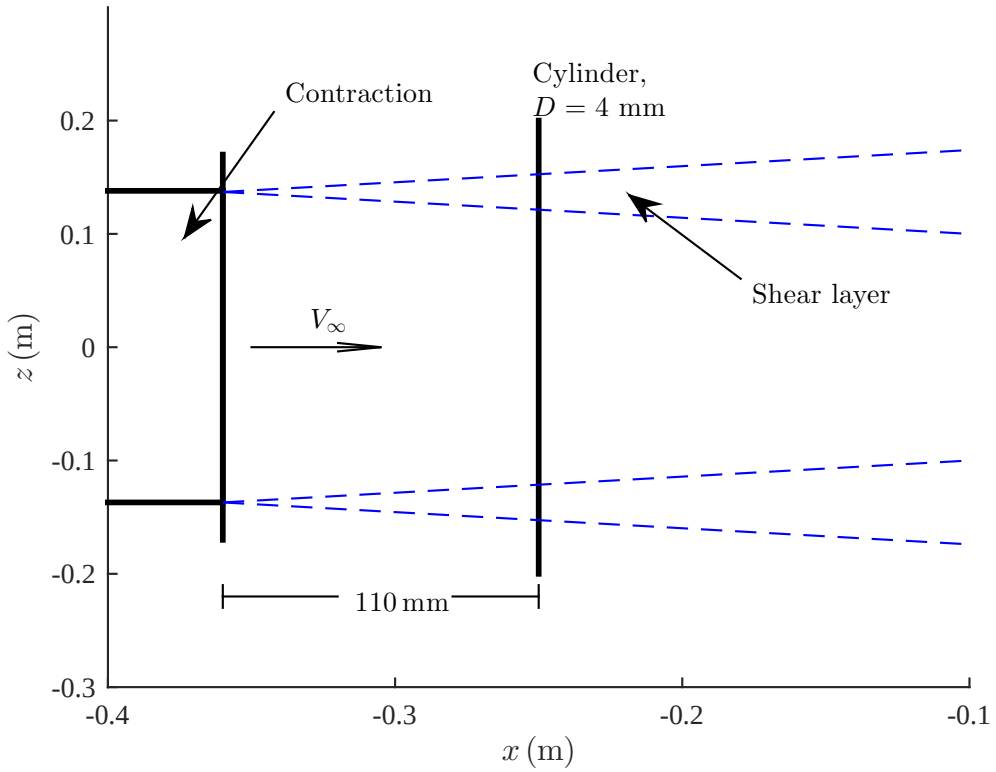

Figure 4.13: A top down view of the experimental set up of the test case used to study the systematic and random error of beamforming images using the AWT top array.

4.5.2 Acoustic reflections from solid wall boundaries

In hard walled wind tunnels, acoustic reflections can create image systems beyond the walls of the tunnels. Generally, these image systems will be much weaker than the real image because of the extra time it takes to propagate to the microphones and that the hard wall will not be a perfect reflector. Additionally, if the scanning grid contains only

the interior of the tunnel, these images will not be seen. One important consideration is that the image system will create side-lobes that do appear in the scanning grid. These side-lobes can theoretically create false images or artificially enhance the integrated power of the source region. In practice, however, these effects have been found to be minimal, even in hard walled wind tunnels (Mueller 2002; Sijtsma 2007). Since the AWT is lined with foam wedges to create an anechoic environment above 300 Hz, reflections are not expected to significantly influence the results at frequencies where beamforming is performed. If, however, acoustic reflections are expected due to interactions between the flow-noise and the model itself, these can be easily accounted for by including the reflected domain in the beamforming grid and applying deconvolution techniques (CLEAN-SC or DAMAS) that remove side-lobes.

For the experimental test case, the contraction nozzle was the only source of possible reflections. To investigate whether reflections from the contraction were significant, two source domains were tested. One source domain ranged from $x = -0.1$ to $x = -0.4$ so that it would not include any reflected images from the cylinder. The second domain ranged from $x = -0.1$ to $x = -0.8$, so it would include any reflected images. The source maps were taken at 2 kHz and 6 kHz respectively using conventional beamforming as shown in Figure 4.14. Comparing the maps at 2 kHz, Figure 4.14a and 4.14c respectively, there is no evidence of reflections interfering with the source map. At 6 kHz there does appear to be a very low level reflected image at $x \approx -0.5$. However, since this image is nearly 6 dB lower than the maximum in the source map, the impact that its side-lobes would have on the source map is negligible.

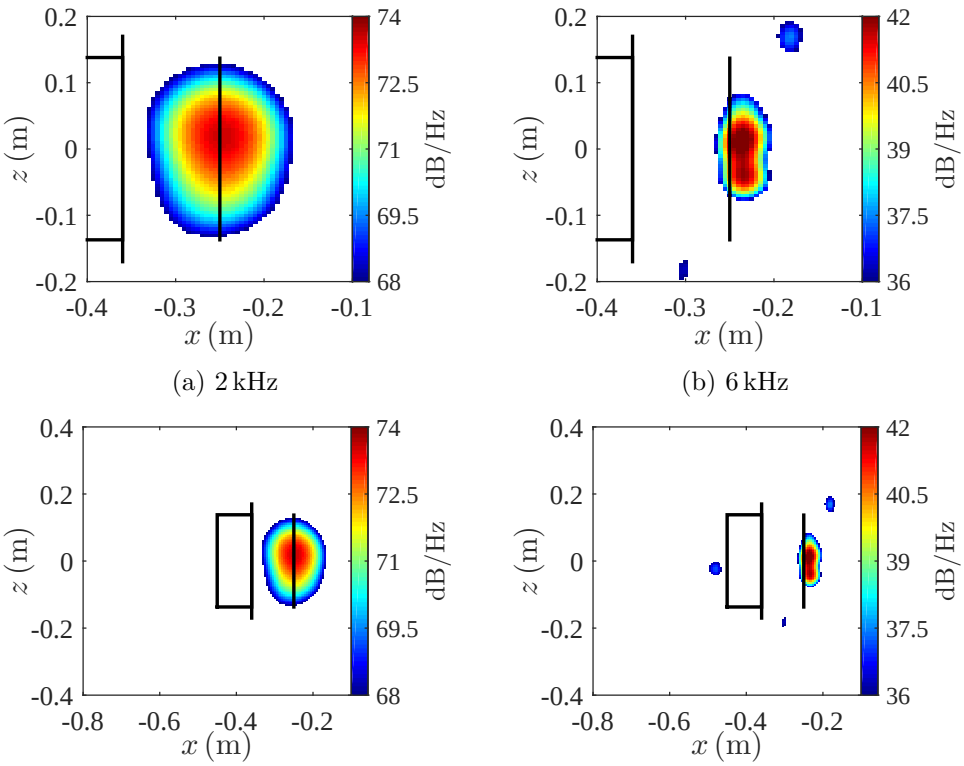

(a) 2 kHz (b) 6 kHz

(c) 2 kHz (d) 6 kHz

Figure 4.14: An illustration of the effect of reflections from the contraction on the beamforming image. The left maps (a and c) were taken at 2 kHz and the right maps (b and d) were taken at 6 kHz.

4.5.3 Shear layer correction

Acoustic measurements in open-jet anechoic wind tunnels are performed with microphones located outside of the mean flow in a quiescent environment. Ray paths exiting the mean flow will cross a shear layer before reaching the microphone. The rays will subsequently be refracted and attenuated because of this difference in acoustic medium, which will change the propogation time of the ray itself from the source to the receiver. This is an important effect to take into account when considering acoustic source localisation with a phased microphone array. The additional time it takes for the source to travel to the microphone manifests itself as a phase error in the steering vector in Equation 4.4. This phase error is magnified at high frequencies. The net result of a shear layer is a downstream shift of the resultant sound map.

For planar beamformers in an open-jet test section, there are three viable approaches to model and correct for the propagation through the shear layer. The first is a simple shift of the entire source map upstream by a distance $d_{shift} = M_\infty h_{1/2}$, where M_∞ is the Mach number of the potential core of the flow and $h_{1/2}$ is the half-width of the potential core. This was originally postulated by Padois et al. (2013a) and shown to work well in practice for low Mach number shear layers (Moreau et al. 2014).

The second method involves analytically solving for the change in propagation time due to the acoustic rays convecting and refracting through the shear layer. Here the shear layer is assumed to be an infinitely thin boundary that separates two media; one medium where there is a mean flow and one where there is no flow. Thus simple geometrical acoustics based on Snell's law can be used to find the propagation time. Koop et al. (2005) calculated the emission path and emission time for a ray travelling through a shear layer by reformulating the problem as time minimisation. The analysis assumed that the source location and microphone location lay in the same plane. Bahr et al. (2011) used ideas presented by Amiet (1978) to extend the analysis Koop et al. (2005) to make it suitable for out-of-plane source receiver combinations.

The procedure calculates the propagation time, t_p, given by

$$t_p = \frac{r_0}{c_0} + \frac{r_1}{c_1}, \tag{4.18}$$

where r_1 is the distance from the source point to the intersection point of the straight ray path with the infinitely thin shear layer, denoted $\mathbf{x}_{Ic} = (x_{Ic}, y_{Ic}, z_{Ic})$, c_1 is the equivalent speed of sound within the moving air-stream based on the angle of emission, r_0 is the distance from the shear layer intersection point and the microphone and c_0 is the speed of sound in a quiescent environment.

The ray speed, c_1, depends on the emission angle, $\cos\theta$, by

$$c_1 = M_\infty c_0 \cos\theta + \sqrt{(M_\infty c_0 \cos\theta)^2 + c_0^2 - (M_\infty c_0)^2}, \tag{4.19}$$

where θ is the ray emission angle relative to the free-stream. The emission angle, in turn, is a function of the intersection point, $\mathbf{x_{Ic}}$, of the ray path with the shear layer, determined by

$$\cos\theta = \frac{x_{Ic}}{|\mathbf{x}_{Ic}|}. \tag{4.20}$$

The intersection point of the shear layer is found by iteratively selecting an intersection point and evaluating the emission time via Equation 4.18. The correct intersection point is found when the emission time is minimised over the shear layer surface (Koop et al. 2005). Bahr et al. (2011) found that this minimisation could be achieved by solving for $\mathbf{x}_{Ic}$ directly using

$$\frac{x_{Ic} - x_s}{|(\mathbf{x}_{Ic} - \mathbf{x_s}) \circ \beta|} - \left(1 - M_\infty^2\right) \frac{x_m - x_{Ic}}{|\mathbf{x_m} - \mathbf{x}_{Ic}|} - M_\infty = 0, \tag{4.21}$$

$$\frac{y_{Ic} - y_s}{|(\mathbf{x}_{Ic} - \mathbf{x}_s) \circ \beta|} - \frac{y_m - y_{Ic}}{|\mathbf{x}_m - \mathbf{x}_{Ic}|} = 0, \tag{4.22}$$

$$z_{Ic} - z_s = h_{1/2}. \tag{4.23}$$

Here $\mathbf{x}_s = (x_s, y_s, z_s)$ is the source position and $\mathbf{x}_i = (x_i, y_i, z_i)$ is the microphone location. The symbol $\circ$ denotes element-wise multiplication. It is unclear whether this calculation is more efficient than simply minimising the time.

A pressure amplitude correction can also be applied to account for spreading of the ray-tube area as it propagates through the shear layer (Mueller 2002). Padois et al. (2013a) show, however, that the amplitude correction is unnecessary for $M \leq 0.1$ since it is less than 1% below $M_\infty < 0.2$. This method has become the standard practice for aeroaocustic studies utilising beamforming (Brooks and Humphreys 2003) because of its computational efficiency. However, this method is only suitable for a planar shear layers and cannot account for shear layers that are curved or not smooth. To overcome this limitation, a modification of the aforementioned shear layer correction method was developed to account for non-smooth and curved shear layer surface (known as the Generalised Shear Layer Correction method or GSLC). The GSLC was not required to analyse the FWMC data presented in this thesis, but is useful when applied to three-dimensional beamforming. Both the GSLC and three-dimensional beamforming are detailed in Appendices B and C respectively.

The third method, which can theoretically account for any shear layer shape, is to numerically integrate the ray path through the assumed or measured velocity field to calculate the propagation time. The differential equations that are integrated are known as the 'ray tracing equations' (Pierce 1989) and come as a direct consequence of an Euler-Lagrange minimisation of the emission time (Fermat's Principle). The ray tracing equations are given by (Pierce 1989),

$$\frac{d\vec{x}}{dt} = \frac{c_0^2 s}{\Omega} + \vec{v}, \tag{4.24}$$

$$\frac{d\vec{s}}{dt} = \frac{\Omega}{c_0} \nabla c_0 + \vec{s} \times (\vec{\nabla} \times \vec{v}) - (\vec{s} \cdot \vec{\nabla})\vec{v}, \tag{4.25}$$

where $\vec{x(t)}$ is the position of the ray path at time t, c_0 is the speed of sound (that may vary spatially), $\vec{s}$ is the 'slowness vector' defined as $\vec{s} = \dfrac{\vec{n}}{c_0 + \vec{v} \cdot \vec{n}}$, $\vec{n}$ is the unit vector normal in the direction of propagation, $\vec{v}$ is the velocity field and $\Omega = \vec{v} \cdot \vec{s}$. These equations are ordinary differential equations and can be integrated using numerical techniques such as Runge-Kutta integration. Although ray tracing is more a accurate and general method, it is computationally expensive. Furthermore, it requires an accurate measurement of the

velocity field and its spatial derivatives in three-dimensions.

In this study, all three methods are compared on the aforementioned experimental test case. For methods 1 and 2, the shear layer was approximated as infinitely thin, while the potential core was assumed to have a half thickness, $h_{1/2} = 0.037\,\text{m}$. For method 3, the actual shear layer velocity profile of the jet was measured using a Pitot tube (with the cylinder removed). The pitot tube was traversed on a grid in the $x - z$ plane (see Figure 4.15) in 2-mm increments and the velocity measured at each point in the grid. The velocity profile was then modelled using a least square regression analysis. The resulting profile is given by the analytic function described in Equations 4.26 and 4.27,

$$\vec{v} = (u, 0, 0), \tag{4.26}$$

$$u = \begin{cases} c_0 M_\infty \exp\left(-\ln(2)\left(\dfrac{y + 0.1(x + 0.36) - 0.035}{0.12(x + 0.36) + 0.0002}\right)^2\right) & y + 0.1(x + 0.36) > 0.035, \\ c_0 M_\infty & y + 0.1(x + 0.36) \leq 0.035, \end{cases} \tag{4.27}$$

where $M_\infty = 0.11$, $c_0 = 343\,\text{m/s}$ and x and y are measured in metres. Figure 4.15 compares Equation 4.27 with the measured velocity. Excellent agreement with the experimental results is observed.

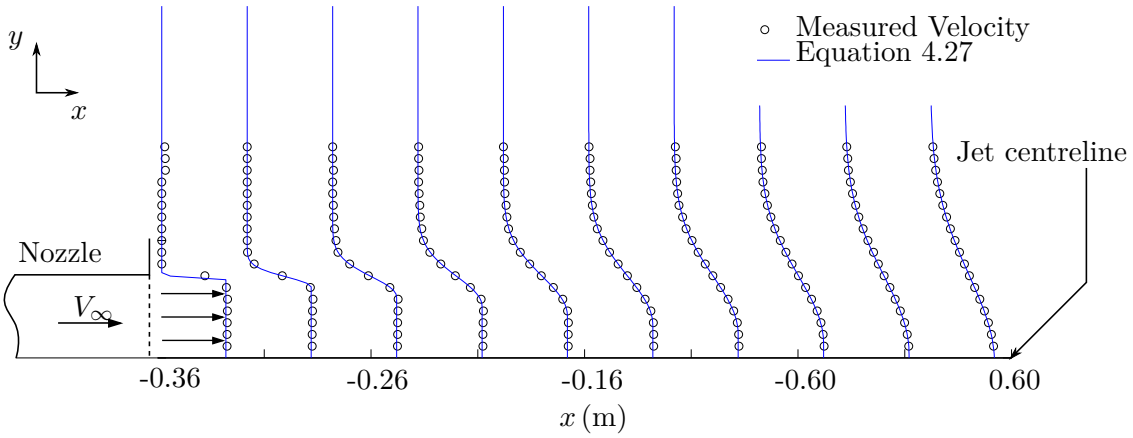

Figure 4.15: The AWT jet profile as modelled by Equation 4.27 (blue line). Equation 4.27 is also compared with experimentally obtained data (black circles) taken with a Pitot tube.

In Equation 4.26 it is assumed that the velocity profile is invariant in the cross-stream direction (z-direction). This assumption appears valid based on the cross-stream velocity results presented in Chapter 3.

After the time delays were calculated for each method, they were used to generate conventional beamforming maps (using Equation 4.1) and sv2 for the test case data. For method 1, the beamforming maps were generated without distortion to the time delays and the correction applied after. Figures 4.16 shows the results at 2 and 6 kHz; Figure 4.16a and b for no correction, 4.16c and d for method 1, 4.16e and f for method 2 and 4.16g and h for method 3.

The results show that if no shear layer correction is applied, the image is shifted downstream. As expected, the effect is greatest at 6 kHz, where the image is shifted by approximately 0.025 m. At 2 kHz the image is only shifted by 7.5 mm. When method 1 is used for correction, the image is perfectly corrected at 2 kHz. At 6 kHz the image is under corrected. When method 2 is used, this time the image at 6 kHz is corrected to within 2.5 mm while the image at 2 kHz is over corrected by 7.5 mm. Method 3 provides very similar results to method 2. There is some distortion to the map at $x = -0.28$ which is due to poor numerical convergence of the ray tracing algorithm leading to high numerical errors.

4.5.4 Coherence loss

Coherence loss is a phenomena where the coherence between microphones in the array is lost because of noise scattering by turbulence in the flow. Coherence loss affects the resolution and dynamic range of the microphone array. Typically, coherence loss increases with frequency, turbulence, microphone separation and directionality of the source (Oerlemanns et al. 2007). This is why in some aeroacoustic studies (Brooks and Humphreys 2003), two nested arrays are used; a large aperture array to measure low frequency noise and a small aperture array to measure high frequency noise.

As demonstrated by Geyer (2011), coherence loss can be indirectly measured using a method described by Sijtsma and Stoker (2004). Here, beamforming sound maps are generated for a test case at a variety of frequencies first using the full array and then using the array with the outer microphones excluded. If coherence loss is present, the beamwidth will reduce when using the full array compared with the reduced array.

To investigate possible coherence loss effects, beamforming maps from the test cylinder were generated twice; once using the full 31 microphone in the array and then using a reduced number of microphones (24) with the outer 7 microphones subtracted from the CSM. Figure 4.17 shows the beamforming map at 2 and 6 kHz. The flow direction is from left to right and no shear layer correction has been applied.

Figure 4.17 shows that at 2 kHz, the beamwidth is much larger when the array size is reduced. Additionally, the peak sound power level is approximately the same in both cases. This indicates that at 2 kHz, coherence loss does not appear to impact the array output. For 6 kHz, the beamwidth for the reduced array is again larger than that of the full array. In this case, the peak sound power level is only 2 dB higher than that of the full array. This indicates that while coherence loss may be slightly affecting the array output at 6 kHz, there is no benefit in array resolution by using a reduced array.

4.5.5 Random errors

There are several major sources of random error when using beamforming (Yardibi et al. 2010). These are (1) errors in the assumed locations of the microphones, (2) random phase errors in the microphones' frequency response, (3) statistical averaging errors in the CSM due to finite microphone record lengths, and (4) errors in the assumed speed of sound.

Random errors propagate through the conventional beamforming equation (Equation 4.1) to create a distribution of the measured beamforming amplitudes at each location in

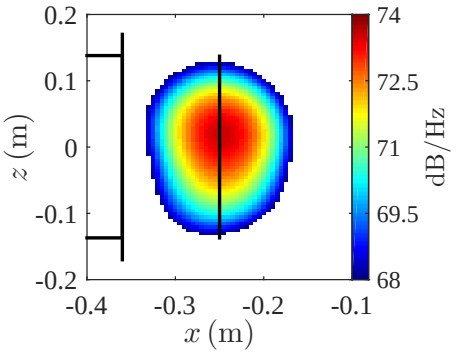

(a) 2 kHz, No correction

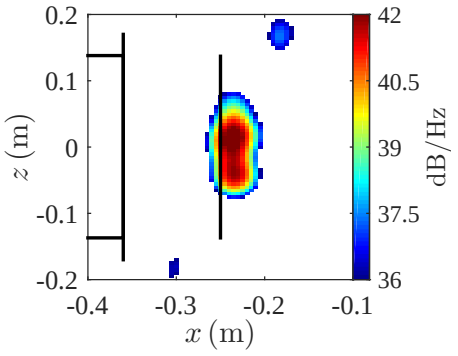

(b) 6 kHz, No correction

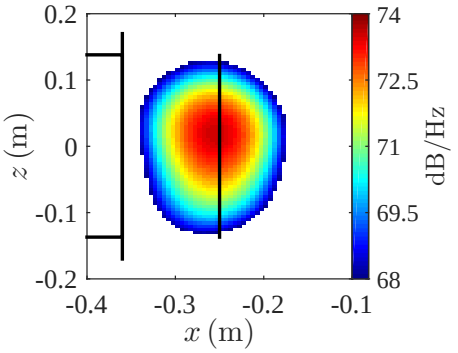

(c) 2 kHz, Padois et al. (2013a) correction

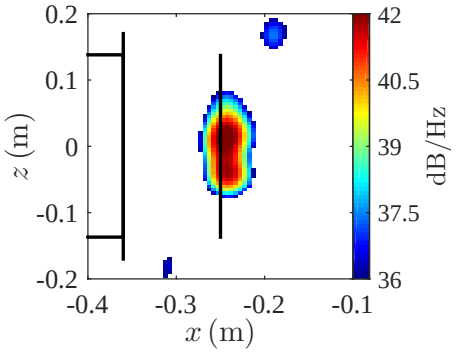

(d) 6 kHz, Padois et al. (2013a) correction

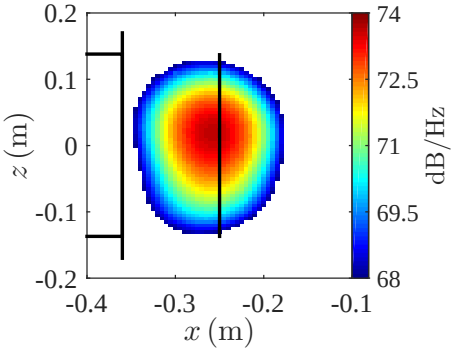

(e) 2 kHz, Bahr et al. (2011) correction

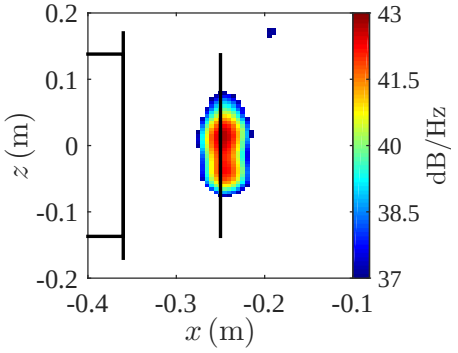

(f) 6 kHz, Bahr et al. (2011) correction

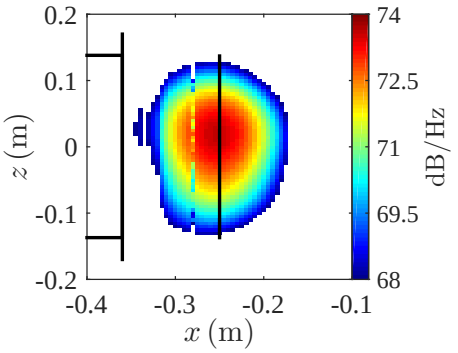

(g) 2 kHz, Ray tracing

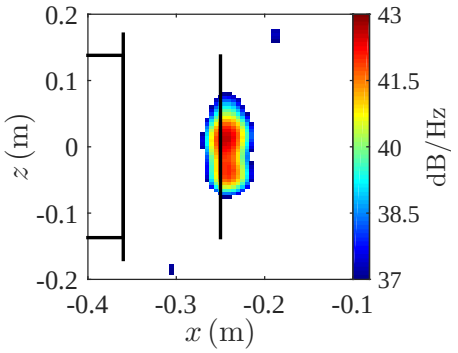

(h) 6 kHz, Ray tracing

Figure 4.16: A comparison of three different shear layer correction methods. Images in the left column were taken at 2 kHz, images in the right column were taken at 6 kHz. Figures (a) and (b) have no correction applied, (c) and (d) using the Padois et al. (2013a) method (method 1), (e) and (f) using the Bahr et al. (2011) method (method 2), and (g) and (h) using ray tracing (method 3).

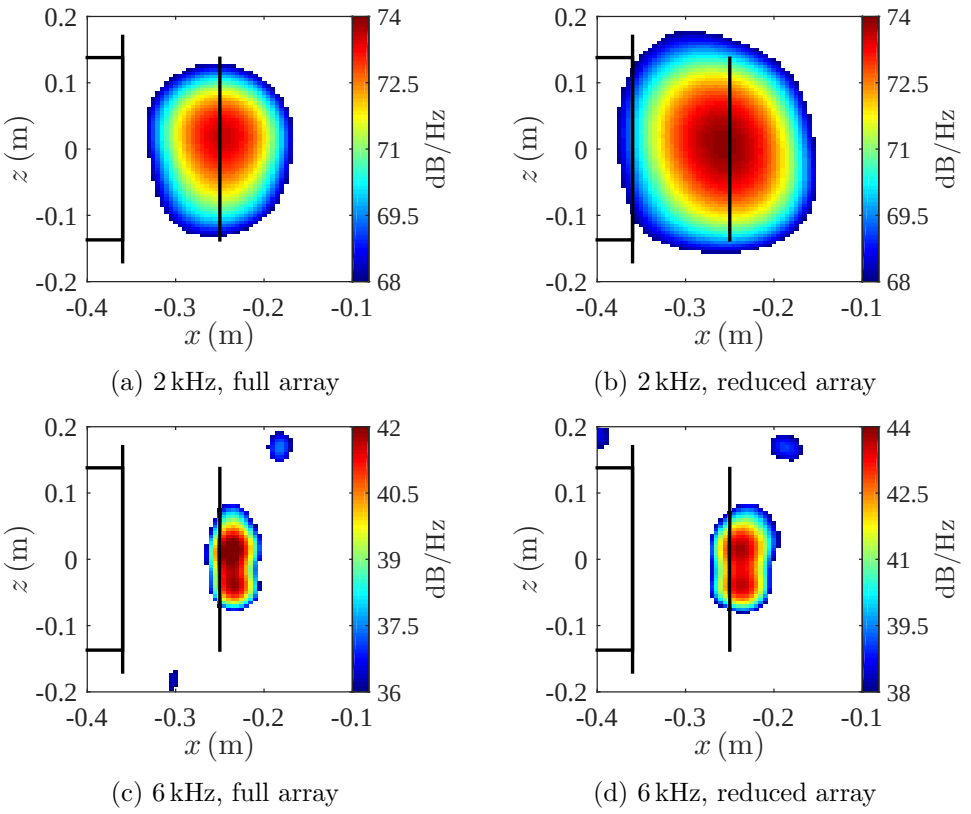

(a) 2 kHz, full array

(b) 2 kHz, reduced array

(c) 6 kHz, full array

(d) 6 kHz, reduced array

Figure 4.17: Source maps of the cylinder test case using the full array (a and c) and a reduced array with the outer microphone shaded (b and d). Images on the left were taken at 2 kHz and images on the right were taken at 6 kHz.

the scanning grid. In this thesis, a *Monte Carlo* analysis is used to understand how random perturbations of the inputs (random errors) propagate through to the beamforming output. The inputs include the microphone spatial locations, the microphones' phase, the temperature (affecting the nominal speed of sound) and statistical errors of the CSM entries.

A Monte Carlo error analysis is a technique where the inputs to a given functional relationship are perturbed randomly according to an assumed probability distribution. Once this has been done for sufficiently many trials, the resulting output distribution is then measured and the standard propagation error can then be quantified based on the measured output distribution.

In this thesis, the distributions of the input sources of error are assumed to be Gaussian, characterised by a mean (or nominal value) and a standard deviation, σ. The microphone locations are perturbed using a standard deviation of σ_x, σ_y and σ_z for the x, y and z-locations respectively. The microphone phases are perturbed using a standard deviation of σ_ϕ and the temperature is perturbed using σ_t. The averaging errors of the CSM entries (which are cross-spectral density values) are calculated using the co-variance formulas presented in Bendat and Piersol (2010) and applied to the CSM using the method of Yardibi et al. (2010).

Technically speaking, errors in the microphone locations and microphone phase are actually a type of systematic error that can be corrected by using an array calibration technique, such as that described by Mueller (2002) where a speaker is placed in the

test section where the test model would normally be. White noise is driven through the speaker and a complex valued array calibration function is generated by focussing the array at the speaker location. Ultimately the calibration function is applied to the cross-spectral matrix as an overall phase correction to perfectly account for the change in microphone positions and deviation in frequency response phase between the assumed and actual values. The 'Dougherty Calibration' method was attempted in this study. A small speaker was driven with white noise at the location of the test cylinder. Special attention was paid to insulating the contraction nozzle to prevent unwanted reflections. Unfortunately, it was found difficult to obtain a uni-directional white noise source at frequencies where the beamformer was intended to be used (3 kHz - 10 kHz). Hence, along with block averaging errors and speed of sound estimate errors, errors in the microphone locations and phase are treated here as random errors, i.e., the microphones are assumed to have a nominal spatial location and zero phase difference with each other. Then, the locations and phase differences are perturbed in a Gaussian manner around the nominal value with a selected standard deviation and the influence on the final beamforming output quantified.

Microphone locations

The top array is constructed of 31 G.R.A.S. 1/4" microphones press fit into a medium density fibre (MDF) board through holes drilled in predetermined locations. The locations of these holes were measured using standard hand-held instruments (a measuring tape and a pencil). Because of this, the error in the microphone locations from their nominal positions in the $x-z$ plane is conservatively assumed to be ± 2 mm (i.e., the positions vary normally with a standard deviation of $\sigma_z = \sigma_x = 2.5$ mm). Since the microphones were only press fit into the MDF, they were free to move when, for example, fitted with a microphone windsock or accidentally knocked. The error in the y-position of the microphone locations is thus estimated to be much larger than that in $x-z$ plane at ± 10 mm (i.e., $\sigma_y = 5$ mm).

Errors in the microphone phase

When performing beamforming, the phase difference between each microphone channel is nominally assumed to be 0. However, according to the transducer documentation, G.R.A.S. 40PH microphones have phase differences (Δ_ϕ) that may vary by $\Delta_\phi = \pm 10$ degrees between 0 to 10 kHz. Thus the standard deviation of the each microphone record's phase is $\sigma_\phi = 3.5$ degrees. This ensures that the standard deviation of the phase *difference* between any two microphones, calculated by multiplying the standard deviation of the phase by $\sqrt{2}$, between two randomly selected microphones, is 5 degrees, with a corresponding 95% confidence level of 10 degrees.

Averaging of the CSM

Averaging of the acoustic records to calculated the CSM lead to statistical errors in the individual CSM entries. However, independent perturbations of the individual CSM entires (as is done for the microphone locations) cannot be done because each entry has a co-variance with each other entry. Therefore, the co-variance matrix of the elements of

the CSM, Σ, must first be calculated and then applied to the nominal CSM as a Gaussian perturbation matrix.

The co-variance matrix Σ was calculated using the method outlined by Yardibi et al. (2010). A Cholesky decomposition of Σ was then applied to obtain a lower triangular matrix, Λ, such that $\Sigma = \Lambda\Lambda^{\mathrm{H}}$. The Gaussian perturbation matrix with co-variance of Σ was then calculated by multiplying Λ by an independent and identically distributed Gaussian random vector, η, with unit variance.

As it turns out, the Guassian perturbation matrix is fully determined by the number of overlapping averaging blocks, B, used in the cross-spectral density estimates (see Equation 3.32). The averaging error in the CSM due to finite averaging is calculated using a block number $B = 959$, which is what was used to generate the CSMs in the FWMC beamforming results presented in Chapter 6.

Errors in the speed of sound estimate

The speed of sound is dependent on the temperature of the air by Bies and Hansen (2009)

$$c = \sqrt{\gamma R T}, \tag{4.28}$$

where T is the temperature in degrees Kelvin, $\gamma = 1.4$ is the ratio of specific heat in air and $R = 287.058\,\mathrm{m}^2/\mathrm{s}^2/\mathrm{K}$ is the ideal gas constant. In this study, the lab temperature was measured at 21° and did not vary significantly when the acoustic data were measured. The standard deviation of the lab temperature is conservatively estimated at ±1°C.

Complete random error analysis

The best way to observe the total effect of all the random sources of error is to perform the Monte Carlo analysis at all frequencies and compare the spatially integrated power in each frequency band to the power spectral density measured by the reference microphone. In the following analysis, the reference microphone was chosen to be the centre microphone and Equation 4.4 was used to reference the amplitudes back to this microphone.

Spatial integration is performed in several ways. If deconvolution is not used, then the PSF of the sources must be taken into account when integrating. To take into account the PSF, Brooks and Humphreys (1999) suggest to scale each of the values in the source map by the sum of the PSF values at that particular point from all the other points in the integration region. Then the integrated value, I, is the sum of these scaled values over the source region. Mathematically, this can be stated via Equation 4.29, where $\mathcal{L}$ denotes the source region, Y_t denotes the beamforming output at scangrid position t and $psf_{\mathcal{L}}(t)$ denotes the sum of the point spread function values over the region $\mathcal{L}$ at position t. This is expressed in Equation 4.30 where $A_{tt'}$ is that which was formulated in Equation 4.10. If deconvolution is used, the direct summation of the source map can be done.

$$I = \sum_{t \epsilon \mathcal{L}} \frac{Y_t}{psf_{\mathcal{L}}(t)} \tag{4.29}$$

$$psf_{\mathcal{L}}(t) = \sum_{t' \epsilon \mathcal{L}} \mathrm{A}_{tt'} \tag{4.30}$$

The Monte Carlo analysis was performed on the infinite cylinder test case using the following steps. First, the nominal locations of the microphones, microphone phase, CSM entries and speed of sound were recorded. Then, these parameters were perturbed randomly in accordance with the Table 4.4, which provides a summary of the discussion above. Once a single random perturbation had been generated, conventional beamforming, CLEAN-SC and DAMAS using sv2, no diagonal removal and unity microphone weighting was performed over all frequencies ranging from 2 kHz to 8 kHz. When generating each individual beamforming map, no shear layer correction was applied and the full microphone array was used. Once all of the maps over all frequencies for a single perturbation had been generated, the maps were spatially integrated over a region that enclosed the cylinder but not the contraction, as shown in Figure 4.18. The data were stored and a new perturbation state generated. This process was repeated for 400 trials.

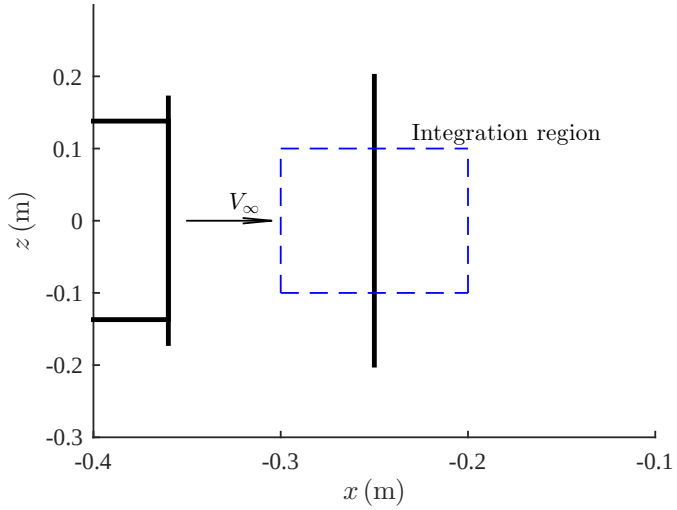

Figure 4.18: The spatial integration region for the experimental test case.

Figure 4.19 shows the PSD of the noise from the test case, as measured by the centre microphone (the reference signal), in black. The reference signal is also compared with the spectra obtained through source map spatial integration. The spectrum using conventional beamforming is shown in blue, while the spectrum using DAMAS and CLEAN-SC are shown in red and green respectively. At each narrow band frequency, the 95% confidence interval of the integrated power based on the 400 Monte Carlo iterations is shown as shaded region.

In general, there is excellent agreement between the spatially integrated spectral density levels and the reference microphone spectral density levels, in particular the

Table 4.4: A summary of inputs used for the Monte Carlo error propagation analysis.

Uncertainty type	Parameter	Value
Microphone location	σ_x	1 mm
Microphone location	σ_y	5 mm
Microphone location	σ_z	1 mm
Phase	σ_ϕ	3.5 degrees
CSM averaging	B	959 blocks
Temperature	σ_t	1 °C

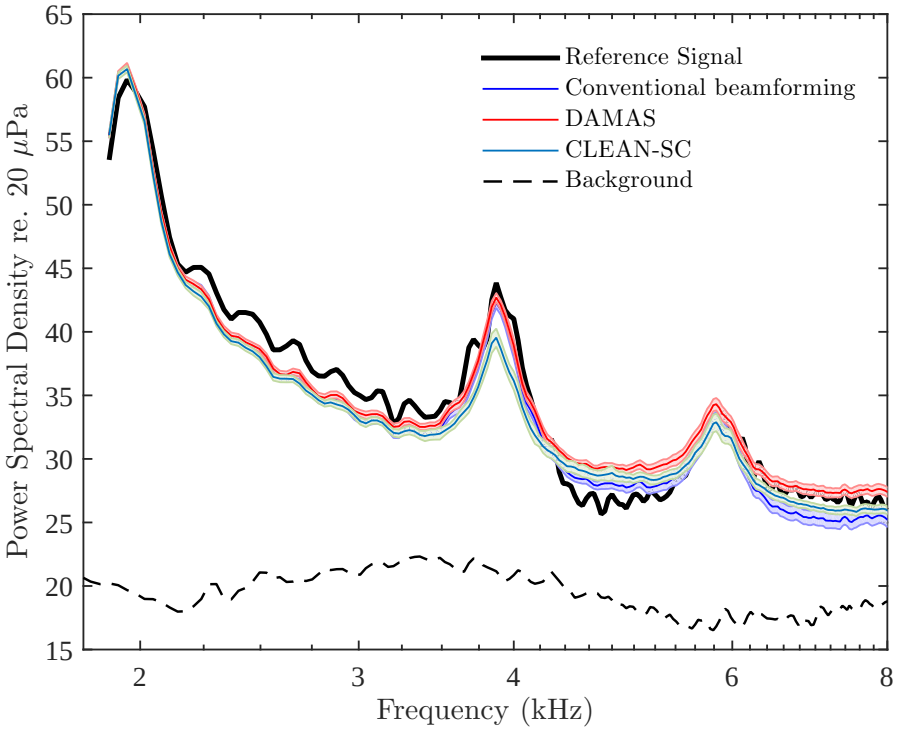

Figure 4.19: A comparison of the reference microphone spectrum with that of spatially integrated levels using conventional beamforming, DAMAS and CLEAN-SC. The shaded regions around each solid line were calculated using a Monte Carlo analysis.

shape of integrated levels, using all three algorithms. Over all frequencies analysed, the 95% confidence intervals of the integrated power spectral density is within ±1 dB/Hz.

The agreement is particularly good at the tonal peaks at 2, 4 and 6 kHz, where the signal-to-noise ratio is higher. At frequencies between the first two peaks, from 2.2 kHz to approximately 4 kHz, the levels are slightly under the reference levels by all three algorithms. This is hypothesised to be caused by both the directionality of the noise at these frequencies as well as weak sources outside of the integration region. It is well understood that at the first harmonic of the fundamental Aeolian tone, the noise will have a dipole-like directivity with the lobes of the dipole orientated in the streamwise direction (commonly referred to as a drag dipole). The streamwise orientation of the dipole is such that poor coherence between the outer microphones is expected. In essence, the aperture of the microphone array for the streamwise dipole is not sufficiently large to capture enough phase information to accurately predict the source autopower. Nevertheless, the predicted levels are at worst only about 2 dB/Hz below the microphone levels.

Between 4 kHz and 8 kHz, there are slight differences between the various algorithms. DAMAS and CLEAN-SC tend to predict higher power density values than conventional beamforming. Similar results were found by Geyer et al. (2012) at frequencies above 5 kHz when comparing CLEAN-SC and DAMAS. The reason for this behaviour is not completely clear although it is suggested by Geyer et al. (2012) that the iterative procedure of DAMAS using the Gauss-Seidel technique may not converge at higher frequencies, thus over predicting the integrated noise. Another reason could be that at higher frequencies, the side-lobe levels become close to the actual source levels. CLEAN-SC and DAMAS may treat these side-lobes as real sources (particularly when no well defined tonal source

is present above 6 kHz), and hence over predict the integrated levels. This is supported by the fact that the difference between the three algorithms is small at 6 kHz, where there is a well defined tone.

Along with spatial integration, frequency integration of the beamforming spatially integrated power spectral density may also be performed to obtain $1/3^{\text{rd}}$ octave band levels or overall sound pressure levels (SPL in dB). To obtain the 95% confidence levels of these frequency integrated levels, each of the 400 aforementioned power spectra were integrated between 1.8 to 8 kHz for conventional beamforming, DAMAS and CLEAN-SC. The normalised distributions of the calculated SPLs are shown in Figure 4.20. The distributions for all three beamforming methods collapse onto one another. From these distributions, the 95% confidence interval of frequency integrated levels due to random error is approximately ± 0.2 dB.

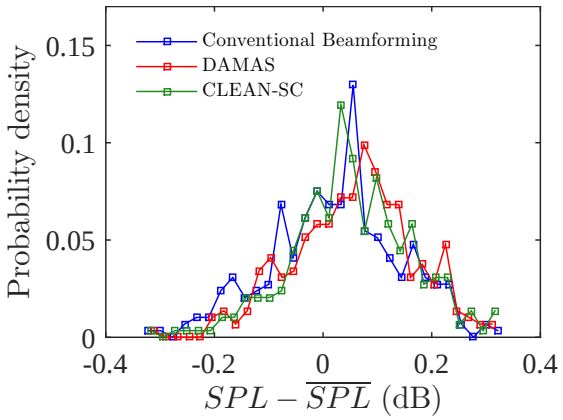

Figure 4.20: The normalised distributions of the frequency integrated SPL levels of the beamforming test case using DAMAS, CLEAN-SC and conventional beamforming.

4.6 Summary

This chapter has provided a comprehensive overview of the methodology behind basic aeroacoustic source localisation using beamforming. The mathematics behind conventional beamforming have been reviewed. Two deconvolution methods, DAMAS and CLEAN-SC have also been discussed. In addition, DAMAS has been rigorously reformulated to accommodate four different steering vector formulations.

Having provided the theoretical background behind beamforming, the specific microphone array used for the FWMC experiments was introduced. The beamformer's performance was then characterised using synthetic data located at the approximate position of the aeroacoustic models to be studied. It was found that for the array configuration (the combination of microphone spiral pattern, array location and test model location) used in the FWMC experiments, steering vector formulation 2 (sv2) provided the best dynamic range and resolution (0.9λ) at the frequencies where the beamformer was intended to be used. As such, it was selected for use in the FWMC cylinder experiments. For the deconvolution methods, the resolution of DAMAS was calculated to be 0.36λ while CLEAN-SC had a lower resolution of 0.9λ.

A detailed study of the sources of error in the beamforming map was also conducted. In general, two major sources of error are present; those associated with the beamforming

algorithm which are systematic and those associated with the experimental implementation of the algorithm, which are either systematic or random. Algorithmic sources of error arise from an artificial amplification of a source's strength as it passes through the beamforming spatial filter. This type of error can be eliminated by applying an 'array gain field' derived from the particular steering vector that is used, and shown to work well for both conventional beamforming and CLEAN-SC. The DAMAS algorithm takes into account the array gain field and no source map correction need be applied.

Systematic experimental errors include reflections, coherence loss and shear layer refraction. Tests on an experimental test case revealed that the impact of coherence loss and reflections were minimal in this study. Several methods to correct for the effect of the shear layer were presented. The method of Bahr et al. (2011) was shown to give results similar to that using high fidelity ray tracing but at a lower computational expense.

Random experimental errors arise from estimates of microphone phase, microphone locations and the speed of sound and statistical errors in the CSM due to finite microphone record lengths. For the specific microphone configuration used in this study, the random errors were quantified based on a Monte-Carlo technique. The random error in the spatially integrated power spectral density was found to be approximately $\pm 1\,\mathrm{dB/Hz}$ across all frequency ranges considered while the random error in the frequency integrated levels was $\pm 0.2\,\mathrm{dB}$. Table 4.5 provides a breakdown of the main source of error and their magnitude.

Table 4.5: A summary of the major sources of error in a beamforming map..

Source of error	Notes	Correction method	Magnitude of uncertainty after correction (if applicable)
Array gain	Artificial amplification of a source's strength.	Apply the array gain field (Table 4.1).	0 dB
Reflections	Reflections due to reflective surfaces in the mapping domain.	Include a larger domain and use deconvolution.	Not necessary in the present study.
Shear layer	Ray paths curve due to interaction with a shear layer leading to phase errors.	Ray tracing, the Bahr et al. (2011) method or the Padois et al. (2013a) method.	Can correct to within grid resolution (±2.5 mm) at frequencies higher than 4 kHz.
Coherence loss	Loss of coherence between array outer microphones due to turbulent scattering.	Can be observed by beamforming with a reduced array.	Coherence loss is minimal in this study.
All random errors	Combined effect of all random errors on the spatially integrated levels.	No correction.	±1 dB/Hz for all frequencies. ±0.2 dB for SPL.

Chapter 5

Flow induced noise from Finite Wall-Mounted Cylinders in the Low Turbulent Boundary Layer

5.1 Introduction

For Reynolds numbers $Re_W > 260$, flow-induced noise from an infinite cylinder is primarily caused by tonal noise generation due to turbulent vortex shedding. As will be shown, an FWMC also generates between 50 to 90% of the overall sound pressure level through tonal components due to periodically shed vortex structures. The behaviour of the vortex structures that generate noise is strongly dependent on the aspect ratio of the cylinder (Sumner et al. 2004; Bourgeois et al. 2011; Kawamura et al. 1984). Therefore, this chapter will discuss the tonal noise components generated by FWMCs and how these components change with aspect ratio. The acoustic and flow results presented in this chapter were obtained from experiments conducted in the AWT and 18WT, the details of which were discussed in Section 3.

This chapter presents the noise and flow results obtained for FWMCs with $0 < L/W < 23$ in the Low Turbulent Boundary Layer (LTB). These include single microphone measurements, hot-wire measurements, surface oil-film visualisation and hot-wire wake measurements. Based on the amalgamation of flow and noise data, the chapter concludes with several proposals to explain the main noise generation mechanisms of the FWMCs in the LTB. The results presented in this chapter are the first to comprehensively demonstrate the highly non-linear behaviour of FWMC noise with changing aspect ratio due to the FWMC's complicated three-dimensional wake structure. Furthermore, this is also the only study to investigate the wake dynamics of square FWMCs for $L/W \geq 14$.

5.2 Single microphone measurements

As discussed in Chapter 3, single microphone measurements (along with directivity measurements and beamforming) were used to characterise the flow-induced noise from the FWMCs, the results of which are presented here. Single microphone measurements were used to measure the Overall Sound Pressure Level (OASPL) and the acoustic spectrum of the flow-induced noise generated by FWMCs as the aspect ratio increased.

5.2.1 Overall Sounds Pressure Levels

According to Phillips (1956), Curle's theory (Curle 1955) can be used to calculate the mean-square sound pressure, $\overline{p_a^2}$, generated by an infinite square cylinder with width W, undergoing vortex shedding at a Strouhal number, $St = fW/V_\infty$, as

$$\overline{p_a^2} = \frac{V_\infty^6 \rho^2 St^2 \overline{C_l^2} LsW}{16 c_0^2 r^2}, \tag{5.1}$$

where r is the distance from the cylinder axis to the far-field microphone (placed orthogonally to the cylinder axis) and the flow, $\overline{C_l^2}$ is the mean-square lift coefficient, s is the spanwise correlation factor, and c_0 is the speed of sound. Equation 5.1 demonstrates that the mean-square acoustic pressure measured by a single microphone is a function of three parameters that characterise the vortex shedding dynamics. These include the mean-square lift coefficient, $\overline{C_l^2}$, that describes the amplitude of vortex shedding, the Strouhal number, St, that characterises the frequency of vortex shedding and the spanwise correlation factor, s, that is a measure of the spanwise three-dimensionality of the vortex filaments as they are shed of the cylinder face. Therefore, from Equation 5.1, changes in the mean-square acoustic pressure measured by a single microphone reflect the dynamical changes in the cylinder near wake.

Many authors (Keefe 1961; Amiet 1975; Schlinker and Fink 1976; Hutcheson and Brooks 2006; Fujita 2010; Leclercq and Doolan 2009; Oguma et al. 2013; Casalino and Jacob 2003; Norberg 2003) have shown good experimental agreement between the mean-square sound pressure measured for infinitely long cylinders (both with square and circular cross-sections) and Equation 5.1. As discussed in Chapter 2, the conditions for an 'infinitely long' cylinder can be achieved when $L/W > 30$ (Fox and West 1993a). Alternatively, according to Fox and West (1990), 'infinitely long' cylinder conditions can also be produced for cylinders with aspect ratios as low as 7 if appropriately sized end-plates are fitted at either end. This means that if end-plates are used, then mean-square sound pressure measurements for low aspect ratio cylinders ($7 < L/W < 30$) can also be predicted using Equation 5.1. Hence, a comparison of the experimentally obtained mean-square sound pressure of FWMCs of various aspect ratio to that predicted by Equation 5.1 for 'infinite' cylinders of the same aspect ratio will yield a direct quantification of the total influence that the free-end and junction have on the overall periodic wake dynamics.

Figure 5.1 shows the variation of the Overall Sound Pressure Levels (OASPL) in dB re. 20μPa with aspect ratio for $0 < L/W < 23$ as measured by a single microphone located 0.5 m directly above the FWMC. To calculate the OASPL, the data (sampled at 2^{15} Hz for 30 seconds each) were first digitally band-pass filtered between 0.3 kHz and 16 kHz using a 6^{th} order band-pass Butterworth filter. The OASPL was then estimated as the mean-square pressure of the filtered time series. The statistical random error in the OASPL estimate is ± 0.4 dB re. 20μPa with 95% confidence. Figure 5.1 also compares the experimental results with the theoretical OASPL calculated by Equation 5.1. The theoretical prediction was calculated using an experimentally obtained Strouhal number of $St = 0.13$, a correlation factor of $s = 6$, and a sectional mean-square lift coefficient, $\overline{C_l^2} = 1.7$ that were acquired from experiments on an infinitely long square cylinder in flow with $Re_W = 4 \times 10^4$ by Vickery (1966). Curle's theory predicts that given

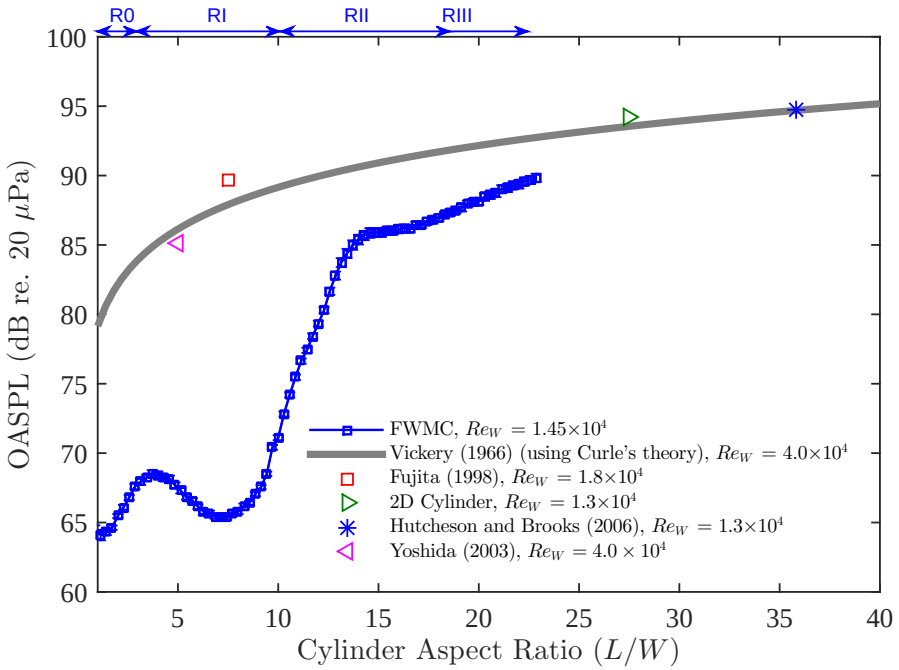

Figure 5.1: A comparison of Overall Sound Pressure Levels (OASPL in dB re. 20μPa) for square FWMCs of aspect ratios ranging from $0 < L/W < 23$. The data are compared to that calculated using Equation 5.1 using measurements of an infinite square cylinder provided by Vickery (1966)($s = 6$, $St = 0.13$ and $\overline{C_l^2} = 1.7$) and experimentally obtained noise data measured by Fujita et al. (1998), Hutcheson and Brooks (2006) and Yoshida et al. (2003) of 2D square cylinders of various length. The boundaries of the different shedding regimes, R0 to RIII, are shown at the top.

constant values of s, St and $\overline{C_l^2}$, the OASPL of an infinite cylinder (with end-plates if $L/W < 30$) will vary linearly with aspect ratio. Figure 5.1 also compares Equation 5.1 with experimentally measured OASPLs of several infinitely long square cylinders with various aspect ratios (ranging from $L/W = 6$ to $L/W = 33$) and Reynolds numbers (ranging from $Re_W = 1.3\times10^4$ to $Re_W = 4\times10^4$). The data has been taken by Fujita et al. (1998) for an infinite square cylinder with $L/W = 8$ (with end-plates), Hutcheson and Brooks (2006) for a 2D square cylinder with $L/W = 33$ (with end-plates), Yoshida et al. (2003) for a 2D square cylinder with $L/W = 6$ (with end-plates) and an infinite square cylinder with $L/D = 27.5$ taken in the AWT (without end-plates). The results have been rescaled to a velocity of 32 m/s and a cylinder width of $W = 7$ mm using Equation 5.1. The experimentally obtained OASPLs for infinitely long cylinders show good agreement with those predicted by Equation 5.1 using the data of Vickery (1966). This indicates that the wake dynamics of infinitely long square cylinders are aspect ratio and Reynolds number invariant within the Reynolds number range of $1.3 \times 10^4 < Re_W < 4 \times 10^4$ and aspect ratio range of $6 < L/W < 33$.

The variation of OASPL for the FWMCs with aspect ratio deviates significantly from that predicted by Equation 5.1, in both trend and magnitude. For all aspect ratios, the OASPL is less than that predicted by Equation 5.1. For very low aspect ratios ($L/W < 2$), it is expected that regular periodicity in the wake is suppressed through strong downwash (Sumner et al. 2004; Hosseini et al. 2013), so a lower OASPL is expected. However, even for $L/W \geq 2$, where vortex shedding is present, the measured OASPL is below that

of the predicted value. This highlights the disruptive impact that the junction and the free-end have on the vortex shedding characteristics across the span of the FWMC.

As the aspect ratio increases above $L/W = 15$, the OASPL approaches the value predicted by Equation 5.1. For example, at $L/W = 23$, the difference between the value of Equation 5.1 and the experimental value of the FWMC is only 3 dB. However, for $0 < L/W < 23$, the variation of OASPL is not monotonic. At this point it is convenient to split the variation of OASPL with FWMC aspect ratio as a transition through four aspect ratio shedding regimes, called R0 through RIII. The aspect ratio ranges over which these regimes are defined are shown in Figure 5.1.

The first regime, known as the 'very low aspect ratio' regime or R0, occurs for $L/W < 2$. For these low aspect ratio cylinders, the noise levels are less than 1 dB above that of background noise levels. As will be shown, in R0, tonal vortex shedding noise is not detected by the microphone.

The second regime, known herein as the 'low aspect ratio regime' or RI, occurs for $2 \leq L/W < 10$ and is characterised by a local maxima in the OASPL that occurs at $L/W \approx 4$ and a local minima in the OASPL, that occurs at $L/W \approx 7$. Similar observations have been made by Moreau and Doolan (2013) on circular FWMCs, where the OASPL was observed to increase at $L/D = 3.1$. In this study, it was explained that below $L/D = 8$, vortex shedding was suppressed except at $L/D = 3.1$, where vortex shedding reappeared. No explanation for this behaviour was given by the authors. One Aeolian tone is measured throughout this regime, although it is substantially weaker at $L/W = 7$ than at $L/W = 4$.

The third regime, known herein as the 'transitional aspect ratio regime' or RII, occurs for $10 < L/W < 18$. In this regime, the OASPL experiences a very rapid rate of increase, increasing by 15 dB between $L/W = 10$ and $L/W = 14$. Afterwards, a small plateau occurs between $L/W = 14$ and $L/W = 16$ where the OASPL remains constant, after which it begins to rise.

The fourth and final regime, known herein as the 'high aspect ratio regime' or RIII occurs for $L/W \geq 18$. Here, the OASPL steadily rises from 87 dB at $L/W = 18$ to 90 dB at $L/W = 23$. Between $L/W = 18$ and $L/W = 23$, the rate of increase of OASPL is much slower than in RII. Nevertheless, this slower rate of increase is still larger than what one would expect for an infinite cylinder and the OASPL is still below that predicted by Equation 5.1. The OASPL will approach that of Equation 5.1 as the aspect ratio is increased towards infinity because the relative influence of the junction and free-end regions become small compared with the mid-span of the cylinder. It is remarkable that end effects can have such a profound impact on the properties of the flow-induced noise from the cylinder even at aspect ratios as high as $L/W \approx 20$. In fact, if the curve for FWMC noise in Figure 5.1 were linearly extrapolated until it intersected the theoretical curve generated by Equation 5.1, it would intersect at approximately $L/D = 30$, consistent with the observations of aerodynamic lift and drag made by Fox and West (1993a) for circular FWMCs.

5.2.2 Power Spectral Density

The Power Spectral Density (PSD) is used to investigate the occurrence of vortex shedding and the relative magnitude of other components of noise. To generate the PSD of the acoustic pressure fluctuations, the same acoustic pressure time records used to calculate the OASPL were digitally band-pass filtered between 0.3 kHz and 16 kHz using a 6^{th} order band-pass Butterworth filter. The autospectra were then estimated using Welch's averaged modified periodogram method (see Chapter 3). The records were divided into $B = 479$ blocks, each with 2^{12} data points, giving a frequency resolution of $\Delta f = 8$ Hz, or $\Delta St = 0.002$. Using Equation 3.36, the uncertainty at each narrowband frequency is ± 0.5 dB/Hz with a 95% level of confidence.

Figure 5.2 is a colourmap (also known as a 'spectral map') showing the variation of acoustic PSD with aspect ratio for a flow speed of 32 m/s. Figure 5.3 is a waterfall diagram showing the shape of the individual autospectra across all aspect ratios. Finally, Figure 5.4 shows the autospectra for select aspect ratio FWMCs compared with the background level, which is the level obtained with the cylinder removed, but with the mounting plate attached to the contraction (see Figure 3.9).

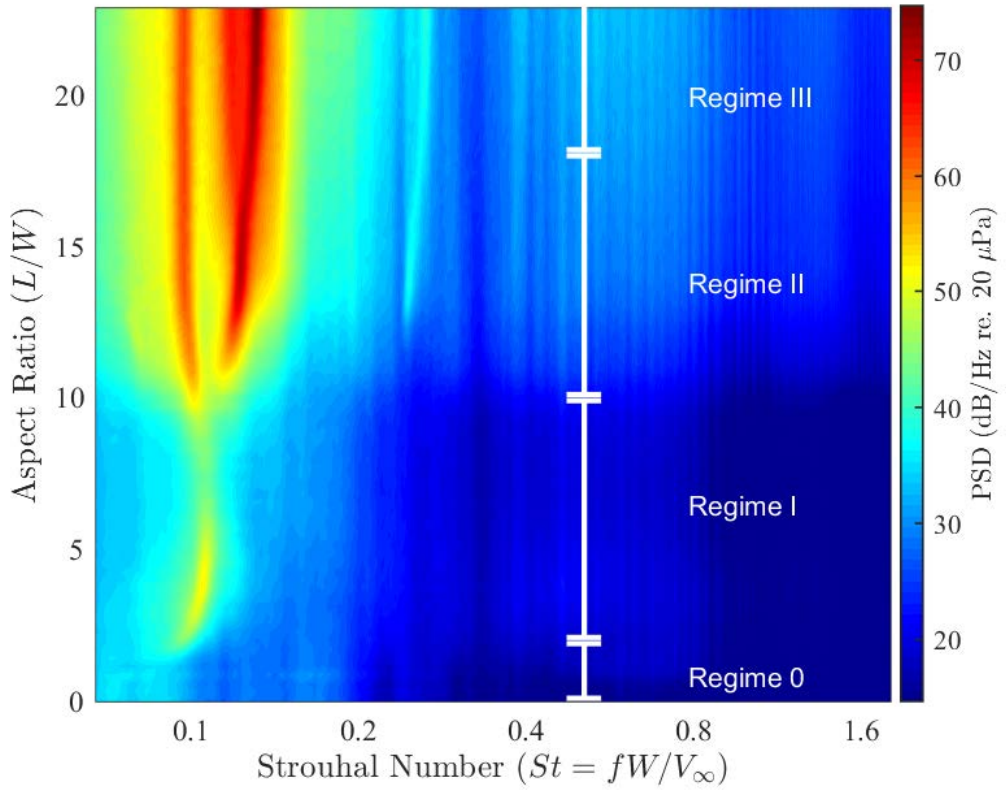

Figure 5.2: A spectral map showing the variation of the Power Spectral Density (PSD) of acoustic pressure fluctuations with FWMC aspect ratio when the FWMC is immersed in the LTB, expressed in dB/Hz re. 20μPa . The shedding regime boundaries are labelled in white. These regimes correspond spectra with 0, 1, 2, and 3 vortex shedding tones respectively.

Figure 5.2, 5.3 and 5.4 show how the spectral characteristics of the flow-induced noise change within each of the aspect ratio regimes. The change in frequency content of the noise with aspect ratio gives further insight to the flow mechanisms responsible for the

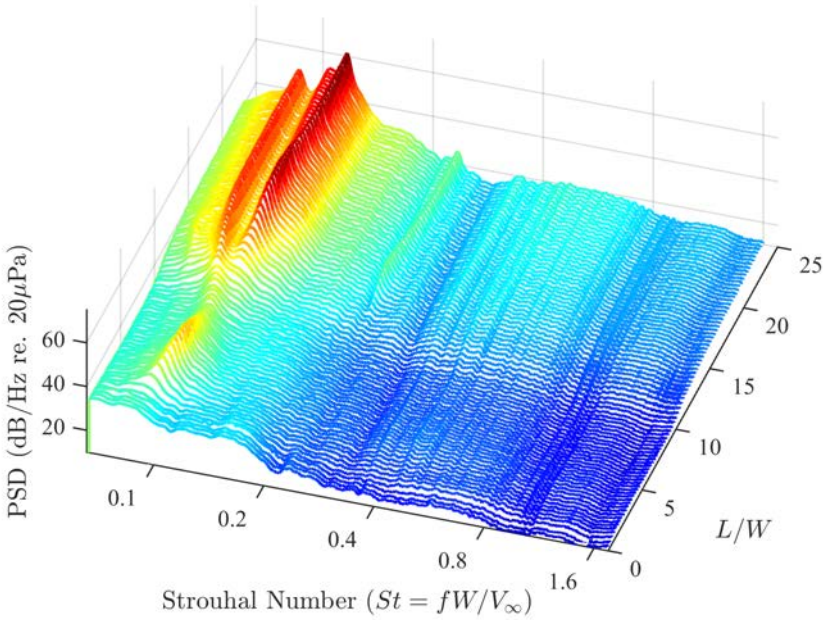

Figure 5.3: The variation of the Power Spectral Density (PSD) of the acoustic pressure fluctuations with aspect ratio of the FWMC, presented as a waterfall diagram, expressed in dB/Hz re. 20μPa . The colour is proportional to the PSD level.

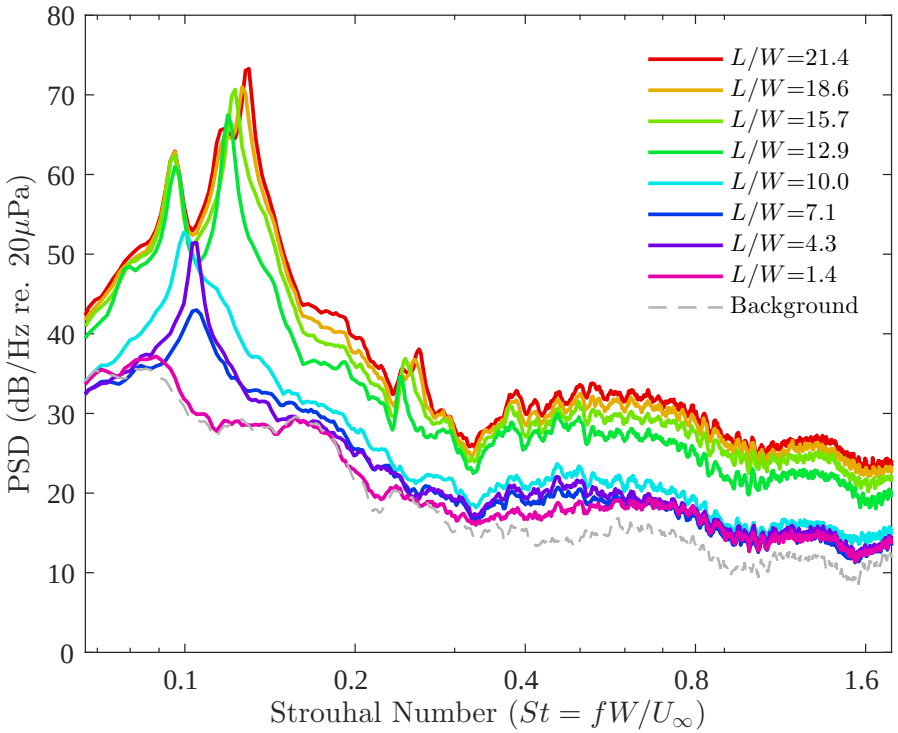

Figure 5.4: Narrowband acoustic spectra for selected aspect ratio FWMCs. The frequency resolution is $\Delta f = 8\,$Hz or $\Delta St = 0.002$.

differences in OASPL between regimes R0, RI, RII and RIII.

According to Becker et al. (2008), the individual frequency spectra of FWMCs can be split into two components. The first component is the 'tonal component' between Strouhal numbers $St = 0.07$ to $St = 0.3$. This region contains one or several narrowband peak(s) (and sometimes their harmonics) generated through vortex shedding at the

mid-span of the FWMC. These peaks can be described by their bandwidth, centre frequency and frequency integrated amplitude. The second component is the 'broadband component' that occupies frequencies $0.3 \leq St < 2$ and consists of stochastic, low amplitude, broadband noise. While this chapter concentrates on the tonal components of noise (the broadband component is better discussed in the context of plate boundary layer effects in the next chapter), some properties of the broadband noise component will be presented for reference.

Figure 5.4 shows that in R0 ($L/W < 2$), no tonal components are measured and the spectrum for $St < 0.3$ collapses onto the background spectrum (the noise measured with the plate and no cylinder in place). The absence of any sharp peak near $St = 0.1$ suggests that regular vortex shedding is either too weak to be detected or completely suppressed. In the broadband range, the power spectral density is slightly elevated above the background.

In RI, the acoustic spectrum is characterised by a single Aeolian peak centred at approximately $St = 0.1$ (see Figure 5.2). This peak is caused by vortex structures that shed periodically from the face of the cylinder, causing periodic pressure fluctuations on the surface of the cylinder. According to Bourgeois et al. (2011) (and discussed in Chapter 2), these structures are either in the form of a 'half-loop', where opposite signed vortices are connected by vortex filaments formed in the shear-layer over the free-end of the cylinder, or a 'full-loop', where vortex filaments are also rotated in the upstream direction at the junction due to interaction with the horseshoe vortex. Figure 5.4 shows that the exact frequency of the dominant peak appears to change as the aspect ratio increases from 2 to 10. An important feature in RI is that the magnitude of the peak at $L/W = 7.1$ is weaker than that at $L/W = 4.3$, which explains the existence of a local minima in the OASPL at $L/W = 7.1$ in Figure 5.1. Similar to R0, the broadband noise is also elevated above the background level.

In RII, the frequency spectrum dramatically changes. A bifurcation occurs at $L/W \approx 10$ and two vortex shedding peaks are observed, one at $St < 0.10$ and one at a $St > 0.10$ (see Figure 5.2). Moreau and Doolan (2013) showed that these two peaks are caused by two different vortex shedding frequencies occurring along the cylinder axis. The dual peaks are indicative of a *cellular* shedding mode that sometimes occurs in infinite circular cylinders (Gerich and Eckelmann 1982) given the right inflow conditions. A cellular shedding mode is where different spanwise portions of the cylinder shed with different frequencies, creating different spanwise 'cells' of constant frequency. According to Moreau and Doolan (2013), the lower frequency peak is associated with a cell of vortex structures towards the free-end of the cylinder and the higher frequency peak with a second cell of vortex structures towards the junction.

In a similar manner as RII, the beginning of RIII is also characterised by a bifurcation that occurs at $L/W \approx 18$ at $St = 0.115$, creating a third peak between the two previous ones. This peak is difficult to observe in Figure 5.2 due to the colour scheme, but can be clearly seen in Figures 5.3 and 5.4. These results demonstrate that a triple cellular shedding mode is occurring in the wake of the cylinder. A triple shedding mode has never before been observed in square FWMC flow, probably because all other investigations have focused on aspect ratios $L/W < 14$. Another salient feature of the flow-induced noise for FWMCs in RII and RIII is that the broadband noise component experiences a

significant increase compared with that of R0 and RI across all frequencies. The increase in broadband noise coincides with the onset of the dual and triple shedding modes.

5.3 Noise component analysis

Section 5.2 showed that the spectrum of flow-induced noise from an FWMC is comprised of a tonal component and a broadband component. The tonal component contains several (up to three) Aeolian-like peaks, while the broadband components contain stochastic noise across a large range of frequencies. This section will quantify how several important properties of these components change with aspect ratio. In the following analysis, four properties will be investigated. These include;

1. the frequency of each peak,
2. the (integrated) magnitude of each peak,
3. the bandwidth of the each peak and,
4. the directivity of each peak.

5.3.1 Peak frequency

As shown in Figure 5.4, the acoustic spectrum of an FWMC will exhibit up to three main peaks in the acoustic spectrum depending on the aspect ratio regime. For regime R0, no peaks occur. In RI, only one dominant peak can be identified. This peak is known as 'P1' and occurs at a frequency lower than what is expected for an infinite square cylinder at $St = 0.13$ (Vickery 1966). The exact frequency of P1 varies with aspect ratio within RI. P1 continues to exist into RII and RIII as the lower frequency peak. In RII, between $10 < L/W < 18$, a secondary, higher frequency peak occurs, referred to as 'P2'. Finally, for $L/W > 18$, a third peak occurs between P1 and P2, known as 'P3'. Like P1, the frequencies of P2 and P3 also vary with aspect ratio within their respective regimes.

Figure 5.5 plots the frequency (Strouhal number) of each peak as a function of aspect ratio. Because of the finite frequency resolution ($\Delta f = 8\,\text{Hz}$), the uncertainty in the peak frequency (at 95% confidence assuming a rectangular distribution) is approximately $f_e = \pm 2\Delta f/\sqrt{3} = \pm 9.2\,\text{Hz}$ corresponding to a Strouhal number uncertainty of $St_e = \pm 0.002$, shown as error bars in Figure 5.5. Also shown are the measured Strouhal numbers of vortex shedding of various aspect ratio square FWMCs measured in other studies. These measurements include that from Becker et al. (2008) for an $L/W = 6$ square FWMC using a far-field microphone and that from Bourgeois et al. (2011), Hosseini et al. (2013) and Wang et al. (2014) for $L/W = 8$, 6 and 4 square FWMCs respectively, using hot-wire anemometry.

Initially, P1 increases from $St = 0.09$ and appears to reach a stable value of $St = 0.102$ between $4 < L/W < 8$. This is the aspect ratio range where most other investigations on square FWMCs have taken place and there is good agreement between the present results and other studies. The exception is the study by Wang et al. (2014), who measured a Strouhal number of $St = 0.11$ for an $L/W = 7$ square FWMC in a boundary layer thickness of $\delta/W = 1.35$ and a Reynolds number of $Re = 0.93 \times 10^4$. The discrepancy is

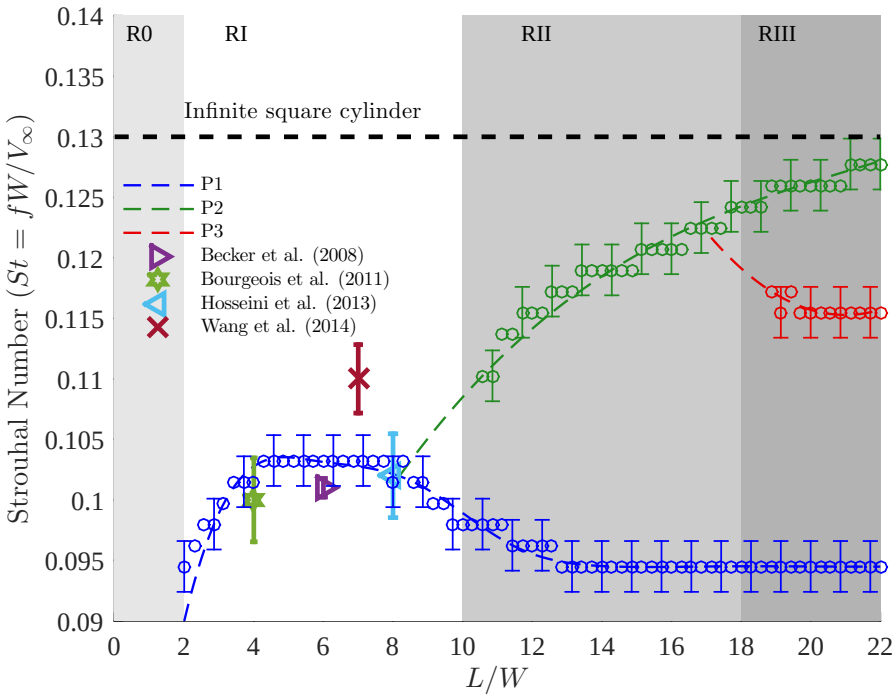

Figure 5.5: The variation of the frequency of each peak (P1, P2 and P3) as a function of FWMC aspect ratio. The data is compared with the vortex shedding peak frequency of square FWMCs from other studies including: Hosseini et al. (2013) ($L/W = 8$, $Re = 1.2 \times 10^4$ and $\delta/W = 0.72$),Wang et al. (2014) ($L/W = 7$, $Re = 0.93 \times 10^4$ and $\delta/W = 1.35$), Becker et al. (2008) ($L/W = 6$, $Re = 3.8 \times 10^4$ and $\delta/W = 0.27$) and Bourgeois et al. (2011)($L/W = 4$, $Re = 1.2 \times 10^4$ and $\delta/W = 0.72$). The frequency, f, is non-dimensionalised as Strouhal number, $St = fW/V_\infty$.

surprising since their boundary layer height of $\delta/W = 1.35$ is comparable to that used in this study ($\delta/W = 1.3$). The discrepancy in the Strouhal number may be caused by an error in their measured velocity of the flow. In their study, the flow velocity was low at 7 m/s and propagation errors in the measured Strouhal number are magnified at low velocities, potentially inflating the estimated Strouhal number.

Between $7.7 < L/W < 14$, the Strouhal number of P1 decreases. At $L/W = 14$, the beginning of RIII, the Strouhal number of P1 reaches a constant value of $St = 0.095$. At the same time, P2 starts to occur at $L/W = 10.6$, the beginning of RII, and the Strouhal number of P2 increases in value towards the two-dimensional value of $St = 0.13$ as the aspect ratio increases. P3 begins to form at $L/W = 18$ and by $L/W = 18.9$ is sufficiently well resolved to be distinct from P2. The Strouhal number of P3 is constant at $St = 0.115$.

5.3.2 Peak magnitude

In this investigation, the magnitude of an individual peak in the acoustic spectrum is defined as the sound pressure level (SPL) obtained when the acoustic spectrum is integrated in a frequency band arranged symmetrically around the peak frequency. This is a similar approach to that taken by Geyer et al. (2015) when investigating the aeroacoustic characteristics of porous cylinders. In this study, the integration bandwidth was set to 48 Hz (much larger than the half-power bandwidth of each peak) to capture all the

spectral energy in each peak. The magnitude of the broadband noise is defined as the level obtained when integrating the acoustic spectrum from $St = 0.3$ to $St = 2$. The uncertainty limits in the magnitude were calculated by integrating the upper and lower limits of the 95%, confidence interval of the acoustic spectrum, given by Equation 3.36, and are shown in the figure.

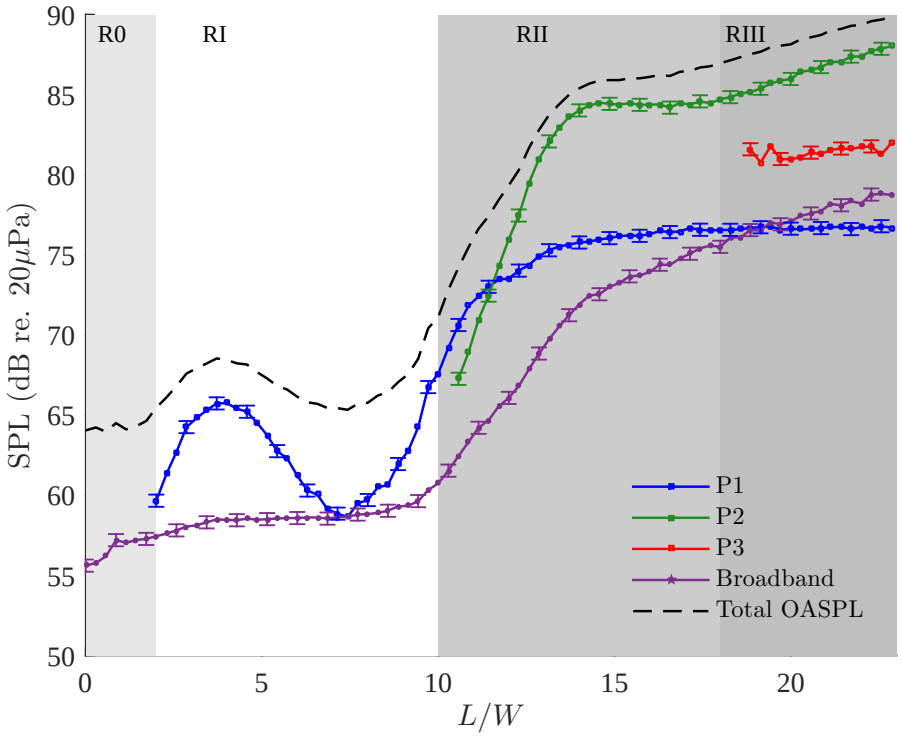

Figure 5.6: The variation of the magnitude of each peak (P1, P2 and P3) and the broadband component as a function of FWMC aspect ratio.

Figure 5.6 shows the magnitudes of P1, P2, P3 and the broadband component against aspect ratio. The OASPL calculated previously is overlaid for reference. Figure 5.7 shows the magnitudes of P1, P2, P3 and the broadband component as a percentage (0 being 0% and 1 being 100%) of the OASPL at a particular aspect ratio. It should be noted that in this analysis alternative sources occurring at frequencies $St < 0.3$ (other than those contained in either P1, P2 or P3) will also contribute to the OASPL, so the sum total of the magnitudes of P1, P2 and P3 and broadband components do not equal the OASPL exactly.

P1 starts to occur at the beginning of RI with a magnitude of approximately 57 dB and rises to a local maximum of 66 dB at $L/W = 4$. At $L/W = 4$, 54% of the total OASPL is contained in P1, indicating that at $L/W = 4$, P1 is the dominant source of noise. In contrast, at $L/W = 7.4$ the magnitude of P1 drops significantly to 58 dB. In fact, the reduction in noise magnitude is so great that the levels become comparable to that of the broadband noise levels. At $L/W = 7.4$, both the broadband component and P1 contribute approximately 20% to the total OASPL, with the remaining 60% contributed by other low frequency sources in the spectrum. The OASPL correspondingly decreases to a level only slightly higher than the background level (the level obtained at $L/W = 0$ in Figure 5.1). Throughout RI, the broadband noise levels stay approximately constant at ≈58 dB, irrespective of the aspect ratio.

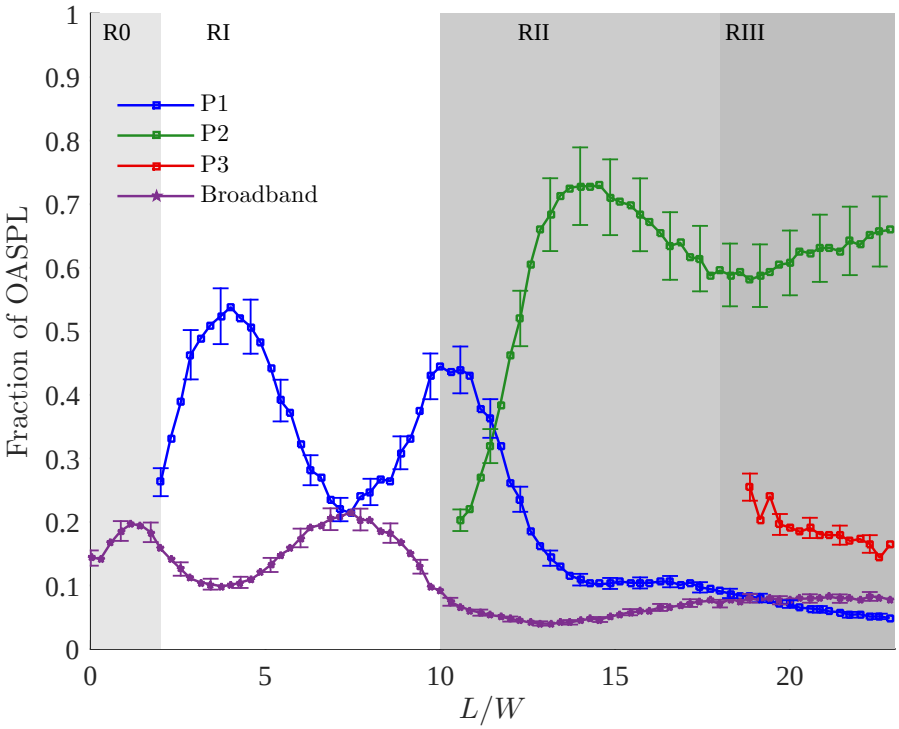

Figure 5.7: The magnitude of each noise component expressed as a proportion of the OASPL at a particular FWMC aspect ratio.

Towards the end of RI there is a rapid increase in the magnitude of P1. From $L/W = 7.4$ to 14 the magnitude of P1 increases from 58 dB to 75 dB. This increase continues into the beginning of RII, after which the rate of increase gradually slows. Beyond $L/W = 14$ (toward the end of RII and into RIII), the magnitude of P1 remains constant at 75 dB.

The beginning of RII also marks the onset of P2. The magnitude of P2 rapidly increases as soon as P2 forms, increasing from 67 dB to 84 dB from $L/W = 10.6$ to 14. The rapid increase of both P1 and P2 at the beginning and end of RII respectively, cause a rapid rise in the OASPL throughout RII. By the end of RII, P2 overtakes P1 as the dominant source of noise, contributing 70% of the OASPL (see Figure 5.7). Unlike P1, the rate of increase in the magnitude of P2 stops abruptly at $L/W = 14$ (see Figure 5.6) to create a distinct 'kink'. This 'kink' is also observed in the broadband noise component at $L/W = 14$. After maintaining a constant level over most of RI, the broadband component increases from $L/W = 10$ to 23. However, like P2, this increase is most rapid in RII and, at $L/W = 14$, the rate of change of the magnitude of the broadband noise suddenly decreases. Based on these observations, it is concluded that $L/W = 14$ marks a significant change in the noise producing mechanisms of FWMCs and that the flow structures that produce P2 (and evidently the broadband noise component) are affected by this change. Conversely, the structures that generate P1 are not affected by this change.

From $L/W = 14$ to 18, the magnitude of P2 plateaus at 84.5 dB, which causes the OASPL to maintain a constant magnitude. During this plateau, P2 contributes increasingly less noise to the OASPL, decreasing from 73% at $L/W = 14$ to 60% at $L/W = 18$. When P3 starts to form at $L/W = 18$ (the boundary between RII and RIII), the magnitude of P2 begins to rise again to a final value of 88 dB and its contribution

increases from 60% at $L/W = 18$ to 66% at $L/W = 23$. From an aspect ratio of $L/W = 18$, the magnitude of P3 remains constant at 81 dB and contributes increasingly less to the OASPL, starting from 24% at $L/W = 18.9$ to 16.3% at $L/W = 23$. Interestingly, when P3 is formed, the magnitude of the broadband component slightly exceeds that of P1. By $L/W = 23$, the broadband component contributes about 7.7% of the OASPL, while P1 contributes only 4%.

5.3.3 Bandwidth

The bandwidth of a spectral peak in the autospectrum is a measure of the degree of modulation of the time signal. For example, the autospectrum of a pure sinusoid is a Dirac delta function at the fundamental frequency, i.e., it has an infinitely narrow bandwidth. Conversely, when the same sinusoid is modulated with a Gaussian signal, the autospectrum will also be a Gaussian curve centred at the sinusoid frequency. In this investigation, the bandwidth of each peak (where they exist) is found by fitting a Gaussian bell curve through the data points either side of the peak in the autospectra. According to Blackburn and Melbourne (1996), the form of this curve is given by

$$S(f) = \frac{w_p}{\sqrt{2\pi}\sigma_b} \exp\left\{\frac{-(f - f_p)^2}{2\sigma_b^2}\right\}, \tag{5.2}$$

where w_p is the integrated magnitude of the peak, calculated in Section 5.3.2, f_p is the frequency at which each peak occurs and σ_b is the 'bandwidth' of the peak. The parameter σ_b was found by performing a least squares regression analysis using 15-20 data points surrounding the peak, and using the values of w_p and f_p calculated in the preceding sections.

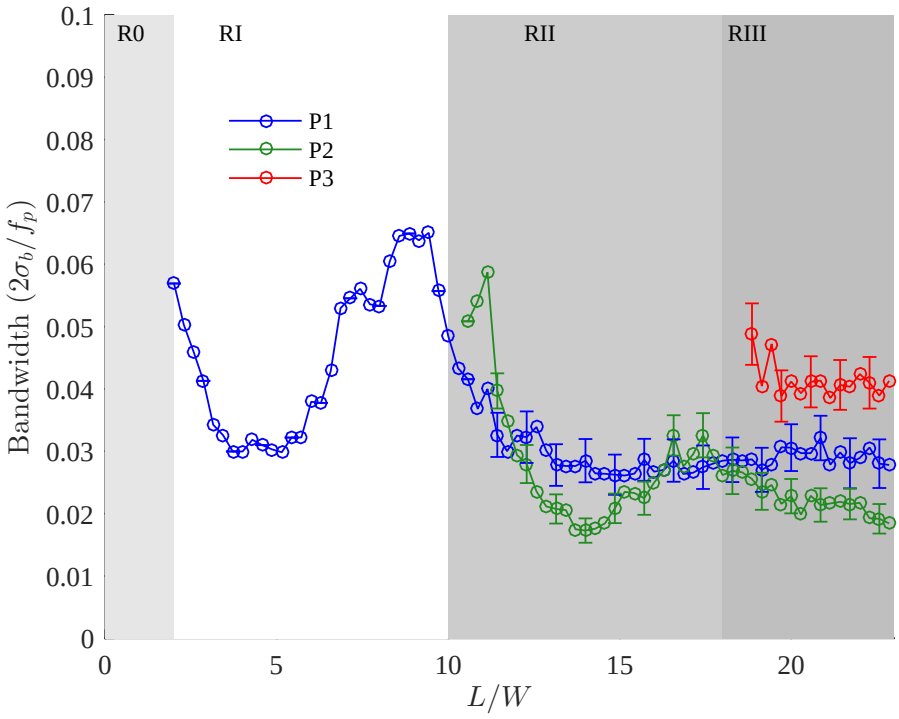

Figure 5.8: The variation of the bandwidth parameter of each tonal peak (P1, P2 and P3) as a function of FWMC aspect ratio.

Figure 5.8 shows the variation of the calculated bandwidth, non-dimensionalised to $2\sigma_b/f_p$, as a function of the aspect ratio. The confidence intervals of the bandwidth parameter were calculated by performing the same curve fitting procedure on the upper and lower limits of the autospectrum.

In RI, the bandwidth of P1 appears to be inversely related to its magnitude. For example, the bandwidth reaches a local minimum and local maximum at $L/W = 4$ and 7.4 respectively, as the magnitude of P1 reaches a local maximum and local minimum respectively (see Figure 5.6). At the boundary between RI and RII, the bandwidth of P1 increases to a maximum at $L/W = 9.4$, coinciding with the occurrence of P2, that forms shortly after. This suggests a higher modulation of the surface pressure fluctuations that generate the acoustic signal as the cylinder transitions from RI to RII. After the formation of P2, the bandwidth of both P1 and P2 rapidly reduce with a small increase in aspect ratio. The bandwidth of P2 at $L/W = 14$, where P2 contributes to the highest proportion of noise, is lower than that of P1. Again, prior to the formation of P3, P2 experiences a significant increase in bandwidth, although it it less pronounced than the increase in the bandwidth of P1 when transitioning from RI to RII. P3 forms with a bandwidth that is slightly larger than both P1 and P2. As the aspect ratio increases beyond $L/W = 18$ the bandwidths of P3 and P2 reduce. By $L/W = 23$, the non-dimensional bandwidths of P2 and P3 are 0.02 and 0.04 respectively, while the non-dimensional bandwidth of P1 is 0.03.

5.3.4 Directivity

The directivity of each peak was found using a single B&K microphone that was traversed in a 60° arc around the cylinder periphery at a radial distance of approximately 510 mm ($\approx 0.7\lambda$, where λ is based on the shedding frequency). The experimental details of the directivity experiments can be found in Chapter 3.

To obtain a baseline directivity pattern with which the FWMC data could be compared, two sets of data were generated. The first was an experimentally obtained directivity pattern of an infinite cylinder measured in the AWT. An infinite cylinder was created using a square cylinder longer than the width of the contraction and mounting it to plates that lay outside of the contraction jet shear layer. The same single B&K microphone was used to measure the directivity of this infinite cylinder, in a 60° arc around the cylinder periphery at a radius of approximately 0.7λ (based on the shedding frequency) from the cylinder.

The second data set was the directivity pattern calculated by computationally *simulating* a perfect two-dimensional point dipole in the AWT facility. The aim of this data set was to model the effect of possible reflections off the contraction outlet. The simulation was implemented by numerically solving the homogeneous 2-D Linearised Euler Equations of a two-dimensional dipole source (with its lobes pointing in the y-direction, towards the array) using a Pseudo-Characteristic Formulation on a rectangular domain that modelled the $x-y$ plane of the AWT (see Mimani et al. (2014) for details of the method). The modelling domain included the effects of the contraction shear layer using Equation 4.27, so that the solution captured any attenuation and refraction caused by propagation through the AWT jet. Two solutions were generated using this code: one with the reflective effects of the contraction outlet included, and one without. The two solutions are compared

in Figure 5.9, which maps the root-mean-square pressure fluctuations in the AWT due to a 2-D point dipole located at the position marked with an 'x' (which was also the position of the FWMCs relative to the AWT contraction). Figure 5.9a shows the solution generated without effects of the contraction flange and Figure 5.9b shows the solution with the effects of the contraction flange included. When no reflections are included, the directivity pattern is symmetric about the y-axis, with the strongest root-mean-square pressure occurring at $\pm 90°$ to the flow. This is exactly the directivity pattern expected of a perfect acoustic dipole (Bies and Hansen 2009). When reflections are included, the measured sound pressures are enhanced at approximately $\pm 75°$, so that the directivity appears skewed downstream. These CAA (Computational AeroAcoustic) simulations show that the major effect of the contraction flange at the wavelengths where the main Aeolian tones are generated is to reflect noise off the contraction flange enhancing the mean-square sound pressure in the direction of the flow. This means that for a perfect point dipole orientated perpendicular to the flow, the directivity pattern is altered so that the lobes lie at $\pm 75°$ instead of $\pm 90°$.

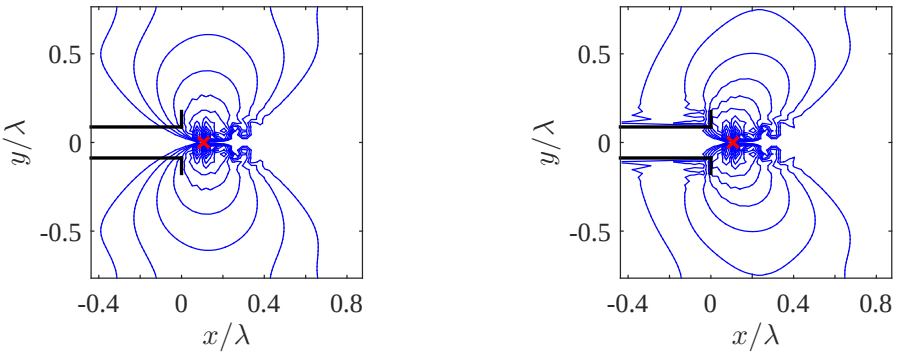

(a) No reflections (b) Reflections

Figure 5.9: A numerical CAA simulation of a two-dimensional point dipole inside the AWT without (a) and with (b) modelling the reflective effects of the contraction flange. The contraction reflective surface is shown as black lines and the position of the simulated dipole is marked with an 'x'. The flow is going from left to right.

Figures 5.10 to 5.12 show the experimentally measured normalised mean-square sound pressures of P1, P2 and P3 as a function of measurement angle, θ_m, for select aspect ratio cylinders. The sound pressures are not logarithmically compressed in order to better illustrate the directional characteristics. To obtain the normalised mean-square sound pressure, the mean-square sound pressures of each peak were calculated using the same spectral integration method used in the previous section, i.e., the peak frequency was found and the acoustic autospectrum was integrated over a 48 Hz band around this frequency. The mean-square sound pressure was then normalised by the highest value measured in the 60° arc for each aspect ratio. In these figures, $\theta_m = 0°$ is the point directly downstream of the cylinder and $\theta_m = 180°$ is the point directly upstream of the cylinder. The data are compared with the directivity pattern of the infinitely long cylinder ('Infinite cylinder') and the simulated CAA results with reflections ('simulated'). The estimated 95% confidence level of each normalised mean-square sound pressure was ± 0.05.

The measured directivity patterns for P2 and P3 (in Figures 5.11 and 5.12 respectively)

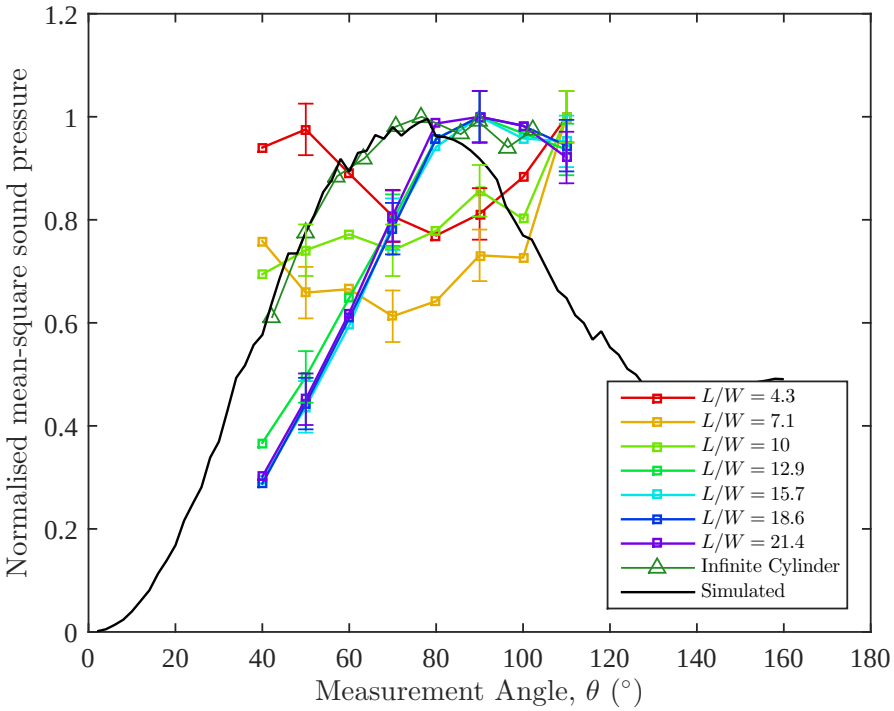

Figure 5.10: The directivity pattern of P1 compared with the directivity pattern of a simulated dipole in the AWT facility and an infinite cylinder in the same facility.

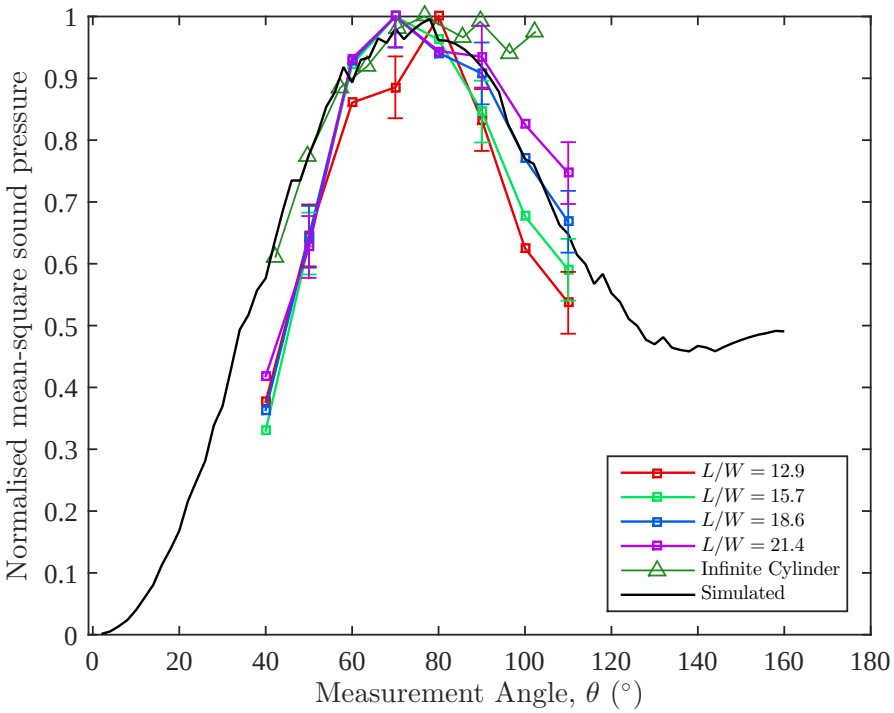

Figure 5.11: The directivity pattern of P2 compared with the directivity pattern of a simulated dipole in the AWT facility and an infinite cylinder in the same facility.

collapse onto the simulated results reasonably well. These results indicate that the primary mechanism that generates P2 and P3 is a dipole with the lobes orientated perpendicular to the flow direction. This is known as a 'lift' dipole, because it is generated by a fluctuating force perpendicular to the free-stream. The maxima in the directivity pattern of the experimental data also occur at approximately 75°. Based on both the directivity pattern

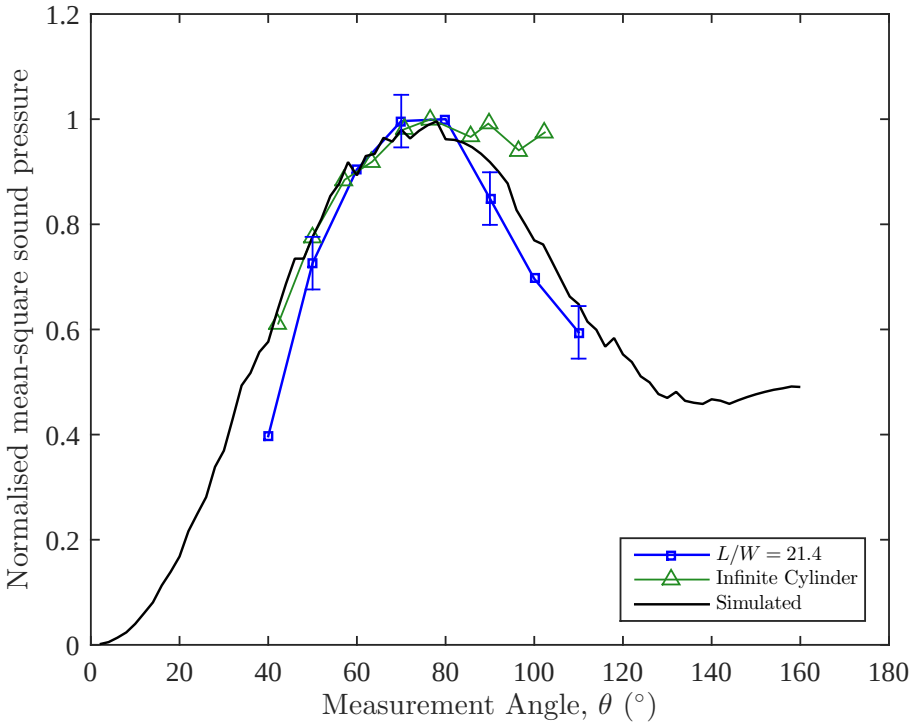

Figure 5.12: The directivity pattern of P3 compared with the directivity pattern of a simulated dipole in the AWT facility and an infinite cylinder in the same facility.

of the simulated CAA data, this shift of 15 degrees is caused by a reflection off the contraction flange. These results support that the conclusion that both P2 and P3 are generated by classical vortex shedding mechanisms.

Contrary to P2 and P3, the directivity patterns of P1 in Figure 5.10 do not follow the simulated results. The directivity pattern of P1 also appears to be aspect ratio dependent. For FWMCs in RI ($2 < L/W < 10$), the peak in directivity occurs at $\theta_m = 110°$ and appears to have a minimum at $\theta_m = 75°$. This suggests a dominant streamwise dipole, where the lobes of the dipole lie parallel to the free-stream. A streamwise dipole is known as a 'drag' dipole because it is generated by force fluctuations parallel to the free-stream.

For $L/W > 10$ (RII and RIII), the directivity patterns of P1 resemble a lift dipole and remain constant with aspect ratio. However, the peak in the pattern is *shifted* upstream to approximately $\theta_m = 90°$. The FWMC with $L/W = 10$ appears to be in a transitional state between the two patterns. Therefore, unlike P2 and P3, the noise generation mechanisms that produce the directivity patterns for P1 cannot be explained by a lift dipole. From the directivity patterns, it can be concluded that the mechanisms that generate P1 are certainly different from that of P2 and P3 and, in addition, the mechanism that generates P1 changes as the aspect ratio transitions from RI into RII.

5.4 Wake velocity measurements

Having characterised the flow-induced noise from an FWMC at different aspect ratios, attention will now turn to the fluid dynamics of the wake. This section presents hot-wire measurements of the mean and fluctuating components of velocity measured in the wake of FWMCs in the Low Turbulent Boundary Layer (LTB). Eight aspect ratios were tested:

$L/W = 1.4$, 4.3, 7.1, 10, 12.9, 15.7, 18.6 and 21.4. Experimental details of the LTB and the hot-wire wake surveying experiments are provided in Chapter 3.

5.4.1 Mean velocity

Figure 5.13 show colourmaps of the mean velocity contours in the wake of the FMWCs. In each map, the mean velocity has been normalised by the free-stream velocity, $V_\infty = 32$ m/s. Additionally, the abscissa axis has been normalised by the span of each cylinder so that $z/L = 1$ is the free-end and $z/L = 0$ is the junction of the cylinder. As discussed in Chapter 3, the measurement plane was at $y/W = 0.6$ to avoid (as much as possible) entering the reverse flow region of the wake. Finally, the relative height of the boundary layer for each aspect ratio is indicated by a dashed red line. Figures 5.14 directly compares the mean velocity between aspect ratios at various downstream stations. The 95% confidence levels shown in Figure 5.14 were calculated by taking the square and the sum of the variances of the statistical and experimental uncertainty, calculated in Chapter 3. The uncertainty at $L/W = 10$ is larger than other aspect ratio FWMCs because of the large hot-wire drift error during the measurement. It should also be noted that the mean streamwise velocity may also be over-predicted by as much as 5% in regions of turbulence intensity $T.I. > 0.3$. In these results, no correction is applied for high turbulence effects, but spatial regions of $T.I. > 0.3$ are shaded in Figure 5.13, and also shown in black in Figure 5.14.

The first salient feature of each map in Figure 5.13 is the size of the region of high velocity fluid in the upper right corner. The region is indicative of velocity recovery in the wake, and is directly related to the descending shear layer over the free-end. The pressure difference between the free-stream and the cylinder base[1] accelerates high velocity, irrotational fluid from the free-stream over the free-end and transports it into the wake core, a process known as 'downwash' (Rostamy et al. 2012). The stronger the downwash, the more rapid the velocity recovery and the deeper the free-stream descends into the wake. According to Wang et al. (2006) and Bourgeois et al. (2011), the presence of downwash implies the presence of a pair of streamwise 'free-end' vortices, whose sense of rotation acts to draw fluid from the free-stream and push it down in the wake.

At $L/W = 1.4$ in Figure 5.13a, the shear layer descends across the entire cylinder span. The velocity, however, never recovers to the free-stream value. This is due to the relatively high height of the boundary layer compared with the span of the cylinder ($\delta/L \approx 0.9$). Because the boundary layer itself contains low velocity fluid, the imminent acceleration of this fluid over the free-end into the wake still results in a streamwise velocity lower than the free-stream. Accordingly, as the aspect ratio increases to $L/W = 4.3$ and 7.1 in Figure 5.13b and 5.13c, the relative height of the boundary layer reduces to $\delta/L \approx 0.3$ and 0.2 respectively, and the velocity recovers to the free-stream value. At $L/W = 10$, Figure 5.14d shows that there is a region at $x/W = 3$ and $z/L = 1$ where the velocity is 20% greater than the free-stream. While this may indicate that there is enhanced acceleration around the free-end implying that the base pressure at the free-end for $L/W = 10$ is higher than for $L/W < 10$, the measurements were taken in regions of high turbulence intensity and could simply be an artificial inflation of the mean velocity. At $L/W \geq 12.9$,

[1] 'base' refers to the leeward wall of the cylinder, not the junction of the cylinder

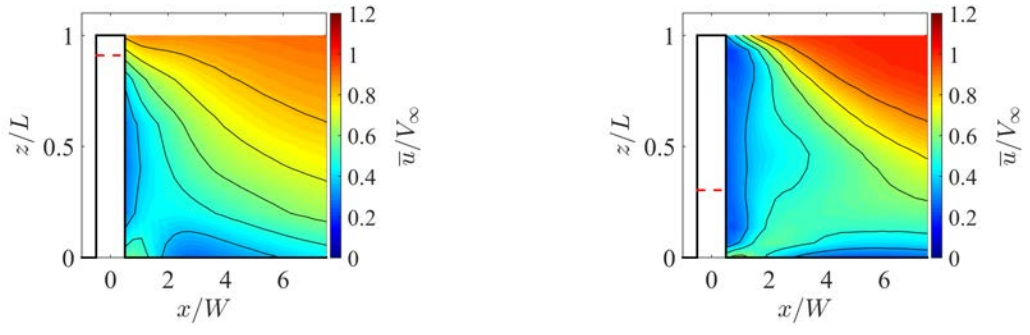

(a) $L/W = 1.4$, R0

(b) $L/W = 4.3$, RI

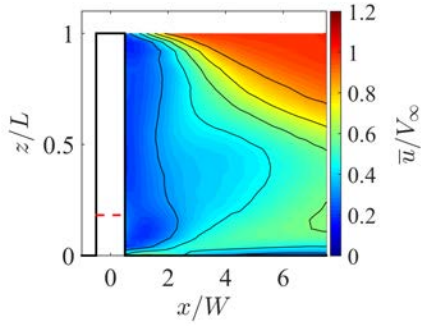

(c) $L/W = 7.1$, RI

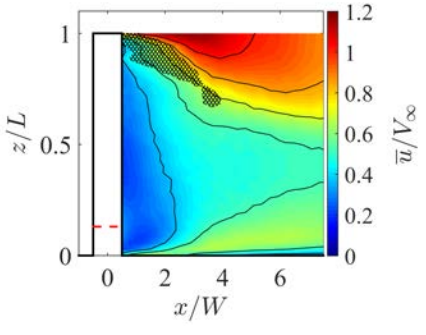

(d) $L/W = 10$, RII

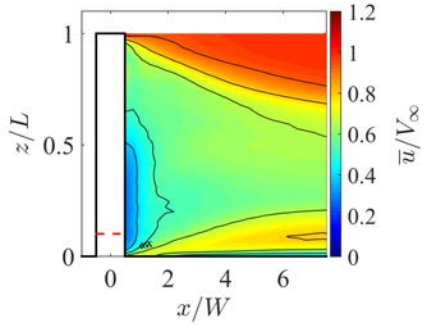

(e) $L/W = 12.9$, RII

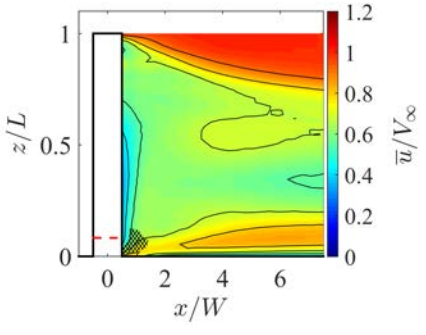

(f) $L/W = 15.7$, RII

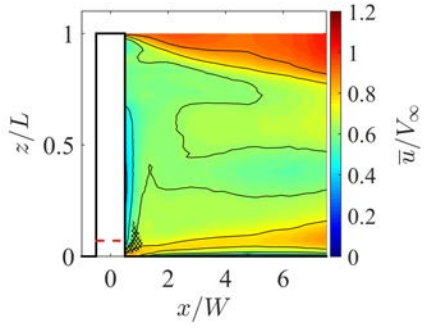

(g) $L/W = 18.6$, RIII

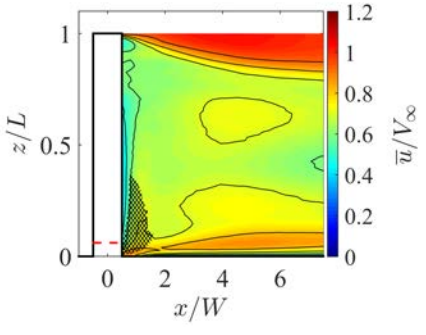

(h) $L/W = 21.4$, RIII

Figure 5.13: Colourmaps showing the mean velocity contours in the wake of 8 different aspect ratio FMWCs. The mean velocity is normalised by the free-stream velocity, $V_\infty = 32$ m/s, while the ordinate axis has been normalised by the height of each cylinder so that $z/L = 1$ is the free-end of the cylinder. The relative height of the boundary layer for each aspect ratio is indicated by a dashed red line. The plane of the hot-wire measurements was $y/W = 0.6$. Regions where the hot-wire measured the turbulence intensity $T.I. > 0.3$ are cross hatched.

the maximum velocity recovery returns to the free-stream value (see Figures 5.13e to 5.13h).

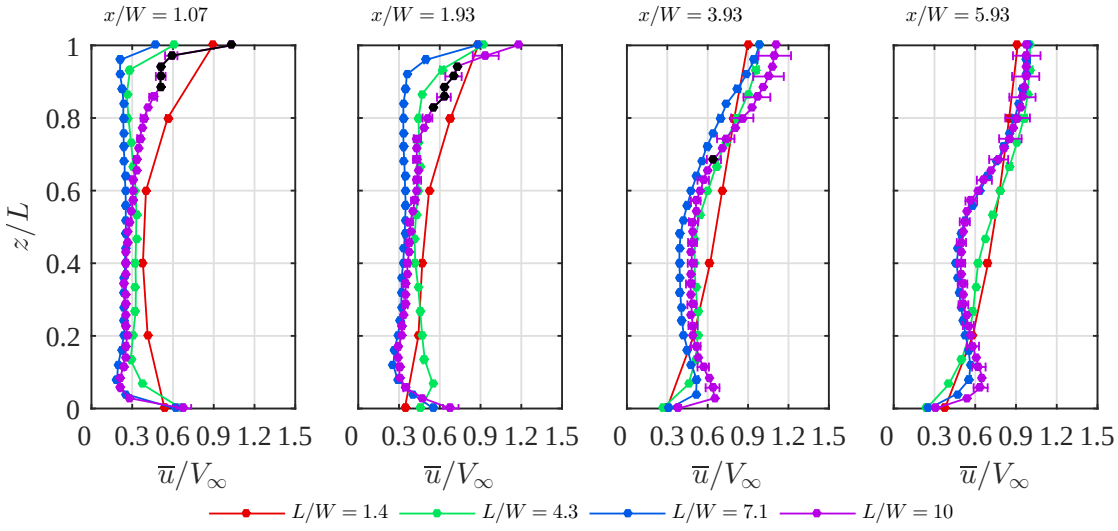

(a) $1.4 \leq L/W \leq 10$

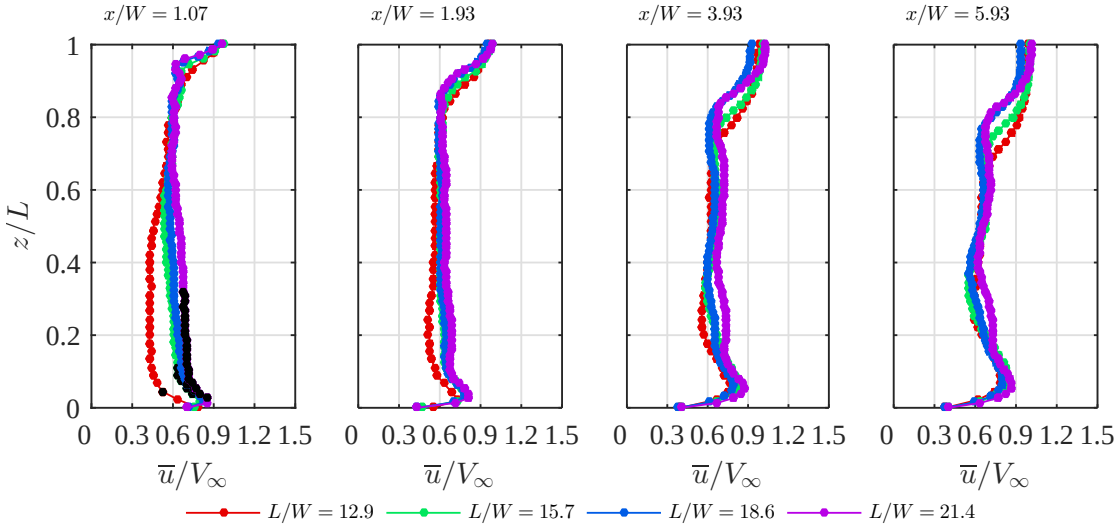

(b) $12.9 \leq L/W \leq 21.4$

Figure 5.14: The spanwise mean velocity profiles at various downstream locations in the wake for (a) $1.4 \leq L/W \leq 10$ and (b) $12.9 \leq L/W \leq 21.4$. Measurements where the turbulence intensity exceeds $T.I. > 0.3$ are shown in black.

As L/W increases from 12.9 to 21.4, the extent that the free-stream penetrates into the wake approaches aspect ratio independence. To illustrate, a 'wake penetration parameter' is defined, which is the point along the cylinder span in the z/L direction at $x/W = 6$ in Figure 5.14 where the velocity reaches 80% of the free-stream value. Figure 5.15 plots the free-stream wake penetration parameter (as the number of cylinder widths from the free-end) against the cylinder aspect ratio. The effect of the shear layer increases linearly with aspect ratio for $L/W \leq 10$. However, for $L/W \geq 12.9$, free-stream penetration is independent of aspect ratio and extends to approximately $3.5W$ from the free-end. The results suggest that at $L/W \geq 12.9$, the wake dynamics of the free-end *decouple* from the wake dynamics of the mid-span and the junction.

The second important feature of the mean velocity maps in Figure 5.13 is the injection of high speed fluid near the junction of the cylinder, starting at $x/W \approx 2$. According

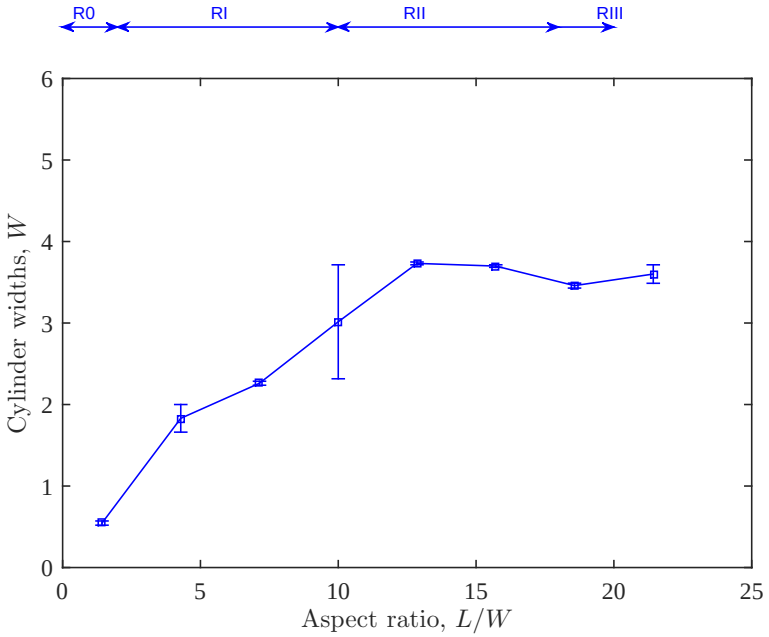

Figure 5.15: The number of FWMC widths below the free-end at $x/W = 6$ where the mean velocity reaches 80% of the free-stream value.

to Bourgeois (2012), high speed fluid near the junction is an indication of the presence of 'upwash', where high speed fluid from the free-stream is entrained into the wake and forced, in a spanwise direction, into the reverse flow region. With this upwash, a significant amount of streamwise flow is present, due to the entrainment of irrotational free-stream fluid. Similar to downwash, Hosseini et al. (2013) has related upwash to the presence of streamwise junction vortices.

From Figure 5.13a, it appears that no upwash exists at $L/W = 1.4$. As the aspect ratio increases to $L/W = 21.4$ in Figure 5.13h, the magnitude of the streamwise velocity at the junction progressively increases. A jet-like injection forms at $x/W \approx 2$, which rises, in the spanwise direction, off the plate as the measurement position moves downstream. A local maximum in the streamwise velocity is measured for $L/W \geq 7.1$ at $z/L \approx 0.1$ and $x/W = 6$, as demonstrated in Figure 5.14. Figure 5.16 quantifies the magnitude of this local maximum at $x/W = 6$, $\overline{u}/V_\infty|_{max}$, against aspect ratio.

For $L/W \leq 4.3$, no local maxima in the junction mean velocity exists (see Figure 5.14), hence upwash is weak or not existent for $L/W < 4.3$. For $7.1 \leq L/W \leq 15.7$, there is a rapid rise in the maximum velocity in the junction region from 55% of the free-stream value to approximately 85% of the free-stream value, after which the upwash becomes independent of aspect ratio. Upwash is still weak at $L/W = 7.1$, but strengthens rapidly as L/W approaches 12.9. By the time the FWMC reaches $L/W = 15.7$, upwash is strong, but invariant with aspect ratio.

5.4.2 Turbulence intensity

Figure 5.17 shows colourmaps of the streamwise turbulence intensity contours in the wake of the FWMCs. Here, streamwise turbulence intensity is denoted $T.I. = \sigma_u/V_\infty$, and is calculated as the standard deviation of the velocity of the signal normalised by

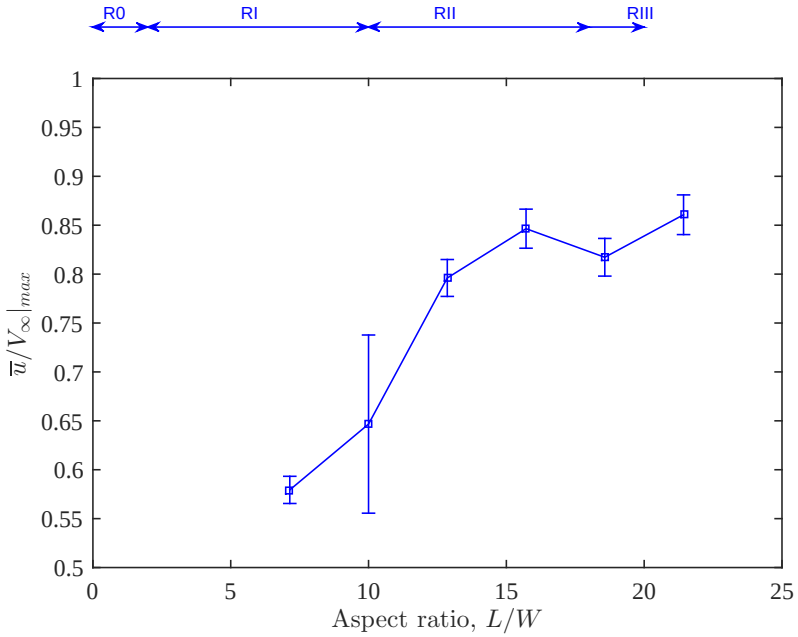

Figure 5.16: The magnitude of the local maximum of the mean velocity profile at $x/W = 6$ near the junction as the aspect ratio increases. This is a measure of the level of upwash at the junction.

the free-stream value. Similar to Figure 5.13, the abscissa-axis has been normalised by the span of each FWMC so that $z/L = 1$ is the free-end. The height of the boundary layer relative to the FWMC span for each aspect ratio is indicated by a dashed red line. Figures 5.18 directly compares the turbulence intensity between aspect ratios at various downstream stations. Figure 5.18a also compare the turbulence intensity results with similar results from Wang et al. (2006) at $x/W = 6$ for an FWMC with $L/W = 6$. The uncertainty bounds of the turbulence intensity were calculated by taking the sum of the square of the experimental uncertainty and statistical uncertainty (using Equation 3.25), discussed in Chapter 3. The large error for the measurements at $L/W = 10$ is a result of the relatively large hot-wire drift error during these measurements. Once again spatial regions of $T.I. > 0.3$ are shaded in Figure 5.17, and also shown in black in Figure 5.18. As discussed in Chapter 3, unlike mean velocity measurements, turbulence intensity measurements are relatively insensitive to transverse turbulence, and the error is estimated to be less than 2% for $T.I. < 0.3$.

Figure 5.17 shows that for $L/W = 4.3$, 7.1 and 10, there are two prominent concentrations of turbulence intensity, one near the free-end and one near the junction. For $L/W = 1.4$, only one concentration exists. The results are qualitatively similar to the PIV measurements presented by Wang and Zhou (2009) for $L/W = 3$, 5 and 7 square FWMCs in a similar boundary layer height of $\delta/W = 1.35$ at a slightly lower Reynolds number of $Re_W = 0.93 \times 10^4$. In that study, the turbulence intensity field of the $L/W = 3$ cylinder wake displayed only one maximum near the free-end, while the turbulence intensity field of the $L/W = 5$ and 7 wakes displayed two maxima. According to Wang and Zhou (2009), the presence of two maxima in the turbulence field is caused by streamwise junction and free-end vortices respectively. A cylinder with $L/W = 3$ was found (using streamwise vorticity measurements) to have a dipole vortex topology, where a pair of counter rotating

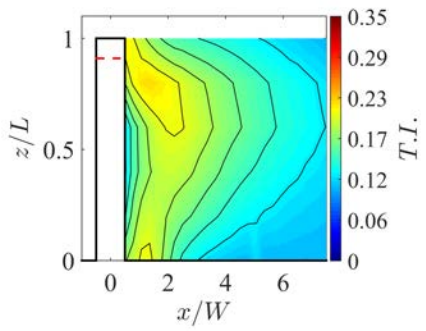

(a) $L/W = 1.4$, R0

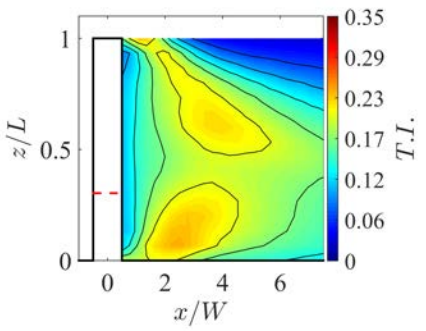

(b) $L/W = 4.3$, RI

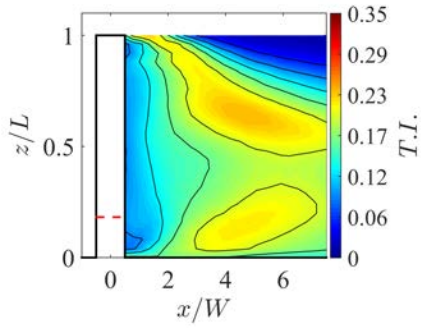

(c) $L/W = 7.1$, RI

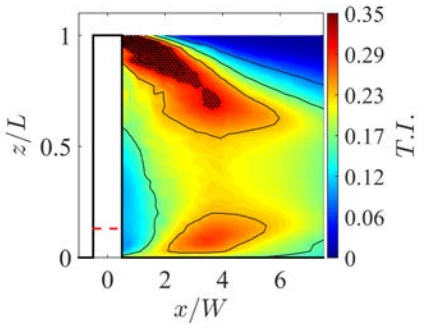

(d) $L/W = 10$, RII

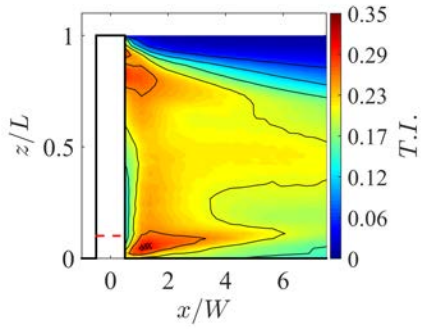

(e) $L/W = 12.9$, RII

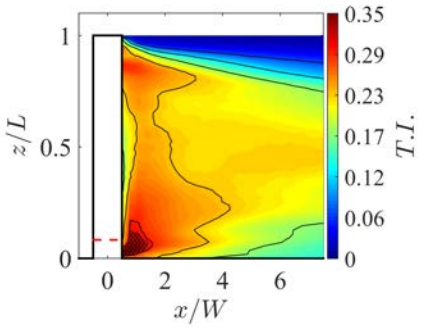

(f) $L/W = 15.7$, RII

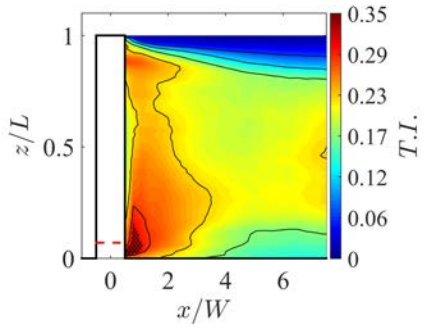

(g) $L/W = 18.6$, RIII

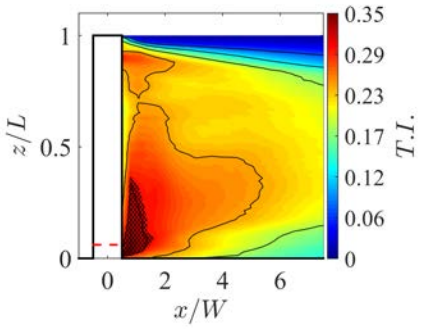

(h) $L/W = 21.4$, RIII

Figure 5.17: Colourmaps showing the turbulence intensity contours in the wake of 8 different aspect ratio FWMCs. The turbulence intensity is denoted $T.I. = \sigma_u/V_\infty$, calculated as the standard deviation of the velocity of the signal normalised by the free-stream value. The ordinate axis has been normalised by the span of each cylinder so that $z/L = 1$ is the free-end of the cylinder. The relative height of the boundary layer for each aspect ratio is indicated by a dashed red line. The plane of the hot-wire measurements was $y/W = 0.6$. Regions where the hot-wire measure the turbulence intensity $T.I. > 0.3$ are cross hatched.

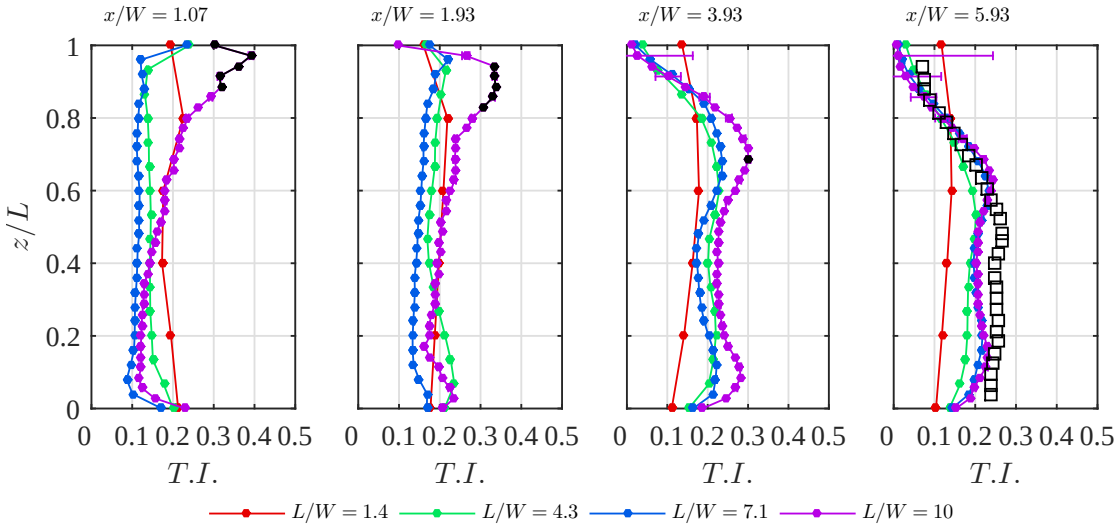

(a) $1.4 \leq L/W \leq 10$

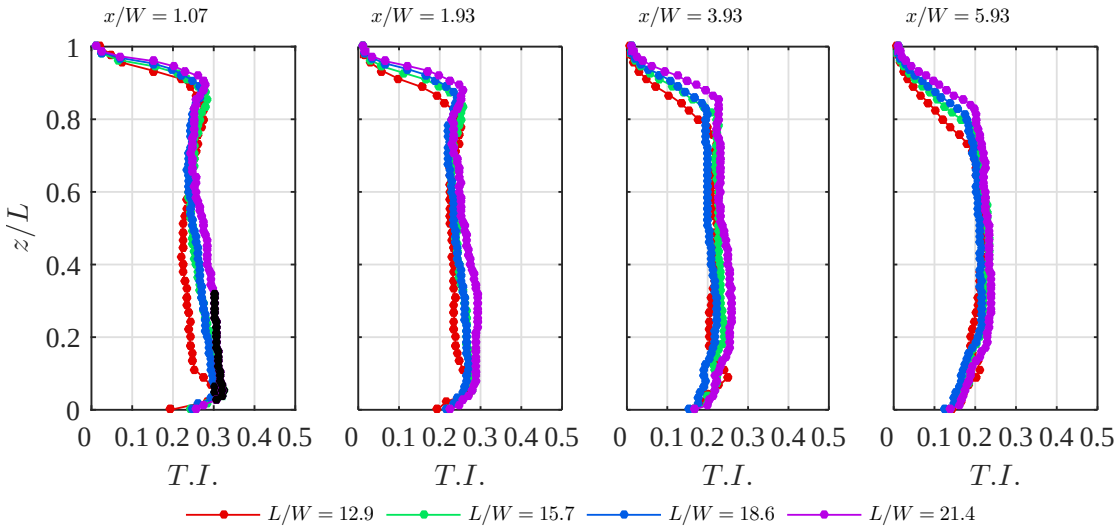

(b) $12.9 \leq L/W \leq 21.4$

Figure 5.18: Spanwise profiles of the turbulence intensity, $T.I.$ of 8 FWMCs with aspect ratios ranging from (a) $L/W = 1.4 \leq L/W \leq 10$ and (b) $12.9 \leq L/W \leq 21.4$ at four downstream locations. The results are also compared with similar results from Wang et al. (2006) at $x/W = 6$ for an $L/W = 6$ FWMC. Measurements above $T.I. > 0.3$ are highlighted in black.

vortices are observed near the free-end. On the other hand, cylinders with $L/W = 5$ and 7 were found to have quadrupole wake topologies, where an additional pair of counter rotating vortices are found near the junction.

Bourgeois (2012) explains that a dipole wake is the result of 'half-loop' shedding where opposite signed vortices are connected by vortex filaments formed in the separating shear-layer over the free-end of the cylinder. These filaments are 'bent' upstream due to Biot-Savart induction and consequently project a pair of counter-rotating streamwise vorticies in the cross-stream plane near the free-end. Similarly, Bourgeois (2012) found that a quadrupole wake is the result of 'full-loop' shedding, where vortex filaments are also rotated in the upstream direction at the junction due to interaction with the horseshoe

vortex. In contrast to the findings of Wang and Zhou (2009), Bourgeois (2012) found that the $T.I.$ field will still exhibit two maxima (one at the free-end and one at the junction) regardless of whether half or full-loop shedding occurs, the only difference being that full-loop shedding tends to shift the concentration of turbulence intensity at the junction much closer to the FWMC base when compared with half-loop shedding. Consequently the present streamwise turbulence intensity maps do not allow for the direct identification of dipole or quadrupole wakes. Hence, there is ambiguity in whether the vortex topologies of $L/W = 1.4$ through 10 are either quadrupole or dipole.

It has been inferred by Bourgeois (2012) that the wake of the $L/W = 6$ FWMC used by Wang et al. (2006) immersed in a boundary layer thickness of $\delta/W = 1$ had a quadrupole style wake because of the presence of upwash at the junction. In the present results, no appreciable upwash flow has been measured (or inferred from the mean velocity maps) until $L/W = 10$. Therefore, while the present results do not allow for the direct identification of the wake topology, it is likely that FWMCs with $L/W < 10$ have dipole wakes. This interpretation seems reasonable, especially when the turbulence intensity fields are compared with those for FWMCs immersed in the HTB (High Turbulent Boundary Layer) in Chapter 6, where the topology is known to be a quadrupole wake. In these maps (see Figure 6.14), while two turbulence intensity concentrations are still present for $L/W < 10$, the junction turbulence concentrations in the HTB are significantly closer to the cylinder base than in the LTB. Ogunremi and Sumner (2015) found that square FWMCs of $3 \leq L/W \leq 9$ in a boundary layer of height $\delta/W = 1.5$ had dipole wakes confirming that the boundary layer must be greater than $\delta/W = 1.5$ for a quadrupole wake to be induced. El Hassan et al. (2015) has also demonstrated that the vortex legs shed off FWMCs with $L/W = 4$ immersed in a boundary layer thickness of $\delta/W = 1.3$ had less severe wake retraction than that of a quadrupole style wake. One possibility raised by El Hassan et al. (2015) is that their FWMC was in a 'transitional' state between quadrupole and dipole vortex topologies.

Unlike their lower aspect ratio counterparts, cylinders in RII and RIII ($L/W > 10$) do not have well established vortex flow topologies. It is unclear whether these FWMCs have quadrupole or dipole wakes or another alternative. Figures 5.17e through 5.17h show that as the aspect ratio increases above $L/W = 10$, the two turbulence intensity concentrations retreat toward the free-end and junction respectively so that they lie at $x/W \approx 1$. The turbulence intensity at the mid-span ($z/L = 0.5$) also generally increases with aspect ratio. The high degree of streamwise turbulence intensity near the free-end and junction region (see Figure 5.18) for these high aspect ratio cylinders indicates that strong free-end and junction vortices are present, consistent with a quadrupole style, full-loop shedding wake. Section 5.2 has shown, however, that multiple Aeolian like tones exist for these high-aspect-ratio FWMCs corresponding to a spanwise cellular vortex structure, where different spanwise regions of the cylinder shed with different frequencies. A cellular variation in vortex shedding frequency across the span implies that multiple independent vortex structures form across the FWMC span. Therefore it is unlikely that conventional full-loop quadrupole or half-loop dipole wake structures, like those described by Wang and Zhou (2009) or Bourgeois et al. (2011), exist at these high aspect ratios.

A flow quantity that is commonly used to characterise the wake of infinite cylinders is the *formation length* (Williamson 1996). As discussed in Chapter 2, the formation

length is defined as the point where the streamwise velocity fluctuations on the wake centreline first reach a local maximum. The physical relevance of the formation length of an infinite cylinder is discussed by Gerrard (1966) and Unal and Rockwell (1988); it is essentially the point downstream of the cylinder where fluid from outside of the wake first crosses the centreline of the cylinder on average. For an infinite cylinder, the length of the formation region is indicative of the strength of vortex shedding; the shorter the formation length, the higher the Reynolds stress production and the stronger the vortex shedding.

Figure 5.19 shows the variation of the turbulence intensity for various downstream stations at the cylinder mid-span ($z/L = 0.5$). Figure 5.20 plots the location of the maximum of the turbulence intensity, a measure of the formation length, L_f, for different aspect ratio cylinders. These measurements are also compared with similar measurements made by Wang and Zhou (2009) ($1 \leq L/W \leq 11$) and Hosseini et al. (2013) ($L/W = 8$) for square FWMCs and Lyn et al. (1995) for an infinite cylinder.

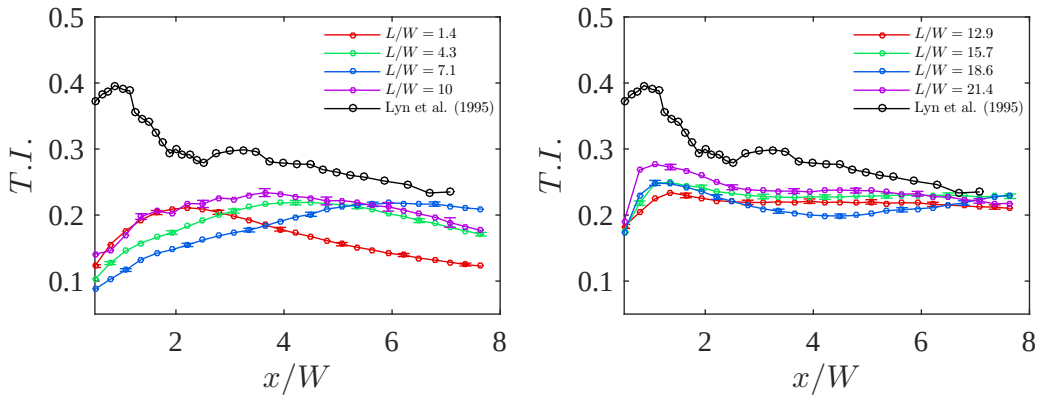

(a) $1.4 \leq L/W \leq 10$ (b) $12.9 \leq L/W \leq 21.4$

Figure 5.19: Streamwise variation of turbulence intensity, $T.I.$, at the mid-span for FWMCs with aspect ratios ranging from (a) $1.4 \leq L/W \leq 10$ and (b) $12.9 \leq L/W \leq 21.4$.

Figure 5.19 shows that for all aspect ratios, the maximum turbulence intensity is below that measured by Lyn et al. (1995). This indicates that the Reynolds stresses produced by the vortex structures are weaker for FWMCs than in the infinite cylinder case. This is corroborated by the location of the maximum turbulence intensity, i.e., the formation length, L_f. Figure 5.20 shows that the formation length increases rapidly from approximately $L_f/W = 2$ at $L/W = 1.4$ to a maximum of $L_f/W = 6$ at $L/W = 7.1$, greater than that expected for an infinitely long cylinder found by Lyn et al. (1995). For higher aspect ratios, the formation length becomes similar to that for an infinite cylinder as the flow at the FWMC mid-span becomes free from the influence of the free-end and junction.

As demonstrated in Figure 5.20, the calculated formation lengths agree well with the individual data point measured by Hosseini et al. (2013) but are several cylinder widths higher than the corresponding measurements by Wang and Zhou (2009). Importantly, however, the general trend compares well with the results of Wang and Zhou (2009) where the maximum formation length occurs for $L/W = 7$. One possibility that may explain why the present calculated formation lengths are higher than the measurements of Wang and Zhou (2009) are Reynolds number effects. The experiments conducted by

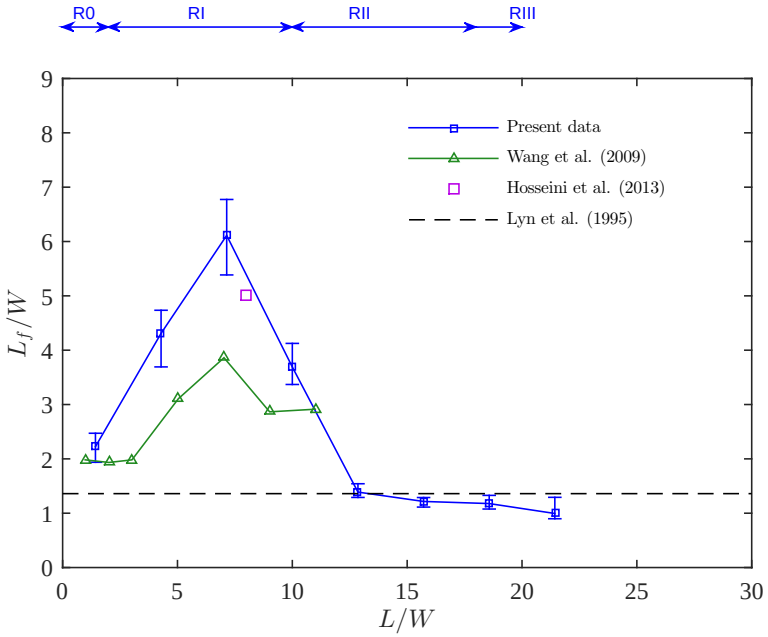

Figure 5.20: The variation of the wake formation length, L_f/W, at the mid-span of the FWMC, with aspect ratio. The results are compared with the data of Wang and Zhou (2009) and Hosseini et al. (2013) for square FWMCs and Lyn et al. (1995) for an infinite cylinder.

Wang and Zhou (2009) were at $Re_W = 0.93 \times 10^4$, whereas the present measurements were performed at $Re_W = 1.45 \times 10^4$. Furthermore, the measurements of Hosseini et al. (2013), for which very good agreement is achieved, were performed at $Re_W = 1.2 \times 10^4$. Thus, the discrepancy between the results of Wang and Zhou (2009) and the present results may be a Reynolds number dependence of the formation length. The present understanding of the large scale vortex structures behind FWMC by Bourgeois et al. (2011) dismisses the impact of Reynolds number on the quasi-periodic flow structures. This assumption, however, was based on observations on low aspect ratio ($L/W < 4$) square FWMCs in a Reynolds number range of $0.65 \times 10^4 < Re_W < 1.2 \times 10^4$. The present results show that Reynolds number effects may begin at higher aspect ratios (i.e., $L/W > 4$). Certainly, in the wake of an infinitely long circular cylinder, the formation length is known to vary with Reynolds number in the range from $1000 < Re_W < 20 \times 10^4$ (Norberg 2003), so it seems reasonable to expect similar behaviour for square cylinders at higher aspect ratios and comparable Reynolds numbers.

The most important observation in these results is that the elongation of the formation length at $L/W = 7$ is coincident with the reduction in the mganitude of P1 (and OASPL) at $L/W = 7$. The turbulence intensity results presented here indicate that the strength of the vortices at $L/W = 7$ are much weaker than those of higher or lower aspect ratio. As will be shown, this reduction in vortex strength corresponds to a wake reformation process prior to the transition from RI to RII at $L/W = 10$. The properties of this wake reformation are studied in-depth using surface pressure measurements and flow visualisation in Section 5.5.

5.4.3 Spectral maps

Figures 5.21 and 5.22 show spectral maps of the PSD of velocity fluctuations, denoted $G_{uu}(f)$, at various downstream positions in the wake for each FWMC. In these maps, the abscissa axis is the Strouhal number of the velocity fluctuations, the ordinate axis is the normalised span of the cylinder and the colour denotes the PSD of the velocity fluctuations in dB/Hz re. 20μm/s. The PSDs were estimated using Welch's averaged modified periodogram method (herein referred to 'Welch's method') (Welch 1967) by dividing each time record into B=240 overlapping blocks of 2^{12} data points. This gave a frequency resolution of $\Delta f = 8$ Hz and a spectral density estimate (based on the statistical uncertainty) with a 95% confidence of ± 0.6 dB/Hz at each narrowband frequency.

The velocity spectral maps at $L/W = 1.4$ in Figure 5.21a show strong fluctuations at $St \approx 0.09$. This indicates that a periodic signal is occurring in the wake of the cylinder, despite the fact that no Aeolian tone is detected at this aspect ratio. At $x/W = 1.07$ in Figure 5.21a, the fluctuations are strongest near the junction region. Moving downstream, the strength of the velocity fluctuations decay, but decay more rapidly at the junction region. Eventually, at $x/W = 5.93$, the peak velocity fluctuations occur at $z/L = 0.7$.

The wakes shown in Figures 5.21b, 5.21c and 5.21d for $L/W = 4.3$, 7.1 and 10 respectively have different characteristics compared with that of 5.21a for $L/W = 1.4$. All three wakes display strong wake periodicity at $St \approx 0.1$. However, unlike Figure 5.21a, strong velocity fluctuations are not measured close to the cylinder at $x/W = 1.07$. Instead, the peak velocity fluctuations occur at $x/W \geq 2$. This is consistent with the observation that the formation length is elongated.

Another characteristic of these wakes is that the highest magnitude fluctuations first form at the junction region of the cylinder. For example, for $L/W = 4.3$ at $x/W = 1.93$ in Figure 5.21b, the strongest velocity fluctuations are localised entirely within the boundary layer. These observations are consistent with the investigation of Casalino and Jacob (2003), who observed that a cylinder will experience enhanced vortex shedding near an end-plate because the end-plate prevents spanwise velocity fluctuations from disrupting the wake in that region, thereby promoting two-dimensional flow.

In fact, the wakes appear to be split into two regions; a region of strong velocity fluctuations at $St = 0.1$ near the junction as previously discussed and a secondary region of weaker velocity fluctuations, also at $St = 0.1$, localised near the free-end. These two regions correspond to the two peaks found in the turbulence intensity maps, thus confirming that the peaks in turbulence intensity are generated by the passage of periodically shed vortices. As demonstrated in the turbulence intensity maps, the spatial separation between the tip and junction fluctuations decreases further downstream. At $x/W \approx 6$ the two peaks merge to form a single 'cell' of vortex shedding.

As the aspect ratio increases toward higher values as in Figure 5.22, the wake is dominated by a stronger vortex shedding and multi-cellular wake structures. At $L/W = 12.9$ in Figure 5.22a two vortex shedding peaks are observed: a lower frequency peak toward the free-end of the cylinder beginning from $z/L = 0.4$ to 1 and a higher frequency peak at the junction region starting from $z/L = 0$ to 0.4. The magnitude of the velocity fluctuations at the free-end cell decay downstream at a much faster rate than that associated with the higher frequency peak at the junction. The same phenomena is

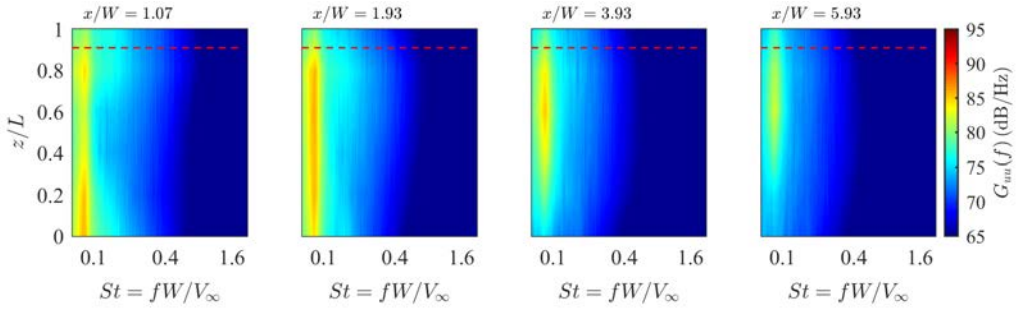

(a) $L/W = 1.4$, R0

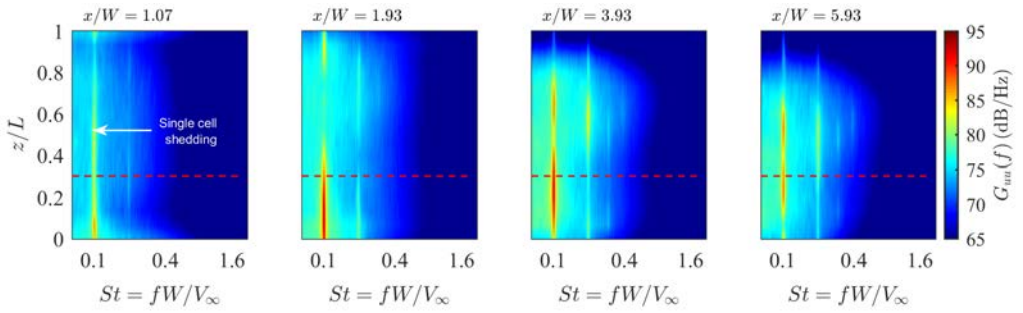

(b) $L/W = 4.3$, RI

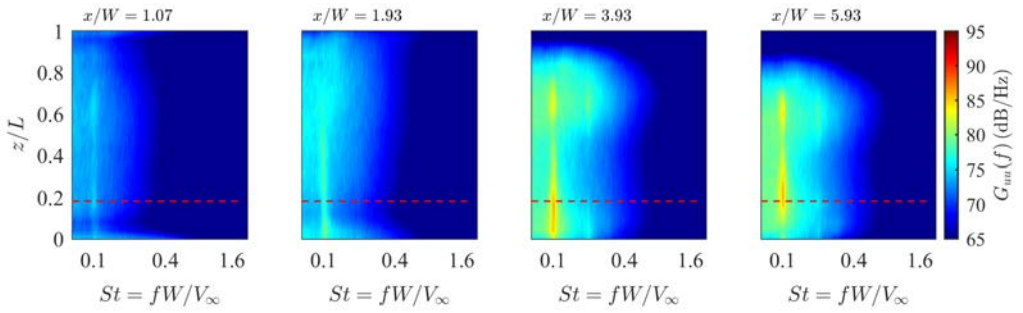

(c) $L/W = 7.1$, RI

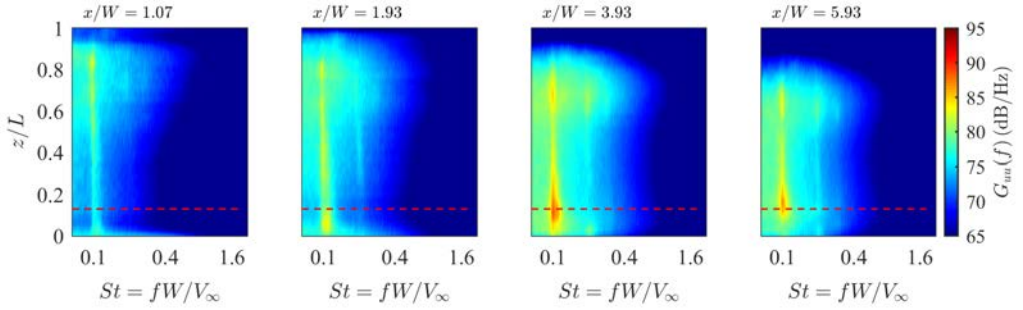

(d) $L/W = 10.0$, RII

Figure 5.21: Spectral maps of the streamwise velocity fluctuations, $G_{uu}(f)$, at various downstream stations for FWMCs with aspect ratios (a) $L/W = 1.4$, (b) $L/W = 4.3$, (c) $L/W = 7.1$ and (d) $L/W = 10$. The values are expressed in dB/Hz re. 20μm/s.

observed for $L/W = 15.7$. However, as the aspect ratio increases, the starting point of the free-end cell moves toward the free-end of the cylinder, so the total length of the free-end cell remains constant. At $L/W = 21.4$, a third cell of vortex shedding is observed at the junction region, that extends from $z/L = 0$ through the boundary layer to $z/L = 0.2$. The frequency of this cell lies between that of the first and second cell. Similar to the free-end cell, the velocity fluctuations associated with this cell decay downstream at a

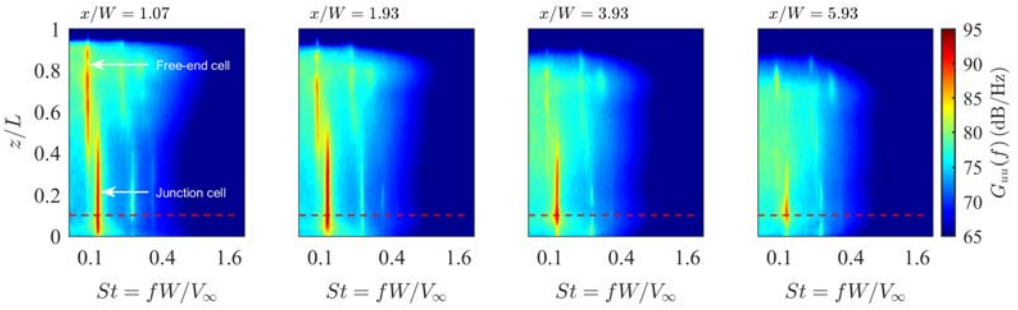

(a) $L/W = 12.9$, RII

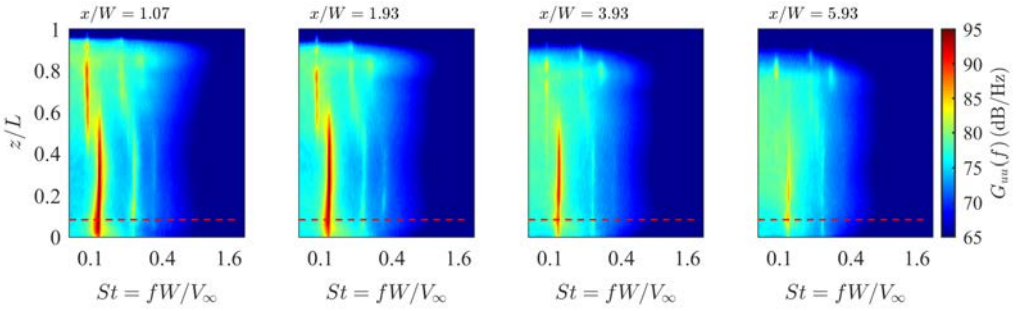

(b) $L/W = 15.7$, RII

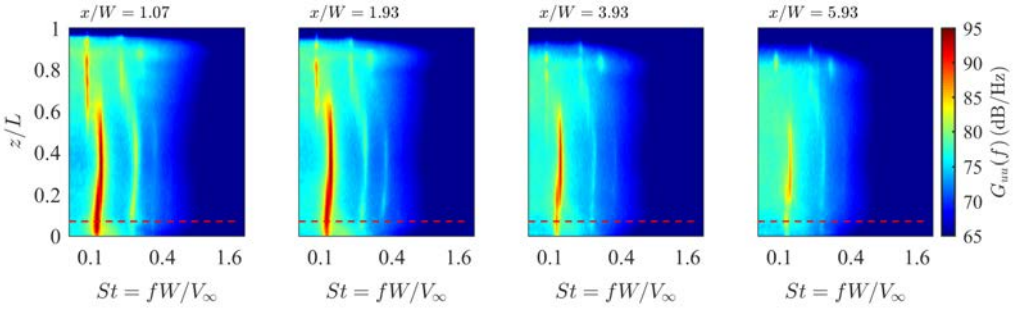

(c) $L/W = 18.6$, RIII

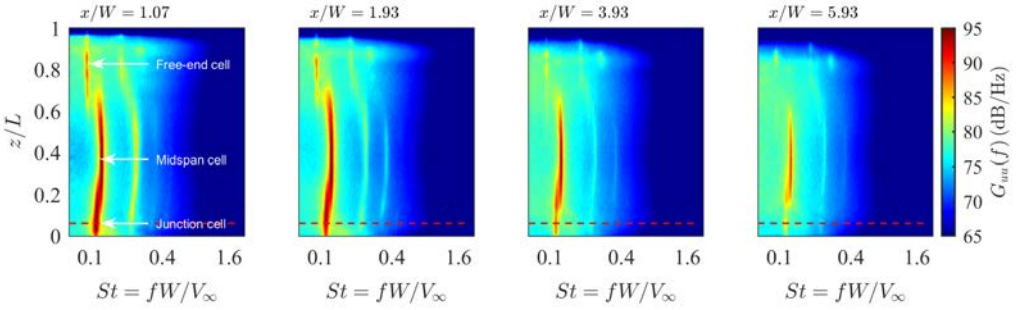

(d) $L/W = 21.4$, RIII

Figure 5.22: Spectral maps of the streamwise velocity fluctuations, $G_{uu}(f)$, at various downstream stations for FWMCs with aspect ratios (a) $L/W = 12.9$, (b) $L/W = 15.7$, (c) $L/W = 18.6$ and (d) $L/W = 21.4$. The values are expressed in dB/Hz re. 20μm/s. Each point is measured to with ± 0.6 dB/Hz with a 95% level of confidence.

more rapid rate than the mid-span cell.

5.4.4 Coherence with a single microphone

Figures 5.23 and 5.24 show the contours of the coherence, $\gamma^2_{xy}(f)$, between the acoustic pressure measured by the microphone located 0.5 m directly above the cylinder and the

velocity fluctuations in the wake. The form of Figures 5.23 and 5.24 is similar to that of Figure 5.21, although the colour level in these figures denotes the coherence, $0 \leq \gamma^2_{xy}(f) \leq 1$. The coherence function was calculated using Welch's method, dividing each time record into $B = 240$ overlapping blocks of 2^{12} data points each, calculating the coherence function of these sub-records, and averaging the result. In the coherence measurements, a small propagation time delay between the velocity fluctuations measured with the hot-wire and the acoustic pressure fluctuations measured with the single microphone meant that the coherence estimates had a small bias error associated with them. This bias error is approximately 2.4% of the coherence, as calculated using Equation 3.40. The variance of the coherence function is dependent on the coherence itself, as indicated by Equation 3.39. The 95% confidence interval of the coherence estimates are calculated as twice the root of the total Mean Square Error (MSE) (95% C.I. $= 2\sqrt{MSE}$), where the MSE is the sum of the square of the bias and the variance. Table 5.1 presents the breakdown of the sources of error in the measured coherence. At high $\gamma^2_{xy} = 0.9$, the uncertainty is approximately ± 0.05, increasing to ± 0.07 at $\gamma^2_{xy} = 0.3$.

Table 5.1: A breakdown of the bias and random error associated with measurement of coherence between the acoustic pressure fluctuations measured by the microphone and the velocity signal measured in the wake the FWMC with a hot-wire.

γ^2_{xy}	bias(γ^2_{xy})	var(γ^2_{xy})	MSE	95% C.I.
0.3	0.0072	0.0013	0.0014	± 0.07
0.5	0.0120	0.0011	0.0013	± 0.07
0.7	0.0168	0.0006	0.0008	± 0.06
0.9	0.0215	0.0001	0.0005	± 0.05

The coherence spatial maps show similar information to the velocity spectral maps, but confirm that the tonal noise detected by the microphone is generated by periodically shed vortical structures. This is even the case for $L/W = 1.4$, where moderate level coherence is detected across the entire span at $x/W = 1.07$ in Figure 5.23a. As discussed in Section 5.2, no Aeolian tone is detected with the microphone for this aspect ratio case. This suggests that while periodic structures definitely form at $L/W = 1.4$, they form *intermittently* so that the Aeolian tone detected by the microphone becomes masked by background noise.

At $L/W = 4.3$ in Figure 5.23b, very strong coherence ($\gamma^2_{xy}(f) \approx 0.95$) at $St = 0.1$ is achieved across the entire span of the cylinder at $x/W = 1.07$. Similar to the fluctuating velocity, the coherence at $St = 0.1$ first forms two distinct regions downstream, one at the junction and one at the free-end, before eventually merging at $x/W = 6$.

At $L/W = 7.1$ in Figure 5.23c, very low coherence is detected close to the cylinder at $x/W = 1.07$. Moderate levels of coherence ($\gamma^2_{xy} = 0.6$) are only attained at $x/W = 3.93$, where two distinct regions of coherence exist at $St = 0.1$, one at the junction centred at $z/L = 0.2$ and one at $z/L = 0.6$. These regions of coherence correspond to the two regions of fluctuating velocity at the same positions. Lower coherence velocity fluctuations are consistent with the idea that shedding occurs intermittently. Moving to higher aspect ratios, at $L/W = 10$ in in Figure 5.23d, strong coherence is once again recovered close to the cylinder at $x/W = 1.07$, suggesting that vortex shedding becomes more regular. Similar to the behaviour of the velocity fluctuations, the coherence at $St = 0.1$ tends to

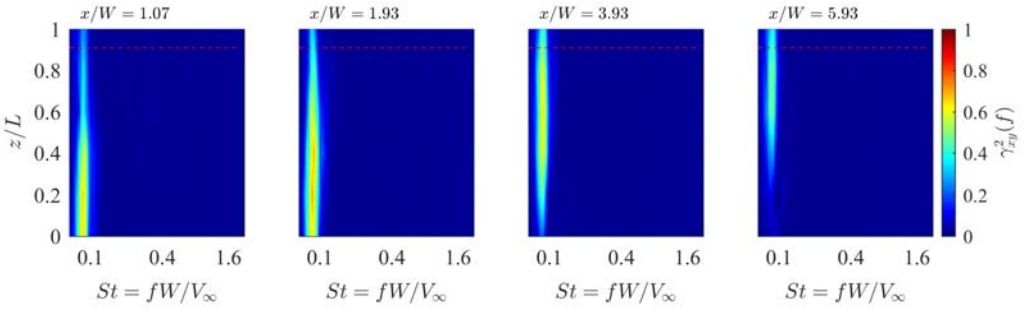

(a) $L/W = 1.4$, R0

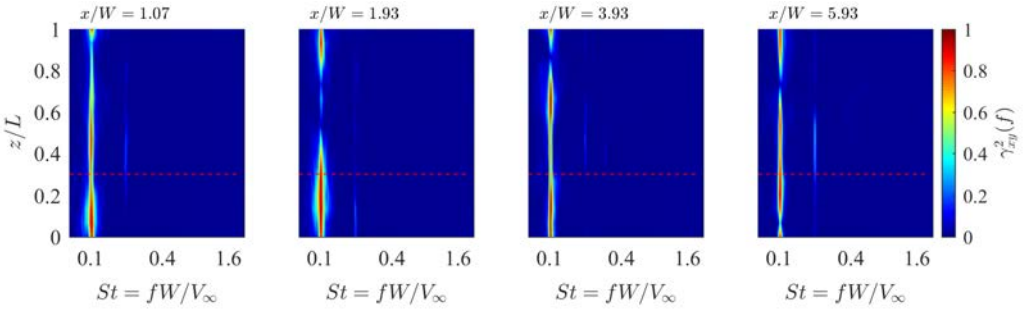

(b) $L/W = 4.3$, RI

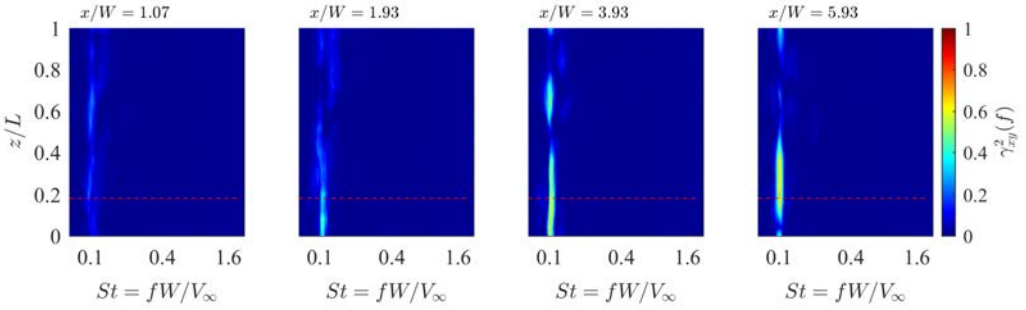

(c) $L/W = 7.1$, RI

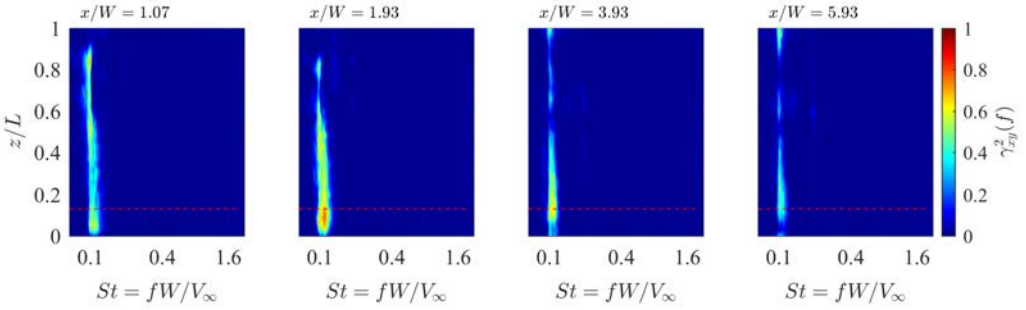

(d) $L/W = 10$, RII

Figure 5.23: Spectral maps of the coherence, $\gamma^2_{xy}(f)$, between velocity fluctuations and the acoustic pressure measured by a single microphone 0.5 m directly above the FWMC at various downstream stations for FWMCs with aspect ratios (a) $L/W = 1.4$, (b) $L/W = 4.3$, (c) $L/W = 7.1$ and (d) $L/W = 10$. The dotted red line denotes the height of the boundary layer, δ, relative to the span of the FWMC.

decay much faster at the free-end that in the junction region.

At higher aspect ratios in Figure 5.24, the coherence levels are high ($\gamma^2_{xy}(f) \approx 0.95$) at the tonal frequencies in the acoustic spectrum. The coherence maps once again confirm that the dual and triple tonal peaks measured in the acoustic spectrum are caused by dual and triple cellular wake structures for FWMCs in RII and RIII ($L/W > 10$).

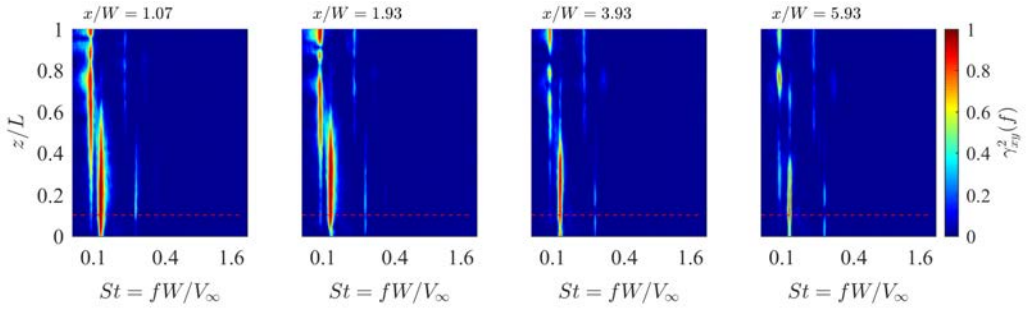

(a) $L/W = 12.9$, RII

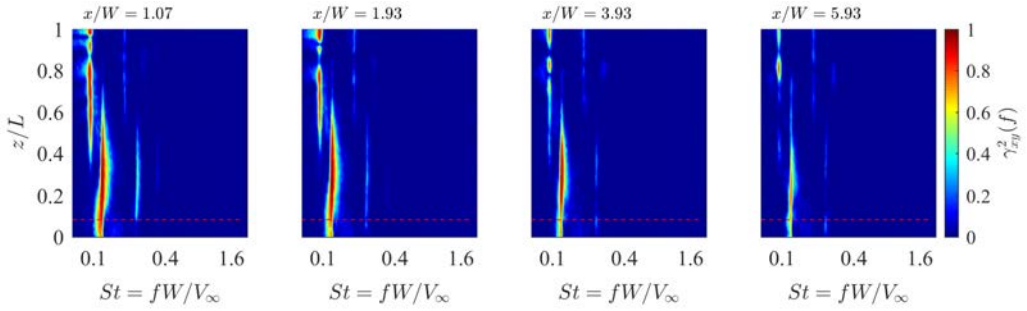

(b) $L/W = 15.7$, RII

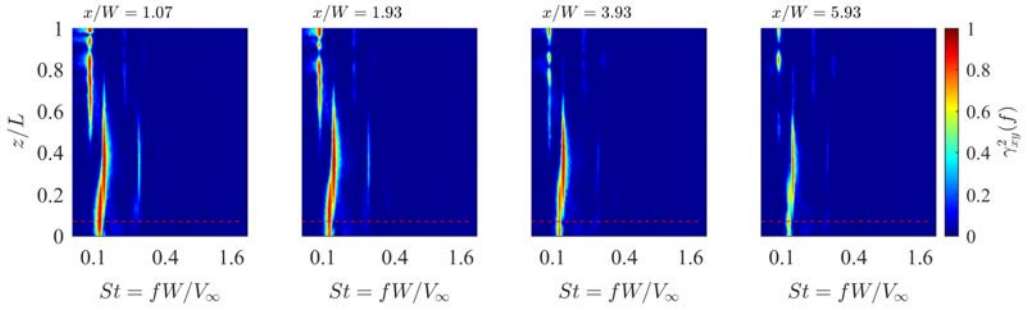

(c) $L/W = 18.6$, RIII

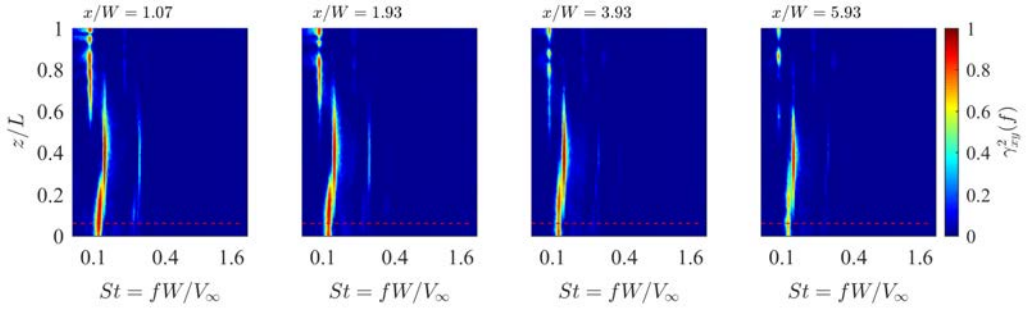

(d) $L/W = 21.4$, RIII

Figure 5.24: Spectral maps of the coherence, $\gamma^2_{xy}(f)$, between velocity fluctuations and the acoustic pressure measured by a single microphone 0.5 m directly above the FWMC at various downstream stations for FWMCs with aspect ratios (a) $L/W = 12.9$, (b) $L/W = 15.7$, (c) $L/W = 18.6$ and (d) $L/W = 21.4$. The dotted red line denotes the height of the boundary layer, δ, relative to the span of the FWMC.

At these higher aspect ratios, the coherence for structures at the junction region tends to decay downstream more slowly than at the free-end region. Strong coherence is always measured for the junction cell regardless of the downstream location, even for locations well inside of the boundary layer (for example see Figure 5.24a). This is true for both the dual and triple cellular wake structures (as in Figure 5.24d). On the other hand, the

coherence of the free-end cell reduces in magnitude at locations further downstream. The free-end cell also splits into three sub-cells at the same frequency further downstream. This behaviour can be observed most prominently at $L/W = 12.9$ at $x/W = 3.93$ in Figure 5.24a, but occurs for all aspect ratios above $L/W = 12.9$ in Figure 5.24b through 5.24d, in what appears to be an exact like-for-like manner.

The coherence maps also show that very close to the cylinder ($x/W \approx 1$), there is significant overlap between the free-end and mid-span cells. At $L/W = 12.9$ in Figure 5.24a, the free-end cell extends from $z/L = 1$ to $z/L = 0.2$ and the junction cell extends from $y/L = 0.6$ to $y/L = 0$. The overlap also occurs for the junction cell in the triple cellular wake structure. Overlapping fundamental frequencies between cells were also found by Williamson (1989) for circular cylinders in low Reynolds numbers ($Re_D \approx 60$). As will be shown in Section 5.5.4, the overlap is caused by the random oscillation of the spanwise location of the cell boundary with time.

5.4.5 Phase maps

Kawamura et al. (1984), Bourgeois et al. (2010), Wang and Zhou (2009) and Hosseini et al. (2013) used dual hot-wires placed either side of square and circular FWMCs to understand the spatial evolution of the vortices under the action of upwash and downwash. In these studies, an upstream curvature of the vortex filaments was visualised by comparing the average phase between each of the hot-wire signals as one hot-wire was traversed along the span. Here, we educe the orientation of the vortex filaments using a similar technique, but with the reference signal being the acoustic pressure measured with a microphone. A similar analysis was performed by Becker et al. (2008) but in a cross-stream plane, rather than a plane that was aligned with the free-stream velocity and the cylinder span. The visualisation technique is based on the fact that the location of the microphone is fixed, so the microphone signal serves as a reference signal with fixed statistical properties. Therefore, if at a certain position the velocity signal has a certain phase difference with the acoustic pressure and at another position, a similar phase difference is measured, then the two points can be thought of as being in-phase. As explained by Bourgeois et al. (2010), the inherent assumption with this visualisation technique is that the fluctuating velocity at a single point is governed primarily by the nearest vortex, with the effect of other vortices in the flow field being negated. As such, iso-contours of constant phase will be aligned with the vortex filaments in the flow.

Figures 5.25 to 5.27 are colourmaps showing the positions in the FWMC wake with similar phase between the velocity fluctuations (measured by the traversing wake hot-wire at $y/W = 0.6$) and acoustic pressure fluctuations (measured by the single microphone 0.5 m directly above the cylinder) at the frequency for which each peak was determined. That is, the position of equal phase at the frequency where P1, P2 and P3 are mapped in Figures 5.25 to 5.27 respectively. To generate these figures, the time averaged phase at a particular frequency was calculated using Equation 3.41. The absolute value of the phase, $|\phi(f_p)|$, where f_p is the peak frequency, was taken to avoid sharp discontinuities in the map due to the ambiguity at the $-\pi$ to π boundary. For visual clarity, the colouring of each map is restricted to only show phase from 0.5π to π.

Like coherence estimates, the error in the phase angle estimate varies with coherence

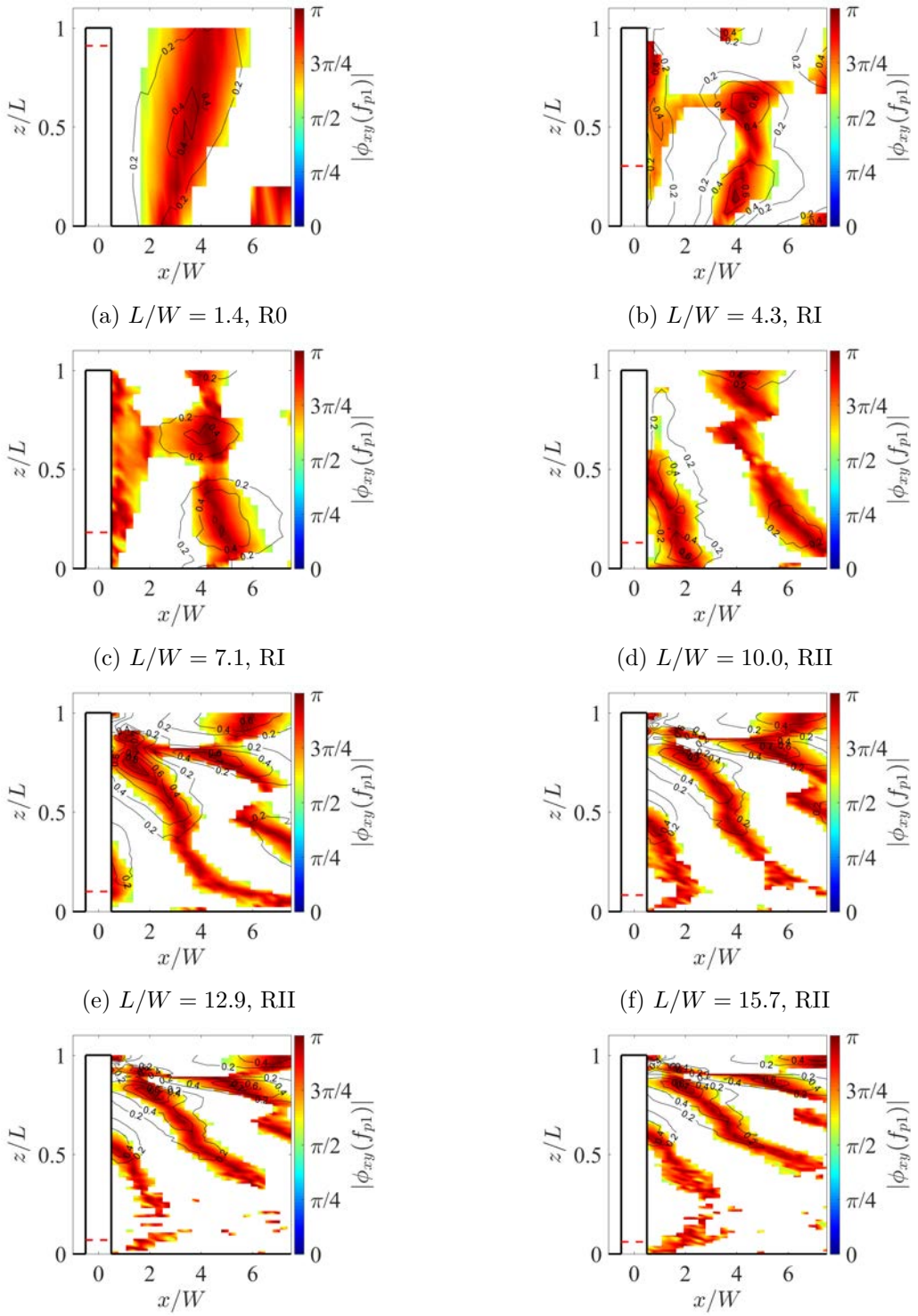

(a) $L/W = 1.4$, R0

(b) $L/W = 4.3$, RI

(c) $L/W = 7.1$, RI

(d) $L/W = 10.0$, RII

(e) $L/W = 12.9$, RII

(f) $L/W = 15.7$, RII

(g) $L/W = 18.6$, RIII

(h) $L/W = 21.4$, RIII

Figure 5.25: The spatial distribution of phase, $|\phi_{xy}(f_{p1})|$, at the frequency where P1 occurs for FWMCs with aspect ratios ranging from (a) $L/W = 1.4$ through (h) $L/W = 21.4$. The colourmaps are restricted to only show $|\phi_{xy}(f_{p1})| = \pi/2$ to π. The contour levels denote those parts of the in-phase structures that are coherent with the acoustic pressure measured with the microphone.

level at the measurement point. Table 5.2 summarises the 95% confidence intervals in the phase angle estimates using Equation 3.42.

As shown in Table 5.2, the phase angle can still be measured to within ± 10% of

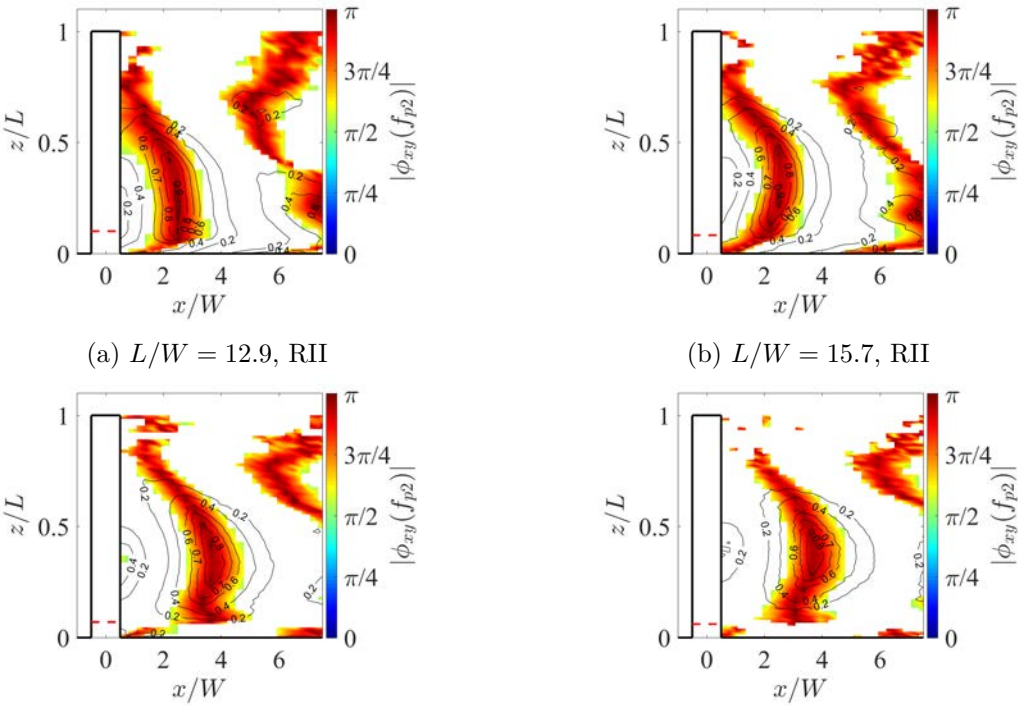

(a) $L/W = 12.9$, RII

(b) $L/W = 15.7$, RII

(c) $L/W = 18.6$, RIII

(d) $L/W = 21.4$, RIII

Figure 5.26: The spatial distribution of phase, $|\phi_{xy}(f_{p2})|$, at the frequency where P2 occurs for FWMCs with aspect ratios ranging from (a) $L/W = 12.9$ through (d) $L/W = 21.4$. The colourmaps are restricted to only show $|\phi_{xy}(f_{p2})| = \pi/2$ to π. The contour levels denote those parts of the in-phase structures that are coherent with the acoustic pressure measured with the microphone.

π even when the coherence is as low as $\gamma^2_{xy} = 0.1$. This is fortunate since, due to the location of the reference microphone (0.5 m directly above the cylinder), only velocity fluctuations associated with structures that continuously generate fluctuating lift (and therefore noise perpendicular to the cylinder) are coherent with the acoustic pressure directly above the cylinder. Nevertheless, even if low coherence is measured, in-phase regions may still be educed using the technique, although with a slightly larger degree of uncertainty. This also means that parts of the same vortex that do not radiate much noise perpendicular to the cylinder (either because they form intermittently or primarily generate fluctuating drag) can also be visualised. As such, in each of the maps, black contours have been added to represent the distribution of the in-phase structures that are coherent with the microphone. This is calculated by multiplying the absolute value of the phase at each point in space by the value of the coherence between the microphone and the hot-wire at the same point, and scaling the result so that 0 indicates no coherence, and 1 indicates full coherence. In this manner, those parts of the vortex structures that are noise producing are shown by the contours.

The maps for P1 (Figure 5.25) show a distinct transition of the noise producing structures moving from cylinders in R0 ($L/W < 2$), through RI ($2 < L/W < 10$) and finally to RII ($10 < L/W < 18$) and RIII ($L/W > 18$). At $L/W = 1.4$ in Figure 5.25a (the only cylinder in R0), there appears to be a single dominant structure across the entire FWMC span. The contours show that this structure is moderately coherent with the acoustic pressure fluctuations, the highest coherence ($\gamma^2_{xy} = 0.5$) occurring at the

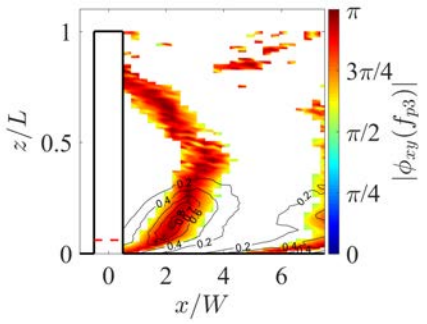

Figure 5.27: The spatial distribution of phase, $|\phi_{xy}(f_{p3})|$, at the frequency where P3 occurs for $L/W = 21.4$ (RIII). The colourmap is restricted to only show $|\phi_{xy}(f_{p3})| = \pi/2$ to π. The contour levels denote those parts of the in-phase structures that are coherent with the acoustic pressure measured with the microphone.

Table 5.2: The uncertainty associated with measurement of phase angle, in radians (Rad), between the acoustic pressure fluctuations measured by the microphone and the velocity signal measured in the wake the FWMC with a hot-wire.

γ^2_{xy}	95% C.I. (Rad)
0.1	$\pm 0.09\pi$
0.3	$\pm 0.05\pi$
0.5	$\pm 0.03\pi$
0.7	$\pm 0.02\pi$
0.9	$\pm 0.01\pi$

mid-span. This is consistent with the idea that this structure forms intermittently. The structure is also inclined downstream from the junction to the free-end. The downstream inclination of the in-phase structures and the coherence contours explains why a high decay rate of fluctuating velocity and coherence was found near the junction region in Figures 5.21 and 5.23 respectively.

The in-phase structures for $L/W = 4.3$ and $L/W = 7.1$ in Figure 5.25b and 5.25c (the cylinders within RI) are very different to that of $L/W = 1.4$, but show some similarity with each other. This similarity indicates that similar noise generating structures are formed within RI. For these aspect ratios, the primary noise producing structure is located near the junction and is parallel to the FWMC span. The primary spanwise structure at $x/W \approx 5$ is also connected to another in-phase structure very close to the cylinder at $x/W \approx 1$. The connection occurs via an in-phase strand at $z/L = 0.6$ with low coherence with the acoustic pressure fluctuations. For $L/W = 4.3$, the structure close to the cylinder has a moderate level of coherence with the Aeolian tone across the entire cylinder span, while the corresponding structure for $L/W = 7.1$ has almost no coherence with the microphone. This is consistent with the elongation of the formation length observed at $L/W = 7.1$, which delays the formation of coherent noise producing structures until much further downstream. It should be noted that the form of the in-phase structures presented in Figures 5.25b and 5.25c bear some resemblance to the half-loop shedding structure proposed by Bourgeois et al. (2011). In this vortex model, alternate upright vortices are shed in the lower portion of the FWMC, near the junction. These filaments are known as the 'principal core' of the loop. As each successive vortex is shed, vorticity over the free-end of the cylinder connects the anteceding vortex filament

from the opposite side. This filament is known as a 'connector strand'. In the present results, it is proposed that the upright structures at $x/W = 5$ are the in-print of the principal cores of the loops, while the connecting structures at $z/L = 0.6$ are the remnants of the connection strands. The results presented here suggest that the principal core of the loop is split into two noise producing components, one near the junction and one near the free-end at $z/L \approx 0.7$. These two concentrations of coherence occur where the peaks in the turbulence intensity maps occur providing evidence that the peaks in the turbulence intensity maps are caused by the passage of these looping structures.

In Figure 5.25d, the map for $L/W = 10$ is yet again different from its predecessors. This aspect ratio cylinder occurs at the boundary of RI and RII. No looping structures appear to be present in the phase map. Instead, vertical structures inclined upstream toward the free-end are visualised. In this manner, the vortices appears to 'peel' off the cylinder as they are shed. Further downsteam, what is presumably the same structure is observed to deform significantly near the free-end. While high coherence with the Aeolian tone is detected close to the cylinder across the majority of the span, the coherence decays rapidly as the structure deforms downstream.

The maps for $L/W > 10$ in Figure 5.25 (those cylinders that lie in RII and RIII) are self-similar. This is unsurprising because, up until this point, the flow and noise results associated with P1 at $L/W \geq 12.9$ have shown little to no variation. As pointed out previously, this indicates that for $L/W \geq 12.9$, the free-end region has reached a state where it is independent from the rest of the cylinder. Hence, the flow-induced noise and fluid dynamic properties related to P1 remain constant, regardless of the aspect ratio. The predominant in-phase structures for these aspect ratios appear to show a series of vortex filaments inclined upstream toward the junction. The highest coherence with the acoustic pressure occurs at the free-end closest to the cylinder. The coherence pattern follows the inclination of the vortices, which are highly deformed and irregular, explaining why the coherence breaks up into a series of sub-cells in Figure 5.24. Moving toward the junction region, there is no coherence with the acoustic pressure. The vortex filaments also lose an organised phase structure, signifying that the vortex filaments do not extend towards the junction region.

Moving to the structures associated with P2 (Figure 5.26), the in-phase components of velocity appear to be similar between each map. Unlike those associated with P1, the structures that generate P2 are large scale, well organised, regular and do not have significant inclination with respect to the axis of the cylinder. The coherence contours demonstrate that the dominant region of noise production from these structures is centralised at the mid-span of the cylinder. The portion of these upright structures close to the cylinder extremities is not coherent with Aeolian tone production. This coincides with the break-down of an organised phase relationship at the cylinder extremities, which is particularly evident in Figures 5.26c and 5.26d.

Finally, the structures that generate P3 are shown in Figure 5.27. Similar to P2, the major noise contribution occurs at the junction where the phase appears to be most organised. This is consistent with P3 being associated with the junction cell of vortex shedding. Near the free-end the structures have no coherence with the Aeolian tone. Like those that generate P1, this structure is inclined downstream, although the angle of inclination is the opposite direction to P1. However, unlike P1, the in-phase filaments

appear to be regularly organised and a complicated lattice of vortex structures are not observed.

5.4.6 The convection velocity

The last quantity to be examined using the measurements of fluctuating velocity is the streamwise convection velocity, u_c, of the shed vortex filaments as they propagate downstream. According to Moreau et al. (2012), the streamwise convection velocity can be estimated using

$$u_c = 2\pi \frac{f}{\partial\phi/dx}, \tag{5.3}$$

where f is the shedding frequency in Hz, and $\partial\phi/\partial x$ is the rate of change of phase (in radians) with streamwise distance. To measure the rate of change of phase, the phase plots presented in Figures 5.25 through 5.27 were 'unwrapped' by changing the absolute value of discontinuities greater than π to their 2π complement. The gradient of the resulting curve was estimated using a least squares approach.

The least squares method was found to be the most well conditioned method for estimating the convection velocity in such a highly three-dimensional environment with the data set available. However, this method inherently calculates the *spatially averaged* convection velocity over the range of data considered in the least squares fit, which extended from the cylinder base to approximately 3 cylinder widths downstream from the cylinder base.

For some points along the span of the FWMCs, a straight line could not be used because the streamwise phase variation was not linear, even when the phase was unwrapped. This generally occurred at positions of high vortex filament curvature or areas of low coherence with the acoustic pressure measured by the microphone. To account for this, those positions where the correlation coefficient (Bendat and Piersol 2010) between the estimated linear trend and the measured data was less than $r^2 = 0.97$ were rejected.

The random uncertainty in the measured convection velocities was calculated by using a Monte Carlo analysis. The measured values of phase were perturbed with a variance given by Equation 3.42 and the curve fitting procedure carried out on the perturbed data. The largest uncertainty bounds are associated with areas of low coherence of the velocity with the acoustic pressure, for example, at $L/W = 7.1$ (5.28c), although generally, the error is small at $\Delta u_c/V_\infty < 0.05$.

Figure 5.28 shows the variation of the measured streamwise convection velocity normalised by the free-stream value, u_c/V_∞, across the normalised span, z/L, of select aspect ratio FWMCs. The right hand side of each sub-figure shows the frequency (expressed as Strouhal number, St) of the dominant tone measured at that particular point to illustrate the single and dual and triple shedding behaviour.

At $L/W = 1.4$ in Figure 5.28a, the convection velocity reaches maximum of $u_c/V_\infty \approx 0.7$ toward the top of the cylinder. This is in general agreement with the observations made previously whereby the top of the vortex filament was shown to incline downstream. These results suggest that secondary free-end flow convects the top of the vortex structure forming off the $L/W = 1.4$ FWMC toward the ground plane. For $L/W = 4.3$ and $L/W \leq 7.1$ in Figure 5.28 and 5.28c the convection velocity data are sparse. This is due

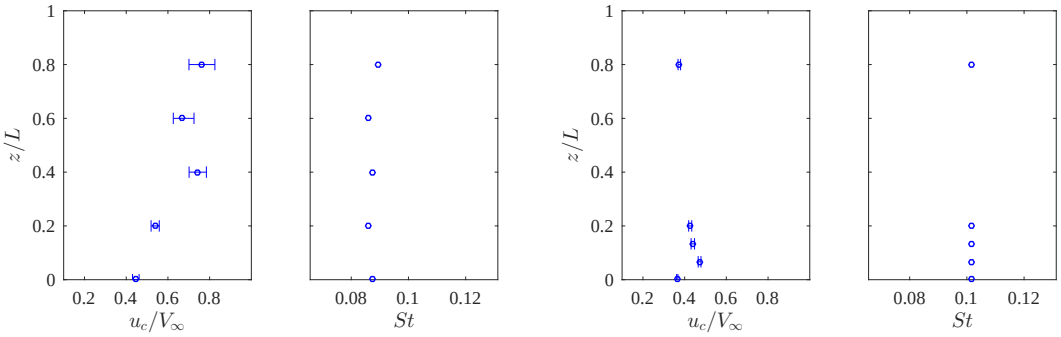

(a) $L/W = 1.4$, R0

(b) $L/W = 4.3$, RI

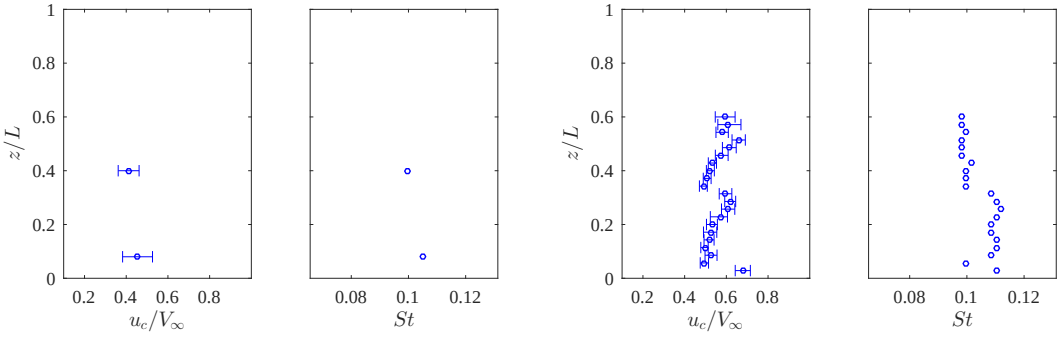

(c) $L/W = 7.1$, RI

(d) $L/W = 10.0$, RII

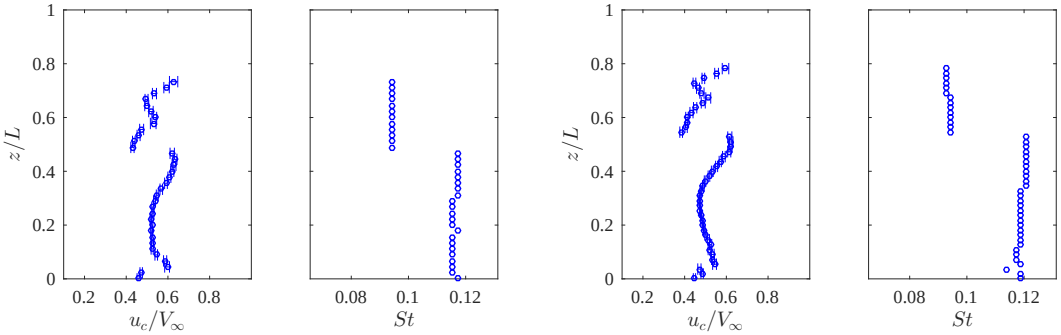

(e) $L/W = 12.9$, RII

(f) $L/W = 15.7$, RII

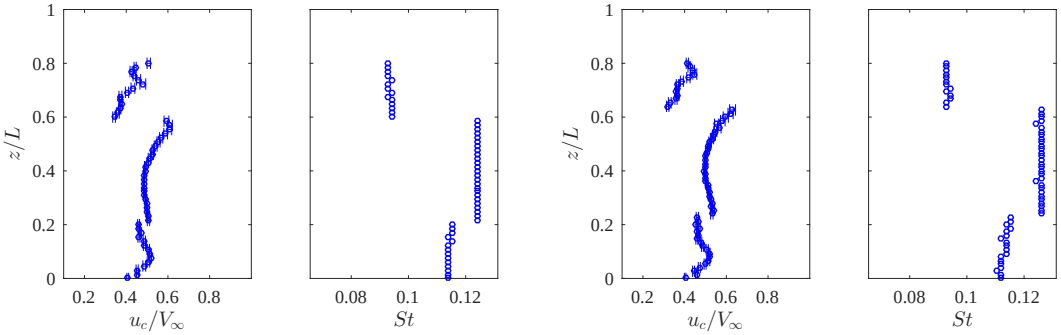

(g) $L/W = 18.6$, RIII

(h) $L/W = 21.4$, RIII

Figure 5.28: The convection velocity, u_c/V_∞, of the most energetic vortices along the span, z/L, of select aspect ratio FWMCs in the LTB. The right hand side of each sub-figure shows the frequency, $St = fW/V_\infty$, of the most dominant vortices at a particular spanwise station.

to a combination of high vortex curvature and low signal coherence. Nevertheless, the nominal convection velocity appears to be slower than that of $L/W = 1.4$ at $u_c \approx 0.4$

and uniform across the span. This is agreement with the observations made by Bourgeois et al. (2010), where a constant convection velocity was measured along the span of an $L/W = 4$ FWMC.

At aspect ratios with $L/W \geq 10$ in Figures 5.28e through 5.28f, multi-cell shedding occurs and spanwise variations in the measured convection velocity become more apparent. At $L/W = 10$ the convection velocity is centred at $u_c = 0.5$ but appears to be split into two regions. Although $L/W = 10$ has been classified as an RI cylinder based on the fact that only one tonal peak was resolved in its flow-induced noise spectrum, it clearly shows evidence of a developing junction cell at a slightly higher frequency than that at the free-end. This is the reason for the two distinct regions of convection velocity. The boundary between the developing junction cell and the free-end cell occurs at $z/L = 0.3$. At this point the convection velocity experiences a marked reduction in magnitude.

The aforementioned upper and lower spanwise regions for the $L/W = 10$ FWMC both appear to be skewed from left to right, indicating that vortices have a higher convection velocity toward the free-end, implying that the vortex filaments are inclined downstream at the free-end. This is in contradiction to was what observed in the phase maps in the Section 5.4.5. In fact, this is in contradiction to the majority of vortex visualisations on FWMCs in the literature, which all describe an upstream tilting of vortex filaments toward the free-end for FWMC in RI. The skewed appearance of the convection velocity is explained through this upstream tilting. When vortices are tilted upstream by an angle α, their apparent streamwise wavelength as measured with a hot-wire becomes larger by a factor of $\sec(\alpha)$ as described by Williamson (1989). For a given shedding frequency (which is constant within each vortex shedding cell) this will inflate the convection velocity from the true value.

Skewed convection velocity profiles continue to higher aspect ratios where dual and triple cellular shedding exist (see Figures 5.28e through 5.28f). The mid-span, free-end and junction regions all show higher convection velocities toward the free-end and junction respectively because they incline upstream at these positions, for example, in Figure 5.28e for $L/W = 12.9$. For these aspect ratios, the convection velocity also reduces substantially very close to the junction plate. This is probably caused by the low velocity deep within the boundary layer significantly retarding the passage of vortices near the junction. Regardless of the shape of the convection velocity profile, the boundary of each cell in Figures 5.28e through 5.28f is characterised by a significant reduction in convection velocity. This suggests that the effect of the downwash from the free-end and from the junction act to retard the rate at which vortices are formed.

Based on these results, the mechanism through which a cellular vortex wake forms for FWMCs in RII and RIII appears to be a spanwise gradient in convection velocity caused by progressively increasing downwash and upwash. For FWMCs in RI, the FWMC is short enough to allow a mutual interaction between downwash near the free-end and spanwise flow near the junction (known as 'spanwise coupling', discussed in Section 5.6). However, for FWMCs in RII, the FWMC is long enough to allow the formation of two-dimensional vortices at the lower portion of the FWMC that are free from the influence of the free-end. Downwash from the free-end retards the formation of vortices near the free-end but not those near the junction. Hence, there is a disparity in convection velocity near the junction and free-end, causing two cells to form. A similar mechanism

occurs for FWMCs in RIII. This mechanism is elaborated upon in Section 5.6.3.

5.5 Surface pressure measurements and oil-film visualisation

To further understand the dynamic behaviour of the vortex structures that were observed in the AWT experiments, surface pressure measurements and oil-film visualisations were conducted in the 18WT. The main objective of these experiments was to understand the vortex dynamics during the transition from RI to RII, since this transition showed signs of a significant wake reformation resulting from heightened interaction of the spanwise downwash and upwash with the nominally two-dimensional vortex street at the FWMC mid-span.

The spanwise variation of the surface pressure coefficient on the cylinder back face (base) and cylinder side face was measured in these experiments. The specific details of this experiment including the equipment used and experimental facility are provided in Section 3.3.2. The aspect ratios of the FWMCs tested were $L/W = 0.75$, 1.5, 4, 6.2, 6.9, 7.7, 8.4, 9.2, 9.9 and 12.5. The ratio of boundary layer thickness to cylinder width was $\delta/W = 0.9$ and the Reynolds number of the experiment was $Re_W = 1.1 \times 10^4$. The ratio of boundary layer thickness to cylinder width was lower than that of the LTB in the AWT. However, according to El Hassan et al. (2015), FWMCs in RI will exhibit similar large scale dynamic behaviour (dipole half-loop shedding) for boundary layer thicknesses $\delta/W \leq 1.3$. Since this condition is met by both the 18WT and the AWT boundary layers, the flow-visualisation and pressure measurements conducted in the 18WT can be used to understand the large scale quasi-periodic structures that occur for FWMCs in the AWT experiments. Unless stated, the pressure data herein are presented as a pressure coefficient, $C_p(t)$, defined as

$$C_p(t) = \frac{p(t) - \overline{p_\infty}}{\overline{p_d}}, \tag{5.4}$$

where $p(t)$ is the pressure time record, $\overline{p_\infty}$ is the time averaged free-stream static pressure in the tunnel and $\overline{p_d}$ is the time averaged dynamic pressure in the wind tunnel.

5.5.1 Mean pressure profiles and oil-film visualisations

Figure 5.29 shows the time averaged mean pressure coefficient profiles for the various aspect ratio cylinders on the FWMC back face ('base'). The experimental uncertainty in the mean pressures are ±0.1%, as given by the Scanivalve documentation (see Chapter 3), yielding an uncertainty in the base pressure coefficient of ±0.2%. The statistical uncertainty in the mean was calculated using Equation 3.23. The total uncertainty (the quadratic sum of the statistical and experimental uncertainty) for the pressure coefficient was $|\Delta\overline{C_{pb}}| < 0.05$ for all measurements. The results are plotted as a function of spanwise location normalised by the span of each cylinder (z/L). Figure 5.30 shows the corresponding oil-film visualisations around the cylinder junction captured in the 18WT using the same cylinders as those for the pressure measurements. The method of oil-film visualisation is also detailed in Section 3.3.3.

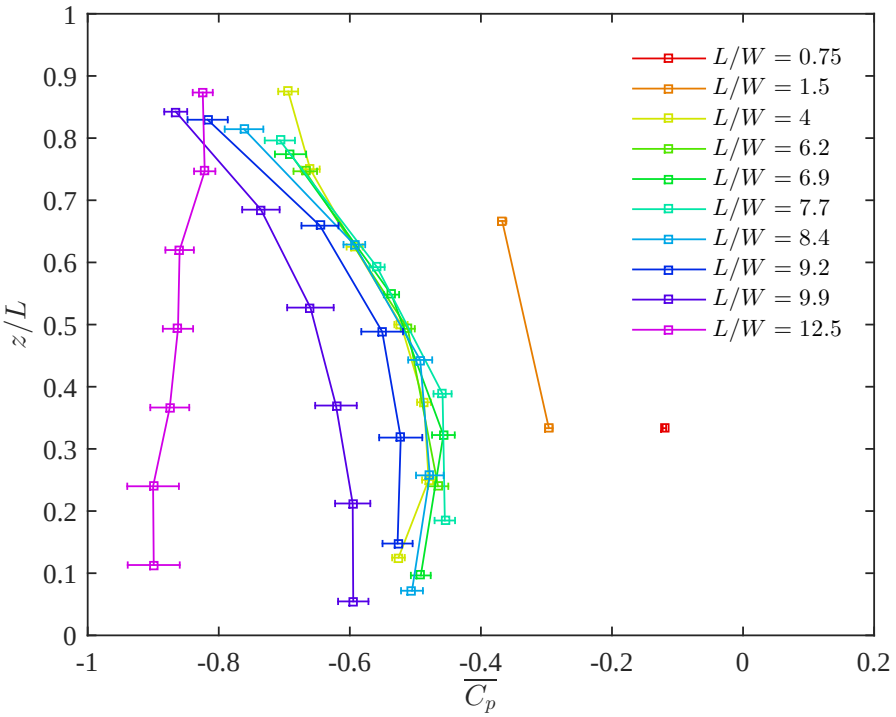

Figure 5.29: The spanwise mean base pressure coefficient, $\overline{C_{pb}}$, profiles for FWMCs with aspect ratios $0.75 < L/W < 12.5$.

Figure 5.29 demonstrates that cylinders in R0 ($L/W = 0.75$ and $L/W = 1.5$) have high base pressure coefficients and therefore relatively low wake suction compared with higher aspect ratio cylinders. Although not measured in these experiments, the base pressure profile for these low aspect ratio FWMCs in R0 reduces towards the free-end, as presented by Lee (1997).

The oil-film visualisations for these two aspect ratio cylinders, shown in Figures 5.30a and 5.30b, show the imprint of two counter rotating vortex cores, marked 'F1' and 'F2', close to the cylinder back face at $x/W < 1$. At the position marked 'R', there is evidence of a jet like feature expanding further downstream. Lastly, the imprint of a horseshoe vortex, marked 'HSV', can be seen upstream of the cylinder. According to Martinuzzi and Tropea (1993), the point R is the reattachment point of the flow that is drawn into the wake via downwash over the free-end. Martinuzzi and Tropea (1993) also discuss that F1 and F2 are imprints of a symmetrically shed arch structure. The possibility of this structure will be elaborated upon in Section 5.6.

Higher pressure recovery (low base suction) combined with a short recirculation zone is consistent with the flow separating on the leading edge of the cylinder side and *reattaching* onto the side face (Sakamoto and Arie 1983). This has also been observed by Martinuzzi and Tropea (1993) on similar aspect ratio cylinders immersed in channel flow. Additionally, the observation of flow reattachment at the point R is consistent with what was observed in the hot-wire data where it was shown that the descending shear layer penetrates deep into the wake (see Figure 5.13a). The high level of base pressure is caused by reverse flow in the wake impinging on the cylinder base. The reverse flow is generated by the reattachment of high speed fluid from the free-end creating an unstable node at position R, that generates mass flux upstream towards the cylinder.

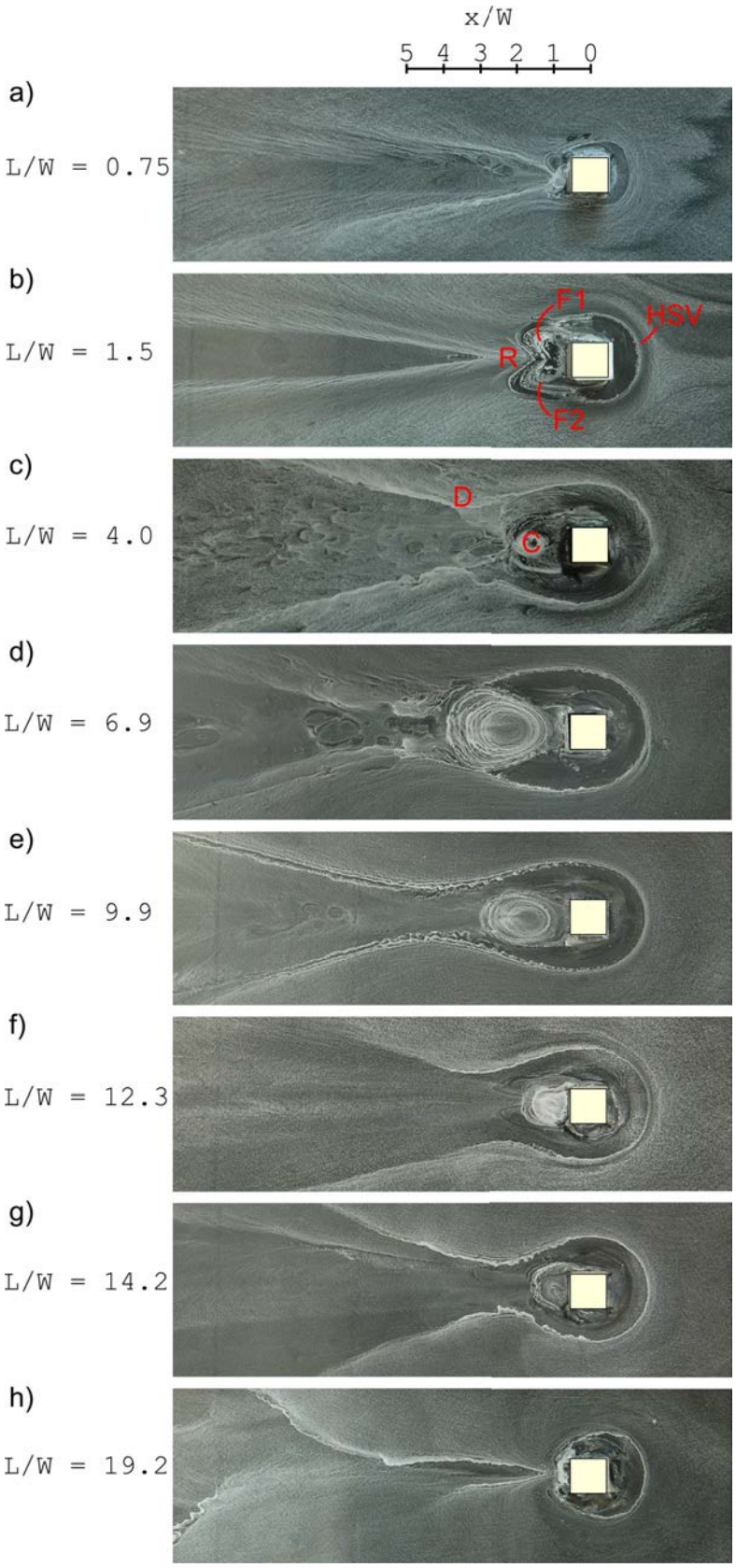

Figure 5.30: Oil-film images of the mounting plate region of select aspect ratio FWMCs in a boundary layer of $\delta/W = 0.9$. In each image, the flow is moving from right to left. The images show the imprint of various flow features in the wake including the horseshoe vortex, 'HSV', the legs of an arch vortex structure, 'F1' and 'F2', the point of flow reattachment, 'R', the wake length where alternately shed vortices coalesce, 'C', and the point of minimum wake width, 'D'.

Figure 5.29 shows that the mid-span base pressure reduces as the aspect ratio of the FWMC increases into RI (from $L/W = 1.5$ to $L/W = 4$). The reduction of base pressure in general indicates a reduction of mass flux toward the cylinder base, consistent with a reduction of the wake penetration from the free-end. The oil-film visualisations in Figures 5.30c to 5.30h show no evidence of a strong jet like wake. In these cases, the descending shear layer does not reattach on the base plate. Instead the downwash clashes with mild upwash from the junction, creating a saddle point slightly above the junction plate, as demonstrated by the LDA measurements of Wang et al. (2006) in the plane of symmetry of an $L/W = 6$ FWMC. Evidently, this allows the formation of a von Kármán-like vortex street toward the junction of the cylinder. The two vortex core imprints, F1 and F2 coalesce into a single vortex core, marked 'C'. Taniguchi et al. (1981) and El Hassan et al. (2015) both demonstrate that this single core is the result of the passage of an alternating von Kármán vortex street. Downstream of the single vortex core, the flow appears to initially contract, at point 'D', and then expand thereafter. The initial contraction is caused by fluid entrainment by the recirculation of alternating vortices. Further downstream, the horseshoe vortex entrains fluid away from the plane of symmetry, causing the subsequent expansion.

In Figure 5.29, FWMCs with $4 \leq L/W \leq 9.9$ have a local maximum in their spanwise base pressure profiles at the mid-span ($z/L = 0.4$ to 0.5). Toward the junction and free-end, the base pressure is considerably reduced. Similar results have been reported by Taniguchi et al. (1981) for circular FWMCs at similar aspect ratios. The low pressure at the extremities is caused by the existence of the low pressure cross-stream connector strand as part of the half-loop shedding structure proposed by Bourgeois et al. (2011). As Rostamy et al. (2012) demonstrates, this connector strand generates cross-stream vorticity in the plane of symmetry of the wake (the x-z plane), leading to a region of low pressure at the extremities.

Figure 5.30d shows that the wake length increases at $L/W = 6.9$. An elongation of the formation length at $L/W = 7.1$ was also found earlier in the hot-wire wake measurements, demonstrated in Figure 5.20. Additionally, a maximum in the wake length at an aspect ratio between 6.5 and 7 has been reported by several other authors for both square FWMCs (Wang and Zhou 2009) and circular FWMCs (Rostamy et al. 2012; Okamoto and Sunabashiri 1992; Etzold and Fiedler 1976). The wake length appears to have an approximately inverse relationship with the mean base pressure at the junction of the cylinder. Figure 5.31 plots the measured wake length, L_w, from the oil-film images against the mean base suction (negative of mean base pressure) at the junction of the cylinder. The wake length was taken to be the downstream extent of the single vortex core (the feature denoted 'C'). For FWMCs with $L/W \geq 4$, there is a local minimum in mean base suction when the wake length experiences a maximum at $L/W = 6.9$. As the wake length retracts at higher aspect ratios, the mean base suction experiences a rapid increase.

The mechanism for this wake elongation is proposed to be the increasing and decreasing influence of downwash from the free-end as the FWMC aspect ratio is increased. The mean velocity results (see Figure 5.15) showed that downwash increased as the aspect ratio increased up until $L/W = 12.9$. Increasing downwash with aspect ratio was also found by Wang and Zhou (2009), who observed that the magnitude of downwash doubled when the aspect ratio of an FWMC increased from $L/W = 3$ to $L/W = 7$.

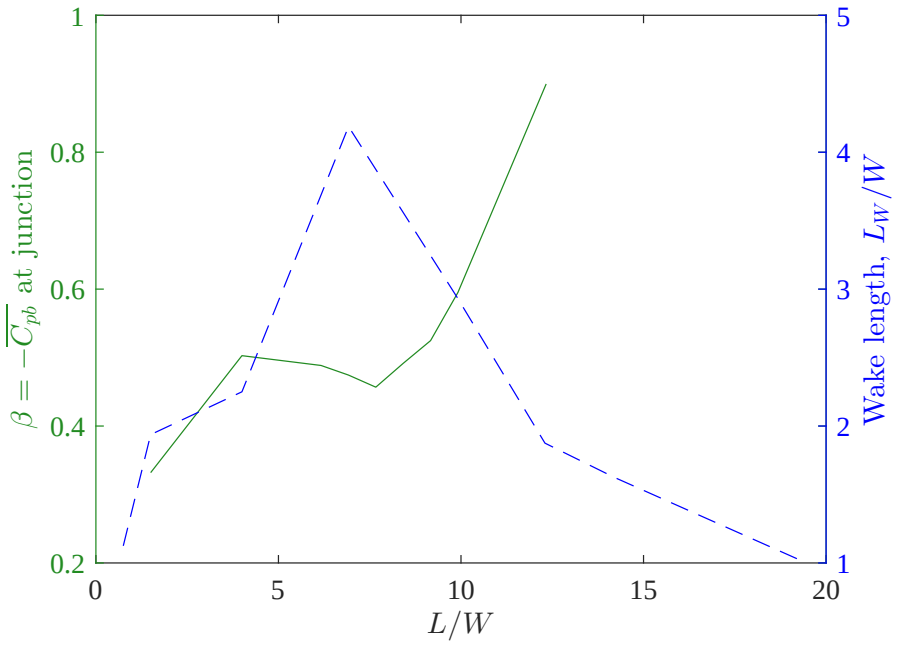

Figure 5.31: The variation of the junction base suction, $\beta = -\overline{C_{pb}}$, and wake length, L_w/W, with FWMC aspect ratio.

At low aspect ratios, i.e., $L/W = 4$, the downwash is weak, possibly because of the close proximity of the free-end with the edge of the plate boundary layer, and spanwise vortices are formed relatively uninhibited toward the junction. Uninhibited vortex formation causes a shorter recirculation zone and lower base pressure. As the aspect ratio increases to $L/W = 7$, downwash increases. This strong downwash acts to prolong the formation of vortices in the lower half of the cylinder, elongating the formation length, while also weakening those at the free-end. This interpretation appears to be consistent with the findings of Wang et al. (2014), who found a positive correlation between the length of the recirculation zone at the mid-span of an $L/W = 7$ FWMC and the level of downwash. As the recirculation length increases at $L/W = 7$, so to does the base pressure near the junction. Higher levels of downwash clash with upwash from the junction and force fluid upstream, increasing the cylinder base pressure. This is corroborated by the findings of Wang and Zhou (2009), who measured higher levels of flow reversal in the wakes of FWMCs with $L/W = 3$, 5 and 7 as the recirculation zone increased.

While downwash is highly dependent on aspect ratio in the range of $4 < L/W < 10$, upwash does not appear to be dependent on aspect ratio in this range. Wang and Zhou (2009) also measured similar levels of upwash on FWMCs wiht $L/W = 5$ and 7 and Rostamy et al. (2012) found that the upwash was significantly weaker than the downwash for circular FWMCs ranging from $L/W = 3$ to 9. The very mild sensitivity of the upwash to aspect ratio is consistent with the half-loop shedding model of Bourgeois et al. (2011). In this model, upwash is only induced through the streamwise rotation of initially spanwise vortices via the boundary layer velocity gradient. Hence, the magnitude of the upwash is only determined by the degree of rotation of the vortices which, by extension, is only determined by the height of the boundary layer, and not the aspect ratio of the cylinder.

After aspect ratio $L/W = 7$, downwash still increases, but with a diminishing effect at the mid-span of the cylinder. The mid-span of the cylinder is subject to less downwash (and upwash) and the ensuing vortex street is allowed to form uninhibited. Consequently, the wake formation length once again retreats (as shown in Figure 5.20 and Figure 5.30). Moving to even higher aspect ratios, the mean base pressure at the junction experiences a rapid decrease, while the formation length also continues to decrease. To illustrate this, Figure 5.29 shows that with a small aspect ratio increase from $L/W = 9.9$ to 12.5, the base pressure at the junction reduces by 50% from $\overline{C_{pb}} = -0.6$ to -0.9. This rapid decrease in base pressure is associated with the removal of the free-end influence from the junction which permits the formation of a localised region near the cylinder junction where a two-dimensional-like vortex street can form relatively uninhibited. The free-end, on the other hand, experiences a slight increase in base pressure so that the base pressure profile now increases towards the free-end. This is also supported by the mean hot-wire wake profile measurements in Figure 5.13. It was shown that the flow experiences the greatest acceleration over the free-end at $L/W = 10$ when compared with other aspect ratio cylinders. These results confirm that this is due to the lowest free-end base pressure occurring at $L/W = 10$. The base pressure profile of $L/W = 12.5$ is different to the preceding profiles of lower aspect ratios which is consistent with the idea that the wake structure of FWMCs in RII are fundamentally different to the half-loop shedding model of FWMCs in RI.

5.5.2 Fluctuating side face pressure and frequency decomposition

Figure 5.32 shows the fluctuating components of the pressure coefficient measured on the side face of the cylinder. The values in this figure were calculated by first band passing the data between 100 and 240 Hz (pressure was sampled at 480 Hz for 10 seconds) using a 6^{th} order Butterworth filter and taking the variance of the resulting time signal, σ_p^2. The results are expressed in dB re. 20μPa . The statistical error in the fluctuating pressure was calculated using Equation 3.25 and is less than ± 0.5 dB for all measurements. Since the gain of the pressure signal through the tubing system was estimated to be less than 2%, no gain corrections have been applied to the raw pressure signal before filtering.

Like the mean base pressure, the behaviour of the fluctuating pressure differs between shedding regimes. Figure 5.32 shows that at $L/W = 0.75$ (in R0) the fluctuating surface side pressure is relatively high at 102 dB. At $L/W = 4$ (in RI), the fluctuating surface side pressure increases substantially toward the junction as two-dimensional vortices are formed, and reduces toward the free-end as downwash restricts vortex formation.

A significant reduction in fluctuating levels occurs between $L/W = 6.2$ and 8.4 during the period of maximum wake elongation and maximum disruption to due downwash. Here the fluctuating pressure profile is mostly uniform, but almost 10 dB lower at the junction when compared with the $L/W = 4$ cylinder.

At higher aspect ratios, the fluctuating side pressure rapidly increases as a two-dimensional region at the cylinder mid-span forms. For example, the increase in fluctuating pressure between $L/W = 7.7$ and 9.9 is approximately 18 dB at the free-end. At $L/W =$ 12.5 (RII) there are two local maxima, one at the free-end and one at the junction. These local maxima correspond with the free-end and junction vortex shedding cell

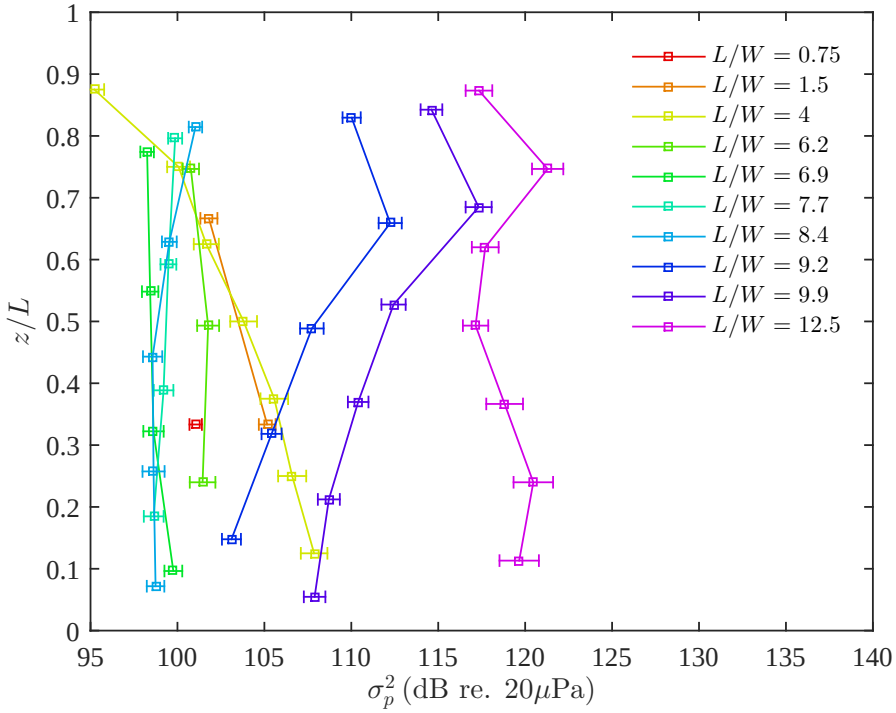

Figure 5.32: The fluctuating side pressure profiles for FWMCs with $0.75 < L/W < 12.5$, σ_p^2 (in dB re. 20μPa).

respectively. Once again, the small increase in aspect ratio from RI ($L/W = 9.2$) and RII ($L/W = 12.5$) is accompanied by a large increase in fluctuating wake properties and suggests a complete wake restructure at the regime boundary.

Figure 5.33 shows spectral maps of the surface pressure fluctuation on the side face of select aspect ratio FWMC. The values are expressed in dB/Hz re. 20μPa . These power spectral densities were calculated using Welch's method, as outlined in Chapter 3. The filtered time records were split into 41 overlapping blocks of 240 points each. From Equation 3.36, the 95% confidence interval for each narrowband level is approximately ± 1.6 dB/Hz. In these plots the ordinate-axis is the height above the junction normalised by the length of the cylinder, z/L.

The maps clearly demonstrate the transition from a single cell (in Figure 5.33a to 5.33e) in RI to a double cell (in Figure 5.33g) in RII. The spectral map for $L/W = 9.9$ (Figure 5.33f) is on the boundary between RI and RII, so shows a very weak junction cell. The aspect ratio regimes measured with these results are generally consistent with those measured by the hot-wire results in Figure 5.21.

The spectral map of the FWMC with $L/W = 1.5$ in Figure 5.33a shows that periodicity is still detected on the surface of the cylinder, which is consistent with what was presented with the fluctuating wake velocity measurements in Figure 5.21. The signal has a wide bandwidth however, with the spectral energy spread between a large range of frequencies centred at $St = 0.09$. A wide bandwidth indicates that the signal is highly modulated. This modulation is probably caused by the deep relative immersion in the turbulent boundary layer, which contains highly turbulent flow with a wide range of flow scales at different velocities.

A salient feature of Figure 5.33 is the change in wake behaviour when the cylinder transitions from a single to double cell from $L/W = 9.2$ to $L/W = 12.5$. This transition

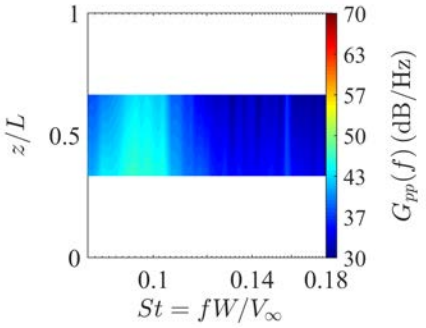

(a) $L/W = 1.5$, R0

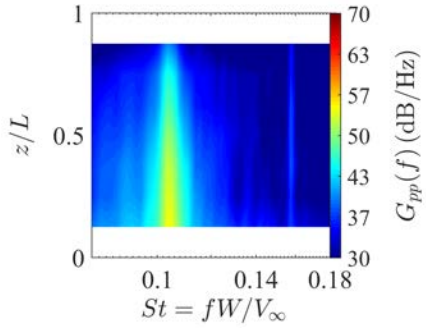

(b) $L/W = 4.0$, RI

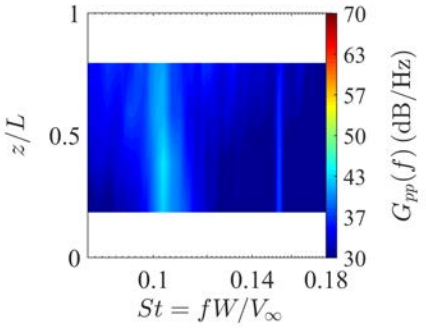

(c) $L/W = 7.7$, RI

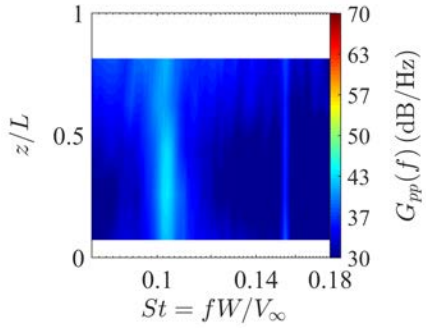

(d) $L/W = 8.4$, RI

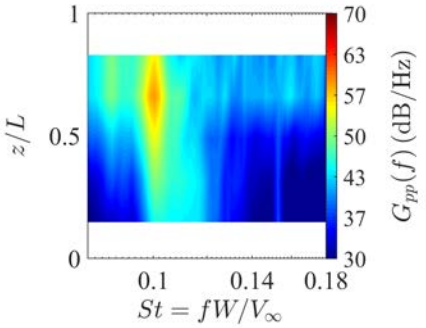

(e) $L/W = 9.2$, RI

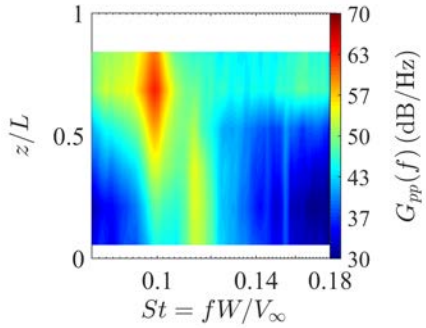

(f) $L/W = 9.9$, boundary between RI and RII

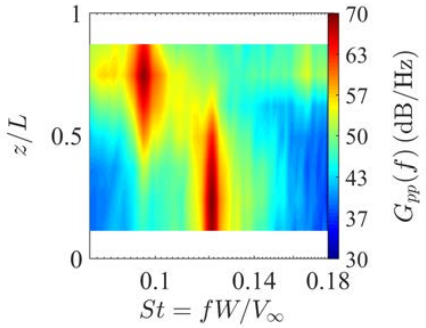

(g) $L/W = 12.5$, RII

Figure 5.33: Spectral maps of the cylinder side face pressure fluctuations, $G_{pp}(f)$ (in dB/Hz re.20μPa), for FWMCs ranging from $L/W = 1.5$ (a) through to $L/W = 12.5$ (g). The white portions of each map indicate that portion of the FWMCs where no pressure data were taken.

was not captured with the fluctuating wake velocity measurements because no data were taken for $7 < L/W < 10$. At $L/W = 4$ in Figure 5.33b, the main vortex shedding peak appears to be located at the junction of the cylinder and reduces in magnitude towards the free-end. Moving through RI ($4 < L/W < 10$), this trend begins to reverse. At

$L/W = 6.9$, the entire cylinder span sheds vortices but with significantly lower magnitude than that of $L/W = 4$. When the boundary between RI and RII is encountered at $L/W = 9.9$ in Figure 5.33f, the map is dominated by a signal at the free-end and a weak junction cell can just be observed. With a small increase in aspect ratio, the amplitude of the junction cell rapidly rises and by $L/W = 12.5$ (in Figure 5.33g), the amplitude of the junction cell exceeds that of the free-end cell. These results demonstrate that as the cylinder transitions from RI to RII the free-end cell forms *first* at approximately $L/W \approx 9$, while the formation of the junction cell is delayed until the conditions at the junction become more favourable for two-dimensional shedding. The delay of the junction cell was also observed in Figure 5.5. In this figure the Strouhal number of P1 starts reducing after $L/W = 8$, but P2 does not form appreciably until after $L/W = 10$.

5.5.3 Spanwise correlation

The axial correlation function is another useful indicator of the changes in shedding properties as the FWMC transitions from a single cell wake structure to a double cell wake structure. As explained by Blake (1986), the axial correlation is interpreted as a measure of the phase uniformity of the vortex filaments as they are shed from the cylinder. The axial correlation function, $R_{12}(\Delta z)$, is mathematically defined as (Bailey et al. 2002)

$$R_{12}(\Delta z) = \frac{1}{T_{acq}\sqrt{\overline{C_p(z_1)^2 C_p(z_1+\Delta z)^2}}} \int_0^{T_{acq}} C_p(z_1,t) C_p(z_1+\Delta z,t) dt, \tag{5.5}$$

where $C_p(z,t)$ is the side pressure coefficient at axial position z and time t, z_1 is the reference location, Δz is the spanwise distance between measuring positions and T_{acq} is the total sampling time. A comparison with Equation 3.27 in Chapter 3 reveals that Equation 5.5 can be rewritten as $\rho_{z_1,z_1+\Delta z}(0)$, where $\rho(0)$ is the cross-correlation coefficient at zero time delay. Thus, the random error of Equation 5.5 can be calculated using Equation 3.29. The 95% confidence interval of each measurement using Equation 3.29 is calculated to be $\pm 10\%$ for all correlation values.

Chapter 3 has demonstrated that the phase variation with frequency of the tubing system is approximately linear and the predicted phase difference due to propagation through the tubing at the frequencies of interest (100-200 Hz) is less than 2 degrees, or a time delay of approximately 27μs. Thus phase off-sets due to the pressure tubing system have not been corrected for. However, the Scanivalve pressure sensor is a multiplexed system, with the pressure scanned cyclically between pressure ports. In these experiments, the sampling frequency was 480 Hz, meaning there was a time offset of 130.31 μs between each successive pressure port, and a maximum delay of 2 milliseconds between the first and last port (the scannivalve has 16 ports). Therefore, prior to calculating the correlation using Equation 5.5, each channel was synchronised by first up-sampling each pressure signal by a factor of 10 (so that the apparent sampling frequency became 4800) and interpolating the up-sampled time series so that each started at a common time origin.

Figure 5.34 presents the correction coefficient of side surface pressure ($R_{12}(z_1, \Delta z)$) between simultaneously sampled spanwise pressure ports, for all FWMCs with aspect

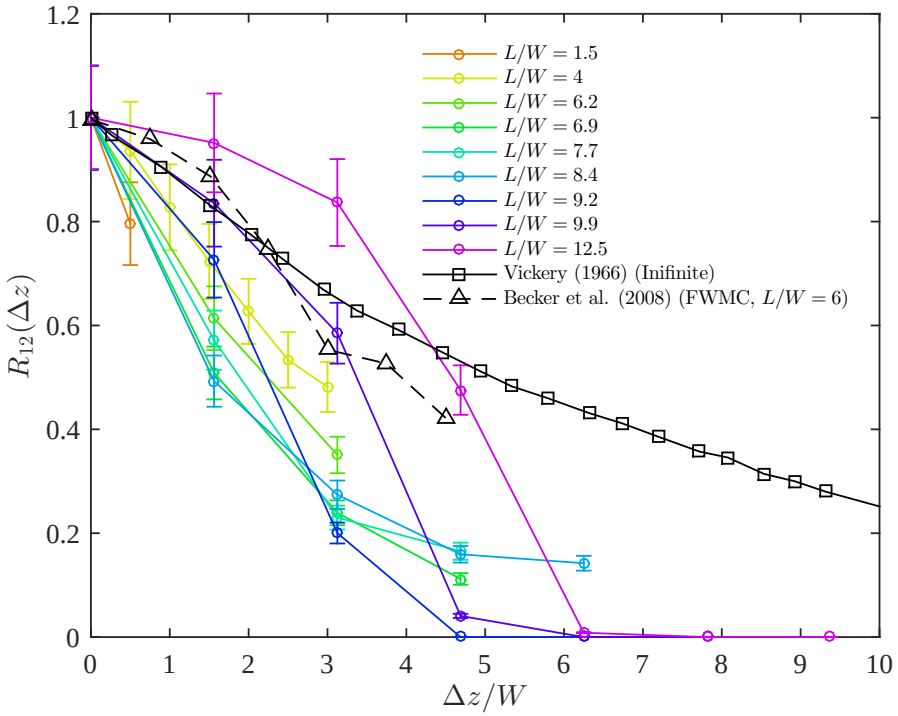

Figure 5.34: Values of the spanwise correlation coefficient of the surface pressure, $R_{12}(\Delta z)$, for various aspect ratio square FWMCs. The results are compared with similar flow measurements behind a square FWMC with $L/W = 6$ from Becker et al. (2008) and an infinitely long square cylinder from Vickery (1966).

ratios $L/W \geq 1.5$. In this figure, the reference position, z_1, was the pressure port closest the junction. This port was chosen in order to maximise the number of points used to estimate the correlation function (maximise Δz). For comparison, Figure 5.34 also shows correlation coefficients obtained for an infinite square cylinder from Vickery (1966) and for a square FWMC with $L/W = 6$ from Becker et al. (2008).

These results show that as the aspect ratio is increased, the rate of decay of spanwise correlation reduces, i.e., the vortices become more axially correlated when the FWMC transitions from RI to RII. For $L/W \leq 9.9$, all values of the correlation function lie below that of the infinite cylinder of Vickery (1966). This is consistent with the finding that FWMCs in RI experience a highly modulated, three-dimensional flow structure generated by downwash into the wake. For these aspect ratios, the high degree of interaction with the free-end downwash not only reduces the base suction and fluctuating side surface pressure, but also decorrelates the axial vortices.

For $L/W = 12.5$, the correlation experiences a rapid decrease beyond $\Delta z/W = 5$. This occurs because this point marks the end of the junction cell. However within the junction cell, the correlation values lie above that of the two-dimensional values. It has been suggested by Casalino and Jacob (2003) that the close proximity of the junction cell with the end plate limits spanwise velocity fluctuations thereby limiting the disruption caused by spanwise flow and enhancing the correlation of the vortices within the cell. A similar effect can also be observed in the results of Becker et al. (2008), where the correlation values lie slightly above that of Vickery (1966) for $\Delta z/W < 2$. It should be noted however that Becker et al. (2008) used an FWMC in a boundary layer that was significantly lower ($\delta/W \approx 0.4$) than the ones in the current experiment.

An integral parameter often used to describe the correlation function is the correlation length. The correlation length, s, is defined as the integral of the correlation function over all possible values of Δz,

$$s = \int_{-\infty}^{\infty} R_{12}(\Delta z).d\Delta z. \tag{5.6}$$

Often the correlation function is modelled using an analytical expression. Casalino and Jacob (2003) suggest that either a Laplacian (exponential) or Gaussian model is suitable as a function for modelling the correlation. That is, the correlation function is modelled as

$$R_{12}(\Delta z) \approx e^{\frac{-\pi|\Delta z|^2}{s^2}}, \tag{5.7}$$

for a Gaussian model or

$$R_{12}(\Delta z) \approx e^{\frac{-2|\Delta z|}{s}}, \tag{5.8}$$

for a Laplacian model. The advantage of these analytical descriptions is that the integral parameter, s, is part of the function itself and can be found by fitting either Equation 5.7 or 5.8 (which ever best represents the decay correlation decay) to the measured correlation data using a least squares approach. This means that the integral in Equation 5.6 can be evaluated with a sparse set of data points.

The correlation length, s, was calculated for FWMCs with aspect ratios $1.5 \leq L/W \leq 12.5$ using this curve fitting procedure. FWMCs with $L/W \leq 8.4$ were fitted with a Laplacian model, while FWMCs with $L/W \geq 9.2$ were fitted with a Gaussian. The results are presented in Figure 5.35. The uncertainty in the correlation length was calculated using a Monte-Carlo analysis. Each point in the spanwise correlation coefficient was allowed to vary independently within their uncertainty bounds ($\pm 10\%$) and the aforementioned curve fitting procedure was carried out on the perturbed data for 500 trials. The uncertainty bounds were then calculated as the interval where 95% of the distribution sits.

In Figure 5.35 the vortices initially become more correlated across the span of the cylinder reaching a local maximum at $L/W = 4$. This corresponds to the increase in Strouhal number (Figure 5.5) and reduction in formation length (Figure 5.20) at this aspect ratio. Between $L/W = 6.8$ and $L/W = 8.4$, the vortices experience a sharp reduction in spanwise correlation, before the correlation increases past $L/W = 10$. The sharp reduction in spanwise correlation is coincident with an increase in formation length and a reduction in fluctuating surface pressure (Figure 5.32) also measured at these aspect ratios. Evidently, the heightened disruption to the regular spanwise vortices due to the increased downwash not only elongates the wake length and reduces the level of fluctuating side pressure, but also decorrelates the spanwise vortices.

5.5.4 Time series analysis

The preceding results have demonstrated that the wake of an FWMC is a highly modulated, three-dimensional environment, especially within RI where the FWMC sheds with

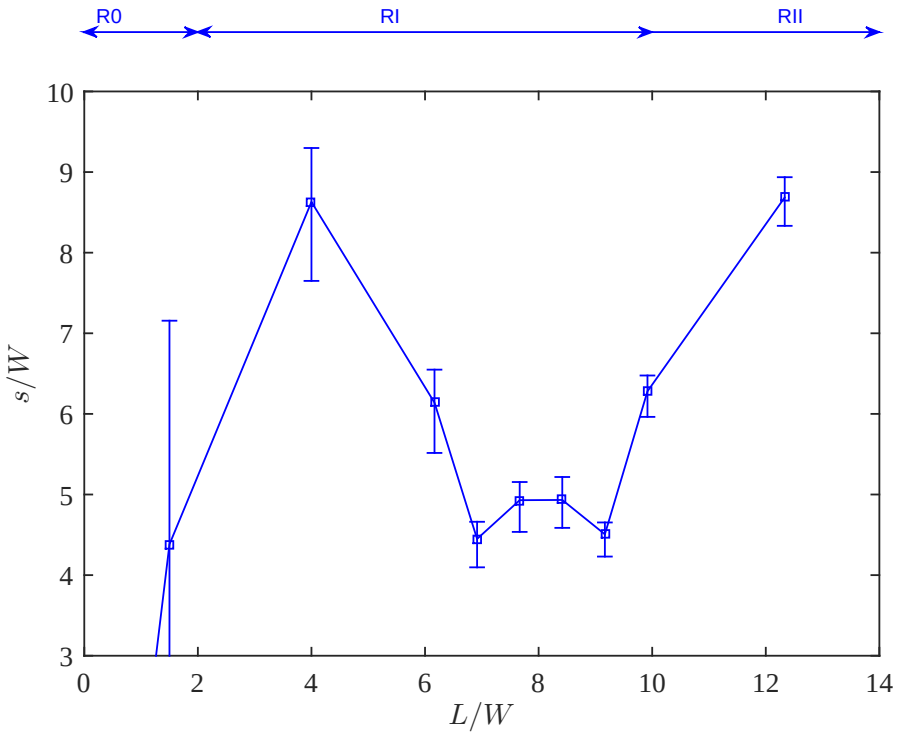

Figure 5.35: Estimated values of the correlation length, s/W, for FWMCs in the range of $1.5 \leq L/W \leq 12.5$.

a single cell structure. A time domain analysis gives insight into the transient behaviour of the shed vortices and, in particular, the different behaviours between a single and double cellular structure.

Intermittent shedding

Figure 5.36 presents the normalised pressure time histories, $C_p(z,t)_{\text{norm}} = C_p(z,t)/\sigma_{C_p}$, where σ_{C_p} is the standard deviation of the pressure signal, for various aspect ratio FWMCs. The pressure was that measured on the side face of the FWMCs. Figure 5.36 purposely displays an enlarged time history to visualise the variation of the pressure fluctuations over a long time scale. Prior to this calculation, the pressure time histories were up-sampled and aligned to begin at a common time origin. In all of the maps, the time axis has been reversed so that events on the right occur before events on the left. This gives the impression of the vortices travelling from left to right.

A striking feature of Figure 5.36 is the intermittency of vortex shedding. The time histories for cylinders in RI ($4 \leq L/W \leq 9.2$) are characterised by long periods of low amplitude fluctuations followed by bursts of high amplitude events. For example, the time history for $L/W = 7.7$ is dominated by low amplitude events with no high amplitude events occurring between $t = 1$ and 4 seconds, equivalent to 450 shedding cycles. In contrast, for $L/W = 12.5$ where the cylinder is in RII, the time history is comprised of regular vortex shedding interspersed with short periods of low amplitude events.

One way to quantify the level of intermittency of a time series is to calculate the probability distribution of the instantaneous amplitude of the time series. According to Bendat and Piersol (2010), the amplitude envelope function of narrowband data will have

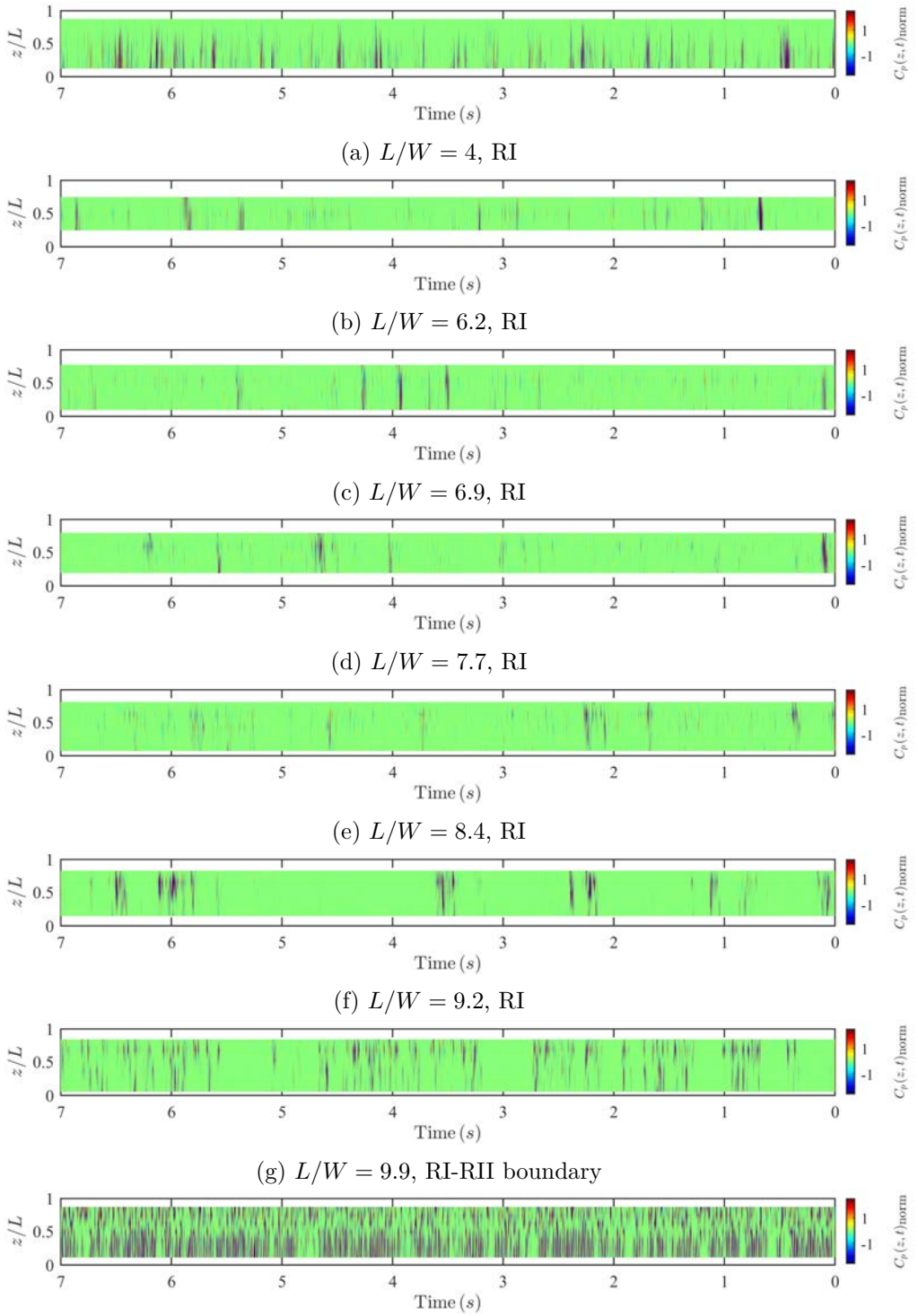

(a) $L/W = 4$, RI

(b) $L/W = 6.2$, RI

(c) $L/W = 6.9$, RI

(d) $L/W = 7.7$, RI

(e) $L/W = 8.4$, RI

(f) $L/W = 9.2$, RI

(g) $L/W = 9.9$, RI-RII boundary

(h) $L/W = 12.5$, RII

Figure 5.36: The spanwise pressure time histories (from $t = 0$ to $t = 7$) of FWMCs with aspect ratios ranging from $L/W = 4$ (a) to $L/W = 12.5$ (h).

a Rayleigh distribution. The more skewed the distribution is towards zero, the more the time series is dominated by low amplitude events (relative to the signal's variance). In this sense, the mean of the envelope distribution is a good integral parameter measuring the level of intermittency. The closer the mean is to 0, the longer the time series spends at low amplitude.

Figure 5.37a and 5.37b shows the PDFs and the mean values of the normalised

amplitude envelope, A/σ_{C_p} (where σ_{C_p} is the standard deviation of the pressure coefficient time series) respectively, for aspect ratios from $L/W = 0.75$ through 12.5. The instantaneous amplitude envelope was calculated using the Hilbert Transform (Bendat and Piersol 2010). The uncertainty in the value of the probability density function was calculated using Equation 3.31. In Figure 5.37, each histogram is vertically displaced by $\Delta\text{Prob} = 0.1$ for clarity. The pressure time histories used for the analysis were those closest to the junction region.

Starting at $L/W = 1.5$ and 4 in Figure 5.37b, the mean fluctuating pressure amplitude is approximately 0.7 standard deviations from the mean of the original signal, indicating relatively regular cycle-to-cycle shedding behaviour. The pressure time history for $L/W = 4$ displays regular bursts of high amplitude shedding. As the aspect ratio increases through $4 < L/W < 8$, the episodes of high amplitude events become increasingly sparse. By $L/W = 8.4$, the mean amplitude of the signal is only 0.3 standard deviations from the mean of the signal. By way of comparison, if the signal were a pure harmonic, the mean amplitude would be $\sqrt{2}$ standard deviations from the mean. Greater vortex shedding sparsity can be added to the list of phenomena that occur for $4 < L/W < 8$ that is suggestive of increased three-dimensional, disorganised activity. For $L/W > 10$, the mean amplitude rapidly increases to 1 standard deviation from the mean of the original signal, indicating a return to organised, regular vortex shedding.

Phase-jitter

The nature of the pressure time series also has a relationship with the spectral bandwidth of the shedding. A wider spectral bandwidth is indicative of a distribution of shedding frequencies included in the signal. Bailey et al. (2002) suggests that variations in spanwise phase ('phase-jitter') between adjacent spanwise locations are indicative of a disruption of the spacing between successively shed spanwise vortices which causes a wider frequency distribution of the vortex shedding signal.

To demonstrate the level of phase jitter, the phase lag, $\Delta\phi(t)$, was calculated between simultaneous pressure taps located near the junction of several aspect ratio cylinders. The instantaneous phase was calculated using the Hilbert transform. The selected pressure taps was the one located closest to the junction and a tap $1.5W$ away from this tap. Once the phase lag time series had been acquired, the phase lag PDFs were calculated.

Figure 5.38a shows the individual phase lag PDFs. Like the amplitude distributions, each phase lag distribution is vertically displaced by $\Delta\text{Prob} = 0.05$ for clarity. Figure 5.38b shows the variance of each distribution as a function of the aspect ratio. At $L/W = 4$, the variance of the phase is relatively low. This suggests that shedding occurs in a mostly organised manner, with relatively few cycle-to-cycle variations in the phase between two spanwise locations. At higher aspect ratios, the phase distribution considerably flattens, which is reflected by a rise in phase lag variance. This continues until $L/W = 9.9$ after which the variance in the phase lag reduces. By way of comparison, the phase lag distribution for $L/W = 12.5$ has a very sharp peak, confirming that the vortices are shed with a low cycle-to-cycle variability between the two locations and thus a heightened organisation.

Figure 5.39 displays the spectral bandwidth of the pressure fluctuations (defined as

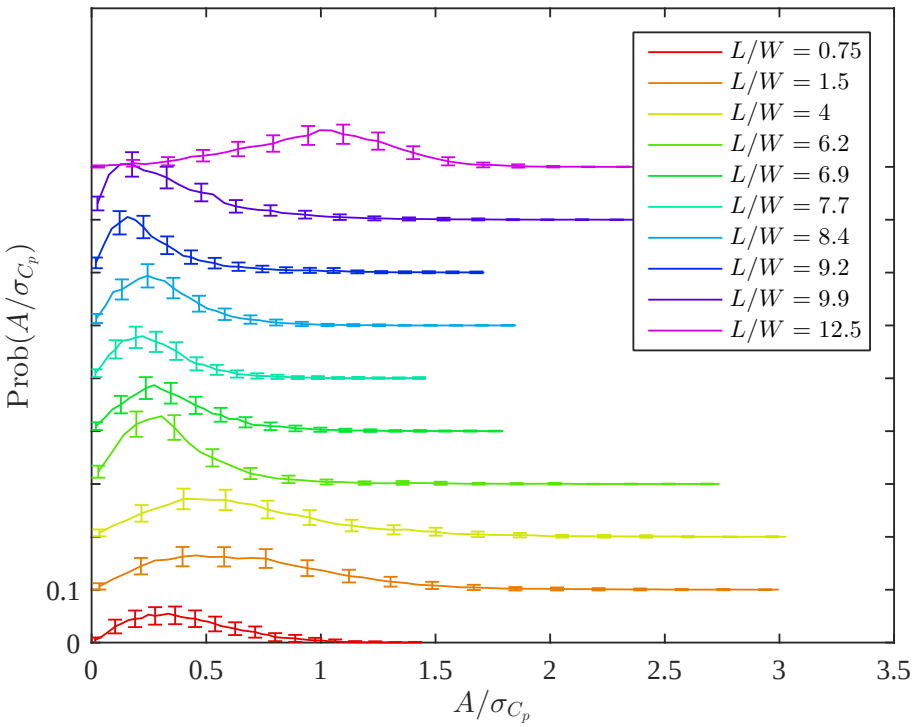

(a) Prob(A/σ_{C_p})

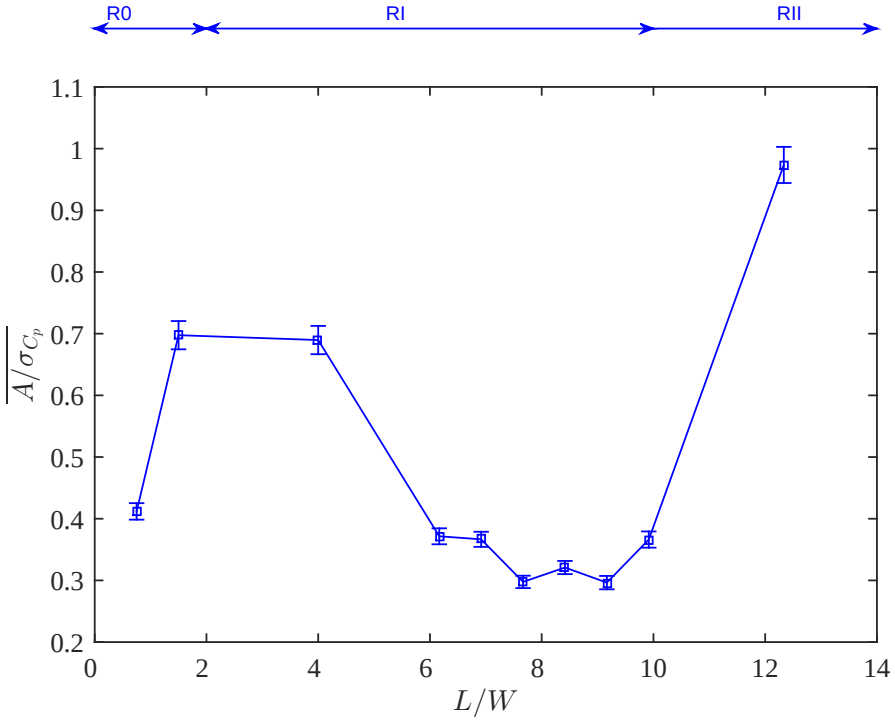

(b) $\overline{A/\sigma_{C_p}}$

Figure 5.37: (a) The measured PDFs of the amplitude envelope function, $A(t)/\sigma_{C_p}$, of the pressure signal of the tap closest the junction for various aspect ratio FWMCs. The bin-width is 0.05. (b) The mean amplitude, $\overline{A(t)/\sigma_{C_p}}$, of the envelope function.

$2\sigma_p/f_p$ as in Section 5.3), measured at the pressure tap closest to the junction against their corresponding phase lag variance measurements (var$(\Delta\phi)$) for each cylinder. There is a positive correlation between the amount of phase-jitter and the bandwidth of the signal, confirming the suggestion of Bailey et al. (2002). That is, A wider distribution of phase

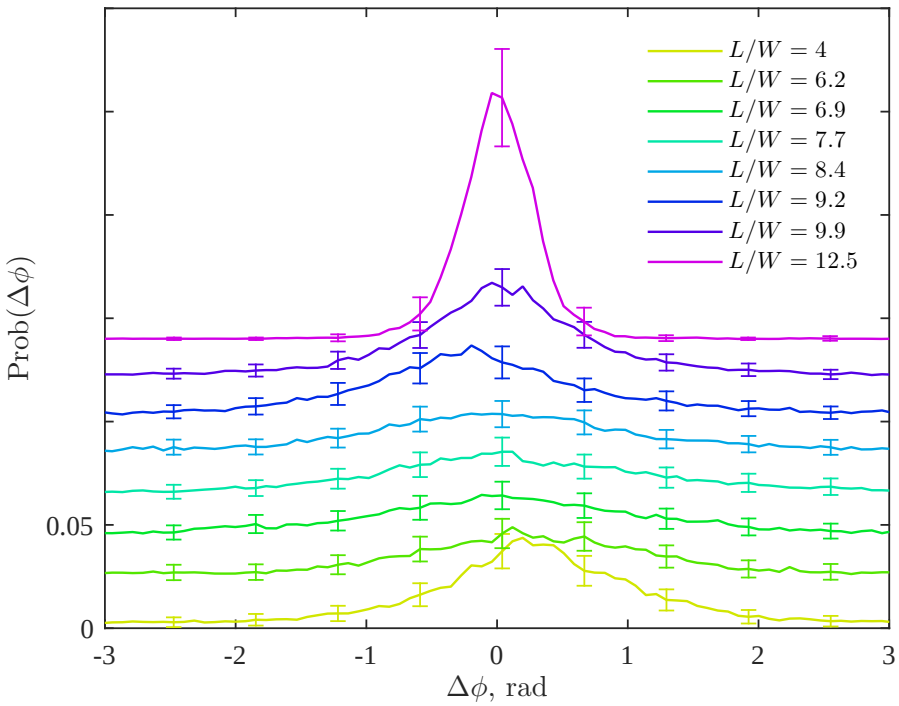

(a) PDF

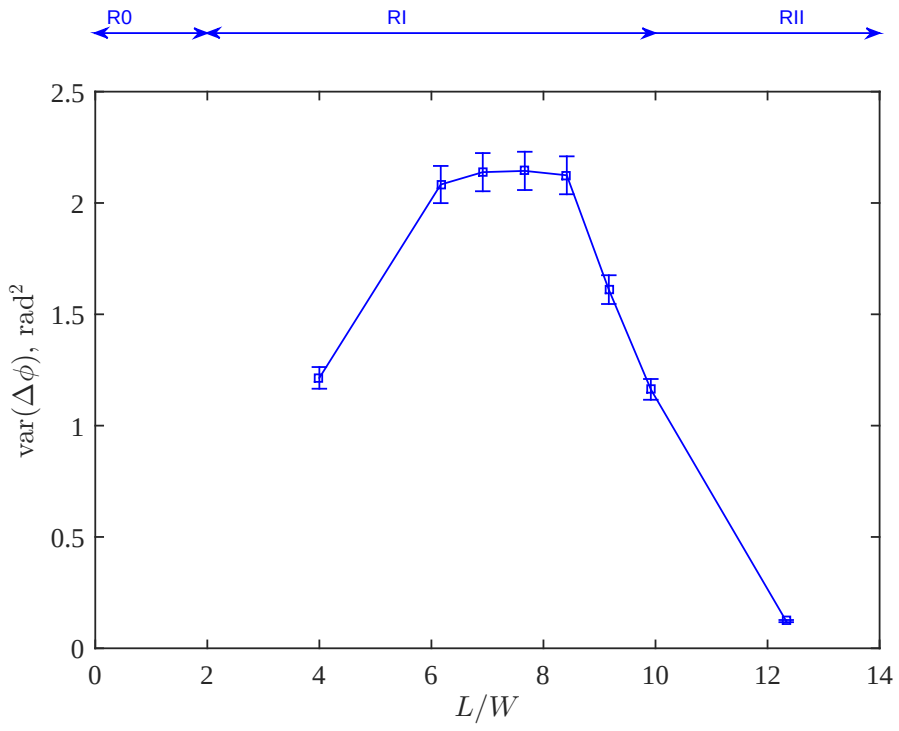

(b) Variance

Figure 5.38: (a) The estimated PDFs of the phase lag between two spanwise pressure taps near the junction for various aspect ratio FWMCs. The bin-width is 0.08 rad. (b) The variance of the distributions in (a). The two taps at the FWMC junction were locate $1.5W$ away from each other.

lag between spatially adjacent locations indicates that the cycle-to-cycle shedding period at these two locations also fluctuates stochastically. This means that the spacing between successively spanwise shed vortices also varies randomly which introduces more frequencies into the signal, widening the signal bandwidth. Higher phase-jitter also indicates that

the shedding process is becoming less coherent between the two measurement points. As such, axial correlation between these points also reduces as the phase-jitter increases, as observed in Figure 5.35.

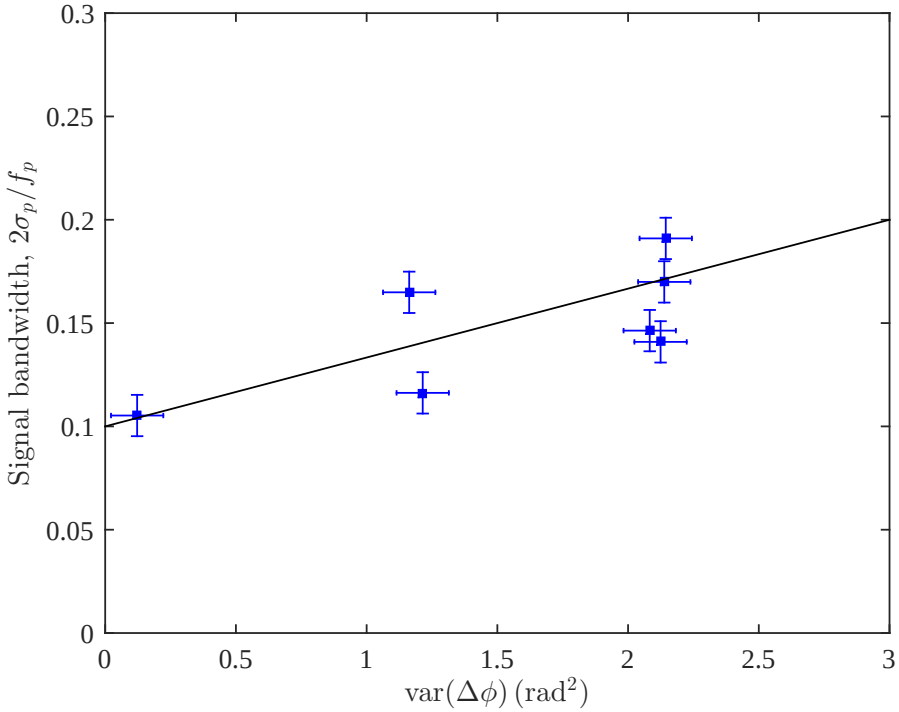

Figure 5.39: The phase lag variance, var($\Delta\phi$) (in rad^2), against surface pressure signal bandwidth, expressed as $2\sigma_p/f_p$ (defined in Equation 5.2).

Cellular shedding

The time series record also allows a deeper understanding of the cycle-to-cycle dynamics of the vortices, in particular, the difference between the single cell structure of RI and the multi-cell structure of RII.

In Figure 5.36h, the time series of $L/W = 12.5$ shows a line of low amplitude events at $z/L \approx 0.6$. This corresponds to the boundary between the junction and free-end cell. Such a line is also evident for the $L/W = 9.9$ case (Figure 5.36g), although, because of the increased sparsity of high amplitude events at lower aspect ratios, the line is not as prominent. As expected, no line occurs for lower aspect ratios that shed with a single cell structure.

Figure 5.40 shows a select time increment ($t = 6$ to 6.2 seconds) of the pressure records for aspect ratios $L/W = 4$, 7.7, 9.9 and 12.5, where the specific cycle-to-cycle behaviour of the spanwise vortices is readily observed. Figure 5.40a (for the $L/W = 4$ case) shows that the pressure time history is comprised of vertical lines of positive and negative amplitude. These correspond to upright columnar vortex filaments (also known as 'rollers' (Bailey et al. 2002)) being alternately shed from the cylinder. For the $L/W = 4$ case, the rollers appear to be in-phase along the FWMC span, consistent with the high level of spatial correlation observed previously. Additionally, the amplitude of the rollers is highest near the junction, consistent with high levels fluctuating velocity found near the junction presented in Section 5.4 in Figure 5.21b. In contrast, for $L/W = 7.7$, upright

rollers do form, but are less organised and much lower in amplitude. This disorganisation leads to a lower spanwise correlation length scale.

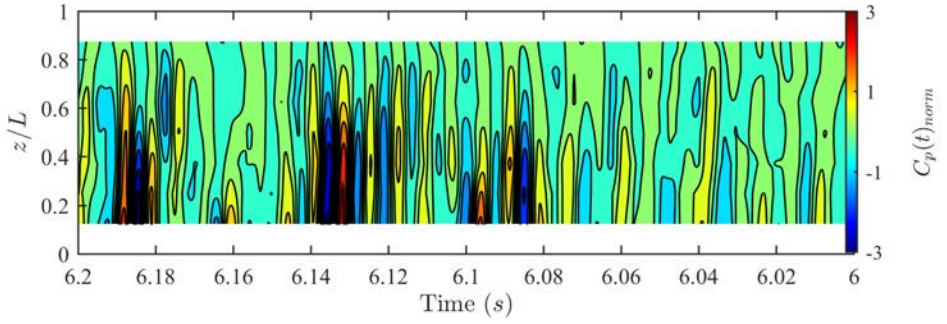

(a) $L/W = 4.0$, RI

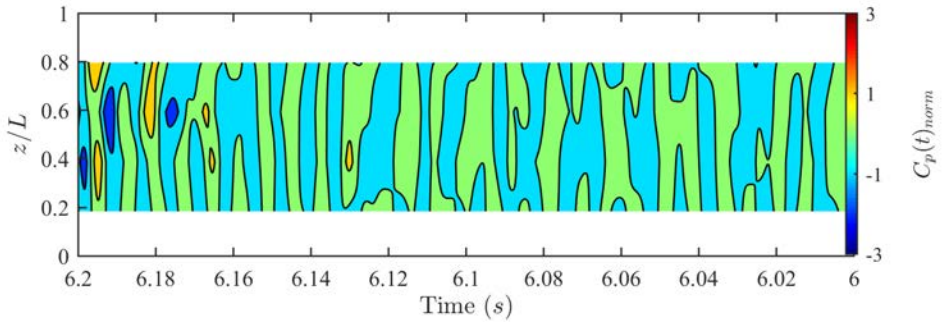

(b) $L/W = 7.7$, RI

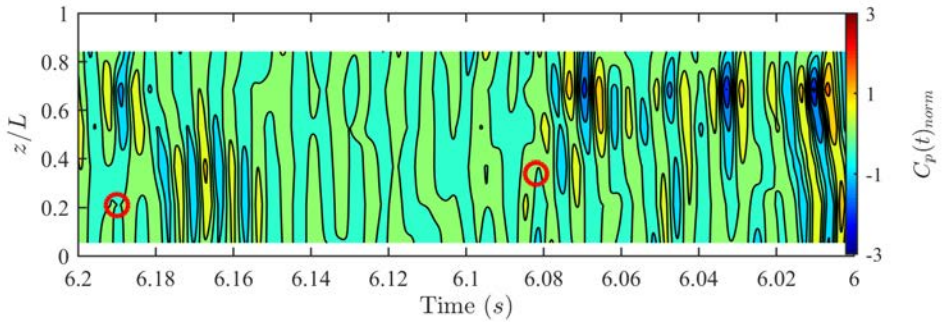

(c) $L/W = 9.9$, RI-RII boundary

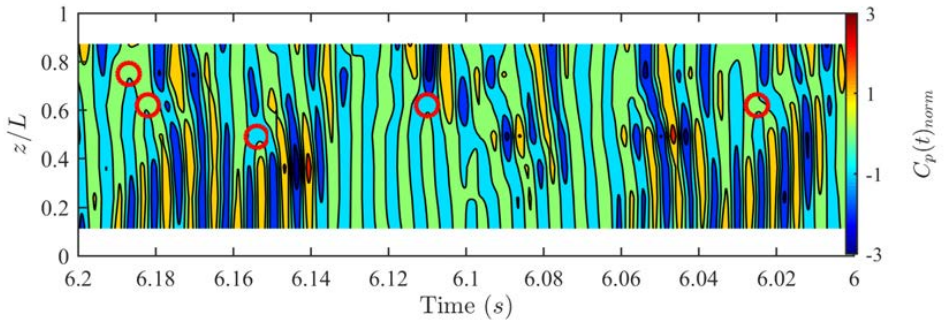

(d) $L/W = 12.5$, RII

Figure 5.40: The spanwise pressure time histories (from $t = 6$ to $t = 6.2$) of FWMCs with aspect ratios ranging from $L/W = 4$ (a) to $L/W = 12.5$ (d).

Figure 5.40d for $L/W = 12.5$ demonstrates that the boundary between the free-end cell and the junction cell is marked by distinct 'phase jumps'. These are essentially bifurcation events where a single roller suddenly splits into two rollers. An additional roller of opposite phase forms between the two original rollers. Several of these phase

jumps are highlighted in Figure 5.40d. Similar mechanisms appear to be occurring in the $L/W = 9.9$ (Figure 5.40c) case, although the magnitude of the junction cell is considerably weaker than that of the latter. The time series in Figure 5.40c suggests that for the $L/W = 9.9$ case, episodes of strong organised shedding at the junction are more sparse than that at the free-end, giving rise to a lower time averaged fluctuating level at the junction. This is consistent with the finding that the formation of the junction cell occurs at a higher aspect ratio than that at the free-end and that $L/W = 9.9$ is in a transitional state between a single (RI) and a double (RII) shedding structure. Regardless, phase jumps occur whenever strong shedding occurs at both the free-end and junction. It is observed that the phase jumps occur at slightly different spanwise locations at any given point in time (although the bulk of the phase jumps are concentrated in a band centred at $z/L \approx 0.6$).

Physically, a phase discontinuity occurs because the rate of shedding near the junction exceeds that of the free-end. As was observed in Section 5.4, the driver for this spanwise difference in shedding frequency is a spanwise gradient of convection velocity, caused by (1) strong downwash retarding vortex formation near the free-end and (2) a sufficiently long cylinder to allow two-dimensional vortices to form near the junction. In Figure 5.40d, vortices are initially shed in-phase along the entire span, for example, at $t = 6.12\,\mathrm{s}$ for $L/W = 12.5$. The phase of the vortices at the junction move ahead of those from the free-end and the vortex rollers from the free-end appear to incline backwards (form later in time). Evidence of this inclination can be observed between $t = 6.14$ to 6.15 at $z/L = 0.7$ for the $L/W = 12.5$ case and at $t = 6.01$ at $z/L = 0.3$ for the $L/W = 9.9$ case. Finally, a phase discontinuity occurs as the rollers from the free-end become completely out of phase with those at the junction, allowing the vortex filament to shed in phase along the span, thereby restarting the process. The time scale over which this process occurs is related to the beating period associated with the difference in shedding frequencies between the two cells. For the $L/W = 12.5$, this difference is approximately 32 Hz, corresponding to a phase jump time scale of $1/32 \approx 31 \times 10^{-3}\,\mathrm{s}$. To verify this, each phase jump in the time pressure history was identified using an algorithm based on the instantaneous phase difference between two points. Then, the time delay between each successive phase jump was calculated. The PDFs of these time delays are shown in Figure 5.41. The uncertainty in the values of the PDF was calculated using Equation 3.31. The large uncertainty in these measurements is due to a low number of phase-jumping events that occurred during the pressure time history (there were only 314 of these events). The histogram shows the most probable time delay is, as expected, approximately 0.03 s, but with an appreciable amount of scatter in the data. This suggests that while the process between phase jumps is the one described above, ultimately the process is turbulent and therefore subject to stochastic variability.

Similar style phase discontinuities (which are sometimes referred as 'dislocations') have been experimentally observed in several studies concerning the flow past circular cylinders near end-plates at low Reynolds numbers. Figure 5.42a shows a smoke flow visualisation by Eisenlohr and Eckelmann (1989) near the end-plate of a circular cylinder at $Re_D = 130$. Near the end-plate a cell of lower frequency vortex shedding was detected using a hot-wire. It was shown that the cell boundary is characterised by a vortex splitting event, shown in red. This event closely resembles what is observed in the present data in

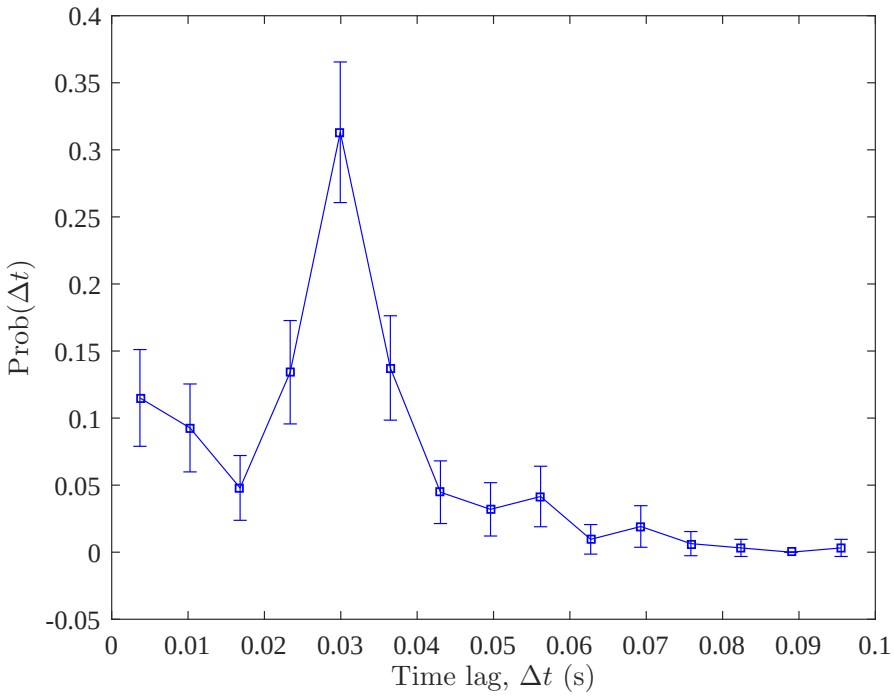

Figure 5.41: The PDF of the time lag (Δt) between successive phase jump events for $L/W = 12.5$. The bin-width is 0.007 s.

Figure 5.40c and 5.40d. Eisenlohr and Eckelmann (1989) explain that in order to conserve total circulation during the dislocation event, the circulation in the lower vortex filament is divided amongst its nearest neighbours.

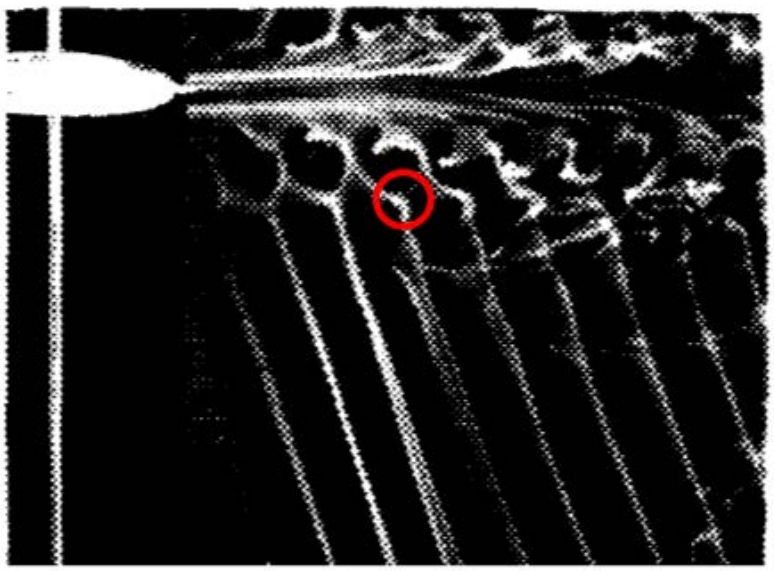

Figure 5.42: A smoke flow visualisation by Eisenlohr and Eckelmann (1989) near the end-plate of a circular cylinder at $Re_D = 130$ demonstrating the division of circulation at the boundary between two vortex cells.

In Section 5.4, the end cell was shown to shed at an oblique angle to the span of the

cylinder whereas the junction cell was shown to be parallel to the span of the cylinder. As previously discussed, backward inclination of the vortices appears to be inherently connected to the phase jumping events that define the cell boundary. Indeed, using the current pressure time history data, it can be shown that the free-end cell vortices do, on average, shed at an oblique angle, thus confirming the previous hot-wire visualisations. The average phase lag between two pressure ports can be related to the angle with which the vortices are shed, θ_{shed}, using (Bailey et al. 2002)

$$\theta_{shed} = \frac{\Delta\phi}{2\pi} \frac{u_c/V_\infty}{St_W} \frac{W}{\Delta z}, \tag{5.9}$$

where Δz is the spanwise distance between pressure ports and u_c is the convection velocity of the shed vortices. Equation 5.9 was used to estimate the physical shedding angles for the free-end and junction cell of the $L/W = 12.5$ cylinder. For the free-end cell, the two measuring taps were the 5^{th} and 6^{th} tap from the junction and for the junction cell, the two measuring taps were the 1^{st} and 2^{nd} from the junction. Thus for each case the spanwise separation of the measuring positions is $\Delta z = 1.5W$. From Figure 5.28, the vortex convection velocity was estimated at $0.5V_\infty$ at the junction and $0.4V_\infty$ at the free-end. The Strouhal number of the free-end cell was set at $St = 0.1$, while the Strouhal number of the junction cell was set at $St = 0.125$ in accordance with the measurements made in Figure 5.33.

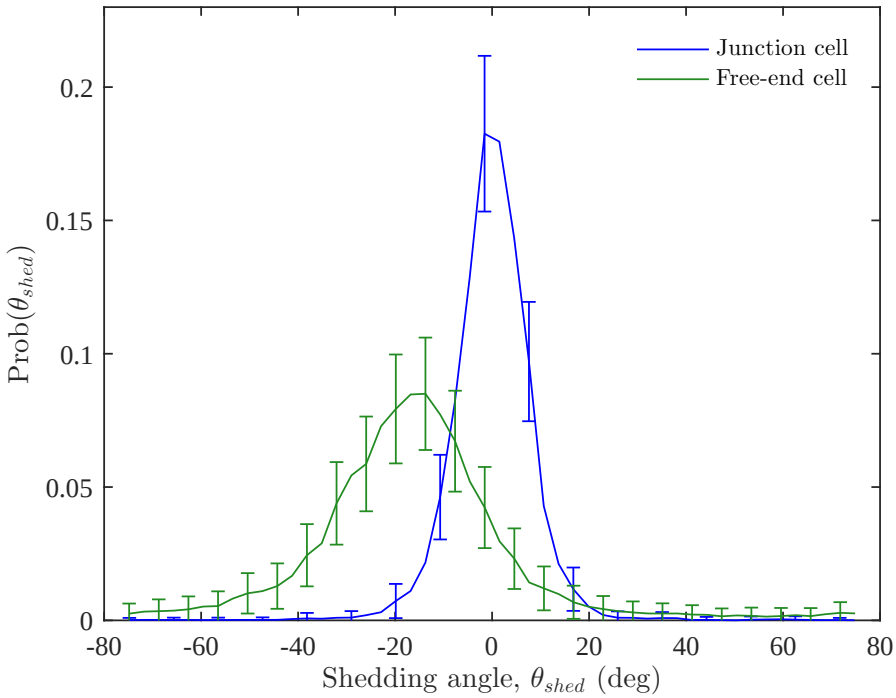

Figure 5.43: A comparison of the shedding angle, θ_{shed}, PDFs at the free-end and the junction of the $L/W = 12.5$ FWMC. The bin-width for each PDF is 3 deg.

Figure 5.43 shows the resulting PDF of the physical vortex shedding angles, in degrees, for the junction cell and free-end cell. It is seen that the junction cell sheds with a time mean shedding angle of -1.3 degrees, indicating nearly parallel shedding. Conversely, the free-end cell sheds at a large negative oblique angle of -17.5 degrees.

5.6 Discussion of results

In this section, the acoustic and fluid dynamic results are consolidated to provide an explanation for the main observed phenomena. Complementary analysis is provided to support the hypotheses that are made.

5.6.1 Arch structures for FWMCs in Regime 0 ($L/W < 2$)

An Aeolian tone was not detected for FWMCs in R0, either by a microphone perpendicular to the cylinder face or a microphone at other measurement angles. This is despite periodic velocity fluctuations being detected in the wake with a hot-wire at $St \approx 0.09$ in Figure 5.21, that were mildly coherent ($\gamma^2_{xy} \approx 0.6$) with the acoustic pressure perpendicular to the cylinder. It is hypothesised that a weak Aeolian tone does exist, but the acoustic signal-to-noise ratio is too low to be observed as a well-resolved tone detected by a single microphone. The hot-wire wake survey also found a single peak in the velocity PSD maps in Figure 5.21. The peak velocity fluctuations were observed to rise from the junction moving downstream, and the phase maps in Figure 5.25 confirmed that the wake structure most coherent when the acoustic pressure perpendicular to the cylinder was bent downstream at the free-end, implying a downstream tilting of the vortex filament.

Vortex filament tilting is in agreement with several experimental results in the literature on low-aspect ratio surface mounted obstacles (not necessarily cylinders) in relatively high boundary layers. Hajimirzaie et al. (2012) observed a pair of counter rotating vortices in the wake of a semi-ellipsoidal obstacle immersed in a relative boundary layer thickness of $\delta/L > 1$, where L is the height of the obstacle from the junction. The sense of rotation of the vortex pair induced upwash into the wake, indicating a downstream tilting of vortices at the free-end. Hajimirzaie et al. (2012) suggests the two opposite vortices are connected through the plane of symmetry so that a half-loop is formed as the structure is shed and convected downstream. Such a structure is known as an 'arch vortex structure'. Strong shear flow over the free-end of the obstacle convects over the top of the arch vortex towards the base plate resulting in a 'hairpin' vortex.

The existence of an arch vortex tilted downstream at the free-end can be predicted by the empirical rule developed by Mason and Morton (1987) for low-aspect-ratio bluff bodies. By experimentally investigating the wakes of a wide range of surface mounted bluff bodies in several boundary layers, Mason and Morton (1987) concluded that obstacles with a velocity maxima over the free-end produce upwash vortex pairs in the wake. Based on this criterion, downstream tilting of the vortex filaments is promoted by low-aspect-ratio cylinders immersed in boundary layers with thicknesses close to the span of the cylinder, where the incoming velocity at the free-end vastly exceeds that at the junction. This is exactly the condition that is found in the current experiments for FWMCs in R0.

Further evidence of an arch type periodic vortex structure for low-aspect-ratio FWMCs are provided by the oil-film visualisation and surface pressure measurements. The oil-film visualisations showed two counter rotating vortices in the wake, which are the imprints of the oppositely signed legs of the arch vortex. Surface pressure measurements for these low aspect ratio FWMCs also showed low base suction levels. Low base suction levels are indicative of possible flow reattachment of the separated shear layer on the *side* of the FWMC (Sakamoto and Arie 1983). Martinuzzi and Tropea (1993) suggest that such

conditions are favourable for the formation of arch type structures.

Based on the above discussion, it is likely that the periodic wakes of FWMCs in R0 are comprised of arch type half loops that are convected downstream at the free-end, giving the appearance of tilted vortex filaments. A vortex skeleton of such a shedding mechanism is given in Figure 5.44. The arch type loops are similar to hairpin vortices found the wakes of wall-mounted hemispheres (Savory and Toy 1986).

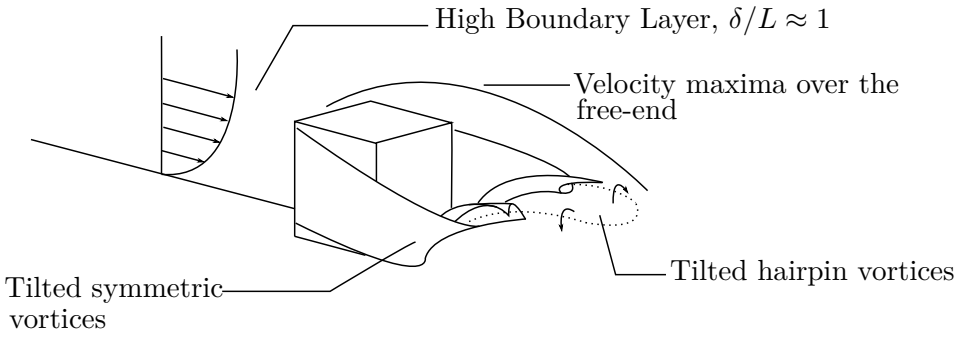

Figure 5.44: A vortex skeleton diagram illustrating the periodic arch vortex structures generated by square FWMCs in R0.

Figure 5.21 indicate that the arch structures are shed quasi-periodically, with a high bandwidth while Figure 5.37 demonstrates that these structures also form intermittently. The noise generated by these arch structures is only mildly coherent with the acoustic pressure measured directly above the FWMC (orthogonal to the span and the flow direction). One factor contributing to the mild level of coherence with the acoustic pressure fluctuations is the intermittent formation of the vortices. Another factor could also be the possible *symmetric* style shedding of the arch structure.

Symmetric shedding is where vortices from either side of the cylinder form and shed simultaneously, unlike a classic von Kármán vortex street, where vortices form alternately (anti-symmetrically). Arch type structures are often synonymous with symmetric shedding (Sakamoto and Arie 1983). Symmetric shedding is associated with small formation lengths, low wake circulation (and hence fluctuating lift) (Wang et al. 2014), wide-band shedding (Okamoto and Sunabashiri 1992) and low Reynolds stress production (Wang and Zhou 2009), all of which were observed in the wakes of FWMCs in R0 through fluctuating velocity measurements (see Figures 5.20, 5.18 and 5.21), surface pressure measurements (see Figure 5.32) and flow visualisation (see Figure 5.30).

The propensity of the arch structures to shed symmetrically also affects the directional characteristics of the flow-induced noise. A predominance of symmetric style shedding would imply that the fluctuating lift is low compared with the fluctuating drag at the shedding frequency. This would give rise to a predominant *drag* dipole, orientated in the streamwise direction (as opposed to a lift dipole orientated perpendicular to the flow). Hence, symmetric shedding in conjunction with intermittent formation of the arch vortices could explain the mild signal coherence with the acoustic pressure perpendicular to the cylinder face. The existence of a dominant drag dipole also has real world implications. For example, way-side noise from FWMC-like protrusions on high speed vehicles would likely reduce if symmetrical vortices were shed instead of anti-symmetric ones.

Poor signal-to-noise ratio in the AWT facility prevents measurement of the directional characteristics of the FWMCs in R0 (and hence the predominance of symmetric shedding).

Therefore, it seems appropriate that future work on FWMC noise include a verification of this predicted streamwise dipole characteristic for low aspect ratio FWMCs with $L/W < 2$.

5.6.2 FWMCs in Regime I ($2 < L/W < 10$)

Noise prediction for FWMCs in RI

FWMCs in RI generate only one tonal peak (P1) in the acoustic pressure spectrum as shown in Figure 5.4. A single tonal peak is consistent with the flow model proposed by Wang and Zhou (2009) and Bourgeois et al. (2011) where a series of fully interconnected vortex loops periodically shed off the cylinder and convect downstream. In this wake vortex model, the entire structure sheds with the same frequency along the span, resulting in only one Aeolian tone being detected. Phase maps of the wakes of FWMCs in RI in Figure 5.25 appear to show evidence of looping vortex structures.

The tonal peak frequency has a constant Strouhal number of $St = 0.102$ between $4 < L/W < 8$, which is the aspect ratio range where most other flow investigations have taken place (Bourgeois et al. 2011; Wang and Zhou 2009; Wang et al. 2006; Sattari et al. 2012; Becker et al. 2008) and the measurements presented in Figure 5.5 agree well with these studies. Below $L/W = 4$, an Aeolian tone is detected, but with progressively weaker sound pressure level and higher bandwidth (Figure 5.8) as the aspect ratio is reduced. Similarly, above $L/W = 5$, the bandwidth also increases. The present results indicate that an increase in acoustic signal bandwidth is attributed to higher axial phase modulation of the acoustic signal (see Figure 5.39). For $L/W < 4$, this modulation occurs due to heightened three-dimensional interaction between the alternating von Kármán vortices and downwash in the wake as the free-end and junction become closer in proximity. Alternatively for $L/W > 4$, a higher signal bandwidth occurs due to increased phase jitter of the alternatively shed vortices, as the cylinder transitions from a single cell structure to a double cell structure.

The most prominent feature in RI is the local maximum of the OASPL at $L/W = 4$ and local minimum of the OASPL at $L/W = 7$ (see Figure 5.1). The minimum in OASPL at $L/W = 7$ is hypothesised to be caused by a maximum disruption by the downwash and upwash on the cylinder wake. As a result of this disruption, the vortices experience an increase in wake formation length, (Figure 5.20), a reduction in wake base suction (Figure 5.31), a spanwise decorrelation (Figure 5.35) and greater intermittency (Figure 5.37) with a wider distribution of phase (Figure 5.38).

Curle's theory can be used to prove the connection between the measured wake properties and the magnitude of the measured flow-induced noise from the FWMC. Here, the most common form of Curle's theory for infinite cylinders (for example that presented by in Equation 5.1) cannot be used because the nature of FWMC flow violates the key assumptions that this formulation is based upon. These key assumptions include the provision that fluctuating lift is constant along the cylinder span, the microphone lies in the far-field and the cylinder length is much longer than the vortex correlation length. Since these assumptions are not true for the FWMC case, a new approach will be taken instead.

To begin, for an acoustically compact source ($\lambda >> W$), Curle's theory (Curle 1955)

predicts that the acoustic pressure, $p(\mathbf{x}, t)$, can be calculated as

$$p(\mathbf{x}, t) = \frac{1}{4\pi c}\frac{x_i}{r^2}\left[\frac{\partial F_i}{\partial t} + \frac{cF_i}{r}\right], \tag{5.10}$$

where x is the observation point, r is the distance from the source to the observation point, F is the total force on the surface of the body, c is the speed of sound, the subscript i denotes the i^{th} spatial direction and the brackets, [], represent the retarded time operator, equivalent to $[f(\mathbf{y})] = f(\mathbf{y}, t - r/c)$. In the present case, the retarded operator can be reasonably neglected because the cylinder is short compared with the distance to the microphone ($r \gg L$) (also known as the geometric far-field). The maximum retarded time difference across the span is of the order of 1% of a typical shedding cycle. The second term in the brackets in Equation 5.10 is a near-field term. In this case it cannot be neglected because $r < \lambda$. A shedding frequency of approximately 450 Hz corresponds to a wavelength of 0.75 m, whereas the observation point is $r = 0.5$ m away from the cylinder. However, by assuming that the force on the cylinder is harmonic, $F_y = \cos(\omega t - \phi(z, t))$, where $\phi(z, t)$ is the stochastic phase variation along the cylinder span, then the near-field term will be phase shifted by 90° from the far-field term. Furthermore, if the observation point is located directly above the cylinder, i.e., $x = r\cos(\theta = \pi/2)$, then the microphone will only sense pressure fluctuations due to lift force fluctuations, i.e., $F_i = F_y$. With these assumptions, the mean square of Equation 5.10 reduces to

$$\overline{p^2(t)} = \left(\frac{\omega}{4\pi c r}\right)^2 \left(1 + \left(\frac{\lambda}{2\pi r}\right)^2\right) \overline{F_y^2}, \tag{5.11}$$

where the over-line denotes a time average and the term $\lambda/2\pi r$ is the near-field correction term. In Equation 5.11 the cross-terms due to the near-field component equate to zero because of the orthogonality properties of sinusoidal functions. The term $\overline{F_y^2}$ is the time average mean-square of the FWMC lift force. This can be calculated from the sectional lift force, f_y, using

$$\overline{F_y^2} = \frac{1}{T}\int_0^T \left(\int_{-L/2}^{L/2} f_y(z, t) dz\right)^2 dt. \tag{5.12}$$

If the vortex shedding is anti-symmetric, the sectional lift force can be approximated by the surface pressure, $p(z, t)$, using

$$f_y(z, t) = 2W p(z, t), \tag{5.13}$$

where W is the width of the cylinder. It is implicitly assumed that the side-face pressure distribution only varies along the span of the cylinder and is uniform along the cylinder chord[2]. Sakamoto and Arie (1983) have shown this to be true for square FWMCs with $L/W > 2$. Expansion of Equation 5.12 yields

$$\overline{F_y^2} = W^2\rho^2 V_\infty^4 \int_{-L/2}^{L/2}\int_{-L/2}^{L/2} \overline{C_p(z_1, t)C_p(z_2, t)} dz_1 dz_2, \tag{5.14}$$

where ρ is the air density, V_∞ is the free-stream velocity, $C_p = 2p(t)/\rho V_\infty^2$ is the pressure

[2]The cylinder 'chord' is the streamwise length of the face parallel to the flow, i.e., the distance from the leading edge to the trailing edge

coefficient and z_1 and z_2 are dummy variables denoting positions along the cylinder span. One of the key differences between a classical reduction of Curle's theory (e.g. Equation 5.1) is that the fluctuating lift is assumed to be constant along the span of the cylinder and the cylinder is much longer than the correlation length, s. If this were the case, the integral in Equation 5.14 reduces to $\overline{C_p^2}Ls$, where s is the correlation length of the spanwise vortices calculated in Section 5.5. For the case of the FWMCs, this is not true, as can be seen in Figure 5.32.

To account for the change in fluctuating lift along the cylinder span, it is assumed that the correlation function defined in Equation 5.5 is independent of the reference position, z_1. This assumption is approximately true for the infinite cylinder case (Norberg 2003), but not necessarily true for the FWMC case. However, in the absence of a set of data that can be used to estimate the change in correlation length across the cylinder span, this assumption is necessary in order to obtain a solution. In this case, the term $\overline{C_p(z_1,t)C_p(z_2,t)} = R_{12}(\Delta z)\overline{C_p^2(z_1)}$, where $R_{12}(\Delta z)$ is the correlation function in terms of the difference variable, $\Delta z = z_1 - z_2$, and $\overline{C_p^2(z_1)}$ is the amplitude of the fluctuating pressure coefficient at any point along the span, z_1. By noting that the correlation function $R_{12}(\Delta z)$ is symmetric about Δz and through a change of variables, the integral in Equation 5.14 can be transformed to

$$\int_{-L/2}^{L/2}\int_{-L/2}^{L/2}\overline{C_p(z_1,t)C_p(z_2,t)}dz_1dz_2 = 2\int_0^L e^{-\frac{\pi|\Delta z|^2}{s^2}}\int_0^{L-\Delta z}\overline{C_p^2(z_1)}dz_1dr\Delta z, \quad (5.15)$$

where s is the correlation length and a Gaussian correlation decay has been assumed. Equation 5.15 is now in a form that can be estimated using sparse data sets. Combining Equation 5.15 with 5.14 and substituting the result into Equation 5.11 yields

$$\overline{p^2(t)} = \left(\frac{St}{2cr}\right)^2\left(1+\left(\frac{\lambda}{2\pi r}\right)^2\right)\rho^2V_\infty^6 2\int_0^L e^{-\frac{\pi|\Delta z|^2}{s^2}}\int_0^{L-\Delta z}\overline{C_p^2(z_1)}dz_1d\Delta z. \quad (5.16)$$

Equation 5.16 is a more general form of Curle's equation that is suitable for predicting the noise produced by FWMCs perpendicular to their periphery. Equation 5.16 still retains the classical V_∞^6 dependence that was derived by Curle (1955) but, as explained, contains terms that account for near-field effects and for variations in fluctuating lift levels across the cylinder span.

Equation 5.16 and the fluctuating pressure data presented in Figure 5.32 and Figure 5.40 were used to predict the fundamental Aeolian tone level for FWMCs in RI. Interpolation was used to approximate the fluctuating pressure levels at positions where there was no pressure tap. Similarly, the pressure levels at the cylinder junction and free-end were approximated using the value of the fluctuating pressure closest to the junction and free-end respectively. The double integral in Equation 5.15 was then calculated using a trapezoidal method. The reflective effects of the mounting plate and contraction were taken into account by doubling the predicted sound pressure level.

The result of this analysis is shown in Figure 5.45 for aspect ratios of $4 < L/W < 10$ and compared with the measured tonal magnitude of P1 presented in Figure 5.6. No

comparison is given for $L/W = 1.5$ because no well resolved Aeolian tone could be measured. The uncertainty in the predicted levels was calculated using a Monte-Carlo analysis. The fluctuating lift, correlation values and Strouhal number estimates were allowed to vary independently according to a Gaussian distributions and the variance of the individual distributions were calculated using Equation 3.25 for fluctuating lift, Equation 3.29 for the correlation and Equation 3.34 for the Strouhal number.

There is relatively good agreement between the trend of the predicted data and the trend of the experimental data, particularly concerning the large decrease in sound pressure level at $L/W = 7$. This shows that the reduction in OASPL at $L/W = 7$ is caused by maximum disruption to the wake by the downwash and upwash at this aspect ratio. The apparent 'tuning' that occurs for $L/W = 4$ is simply caused by a combination of low downwash, low upwash and a long enough span to allow the organised formation of vortices near the junction, increasing the spanwise correlation of vortices and ultimately increasing Aeolian tone level.

For $L/W < 8$, the magnitude of the predicted levels tend to be 4-5 dB lower than that of the measured values with a better comparison achieved at higher aspect ratios. The predicted sound levels are lower due to a number of factors. These include the assumption of a correlation length independent of reference position, different turbulence intensities between facilities, blockage ratios, cylinder vibration, near-field effects, and unknown reflective and diffractive characteristics of the AWT contraction and mounting plate.

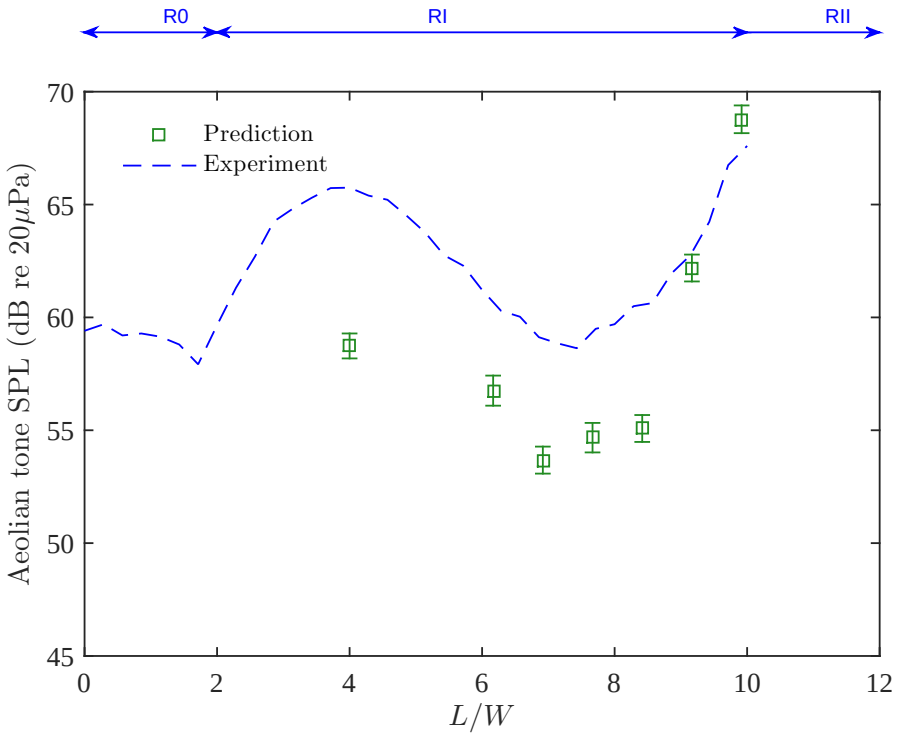

Figure 5.45: A comparison between semi-empirical values of the Aeolian tonal level from an FWMC using Equation 5.16 and the measured experimental values using a microphone 0.5 m directly above the FWMC.

The role of the wake formation length

This study has argued that downwash and upwash increase the formation length, reduce the base pressure and disrupt the organised development of spanwise vortices. However, as yet no formal mechanism has been proposed to explain why a reduction in base pressure by itself would lead to a reduction in fluctuating lift and therefore Aeolian tone level. The following simple argument can be made to explain why this must be the case.

The Kutta-Joukowski theorem dictates that the sectional lift force is proportional to the sectional circulation generated inside of the cylinder. That is, in a completely inviscid situation, the cylinder sectional lift force, F_L, and the circulation, Γ, are related by

$$F_L = \rho V_\infty \Gamma. \tag{5.17}$$

In reality, the circulation in each vortex is generated by the roll-up of the free-shear layers that separates from the leading edge of the square cylinder. Roshko (1993) derived that the rate of circulation available for roll up generated by a separating free-shear layer, $\partial\Gamma/\partial t$, is

$$\frac{\partial \Gamma}{\partial t} = (1 - C_{pb})V_\infty^2, \tag{5.18}$$

where V_∞ is the free-stream velocity and C_{pb} is the base pressure coefficient. In practice, the total circulation measured in each vortex downstream of the cylinder is only a fraction of what is available in Equation 5.18. In a two-dimensional situation, this is because velocity with opposite signed vorticity is drawn across the wake during shear layer roll up effectively reducing the total circulation of the fully formed vortex (Gerrard 1966). In the presence of downwash in a three-dimensional situation, the fraction of total circulation available would be even less given the increased rate of mixing.

Regular periodicity in the shear layer roll-up process implies that the time rate of change of circulation generated inside of the cylinder is given by

$$\frac{\partial \Gamma}{\partial t} = \omega \Gamma. \tag{5.19}$$

In Equation 5.10, the magnitude of the Aeolian tone level is proportional to the term ωF, which, through Equation 5.17, is simply the rate of change of circulation in the wake, i.e., Equation 5.19. Therefore, as the base pressure is relaxed (increases to less negative values), less circulation is available for roll up (Equation 5.18), and, as a consequence, less fluctuating lift is generated.

Intuitively, one would expect an approximate inverse relationship between the base suction and the wake formation length. This is because the separating shear layer would be more violently drawn across the wake as the base suction increases, leading to a faster rate of formation, closer to the cylinder base. Roshko (1993) quantitatively relates the base pressure to the wake length using the free streamline theory of Riabouchinksy (1920). In his formulation, Riabouchinksy (1920) modelled the wake behind a thin flat plate as the stagnant area between two parallel flat plates where the streamlines joining the flat plates were such that they connected the plate edges. The base pressure was calculated as a function of wake length, and was approximately given by

$$-C_{pb} \approx \frac{9}{2}\left(\frac{L_W}{W}\right)^{-5/3}, \tag{5.20}$$

where L_W is the wake length. Hence, as base pressure is increased to less negative values, the wake formation length naturally increases. For a given shedding frequency, less circulation is available for roll-up and the fluctuating lift reduces. In turn, the acoustic sound pressure level reduces.

A relationship between the cylinder wake formation length and the far-field acoustic pressure fluctuations has been discussed by several other authors. The numerical simulations of Ali et al. (2011) for low Reynolds number flow over a square cylinder showed that placing a splitter plate in the wake of the cylinder prevented the shear layers from either side of the cylinder from interacting, effectively increasing the formation length of the wake. By increasing the formation length, the concentration of hydrodynamic pressure fluctuations caused by the periodic vortex roll-up was moved further downstream from the cylinder base. In the study of Ali et al. (2011), a direct link between the proximity of hydrodynamic pressure fluctuations to the cylinder wall in the near wake and the magnitude of the fluctuating pressure on the surface of the cylinder was made. This link has been verified experimentally by Oguma et al. (2013). By using the Poisson equation on single PIV images, Oguma et al. (2013) showed that a downstream movement of hydrodynamic pressure fluctuations reduces the fluctuating surface pressure of the cylinder, thereby reducing the sectional lift coefficient and hence the far-field acoustic pressure fluctuations.

Directivity

The last point of discussion for FWMCs in RI is the measured directivity characteristics. The directivity of FWMCs in RI in Figure 5.10 have some similarities with a drag dipole, that is, a streamwise dipole with its lobes orientated upstream and downstream. As the cylinder moves towards RII, the directivity of the dominant tone shifts to a classical lift dipole pattern. As discussed, a drag dipole is indicative of a propensity of the vortices to shed *symmetrically*. This agrees with the results of Wang et al. (2006), who found that an FWMC with $L/W = 6$ will, on average, shed symmetric vortices 50-70% of the time at the upper half of the cylinder.

The existence of symmetric shedding is in contradiction with the assumption in Equation 5.16 that the fluctuating surface pressure is perfectly out of phase. The directivity results presented in Section 5.3 suggest that shedding, most of the time, occurs in-phase. Does this then render the above analysis incorrect at different measurement angles? Would a minimum in the OASPL still occur at $L/W = 7$ if measured at, say, $\theta_m = 40°$? To answer this, the OASPL of the FWMCs at different measuring stations is plotted in Figure 5.46. This figure demonstrates that a large reduction in measured sound pressure level still occurs at $L/W = 7$ regardless of the microphone measurement angle. This demonstrates that there is a definite disruption to the FWMC wake at $L/W = 7$ and that the three-dimensional processes that reduce the fluctuating lift that generate P1 as measured at $\theta_m = 90°$ equally disrupt and reduce the fluctuating drag at other measurement angles.

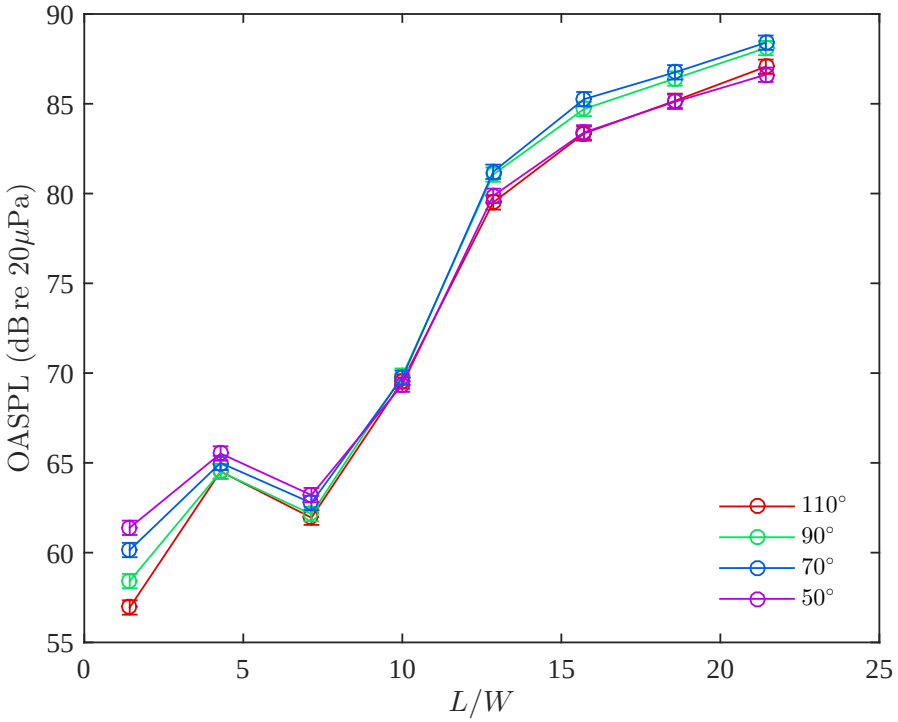

Figure 5.46: The change in OASPL with FWMC aspect ratio at four different measurement angles, $\theta_m = 110°$, $90°$, $70°$ and $50°$.

5.6.3 Vortex shedding in Regimes II and III ($L/W > 10$)

General characteristics

Cylinders in RII and RIII are characterised by low formation lengths (Figure 5.20), low base pressures (Figure 5.29), high values of fluctuating velocity across the cylinder span (Figure 5.18), very high Aeolian tone levels (Figure 5.6), and cellular shedding (Figure 5.22). The wake characteristics in the mid-span and lower portion of the cylinder are indicative of a near wake structure similar to that of the infinite cylinder wake. This is supported by the directivity measurements in Figure 5.11 and 5.12, which show the directivity of P2 and P3 to agree well with a theoretical lifting dipole generated by classical anti-symmetric vortex shedding.

The increasingly 'two-dimensional' behaviour at the mid-span of the FWMC is best illustrated by examining the frequency of the Aeolian tones. The beginning of RII at $L/W = 10$ marks the onset of a dual cell shedding structure which generates a secondary tone, P2 (Figure 5.5). The shedding frequency of P2 rapidly asymptotes towards that of an infinite cylinder, $St = 0.13$. This is because as the aspect ratio increases, the relative influence of the free-end and junction on the flow structures that generate P2 diminish, allowing the vortex street to form uninhibited, as evidenced by the sudden reduction in base pressure and formation length at $L/W = 12.5$ (in Figures 5.29 and 5.20 respectively). With increasing two-dimensionality comes increasing Aeolian tone strength (Figure 5.6) and a reduction in the Aeolian tone bandwidth (Figure 5.8). Figure 5.26 demonstrates that for $10 < L/W < 18$, P2 is associated with structures toward the junction of the cylinder and for $L/W > 18$, P2 is associated with a vortex cell at the mid-span. A third tone, P3, forms when $L/W > 18$ and is associated with structures near the junction (Figure 5.27). The P3 vortex cell also exhibits both two-dimensional

and three-dimensional like behaviour, having a well organised phased relationship and a relatively high Strouhal number (Figure 5.5), but with an inclined vortex structure (Figure 5.27).

In contrast, near the free-end there is a localised region of three-dimensional flow that interacts with the vortex shedding process, giving rise to P1. The properties of P1 are invariant across RII and RIII, suggesting that for these higher aspect ratios, as the flow near the junction becomes independent from that of the free-end, so to the flow near the free-end region becomes independent from the rest of the cylinder. Supporting this view, Figure 5.15 shows that the extent that the free-end downwash for $L/W \geq 12.9$ is restricted to approximately 3.5 cylinder widths. Furthermore, Figure 5.5 shows that P1 has a Strouhal number that is constant and suppressed below that of the two-dimensional value regardless of the aspect ratio. Both Figures 5.25 and 5.40d demonstrate that P1 is associated with a complex network of highly deformed inclined vortex filaments. Figure 5.10 shows that the directional characteristics of P1 are distinctly different to that of P2 and P3, the directivity being directed further upstream than P2 or P3, called a 'shifted lifting dipole'. This gives further evidence of the increased three-dimensional behaviour of P1.

Cellular shedding and the transition from RII to RIII

What is the reason for the sudden development of a dual cellular wake at $L/W = 10$ and a triple cellular wake at $L/W = 18$? As elaborated upon in Chapter 2, cellular shedding is caused by one of three factors: a spanwise change in geometric conditions (for example in the wakes of tapered cylinders (Abuomar and Martinuzzi 2008) or stepped cylinders (Morton and Yarusevych 2014)), a spanwise change in inflow conditions (such as cylinders in shear flow (Griffin 1985)) or a spanwise change in wake conditions. Since the FWMCs in RII and RIII in the LTB do not have any appreciable variation in geometric or inflow conditions (the boundary layer is relatively low), the driver for the cellular wake must be a spanwise variation in wake conditions.

The change in wake condition along the span of the FWMC is driven by three-dimensional flow (also known was 'secondary flow' (Zdravkovich 1997)) at the free-end. As demonstrated in Figure 5.15, while the FWMC aspect ratio increases, the downwash also increases. However, past aspect ratio $L/W \approx 7$, the influence of downwash on the lower portion of the cylinder begins to diminish, allowing a region of two-dimensional flow to form near the junction. In general, downwash acts to reduce the convection velocity of vortices forming off the FWMC. For short cylinders (FWMCs with $L/W < 10$) spanwise coupling is enhanced (elaborated upon in the next section), so the FWMC still sheds as a single cell even when there is a convection velocity gradient along the span caused by downwash near the free-end. However, when the FWMC increases in span so that it enters RII ($L/W > 10$), the free-end flow decouples from the junction. The difference in convection velocity between the free-end and the junction becomes sufficiently large and the cylinder is sufficiently long, so a secondary cell forms, with a lower vortex shedding frequency.

The spanwise base pressure profiles of the FWMCs are also indicative of the effect of secondary flow as the FWMC aspect ratio increases. As has been discussed, the transition

from RI to RII at $L/W = 10$ is marked by a rapid increase in base suction at the junction region signifying strengthening of the spanwise vortices in that region (Figure 5.29). This change is also accompanied by a slight decrease in base suction toward the free-end so that cylinders in RII have higher base suction at the junction than at the free-end.

Most importantly the spanwise base pressure profile for $L/W = 12.5$ in RII has a very mild gradient, unlike the base pressure profiles for FMWCs in RI, where extreme differences between the free-end and junction are observed. From the current results, a high spanwise base pressure gradient appears to be preclude the existence of a strong cellular wake structure. This is because high base pressure gradients signify a highly modulated three-dimensional environment, i.e., a wake with cross-stream connector strands, large streamwise and cross-stream vorticity magnitudes, significant differences in flow reversal magnitudes across the span and large cycle-to-cycle variations in time. These factors suppress the development of a two-dimensional wake altogether. On the other hand, a mild base pressure gradient signifies that each spanwise slice of the cylinder acts similar to adjacent slices, a condition favourable to the development of a two-dimensional vortex street. As such, this environment is more suited to supporting a cellular wake, since the cycle-to-cycle variations are mild (e.g Figure 5.36d) and spanwise coupling is low. The lower base suction toward the free-end is also indicative of a lower shedding frequency in that part of the cylinder, in accordance with Roshko's theory, where the frequency of vortex shedding is related to the base pressure by Equation 5.18.

The experimental observations made for cylinders transitioning from RI to RII at $L/W = 10$ can also be used to explain the transition from RII to RIII at $L/W = 18$. Within RII, there is still a mild level of spanwise flow owing to increasing upwash at the cylinder junction (Figure 5.16). This spanwise flow causes the junction cell to form with a slightly lower frequency than that of the two-dimensional value. As the cylinder increases in length, the mid-span experiences less of this spanwise flow, and the frequency of vortex shedding steadily increases toward the two-dimensional value (Figure 5.5). Due to spanwise coupling, the entire junction cell increases in vortex shedding frequency. Meanwhile, the upwash continues to increase with increasing aspect ratio (the reason why this occurs is discussed in Chapter 6). At $L/W = 14$, the upwash is large enough to begin to impact the junction cell in a similar manner to the downwash flow in RI. Spanwise coupling and three-dimensional effects are still sufficiently high to cause a significant reduction in correlation and surface pressure fluctuations near the junction, similar to that observed in Figures 5.34 and 5.32. This is the reason for the plateau in the OASPL and the magnitude of P1 in Figure 5.6 at $L/W = 14$. Further increases in FWMC length increase the upwash, reduce the correlation and cause the overall sound level from P1 to remain constant. Just prior the transition from RII to RIII at $L/W = 18$, the upwash flow reaches its maximum value (see Figure 5.16). Spanwise coupling of the junction cell is limited and once again further increases in cylinder length allow increasing two-dimensionality near the mid-span. Finally, the mid-span is sufficiently decoupled from the junction that a third cell of lower frequency vortex shedding is formed near the junction. The mid-span of the cylinder experiences no influence from either the upwash or the downwash, permitting a quasi-infinite cylinder wake at the mid-span, and the OASPL once again increasing with cylinder length. The junction, however, experiences a localised region of three-dimensional flow where a third cell of inclined vortices forms

with a lower frequency than that of the the mid-span.

Understanding cellular shedding using an oscillator analogy

From the preceding section, spanwise vortex coupling is observed to be an important aspect of FWMC flow, and plays a critical role in determining the dynamics of the transitions from RI to RII at $L/W = 10$ and RII to RIII at $L/W = 18$. Formally, spanwise coupling is the tendency of the vortices at a particular spanwise location to synchronise with other vortices shed from adjacent spanwise locations, even though the local inflow conditions may vary significantly across the span. For example, this is the mechanism by which vortex shedding continues deep within the boundary layer for FWMCs with $L/W = 4.3$ and 7.1 in Figure 5.21.

Spanwise coupling along the cylinder span can be modelled using the van der Pol oscillator analogy of Noack et al. (1991). For a van der Pol oscillator, the frequency of the oscillator will synchronise with the natural frequency of the driver if the two are sufficiently close together. Noack et al. (1991) modelled the wake of cylinders as the sum of a series of infinitely thin sectional fluid packets along the cylinder span, z. The dynamics of an isolated fluid packet at any point along the span was modelled as a van der Pol oscillator. Each fluid packet was also viscously coupled to adjacent fluid packets, providing a means by which the an individual fluid packet may be driven at a frequency other than their natural frequency, thereby mimicking the spanwise coupling effect.

Not only can the van der Pol oscillator analogy be used to study spanwise coupling, it also allows a better understanding of the dynamic nature of spanwise cellular shedding that has been observed using the experimentally obtained wake velocity profiles (Figure 5.22) and surface pressure time histories (Figure 5.40). In the van der Pol oscillator model, if there is a spanwise variation in natural frequency and the viscous coupling between adjacent fluid packets is large, spanwise regions of constant shedding frequency (i.e., cells) will develop rather than a continuously varying shedding frequency. In this manner, the van der Pol oscillator analogy is useful to model the interaction between two cells at the cell boundaries.

According to Noack et al. (1991), by modelling each cross section of the cylinder as a van der Pol oscillator, the dynamics of the wake can be described by

$$\frac{\partial^2\eta}{\partial\tau} + \epsilon\omega_0(4\eta^2 - 1)\frac{\partial\eta}{\partial\tau} + \omega_0^2\eta = p\kappa\frac{\partial^3\eta}{\partial^2\zeta\partial\tau}, \tag{5.21}$$

where $\omega_0 = St(\zeta)/St_{ref}$ is the ratio of the local driving frequency to reference natural frequency, St_{ref} is the reference natural frequency (as Strouhal number), $\tau = tSt_{ref}Re_W\nu/W^2$ is the non-dimensional time, $\kappa = \dfrac{1}{St_{ref}(L/W)^2Re_W}$ is the non-dimensional viscous coupling constant, $0 < \zeta = z/L < 1$ is the non-dimensional length, ϵ is the strength of the oscillator in relation to the other coupling forces, typically set at $\epsilon = 0.2$ and p is a correction factor used to increase or decrease the strength of viscous coupling. Finally, the term $\eta(\zeta, \tau)$ is the aforementioned non-dimensional fluid packet, the solution of which describes the dynamic behaviour of each section of the wake. It could represent any fluctuating quantity along the span of the cylinder, for example, streamwise velocity or surface pressure. This model can be solved for $\eta(\zeta, \tau)$ numerically with appropriate

boundary conditions. For an FWMC, the boundary conditions of the problem are Dirichlet and von Nuemann condition for the junction and free-end respectively, i.e.,

$$\eta(0,\tau) = 0, \tag{5.22}$$

for the junction and

$$\frac{\partial \eta(0,\tau)}{\partial \tau} = 0, \tag{5.23}$$

at the free-end.

In the model, spanwise viscous coupling is provided by the term $p\kappa = \dfrac{p}{St(L/W)^2 Re_W}$. When $p = 1$, spanwise coupling is only facilitated by molecular friction. As Reynolds number increases, the ratio of inertial forces to viscous forces increases, and spanwise viscous coupling reduces. However, according to Noack et al. (1991), spanwise velocity components, facilitated by spanwise downwash, increase macroscopic momentum exchange between fluid layers, effectively increasing the level of effective coupling. The parameter p therefore represents the inflated spanwise coupling due to spanwise flow. Additionally, for a given value of p, when the aspect ratio of the cylinder, L/W is increased, the non-dimensional spanwise coupling factor κ decreases by $1/(L/W)^2$. Hence, as aspect ratio increases, spanwise coupling reduces.

The connection between spanwise coupling and cellular shedding was studied by Noack et al. (1991) for tapered cylinders using Equation 5.21. It was observed that for a given set of inflow and geometric conditions, the number of constant frequency 'cells' given by the solution of Equation 5.21 increased as the term $p\kappa$ decreased, i.e., more cells form when spanwise coupling is low. That is, more spanwise cells form the longer the cylinder, the lower the Reynolds number, or the lower the spanwise flow. When the spanwise coupling factor reduces, the influence that adjacent fluid packets have on one another decreases, meaning that individual fluid packets can act independently from one another, increasing the number of independently forming regions of flow.

This suggests that two conditions must be met for multiple shedding cells to form. The first is that a spanwise change in vortex shedding driving frequency exists. For FWMCs, this is facilitated by downwash which reduces the convection velocity at the free-end. The second is that spanwise coupling between adjacent cells is low. For FWMCs, spanwise coupling is facilitated by the length of the cylinder and the level of downwash (which is also aspect ratio dependent). For example, if there was no change in spanwise driving frequency, then regardless of how little spanwise coupling there was, each individual cross section of the cylinder would shed with the same frequency. On the other hand, if spanwise coupling was sufficiently high then the cylinder could conceivably still shed with a single cell regardless of how different the driving frequency between different spanwise locations was. Thus, a dual cellular shedding structure will only occur if spanwise coupling is low and a driving frequency gradient exists.

The acoustic and flow results of FWMCs transitioning from RI to RII perfectly illustrate this concept. When the FWMC is in RI ($L/W < 10$), the FWMC's length is short enough and downwash low enough to ensure a single vortex cell occurs over the length of the cylinder. As the aspect ratio increases, both cylinder length and downwash (Figure 5.15) increase. As such, spanwise coupling is simultaneously reduced

and enhanced by these competing effects. However, as demonstrated in Figure 5.15, the marginal increase of downwash with aspect ratio reduces as the aspect ratio increases. Eventually at $L/W = 10$, the cylinder length becomes long enough to permit a dual cellular wake, regardless of the spanwise coupling facilitated by the downwash. At the same time, because downwash exists, a spanwise gradient of wake condition (the convection velocity) exists, which drives a vortex shedding frequency gradient along the span. Hence a dual cellular wake is formed. Beyond $L/W = 10$, the vortex dynamics at free-end are no longer influenced by that near the mid-span and the free-end is said to decouple from the mid-span.

Having understood the role that spanwise coupling plays in the dynamics of the wake, the specific nature of cellular shedding can be investigated using Equation 5.21 to simulate the dual cell wake of an FWMC in RII. The numerical parameters that were used to simulate an FWMC in RII were chosen to closely simulate the $L/W = 12.5$ case in the 18WT and are given in Table 5.3. A cylinder of $L/W = 12.5$ is simulated so a direct comparison with the surface pressure time histories can be obtained.

Table 5.3: Parameters used when solving Equation 5.21 simulating the wake of an FWMC in RII.

Parameter	Value
W	12 mm
$Re_W(\zeta)$	1.1×10^4
St_{ref}	0.122
ϵ	0.2
L/W	12.5
$\omega_0(\zeta)$	$1 - 0.2\zeta$
p	2600

In the simulation, the natural frequency, $\omega_0(\zeta)$, is varied linearly along the span of the cylinder. This was done in order to force a change in shedding frequency between the free-end and junction region. In reality this change in natural frequency along the span is facilitated by a change in convection velocity along the span (because of downwash). Unfortunately, while the measurements in Section 5.4 demonstrate a reduction in convection velocity toward the free-end, the measurements are highly skewed due to the deformation of the vortices as they are convected downstream. As such, the measurements are not suitable for use in this model. However, since the purpose of this model is to study the dynamics of the boundary between two cells specifically and not to predict the onset of cellular vortex shedding due to changes in convection velocity, a linear spanwise gradient of natural frequency is an adequate method for forcing a cellular solution. The natural frequencies at the free-end and the junction are set at $St = 0.122$ and 0.097, respectively, which are the same Strouhal numbers measured at the free-end and junction of the $L/W = 12.5$ FWMC in the 18WT. It should also be noted that the value of 'p' is chosen to be just high enough to yield two cells across the span.

Equation 5.21 is solved by first descretising ζ using a central finite-differencing scheme and integrating in time (τ) using a fourth order Runge-Kutta scheme. At each time step, the aforementioned boundary conditions are enforced. The solution is taken for over 5000 shedding cycles to allow for the solution to reach an asymptotic state. The

initial conditions of $\eta(\zeta, 0)$ and $\dfrac{\partial \eta(\zeta, 0)}{\partial t}$ are arbitrarily set, as the final solution does not depend on them.

Figure 5.47a is the autospectral density of $\eta(t)$ across the cylinder span, denoted $G_{\eta\eta}(f)$. For reference, the spectral maps of surface pressure fluctuations for the $L/W = 12.5$ FWMC is given in Figure 5.47b. There is a very close similarity between the numerically modelled result and the experimentally obtained result. Two distinct regions of lower frequency shedding and higher frequency shedding are observed at the free-end and junction respectively. The boundary of the cell in the numerical simulation is at $z/L = 0.6$, which is similar to where the cell boundary was found to occur experimentally. Additionally, at the cell boundary there is, on average, lower amplitude shedding which is again mirrored in the experimental results (see for example Figure 5.36).

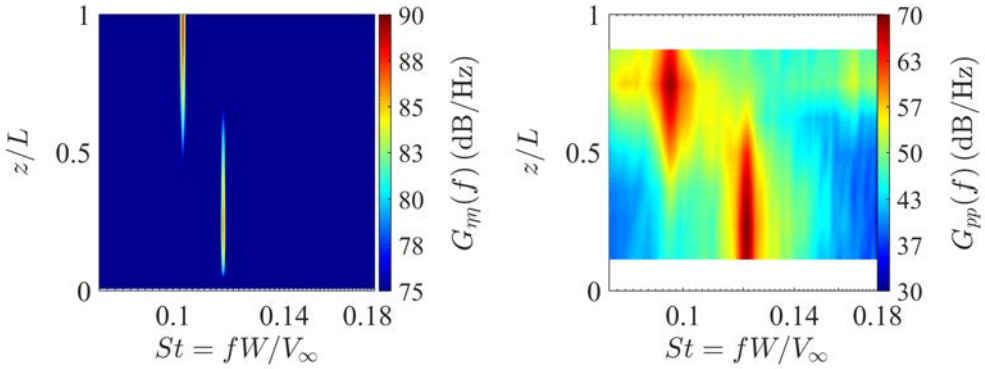

(a) Numerical results, $L/W = 12.5$ (b) Experimental results, $L/W = 12.5$

Figure 5.47: A comparison of the spectral map of $\eta(t)$ obtained numerically by solving Equation 5.21 (a) and the spectral map of surface pressure for $L/W = 12.5$ obtained experimentally (b).

Figure 5.48a is the time history of η as it varies across the span. For reference, the spanwise pressure time history for the $L/W = 12.5$ FWMC is given in Figure 5.48b. Once again, there are remarkable similarities. Much like the numerical results, the cell boundaries are characterised by a regular discontinuity in the spanwise phase. The vortices are initially synchronised across the span of the cylinder. As the vortices from the free-end begin to lag those at the junction, they are 'bent backwards' until they become completely out of phase with those at the junction. At this point the phase jump occurs as the vortices 'snap back' into synchronisation once again. This process is best highlighted by observing the time history of the phase difference between a point in the junction cell (at $z/L = 0.3$) and a point at the boundary of the free-end cell (at $z/L = 0.6$). This is shown in Figure 5.49 and phase jumps can be seen at time instances 'a', 'b' and 'c'. By using this figure, the probability density function of the phase difference can be constructed, and the result, shown in Figure 5.50, is a normal-like distribution centred at a negative mean phase difference of -2 rad. This bears striking similarity with that observed experimentally using the time series of the side surface pressure (Figure 5.36) also measured between points at $z/L = 0.3$ and $z/L = 0.6$, also shown in Figure 5.50. This result is important because it implies that the upstream tilting of the vortex filaments inside a dual cell wake is a phenomenon related to the difference in frequencies. It is not necessarily related to the downwash flow itself 'pushing' the vortex filaments

backward like what was described for cylinders in R0 nor is it caused by Biot-Savart self induction as is described for cylinders in RI by Bourgeois et al. (2011). Rather it is an indirect consequence of the downwash flow reducing the rate of formation of the vortices, which causes the vortices in the junction cell to 'pull' the lower portion of the free-end cell vortices forwards, ultimately driving the inclination process.

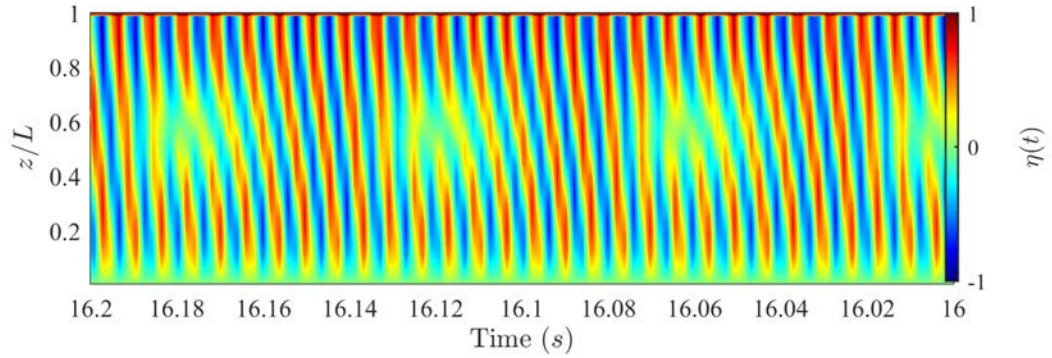

(a) Numerical results, $L/W = 12.5$

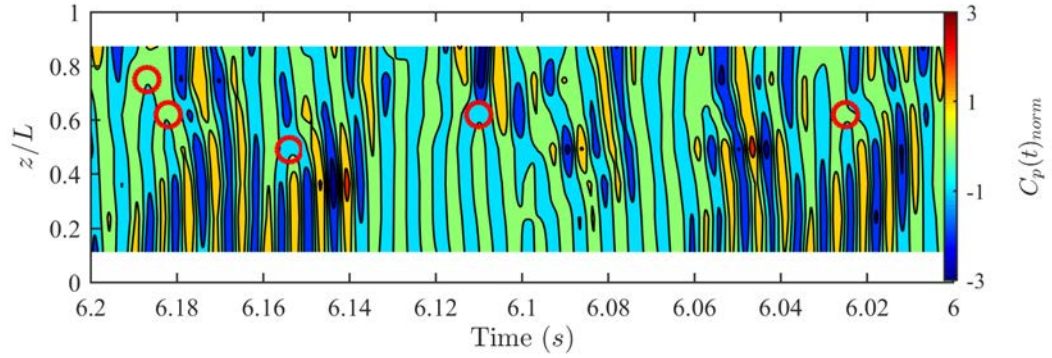

(b) Experimental results, $L/W = 12.5$

Figure 5.48: A comparison of (a) the numerically calculated time history of $\eta(t)$ using the van der Pol oscillator model and (b) the experimentally obtained time pressure history, $C_p(t)_{norm}$, for $L/W = 12.5$ at a select time increment.

Directivity

The directivity pattern of the P1 tones for FWMCs in RIII are puzzling. While the corresponding patterns of P2 and P3 were shown to collapse onto a classical dipole, the P1 tones for FWMCs in RII and RIII were directed upstream in what was called a 'shifted lifting dipole'. The main implication of this result was that the flow mechanism that generates P1 is more 'three-dimensional' than P2 and P3. This has already been shown to be true using the wake velocity and surface pressure data sets. Significant inclination and distortion of the vortex filaments were observed in the wake phase maps.

It is believed that a complicated interaction of these inclined vortex filaments with the free-end surface act to rotate the time-averaged acoustic dipole directivity pattern upstream. This seems plausible since the free-end surface is perpendicular to the sides of the FWMC, meaning it would generate a dipole orthogonal to both the lift and the drag dipoles. Such a dipole could be generated by the periodic passage of cross-stream vorticity connecting the two oppositely signed vortices on either side of the FWMC.

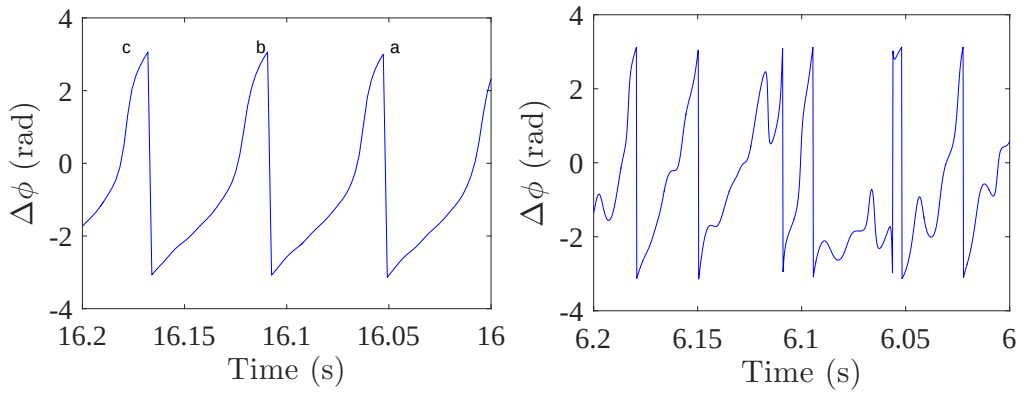

(a) Numerical results, $L/W = 12.5$

(b) Experimental results, $L/W = 12.5$

Figure 5.49: A comparison of the instantaneous phase difference between two points along the FWMC span, one in the junction cell and one in the free-end cell. (a) shows the results using the numerical van der Pol oscillator model and (b) shows the results obtained experimentally using surface pressure measurements.

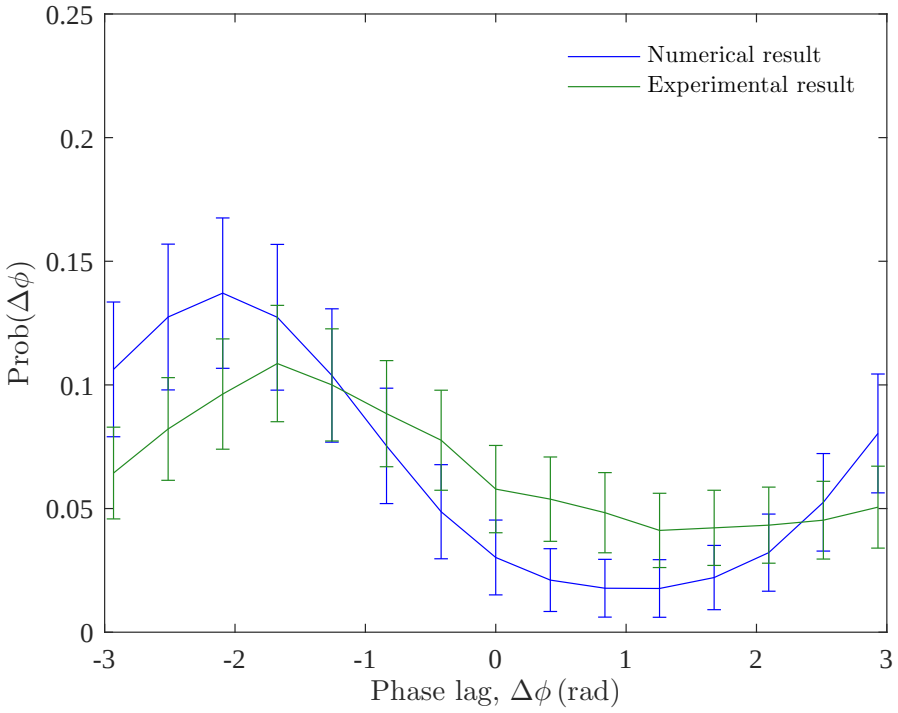

Figure 5.50: The PDF of the phase difference the fluctuating wake between two points along the span of the $L/W = 12.5$ FWMC obtained using the numerical van der Pol oscillator model. The two points were a point inside the junction cell and a point inside the free-end cell. The results are compared with that measured experimentally using the time series of the side surface pressure. Each PDF was created with a bin-width of 0.4 rad.

5.7 Summary

A comprehensive study characterising the flow-induced noise from square FWMCs with aspect ratios ranging from $0 < L/W < 23$ in low boundary layers has been conducted. The investigation is novel in that it is the first time aspect ratios greater than 14 have been studied. Based on the aspect ratio of the FWMCs, four shedding regimes were identified, namely R0 ($L/W < 2$), RI ($2 < L/W < 10$), RII ($10 < L/W < 18$) and RIII ($L/W > 18$). RIII had never previously been identified in the literature. Each shedding regime was characterised by a progressively higher number of tonal components in the acoustic spectrum. Based on the magnitude, bandwidth, frequency and directivity of these components, RI was found display higher three-dimensional characteristics, while RII and RIII were associated with ever increasing two-dimensionality.

A hot-wire wake survey was undertaken to understand the fluid dynamics responsible for the observed noise generation. The results indicated that at low aspect ratios (R0 and RI), spanwise flow or downwash, dominates the wake, creating a highly three-dimensional shedding environment. In particular, the effect of downwash on the cylinder is maximised at $L/W \approx 7$, leading to an elongation of the vortex formation length, and a significant reduction in the flow-induced noise. For these FWMCs, the looping vortex structures found by Bourgeois et al. (2011) and Hosseini et al. (2013) were visualised using a novel phase eduction technique that spatially mapped those points in space where the velocity signal was in-phase with the acoustic pressure measured by a microphone. It was found that the principal core of the loops generates the most noise perpendicular to the cylinder. For higher aspect ratios in RII and RIII, the main noise producing structures are significantly different, consisting of a series of inclined vortex filaments, where the angle of inclination varied between vortex cells.

A series of surface pressure measurements was conducted to further investigate the dynamic characteristics of RI, study the transition between RI and RII and understand the cycle-to-cycle dynamics of cellular shedding. At $L/W = 7$, the maximum relative downwash not only elongates the formation length (this time shown using an oil-film visualisation technique), but also reduces the fluctuating surface pressure and reduces the spanwise correlation of vortices. A reduction in correlation is also related to heightened shedding intermittency, increased phase jitter and a wider signal bandwidth.

Measurements of spanwise correlation of surface pressure and fluctuating surface pressure levels were then used to predict the Aeolian tone level using a modified version of Curle's theory. Good agreement was achieved when comparing the predicted values with the experimentally obtained values.

The transition from RI to RII is characterised by a rapid reduction in cylinder base pressure near the junction and more organised, regular vortex shedding. This coincides with the decoupling of free-end flow from the mid-span of the cylinder. The localised region near the free-end has a lower convection velocity than that near the junction, which, when combined with the decoupled spanwise flow, causes a dual cellular wake to form. The boundary between the two cells, known as the junction and free-end cells respectively, is marked by periodic phase dislocations mostly occurring at the frequency difference between the two cells. It was found that because of the difference in shedding frequencies between the upper and lower cells, vortices in the free-end cell are periodically

'pulled' forward. The difference in spanwise phase as the vortices are shed causes an observed inclination of the free-end cell. The phenomena was recreated numerically by modelling the cylinder dynamics using a van der Pol oscillator analogy. General agreement of the numerical results with the experimental results confirmed that the inclination of free-end vortices is caused primarily by a shedding frequency difference, and not by Biot-Savart self-induction.

Chapter 6

The effect of the boundary layer

6.1 Introduction

Having presented a discussion of the flow-induced noise produced by FWMCs of various aspect ratios in low boundary layers in Chapter 5, attention can now turn to FWMCs immersed in high boundary layers. The effect of the boundary layer on the wakes of FWMCs (and by extension the flow-induced noise) is the least well understood facet of FWMC flow (see Chapter 2).

This chapter presents and discusses the results of the experiments conducted in the AWT for FWMCs immersed the High Turbulent Boundary Layer (HTB). The HTB is considerably thicker ($\delta/W = 3.7$) than that of the LTB ($\delta/W = 1.3$). The experimental method for the HTB experiments was exactly the same as that employed for the FWMCs immersed in the LTB (presented in Chapter 5). In-depth details of the experimental method and HTB characteristics can be found in Chapter 3.

The results presented in this chapter demonstrate that the effect of the boundary layer on FWMC flow are either *non-localised*, affecting those portions of the FWMC that lie outside the boundary layer, or *localised*, affecting those portions of the cylinder that are inside the boundary layer. The most influential non-localised effect is that the height of the boundary layer, δ, changes the balance between upwash and downwash across the span, resulting in a delayed onset of each shedding regime. This means that phenomena that are only observed for lower aspect ratio FWMCs in the LTB, such as single cellular shedding, are observed at higher aspect ratios in the HTB. The most influential localised effect is that the third junction cell that generates P3 in the LTB is not observed in the acoustic spectra because of the heightened turbulence inside the HTB.

This chapter also characterises the broadband, high frequency part of the acoustic spectrum of FWMC flow-induced noise. The broadband noise level appears to have a relationship with the relative levels of upwash and downwash. For sufficiently high aspect ratios, broadband noise is reduced with a higher boundary layer. This is because the relative levels of upwash and downwash are changed by the higher boundary layer.

The data presented in this chapter are unique. Not only are studies that vary the boundary layer thickness rare (there are only three studies in the literature that change the boundary layer height for a given aspect ratio FWMC), there are no studies that vary the boundary layer and simultaneously vary the aspect ratio. Furthermore, there have been no studies that have related the high frequency broadband flow-induced noise

from FWMCs with its flow structure. These are new contributions to the literature that are addressed in this chapter.

6.2 Single microphone measurements

This section presents the results of the single microphone measurements for FWMCs in the HTB. Similar to Section 5.2, these results include the Overall Sound Pressure Level (OASPL), the narrowband acoustic spectrum, the magnitude, the bandwidth and the frequency of each of the major tones in the acoustic spectrum and the directivity of these tones.

6.2.1 Overall Sound Pressure Levels

Figure 6.1 plots the variation of Overall Sound Pressure Level (OASPL) in dB re. 20μPa with aspect ratio (from $0 < L/W < 23$) for FWMCs in the HTB. The data were processed in exactly the same manner as that for the LTB in Chatper 5. Each data point has a statistical uncertainty of ± 0.4 dB at 95% confidence. Figure 6.1 also compares the results with the OASPL of FWMCs in LTB, as shown previously in Figure 5.1. Finally, the top of Figure 6.1 compares the different regime boundaries between the LTB and the HTB. The reason for the difference in regime boundaries between the LTB and HTB is elaborated upon in the next section. For now it is sufficient to observe that the regime boundaries for FWMCs in the HTB are shifted to higher aspect ratios than in the LTB.

Figure 6.1 shows that the plate boundary layer has a large influence on the OASPL, even for very high aspect ratios ($L/W > 15$). As the aspect ratio increases from $L/W = 0$ to 7, the OASPL increases at its fastest rate (i.e., dB increase per unit L/W). Unlike FWMCs in the LTB, there is no reduction in OASPL after $L/W = 4$, which results in an OASPL at $L/W = 7$ that is 11 dB greater in the HTB case than in the LTB case. However, from $L/W = 7$ to 12, the OASPL remains constant. This behaviour is similar to what was observed during the transition from RII to RIII for FWMCs in the LTB (shown in Figure 5.1) and suggests that the FWMCs in the HTB undergo a similar transitional state at these aspect ratios. After $L/W = 12$, the OASPL once again begins to increase with aspect ratio, this time at a noticeably slower rate than between $0 < L/W < 7$. This also marks the point where the OASPL of cylinders in the HTB becomes lower than that of the LTB. Finally, at $L/W = 18$, the rate of increase slows again to now follow the rate of increase of the LTB. At these aspect ratios, the OASPL of FWMCs in the HTB is constantly 3 dB lower that of FWMCs in the LTB.

6.2.2 Power Spectral Density noise component analysis

Chapter 5 formulated several links between the characteristics of the acoustic spectrum and the dynamics of the wake of FWMCs over a wide aspect ratio range in the LTB. Therefore, a comparison of the acoustic spectra of FMWCs in the HTB with the acoustic spectra of those immersed in the LTB can be used to infer how the boundary layer influences the dynamics of the FWMC wake flow at a given aspect ratio.

Figure 6.2 presents a spectral map of the acoustic Power Spectral Density for varying aspect ratio FWMCs in the HTB, while Figure 6.3 directly compares the narrowband

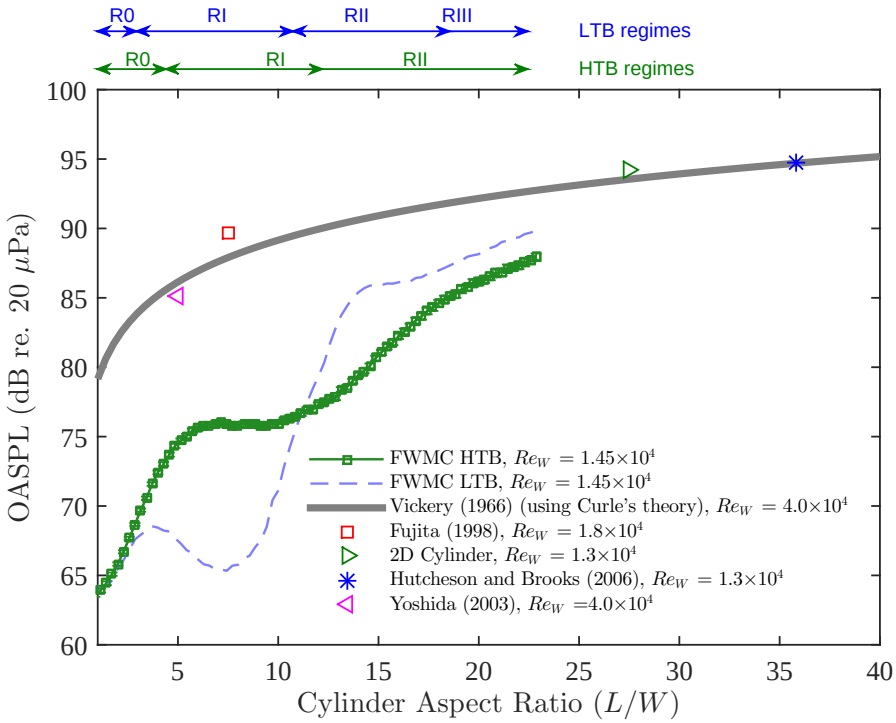

Figure 6.1: A comparison of Overall Sound Pressure Levels (OASPL in dB re. 20μ.Pa) for square FWMCs in the HTB for $0 < L/W < 23$. The OASPL of FWMCs in the LTB (from Figure 5.1) are also shown for reference. The data is compared with that calculated using Equation 5.1 using measurements of an infinite square cylinder provided by Vickery (1966) ($s = 6$, $St = 0.13$ and $\overline{C_L}^2 = 1.7$) and experimentally obtained noise data of infinite square cylinders measured by Fujita et al. (1998), Hutcheson and Brooks (2006) and Yoshida et al. (2003). The extent of each shedding regime for the HTB and the LTB are shown at the top of the figure.

acoustic spectra of select FWMCs in the HTB with the corresponding spectra for the same aspect ratio FWMCs in the LTB. The spectral uncertainty is 0.5 dB/Hz with a 95% level of confidence.

Figure 6.2 shows that when the inflow conditions are changed from the LTB to the HTB, the spectral content of the acoustic pressure fluctuations are also altered. The most prominent change appears to be that the aspect ratios where single and multiple Aeolian tones are measured are shifted to higher aspect ratios. As a result, the shedding regime boundaries are shifted. The differences in shedding regime boundaries are also shown graphically in Figure 6.1 and can be used as a reference to aid in the proceeding discussion. R0, the low aspect ratio regime, continues until $L/W = 4$, whereas in the LTB, R0 only continues until $L/W = 2$. RI now occurs from $L/W = 4$ through to $L/W = 12$, only generating a single Aeolian tone, P1. At $L/W = 12$ a bifurcation occurs and two tones are generated, P1 and P2, up until $L/W = 23$. In the LTB, the corresponding bifurcation occurred at $L/W = 10$.

There is a common observation in the literature that boundary layers with large δ/L suppress cellular shedding along the span of FWMCs (Sumner et al. 2004; Sakamoto and Oiwake 1984). Further evidence of this fact is provided in a recent study by Hu et al. (2015), who presented LES data on the wake of a square FWMC with $L/W = 18$. In the LTB such a high aspect ratio would normally place this cylinder in RII or RIII, but the

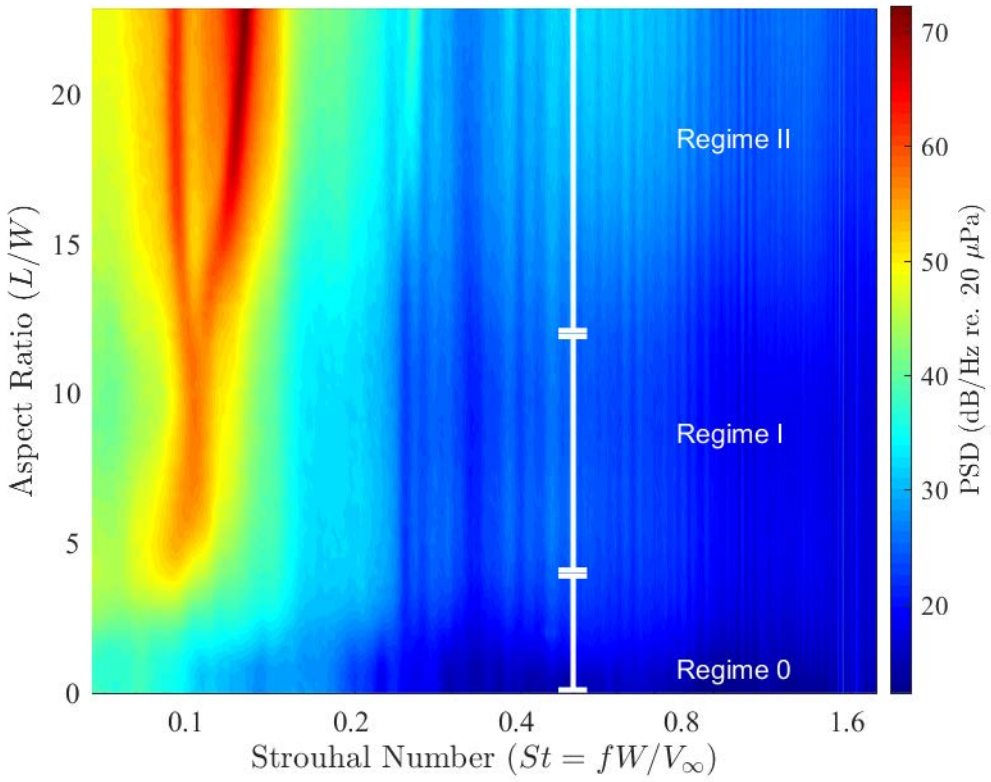

Figure 6.2: A colour map showing the variation of Power Spectral Density (PSD) of acoustic pressure fluctuations with aspect ratio when the FWMC is immersed in the HTB, expressed in dB/Hz re. 20μPa . The shedding regime boundaries are labelled in white.

boundary layer height in this numerical investigation was over 18 times the width of the cylinder, making $\delta/L \approx 1$. In agreement with the arguments provided by Sumner et al. (2004) and Sakamoto and Oiwake (1984), no cellular variation of shedding frequency was found along the cylinder span.

The results of the present study yield more insight into the phenomenon. For aspect ratios near the transition from RI to RII in the LTB ($L/W = 10$), cellular shedding is 'suppressed' when in the HTB. However, the suppression is only effective for a few diameters. Once the FWMC span is long enough so that free-end lies sufficiently far from the edge of the boundary layer, cellular shedding occurs once again. In this sense, a higher boundary layer does not 'suppress' cellular shedding, but *delays* cellular shedding through shifting the shedding regime boundaries. The observed suppression of cellular vortex shedding due to the boundary layer height in other studies is a consequence of the aspect ratios considered being close to the transition between RI and RII. For example, in the study of Hu et al. (2015), the higher boundary layer ($\delta/W = 18$) shifts the shedding regime boundaries so much that their FWMC with $L/W = 18$ lies in RI. It is hypothesised that if their cylinder had been longer in the same boundary layer, cellular shedding would have occurred.

Directly comparing the narrowband acoustic spectra of FWMCs in the HTB with those in the LTB (in Figure 6.3) shows large differences in the magnitude, frequency and bandwidth of the observed tones. These differences are quantified in Figures 6.4 to 6.6,

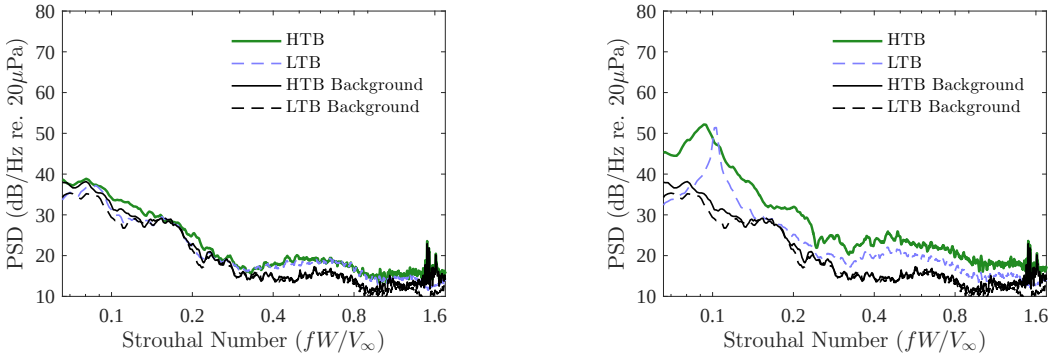

(a) $L/W = 1.4$

(b) $L/W = 4.3$

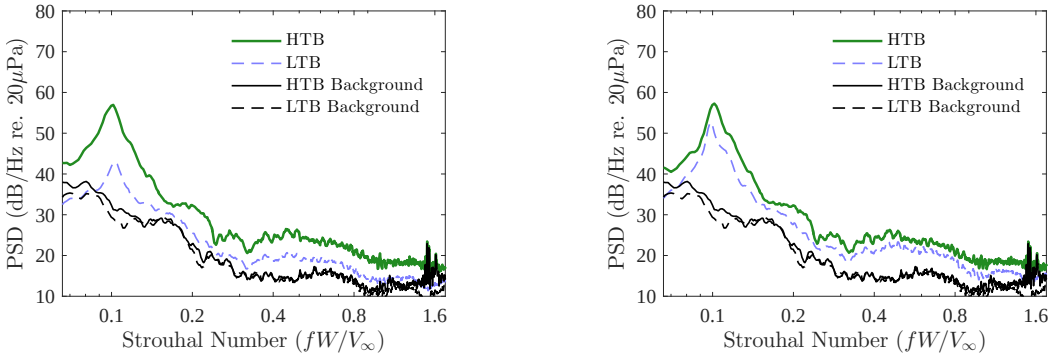

(c) $L/W = 7.1$

(d) $L/W = 10.0$

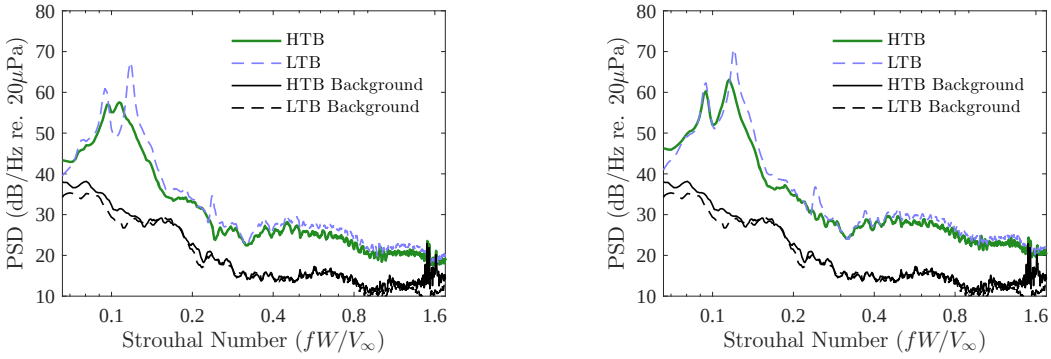

(e) $L/W = 12.9$

(f) $L/W = 15.7$

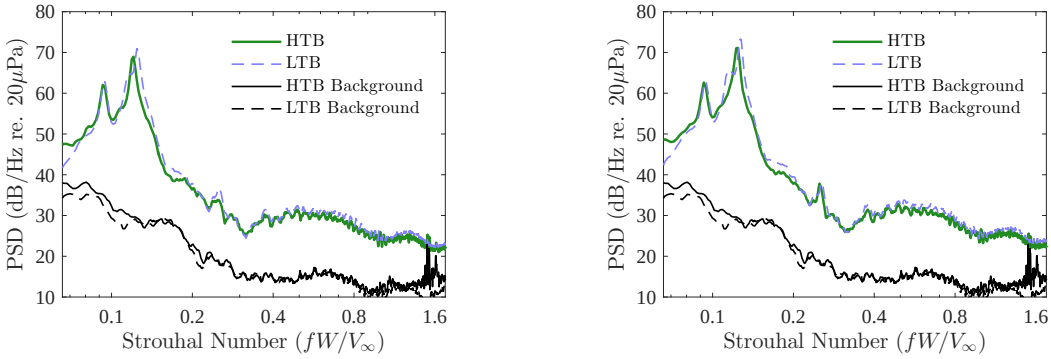

(g) $L/W = 18.6$

(h) $L/W = 21.4$

Figure 6.3: A comparison of the narrowband acoustic spectra measured by a microphone 0.5 m directly above the FWMC, for FWMCs in the HTB compared with those in the LTB for aspect ratios ranging from $1.4 \leq L/W \leq 21.4$.

respectively, which show the magnitude, frequency and bandwidth of P1 and P2 (at the aspect ratios where they occur) against their LTB counterparts as a function of aspect ratio. The definition, method of calculation and uncertainty estimates of these parameters are the same as for the LTB in Chapter 5. The shift of each shedding regime to higher aspect ratios is best observed in Figure 6.5, showing the Strouhal number of each tonal peak as a function of aspect ratio. The results are compared with the corresponding measurements made for FWMCs in the LTB. The shapes of the HTB and LTB curves are nearly identical but with the HTB curves shifted by approximately two aspect ratios to the right (to higher aspect ratios).

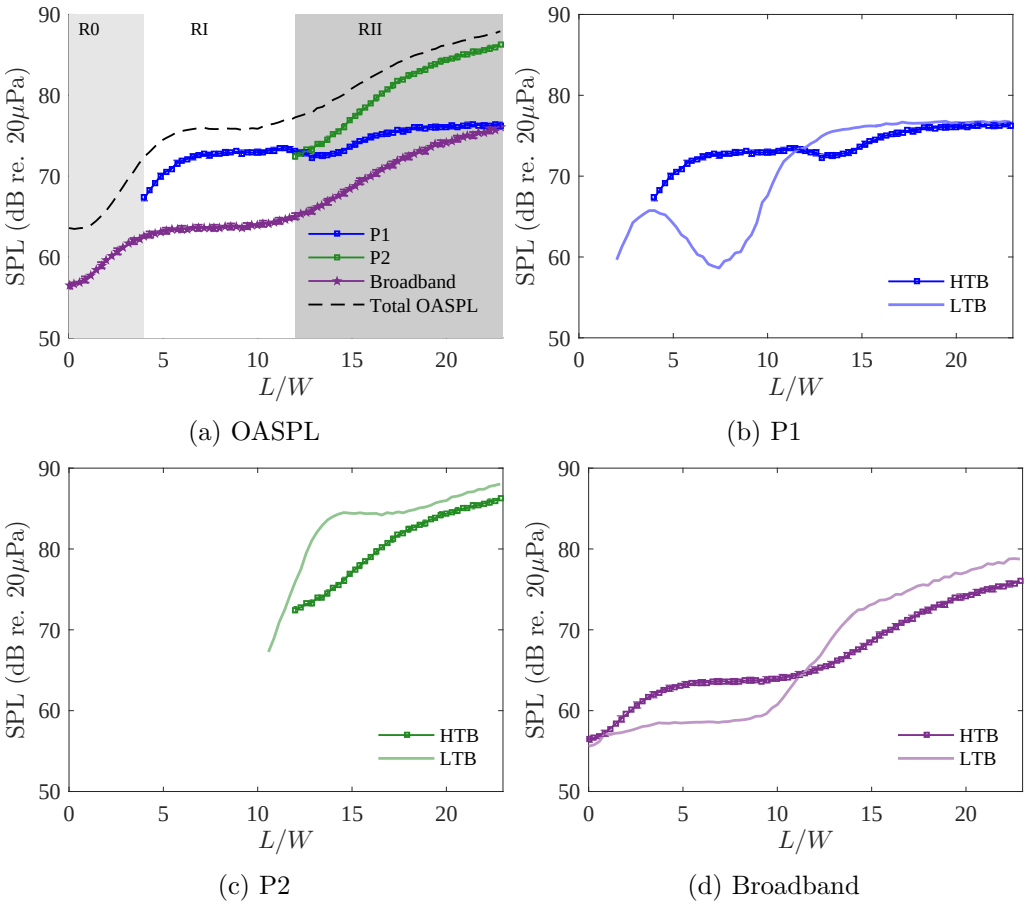

(a) OASPL (b) P1

(c) P2 (d) Broadband

Figure 6.4: (a) A breakdown of the magnitude of each component, P1, P2 and the broadband component, that comprise the acoustic spectra of FWMCs of various aspect ratios in the HTB. Subfigures (b), (c) and (d) compare the magnitudes of P1, P2 and the broadband part of the spectrum respectively to their LTB counterparts.

At $L/W = 1.4$, Figure 6.3a shows that no coherent vortex shedding can be observed for both boundary layer cases. The spectrum appears to be very similar across all frequencies, with a slight increase of broadband noise levels (above the background level) between $St = 0.4$ to $St = 0.8$ for both the LTB and the HTB. The occurrence of several narrow peaks at $St \approx 1.6$ for the HTB is attributed to electrical interference. It occurs in both the background signal and in the FWMC measurements for low aspect ratios when the signal-to-noise ratio is low.

At $L/W = 4.3$, Figure 6.3b shows that a single Aeolian tone (P1) exists in both the LTB and HTB. The HTB tone has a similar magnitude to that of the LTB but with a much higher bandwidth (see Figure 6.6). For this aspect ratio the Aeolian tone

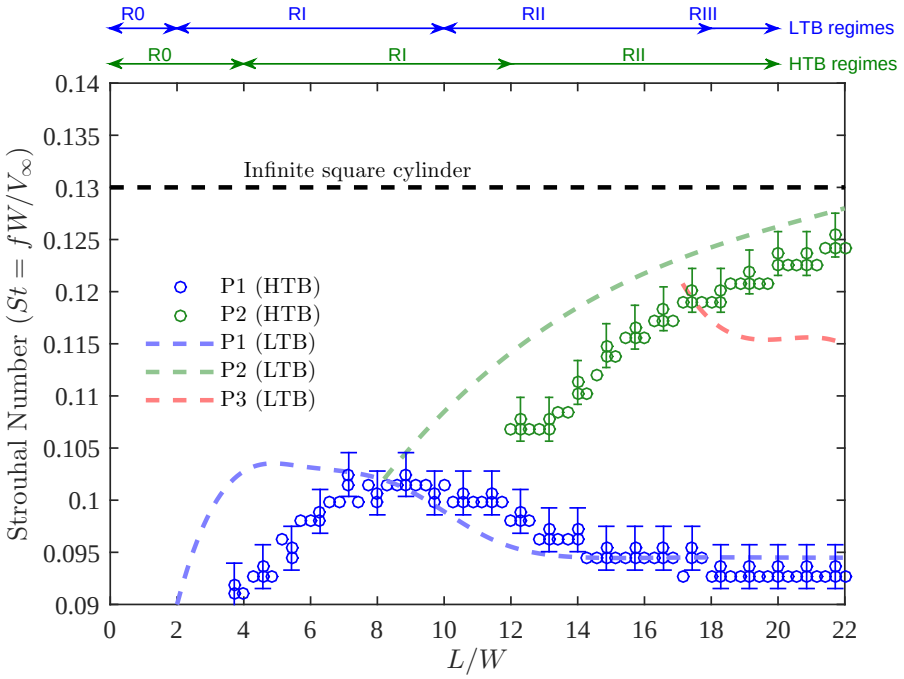

Figure 6.5: The variation of the centre frequency of each tonal peak (P1 and P2) as a function of aspect ratio. The data is compared with the corresponding results in the LTB.

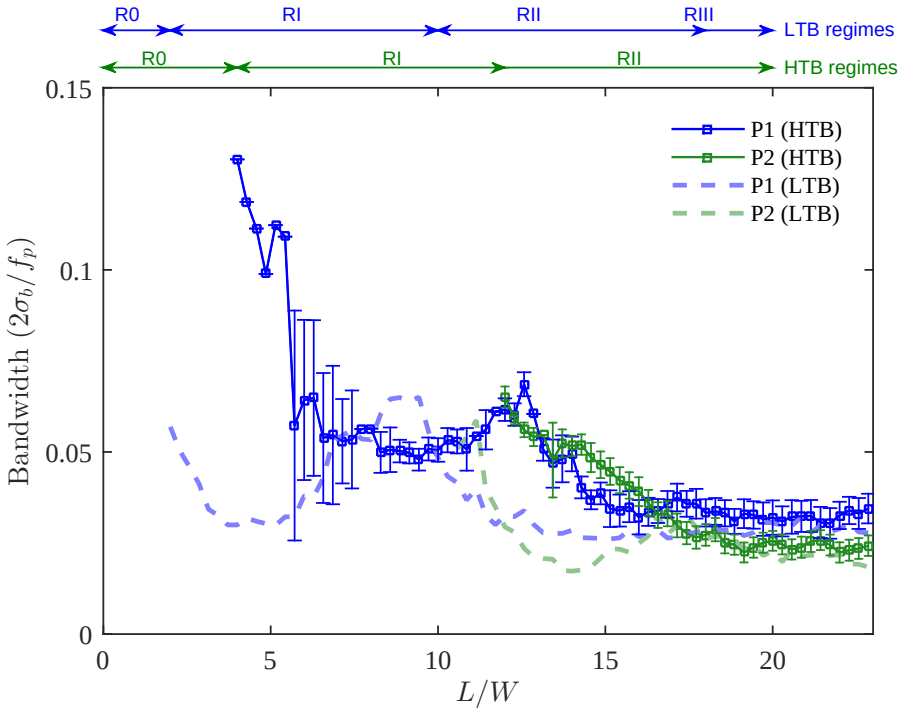

Figure 6.6: The variation of the bandwidth parameter of each tonal peak (P1 and P2) as a function of aspect ratio. The data is compared with the corresponding results in the LTB.

frequency and bandwidth characteristics are similar to that measured for $L/W = 1.4$ in the LTB. In fact, the $L/W = 4.3$ FWMC in the HTB and the $L/W = 1.4$ FWMC in the LTB share a dynamic similarity. In the LTB, the FWMC with $L/W = 1.4$ is slightly higher than the boundary layer height of $\delta/W = 1.3$, meaning that $\delta/L = 0.92$. In the

HTB for $L/W = 4.3$, the boundary layer height is $\delta/W = 3.7$, yielding a very similar boundary layer thickness to span ratio, $\delta/L = 0.86$. The similarity of spectral component characteristics and in-flow conditions suggest that the noise generation mechanism for the $L/W = 4.3$ FWMC in the HTB is similar to the $L/W = 1.4$ case in the LTB. This is consistent with the interpretation that a higher boundary layer shifts the shedding regime boundaries (and so too cylinders with dynamically similar wakes) to higher aspect ratios.

Figure 6.4b shows that the magnitude of P1 increases from $L/W = 4$ to $L/W = 7$ but is constant beyond $L/W = 7$. In this aspect ratio range, the bandwidth steadily reduces (see Figure 6.6) and the frequency steadily increases (see Figure 6.5) so that the FWMC with $L/W = 7$ has the lowest bandwidth and the highest Strouhal number in RI. This aspect ratio is analogous to the $L/W = 4$ case in the LTB, where the cylinder is long enough and the downwash low enough for the wake to be stable and the Aeolion tone to experience 'tuning'. This tuning phenomenon occurs at a much higher aspect ratio than in the LTB, explaining why the magnitude of P1 at the tuning aspect ratio is much greater in the HTB than in the LTB. In contrast, the FWMC with $L/W = 7$ in the LTB marks the aspect ratio where significant wake decorrelation occurs and the result is a 'detuning' of the aspect ratio. The concurrence of tuning in the HTB and detuning in the LTB at $L/W = 7$ causes the 11 dB difference in OASPL at this aspect ratio.

Unlike in the LTB, the magnitude of P1 in the HTB does not reduce for aspect ratios higher than the tuning aspect ratio ($L/W = 7$). Instead, with increases in aspect ratio between $7 < L/W < 12$, the magnitude of P1 remains constant. For $7 < L/W < 10$ the shedding frequency (in Figure 6.5) remains constant at $St = 0.103$ and the bandwidth (in Figure 6.6) remains constant at $2\sigma_b/f_b = 0.05$. Just prior to the formation of P2 between $10 < L/W < 12$, the bandwidth of P1 increases to $2\sigma_b/f_b = 0.07$ and the shedding frequency reduces slightly to $St = 0.0998$. These characteristics suggest that prior to the transition between RI and RII (during $7 < L/W < 10$) a wake reorganisation occurs. However, when this wake reorganisation is forced to occur at a higher aspect ratio due to the higher boundary layer, the decorrelation of the spanwise vortices is considerably milder when compared with the analogous transition period in the LTB. Evidently, changes in intermittency and correlation length during the transition period are not high enough to reduce the tonal levels with increases in aspect ratio, as in the LTB case. As such, the transition between RI and RII for FWMCs in the HTB appears similar to the transition between RII and RIII for FWMCs in the LTB.

At $L/W = 13$, two Aeolian tones (P1 and P2) exist for both boundary layer cases. Figure 6.3e shows that the magnitudes of P1 and P2 for FWMCs in the HTB are both considerably less than in the LTB. This is because the transition from RI to RII occurs at $L/W = 12$ in the HTB case, rather than $L/W = 10$ for the LTB case. This means that in the LTB, by $L/W = 13$, stronger junction flow shedding has already been established as the free-end flow becomes fully independent of the junction. In contrast, weaker junction and free-end shedding occurs in the HTB case since the free-end flow is not yet decoupled from the rest of the cylinder.

After the formation of P2, the magnitude, frequency and bandwidth of P1 in the HTB asymptote toward the value of that of the LTB. This occurs in a like-for-like manner when compared with the LTB. Figure 6.4b shows that the shapes of the curve of P1

after $L/W = 13$ in the HTB is very similar to that of P1 after $L/W = 10$ in the LTB. This indicates that the process by which the free-end cell becomes decoupled from the junction cell is similar in each boundary case, but obviously occurs at a greater aspect ratio in the higher boundary layer due to the shifted regime.

On the other hand, the influence of the boundary layer on P2 appears to be much larger in the HTB than in the LTB. In the LTB, from $10 < L/W < 14$, P2 rapidly attains 'two-dimensionality' (see Figure 6.4c) because the downwash is sufficiently decoupled from the junction and the upwash near the junction region is weak. This allows the formation of a region in the lower half of the cylinder that is relatively free from spanwise flow. The lock-in effect is strong enough that two-dimensional vortex shedding persists deep into the boundary layer. As presented in Section 5.5, during this aspect ratio range, the cylinder length, vortex correlation length and sectional fluctuating lift coefficient simultaneously increase. As a result, the magnitude of P2 rises by 4.5 dB per unit aspect ratio. This does not occur in the HTB. It is likely that the HTB increases the interaction of the flow in the lower half of the cylinder with junction flow during RII, suppressing the ability of the junction cell to rapidly reach a two-dimensional state. Consequently the magnitude of P2 increases at a reduced rate of 1.7 dB per unit aspect ratio (see Figure 6.4c) from $L/W = 13$ to 17 in the HTB.

An important observation in Figure 6.2 is that a second transition period does not occur for FWMCs in the HTB (to RIII) and a third tone, P3, is not observed in the narrowband acoustic spectra. This suggests that a junction cell is not formed. In the LTB, a transition period occurs between $L/W = 14$ to 17 resulting in the magnitude of P2 remaining constant over this aspect ratio range. This transition period occurs because upwash increases as the flow around the mid-span region becomes two-dimensional and fluid is entrained from within the boundary layer. When this upwash is sufficiently large, it acts to decorrelate the vortices in the junction cell. The increase of P2 in the LTB occurs after entering RIII ($L/W = 18$) as the aspect ratio becomes higher enough so that flow at the mid-span becomes decoupled from the junction. On the other hand, FWMCs in the HTB do not experience a plateau of OASPL due to the formation of this third cell. Therefore, as shown in Figure 6.1, the OASPL rises steadily throughout RII, allowing the difference between the OASPL in the LTB and the OASPL in the HTB to reduce. Consequently, by $L/W = 18$, there is only a 3 dB difference in OASPL and from Figure 6.4c the rate of increase in OASPL and P2 are identical.

6.2.3 Directivity

Figures 6.7 and 6.8 plot the directivity pattern of the frequency integrated magnitude of P1 and P2 for select aspect ratio FWMCs in the HTB. Like Figures 5.10 to 5.12, the results are compared with a simulated directivity pattern obtained using a CAA code modelling a point dipole in the AWT environment (denoted 'Simulated') and the experimentally obtained directivity pattern of a cylinder that spanned the full width of the contraction outlet (denoted 'Infinite Cylinder'). The 95% confidence level of the normalised mean-square pressure values is approximately ± 0.05.

The directivity patterns of the P2 tones in the HTB (Figure 6.7) are similar to the directivity pattern of the P2 tones measured in the LTB (Figure 5.11). The pattern

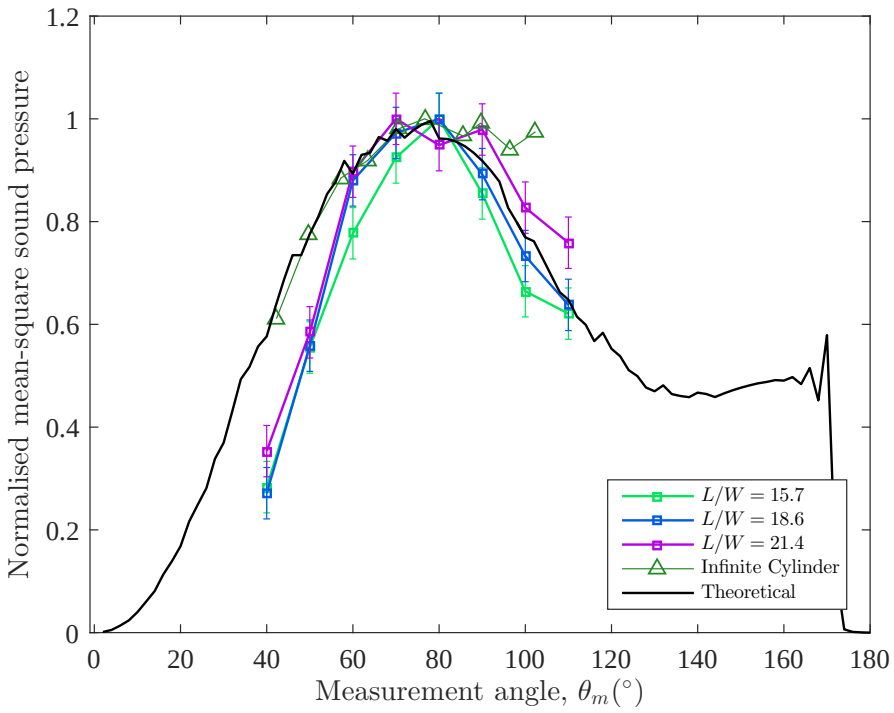

Figure 6.7: The directivity pattern of P2 for FWMCs in the HTB compared with the directivity pattern of a simulated dipole in the AWT facility and the experimentally obtained pattern from infinite cylinder in the same facility.

resembles a lift dipole, with its lobe perpendicular to the free-stream direction. The maximum sound pressure level occurs at approximately θ_m =70-80° anti-clockwise from the streamwise direction, which is caused by a reflection off the contraction flange, as predicted by the simulated CAA results (see Figure 5.9 in Chapter 5). It can be concluded that the mechanism of noise generation for P2 in the HTB is similar to that of P2 in the LTB; that is, P2 is generated by classic anti-symmetric vortex shedding. It was discussed in Section 6.2.2 that the reduced rate of increase of the magnitude of P2 with aspect ratio during RII in the HTB implied that P2 was disrupted by the increased three-dimensional flow near the junction of the cylinder. Evidently, however, the increased interaction of the structures that generate P2 with the boundary layer do not alter the directivity pattern of noise generation.

Similarities between the LTB and the HTB also exist when interrogating the directivity patterns of P1. Figure 6.8 shows that P1 has a shifted lifting dipole for FWMCs in RII ($L/W > 12$ for the HTB) and has a streamwise dipole characteristic for FWMCs in RI. A streamwise dipole is evidenced by low values of sound pressure level at $\theta_m = 90°$ and higher levels away from this measurement angle for these aspect ratios. The $L/W = 12.9$ FWMC in the HTB appears to be in a transitional state between the a streamwise dipole and a shifted lifting dipole, as it lies close to the boundary between RI and RII. For comparison, when FWMCs in the LTB are in RI, P1 have streamwise dipole directivity characteristics while those in RII have a shifted lifting dipole directivity pattern (see Figure 5.10). The difference between the LTB and the HTB is that transition point between a streamwise dipole and a shifted lifting dipole occurs at $L/W = 12$ for FWMCs in the HTB and $L/W = 10$ for FWMCs in the LTB. These results are consistent with the finding that the boundary layer shifts the shedding regime boundaries to slightly

higher aspect ratios.

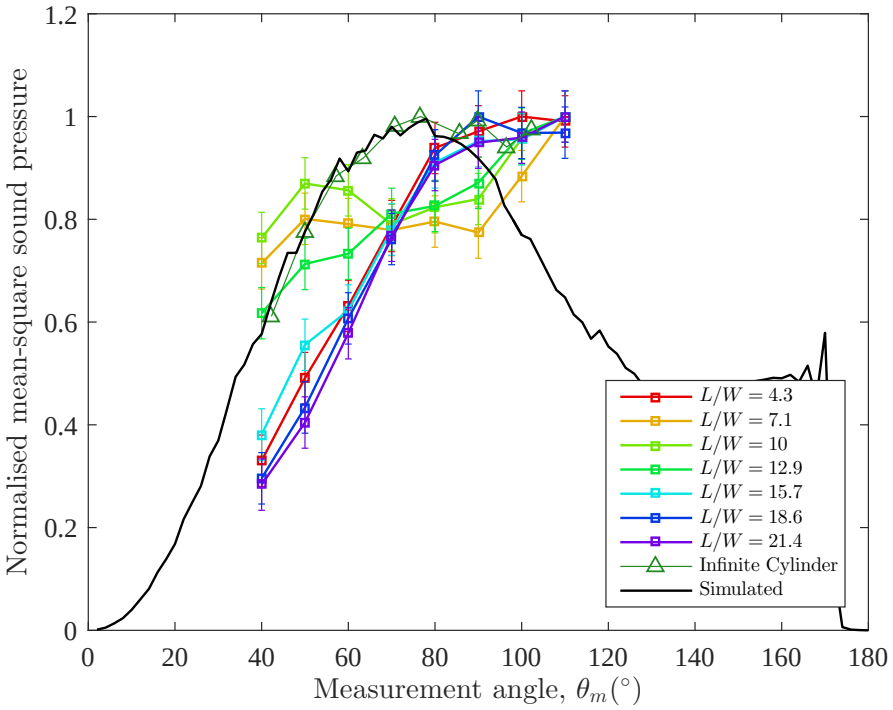

Figure 6.8: The directivity pattern of P1 for FWMCs in the HTB compared with the directivity pattern of a simulated dipole in the AWT facility and the experimentally obtained pattern from infinite cylinder in the same facility.

Curiously, the directivity pattern of P1 at $L/W = 4.3$ in the HTB in Figure 6.8 resembles a shifted lifting dipole. This is in contrast to what was measured in the LTB for the $L/W = 4.3$ FWMC, where the directivity pattern clearly resembles a streamwise dipole (see Figure 5.10). In this case, for $L/W = 4.3$ in the HTB, $\delta/L = 0.86$ while for $L/W = 4.3$ in the LTB, $\delta/L = 0.3$. The boundary layer must therefore have an influence on the noise generation mechanism when cylinder length is close to the height of the boundary layer. Furthermore, this noise generating mechanism appears similar to that of the free-end cell mechanism that generates P1 in RII.

As discussed in Section 6.2.2, the $L/W = 4.3$ FWMC is suggested to have a similar noise generation mechanism to $L/W = 1.4$ in the LTB due to the dynamic similarity of their span relative to the height of the boundary layer. However, in Chapter 5 the directional characteristics of P1 produced by the $L/W = 1.4$ FWMC could not be studied because of the poor signal-to-noise ratio. In contrast, the signal-to-noise ratio of the $L/W = 4.3$ FWMC in the HTB is much higher. Therefore by extrapolation, it is hypothesised that the $L/W = 1.4$ FWMC in the LTB may have a similar directivity pattern to the $L/W = 4.3$ FWMC in the HTB had the signal-to-noise ratio of the AWT been higher.

Unfortunately, this extrapolation is in disagreement with the argument put forth in Section 5.6.1, where it was hypothesised that such low FWMCs in the LTB should display a drag dipole directivity pattern owing to the formation of a periodically shed symmetric arch structure.

The inconsistency of the directivity results presented here with the hypothesis in Section 5.6.1 renders the origin of this shifted lifting dipole enigmatic. One conclusion

that can be drawn is that the shifted lifting dipole is related to free-end flow, which is the only commonality between all instances where a shifted lifting dipole is measured. When free-end flow dominates, as it does when an end-cell forms, or, evidently when the edge of the boundary layer and the span of the cylinder are approximately equal, a shifted lifting dipole is measured.

6.3 Wake velocity measurements

In this section the fluid dynamical mechanisms responsible for the observations on noise generation from FWMCs in the HTB in Section 6.2 are discussed. Evidence of these mechanisms is provided using the results of a hot-wire wake survey. The experimental methodology and details of this wake survey are the same as those when measuring FWMCs in the LTB. The same hot-wire was used in both sets of experiments and wake surveys were conducted on the same aspect ratio FWMCs. The aspect ratios were $L/W = 1.4$, 4.3, 7.1, 10, 12.9, 15.7, 18.6 and 21.4. Unlike in Chapter 5, the full set of hot-wire results are not presented here. Instead, only the most salient results will be presented in order to facilitate a discussion of the differences between FWMC wakes in the HTB compared with those in the LTB. Where appropriate, results already presented in Chapter 5 will be repeated to highlight the impact of the HTB. The reader is directed to Appendix A for the full set of HTB hot-wire results. Unless otherwise stated, the uncertainty estimates for the results presented in this section were calculated in the same manner as the corresponding results in Chapter 5.

6.3.1 Mean velocity maps

Figure 6.9 compares the mean velocity colourmaps for various aspect ratio FWMCs in the HTB (on the left) and the LTB (on the right). The higher boundary layer in the HTB has a slightly lower wake penetration level than that of the LTB. This is particularly noticeable for the $L/W = 4.3$ case (comparing Figures 6.9c and 6.9d). Higher levels of upwash are also observed near the junction for cylinders in RI ($4 \leq L/W \leq 12$) in the HTB when compared with the LTB. This is best visualised by comparing the maps for $L/W = 7.1$ for the HTB (Figure 6.9e) and the LTB (Figure 6.9f). The jet-like ejection of streamwise fluid at $x/W = 6$ from the junction region in the HTB is very prominent. Conversely, at higher aspect ratios (e.g., $L/W = 15.7$ in Figure 6.9i), the magnitude of the upwash appears to be lower in the HTB, despite the fact that the jet-like ejection of streamwise fluid penetrates higher into the wake. Here the reduced streamwise velocity at $x/W = 6$ and $z/L = 0.1$ is approximately $\overline{u}/V_\infty = 0.6$ whereas the corresponding measurement in the LTB is $\overline{u}/V_\infty = 0.8$.

Figures 6.10 and 6.11 quantify the aforementioned observations. Figure 6.10 compares the extent of wake penetration of the separating shear layer over the cylinder free-end for the two boundary layer cases. Once again this parameter is defined as the number of cylinder widths below the free-end at $x/W = 6$ where the mean velocity reaches 80% of the free-stream value and is interpreted as an indicator of the magnitude of the downwash. The curves demonstrate that downwash for FWMCs in the HTB is slightly lower than that of FWMCs in the LTB for all aspect ratios up to $L/W = 15.7$. Beyond this aspect

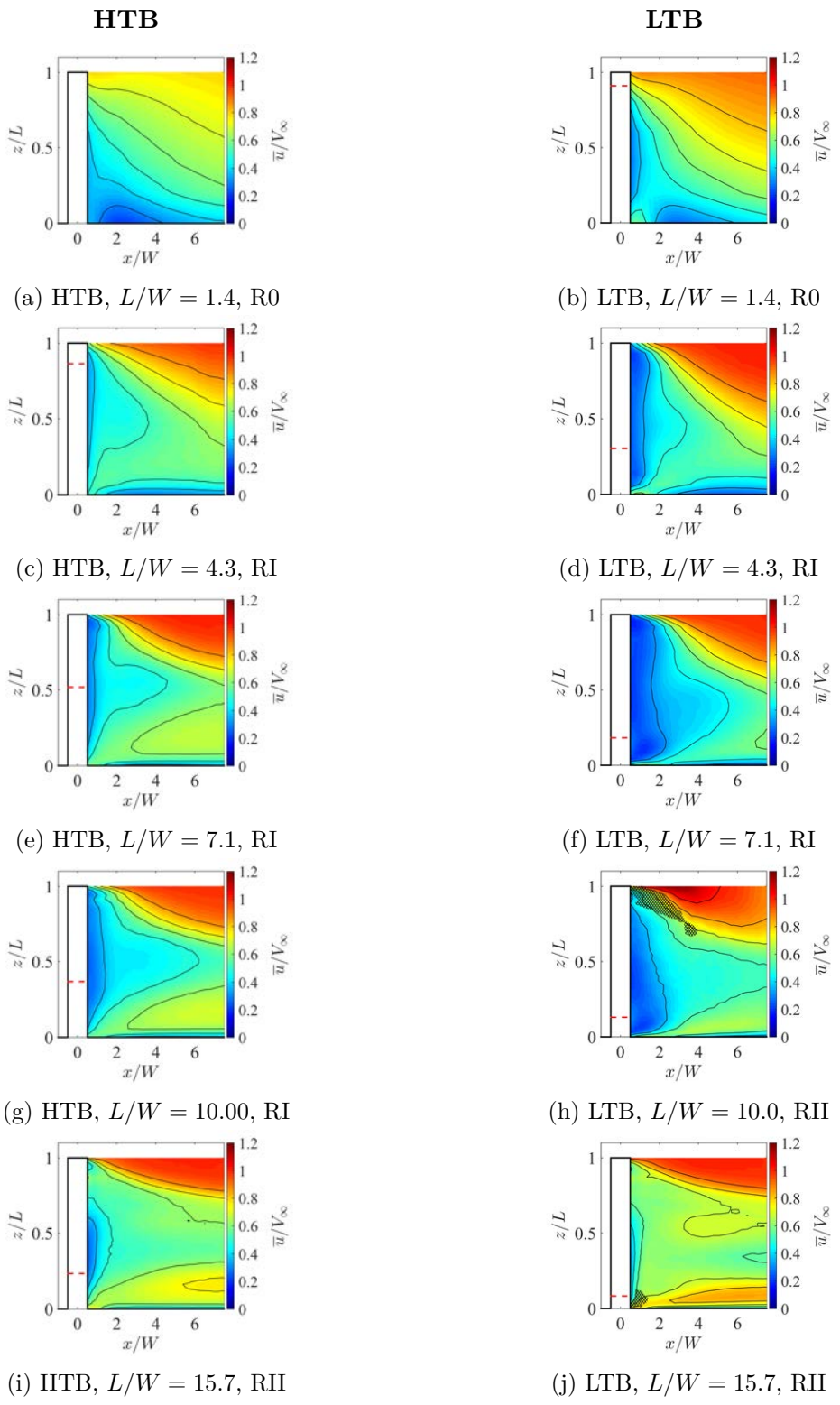

(a) HTB, $L/W = 1.4$, R0

(b) LTB, $L/W = 1.4$, R0

(c) HTB, $L/W = 4.3$, RI

(d) LTB, $L/W = 4.3$, RI

(e) HTB, $L/W = 7.1$, RI

(f) LTB, $L/W = 7.1$, RI

(g) HTB, $L/W = 10.00$, RI

(h) LTB, $L/W = 10.0$, RII

(i) HTB, $L/W = 15.7$, RII

(j) LTB, $L/W = 15.7$, RII

Figure 6.9: Colourmaps showing the mean velocity contours in the wake of select aspect ratio FWMCs in the HTB (left) compared with those measured in the LTB (right) measured using a hot-wire. The relative heights of the boundary layers are indicated by the dashed red line for each case. The plane of the hot-wire measurements was $y/W = 0.6$. Regions where the hot-wire measured the turbulence intensity $T.I. > 0.3$ are cross hatched.

ratio, the LTB and HTB cases have equivalent downwash because the free-end flow becomes fully decoupled from the junction. At $L/W = 21.4$ the downwash of FWMCs

in the HTB reduces; however, this is attributed to the relatively large drift error in the hot-wire measurements at $L/W = 21.4$ in the HTB case (see Section 3.2.5).

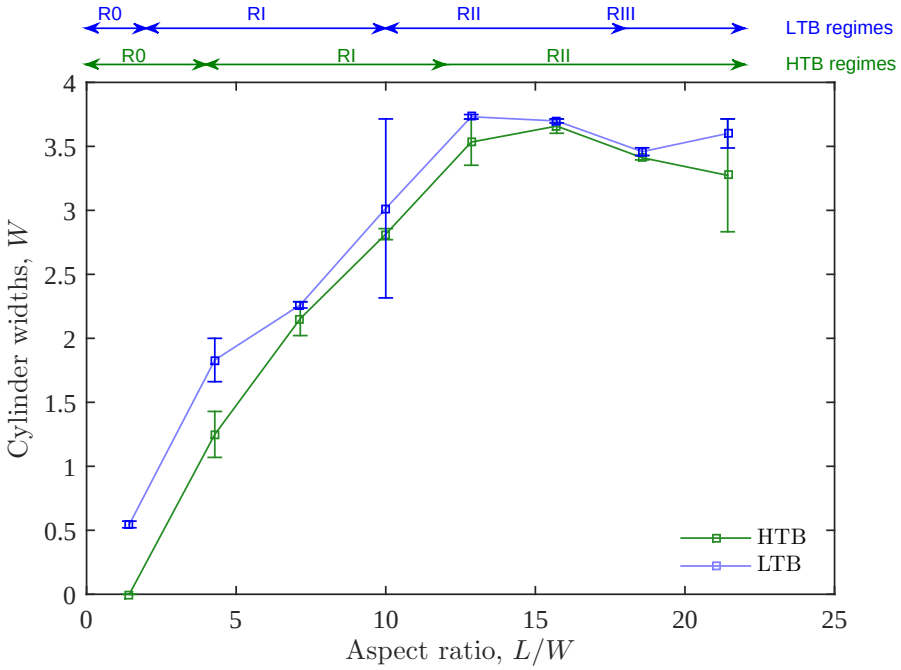

Figure 6.10: The number of cylinder widths below the free-end at $x/W = 6$ where the mean velocity of cylinders in the HTB (green) and LTB (blue) reaches 80% of the free-stream value.

Lower downwash explains why shedding regime RII is shifted to higher aspect ratios (from $L/W = 10$ in the LTB to $L/W = 12$ in the HTB). Section 5.6.3 discussed that cellular shedding will only occur if two conditions are met: (1) A variation in cylinder wake properties exists along the cylinder span and (2) the cylinder is long enough so that spanwise coupling (which is enhanced by spanwise flow) is weak. For a given aspect ratio in the LTB in RII, the aspect ratio is high enough and downwash large enough that the vortices near the free-end are retarded sufficiently from those near the mid-span to cause an independent cell of lower frequency vortex shedding. In these cases, secondary flow over the free-end dominates the wake only in a confined region near the free-end. For lower aspect ratios, secondary free-end flow and primary mid-span vortex flow are coupled because the cylinder is short. Combined with lower downwash at lower aspect ratios, only a single cell forms. Now consider the situation of an FMWC with a span just long enough so that it sheds with two spanwise cells in the LTB, e.g., $L/W = 10.5$. When the plate boundary layer height is substantially increased, downwash from the free-end is reduced. This reduces the spanwise gradient in wake conditions, i.e., the spanwise variation in convection velocity. In this situation free-end cellular shedding ceases because Condition 1 is not met (even though Condition 2 might be met). When the aspect ratio increases to say $L/W = 13$, downwash increases so Condition 1 is met, and cellular shedding occurs. This is the mechanism through which cellular shedding is delayed to higher aspect ratios in the HTB.

For $L/W < 12$, a reduction in downwash is accompanied by an increase in upwash near the junction. Figure 6.11 compares the magnitude of the local maximum in the velocity profile near the junction region at $x/W = 6$. As observed qualitatively, the

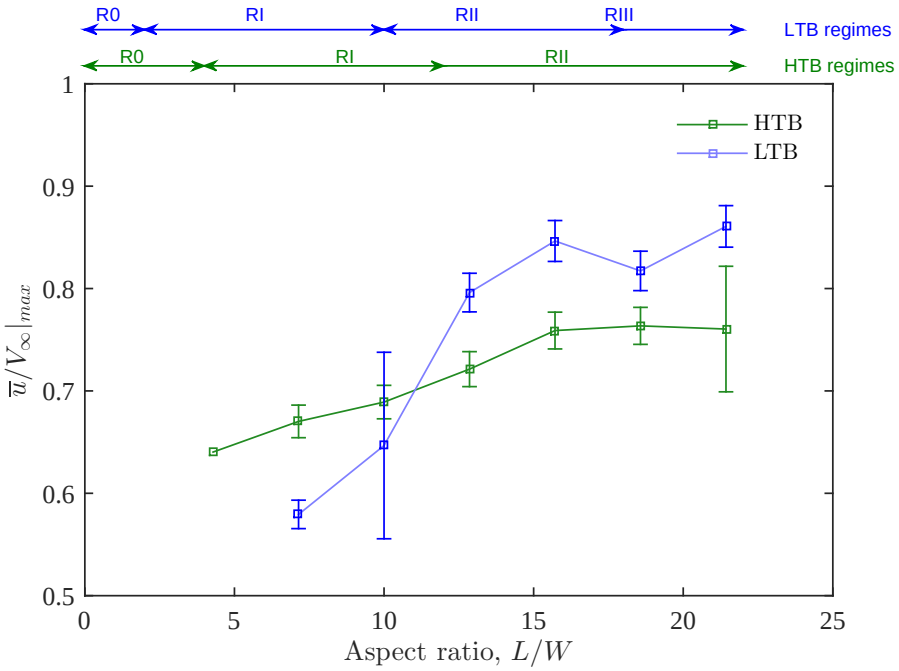

Figure 6.11: The magnitude of the local maximum of the mean velocity profile at $x/W = 6$ near the junction for FWMCs in the HTB (green) compared with the LTB (blue) as the aspect ratio increases.

magnitude of the upwash for $L/W < 12$ is greater for FWMCs in the HTB compared with in the LTB. However, upwash for FMWCs in the LTB appears to increase rapidly after the transition from RI to RII at $L/W = 12$. While the upwash steadily increases with aspect ratio in the HTB case, there is no rapid increase in upwash after transitioning from RI to RII as there is for FWMC in the LTB at $L/W = 10$. As a result, FWMCs in the LTB experience greater levels of upwash than those in the HTB for $L/W \geq 12.9$.

Higher upwash and lower downwash are observations also found by Hosseini et al. (2013) and Wang et al. (2006) when comparing FWMCs with $L/W<8$ in high and low boundary layers. In these studies, the FWMCs shed vortices with a single frequency regardless of the boundary layer height and hence were in RI for both high and low boundary layers. Hosseini et al. (2013) showed that the higher velocity gradient in the plate boundary layer rotates the lower portion of the initially vertical spanwise vortex in the streamwise direction to create streamwise vorticity, with a sense of rotation that entrains fluid into the wake, increasing upwash. Wang et al. (2006) showed that the increased mass flux from the junction to the mid-span of the cylinder raises the position of the saddle point in the wake where the downwash clashes with the upwash. Bourgeois (2012) also shows that the higher upwash promotes greater mass flux toward the cylinder back face. This reduces the base pressure of the FWMC and therefore reduces the downwash entrained into the wake due to the pressure difference between the free-stream and cylinder base.

Here it becomes useful to classify the impact of the boundary layer on FWMCs in RI as either *localised* or *non-localised*. The term *localised* is used to described boundary layer effects confined to that part of the FWMC that lie in the boundary layer while *non-localised* effects are used to describe secondary consequences of *localised* effects that impact the entire cylinder. For example, the added streamwise rotation of vortex filaments

due to the higher velocity gradient in the HTB is a localised effect. A non-localised effect is that the downwash is indirectly reduced. Because of this, the shedding regimes are shifted to higher aspect ratios. This makes it possible for the non-localised effect of the boundary layer to be experienced at aspect ratios where the free-end lies over 10 diameters from the edge of the boundary layer.

The studies by Hosseini et al. (2013) and Wang et al. (2006) have both only focused on cylinders in RI ($L/W < 10$). To date, there has been no study other than the present one that has varied the boundary layer height for FWMCs in RII or RIII where cellular shedding occurs ($L/W > 10$). Figure 6.11 shows that upwash for cylinders in RII in the HTB ($L/W > 12$) has a lower magnitude than in the LTB, the reverse of what was observed for lower aspect ratio cylinders for $L/W \leq 10$. These observations are supported by the acoustic results presented in Section 6.2. Figures 6.4 and 6.5 demonstrate that in the LTB, P2 reaches a two-dimensional state rapidly after it is formed at $L/W = 10$, indicating that the base pressure at the mid-span of the cylinder is decreasing. Figure 6.11 shows that for the LTB case, as soon as P2 forms the upwash rapidly increases. This upwash is hypothesised to be not be caused by a streamwise rotation of the vortex filaments like it was in RI, but rather an entrainment mechanism due the large pressure difference between the base of the cylinder and the free-stream. This is a similar mechanism that causes downwash to occur, but requires a much higher pressure difference because of the stabilising influence of the base plate. In the HTB, the upwash flow is not enhanced to the same degree as it is in the LTB during the analogous period. This is because of the restricted ability of the mid-span to rapidly attain a two-dimensional state. As a result, at a given aspect ratio, the pressure difference between the free-stream and cylinder base is lower. Additionally, the HTB contains more low momentum fluid close to the junction plate of the cylinder when compared with the LTB, so any fluid that is entrained has a low velocity because it is drawn from deep within the boundary layer. These two factors contribute to lower upwash for higher aspect ratio FWMCs in the HTB.

6.3.2 Turbulence intensity maps

In Section 6.2, it was observed that the shedding regimes were shifted to higher aspect ratios as a consequence of the heightened boundary layer. The results presented in this section show that the turbulent profiles of the wakes of FWMCs in the LTB and HTB are similar provided that the FWMCs are in the same shedding regime.

Figure 6.12 compares colourmaps of the wake turbulence intensity for various aspect ratio FWMCs in the HTB (on the left) and the LTB (on the right). The turbulence intensity maps of the HTB show that cylinders with a higher aspect ratio in the HTB have similar turbulent wake structures when compared with cylinders of lower aspect ratio in the LTB. This is most evident when comparing the turbulent intensity maps of $L/W = 4.3$ in the HTB with $L/W = 1.4$ in the LTB. In both cases there are two concentrations of high turbulence production, one near the junction at $z/L \approx 0.1$ at $x/W \approx 1$ and one near the free-end at $z/L \approx 0.9$. With increasing aspect ratio, the FWMCs in both boundary layer cases experience the same sequence of changes. That is, the peak turbulence at the cylinder mid-span begins to move downstream from the cylinder back face. This is quantified in Figure 6.13, which compares the formation length

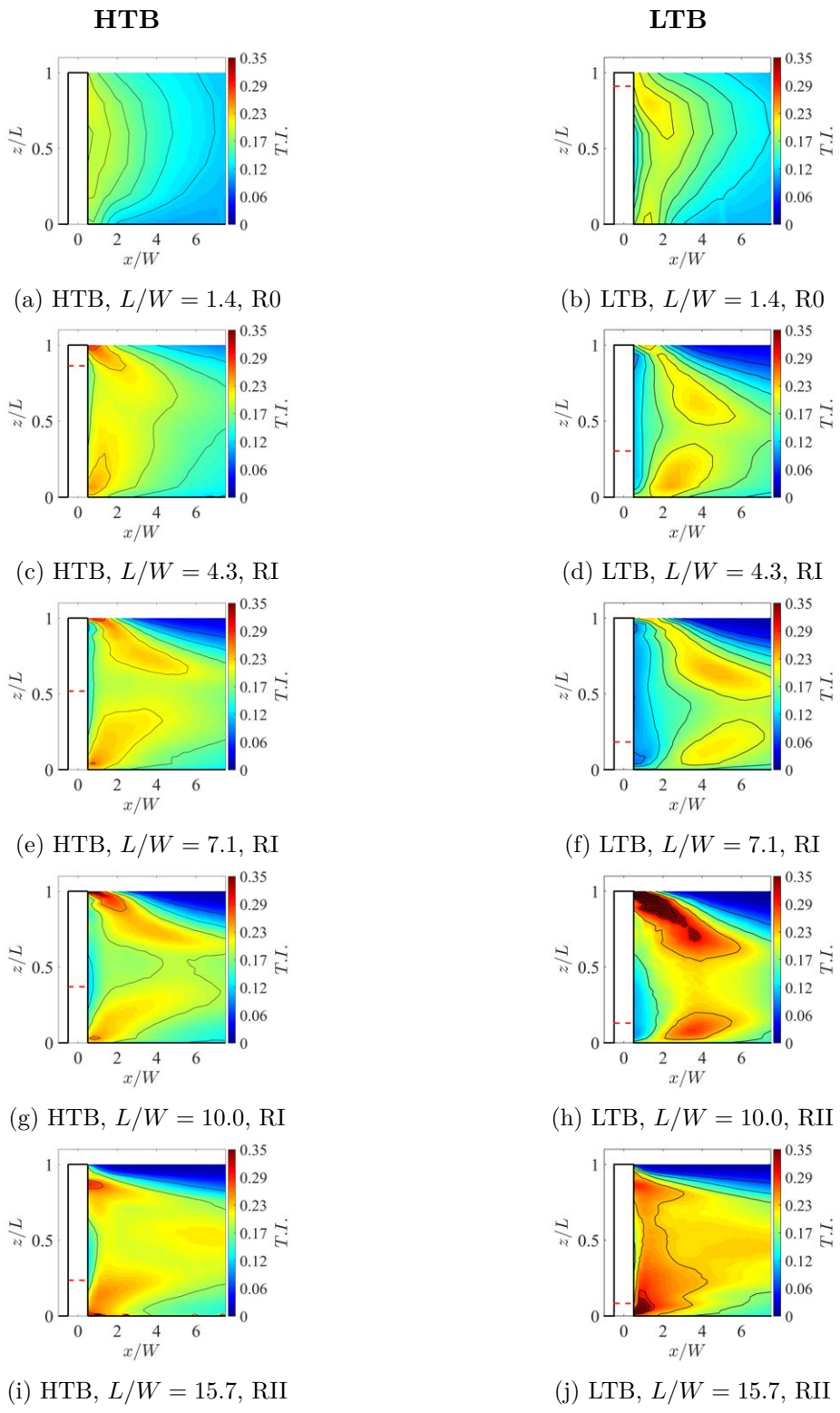

(a) HTB, $L/W = 1.4$, R0

(b) LTB, $L/W = 1.4$, R0

(c) HTB, $L/W = 4.3$, RI

(d) LTB, $L/W = 4.3$, RI

(e) HTB, $L/W = 7.1$, RI

(f) LTB, $L/W = 7.1$, RI

(g) HTB, $L/W = 10.0$, RI

(h) LTB, $L/W = 10.0$, RII

(i) HTB, $L/W = 15.7$, RII

(j) LTB, $L/W = 15.7$, RII

Figure 6.12: Colourmaps showing the turbulence intensity contours in the wake of select aspect ratio FWMCs in the HTB (left) and the LTB (right). The relative height of the boundary layer for each aspect ratio is indicated by a dashed red line. The plane of the hot-wire measurements was $y/W = 0.6$. Regions where the hot-wire measured the turbulence intensity $T.I. > 0.3$ are cross hatched.

(defined as the first point downstream where a local maximum turbulence intensity occurs) at the mid-span of the cylinder for both LTB and HTB cases. The largest extent of this downstream migration occurs at $L/W = 7.1$ in the LTB and $L/W = 10$ in the HTB. In

Chapter 5 it was explained that the maximum influence of the downwash is felt at the mid-span of the cylinder during the point of maximum formation length. In the LTB this leads to a reduction in the magnitude of P1 at $L/W = 7$, while the influence on the wake is milder in the case of the HTB, and so the magnitude of P1 plateaus instead of reducing (Figure 6.4b).

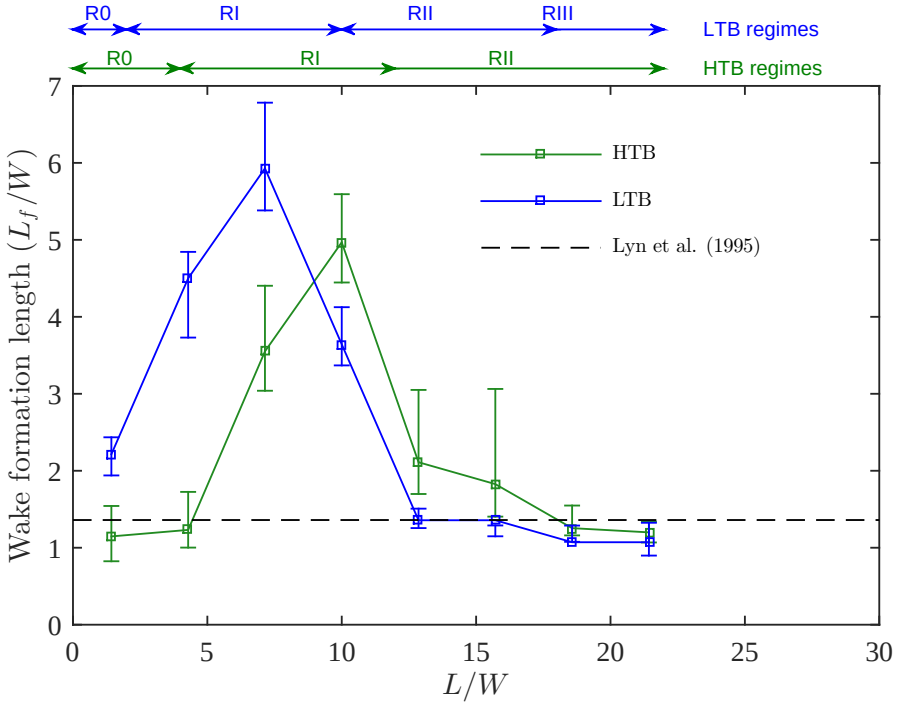

Figure 6.13: The variation of the wake formation length in the mid-span of FWMCs in the HTB (green) with aspect ratio. The results compared with that measured in the LTB (blue).

One of the key differences between the turbulence intensity maps for FWMCs in the HTB compared with those in the LTB is that the turbulence concentration at the junction of FWMCs in the HTB in RI ($4 < L/W < 12$) appear to be located much closer to the base of the cylinder. This is caused by the added streamwise rotation of the vortex filaments in the HTB as they are formed (Hosseini et al. 2013). The added streamwise rotation causes the increased upwash observed in Figure 6.11. For cylinders with higher aspect ratios, i.e., $L/W = 15.7$, there does not appear to be any difference in the downstream location of the turbulence intensity concentrations suggesting that similar levels of streamwise rotation are occurring in both boundary layer cases. The fact that higher levels of upwash are observed for FWMCs in the LTB for these higher aspect ratios confirms that a different upwash mechanism must occur between the two boundary layer cases.

In fact, the turbulence intensity production is much higher in the LTB case than in the HTB case at higher aspect ratios (e.g. $L/W = 15.7$ in Figure 6.12). This result is consistent with what was observed for the behaviour of the magnitude of the P2 acoustic tone in Section 6.2. In Figure 6.4c, the magnitude of P2 in the HTB is measured to be consistently lower than that of P2 in the LTB. Since P2 is correlated with periodic turbulence production near the mid-span and junction of the cylinder, these results confirm that weaker vortex shedding occurs at the junction of FWMCs in the HTB.

6.3.3 Fluctuating components of velocity

Figures 6.14 and 6.15 decompose the velocity fluctuations in the wake of various aspect ratio FWMCs in the HTB into their frequency components (as the autospectral density) and map how these components evolve downstream of the cylinder. In these maps, the ordinate axis is the normalised height of the cylinder, z/L, the abscissas axis is the frequency expressed as Strouhal number, $St = fW/V_\infty$, and the colour denotes the Power Spectral Density of the velocity fluctuations in dB/Hz re. 20μm/s. Along with the autospectral density, Figures 6.16 and 6.17 map the spatial evolution of the coherence, γ^2_{xy}, between the velocity fluctuations and the acoustic pressure measured by the single microphone, located 0.5 m directly above the FWMC.

No spectral peak is evident in the map for $L/W = 1.4$. Instead, low frequencies contain high levels of energy that gradually decay as the frequency increases and as the measurement position moves farther downstream. For this aspect ratio cylinder the coherence maps demonstrate that there is little to no coherence of the velocity fluctuations with the acoustic pressure. For low aspect ratio FWMCs immersed deep within the HTB, vortex shedding is truly suppressed. Unlike the $L/W = 1.4$ FWMC in the LTB, no periodic structure is generated and no tonal noise is produced. The noise that is detected is solely the result of interaction of turbulence in the boundary layer with the cylinder creating a broadband hump at $St = 0.4$.

For cylinders not in R0 ($L/W > 4$), the maps of the velocity fluctuations show a strong peak around $St \approx 0.1$ depending on the aspect ratio. The exact frequency of the spectral peak varies with aspect ratio according to Figure 6.5. This confirms that periodic structured vortex shedding is occurring in the wake of these FWMCs. The coherence maps for these cylinders (in Figures 6.16 and 6.17) show that these periodic components are the dominant sources of noise at the microphone location.

The map for the FWMC with $L/W = 4.3$ in the HTB shows a strong similarity with that of $L/W = 1.4$ in the LTB. Again this is due to the shift in regime boundaries caused by the change in boundary layer. Strong vortex shedding first develops in the lower half of the cylinder at $St = 0.09$. In both the velocity and coherence measurements, the fluctuating energy at $St = 0.09$ migrates up the span of the cylinder as the measurement station moves downstream. Like the analogous cylinder in the LTB, this is due to the downstream tilting of the vortex filament near the free-end of the cylinder.

The fluctuating velocity map for $L/W = 7.1$ in Figure 6.14c shows very strong similarities with the $L/W = 4.3$ fluctuating velocity map in the LTB in Figure 5.21c. Periodic velocity fluctuations first develop near the junction inside of the boundary layer at $x/W = 1.07$. Close to the cylinder, the highest coherence is measured inside the boundary layer, but moderate levels of coherence are still measured outside of the boundary layer (see Figure 6.16c), despite there being relatively low magnitudes of velocity fluctuations (see Figure 6.14c). Moving downstream, stronger periodic velocity fluctuations with increasing coherence develop outside of the boundary layer in this region. The fluctuations outside of the boundary layer eventually meet those inside of the boundary layer at $z/L = 0.6$ and $x/W = 4$ as each respectively migrates towards the mid-span downstream. The fluctuations form a single 'cell' of vortex shedding across the span. Very similar behaviour is observed for the $L/W = 10$ FWMC. Surprisingly, at

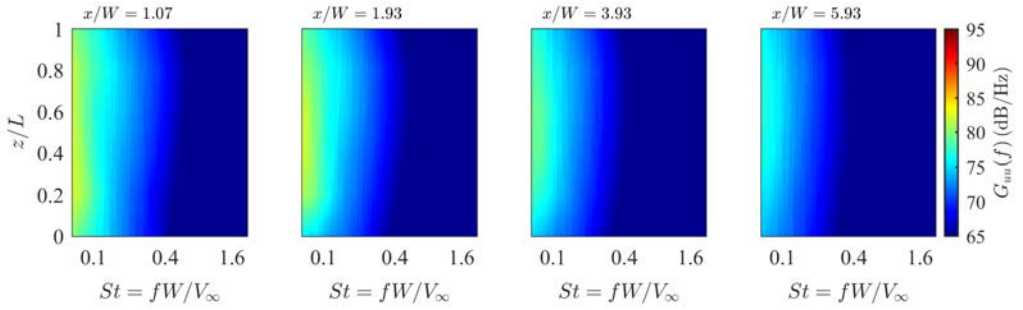

(a) $L/W = 1.4$, R0

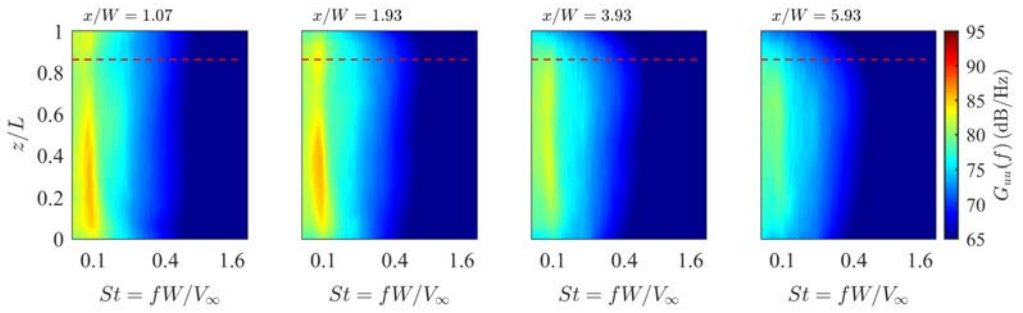

(b) $L/W = 4.3$, RI

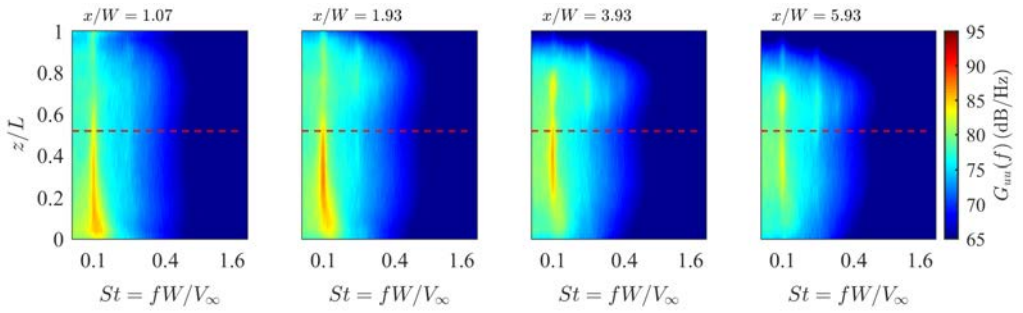

(c) $L/W = 7.1$, RI

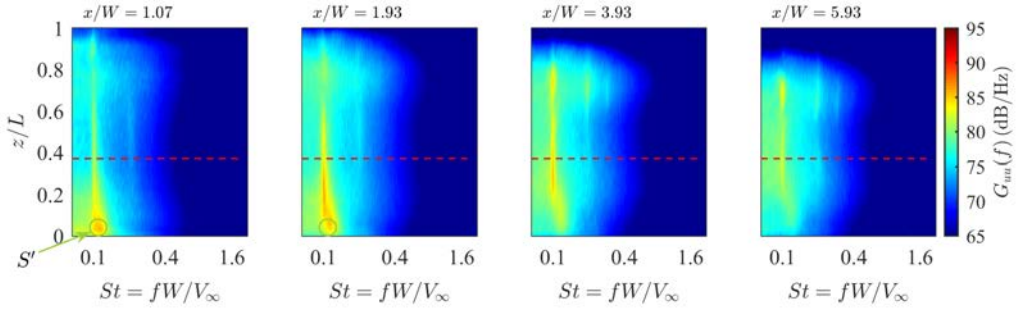

(d) $L/W = 10.0$, RI

Figure 6.14: Spectral maps of the streamwise velocity fluctuations, $G_{uu}(f)$, at various downstream stations for FWMCs in the HTB with aspect ratios (a) $L/W = 1.4$, (b) $L/W = 4.3$, (c) $L/W = 7.1$, (d) $L/W = 10$. The values are expressed in dB/Hz re. 20μm/s.

these aspect ratios, the heightened turbulence intensity inside of the boundary does little to prevent the periodic formation of vortex shedding, except possibly very close to the cylinder-wall junction, where the bandwidth of the signal increases and the coherence reduces. Once again, this demonstrates that the close proximity of the upwash at the junction, downwash near the free-end and primary flow at the mid-span stabilise the vortex shedding process through strong spanwise coupling. This stability is strong enough

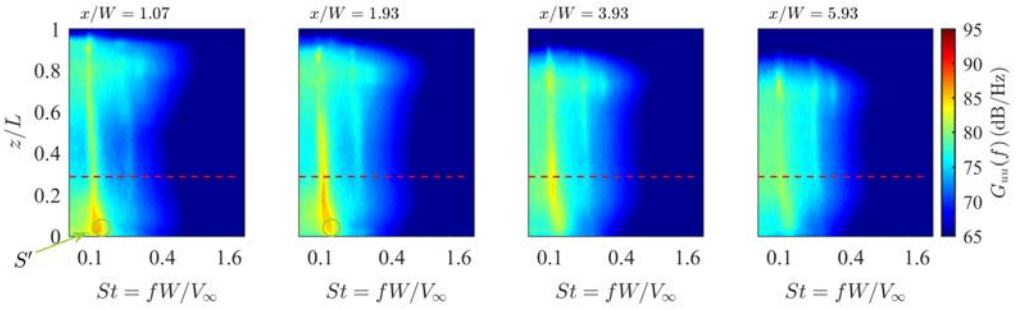

(a) $L/W = 12.9$, RII

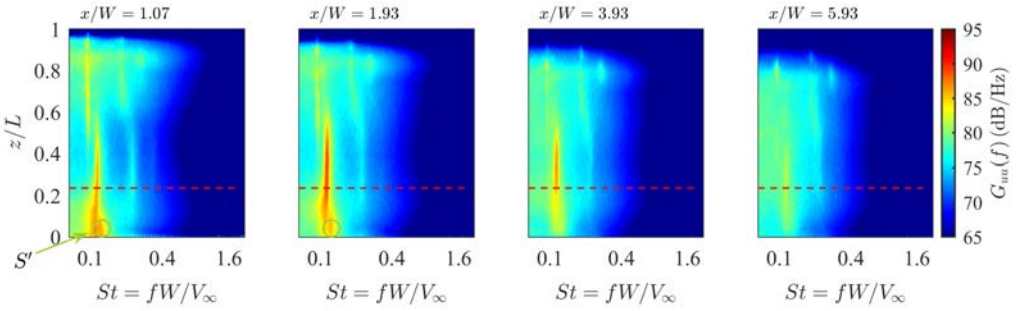

(b) $L/W = 15.7$, RII

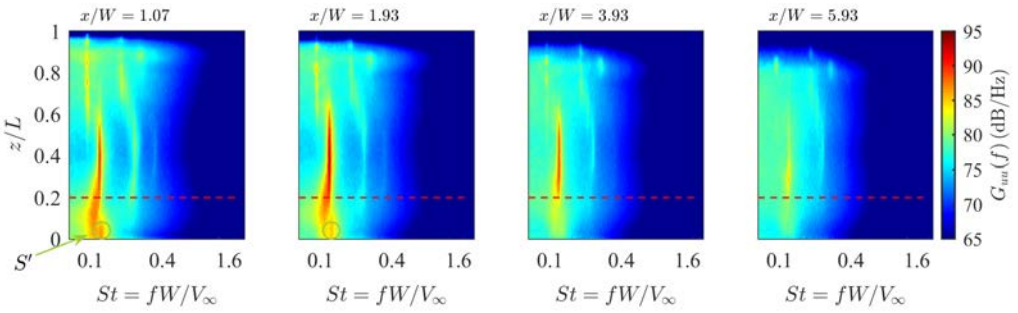

(c) $L/W = 18.6$, RII

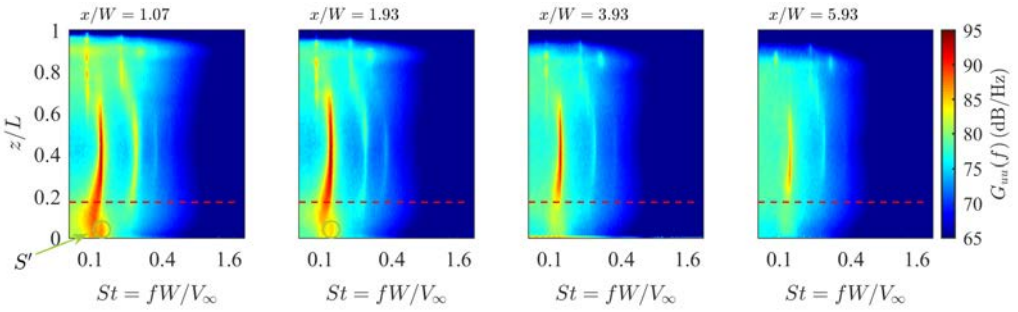

(d) $L/W = 21.4$, RII

Figure 6.15: Spectral maps of the streamwise velocity fluctuations, $G_{uu}(f)$, for FWMCs in the HTB with aspect ratios (a) $L/W = 12.9$, (b) $L/W = 15.7$, (c) $L/W = 18.6$, (d) $L/W = 21.4$. The values are expressed in dB/Hz re. 20μm/s.

to overcome the disrupting, localised effects of the boundary layer.

For FWMCs with $L/W > 12.9$ (in RII), the mid-span of the cylinder lies above the boundary layer. The velocity spectral maps in Figure 6.15 show that at the mid-span of these FWMCs, a sharp spectral peak occurs at $St \approx 0.125$. The magnitude of this signal is low at $L/W = 12.9$, but increases with aspect ratio. The coherence maps in Figure 6.16 show that this signal is coherent with the tone that causes P2. These cylinders also

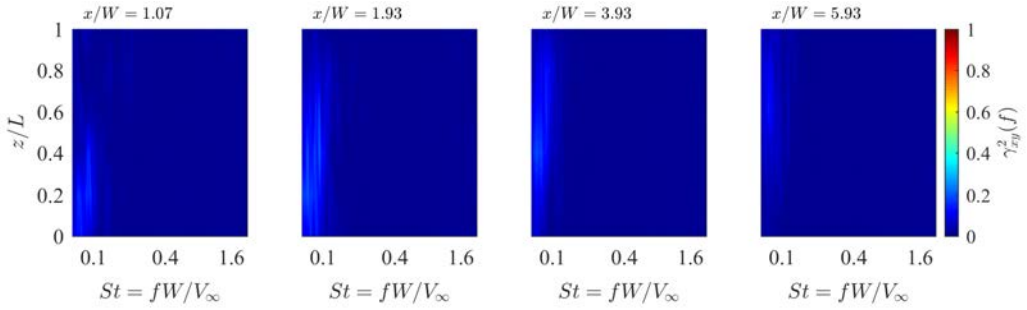

(a) $L/W = 1.4$, R0

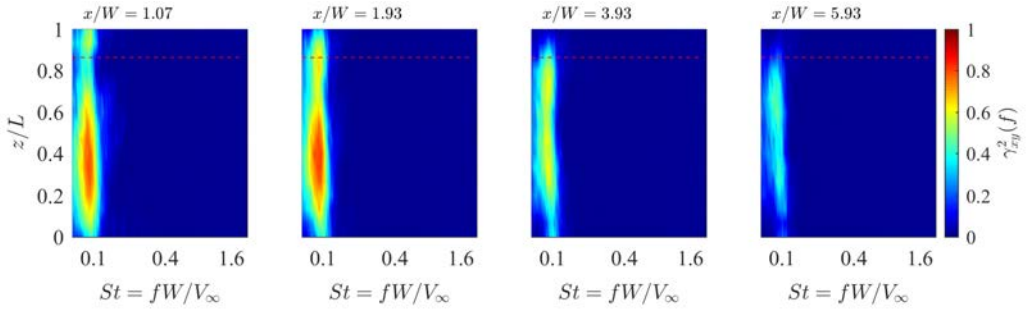

(b) $L/W = 4.3$, RI

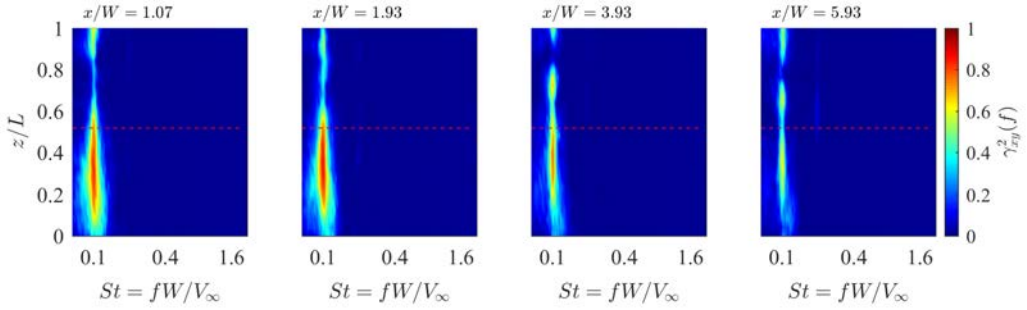

(c) $L/W = 7.1$, RI

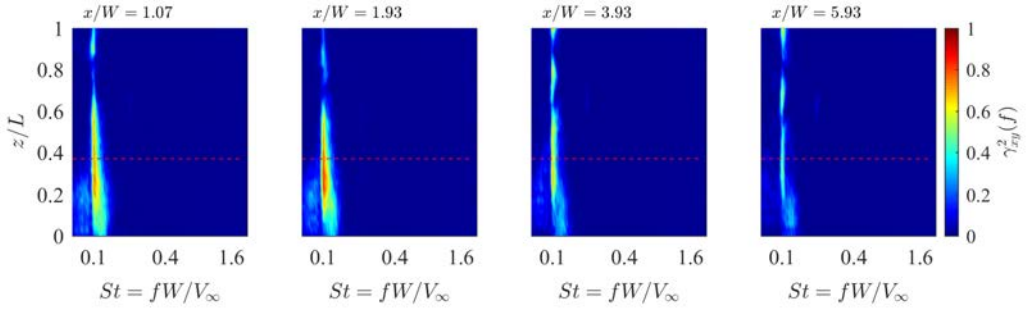

(d) $L/W = 10.0$, RI

Figure 6.16: Spectral maps of the magnitude squared coherence, $\gamma^2_{xy}(f)$, between wake velocity fluctuations and the acoustic pressure measured by a single microphone 0.5 m directly above the FWMC at various downstream stations for FMWCs in the HTB with aspect ratios (a) $L/W = 1.4$, (b) $L/W = 4.3$, (c) $L/W = 7.1$, (d) $L/W = 10$. The dotted red line denotes the height of the boundary layer, δ, relative to the span of the FWMC.

shed with a free-end cell that generates P1. At $z/L \approx 0.6$, there is a discrete frequency jump to a lower frequency, indicating the beginning of the free-end cell that generates P1. The cell boundary occurs at the same spanwise position ($z/L \approx 0.6$) in both the HTB and the LTB. In this regard, the dynamics of the free-end cell for FWMCs in the HTB (where it occurs) is very similar to that observed in the LTB, which is consistent with

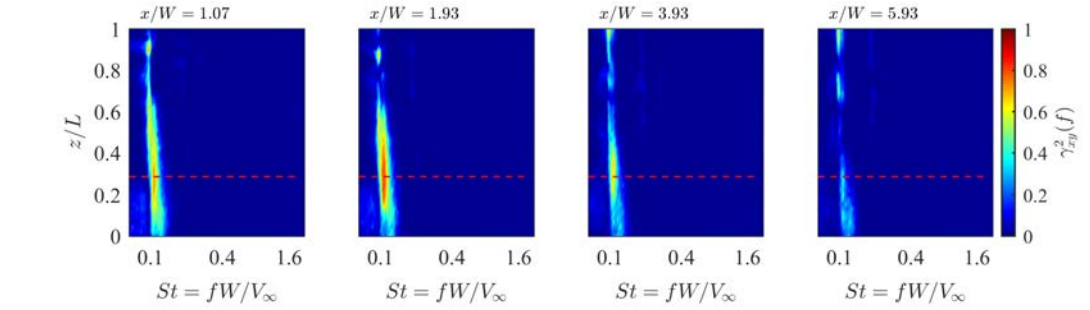

(a) $L/W = 12.9$, RII

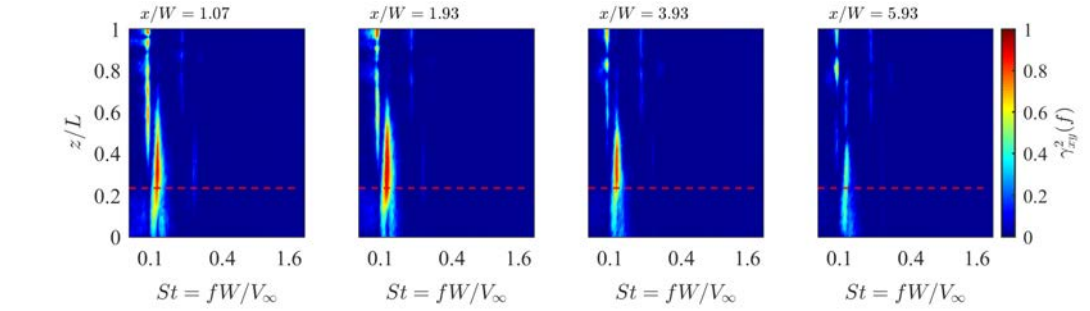

(b) $L/W = 15.7$, RII

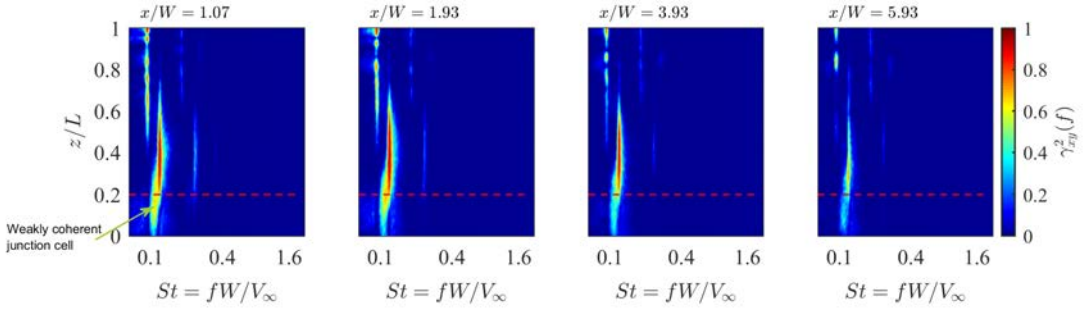

(c) $L/W = 18.6$, RII

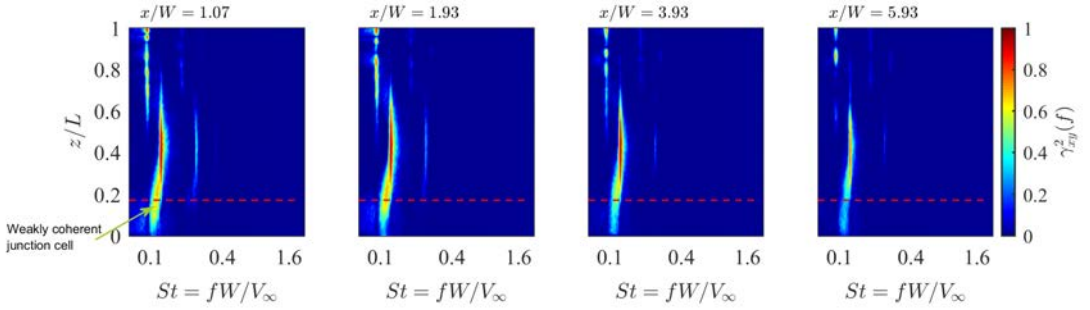

(d) $L/W = 21.4$, RII

Figure 6.17: Spectral maps of the magnitude squared coherence, $\gamma^2_{xy}(f)$, between wake velocity fluctuations and the acoustic pressure measured by a single microphone 0.5 m directly above the FWMC at various downstream stations for FMWCs in the HTB with aspect ratios (a) $L/W = 12.9$, (b) $L/W = 15.7$, (c) $L/W = 18.6$, (d) $L/W = 21.4$. The dotted red line denotes the height of the boundary layer, δ, relative to the span of the FWMC.

the acoustic observations made in Section 6.2.

The effect of the HTB on the spectral content of the velocity fluctuations in the wake of FWMCs in RII ($L/W > 12$) is more profound near the junction. Unlike the free-end, at these higher aspect ratios, the flow is heavily disrupted within the boundary layer.

The velocity maps show that vortex shedding near the junction has a wider bandwidth and lower magnitude than in the LTB (for example the velocity maps of $L/W = 12.9$ and $L/W = 15.7$ in Figures 6.15a and 6.15b). The coherence measurements show that velocity fluctuations in this region (see Figures 6.17a and 6.17b) for these aspect ratios are weakly coherent with the acoustic pressure measured by the microphone. There is also evidence of an additional signal, called S', that occurs at frequencies of $St \approx 0.125$ deep in the boundary layer and is also weakly coherent with the acoustic pressure fluctuations. The signal S' will be discussed at the end of this section.

The combination of high bandwidth and low coherence suggests that vortices formed from that part of the FWMC immersed in the boundary layer have a high degree of intermittency. As Ross et al. (2008) explain, the heightened variability of the approach speed and turbulent scales in the HTB acts to significantly modulate the vortex shedding frequency and amplitude creating this intermittency, in a localised boundary layer effect. This localised effect, however, influences the immediate region in the wake *above* the boundary layer as a non-localised effect. Mutual coupling between the disturbed flow in the boundary layer and the undisturbed region above of the boundary layer act to reduce the spanwise correlation and heighten the intermittency in the undisturbed region, resulting in a reduced rate of increase of in magnitude of P2 from $12 < L/W < 18$. This non-localised effect also continues to the highest aspect ratio tested and is the reason why the magnitude of P2 in the HTB is constantly 3 dB lower than that in the LTB for $L/W > 20$, as observed in Figure 6.4c.

Figures 6.17c and 6.17d show that for $L/W \geq 18$, a weakly coherent third junction cell forms, indicated in the figures. The span over which the junction cell occurs, from $0 < z/L < 0.2$, is very similar to that of the junction cell in the LTB for $L/W \geq 18$. The frequency with which this cell occurs ($St \approx 0.107$) is slightly lower than that in the LTB ($St \approx 0.114$). Its weak coherence with the acoustic pressure suggests that the junction cell also forms intermittently, which is why a third spectral peak is not observed in the acoustic spectrum. These observations suggest that when the aspect ratio is sufficiently high ($L/W \geq 18$), a junction cell will occur, regardless of the boundary layer type. However, the frequency, strength and continuity of this junction cell is obviously affected by the presence of a different boundary layer thickness.

The discovery of a weak third junction cell in the presence of the HTB provides more insight into the nature of the junction cell and suggests that it is an inherent part of FWMC flow. In the LTB, a junction cell forms because three-dimensional flow at the junction of the cylinder disturbs the lower portion of the nominally two-dimensional vortex filament, creating two separate regions of vortex shedding. The discussion in Section 5.6 postulated two necessary conditions for the formation of a junction cell separate to the mid-span cell. The first condition (Condition 1) is that the retarding influence of the three-dimensional flow near the junction must be sufficiently high to create a large enough difference in wake properties between the junction and the mid-span. The second condition (Condition 2) is that the aspect ratio must be sufficiently high to reduce spanwise coupling of vortex flow at the junction and the mid-span regions. Before entering RIII, the FWMCs in the LTB undergo two aspect ratio ranges; (1) a range between $10 < L/W < 14$, where the magnitude of P2 rises rapidly as it attains two-dimensionality and (2) a transitional range between $L/W = 14$ to 17, where the

magnitude of P2 plateaus (see Figure 6.4c). During the first period, the upwash also increases rapidly as the pressure difference between the free-stream and the FWMC base increases, which progressively retards the flow. Thus, at $L/W = 14$, Condition 1 is met. However, Condition 2 is not met since the aspect ratio is low enough to allow the three-dimensional effects of the junction to couple vortex shedding at with the mid-span. Thus during the second period, further increases in aspect ratio result in a plateau of the Aeolian tone level as the spanwise coupling and heightened three-dimensional interaction reduces correlation across the span. When the aspect ratio increases above $L/W = 18$, Condition 2 is met and two separate cells form, one at the junction that contains the effect of the highly retarded flow and one at the mid-span which is 'two-dimensional'.

For FWMCs in the HTB in RII ($L/W > 12$), the mid-span does not reach two-dimensionality as rapidly as those in the LTB in RII ($10 < L/W < 18$). This is because of the non-localised boundary layer influence described above. As a result, upwash is not as rapidly enhanced during this period (although it still increases). This means that at $L/W = 14$, neither Condition 1 nor Condition 2 are met. Since Condition 1 is not met, the magnitude of P2 rises steadily with aspect ratio.

When $L/W = 18$, Condition 2 is met. Additionally, the HTB contains a much larger range of turbulent scales that vary stochastically in time over a larger portion of the cylinder. Therefore, there will be intermittent periods when Condition 1 is met creating an intermittent junction cell with weaker coherence with the acoustic pressure. This junction cell occurs at a slightly lower frequency presumably because the mid-span cell also sheds with a lower frequency and because of the lower velocity in the boundary layer. During periods of time when Condition 1 is not met, the localised disruptive effects of the HTB preclude the existence of a junction cell and reduce the magnitude of P2 below that of the corresponding aspect ratio in the LTB case.

The last point of discussion concerning the fluctuating components of velocity is a secondary signal detected deep in the boundary layer, which is referred to as S'. The signal S' is another facet of FWMC flow in the HTB related to heightened three-dimensional interaction of various elements of the wake and is visible in Figures 6.14d and 6.15 at $x/W = 1.93$ for FWMCs with $L/W \geq 10$. For $L/W \leq 12.9$ (Figure 6.14d) the frequency of S' is close enough to the frequency of the primary signal near the junction so that a merged single broad shedding peak is created close to the junction. For $L/W > 12.9$ (Figure 6.15), the frequency of S' becomes sufficiently higher than that of the primary signal in the junction so that two separate peaks are distinguishable. For these cases, the primary signal is associated with either P2 for FWMCs with $L/W \leq 15.7$ or the weak junction cell (that would generate P3) for FWMCs in the HTB with $L/W \geq 18$. Figure 6.18 better illustrates these observations. Here the *Coherent Output Power* (COP) spectrum of the velocity fluctuations with the acoustic pressure for hot-wires placed at $x/W = 1.93$ is shown. The COP spectrum is defined as

$$COP_{xy}(f) = \gamma^2_{xy}(f) G_{xx}(f), \tag{6.1}$$

where $\gamma^2_{xy}(f)$ is the magnitude squared coherence between the two signals $x(t)$ and $y(t)$ and $G_{xx}(f)$ is the autospectral density of signal $x(t)$. In Figure 6.18, the abscissa axis of each sub-figure is the Strouhal number, St, while the ordinate axis is the aspect

ratio of the cylinder, L/W. The colour denotes the magnitude of the COP, expressed as dB/Hz re. 20μPa . Moving from left to right, the location of the hot-wire moves away from the junction plate, as indicated by its relative position in the boundary layer, z/δ. For example, in Figure 6.18a, the hot-wire is located at $x/W = 1.93$ and $z/\delta = 0.15$, 0.54, 1 and 1.30 moving from left to right, where δ is the height of the boundary layer. Additionally, the frequency of each tone, as measured in the acoustic results, i.e., P1, P2 and P3 (where it exists), is overlaid. Figure 6.18a shows the results for cylinders in the HTB, while Figure 6.18b shows the results for cylinders in the LTB.

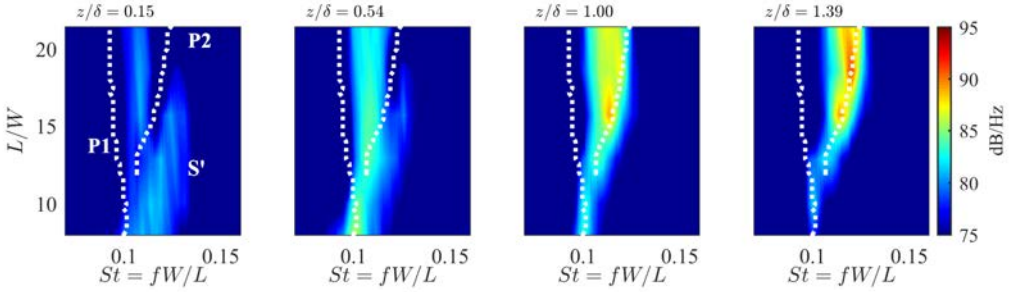

(a) HTB

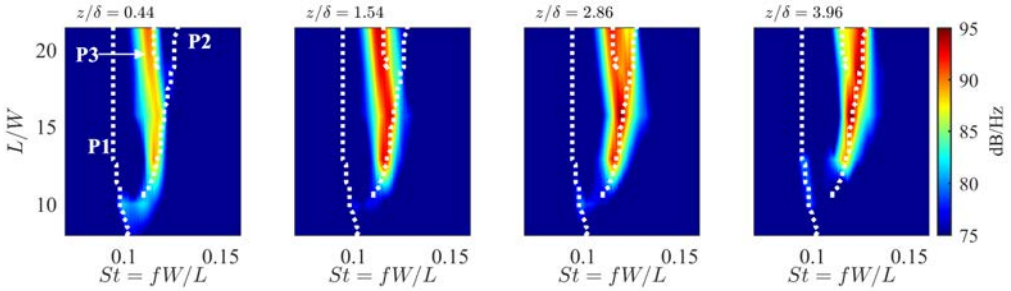

(b) LTB

Figure 6.18: The change of Coherent Output Power spectrum (COP in dB/Hz re. 20μPa) with FWMC aspect ratio between a hot-wire placed at $x/W = 1.93$ and $y/W = 0.6$ and the acoustic pressure measured 0.5 m directly above the FWMC. Moving from left to right, the hot-wire is located at progressively higher spanwise locations (z/L) relative to the height of the boundary.

Figure 6.18a shows that the signal S' is strongest deep in the HTB at z/δ=0.15. Evidently S' has a wide bandwidth and a centre frequency above that of P1. As the aspect ratio increases from $L/W = 7.1$ to $L/W = 15.7$, the centre frequency of S' also increases. At this point in the boundary layer, S' appears to be the velocity signal most coherent with the microphone signal. However, when the aspect ratio increases to $L/W = 18$ and above, where the conditions become favourable for an intermittent third junction cell to form, the COP of S' reduces significantly. In contrast, S' cannot be observed at higher positions in the boundary layer, for example at z/δ=0.54. At this spanwise position, the frequency of the velocity signal that is most coherent with the microphone is either at P1 (for $L/W \leq 10$), P2 (for $12.9 < L/W \leq 15.7$) or the weakly coherent third junction cell that would have been P3 (for $L/W \geq 18.6$). At even higher spanwise stations, the signal most coherent with the microphone is that detected at the mid-span of each aspect ratio cylinder, i.e., either P1 for $L/W \leq 10$ or P2 for $L/W \geq 12.9$.

Figure 6.18b shows that a similar progression of events occur for FWMCs in the LTB

except that S' is not observed. At $z/\delta = 0.44$, the coherent signal is either that which generates P3 (for FWMCs with $L/W > 18$) or that which generates P2 (for FWMCs with $10 < L/W < 18$). Moving away from the plate up the span of the cylinder, the coherent signal at higher aspect ratios gradually shifts from being associated with P3 to being associated with P2. This is because of the hot-wire exiting the third junction cell and entering the mid-span cell.

The structures associated with S' are clearly confined to positions deep within the HTB. Additionally, S' only occurs in the HTB, suggesting that its existence depends on the height of the boundary layer relative to the width of the cylinder. One possible explanation for S' is that it is a signal associated with the interaction of the spanwise vortices with the horseshoe vortex. El Hassan et al. (2015) recently used proper orthogonal decomposition (POD) of PIV data to decompose the flow at the junction of an $L/W = 4$ square FWMC into a series of modes. Junction flow in two boundary layers, a high boundary layer ($\delta/W = 2.56$) and a low boundary layer ($\delta/W = 0.72$), were investigated. In the low boundary layer, the junction flow was dominated by an anti-symmetric mode of shedding. In the high boundary layer, the junction flow was dominated by several modes associated with the complex interaction of the spanwise vortices with the legs of the horseshoe vortex. As a result of these additional interactions, a spectral peak in the velocity fluctuations associated with these modes was not observed. However, while not elaborated upon in the study, one of the less dominant flow modes in the higher boundary layer ('Mode 3') was associated with vortex flow completely free from the influence of the horseshoe vortex. Fourier analysis of this mode resulted in a broad spectral peak at $St \approx 0.12$. It is possible that at higher aspect ratios, $4 < L/W < 18$, this mode begins to become more dominant, thereby generating a broad spectral peak in the velocity fluctuations measured by a hot-wire, S'. The signal is weakly coherent with the microphone signal because the junction region also contains other high energy modes that do interact with the legs of the horseshoe vortex. As the aspect ratio becomes high enough ($L/W > 18$) the conditions become favourable for an intermittent third junction cell. When this occurs, S' reduces in coherence with the acoustic pressure while the coherence of the mode associated with a third junction cell increases.

6.3.4 Coherent phase analysis

Figure 6.19 shows the coherent phase magnitude maps for FWMCs in the HTB with $L/W = 4.3$, 7.1, 10 and 15.7 at the frequency that generates P1 for each case. These maps were generated in the same manner as in Chapter 5 with the coloured regions indicating points in space that are in phase with one another and the black contours denote the magnitude squared coherence levels with the acoustic pressure measured by a microphone 0.5 m directly above the cylinder.

Once again, the $L/W = 4.3$ FWMC shows similarities with its $L/W = 1.4$ counterpart in the LTB. The phase maps show a single vortex filament across the span of the cylinder that inclines downstream at the free-end of the cylinder. The structure is moderately coherent with the acoustic pressure fluctuations measured with the microphone. As discussed, the likely vortex structure is an arch type structure that is connected through the plane of symmetry of the cylinder wake at the free-end.

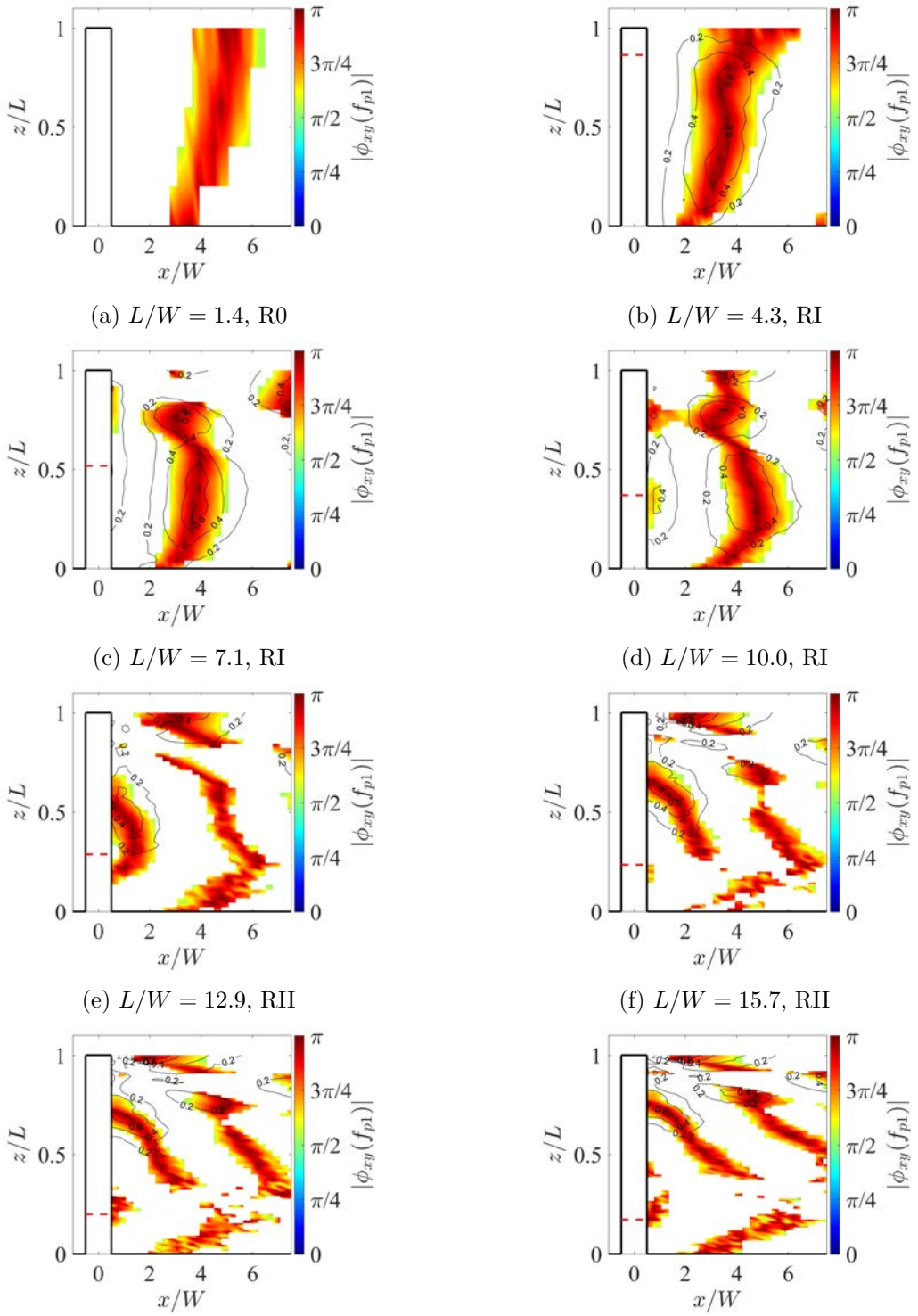

(a) $L/W = 1.4$, R0

(b) $L/W = 4.3$, RI

(c) $L/W = 7.1$, RI

(d) $L/W = 10.0$, RI

(e) $L/W = 12.9$, RII

(f) $L/W = 15.7$, RII

(g) $L/W = 18.6$, RII

(h) $L/W = 21.4$, RII

Figure 6.19: The spatial distribution of phase, $|\phi_{xy}(f_{p1})|$, at the frequency where P1 occurs for FWMCs in the HTB with aspect ratios ranging from (a) $L/W = 1.4$ through (h) $L/W = 21.4$. The colourmaps are restricted to only show $|\phi_{xy}(f_{p1})| = \pi/2$ to π. The contour levels denote those parts of the in-phase structures that are coherent with the acoustic pressure measured with the microphone.

From Figure 6.19c and 6.19d, the FWMCs with $L/W = 7.1$ and 10 show evidence of a looping type vortex structure. As primary vortices at the mid-span are shed alternately they are connected to the anteceding vortex via a cross stream connector strand. Like

the LTB results, the principal core is the dominant source of noise, as it is associated with the highest levels of coherence with the acoustic pressure fluctuations.

At $L/W = 15.7$, the structures associated with P1 are inclined with respect to the cylinder span (see Figure 6.19f). These are similar structures to those found for P1 FWMCs in the LTB with $10 < L/W < 21.4$ (RII and RIII). Like FWMCs in the LTB, the structures show significant deformation downstream from the cylinder. From these results, it can be concluded that P1 in the LTB and P1 in the HTB for cylinders in RII ($L/W > 10$ for FWMCs in the LTB and $L/W > 12$ for FWMCs in the HTB) are generated by the same mechanism.

Figure 6.20 shows the coherent phase magnitude maps for FWMCs in the HTB with $L/W = 12.9$, 15.7, 18.6 and 21.4 at the frequency that generates P2 for each case. As in the LTB, these structures are associated with a classical two-dimensional vortex shedding process at the FWMC mid-span. As expected, the phase maps show a mostly upright structure with high levels of coherence concentrated in the mid-span of the cylinder. There is a breakdown of an organised phase relationship at the free-end of the cylinder, indicating that the structure does not extend to the free-end, consistent with the interpretation that this upright structure is confined to a region in the lower portion of the cylinder. For $L/W \geq 18.6$, a speckled region near the junction forms. This coincides with the formation of the weak, intermittent junction cell. Despite the added intermittency and weaker coherence of the junction cell due to the disruption of the boundary layer, the mid-span cell still cannot penetrate the boundary layer. This is further evidence of the localised disruptive effect of the HTB that prevents 'two-dimensional' shedding within the region engulfed by the boundary layer.

6.3.5 Convection velocity

The convection velocity, u_c (and the associated uncertainty in the convection velocity) was calculated in the same manner as for the LTB case in Section 5.4.6. That is, the phase plots presented in Figures 6.19 and 6.20 were unwrapped and the gradient of the phase difference between the microphone and hot-wire in the downstream (x) direction was estimated using a least squares approach. Those positions where Pearson's correlation coefficient (Bendat and Piersol 2010) between the estimated linear trend and the measured data was less than 0.97 were rejected. The convection velocity was then measured using Equation 5.3.

Figure 6.21 shows the variation of streamwise convection velocity across the span of selected aspect ratio cylinders. The corresponding results obtained in the LTB are shown for reference. The right hand side of each sub-figure shows the frequency of the dominant tone measured at that particular point to illustrate the single and multi-cell shedding behaviour. No data are presented for $L/W = 1.4$ for the HTB case since shedding is suppressed at this aspect ratio.

At high aspect ratios ($L/W \geq 15.7$), the measured convection velocities across the span are similar to those measured at similar aspect ratios in the LTB and generally show the same trends. The convection velocity increases toward the free-end and junction in the mid-span and free-end cells, but this is attributed to the upstream tilting of the vortex filaments, as explained in Chapter 5. At the mid-span, the convection velocity is

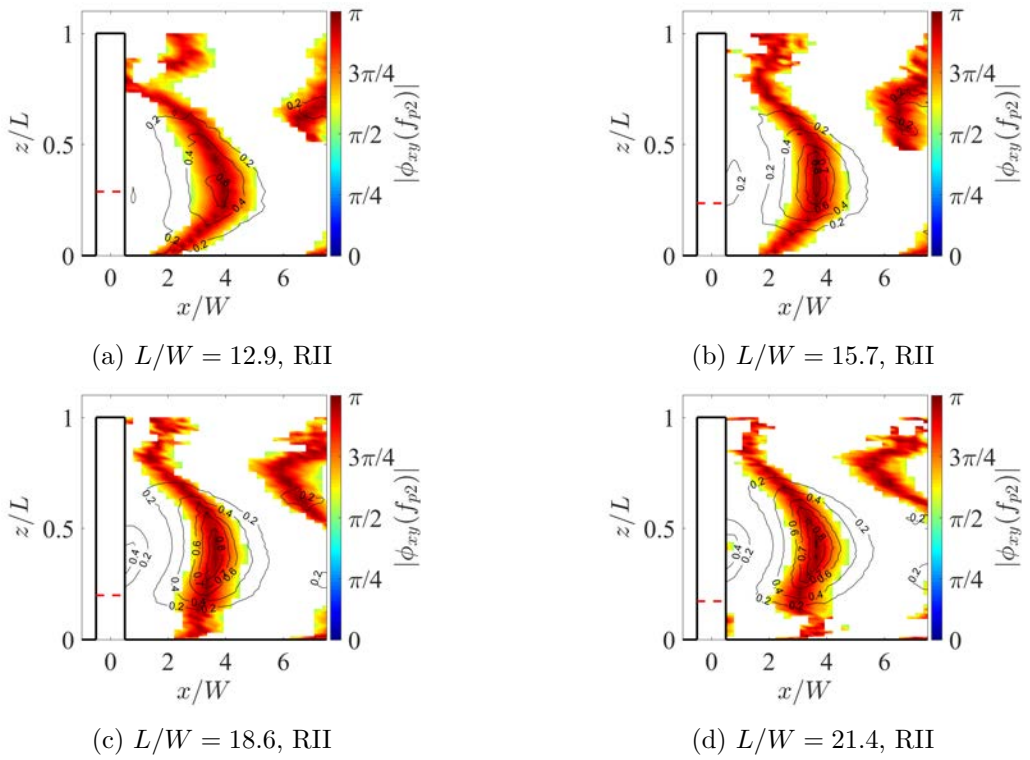

(a) $L/W = 12.9$, RII

(b) $L/W = 15.7$, RII

(c) $L/W = 18.6$, RII

(d) $L/W = 21.4$, RII

Figure 6.20: The spatial distribution of phase, $|\phi_{xy}(f_{p2})|$, at the frequency where P2 occurs for FWMCs in the HTB with aspect ratios ranging from (a) $L/W = 12.9$ through (d) $L/W = 21.4$. The colourmaps are restricted to only show $|\theta_{xy}(f_{p2})| = \pi/2$ to π. The contour levels denote those parts of the in-phase structures that are coherent with the acoustic pressure measured with the microphone.

slightly lower than that of the LTB, at $u_c = 0.45$ compared with $u_c = 0.5$, confirming that vortices at the mid-span of high aspect ratio FWMCs are being retarded more in the HTB than in the LTB. This is despite the fact that in both cases, the mid-span lies well outside of the boundary layer. It is this added interaction that causes the slight reduction in shedding frequency at the mid-span. Toward the junction, u_c in the HTB is lower than u_c in the LTB. This is attributed to the FWMC being immersed in lower momentum fluid in the HTB.

The data are less sparse for FWMCs with $4.3 \leq L/W \leq 12.9$ than the corresponding data for the LTB case (Figure 5.28), largely owing to the increased coherence of vortices from FWMCs with $L/W = 4.3$ and 7.1. The data in Figure 6.21 give more insight into the causes of dual cell behaviour for FWMCs in both the HTB and the LTB. At $L/W = 4.3$, a single cell at $St = 0.1$ forms across the span. Similarly, the convection velocity remains relatively constant across the span at $u_c \approx 0.5$. At $L/W = 7.1$, a single frequency is again detected across the span. In this case, however, the convection velocity is observed to reduce considerably at $z/L = 0.6$ before the data become poorly conditioned. At $L/W = 10$, the same phenomenon occurs, except the difference in convection velocity between the free-end and junction is larger. This is confirmation that during the transition from RI to RII between $7.1 < L/W < 10$, the convection velocity at the free-end becomes lower than that at the junction as the vortices forming at the free-end are retarded by the action of the free-end flow. As the aspect ratio increases and the difference in convection velocity between the free-end and junction becomes too great, spanwise coupling can no

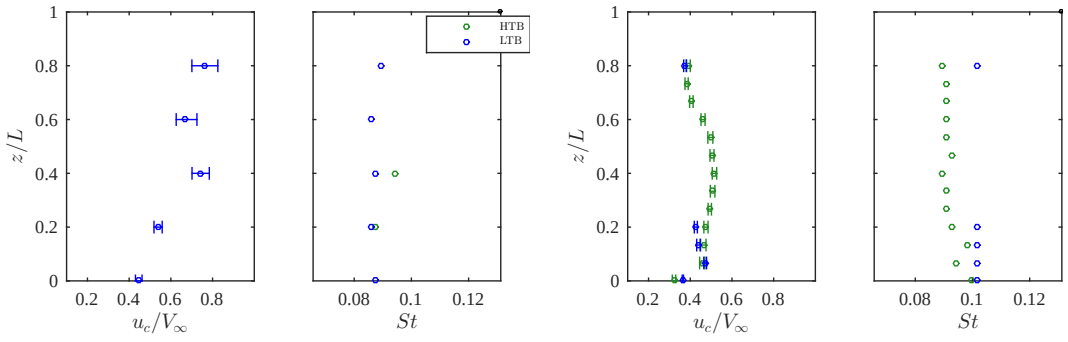

(a) $L/W = 1.4$, (HTB: R0, LTB: R0)

(b) $L/W = 4.3$, (HTB: RI, LTB: RI)

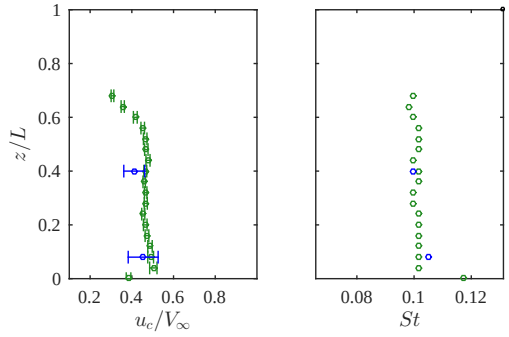

(c) $L/W = 7.1$, (HTB: RI, LTB: RI)

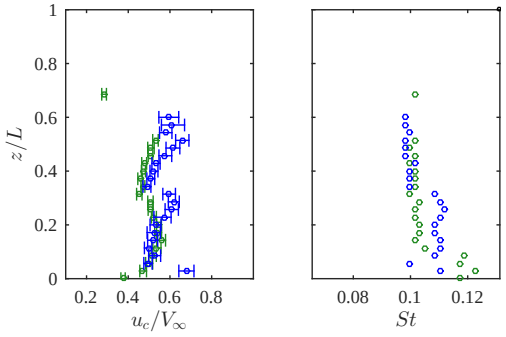

(d) $L/W = 10.0$, (HTB: RI, LTB: RII)

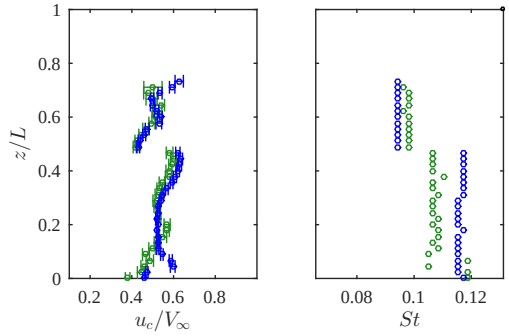

(e) $L/W = 12.9$, (HTB: RII, LTB: RII)

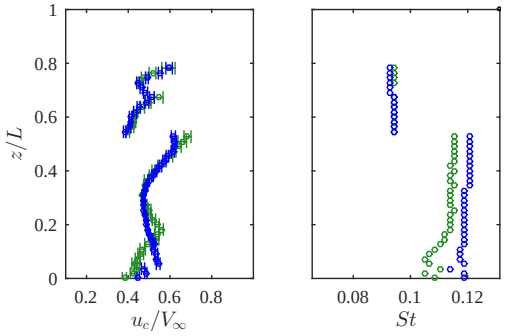

(f) $L/W = 15.7$, (HTB: RII, LTB: RII)

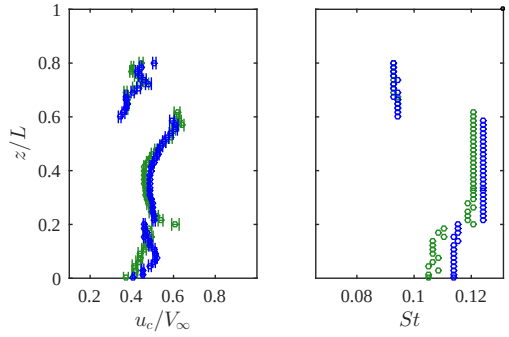

(g) $L/W = 18.6$, (HTB: RII, LTB: RIII)

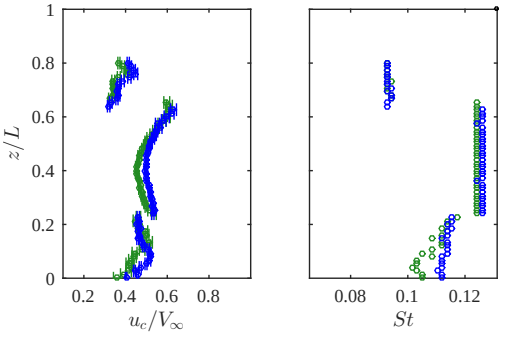

(h) $L/W = 21.4$, (HTB: RII, LTB: RIII)

Figure 6.21: The convection velocity, u_c/V_∞, of the most energetic vortices along the span, z/L, of select aspect ratio FWMCs in the HTB (shown in green). The right hand side of each sub-figure shows the frequency, $St = fW/V_\infty$, of the most dominant vortices at a particular spanwise station. The results are compared with the corresponding measurements made for FWMCs in the LTB (shown in blue).

longer compensate for such a large disparity in spanwise conditions, and a cell of lower frequency vortices forms at the free-end.

6.4 Broadband noise for FWMCs in RII

As shown in Figures 6.4c and 6.4d, the 3 dB reduction of OASPL of FWMCs in the HTB with $L/W > 18$ compared with those in the LTB is comprised of a reduction in both the magnitude of P2 and a reduction in the broadband part of the spectrum. Up until this point, the broadband part of the spectrum has been ignored because it contributes little to the OASPL. Figure 6.4d, however, shows that the magnitude of the broadband part of the spectrum has a strong correlation with the magnitude of the OASPL for both the HTB and LTB cases. This means that the relative magnitude of the broadband noise must be related to the wake dynamics of the cylinder. This is further evidenced by the surprising result that the broadband noise level in the HTB is significantly lower than that in the LTB for FWMCs with $L/W > 10$. By no coincidence this is the aspect ratio range where the magnitude of P2 in the LTB exceeds the magnitude of P2 in the HTB. Therefore, a study of the generation of broadband noise complements understanding of the noise generation mechanisms of FWMCs.

Broadband noise is studied using beamforming source localisation for FWMCs with $L/W > 10$. Details of the properties of the phased array used in the AWT experiments are given in Chapter 4. Importantly, the maximum resolution of the array (using DAMAS deconvolution techniques) at positions close to the location of the FWMC relative to the array is 0.36λ where λ is the wavelength of sound. At a Strouhal number of $St = 0.1$ where vortex shedding typically occurs, the minimum beamwidth (maximum resolution) is 250 mm, which is larger than the length of the highest aspect ratio cylinder. Therefore, beamforming cannot be used to localise the noise produced by the large scale vortex structures at the frequency of the Aeolian tone and is suited to the broadband part of the spectrum in the range of 3 kHz to 10 kHz.

6.4.1 Data processing and beamforming parameters

An in-depth analysis of beamforming theory, the microphone array, the data acquisition system available in the AWT and the likely magnitudes of beamforming uncertainty were presented in Chapter 4. Here, a brief summary of the specific data processing techniques and parameters used for the FWMC experiments is given.

For each FWMC in the LTB and HTB, beamforming data were taken with a 31-channel microphone array located 0.5 m directly above the FWMC. Data were taken for 30 seconds at a sampling rate of 2^{15} Hz. The cross-spectral matrices (CSMs) were generated using Welch's averaged modified periodogram method (see Section 3.4). Each data record was split into 959 overlapping blocks of length 2^{11} giving a frequency resolution of 16 Hz.

To calculate the beamforming maps, CLEAN-SC with 'sv2' (see Section 4.4.1) and diagonal removal was used because it had the lowest side-lobe levels over the 3 kHz to 10 kHz range (see Figure 4.7). All maps were corrected for the array gain using Table 4.3 to eliminate algorithmic systematic error. Additionally, in all maps, the background level was removed using the background removal technique presented by Brooks and Humphreys (2006). For CLEAN-SC, the clean beamwidth was set at 0.5λ and the damping coefficient at $\psi = 0.99$.

DAMAS was used for spatial integration calculations. In this case the pixel width was 10 mm across all frequencies. This pixel size was small enough to avoid 'power leakage'

due to spatial aliasing (see Section 4.4.2) over all frequencies mapped. At each narrow band frequency, the DAMAS algorithm was allowed to run for 1000 iterations.

For both CLEAN-SC and DAMAS, shear layer interference was corrected for using the method of Bahr et al. (2011). It was shown in Section 4.5.3 that this method gives results comparable with that of ray tracing but at a greatly reduced computational expense.

Using the results from the uncertainty analysis in Section 4.5.5, the uncertainty in the spatially integrated narrowband levels are approximately as $\pm 1\,\mathrm{dB/Hz}$. The uncertainty in frequency integrated levels are approximately $\pm 0.2\,\mathrm{dB}$.

6.4.2 Source maps

Figures 6.22a through 6.22j show beamforming source maps of selected aspect ratio cylinders at a $1/3^{\mathrm{rd}}$ octave band centre frequency of 6.3 kHz. This centre frequency was chosen for demonstrative purposes and results shown are representative of the beamforming results across all frequencies. The full set of beamforming images is given in Appendix A. To obtain the maps across an octave band, each beamforming map was generated at a single narrowband frequency and the result integrated (in frequency) across the frequency band of interest. To reiterate, Figures 6.22a through 6.22j have been obtained using the CLEAN-SC algorithm (Sijtsma 2007).

In the LTB, the broadband noise of the FWMC with $L/W = 10$ is dominated by a source near the free-end of the cylinder, as shown in Figure 6.22a. As the aspect ratio increases, a source at the junction of the cylinder increases in magnitude. Although the free-end noise source does increase with aspect ratio, the junction source increases at a faster rate and by $L/W = 18.6$ in Figure 6.22g it is the dominant noise source in the map. At higher aspect ratios, the junction noise source continues to increase while the free-end noise source remains at constant magnitude.

In contrast, in the HTB the broadband noise of the $L/W = 10$ FWMC is dominated by a source near the junction of the cylinder (see Figure 6.22b). The junction source has a much larger amplitude in the HTB than the corresponding junction source in the LTB. However, the peak magnitude of the free-end noise source slightly reduces by the increase in boundary layer height. At $L/W = 12.9$ (Figure 6.22d), both the junction and free-end source strengthen. Again the free-end noise source is lower in peak magnitude when compared with that of the LTB. This trend continues as the aspect ratio increases. Finally, at $L/W = 21.4$ in Figure 6.22j, the magnitude of the free-end noise sources appear to be similar in both the LTB and the HTB. Another salient feature of these maps is the reduction in junction noise source magnitude for $L/W > 12.9$, which can be observed by comparing Figures 6.22e, 6.22g and 6.22i with 6.22f, 6.22h and 6.22j. Unlike the free-end noise sources, the junction noise source in the HTB never reaches the magnitude of that in the LTB. The observation is somewhat expected, since the boundary layer effect of an FWMC with $L/W \to \infty$ would be localised only at the cylinder junction.

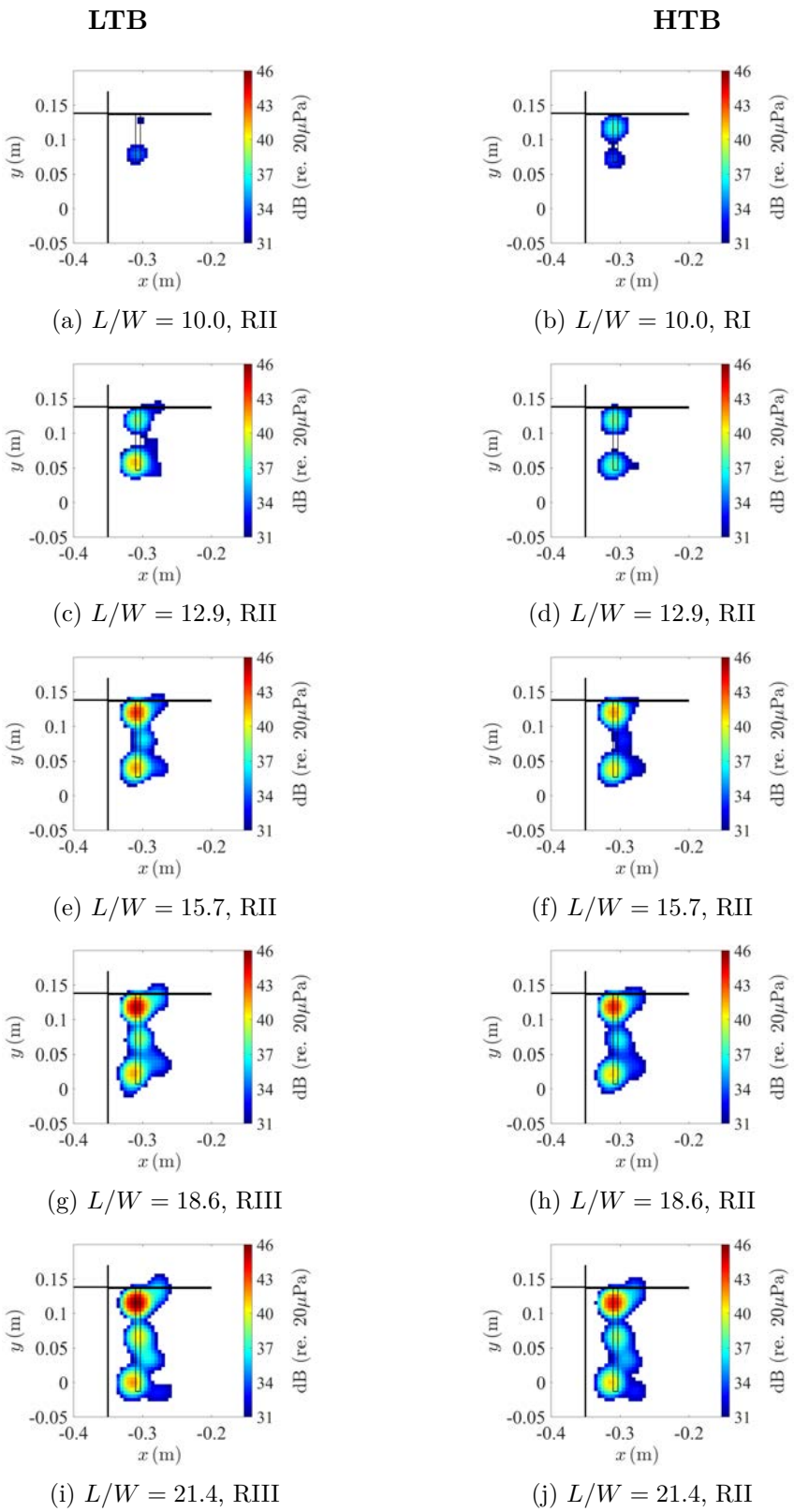

(a) $L/W = 10.0$, RII (b) $L/W = 10.0$, RI

(c) $L/W = 12.9$, RII (d) $L/W = 12.9$, RII

(e) $L/W = 15.7$, RII (f) $L/W = 15.7$, RII

(g) $L/W = 18.6$, RIII (h) $L/W = 18.6$, RII

(i) $L/W = 21.4$, RIII (j) $L/W = 21.4$, RII

Figure 6.22: Beamforming maps for FWMCs between $10 \leq L/W \leq 21.4$ at a $1/3^{\text{rd}}$ octave band centre frequency of 6.3 kHz. The left column shows the maps for FWMCs in the LTB while the right column shows maps for FWMCs in the HTB. In each map the flow is travelling from left to right.

6.4.3 Spatial integration analysis

Integration analysis of the beamforming maps allows an isolation of the noise generated by a particular portion of the cylinder. Four spatial integration sectors, labeled 'the junction', the 'free-end', the 'mid-span' and the 'total' cylinder are used in the following analysis. The bounds of these regions are shown in Figure 6.23 and quantified in Table 6.1.

The 'free-end' integration region extends from 10 mm above the free-end to 30 mm below the free-end. The 'junction' integration region extends from the plate to 40 mm up the span of the cylinder. The 'mid-span' region is the area between the junction and free-end and the 'total' region is simply the sum of the free-end, junction and mid-span of the cylinder. Thus, as the cylinder aspect ratio increases, the area of the total and mid-span regions also increases, while the junction and free-end areas remain constant. It should be noted that at $L/W = 10$, the total portion of the cylinder is equal to the sum of the free-end and junction regions respectively and mid-span region is non-existent. Each region extends 50 mm upstream and downstream from the cylinder. This is done to capture sources that may appear removed from the surface of the cylinder due to either shear layer refraction, random errors in the assumed location of the microphones or spatial aliasing.

To perform spatial integration within a particular region, the source map levels were summed over the spatial region of interest for each narrowband frequency. To obtain $1/12^{\text{th}}$ octave band levels, the resulting narrowband levels were integrated over the frequency band of interest.As explained, before spatial integration was performed, the maps were deconvolved using the DAMAS algorithm to remove the effects of the point spread function (described in Section 4.2.2).

Figure 6.24 shows the $1/12^{\text{th}}$ octave band integrated levels of the junction, mid-span and free-end for select aspect ratio FWMCs. The left columns show data for FWMCs in the LTB and the right column shows data for FWMCs in the HTB. The levels are shown for centre frequencies ranging from 3 kHz ($St = 0.65$) to 10 kHz ($St = 2.2$). For frequencies lower than 3 kHz, the beamwidth of the array is too large to separate the junction and free-end regions for all cylinders.

The junction noise spectra appear in Figure 6.24a and 6.24b to be have similar shapes for LTB and HTB cases respectively, with the spectra having a small hump at $St = 0.9$. In both boundary layers, as the FWMC increases in aspect ratio, the magnitude of the junction noise increases across all frequencies equally, so that the shape of the spectra is invariant to changes in aspect ratio. For FWMCs in the LTB, the magnitude of the spectra increases asymptotically. Between $L/W = 18.6$ and $L/W = 21.4$, there is only

Table 6.1: The numerical bounds of the spatial integration regions defined in Figure 6.23. Here L denotes the length of the FWMC model in metres.

Region	$x_{\min}$	$x_{\max}$	$y_{\min}$	$y_{\max}$
Junction	-0.35	-0.25	0.095	0.135
Mid-span	-0.35	-0.25	0.135-L	0.095
Free-end	-0.35	-0.25	0.125-L	0.165-L
Total	-0.35	-0.25	0.125-L	0.135

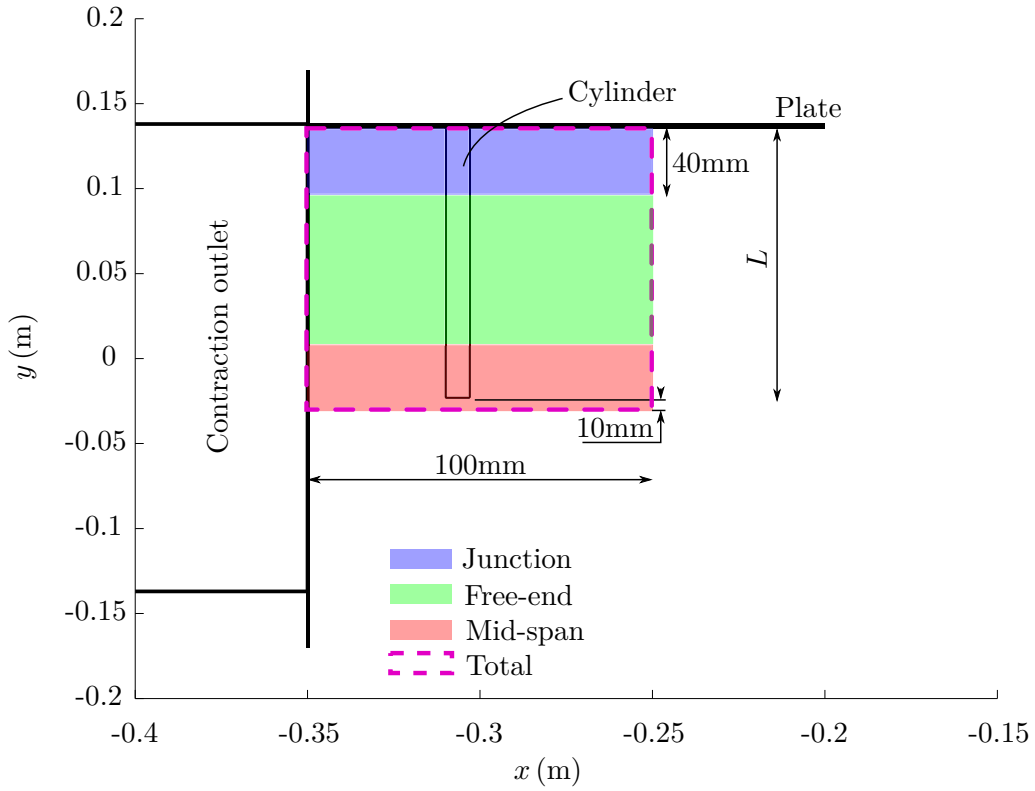

Figure 6.23: An illustration of the bounds of the integration regions used for the source localisation spatial integration analysis. Four integration regions, called the 'junction', the 'free-end',' the 'mid-span' and the 'total' cylinder are used.

a 1 dB increase in noise levels at each centre frequency. In the HTB, the junction noise generated by the $L/W = 10$ cylinder appears to be much higher than its LTB counterpart. This is consistent with the heuristic observations based on the beamforming source maps in Figure 6.22. As the FWMC increases in aspect ratio, the spectra increase in magnitude, maintaining their spectral shape, until their magnitude asymptotes at $L/W = 21.4$.

The magnitude of the free-end noise in Figure 6.24c and 6.24d show a greater disparity between the LTB and HTB cases. In the LTB, the free-end noise spectrum starts at a similar magnitude to the junction noise spectrum at $L/W = 10$. The free-end noise spectrum is slightly higher than that of the junction for frequencies greater than 5 kHz, which is why the map in Figure 6.22a is dominated by a free-end source. At $L/W = 12.9$ the magnitude of the free-end noise spectrum increases by approximately 7 dB. Subsequent increases in aspect ratio do not change the free-end noise spectra. Consequently, the spectral shape and magnitude become invariant with aspect ratio.

In the HTB, the magnitude of the free-end spectrum at $L/W = 10$ in Figure 6.24d is very similar to that of the LTB case. However, unlike in the LTB case, where an asymptotic value was reached at aspect ratios as low as $L/W = 12.9$, when the apsect ratio increases for FMWCs in the HTB, the magnitude of the free-end noise spectrum slowly increases, and reaches its invariant state at $L/W = 21.4$. The magnitude of the free-end spectrum at $L/W = 21.4$ for FWMCs in the HTB is very similar to that of the LTB at the same aspect ratio.

A similar trend is observed for sources generated at the mid-span of the cylinder in

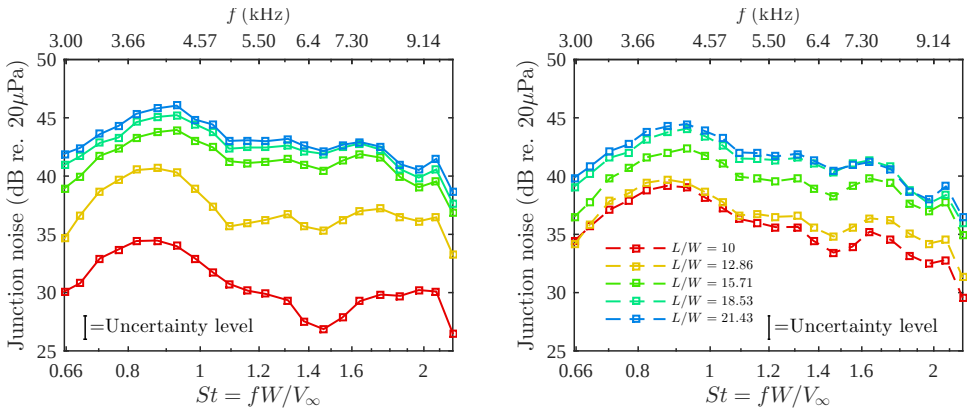

(a) LTB junction noise spectra

(b) HTB junction noise spectra

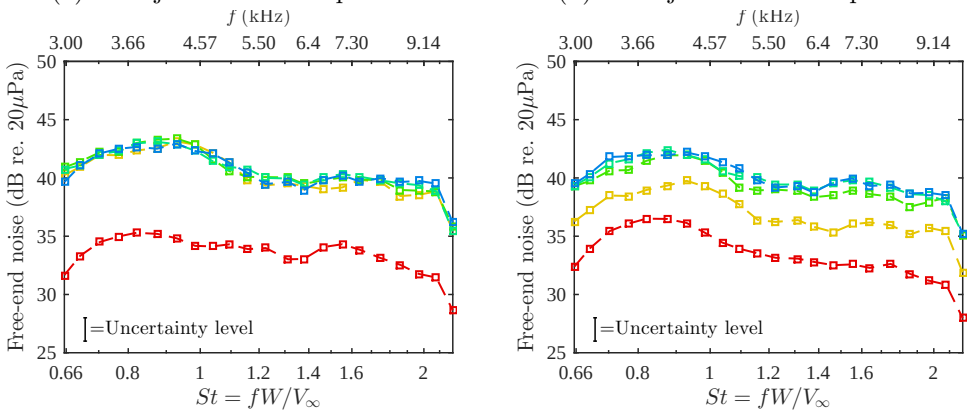

(c) LTB free-end noise spectra

(d) HTB free-end noise spectra

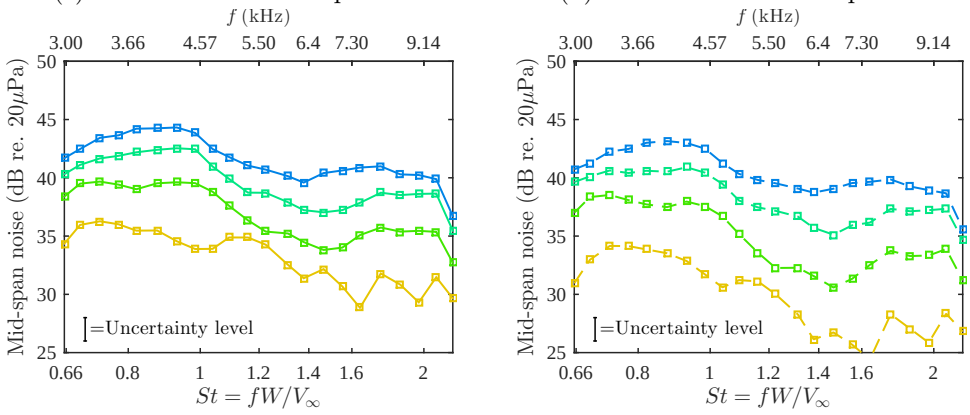

(e) LTB mid-span noise spectra

(f) HTB mid-span noise spectra

Figure 6.24: The $1/12^{\text{th}}$ octave band spectra obtained by spatially integrating the junction, free-end and mid-span regions for FWMCs in the HTB (right) and the LTB (left). The spectra for FWMCs with $10 \leq L/W \leq 21.4$ are shown.

Figure 6.24e and in 6.24f. Unlike the free-end and junction region, the area over which the mid-span region is integrated increases as the aspect ratio increases. Correspondingly the spectra in both the HTB and LTB cases are expected to increase with increasing aspect ratio. The spectral shape of the mid-span noise component is similar to that of the junction region, where the spectra are dominated by a small hump at $St = 0.9$. In general, for a given aspect ratio FWMC, the magnitude of the mid-span noise source spectrum for FWMCs in the LTB tend to be larger than that in the HTB.

6.4.4 Relationship with FWMC flow

The shape of the spectra in Figure 6.24 appear to be aspect ratio invariant for each integration region. Hence, one feasible way to observe the overall differences in the broadband noise between FWMCs in the HTB and LTB is to compare each region's total frequency integrated magnitude. As such, the spectra for each region (shown in Figure 6.23) were integrated across frequencies 3 kHz to 10 kHz. The results are shown in Figure 6.25 for the junction, free-end and mid-span regions.

The trends observed in these figures show an interesting symmetry with the trends measured in the relative magnitudes of the Aeolian tones in Section 6.2. For example, from $L/W = 10$ to 12.9, the free-end noise for FWMCs in the LTB, shown in Figure 6.25b increases from 47 dB to 53 dB, while it then remains constant for higher aspect ratios. Comparatively, while the free-end noise of the $L/W = 10$ FWMC in the HTB has the same magnitude as that of the LTB, the noise increase is less drastic with increasing aspect ratio. This is the same trend that was observed in Figure 6.4b, showing the relative magnitudes of P1. At $L/W = 10$, the magnitudes of P1 are roughly equal in the two boundary layers, but with further increases of aspect ratio, the magnitude of P1 increases but asymptotes quicker in the LTB case. It was explained that in the LTB, the free-end flow reaches a decoupled, independent state at approximately $L/W = 12.9$, where the dynamics of the free-end flow do not change with subsequent increases in aspect ratio. On the other hand, the thicker boundary layer changes the balance of upwash and downwash, meaning that the free-end reaches the independent state at a higher aspect ratio. The results from the beamforming integration also suggest that such a process occurs. Further evidence is provided by the fact that the magnitude of the free-end noise source approaches a similar value (<0.5 dB difference) for high aspect ratio FWMCs regardless of the boundary layer type.

At the other cylinder extremity, the junction noise (in Figure 6.25a) is enhanced by the HTB at lower aspect ratios ($L/W = 10$). However, as the aspect ratio increases, the junction noise increases drastically in the LTB, meaning that it has a consistently greater magnitude than the HTB case for $L/W \geq 12.9$. Once again, there appears to be a fundamental connection between the magnitude of the broadband junction noise source and the dynamics that influence the generation of Aeolian tones originating from structures on the lower portion of the FWMC.

For $L/W = 10$, FWMCs in both the LTB and HTB are still in RI, both generating a single Aeolian tone. Thus, as discussed in Section 6.3, the dominant mechanism by which upwash is produced is through a streamwise turning of the initially vertical vortex filaments near the junction region. As a result, high frequency velocity fluctuations are brought closer to the cylinder junction in the HTB case. This can be observed in Figure 6.12g and 6.12h, where the concentration of turbulence near the junction region in the LTB case lies further downstream than that of the HTB case. This means that there is heightened interaction of this turbulence with the cylinder face and the broadband noise is increased at the junction of the cylinders in the HTB.

As the aspect ratio increases, the FWMCs transition into RII. Again, this occurs for $L/W = 10$ for FWMCs in the LTB and $L/W = 12$ for FWMCs in the HTB. For FWMCs in the LTB, there is a rapid increase in the amount of high-speed fluid entrained into the

wake. It was proposed in Section 6.3 that this rapid increase in entrained fluid is caused by a reduction in base pressure at the mid-span region as it becomes two dimensional. A similar mechanism occurs for FWMCs in the HTB, except that the entrained fluid has significantly less momentum (since the boundary layer is higher) and that the base pressure at the mid-span is higher owing to increased interaction of the boundary layer with the nominally two-dimensional flow of at mid-span. This reduces the upwash in the HTB case compared with the LTB case (although the total level of upwash is still enhanced compared with low aspect ratios). As explained previously, the reduction of upwash (compared with similar aspect ratio FWMCs in the LTB) is indicative of a reduction in high amplitude two-dimensional structured vortex shedding, which reduces the turbulence intensity near the junction of the cylinder (as can be seen in Figures 6.12i and 6.12j). In turn, this reduces the level of junction broadband noise in the HTB case.

The broadband noise generated by the mid-span region increases rapidly from $L/W = 12.9$ for both the HTB and LTB cases. An increasing mid-span noise level is a natural consequence of the integration area increasing as the aspect ratio increases. The rate of increase of mid-span noise is similar between both boundary layer cases but the magnitude of the noise produced by the HTB is lower than that of the LTB. This is consistent with the idea that although similar two-dimensional noise generation mechanisms occur in both boundary layers at high aspect ratios, a higher boundary layer upsets the coherent formation of the lower portion of the structures that generate P2 through a non-localised effect, ultimately reducing the overall fluctuation levels and reducing the broadband noise.

Figure 6.26 shows the variation of the broadband noise generated by the entire cylinder (the 'total' region). The results are expressed as stacked bar charts to demonstrate the relative proportion of the total noise that is generated by each region. For each bar, the yellow, green and blue regions indicate the relative proportion of the total noise generated by the free-end, mid-span and junction region respectively. The total height of the each bar is proportional to the pressure squared (linear) value of the total noise generated by the entire cylinder and is mapped to the dB value (re. 20μPa) by a logarithmic ordinate axis. In Figure 6.26 the solid colours represent cylinders in the HTB while the faded colours represent cylinders in the LTB.

The variation of the total noise with aspect ratio resembles that of the junction region. This is because the majority of the total broadband noise is generated by the sources located at the junction region for every aspect ratio, with the exception of the $L/W = 12.9$ FWMC in the LTB, where the free-end noise reaches its asymptotic value. In Figure 6.4d, a change in the rate of increase of broadband noise occurs at $L/W = 14$ in the LTB case, creating a noticeable 'kink'. Figure 6.26 demonstrates that this kink is due to the free-end region reaching an asymptotic state, reducing the rate of increase of the overall broadband noise level. For the HTB case, Figure 6.4d shows the rate of increase of broadband noise levels increases at L/W = 12.9, creating a reverse 'kink'. Figure 6.26 shows that this is because the junction noise begins to increase at a faster rate beyond $L/W = 12.9$, where the upwash flow begins to be dominated by the entrainment mechanism.

At high aspect ratios ($L/W = 21.4$), approximately 50% of the noise is generated by the junction of the FWMC in both boundary layer cases, with the remaining 50%

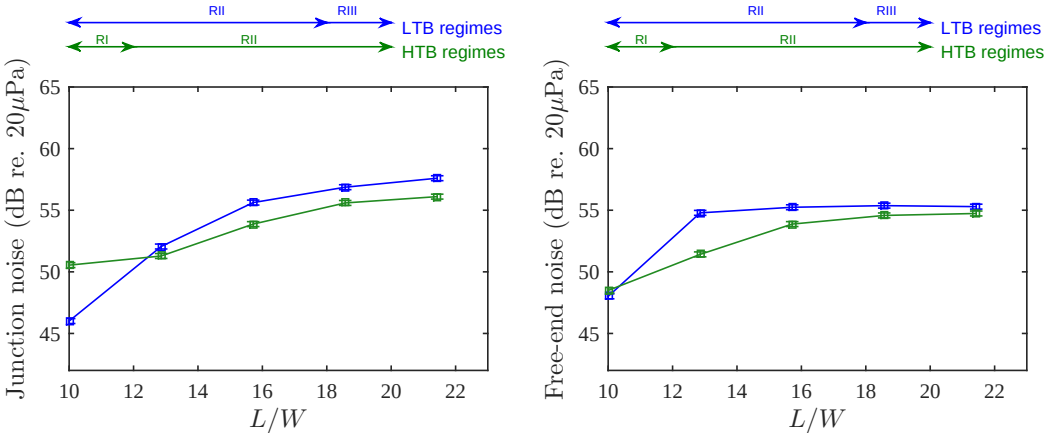

(a) Junction region

(b) Free-end region

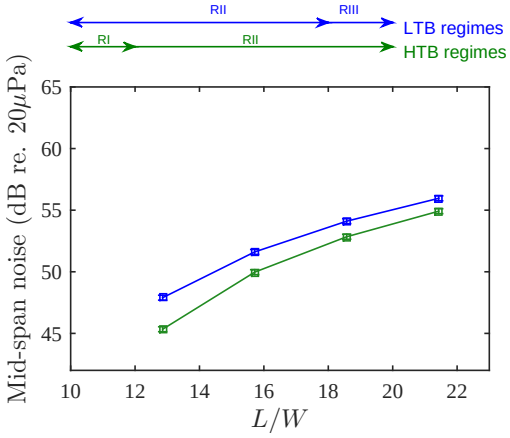

(c) Midspan region

Figure 6.25: A comparison of the total integrated sound levels against aspect ratio for the junction, free-end, mid-span and total regions for cylinders in the LTB and cylinders in the HTB. The values in each Figures were obtained by integrating the area under the curves shown in Figure 6.24.

of the noise shared approximately equally between the free-end and the mid-span. The dominance of the junction noise source in the broadband spectrum of FWMCs is an important consideration when formulating appropriate noise mitigation strategies. Evidently, efforts to reduce broadband noise levels from FWMC like bluff-bodies, e.g., pantograhs or landing gear, should concentrate on the point of the connection of the bluff body with the main structure. These results demonstrate that an increase in the boundary layer thickness can sufficiently disturb the structured wake dynamics of the FWMC and result in a reduction of broadband junction noise levels by approximately 30% (1.7 dB). For even higher aspect ratios, the spectrum will most likely be dominated by the mid-span section, as it increases in size. In these cases, mitigation strategies should be concentrated at the mid-span of the protrusion.

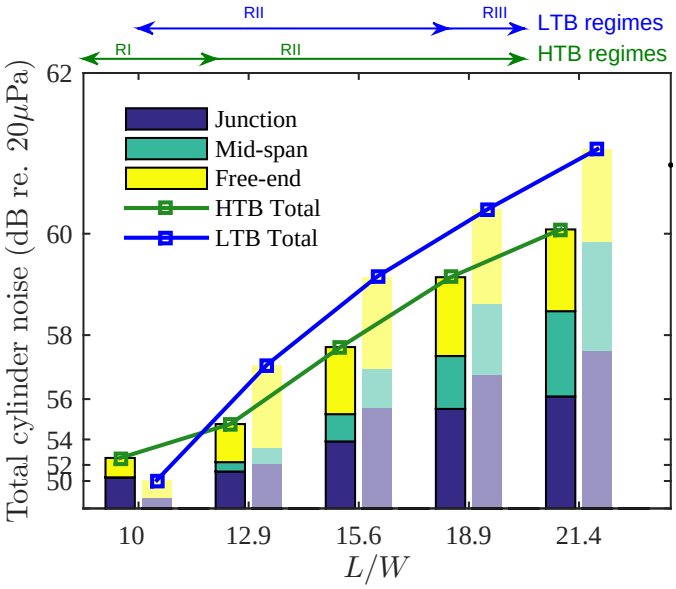

Figure 6.26: A bar chart demonstrating the relative proportions of total broadband noise for FWMCs in the HTB and the LTB that comprise of free-end noise, mid-span noise and junction noise.

6.5 Summary

Prior to this study, the effect of the boundary layer on FWMC flow was poorly understood. Of the few studies that do exist, the effect of the boundary layer has only been studied for a single aspect ratio FWMC in with $L/W < 10$ (Wang et al. 2006; Hosseini et al. 2013). This chapter has taken a holistic approach to investigating the effect of the boundary layer on FWMC flow by studying its impact on the flow-induced noise produced by FWMCs across a wide range of aspect ratios, $L/W < 23$. This chapter compares the results obtained in Chapter 5 for FWMCs in the Low Turbulent Boundary Layer (LTB) with $\delta/W = 1.3$ with results of FWMCs in a High Turbulent Boundary Layer (HTB) with $\delta/W = 3.7$. Given the strong links that the flow-induced noise has with the periodic structure of the wake, as shown in Chapter 5, a comparison of the noise generated by FMWCs in the LTB and HTB is used to infer the effect of the boundary layer on the dynamics of the wake.

Increasing the height of the boundary layer from $\delta/D = 1.3$ (LTB) to $\delta/D = 3.7$ (HTB) shifts the first two shedding regime boundaries to higher aspect ratios. In the HTB, RI starts at $L/W = 4$, while RII started at $L/W = 12$, compared with $L/W = 2$ and 10 in the LTB respectively. As a consequence, the onset of cellular shedding is delayed to higher aspect ratios.

Within RI ($4 < L/W < 12$), the magnitude of the primary Aeolian tone, P1, in the HTB is significantly higher than that of P1 in the LTB. Additionally, the transition from RI to RII at $L/W = 12$ in HTB is not accompanied by a large reduction in OASPL as it was in the LTB. However, within RII ($L/W > 12$), the magnitude of P2 in the HTB is considerably lower than that in the LTB. Another key observation is the disappearance of a third Aeolian tone for FWMCs in the HTB and consequently the disappearance of a third shedding regime.

It is found that the boundary layer had two types of effects on the FWMC flow.

The first, described as localised effects, are changes to the FWMC wake that lie inside of the boundary layer region. For lower aspect ratio FWMCs in RI ($4 < L/W < 12$), the dominant localised effect of the HTB is to increase the upwash at the junction of the cylinder. As explained by Hosseini et al. (2013), this effect is due to an enhanced streamwise rotation of the lower half of the spanwise vortex that induces more upwash. The enhanced upwash from the junction lowers the downwash over the free-end as a secondary, non-localised effect, i.e., an effect that occurs to those parts of the wake that lie outside of the boundary layer. The change in downwash and upwash level ultimately drive the regime shifting behaviour of the FWMCs in the HTB.

For higher aspect ratio FWMCs in RII ($L/W > 12$), the dominant localised effect is a complete disruption to the regularity of vortex shedding within the boundary layer. As a consequence, the HTB also appears to disrupt mid-span vortex shedding as a non-localised effect, which hinders its ability to form two-dimensionally. As a result, the upwash from the junction is reduced in the HTB case. Furthermore, the junction cell that would normally produce a third acoustic tone, P3, is disrupted by the HTB.

The wake dynamics of the FWMCs are also connected to the levels of broadband noise generated by the FWMCs in the two boundary layer types. For FWMCS in RI that generate a single Aeolian tone, broadband noise levels are generally higher in the HTB than in the LTB. This is because junction broadband noise is enhanced by a streamwise rotation of the initially vertical vortex filaments as it sheds as a single coherent structure. The degree of rotation, and thus broadband noise level, is enhanced by higher boundary layers. As the aspect ratio increases, both free-end noise and junction noise are enhanced in the LTB case above that of the HTB case, leading to a reduction of broadband noise levels for FWMCs in the HTB. This behaviour is caused by a combination of regime shifting, which lowers the free-end noise for a given aspect ratio, and disrupted two-dimensional shedding at the FWMC midspan, which lowers upwash in the HTB case, thus reducing junction broadband noise.

Chapter 7

Concluding remarks

7.1 Thesis summary

Community noise is a major man-made pollutant that can have damaging effects on human health. Compared with other man-made pollutants, community noise is poorly controlled. Research into the noise generated by bluff-body flow can help alleviate community noise generated by transportation systems, including aircraft and highspeed rail. The work of this dissertation is an investigation of the flow induced noise generated by square Finite Wall-Mounted Cylinders (FWMCs). An FWMC models the major noise generating components of transportation systems such as landing gear or pantographs.

An extensive literature review of FWMC flow and noise in Chapter 2 concluded that there was a significant lack of knowledge on the effect of aspect ratio, L/W, and incoming boundary layer thickness, δ, on the flow-induced noise generated by square FWMCs, particularly for $L/W > 14$. Thus, the primary aims of this research were to (1) experimentally characterise the flow-induced noise from FWMCs over a range of aspect ratios and boundary layer thicknesses and (2) link the measured flow-induced noise to the flow physics of FWMCs.

To achieve these aims, the flow and noise of square FWMCs with aspect ratios ranging from $0 < L/W < 23$ were measured using a variety of experimental techniques. These included single microphone and phased microphone array measurements of the acoustic pressure directly above the FWMCs, sound directivity measurements around the periphery of the FWMCs, fluctuating velocity measurements in the wakes of the FWMCs, oil-film flow visualisation and mean and fluctuating pressure measurements on the surface of the FWMCs. The measurements were conducted on FWMCs immersed in several different boundary layers, with $\delta/W = 0.9$, $\delta/W = 1.3$ (called the LTB) and $\delta/W = 3.7$ (called the HTB).

In low boundary layers ($\delta/W \leq 1.3$), the flow-induced noise generated by square FWMCs varied significantly with aspect ratio. The Overall Sound Pressure Level (OASPL) measured with a single microphone varied non-monotonically as the aspect ratio increased, most notably with a local OASPL minimum occurring at $L/W = 7$. The acoustic pressure spectrum of FWMCs was comprised of a series of low frequency tonal peaks and higher frequency 'broadband' noise. The number of tonal peaks increased as the aspect ratio increased. On these observations, four different shedding regimes were identified, R0, RI, RII and RIII, corresponding to the number of tones present in their acoustic pressure

spectrum. In the LTB, R0 ranged from $0 < L/W < 2$, RI ranged from $2 < L/W < 10$, RII ranged from $10 < L/W < 18$ and RIII ranged from $18 < L/W < 23$.

FWMCs in R0 and RI had highly three-dimensional wakes. Measurements of fluctuating velocity in the wake demonstrated that periodic vortex shedding still exists at a lower frequency than one would expect for a two-dimensional cylinder and downwash from the free-end dominates the flow. Using the wake mean velocity profiles, it was shown that downwash increases as the FWMC aspect ratio increases, until the FWMC reaches RII, where the level of downwash becomes independent of the aspect ratio. Oil-film visualisations of FWMCs in R0 and RI demonstrated that the primary effect of downwash is to delay the conflation of spanwise vortices so that the FWMCs in RI have higher wake recirculation lengths when compared with a two-dimensional cylinder. This was confirmed through a direct measurement of the wake formation lengths.

The effect of downwash on vortex shedding is maximised at $L/W = 7$. At this aspect ratio, a maximum wake elongation was measured in both the hot-wire and oil-film results and a minimum in the OASPL was measured by the single microphone. One of the key findings of this research is that at $L/W = 7$ the FWMC is long enough so that downwash is large, but short enough so that downwash acts over the entire cylinder span. A heuristic, phenomenological argument was put forth to explain the relationship between the OASPL and the wake length.

Pressure measurements on the surface of FWMCs in RI illustrated the effect of downwash on the cycle-to-cycle dynamics of the vortices. During RI vortex shedding is highly irregular, consisting of intermittent periods of low amplitude events inter-spaced with bursts of high amplitude periodic shedding. The intermittency increases the cycle-to-cycle axial phase variations, contributing to wider bandwidth and lower amplitude vortex shedding. The disruptive effect of downwash is maximised at $L/W = 7$ where spanwise correlation and surface pressure levels are minimised. Measurements of the spanwise correlation and surface pressure were also used to predict the Aeolian tone level using a modified version of Curle's Aeolian tone theory (Curle 1955). Good agreement was achieved when comparing the predicted levels with that measured experimentally.

A novel phase eduction technique was used to visualise the orientation of the vortex filaments from FWMCs in R0 and RI as they convected downstream. The visualisation showed that vortex filaments for these FWMCs are spatially deformed, either inclining downstream near the free-end (for FWMCs in R0) forming an arch structure or inclining upstream near the free-end (for FWMCs in RI) to form 'half-loop' vortex structures, similar to those described by Bourgeois et al. (2011).

Directivity measurements of the primary acoustic tones generated for FWMCs in RI showed evidence of a drag dipole pattern, where the lobes of the dipole are orientated downstream. This directivity pattern was related to the propensity of spanwise vortices to shed symmetrically (rather than anti-symmetrically), further demonstrating the highly three-dimensional wake of FWMCs at low aspect ratios.

Unlike those in RI, FWMCs in RII and RIII showed similarities with two-dimensional cylinder flow. For these FWMCs, multiple Aeolian tones were measured in the acoustic spectrum. Simultaneous measurements of the fluctuating velocity in the wake with the acoustic pressure demonstrated that these multiple acoustic tones are due to the formation of a *cellular* wake structure, where different spanwise regions shed at different frequencies.

A maximum of three cells were found along the cylinder span for RIII ($L/W > 18$); a free-end cell, a mid-span cell and a junction cell. No junction cell independent of that of the midspan was observed for FWMCs in RII, and only two cells formed.

The phase eduction technique demonstrated that the free-end and junction cells consist of a series of inclined vortex filaments, while the mid-span cell consists of vertical vortex filaments. Directivity patterns of the acoustic tones associated with the junction and mid-span cells are similar to that measured for a two-dimensional cylinder, while directivity measurements of the free-end cell tones indicate a 'shifted lifting dipole'. The noise generation mechanism of a shifted lifting dipole remains unknown, however, it was postulated to be related to vortex flow over the free-end.

Surface pressure measurements of FWMCs in RII showed that at the mid-span, the cylinder base pressure, the vortex formation length and the cycle-to-cycle vortex dynamics become similar to that of infinitely long cylinders. This coincides with the 'decoupling' of the free-end flow from the mid-span of the cylinder. In RII, the free-end flow experiences a localised region of three-dimensional flow while the mid-span region forms uninhibited from the influence of downwash and therefore with more two-dimensionality.

The idea of a 'coupled' or 'decoupled' wake flow is central to the formation of a cellular wake. By modelling the wakes of FWMCs using a van der Pol oscillator analogy, it was found that spanwise coupling of vortex filaments is increased by two factors: lowering the aspect ratio and increasing the level of downwash. FWMCs in RII and RIII have high enough aspect ratios so that the free-end and junction flow from independently from the mid-span.

The driver of lower frequency shedding in the free-end and junction cells during RII and RIII is the spanwise flow at those regions. Free-end downwash acts to retard the vortices near the free-end. In doing so, the local convection velocity is reduced. Since the convection velocity is proportional to the frequency of vortex shedding, the free-end cell is driven to form at a lower frequency. Similar mechanisms occur at the junction during RIII.

The van der Pol oscillator analogy was also used to understand the cycle-to-cycle dynamics of cellular shedding. The simulated results using the model indicated that the boundary between cells is characterised by 'phase jumps', where vortex filaments periodically split and distribute circulation to adjacent vortices across the cell boundary. The numerically simulated results matched well with experimental observations using surface pressure measurements. Furthermore, it was found that between phase jumping events, vortices in the higher frequency mid-span cell would 'pull' vortices generated in the lower frequency free-end cell forward, thereby inclining the free-end cell vortices upstream near the free-end. Inclination of the free-end vortices was also visualised using the hot-wire wake velocity measurements. Good agreement was achieved comparing the average angle of inclination of free-end vortices between the numerical and experimental results. This suggests that the free-end cell vortex inclination is mostly driven at the cylinder face by the difference in vortex shedding frequency between cells and not due to Biot-Savat induction.

Thickening the boundary layer to $\delta/W = 3.7$ shifts the boundaries of R0, R1 and RII to higher aspect ratios. A thicker boundary layer increases upwash for FWMCs in R1. In turn, the downwash is reduced for a given aspect ratio, thereby delaying the onset of

cellular shedding. This phenomena was described as a non-localised boundary layer effect because parts of the wake that lie outside of the boundary layer are impacted. Within R1, the acoustic tone is enhanced significantly because of the reduced downwash.

In contrast, for FWMCs in RII, the heightened turbulence in the thickened boundary layer disrupts the regularity of vortex shedding for spanwise regions that lie within the boundary layer, in a localised effect. Upwash is reduced when compared with the lower boundary layer case and an independent junction cell is not allowed to form. The acoustic tones measured in RII are much weaker in the thicker boundary layer case when compared with the low boundary layer case because of this added disruption.

Phased array beamforming was used to characterise and investigate the higher frequency 'broadband' noise generated by FWMCs in RII and RIII. Surprisingly, broadband noise was reduced by 30% when the boundary layer was thickened compared with the low boundary layer case. This is due to lower upwash in the HTB reducing the turbulence intensity of velocity fluctuations near the FWMC junction. In turn higher frequency noise generated at the FWMC junction is also reduced.

7.2 Future work

Many avenues of potential future work exist, some of which are described here.

7.2.1 Directivity

Flow-induced noise directivity measurements were conducted in this study. For FWMCs in RII and RIII, the directivity of noise associated with structures forming at the mid-span resembled that of a classical lifting dipole. However, directivity measurements of noise generated by structures near the free-end of FWMCs in RI showed either a 'shifted lifting dipole' or a streamwise, drag dipole.

The origins of these alternative noise directivity patterns are enigmatic. Apart from inferring that a streamwise dipole noise directivity pattern indicates the propensity of vortices to shed symmetrically (as opposed to anti-symmetrically), no other information about the mechanisms that generate these noise directivity patterns could be concluded. Therefore a link between the directivity pattern and the flow-structures that generate it needs to be established.

A viable strategy to do this may be use of a polar array of microphones to simultaneously measure the directivity at a given point in time. Not only would this elucidate the time-averaged directivity, but also the instantaneous directivity. This is important when considering that the instantaneous noise directivity is directly related to the instantaneous phase of the periodic vortices that shed from the cylinder. Extending this idea, simultaneous measurement of the surface pressure and instantaneous directivity could be used to calculate the phase averaged directivity, which could also be used to relate the measured directivity patterns to the quasi-periodic flow structures that generate them.

One of the issues faced in this study was reduction in signal-to-noise ratio as the aspect ratio reduced into R0. This can be overcome by using multiple microphones, placed at $+\theta_m$ and $-\theta_m$ (where θ_m is the measurement position) with respect to the cylinder to simultaneously measure the noise. Subtraction of the two signals will filter

out uncorrelated signals that are in-phase, i.e, it will enhance the noise produced by anti-symmetric vortex structures that generate fluctuating lift. Similarly, an addition of the two signals will enhance the noise produced by symmetric vortex structures that generate fluctuating drag. A similar technique has been described by Moreau et al. (2010) when measuring aerofoil leading edge noise.

7.2.2 Advanced source localisation

Beamforming was used to localise the higher frequency broadband noise generated by FWMCs. Beamfoming was chosen because it has good resolution at higher frequencies. Lower frequency tonal noise was investigated using simultaneous single microphone and wake velocity measurements.

There is, however, scope to investigate the spatial location of the lower frequency, tonal noise generated by FWMCs using Near-Field Acoustic Holography (NAH). Classical NAH would yield the time average spatial location of the acoustic tones, P1, P2 and P3, which could then be related to the flow structures forming around the FWMC.

An advancement of this technique would be use of *phase averaged* NAH. Three-dimensional phase averaged visualisation of the flow-field of FWMCs using PIV has already been performed by Bourgeois et al. (2011). Here the reference signal used to conditionally sample the flow-field was the FWMC surface pressure. Similar techniques could be applied to acoustic source localisation by simultaneously sampling the acoustic pressure, using an array of microphones, and the surface pressure using embedded surface pressure transducers or pressure sensitive paint (as in Roozeboom et al. (2016)). A robust method for phase averaging acoustic data for source localisation is given by Prime et al. (2014a). In this manner, a direct link between the phases of the vortex structures (and therefore the work of Bourgeois et al. (2011)) that shed off the cylinder and the noise that is produced on the surface of the cylinder could be established.

7.2.3 Circular cross-sections

Square cross-sectioned FWMCs were chosen in this study because knowledge of the flow physics is more advanced when compared with alternative cross-sections. However, a natural extension to the work presented in this thesis is to investigate FWMCs with circular cross-sections. Like square FWMCs, the flow around circular FWMCs is an area of great interest with very few studies having ever investigated the flow-induced noise characteristics and mechanisms. Furthermore, circular FWMCs are more representative of 'real-life' bluff bodies because they produce less noise and have lower drag coefficients.

As explained in Chapter 2, the flow around circular FWMCs is fundamentally different to that of square FWMCs, in particular for FWMCs with $L/W < 10$. As such, the flow-induced noise characteristics would also be fundamentally different. Benchmarking the flow-induced noise characteristics of circular FWMCs against those presented for square FWMCs would therefore provide a holistic understanding of how the flow physics differ between the two cases.

7.2.4 Mitigation strategies

The conclusions drawn from this thesis can be used to investigate several passive noise mitigation options for FWMCs. In Chapter 5 it was observed that at the point of maximum disruption to the wake at $L/W = 7$, the flow-induced noise could be reduced to near background levels. It was found that one of the effects of downwash was to delay vortex formation and shift the concentration of hydrodynamic pressure fluctuations formed by the vortex cores away from the surface of the cylinder. This is a similar mechanism to that of placing a splitter plate in the wake (Ali et al. 2011). From this result, it appears that noise mitigation strategies that delay vortex conflation are effective in significantly reducing flow-induced noise production. Furthermore, this thesis provides evidence that this delay can be achieved simply through flow manipulation. This is advantageous because it does not require placing additional structural components in the wake, which potentially increase weight and drag.

Therefore, future work could investigate ways to delay vortex formation in the wake of FWMC using flow manipulation, with the goal of reducing Aeolian tone levels. This could be achieved through, say, optimal design of the free-end (i.e, using a hemispherical cap or another shape to promote downwash) or bleeding fluid into the wake to increase the cylinder base pressure, which has been shown here to have an inverse relationship with the Aeolian tone level.

References

Abuomar, M. and R. Martinuzzi (2008). "Vortical structures around a surface-mounted pyramid in a thin boundary layer". In: *Journal of Wind Engineering and Industrial Aerodynamics* 96(6), pp. 769–778. DOI: 10.1016/j.jweia.2007.06.009 (cit. on p. 184).

Afgan, I., C. Moulinec, R. Prosser, and D. Laurence (2007). "Large eddy simulation of turbulent flow for wall mounted cantilever cylinders of aspect ratio 6 and 10". In: *International Journal of Heat and Fluid Flow* 28, pp. 561 –574. DOI: 10.1016/j.ijheatfluidflow.2007.04.014 (cit. on p. 6).

Agui, J. H. and J. Andreopoulos (1992). "Experimental investigation of a three-dimensional boundary layer flow in the vicinity of an upright wall-mounted cylinder". In: *Journal of fluids engineering* 114(4), pp. 566 –576. DOI: 10.1115/1.2910069 (cit. on pp. 13, 65).

Ali, M. S. M., C. J. Doolan, and V. Wheatley (2011). "The sound generated by a square cylinder with a splitter plate at low Reynolds number". In: *Journal of Sound and Vibration* 330(15), pp. 3620–3635. DOI: 10.1016/j.jsv.2011.03.008 (cit. on pp. 2, 8, 10, 182, 241).

— (2013). "Aeolian tones generated by a square cylinder with a detached flat plate". In: *AIAA Journal* 51(2).2, pp. 291 –301. DOI: 10.2514/1.J051378 (cit. on pp. 10, 15).

Amiet, R. K. (1975). "Correction of open jet wind tunnel measurements for shear layer refraction". In: *2nd AIAA Aeroacoustics Conference, March 24-26, Hampton, U.S.A, 1975, AIAA Paper 75-532*. DOI: 10.2514/6.1975-532 (cit. on pp. 10, 115, 264, 265, 268, 272).

— (1978). "Refraction of sound by a shear layer". In: *Journal of Sound and Vibration* 54, pp. 467–482. DOI: 10.1016/0022-460X(78)90353-X (cit. on pp. 101, 269).

Astley, R. J. (2014). "Can technology deliver acceptable levels of aircraft noise". In: *Proceedings of INTERNOISE, November 16-19, 2014, Melbourne, Australia* (cit. on p. 1).

Ayoub, A. and K. Karamcheti (1982). "An experiment on the flow past a finite circular cylinder at high subcritical and supercritical Reynolds numbers". In: *Journal of Fluid Mechanics* 118, pp. 1 –26. DOI: 10.1017/S0022112082000937 (cit. on p. 13).

Baban, F. and R. M. C. So (1991). "Aspect ratio effect on flow-induced forces on circular cylinders in a cross-flow". In: *Experiments in Fluids* 10(6), pp. 313–321. DOI: 10.1007/BF00190247 (cit. on p. 13).

Bahr, C., N. S. Zawondny, T. Yardibi, and F. Liu (2011). "Shear layer correction validation using a non-intrusive acoustic point source". In: *16th AIAA/CEAS Aeroacoustic*

conference, June 07-09, Stockholm, Sweden, AIAA Paper 2010-3735. DOI: 10.2514/6.2010-3735 (cit. on pp. 101, 102, 105, 112, 113, 226, 265).

Bahr, C. J., T. F. Brooks, W. H. Humphreys, T. B. Spalt, and D. J. Stead (2014). "Acoustic data processing and transient signal analysis for the hybrid wing body 14-by 22-foot subsonic wind tunnel test". In: *20th AIAA/CEAS Aeroacoustics conference, June 16-20, 2014, Atlanta, USA, AIAA Paper 2014-2345*. DOI: 10.2514/6.2014-2345 (cit. on p. 265).

Bailey, S. C. C., R. J. Martinuzzi, and G. A. Koop (2002). "The effects of wall proximity on vortex shedding from a square cylinder: Three-dimensional effects". In: *Physics of Fluids* 14 (4160). DOI: 10.1063/1.1514972 (cit. on pp. 9, 32, 162, 167, 168, 170, 174).

Baker, C. J. (1980). "The turbulent horseshoe vortex". In: *Journal of Wind Engineering and Industrial Aerodynamics* 6(1), pp. 9 –23. DOI: 10.1016/0167-6105(80)90018-5 (cit. on pp. 11, 13).

Bearman, P. W. (1984). "Vortex shedding from oscillating bluff bodies". In: *Annual Review of Fluid Mechanics* 16, pp. 195–222. DOI: 10.1146/annurev.fl.16.010184.001211 (cit. on p. 46).

Becker, S., H. Lienhart, and F. Durst (2002). "Flow around three-dimensional obstacles in boundary layers". In: *Journal of Wind Engineering and Industrial Aerodynamics* 90, pp. 265 –279. DOI: 10.1016/S0167-6105(01)00209-4 (cit. on pp. 13, 65, 73).

Becker, S., C. Hahn, M. Kaltenbacher, and R. Lerch (2008). "Flow-induced sound of wall-mounted cylinders with different geometries". In: *AIAA Journal* 46(9), pp. 2265–2281. DOI: 10.2514/1.34865 (cit. on pp. 6, 13, 28, 30, 119, 121, 122, 146, 163, 177).

Bendat, J. S. and A. G. Piersol (2010). *Random Data: Analysis and Measurement Procedures, 4^{th} Edition*. Ed. by Balding, D. J. New Jersey: John Wiley and Sons, Inc (cit. on pp. 64, 68–71, 106, 151, 165, 167, 222).

Bies, D. A. and C. H. Hansen (2009). *Engineering Noise Control: Theory and Practice*. Abingdon: CRC press (cit. on pp. 108, 127).

Blackburn, H. M. and W. H. Melbourne (1996). "The effect of free-stream turbulence on sectional lift forces on a circular cylinder". In: *Journal of Fluid Mechanics* 11, pp. 267–292. DOI: 10.1017/S0022112096001309 (cit. on pp. 72, 125).

Blake, W. K. (1986). *Mechanics of flow-induced sound and vibration. Volume 1 General concepts and elementary sources*. Ed. by Frenkiel, F. N. Orlando: Academic Press, Inc (cit. on pp. 9, 10, 15, 162).

Bourgeois, J. A. (2012). "Three-dimensional topology and dynamical modelling of vortex shedding from finite surface-mounted bluff bodies". PhD thesis. University of Calgary (cit. on pp. 14, 18–20, 65, 133, 136, 137, 208).

Bourgeois, J., P. Sattari, and R. Martinuzzi (2011). "Alternating half-loop shedding in the turbulent wake of a finite surface-mounted square cylinder with a thin boundary layer". In: *Physics of Fluids* 23(9), p. 095101. DOI: 10.1063/1.3623463 (cit. on pp. 10–13, 15, 16, 24, 32, 72, 114, 120–122, 130, 137, 139, 149, 157, 158, 177, 190, 192, 237, 240).

Bourgeois, J. A., P. Sattari, and R. J. Martinuzzi (2010). "Quasi-periodic structure of vortical flows produced in the wake of finite bluff bodies partially immersed in a boundary layer". In: *ASME 2010 3rd Joint US-European Fluids Engineering Summer*

Meeting: Volume 1, Symposia Parts A, B, and C, August 1-5, 2010, Montreal, Quebec, Canada, (cit. on pp. 146, 153).

Bradbury, L. J. S. (1976). "Measurements with a pulsed-wire and a hot-wire anemometer in the highly turbulent wake of a normal flat plate". In: *Journal of Fluid Mechanics* 77(03), pp. 473–497. DOI: 10.1017/S0022112076002218 (cit. on p. 61).

Brooks, T. F. and W. M. Humphreys (1999). "Effect of directional array size on the measurement of airframe noise components". In: *5th AIAA/CEAS Aeroacoustic Conference, May 10-12, 1999, Bellevue, USA, AIAA Paper 99-1958* (cit. on pp. 79, 108).

— (2003). "Flap-edge aeroacoustic measurements and predictions". In: *Journal of Sound and Vibration* 261(1), pp. 31–74. DOI: 10.1016/S0022-460X(02)00939-2 (cit. on pp. 79, 80, 83, 102, 104, 283).

— (2005). "Three-dimensional application of DAMAS methodology for aeroacoustic noise source definition". In: *11th AIAA/CEAS Aeroacoustics Conference, May 23-25, 2005, Monterey, USA, AIAA Paper 2005-2960*. Vol. 2960, p. 2005 (cit. on pp. 273, 274).

— (2006). "A deconvolution approach for the mapping of acoustic sources (DAMAS) determined from phased microphone arrays". In: *Journal of Sound and Vibration* 294(4), pp. 856–879. DOI: 10.1016/j.jsv.2005.12.046 (cit. on pp. 3, 79, 80, 82, 84, 85, 93, 95, 96, 225, 273, 277).

Bruun, H. H. (1995). *Hot-wire Anemometry: Principles and Signal Analysis*. Great Britain: Oxford University Press (cit. on pp. 51, 53).

Budair, M., A. Ayoub, and K. Karamcheti (1991). "Frequency measurements in a finite cylinder wake at a subcritical Reynolds number". In: *AIAA Journal* 29(12), pp. 2163–2168. DOI: 10.2514/3.10854 (cit. on p. 13).

Casalino, D. and M. Jacob (2003). "Prediction of aerodynamic sound from circular rods via spanwise statistical modelling". In: *Journal of Sound and Vibration* 262, pp. 815–844. DOI: 10.1016/S0022-460X(02)01136-7 (cit. on pp. 3, 9, 10, 115, 140, 163, 164).

Cheong, C., P. Joseph., Y. Park, and S. Lee (2008). "Computation of an Aeolian tone from a circular cylinder using source models". In: *Applied Acoustics* 69(2), pp. 110–126. DOI: 10.1016/j.apacoust.2006.10.004 (cit. on p. 10).

Christensen, J. J. and J. Hald (2004). *Beamforming: Technical Review*. Tech. rep. Bruel and Kjaer (cit. on pp. 87, 90).

Clauser, F. H. (1954). "Turbulent boundary layers in adverse pressure gradients". In: *Journal of Aeronaturical Sciences* 21(2), pp. 91–108 (cit. on p. 76).

Coles, D. (1956). "The law of the wake in the turbulent boundary layer". In: *Journal of Fluid Mechanics* 1(2), pp. 191–226 (cit. on pp. 73, 75).

Cox, J. S. (1998). "Computation of vortex shedding and radiated sound for a circular cylinder: subcritical to transcritical Reynolds numbers". In: *Theoretical Computational Fluid Dynamics* 12(4), pp. 233–253. DOI: 10.1007/s001620050108 (cit. on p. 10).

Curle, N. (1955). "The influence of solid boundaries upon aerodynamic sound". In: *Proceedings of the Royal Society of London. Series A, Mathematical and Physical Sciences* 231(1187), pp. 505–514. DOI: 10.1098/rspa.1955.0191 (cit. on pp. 3, 9, 115, 177, 179, 237, 275).

Dobrzynski, W. M. (2010). "Airframe noise: landing gear noise". In: *Encyclopedia of Aerospace Engineering* (cit. on p. 1).

Doolan, C. J. (2010). "Computational bluff body aerodynamic noise prediction using a statistical approach". In: *Applied Acoustics* 71(12), pp. 1194 –1203. DOI: 10.1016/j.apacoust.2010.08.004 (cit. on p. 10).

Dougherty, R. P. (2010). "Jet noise beamforming with several techniques". In: *Berlin Beamforming Conference, Feburary 23-24, 2010, Berlin, Germany*, pp. 24–25 (cit. on pp. 80, 88, 96, 273).

Dougherty, R. P., R. C. Ramachandran, and G. Raman (2013). "Deconvolution of sources in aeroacoustic images from phased microphone arrays using linear programming". In: *International Journal of Aeroacoustics* 12(7) (cit. on pp. 82, 85).

Eisenlohr, H. and H. Eckelmann (1989). "Vortex splitting and its consequences in the vortex street wake of cylinders at low Reynolds number". In: *Physics of Fluids* 2.2, pp. 189 –192. DOI: 10.1063/1.857488 (cit. on pp. 24, 172, 173).

El Hassan, M., J. A. Bourgeois, and R. Martinuzzi (2015). "Boundary layer effect on the vortex shedding of a wall-mounted rectangular cylinder". In: *Experiments in Fluids* 56:33. DOI: 10.1007/s00348-014-1882-6 (cit. on pp. 11–14, 18, 20, 76, 77, 137, 154, 157, 220).

Etzold, F and H Fiedler (1976). "The near-wake structures of a cantilevered cylinder in cross flow". In: *Zeitschrift fur Flugwissenschaften* 24, pp. 77–82 (cit. on p. 157).

European Commission (2011). *FLIGHTPATH2050: Europe's vision for aviation.* Tech. rep. Directorate-General for Research and Innovation (cit. on p. 1).

Farivar, D. (1981). "Turbulent uniform flow around cylinders of finite length". In: *AIAA Journal* 19.3, pp. 275 –281. DOI: 10.2514/3.7771 (cit. on pp. 13, 25).

Faszer, A., T. Hynes, C. Blaabjerg, and H.-C. Shin (2006). "Acoustic beamforming and holography measurements of modified boundary layer trailing-edge noise". In: *12th AIAA/CEAS Aeroacoustics Conference, May 8-10, 2006, Cambridge, USA, AIAA Paper 2006-2566.* DOI: 10.2514/6.2006-2566 (cit. on p. 79).

Ffowcs-Williams, J. E. and L. H. Hall (1970). "Aerodynamic sound generation by turbulent flow in the vicinity of a scattering half plane". In: *Journal of Fluid Mechanics* 40(4), pp. 657–670. DOI: 10.1017/S0022112070000368 (cit. on p. 42).

Fox, T. A and J. Apelt (1993). "Fluid-induced loading of cantilevered circular cylinders in a low-turbulence uniform flow Part 3: fluctuating loads with aspect ratios 4 to 25". In: *Journal of Fluids and Structures* 7(4), pp. 375 –386. DOI: 10.1006/jfls.1993.1022 (cit. on pp. 13, 25).

Fox, T. A. and G. S. West (1990). "On the use of end plates with circular cylinders". In: *Experiments in Fluids* 9, pp. 237–239 (cit. on p. 115).

— (1993a). "Fluid-induced loading of cantilevered circular cylinders in a low-turbulence uniform flow Part 1: mean loading with aspect ratios in the range 4 to 30". In: *Journal of Fluids and Structures* 7(1), pp. 1 –14. DOI: 10.1006/jfls.1993.1001 (cit. on pp. 13, 30, 115, 117).

— (1993b). "Fluid-induced loading of cantilevered circular cylinders in a low-turbulence uniform flow Part 2: fluctuating loads on a cantilever of aspect ratio 30". In: *Journal of Fluids and Structures* 7(1), pp. 15 –28. DOI: 10.1006/jfls.1993.1002 (cit. on p. 27).

Frederich, O., E. Wassen, F. Thiele, M. Jensch, M. Brede, F. Hüttmann, and A. Leder (2008). "Numerical Simulation of the Flow Around a Finite Cylinder with Ground Plate in Comparison to Experimental Measurements". In: *New Results in Numerical and Experimental Fluid Mechanics VI: Contributions to the 15th STAB/DGLR Symposium Darmstadt, Germany, 2006*. Ed. by Tropea, C., Jakirlic, S., Heinemann, H.-J., Henke, R., and Hönlinger, H. Berlin, Heidelberg: Springer Berlin Heidelberg, pp. 348–355. ISBN: 978-3-540-74460-3. DOI: 10.1007/978-3-540-74460-3_43. URL: http://dx.doi.org/10.1007/978-3-540-74460-3_43 (cit. on pp. 20, 22–24).

Fujita, H. (2010). "The characteristics of the Aeolian tone radiated from two-dimensional cylinders". In: *Fluid Dynamics Research* 42.1, pp. 1–25. DOI: 10.1088/0169-5983/42/1/015002 (cit. on pp. 10, 115).

Fujita, H., W. Sha, H. Furutani, and H. Suzuki (1998). "Experimental investigation and prediction of aerodynamic sound generated from square cylinders". In: *4th AIAA/CEAS Aeroacousitcs Conference, June 02-04, 1998, Toulouse, France, AIAA Paper 98-2369*. DOI: 10.2514/6.1998-2369 (cit. on pp. 116, 196).

Gerich, D. and H. Eckelmann (1982). "Influence of end plate and free ends on the shedding frequency of circular cylinders". In: *Journal of Fluid Mechanics* 122, pp. 109 –121. DOI: 10.1017/S0022112082002110 (cit. on pp. 13, 26, 120).

Gerrard, J. H. (1955). "Measurements of the sound from circular cylinders in an air stream". In: *Proceedings of the Royal Society of London, Series B* 68, pp. 453–461 (cit. on p. 2).

— (1966). "The mechanics of the formation region of vortices behind bluff bodies". In: *Journal of Fluid Mechanics* 25, pp. 401 –413. DOI: 10.1017/S0022112066001721 (cit. on pp. 7, 138, 181).

Geyer, T., E. Sarradji, and C. Fritzsche (2010). "Measurement of the noise generation at the trailing edge of porous airfoils". In: *Experiments in Fluids* 48, pp. 291–308. DOI: 10.1007/s00348-009-0739-x (cit. on pp. 265, 270).

Geyer, T., E. Sarradji, and J. Giesler (2012). "Application of a beamforming technique to the measurement of airfoil leading edge noise". In: *Advances in Acoustics and Vibration* Article ID 905461. DOI: 10.1155/2012/905461 (cit. on pp. 79, 80, 110, 273, 274).

Geyer, T., E. Sarradj, and G. Herold (2015). "Flow noise generation of cylinders with soft porous cover". In: *21st AIAA/CEAS Aeroacoustics Conference, June 22-26, 2015, Dallas, USA, AIAA Paper 2015-3147*. DOI: 10.2514/6.2015-3147 (cit. on p. 122).

Geyer, T. F. (2011). "Trailing Edge Noise Generation of Porous Airfoils". PhD thesis. Brandenburg University of Technology (cit. on p. 104).

Griffin, O. M. (1985). "Vortex shedding from bluff bodies in a shear flow: a review". In: *Transactions of the ASME: Journal of Fluids Engineering* 107, pp. 298 –306. DOI: 10.1115/1.3242481 (cit. on pp. 24, 26, 29, 184).

Guidelines for community noise (1999). World Health Organisation (cit. on p. 1).

Guo, Y. P., K. J. Yamamoto, and R. W. Stoker (2006). "Experimental study on aircraft landing gear noise". In: *Journal of Aircraft* 43, pp. 306 –317. DOI: 10.2514/1.11085 (cit. on p. 1).

Hain, R., C. J. Kahler, and D. Michaelis (2008). "Tomographic and time resolve PIV measurements on a finite cylinder mounted on a flat plate". In: *Experiments in Fluids* 45.4, pp. 715 –724. DOI: 10.1007/s00348-008-0553-x (cit. on pp. 13, 24).

Hajimirzaie, S. M., C. J. Wojcik, and J. H. J. Buchholz (2012). "The role of shape and relative submergence on the structure of wakes of low-aspect-ratio wall-mounted bodies". In: *Experiments in Fluids* 53.6, pp. 1943 –1962. DOI: 10.1007/s00348-012-1406-1 (cit. on pp. 6, 13, 175).

Heseltine, J. L. (2003). "Flow around a circular cylinder with a free-end". MA thesis. Department of Mechanical Engineering, University of Sakatchewan (cit. on pp. 10, 11).

Hileman, J., B. Thruow, and M. Samimy (2004). "Development and evaluation of a 3-D microphone array to locate individual acoustic sources in a high-speed jet". In: *Journal of Sound and Vibration* 276(3), pp. 649–669. DOI: 10.1016/j.jsv.2003.08.022 (cit. on p. 80).

Holman, J. P. (2012). *Experimental Methods for Engineers*. Boston: McGraw-Hill Education (cit. on p. 63).

Hosseini, Z., J. A. Bourgeois, and R. J. Martinuzzi (2013). "Large-scale structures in dipole and quadrupole wakes of a wall-mounted finite rectangular cylinder". In: *Experiments in Fluids* 54. DOI: 10.1007/s00348-013-1595-2 (cit. on pp. 12–14, 16–19, 116, 121, 122, 133, 138, 139, 146, 192, 208, 209, 211, 234, 235).

Howe, M. S. (1998). *Acoustics of fluid-structure interactions*. Cambridge University Press (cit. on p. 274).

Hu, G, K. Tse, K. Kwok, and Y. Zhang (2015). "Large eddy simulation of flow around an inclined finite square cylinder". In: *Journal of Wind Engineering and Industrial Aerodynamics* 146, pp. 172–184. DOI: 10.1016/j.jweia.2015.08.008 (cit. on pp. 196, 197).

Humphreys, W. M., T. F. Brooks, W. W. Hunter, and K. R. Meadows (1998). "Design and use of microphone directional arrays for aeroacoustic measurements". In: *36th Aerospace Sciences Meeting and Exhibit, Janurary 12-15, 1998, Reno, USA, AIAA Paper 98 - 0471* (cit. on p. 277).

Hutcheson, F. V. and T. F. Brooks (2006). "Noise radiation from single and multiple rod configurations". In: *12th AIAA/CEAS Aeroacoustics Conference, May 08-10, 2006, Cambridge, USA, AIAA Paper-2006-2629* (cit. on pp. 10, 115, 116, 196).

Iglesias, E. L., D. Thompson, and M. Smith (2016). "Experimental study of the aerodynamic noise radiated by cylinders with different cross-sections and yaw angles". In: *Journal of Sound and Vibration* 361, pp. 108–129. DOI: 10.1016/j.jsv.2015.09.044 (cit. on pp. 2, 10).

Javadi, K. and F. Kinai (2014). "On the turbulent flow structures over a short finite cylinder: numerical investigation". In: *Proceedings of the International Conference on Heat Transfer and Fluid Flow, Praque, Czech Republic* (cit. on p. 6).

Johnson, D. H. and D. E. Dudgeon (1993). *Array Signal Processing*. Ed. by Oppenheim, A. v. Upper Saddle River: Pearson Education (cit. on pp. 79, 80, 83).

Jørgensen, F. E (2002). *How to measure turbulence with hot-wire anemometers - a practical guide*. Dantec Dynamics (cit. on p. 57).

Joubert, E., T. Harms, and G. Venter (2015). "Computational simulation of the turbulent flow around a surface mounted rectangular prism". In: *Journal of Wind Engineering and Industrial Aerodynamics* 142, pp. 173–187. DOI: 10.1016/j.jweia.2015.03.019 (cit. on p. 6).

Kaltenbacher, M., M. Escobar, S. Becker, and I. Ali (2010). "Numerical simulation of flow-induced noise using LES/SAS and Lighthill's acoustic analogy". In: *International Journal for Numerical Methods in Fluids* 63, pp. 1101–1122. DOI: 10.1002/fld.2123 (cit. on pp. 28, 30).

Kawamura, T., M. Hiwada, T. Hibino, I. Mabuchi, and M. Kumada (1984). "Flow around a finite circular cylinder on a flat plate (Cylinder height greater than turbulent boundary layer thickness)". In: *Bulletin of Japan Society of Mechanical Engineers* 27(232), pp. 2142 –2151. DOI: 10.1299/jsme1958.27.2142 (cit. on pp. 12–14, 20–23, 25, 27, 31, 65, 114, 146).

Keefe, R. T. (1961). *An investigation of the fluctuating forces acting on a stationary circular cylinder in a subsonic stream, and of the associated sound field*. Tech. rep. UTIA (cit. on pp. 10, 115).

King, W. and E. Pfizenmaier (2009). "An experimental study of sound generated by flow around cylinders of different cross-section". In: *Journal of Sound and Vibration* 328(3), pp. 318 –337. DOI: 10.1016/j.jsv.2009.07.034 (cit. on pp. 13, 28–30, 34).

Kitagawa, T., Y. Fujino, and K. Kimura (1999). "Effects of free-end conditions on end-cell-induced vibration". In: *Journal of Fluids and Structures* 13.4, pp. 499–518. DOI: 10.1006/jfls.1999.0214 (cit. on pp. 25, 27, 46).

Klebanoff, P. (1954). *Characteristics of turbulence in a boundary layer with zero pressure gradient*. Tech. rep. NASA Technical Note no. 1946 (cit. on pp. 74, 75).

Koop, L., K. Ehrenfried, and S. Krober (2005). "Investigation of the systematic phase mismatch in microphone-array analysis". In: *11th AIAA/CEAS Aeroacoustics Conference, May 23-25, 2005, Monterey, USA, AIAA Paper 2005-2962*. DOI: 10.2514/MAERO05 (cit. on pp. 101, 102, 266).

Krajnovic, S. (2011). "Flow around a tall finite cylinder explored by large eddy simulation". In: *Journal of Fluid Mechanics* 676, pp. 294 –317. DOI: 10.1017/S0022112011000450 (cit. on pp. 6, 12, 20, 22–24, 27).

Kurita, T., M. Hara, H. Tamada, Y. Wakabayashi, F. Mizushima, H. Satoh, and T. Shikama (2010). "Reduction of pantograph noise of high-speed trains". In: *Journal of Mechanical Systems for Transportation and Logistics* 3, pp. 63 –74. DOI: 10.1299/jmtl.3.63 (cit. on p. 1).

Lanslots, J., F. Deblauwe, and K. Janssens (2010). "Selecting sound source localization techniques for industrial applications". In: *Sound and Vibration* 44(6), p. 6 (cit. on p. 79).

Leclercq, D. and C. J. Doolan (2009). "The interaction of a bluff body with a vortex wake". In: *Journal of Fluids and Structures* 25(5), pp. 867 –888. DOI: 10.1016/j.jfluidstructs.2009.02.005 (cit. on pp. 10, 115).

Lee, L. (1997). "Wake structure behind a circular cylinder with a free end". In: *Proceedings of the heat transfer and fluids mechanics institute* 35, pp. 241 –251 (cit. on pp. 10, 13, 14, 20, 21, 23, 25, 27, 65, 155).

Legg, M. and S. Bradley (2014). "Automatic 3D scanning surface generation for microphone array acoustic imaging". In: *Applied Acoustics* 76, pp. 230–237. DOI: 10.1016/j.apacoust.2013.08.008 (cit. on p. 273).

Levinson, D., J. M. Mathieu, D. Gillen, and A. Kanafani (1997). "The full cost of high-speed rail: an engineering approach". In: *The Annals of Regional Science* 31, pp. 189–215. DOI: 10.1007/s001680050045 (cit. on p. 1).

Lighthill, M. (1952). "On sound generated aerodynamically". In: *Proceedings of the Royal Society of London. Series A, Mathematical and Physical Sciences* 211, pp. 564–87. DOI: 10.1098/rspa.1952.0060 (cit. on p. 10).

Lira, I. (2002). *Evaluating the Measurement Uncertainty: Fundamentals and Practical Guidance*. Ed. by Afsar, M. Bristol: Institute of Physics Publishing (cit. on pp. 57–60).

Liu, Y., A. R. Quayle, A. P. Dowling, and P. Sijtsma (2008). "Beamforming correction for dipole measurement using two-dimensional microphone arrays". In: *Journal of Acoustical Society of America* 124 (1), pp. 182–191. DOI: 10.112/1.2931950 (cit. on pp. 82, 275).

Loucks, D. P., E. Van Beek, J. R. Stedinger, J. P. Dijkman, and M. T. Villars (2005). *Water resources systems planning and management: an introduction to methods, models and applications*. Paris: UNESCO (cit. on p. 68).

Lu, F. K. (2010). "Surface oil flow visualization: Still useful after all these years". In: *European Physics Journal Special Topics* 182, pp. 51–63. DOI: 10.1140/epjst/e2010-01225-0 (cit. on p. 65).

Lyn, D. A., S. Einav, W. Rod, and J. H. Park (1995). "A laser-doppler velocimetry study of ensemble-averaged characteristics of the turbulent near wake of a square cylinder". In: *Journal of Fluid Mechanics* 304, pp. 285 –319. DOI: 10.1017/S0022112095004435 (cit. on pp. 15, 138, 139).

Maltby, R. (1962). *Flow visualization in wind tunnels using indicators*. Tech. rep. North Atlantic Treaty Organization Advisory Group for Aeronautical Research and Development (cit. on p. 65).

Martinuzzi, R. and C. Tropea (1993). "The flow around surface mounted, prismatic obstacles placed in a fully developed channel flow". In: *Transactions of the ASME: Journal of Fluids Engineering* 115, pp. 85–92. DOI: 10.1115/1.2910118 (cit. on pp. 66, 67, 155, 175).

Mason, P. J. and B. R. Morton (1987). "Trailing vortices in the wakes of surface-mounted obstacles". In: *Journal of Fluid Mechanics* 175, pp. 247 –293. DOI: 10.1017/S0022112087000387 (cit. on pp. 6, 175).

McClean, J. F. and D. Sumner (2014). "An experimental investigation of aspect ratio and incidence angle effects for the flow around surface-mounted finite-height square prisms." In: *Journal of Fluids Engineering* 136 (cit. on p. 20).

Mimani, A., C. Doolan, and P. R. Medwell (2014). "Aeroacoustic time-reversal in the presence of a reflecting surface". In: *Proceedings of INTERNOISE, November 16-19, 2014, Melbourne, Australia* (cit. on p. 126).

Mimani, A., Z. Prime, D. J. Moreau, and C. J. Doolan (2016). "An experimental application of aeroacoustic time-reversal to the Aeolian tone". In: *The Journal of the Acoustical Society of America* 139(2). DOI: 10.1121/1.4941564 (cit. on p. 79).

Moreau, D. and C. Doolan (2013). "Flow-induced sound of wall-mounted finite length cylinders". In: *AIAA Journal* 51, pp. 2493–2502. DOI: 10.2514/1.J052391 (cit. on pp. 6, 13, 15, 27–34, 117, 120).

Moreau, D, M Tetlow, L Brooks, and C Doolan (2010). "Acoustic analysis of flat plate trailing edge noise". In: *20th International Congress on Acoustics, August 23-27, 2010, Sydney, Australia* (cit. on p. 240).

Moreau, D. J., Z. Prime, R. Porteous, C. J. Doolan, and V. Valeau (2014). "Flow-induced noise of a wall-mounted finite airfoil at low-to-moderate Reynolds number". In: *Journal of Sound and Vibration* 333, pp. 6924–6941. DOI: 10.1016/j.jsv.2014.08.005 (cit. on pp. 2, 5, 11, 15, 20, 79, 101, 264, 275, 283).

Moreau, D. J., L. A. Brooks, and C. J. Doolan (2012). "The effect of boundary layer type on trailing edge noise from sharp-edged flat plates at low-to-moderate Reynolds number". In: *Journal of Sound and Vibration* 331(17), pp. 3976–3988. DOI: 10.1016/j.jsv.2012.04.016 (cit. on p. 151).

Morphey, C. L. and P. F. Joseph (2001). "Shear layer refraction corrections for off-axis sources in a jet flow". In: *Journal of Sound and Vibration* 239(4), pp. 819–848. DOI: 10.1006/jsvi.2000.3218 (cit. on p. 265).

Morton, C. and S. Yarusevych (2014). "On vortex shedding from low aspect ratio dual step cylinders". In: *Journal of Fluids and Structures* 44, pp. 251 –269. DOI: 10.1016/j.jfluidstructs.2013.10.007 (cit. on pp. 24, 184).

Mueller, T. (2002). *Aeroacoustic Measurements*. Berlin: Springer (cit. on pp. 79, 86, 100, 102, 106).

Noack, B. R, F. Ohle, and H. Eckelmann (1991). "On cell formation in vortex streets". In: *Journal of Fluid Mechanics* 227, pp. 293 –308. DOI: 10.1017/S0022112091000125 (cit. on pp. 24, 186, 187).

Norberg, C. (2003). "Fluctuating lift on a circular cylinder: review and new measurements". In: *Journal of Fluids and Structures* 17(1), pp. 57 –96. DOI: 10.1016/S0889-9746(02)00099-3 (cit. on pp. 3, 9, 72, 73, 115, 139, 179).

Oerlemanns, S., L. Broersma, and P. Sijtsma (2007). "Quantification of airframe noise using microphone arrays in open and closed wind tunnels". In: *International Journal of Aeroacoustics* 6, pp. 309–331. DOI: 10.1260/147547207783359440 (cit. on pp. 81, 104).

Oerlemanns, S., M Fisher, T Maeder, and K Kgler (2009). "Reduction of wind turbine noise using optimized airfoils and trailing-edge serrations". In: *AIAA Journal* 47(6), pp. 1470–1481. DOI: 10.2514/6.2008-2819 (cit. on p. 79).

Oguma, Y., T. Yamagata, and N. Fujisawa (2013). "Measurement of sound source distribution around a circular cylinder in a uniform flow by combined particle image velocimetry and microphone technique". In: *Journal of Wind Engineering and Industrial Aerodynamics* 18, pp. 1 –11. DOI: 10.1016/j.jweia.2013.04.003 (cit. on pp. 10, 115, 182).

Ogunremi, A. R. and D. Sumner (2015). "The effect of a splitter plate on the flow around a finite prism". In: *Journal of Fluids and Structures* 59, pp. 1–21. DOI: 10.1016/j.jfluidstructs.2015.09.001 (cit. on pp. 13, 19, 137).

Okamoto, S. and Y. Sunabashiri (1992). "Vortex shedding from a circular cylinder of finite length places on a ground plane". In: *Transactions of the ASME: Journal of Fluids Engineering* 114(4), pp. 512 –521 (cit. on pp. 13, 65, 157, 176).

Padois, T., Robin, and A. Berry (2013a). "3D source localisation in a closed wind-tunnel using microphone arrays". In: *19th AIAA/CEAS Aeroacoustics Conference, May 27-29, 2013, Berlin, Germany*. Vol. 2213, p. 2013. DOI: 10.2514/6.2013-2213 (cit. on pp. 80, 101, 102, 105, 113, 265, 270, 273, 274).

Padois, T., C. Prax, and V. Valeau (2013b). "Numerical validation of shear flow correction for beamforming acoustic source localisation in open wind-tunnels". In: *Applied Acoustics* 74, pp. 591–601. DOI: 10.1016/j.apacoust.2012.09.013 (cit. on p. 264).

Palau-Salvador, G., T. Stoesser, J. Frohlich, M. Kappler, and W. Rodi (2010). "Large Eddy Simulation and experiments of flow around finite-height cylinders". In: *Flow Turbulence and Combustion* 84, pp. 239 –275. DOI: 10.1007/s10494-009-9232-0 (cit. on p. 6).

Park, C. W. and S. J. Lee (2000). "Free-end effects on the near wake flow structure behind a finite circular cylinder". In: *Journal of Wind Engineering and Industrial Aerodynamics* 88(2), pp. 231 –246. DOI: 10.1016/S0167-6105(00)00051-9 (cit. on pp. 13, 26, 27).

— (2002). "Flow structure around a finite circular cylinder embedded in various atmospheric boundary layers". In: *Fluid Dynamics Research* 30(4), pp. 197 –215. DOI: 10.1016/S0169-5983(02)00037-0 (cit. on pp. 13, 27).

Pattenden, R. J., S. R. Turnock, and X. Zhang (2005). "Measurements of the flow over a low-aspect-ratio cylinder mounted on a ground plane". In: *Experiments in Fluids* 39(1), pp. 10 –21. DOI: 10.1007/s00348-005-0949-9 (cit. on pp. 13, 20, 22, 23).

Perry, A. E. (1982). *Hot-wire Anemometry*. Oxford: Clarendon (cit. on pp. 51, 53, 61).

Phillips, O. (1956). "The intensity of Aeolian tones". In: *Journal of Fluid Mechanics* 1(06), pp. 607 –624. DOI: 10.1017/S0022112056000408 (cit. on pp. 9, 10, 99, 115).

Pierce, A. D. (1989). *Acoustics: An Introduction to its Physical Principles and Applications*. Woodbury: Acoustical Society of America (cit. on pp. 102, 264, 265).

Pope, S. B. (2000). *Turbulent Flows*. New York: Cambridge University Press (cit. on pp. 73, 74).

Porteous, R., C. Doolan, and D. Moreau (2013). "Directivity pattern of flow-induced noise from a wall-mounted, finite length circular cylinder". In: *Proceedings of Acoustics 2013, November 17-20, 2013, Victor Harbor* (cit. on pp. 27–30).

Porteous, R., D. J. Moreau, and C. J. Doolan (2014a). "A review of flow-induced noise from finite wall-mounted cylinders". In: *Journal of Fluids and Structures* 51, pp. 240–254. DOI: 10.1016/j.jfluidstructs.2014.08.012 (cit. on pp. 5, 283).

Porteous, R., D. Moreau, C. Doolan, and Z. Prime (2014b). "The flow-induced noise of square finite wall-mounted cylinders in different boundary layers." In: *Proceedings of INTERNOISE, November 16-19, 2014, Melbourne, Australia* (cit. on p. 5).

Porteous, R., D. Moreau, and C.Doolan (2014c). "Wake dynamics of circular finite wall-mounted cylinders in different boundary layers". In: *19th Australasian Fluid Mechanics Conference, December 8-11, 2014, Melbourne, Australia* (cit. on p. 12).

Porteous, R., Z. Prime, V. Valeau, C. Doolan, and D. Moreau (2015). "Three-dimensional beamforming of dipolar aeroacoustic sources". In: *Journal of Sound and Vibration* 355, pp. 117–134. DOI: 10.1016/j.jsv.2015.06.030 (cit. on pp. 5, 273).

Powell, A (1964). "Theory of vortex sound". In: *Journal of the Acoustical Society of America* 36(1), pp. 177 –195. DOI: 10.1121/1.1918931 (cit. on p. 18).

Prasad, A. and C. H. K. Williamson (1997). "Three-dimensional effects in turbulent bluff-body wakes". In: *Journal of Fluid Mechanics* 343, pp. 235–265. DOI: 10.1016/S0894-1777(96)00107-0 (cit. on pp. 9, 24).

Prime, Z. and C. J. Doolan (2013). "A comparison of popular beamforming arrays". In: *Proceedings of Acoustics 2013, November 17-20, 2013, Victor Harbor* (cit. on p. 86).

Prime, Z., C. Doolan, and B. Zajamsek (2014a). "Beamforming array optimisation and phase averaged sound source mapping on a model wind turbine." In: *Proceedings of INTERNOISE, November 16-19, 2014, Melbourne, Australia* (cit. on p. 240).

Prime, Z., A. Mimani, D. J. Moreau, and C. J. Doolan (2014b). "An experimental comparison of beamforming, time reversal and near-field acoustic holography for aeroacoustic source localization". In: *20th AIAA/CEAS Aeroacoustics Conference, June 16-20, 2014,AIAA Paper 2014-2917*, pp. 16–20. DOI: 10.2514/6.2014-2917 (cit. on p. 79).

Riabouchinksy, D (1920). "On steady fluid motion with free surfaces". In: *Proceedings of London Mathematics Society Series 2* 19, pp. 206–215 (cit. on p. 181).

Roh, S. C. and S. O. Park (2003). "Vortical flow over the free end surface of a finite circular cylinder mounted on a flat plate". In: *Experiments in Fluids* 32(1), pp. 62 –67. DOI: 10.1007/s00348-002-0532-6 (cit. on pp. 13, 24).

Roozeboom, N. H., L. T. Diosady, B. N. J., J. Panda, and J. C. Ross (2016). "Unsteady PSP measurements on a rectangular cube". In: *54th AIAA Aerospace Sciences Meeting, January 04-08, 2016, AIAA Paper 2016-2017*. DOI: 10.2514/6.2016-2017 (cit. on p. 240).

Roshko, A. (1954). *On the development of turbulent wake from vortex streets*. Tech. rep. 1191. National Advisory Committee for Aeronautics (cit. on pp. 7, 15, 17).

— (1993). "Perspectives on bluff body aerodynamics". In: *Journal of Wind Engineering and Industrial Aerodynamics* 49, pp. 79–100. DOI: 10.1016/0167-6105(93)90007-B (cit. on pp. 3, 8, 9, 181).

Ross, M. H., D. W. Shannon, and S. C. Morris (2008). "Unsteady lift and radiated sound generated by a circular cylinder in a single stream shear layer". In: *14th AIAA/CEAS Aeroacoustics Conference, May 05-07, 2008, AIAA Paper 2008-2962*. DOI: 10.2514/6.2008-2962 (cit. on pp. 10, 217).

Rostamy, N., D. Sumner, D. J. Bergstrom, and J. D. Bugg (2012). "Local flow field of a surface-mounted finite circular cylinder". In: *Journal of Fuids and Structures* 34, pp. 105–122. DOI: 10.1016/j.jfluidstructs.2012.04.014 (cit. on pp. 130, 157, 158).

Rostamy, N., D. Sumner, D. Bergstrom, and J. Bugg (2013). "Instantaneous flow field above the free end of finite-height cylinders and prisms". In: *International Journal of Heat and Fluid Flow* 43, pp. 120–128. DOI: 10.1016/j.ijheatfluidflow.2013.04.005 (cit. on pp. 13, 14, 61).

Saeedi, M., P. Lepoudre, and B. Wang (2014). “Direct numerical simulation of turbulent wake behind a surface-mounted square cylinder”. In: *Journal of Fluids and Structures* 51, pp. 20–39. DOI: 10.1016/j.jfluidstructs.2014.06.021 (cit. on p. 6).

Saha, A. K. (2013). “Unsteady flow past a finite square cylinder mounted on a wall at low Reynolds number”. In: *Computers and Fluids* 88, pp. 599 –615. DOI: 10.1016/j.compfluid.2013.10.010 (cit. on p. 6).

Sahin, B., N. A. Ozturk, and H. Akilli (2007). “Horseshoe vortex system in the vicinity of the vertical cylinder mounted on a flat plate”. In: *Flow Measurement and Instrumentation* 18, pp. 57 –68. DOI: 10.1016/j.flowmeasinst.2006.12.002 (cit. on p. 13).

Sakamoto, H. and M. Arie (1983). “Vortex shedding from a rectangular prism and a circular cylinder placed vertically in a turbulent boundary layer”. In: *Journal of Fluid Mechanics* 126, pp. 147 –165. DOI: 10.1017/S0022112083000087((cit. on pp. 12–18, 20–23, 27, 31, 155, 175, 176, 178).

Sakamoto, H. and S. Oiwake (1984). “Fluctuating forces on a rectangular prism and a circular cylinder placed vertically in a turbulent boundary layer”. In: *Transactions of the ASME: Journal of Fluids Engineering* 106, pp. 160 –166 (cit. on pp. 13, 18, 26, 196, 197).

Sarradj, E. (2010). “A fast signal subspace approach for the determination of absolute levels from phased microphone array measurements”. In: *Journal of Sound and Vibration* 329, pp. 1553–1569. DOI: 10.1016/j.jsv.2009.11.009 (cit. on p. 82).

— (2012). “Three-dimensional acoustic source mapping with different beamforming steering vector formulations”. In: *Advances in Acoustics and Vibration* Article ID 292695. DOI: 10.1155/2012/292695 (cit. on pp. 80, 82, 83, 265, 273, 275).

Sattari, P., J. A. Bourgeois, and R. J. Martinuzzi (2012). “On the vortex dynamics in the wake of a finite surface-mounted square cylinder”. In: *Experiments in Fluids* 52.5, pp. 1149 –1167. DOI: 10.1007/s00348-011-1244-6 (cit. on pp. 12, 13, 15, 18, 177).

Savory, E. and N. Toy (1986). “Hemispheres and hemisphere-cylinders in turbulent boundary layers”. In: *Journal of Wind Engineering and Industrial Aerodynamics* 23, pp. 345–364. DOI: 10.1016/0167-6105(86)90054-1 (cit. on p. 176).

Schlinker, R. H. and M. R. Fink (1976). “Vortex noise from nonrotating cylinders and airfoils”. In: *14th Aerospace Sciences Meeting, Janurary 26-28, 1976, Washington, USA, AIAA Paper 76 - 81*. DOI: 10.2514/6.1976-81 (cit. on pp. 2, 3, 10, 115).

Sijtsma, P. (2007). “CLEAN based on spatial source coherence”. In: *13th AIAA/CEAS Aeroacoustics Conference, May 21-23, 2007, Rome, Italy, AIAA Paper 2007-3436*. Vol. 3436, p. 2007 (cit. on pp. 80, 85, 86, 100, 226, 274).

Sijtsma, P. and R. W. Stoker (2004). *Determination of absolute contributions of aircraft noise components using fly-over array measurements*. Tech. rep. National Aerospace Laboratory NLR (cit. on pp. 82, 104, 277).

Siller, H., M. Drescher, G. Saueressig, and R. Lange. (2010). “Fly-over source localisation on a Boeing 747-400”. In: *Proceedings from the Berlin Beamforming Conference, Feburary 27-28, 2010, Berlin, Germany* (cit. on pp. 2, 79).

Simpson, R. L. (2001). “Junction flows”. In: *Annual Review of Fluid Mechanics* 33, pp. 415 –443. DOI: 10.1146/annurev.fluid.33.1.415 (cit. on p. 11).

Spalart, P. R. (1988). "Direct simulation of a turbulent boundary layer up to $R_\theta = 1410$". In: *Journal of Fluid Mechanics* 187, pp. 61–98. DOI: 10.1017/S0022112088000345 (cit. on pp. 74–76).

Sumner, D. (2013). "Flow above the free end of a surface-mounted finite height circular cylinder: A review". In: *Journal of Fluids and Structures* 43, pp. 41 –63. DOI: 10.1016/j.jfluidstructs.2013.08.007 (cit. on pp. 24, 31).

Sumner, D., J. Heseltine, and O. Dansereau (2004). "Wake structure of a finite circular cylinder of small aspect ratio". In: *Experiments in Fluids* 37(5), pp. 720–730. DOI: 10.1007/s00348-004-0862-7 (cit. on pp. 13, 14, 23–25, 27, 31, 114, 116, 196, 197).

Sumner, D., Rostamy, D. J. Bergstrom., and J. Bugg (2015). "Influence of aspect ratio on the flow above the free end of a surface-mounted finite cylinder". In: *International Journal of Heat and Fluid Flow* 56, pp. 290–304. DOI: 10.1016/j.ijheatfluidflow.2015.08.005 (cit. on pp. 11, 13).

Susuki, T. (2011). "L_1 generalised inverse beamforming algorithm resolving coherent/incoherent, distributed and multipole sources". In: *Journal of Sound and Vibration* 330, pp. 5835–5851. DOI: 10.1016/j.jsv.2011.05.021 (cit. on p. 82).

Suzuki, T. (2006). "Identification of multiple noise sources in low Mach number jets near the peak frequency". In: *Journal of the Acoustical Society of America* 119(6), pp. 3649–3659. DOI: 10.1121/1.2200070 (cit. on p. 79).

Szepessy, S. and P. W. Bearman (1992). "Aspect ratio and end plate effects on vortex shedding from a circular cylinder". In: *Journal of Fluid Mechanics* 234, pp. 191 –217. DOI: 10.1017/S0022112092000752 (cit. on pp. 9, 13).

Taniguchi, S, H. Sakamoto, and M Arie (1981). "Flow around circular cylinders of finite height placed vertically in turbulent boundary layers". In: *Bulletin of JSME* 24, pp. 37–44. DOI: 10.1299/jsme1958.24.37 (cit. on p. 157).

Uematsu, Y. and M. Yamada (1994). "Aerodynamic forces on circular cylinders of finite height". In: *Journal of Wind Engineering and Industrial Aerodynamics* 51, pp. 249 –265. DOI: 10.1016/0167-6105(94)90007-8 (cit. on p. 13).

Uematsu, Y., M. Yamada, and K. Ishii (1990). "Some effects of free-stream turbulence on the flow past a cantilevered circular cylinder". In: *Journal of Wind Engineering and Industrial Aerodynamics* 33, pp. 43 –52. DOI: 10.1016/0167-6105(90)90019-9 (cit. on pp. 13, 65).

Uffinger, T., I. Ali, and S. Becker (2013). "Experimental and numerical investigation of the flow around three different wall-mounted cylinder geometries of finite length". In: *Journal of Wind Engineering and Industrial Aerodynamics* 119, pp. 13 –27. DOI: 10.1016/j.jweia.2013.05.006 (cit. on pp. 6, 11, 13).

Unal, M. F. and D. Rockwell (1988). "On vortex formation from a cylinder. Part 1. The initial instability". In: *Journal of Fluid Mechanics* 190, pp. 491–512. DOI: 10.1017/S0022112088001429 (cit. on p. 138).

Vallentine, H. R. (1967). *Applied Hydrodynamics*. London : Butterworths (cit. on p. 8).

van Driest, E. R (1956). "On turbulent flow near a wall". In: *Journal of the Aeronautical Sciences* 23(11), pp. 1007–1011. DOI: 10.2514/8.3713 (cit. on pp. 74, 75, 77).

Vickery, B. J. (1966). "Fluctuating lift and drag on a long cylinder of square cross-section in a smooth and in a turbulent stream". In: *Journal of Fluid Mechanics* 25 (3), pp. 481 –494. DOI: 10.1017/S002211206600020X (cit. on pp. 115, 116, 121, 163, 196).

Vinuesa, R., P. Schlatter, J. Malm, C. Mavriplis, and D. S. Henningson (2015). "Direct numerical simulation of the flow around a wall-mounted square cylinder under various inflow conditions". In: *Journal of Turbulence* 16 (6), pp. 555–587. DOI: 10.1080/14685248.2014.989232 (cit. on p. 6).

Wang, H. and Y. Zhou (2009). "The finite-length square cylinder near wake". In: *Journal of Fluid Mechanics* 638, pp. 453 –490. DOI: 10.1017/S0022112009990693 (cit. on pp. 12–14, 16–20, 32, 61, 134, 137–139, 146, 157, 158, 176, 177).

Wang, H., Y. Zhou, C. K. Chan, and K. S. Lam (2006). "Effect of initial conditions on interaction between boundary layer and a wall-mounted finite-length-cylinder wake". In: *Physics of Fluids* 18, p. 065106. DOI: 10.1063/1.2212329 (cit. on pp. 12, 13, 18, 19, 31, 130, 134, 136, 137, 157, 177, 182, 208, 209, 234).

Wang, H. F., H. L. Cao, and Y. Zhou (2014). "POD analysis of a finite-length cylidner near wake". In: *Experiments in Fluids* 55, pp. 1790–1805. DOI: 10.1007/s00348-014-1790-9 (cit. on pp. 13, 15, 17, 19, 65, 121, 122, 158, 176).

Wang, H., Y. Zhou, C. Chan, W. Wong, and K. Lam (2004). "Flow structure around a finite-length square prism". In: *15th Australasian Fluid Mechanics Conference, December 13-17, 2004, Sydney, Australia* (cit. on pp. 10, 12–16).

Welch, P. (1967). "The use of Fast Fourier Transform for the estimation of power spectra: A method based on time averaging over short, modified periodograms". In: *IEEE Transactions on Audio and Electroacousticics* AU-15, pp. 70–73. DOI: 10.1109/TAU.1967.1161901 (cit. on pp. 70, 140).

Wilcox, D. C. (2006). *Turbulence modeling for CFD*. La Canada, Calif. : DCW Industries (cit. on pp. 74, 75).

Williamson, C. H. K. (1989). "Oblique and parallel modes of vortex shedding in the wake of a circular cylinder at low Reynolds Numbers". In: *Journal of Fluid Mechanics* 206, pp. 579 –627. DOI: 10.1017/S0022112089002429 (cit. on pp. 24, 26, 27, 47, 146, 153).

— (1996). "Vortex dynamics in the cylinder wake". In: *Annual Review of Fluid Mechanics* 28, pp. 477 –539. DOI: 10.1146/annurev.fl.28.010196.002401 (cit. on pp. 3, 7–9, 15, 18, 137).

Yakhot, A., T. Anor, H. Liu, and N. Nikitin (2006). "Direct numerical simulation of turbulent flow around a wall-mounted cube: spatio-temporal evolution of large-scale vortices". In: *Journal of Fluid Mechanics* 566, pp. 1–9. DOI: 10.1017/S0022112006002151 (cit. on pp. 66, 67).

Yardibi, T., J. Li, P. Stoica, and L. N. Cattafesta (2008). "Sparsity constrained deconvolution apapproach for acoustic source mapping". In: *Journal of the Acoustical Society of America* 123, pp. 2631–2642. DOI: 10.1121/1.2896754 (cit. on p. 85).

Yardibi, T., C. Bahr, N. Zawodny, F. Liu, L. C. III, and J. Li (2010). "Uncertainty analysis of the standard delay-and-sum beamformer and array calibration". In: *Journal of Sound and Vibration* 329, pp. 2654–2682. DOI: 10.1016/j.jsv.2010.01.014 (cit. on pp. 70, 82, 104, 106, 108).

Yoshida, M., M. Koike, and T. Fukano (2003). "A study on the Aeolian tones generated from square cylinders with rounded corners". In: *9th AIAA/CEAS Aeroacoustics Conference and Exhibit, May 12-14, 2003, Hilton Head, USA, AIAA Paper 2003-3218*. DOI: 10.2514/6.2003-3218 (cit. on pp. 116, 196).

Zdravkovich, M. M. (1997). *Flow around Circular Cylinders: Volume 1: Fundamentals.* Oxford : Oxford University Press (cit. on p. 184).

Appendix A

Additional data presentation

Some results from the hot-wire wake survey experiments and beamforming images were not included in the main text because they did not add to the discussion. The complete set of results from these experiments are shown here. These include the mean velocity and turbulence intensity maps for all FWMCs tested in the HTB and the full set of beamforming source maps for all FWMCs tested in both the LTB and the HTB over the full broadband frequency range (3 kHz to 10 kHz).

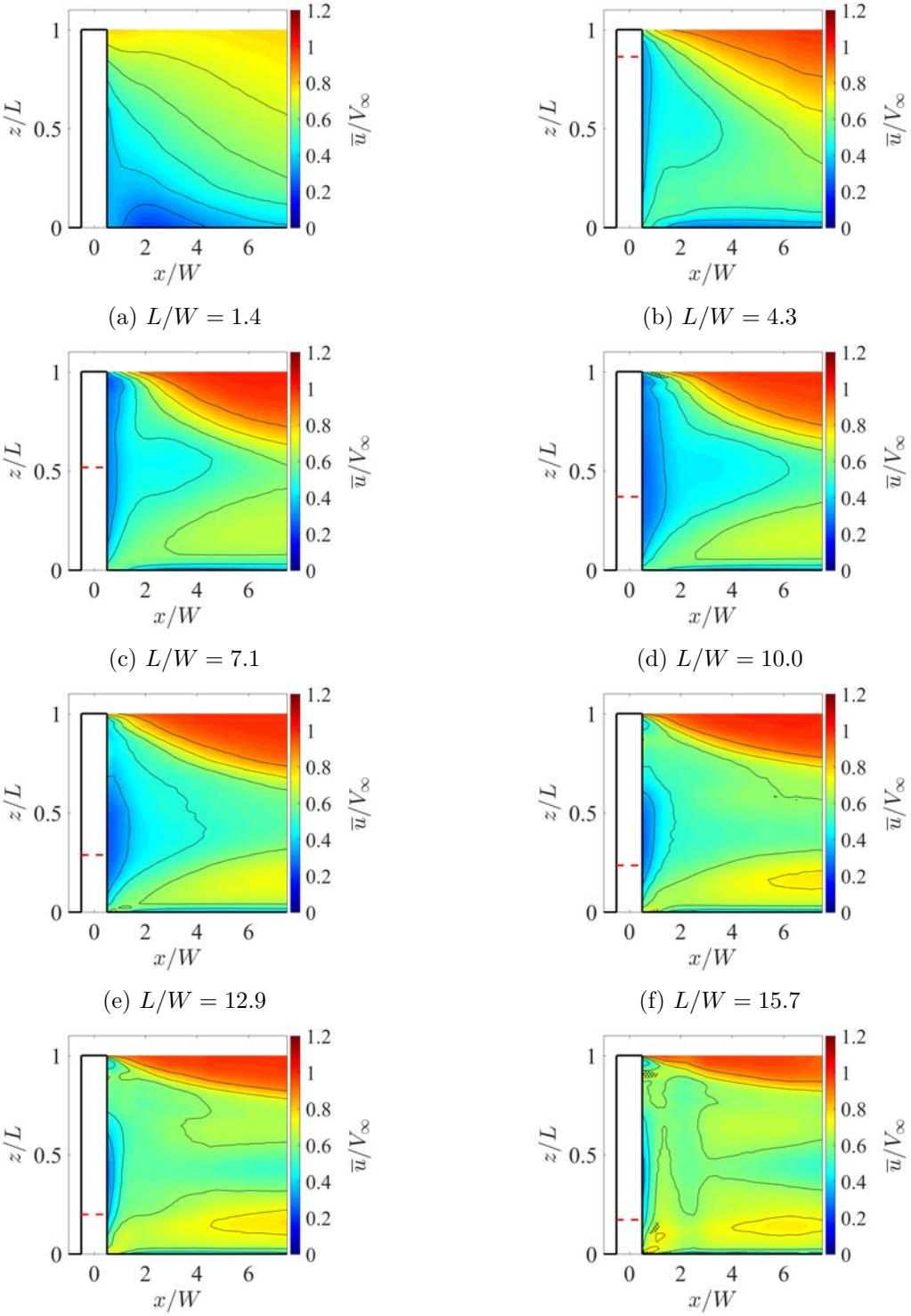

(a) $L/W = 1.4$ (b) $L/W = 4.3$

(c) $L/W = 7.1$ (d) $L/W = 10.0$

(e) $L/W = 12.9$ (f) $L/W = 15.7$

(g) $L/W = 18.6$ (h) $L/W = 21.4$

Figure A.1: Colourmaps showing the mean velocity contours in the wake of 8 different aspect ratio FWMCs in the HTB. The mean velocity is normalised by the free-stream velocity, $V_\infty = 32$, while the ordinate axis has been normalised by the height of each cylinder so that $z/L = 1$ is the free-end of the cylinder. The relative height of the boundary layer for each aspect ratio is indicated by the red dashed line. The plane of the hot-wire measurements was $y/W = 0.6$. Regions where the hot-wire measured the turbulence intensity $T.I.$>0.3 are cross hatched.

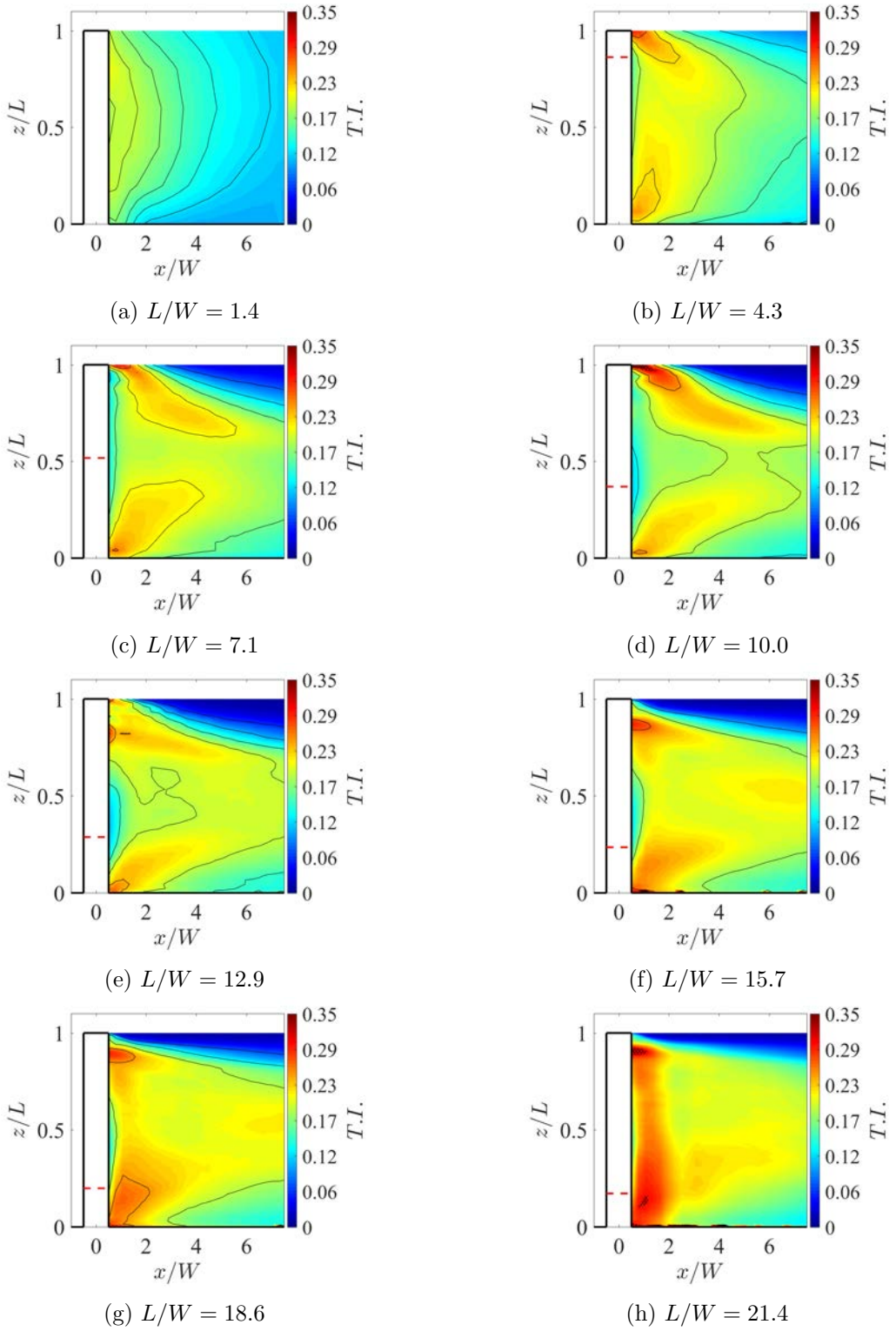

(a) $L/W = 1.4$ (b) $L/W = 4.3$

(c) $L/W = 7.1$ (d) $L/W = 10.0$

(e) $L/W = 12.9$ (f) $L/W = 15.7$

(g) $L/W = 18.6$ (h) $L/W = 21.4$

Figure A.2: Colourmaps showing the turbulence intensity contours in the wake of 8 different aspect ratio FWMCs in the HTB. The turbulence intensity is denoted $T.I. = \sigma_u/V_\infty$, calculated as the standard deviation of the velocity of the signal normalised by the free-stream value. The ordinate axis has been normalised by the span of each cylinder so that $z/L = 1$ is the free-end of the cylinder. The relative height of the boundary layer for each aspect ratio is indicated by a dashed red line. The plane of the hot-wire measurements was $y/W = 0.6$. Regions where the hot-wire measure the turbulence intensity $T.I. > 0.3$ are cross hatched.

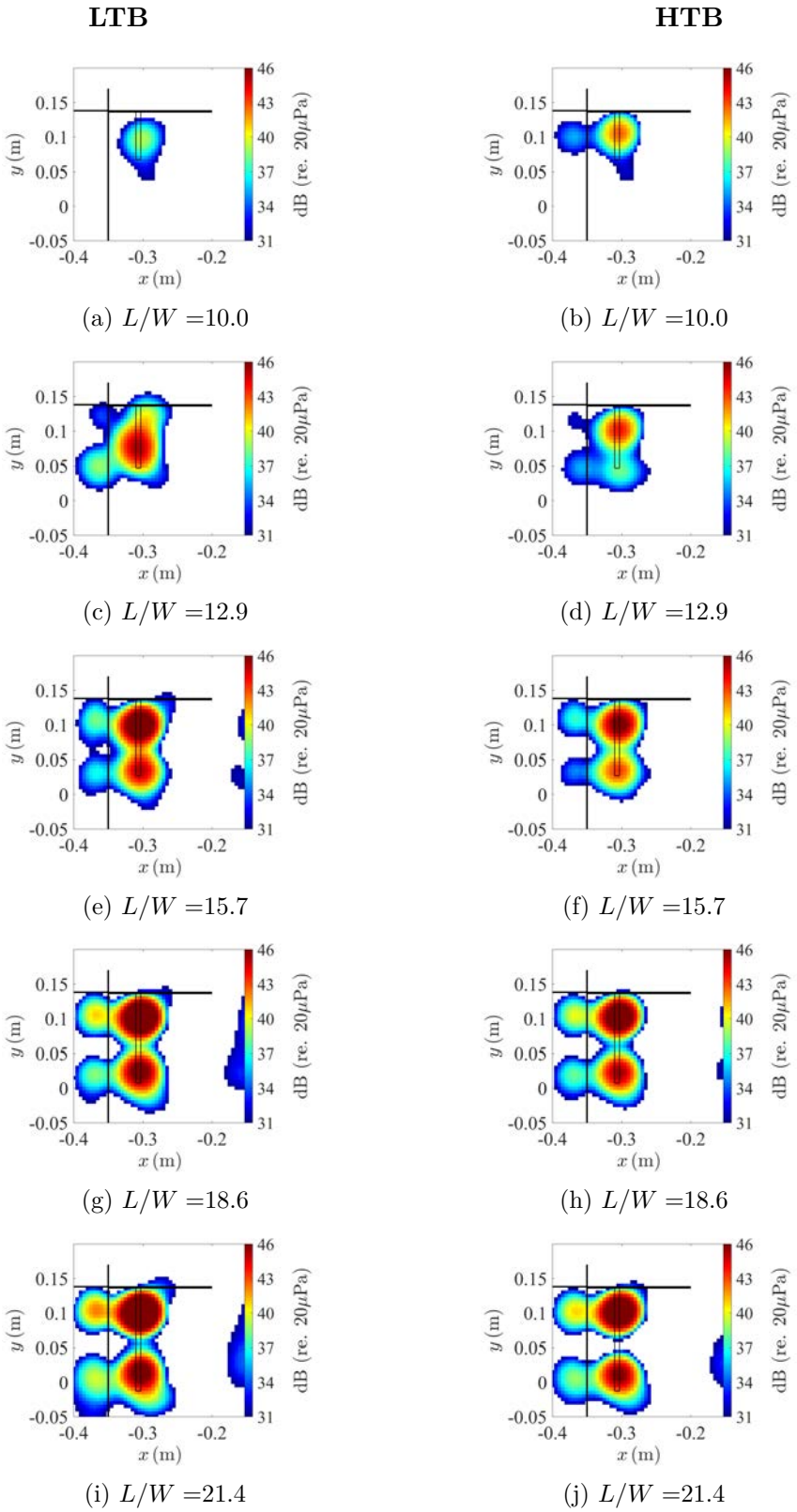

(a) L/W =10.0 (b) L/W =10.0

(c) L/W =12.9 (d) L/W =12.9

(e) L/W =15.7 (f) L/W =15.7

(g) L/W =18.6 (h) L/W =18.6

(i) L/W =21.4 (j) L/W =21.4

Figure A.3: Beamforming maps for FWMCs between $10 < L/W < 21.4$ at a $1/3^{\text{rd}}$ octave band centre frequency of 4 kHz. The left column shows the maps for FWMCs in the LTB while the right column shows maps for FWMCs in the HTB. In each map the flow is travelling from left to right.

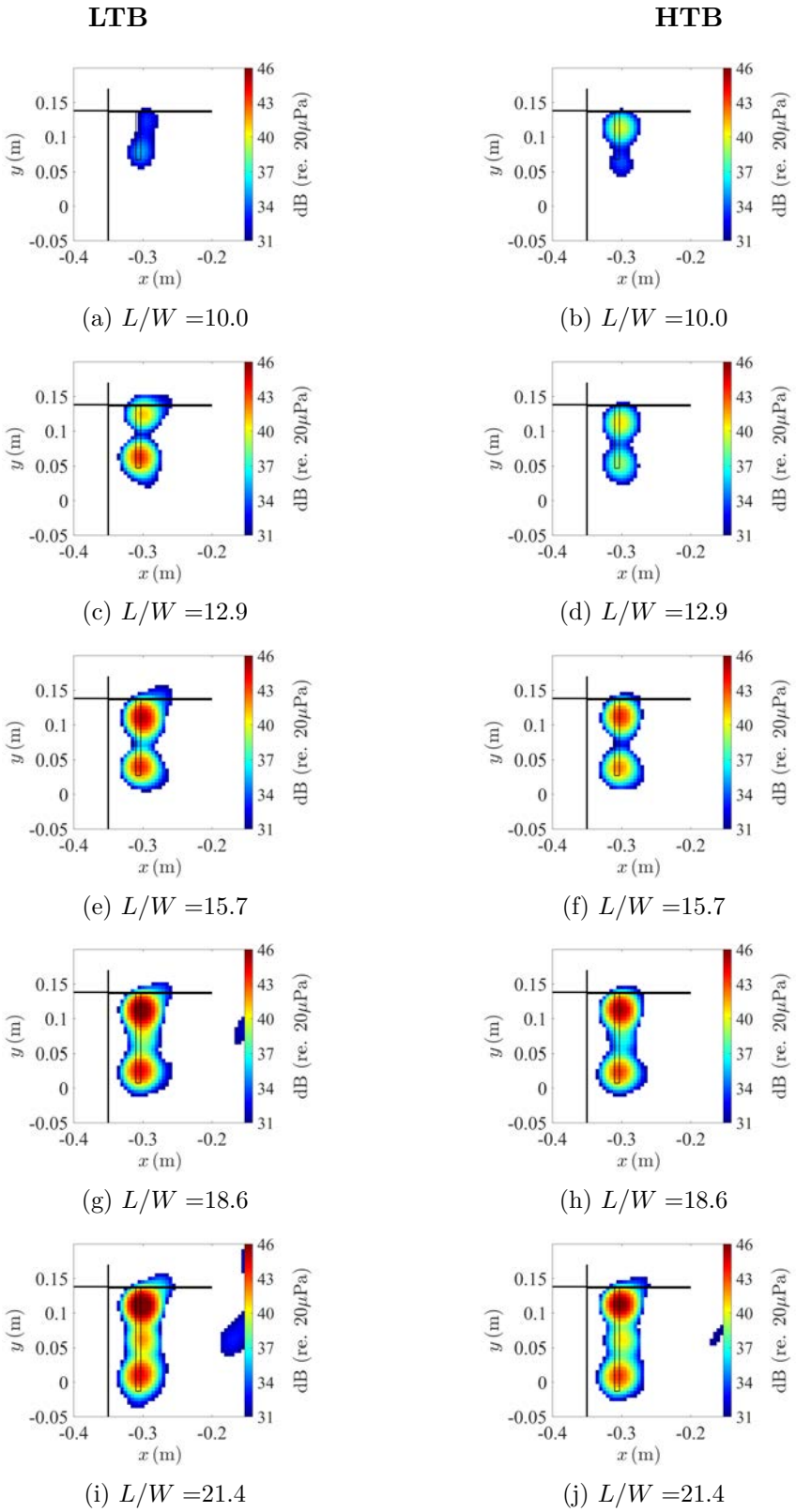

(a) L/W =10.0 (b) L/W =10.0

(c) L/W =12.9 (d) L/W =12.9

(e) L/W =15.7 (f) L/W =15.7

(g) L/W =18.6 (h) L/W =18.6

(i) L/W =21.4 (j) L/W =21.4

Figure A.4: Beamforming maps for FWMCs between $10 < L/W < 21.4$ at a $1/3^{\text{rd}}$ octave band centre frequency of 5 kHz. The left column shows the maps for FWMCs in the LTB while the right column shows maps for FWMCs in the HTB. In each map the flow is travelling from left to right.

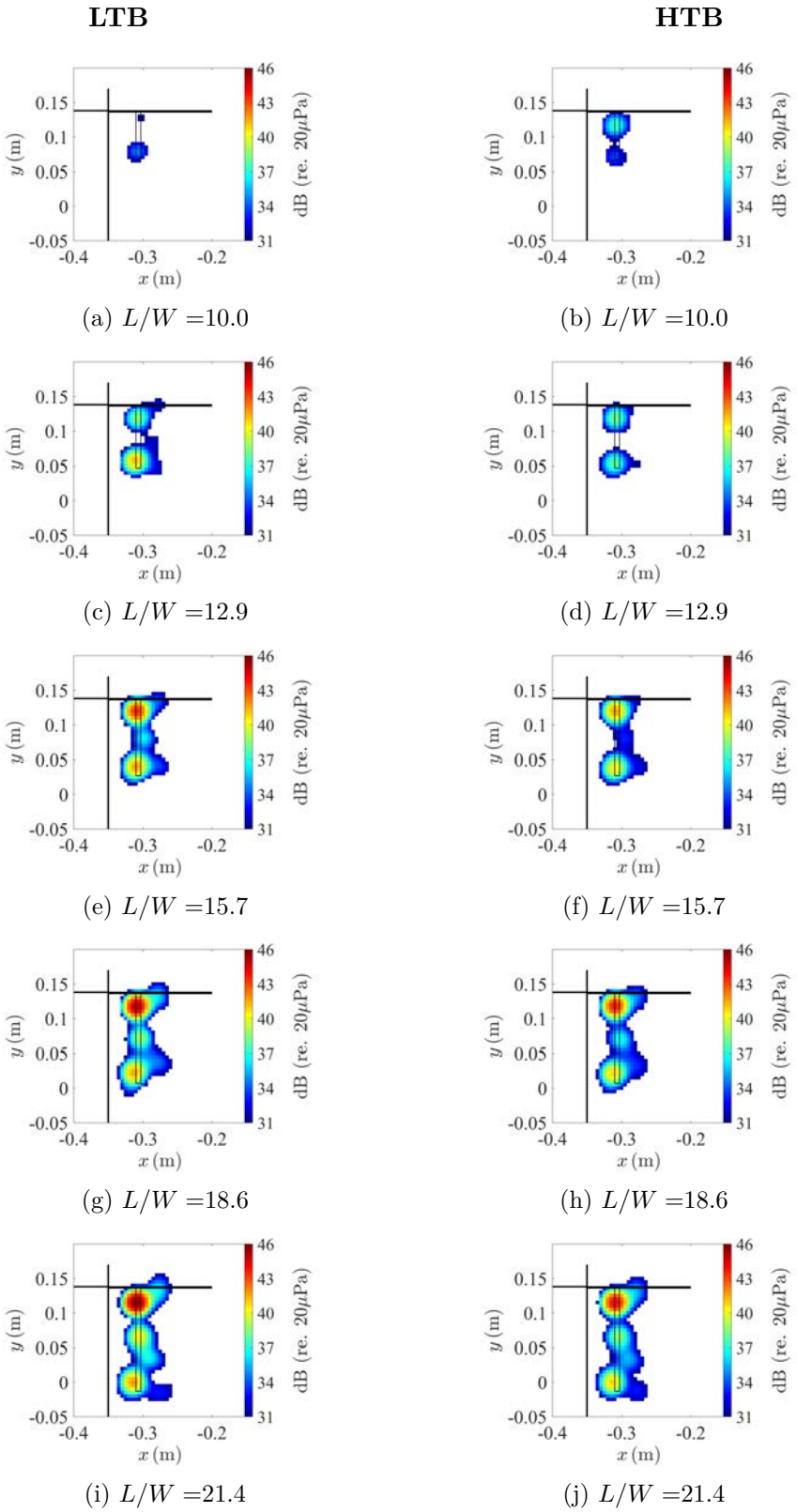

(a) L/W =10.0 (b) L/W =10.0

(c) L/W =12.9 (d) L/W =12.9

(e) L/W =15.7 (f) L/W =15.7

(g) L/W =18.6 (h) L/W =18.6

(i) L/W =21.4 (j) L/W =21.4

Figure A.5: Beamforming maps for FWMCs between $10 < L/W < 21.4$ at a $1/3^{\text{rd}}$ octave band centre frequency of 6.3 kHz. The left column shows the maps for FWMCs in the LTB while the right column shows maps for FWMCs in the HTB. In each map the flow is travelling from left to right.

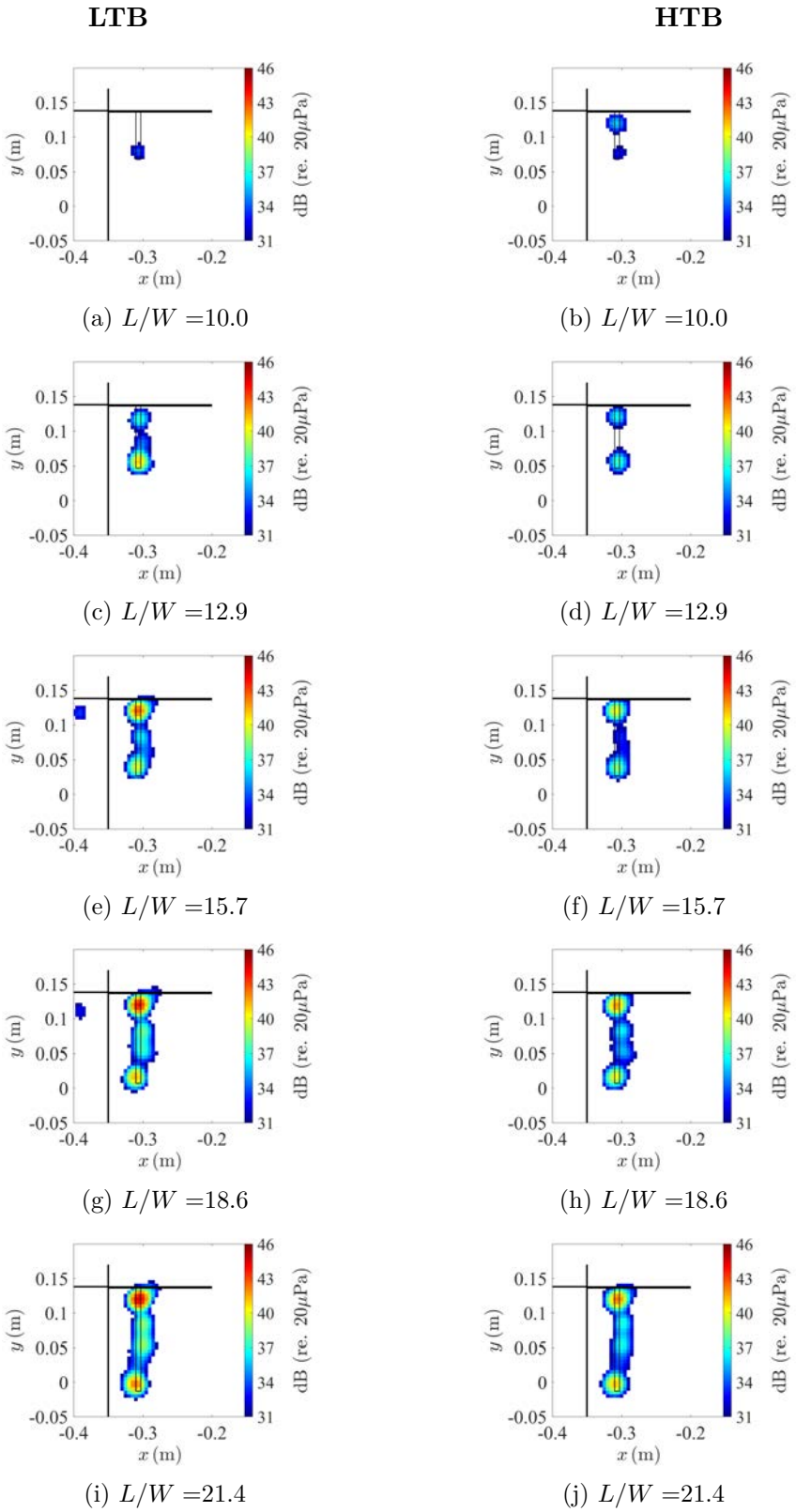

(a) L/W =10.0 (b) L/W =10.0

(c) L/W =12.9 (d) L/W =12.9

(e) L/W =15.7 (f) L/W =15.7

(g) L/W =18.6 (h) L/W =18.6

(i) L/W =21.4 (j) L/W =21.4

Figure A.6: Beamforming maps for FWMCs between $10 < L/W < 21.4$ at a $1/3^{\text{rd}}$ octave band centre frequency of 8 kHz. The left column shows the maps for FWMCs in the LTB while the right column shows maps for FWMCs in the HTB. In each map the flow is travelling from left to right.

Appendix B

The generalised shear layer correction method

Chatper 4 compared three different beamforming shear layer correction methodologies including the method of Padois et al. (2013b), Amiet's method (Amiet 1975) and Ray Tracing (Pierce 1989). In this chapter, a fourth methodology is formulated, known as the Generalised Shear Layer Correction method (GSLC). The GSLC makes possible computationally efficient shear layer corrections for a *three-dimensional* scan-grid. This is necessary when performing three-dimensional beamforming, which is developed in Appendix C.

B.1 Introduction

Acoustic measurements in open-jet anechoic wind tunnels are often performed with the microphones located outside of the mean flow in a quiescent environment. This means that ray paths exiting the potential core of the jet will cross a shear layer (the layer of fluid between the potential core and the stagnant flow) before reaching the microphone. Consequently, the ray paths will be refracted during their path toward the microphone, changing the propagation time of the ray from what it would have been had the entire domain consisted of stagnant air.

This is an important effect to model when considering acoustic source localisation with a phased microphone array. Phased arrays utilise the expected differences in propagation time between array microphones to phase shift each signal the appropriate amount and accurately localise an acoustic source. Therefore, in the presence of a shear layer, time delays based on a simple straight-line source-to-receiver model will cause erroneous source localisation results.

Currently, there are several practical methods to correct for shear layer refraction in aeroacoustic beamforming. The first, originally proposed by Padois et al. (2013b), is a simple shift of the entire source map upstream by a distance $x_s = M_\infty h$, where M_∞ is the Mach number of the potential core of the flow and h is the distance from the source to the shear layer. The method is an approximation based on an order of magnitude estimate of a two-dimensional situation, but has been shown to work sufficiently well in practice for planar beamformers with low Mach number shear layers (Moreau et al. 2014).

The most commonly employed method is the method of Amiet (Amiet 1975). This involves analytically solving for the change in propagation time due to the acoustic rays convecting and refracting through the shear layer. Here the shear layer is assumed to be an infinitely thin boundary (a line) that separates two media; one medium where there is a mean flow and one where there is no flow. The method is mathematically simple, but implicit for source-receiver locations, so iterative schemes must be employed to solve for the propagation time. As mentioned, the method is strictly only suitable for a two-dimensional case, where the microphone and the source lie in the same plane. However, the method has been extended by Bahr et al. (2011) to make it suitable for out-of-plane source/microphone combinations (although it still has the restriction of a planar shear layer shape). More recently, Bahr et al. (2014) described a modification to this method to allow for a quasi 3D shear layer (a rectangle), but it relies on several assumptions that may be erroneous.

A third method is to numerically integrate the ray path through the assumed (or measured) velocity field to calculate the propagation time. The differential equations that are integrated are known as the 'ray tracing equations' (Pierce 1989) and come as a direct consequence of an Euler-Lagrange minimisation of the emission time (Fermat's Principle). While this method can theoretically account for any shear layer shape and is more accurate than the aforementioned methods, it is extremely computationally expensive and not practical when a large scanning grid is used.

Recently, several articles (Sarradj 2012; Padois et al. 2013a) have been published on extending source localisation into the third-dimension and it now appears practical to do so using non-planar arrays arranged around an open-jet (see Appendix C). However, with the exception of ray tracing (and possibly the modified Amiet method of Bahr et al. (2014)), the shear layer correction methods described above are exclusively for 2D (planar) shear layers, and are therefore not suitable for three-dimensional beamforming.

Additionally, there are several instances where shear layer refraction effects cannot be accounted for accurately using Amiet's method, even when using a planar array to beamforming a 2D scanning grid. This situation would occur when the shape of the open jet is not planar but curved such as circular jet exit (as in the work of Geyer et al. (2010)) or an octagonal jet. Morphey and Joseph (2001) have developed an analytical, but still implicit, method to calculate the ray propagation times for the specific case of off-axis sources inside a circular jet. The method, however, is not suitable for other jet exit profiles, such as rectangles or ellipses.

Having provided an overview of the most popular shear layer correction schemes, it is apparent that the current methods available are either restricted to only 2D planar shear layers (Amiet's solution), are too specific (Morphey and Joeseph's solution), or too computationally expensive (ray tracing). There is thus a requirement for the development of a computationally inexpensive, generalised method to solve the shear layer refraction problem for use in beamforming. In this chapter, the *generalised shear layer correction* (GSLC) method is proposed as a potential solution. The scheme is computationally fast and can be applied to any smooth convex shear layer profiles (including circles and ellipses) thus making it highly suitable for three-dimensional beamforming with non-planar arrays.

This chapter will first mathematically develop the GSLC in Section 2. Section 3 of

this chapter will mathematically prove that for a planar shear layer case, solving the GSLC is equivalent to solving Amiet's correction scheme. In the fourth section, the GSLC will be used on an experimental test case. The chapter is concluded in Section 5.

B.2 The generalised shear layer correction scheme

The Generalised Shear Layer Correction scheme (herein denoted GSLC) is inspired by the emission time calculation method presented by Koop et al. (2005). In this paper, the emission time of a ray from a source to a receiver through a planar shear layer is calculated as a one-dimensional time minimisation problem. Here, we extended the analysis to three-dimensions.

Consider a point source located at position **S** that lies in a uniform flow travelling in the x-direction. The flow is bounded by a surface **r** that is smooth, continuous and convex in the $y-z$ plane. Outside of this boundary, the flow is quiescent ($V=0$). Within the boundary defined by **r**, the free-stream velocity is $V_\infty\hat{\mathbf{i}}$. The microphones are assumed to lie outside of the boundary defined by **r** at position **R**. The speed of sound in quiescent air is denoted c_0.

The shear layer surface, **r**, is assumed to have a constant cross-section in the $y-z$ plane, i.e., it does not spread downstream. Therefore, the surface can be parameterised by two variables, u and v, such that

$$\mathbf{r}(u,v) = u\hat{\mathbf{i}} + y(v)\hat{\mathbf{j}} + z(v)\hat{\mathbf{k}} \tag{B.1}$$

The microphone receives acoustic rays that travel from **S** through the shear layer to position **R**. The point where the acoustic rays intersect the shear layer is denoted position **I**. Figure B.1 summarises the nomenclature used above.

The total time, τ_{total}, that it takes a ray to travel from **S** to **R** is given by

$$\tau_{total} = t_1 + t_2 \tag{B.2}$$

where t_1 is the time is takes to travel from **S** to **I** and t_2 is the time is takes to travel from **I** to **R**. The unknown variable in this situation is the shear layer intersection point, **I**. However, according to Fermat's principle the variable **I** will be such that the total time, τ, is minimised. Hence, to find **I** (and therefore τ_{total}), the dependence of τ_{total} on **I** must be calculated and the minimum found.

From Figure B.1, the path adjoining **I** to **R** is a straight line segment through quiescent air. Hence, t_2 can be calculated by

$$t_2 = \frac{|\mathbf{I}-\mathbf{R}|}{c_0} \tag{B.3}$$

where $|.|$ denotes the L-2 norm of a vector. To determine t_1, the approach of (Koop et al. 2005) is used. Here, a wave front is emitted from point **S** and travels to point **I** after a time t_1. The wave front can be thought of as a vector sum of the wave front without the mean flow and that with the mean flow. In this sense, the wave front reaches point **E** after a time t_1 on the surface that is $c_0 t_1$ distance away from **S** and is instantaneously transported to **I**, which lies a distance $V_\infty t_1$ away from **E**. We can then make use of the

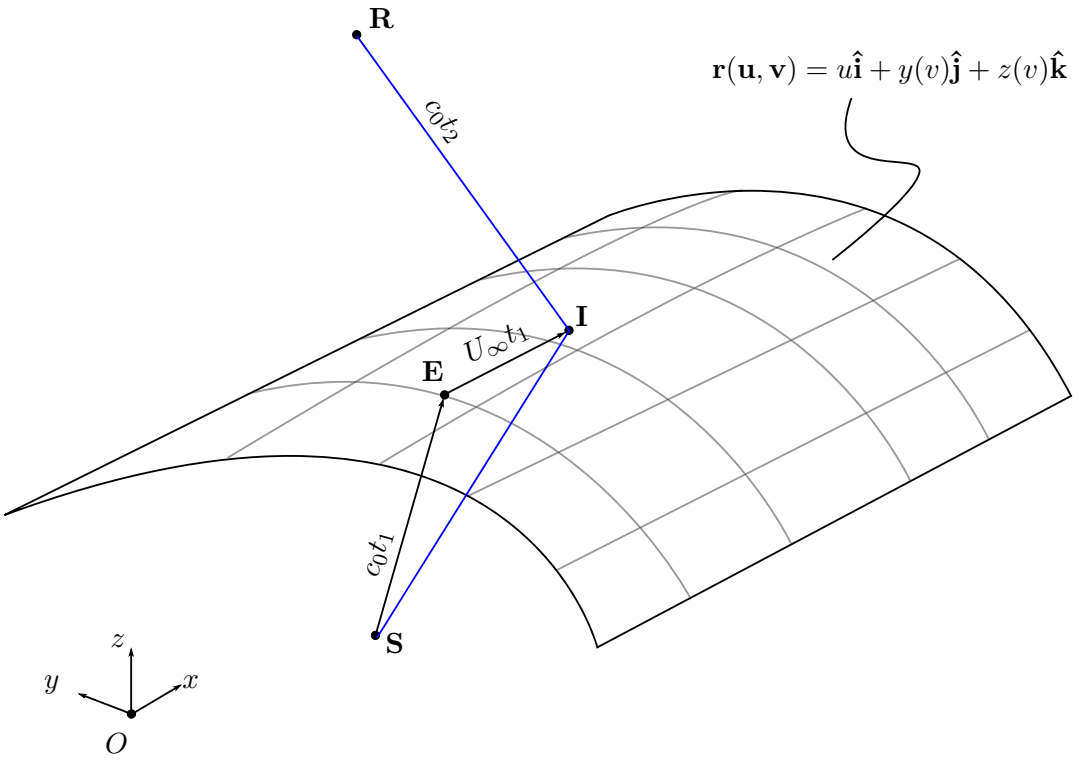

Figure B.1: Possible travel path of a ray travelling from source location **S** to receiver **R**. The rays will be propagated by the mean flow so that the ray intersects the shear layer at **I**.

cosine rule on the triangle that connect points **I**, **S** and **E** to equate **I** with t_1. That is

$$|\mathbf{I}-\mathbf{S}|^2 = (c_0t_1)^2 + (V_\infty t_1)^2 - 2c_0V_\infty t_1^2\cos(\theta) \tag{B.4}$$

In this equation, $\cos(\theta)$ is the angle between the vector **SE** and the mean flow, $V_\infty\hat{\mathbf{i}}$. Using the dot-product rule,

$$\cos(\theta) = \frac{(\mathbf{I}-\mathbf{S}+V_\infty\hat{\mathbf{i}})\cdot\hat{\mathbf{i}}}{c_0t_1} \tag{B.5}$$

Substituting Equation B.5 into Equation B.4 yields

$$|\mathbf{I}-\mathbf{S}|^2 = (c_0t_1)^2 - (V_\infty t_1)^2 - 2V_\infty t_1[(\mathbf{I}-\mathbf{S})\cdot\hat{\mathbf{i}}] \tag{B.6}$$

Equation B.6 can be solved for t_1 using the quadratic formula. The solution will have two real solutions, one being positive and one being negative. Taking the positive solution and noting that $M_\infty = V_\infty/c_0$,

$$t_1 = \frac{M}{c_0(1-M^2)}(\mathbf{I}-\mathbf{S})\cdot\hat{\mathbf{i}} + \frac{1}{c_0(1-M^2)}|(\mathbf{I}-\mathbf{S})\cdot\beta| \tag{B.7}$$

where $\beta = 1\hat{\mathbf{i}} + \sqrt{1-M^2}\hat{\mathbf{j}} + \sqrt{1-M^2}\hat{\mathbf{k}}$. Hence, the total time can be expressed as

$$\tau_{total} = \frac{M}{c_0(1-M^2)}(\mathbf{I}-\mathbf{S})\cdot\hat{\mathbf{i}} + \frac{1}{c_0(1-M^2)}|(\mathbf{I}-\mathbf{S})\cdot\beta| + \frac{1}{c_0}|\mathbf{I}-\mathbf{M}| \tag{B.8}$$

The intersection point, $\mathbf{I}$, is constrained to lie on the surface $\mathbf{r}(u,v)$ and is therefore a function of u and v, i.e $\mathbf{I} = \mathbf{I}(u,v)$. The parameters u and v are such that they minimise τ_{total}. A necessary condition for minimisation is to find u and v such that

$$\frac{\partial \tau_{total}}{\partial u} = 0 \tag{B.9}$$

$$\frac{\partial \tau_{total}}{\partial v} = 0 \tag{B.10}$$

Taking these derivatives in Equation B.8 yields

$$\frac{u - x_m}{|\mathbf{I} - \mathbf{M}|} + \frac{1}{(1-M^2)}\left[-M + \frac{u - x_s}{\sqrt{(u-x_s)^2 + (1-M^2)((y(v)-y_s)^2 + (z(v)-z_s)^2)}}\right] = 0 \tag{B.11}$$

$$\left[(y(v)-y_m)\frac{\partial y}{\partial v} + (z(v)-z_r)\frac{\partial z}{\partial v}\right]\frac{1}{|\mathbf{I}-\mathbf{M}|} + \left[\frac{(y(v)-y_s)\dfrac{\partial y}{\partial v} + (z(v)-z_s)\dfrac{\partial z}{\partial v}}{\sqrt{(u-x_s)^2 + (1-M^2)((y(v)-z_s)^2 + (z(v)-z_s)^2)}}\right] = 0 \tag{B.12}$$

Equations B.11 and B.12 are herein known as the generalised shear layer correction equations. Once these equations are solved for u and v, Equation B.8 can be solved to find the emission time. Equations B.11 and B.12 can be solved efficiently using Newton iteration.

B.3 The GSLC is equivalent to Amiet's method for a one-dimensional shear layer

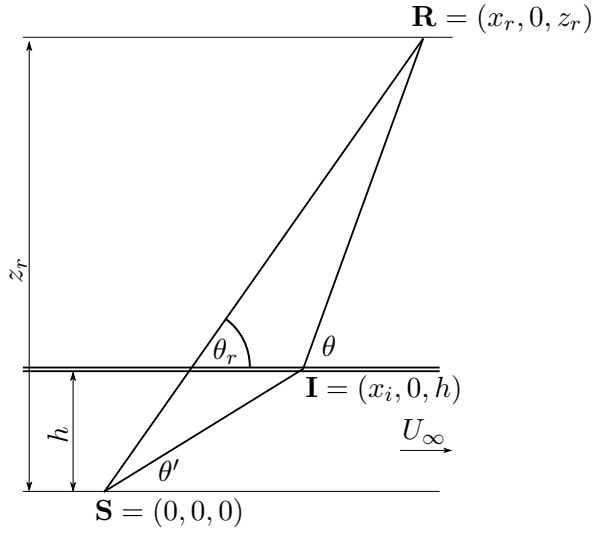

Figure B.2: The nomenclature used in the shear layer correction scheme of Amiet (1975).

Here we formally prove that the GSLC is equivalent to Amiet's (Amiet 1975) correction method for a one-dimensional shear layer, where the source and receiver lie in the same plane. The nomenclature used for Amiet's solution is provided in Figure B.2. The main objective of this proof is to demonstrate that the physical reasoning on which the GSLC is based is correct (within the constraints of the problem) and that the GSLC is adequate for use on a three-dimensional problem.

To review, Amiet's correction method is to solve Equation B.13 and B.14 to obtain θ' given knowledge of z_r, h, M and θ_r. Once θ' is found, the intersection point is calculated as $x_i = h\cot(\theta')$ and the emission time can be found using Equation B.8.

$$\tan(\theta') = \frac{\sqrt{(1 - M\cos(\theta))^2 - \cos^2(\theta)}}{(1 - M^2)\cos(\theta) + M} \tag{B.13}$$

$$z_r \cot(\theta_r) = h\cot(\theta') + (z_r - h)\cot(\theta) \tag{B.14}$$

Equation B.14 is derived based on simple geometry, while Equation B.13 is derived by integrating the Lilly Equation for a plane shear layer (Amiet 1978) or using ray tracing methods. To prove equivalence of the GSLC and Amiet's method, it must be shown that the intersection point found using Equations B.11 and B.12 would be equal to that using Equation B.13.

For the GSLC, the shear layer surface in Figure B.2 can be represented as;

$$\mathbf{r}(u, v) = u\hat{\mathbf{i}} + 0\hat{\mathbf{j}} + h\hat{\mathbf{k}} \tag{B.15}$$

With this surface, Equation B.12 is necessarily true and Equation B.11 reduces to:

$$x_r - u = \left[-M + \frac{u}{\sqrt{u^2 + (1 - M^2)h^2}}\right] \frac{\sqrt{(x_r - u)^2 + (z_r - h)^2}}{1 - M^2} \tag{B.16}$$

where $u = x_i$ is the intersection point. From Figure B.2

$$x_r - u = (z_r - h)\cot(\theta) \tag{B.17}$$

and substituting this expression into Equation B.16 and rearranging yields:

$$(1 - M^2)\cos(\theta) + M = \frac{u}{\sqrt{u^2 + (1 - M^2)h^2}} \tag{B.18}$$

Equation A18a in Amiet 1978 shows that

$$\frac{h}{\sqrt{x_i^2 + (1 - M^2)h^2}} = \sqrt{(1 - M\cos(\theta))^2 - \cos^2(\theta)} \tag{B.19}$$

Noting that $x_i = u$, it is trivial to show that

$$\frac{h}{u} = \frac{\sqrt{(1 - M\cos(\theta))^2 - \cos^2(\theta)}}{(1 - M^2)\cos(\theta) + M} \tag{B.20}$$

Finally, $u = h\cot(\theta')$ implying that $h/u = \tan\theta'$. Thus, for the one-dimensional case, solving Equation B.11 is exactly the same as solving Equation B.13. This ends the proof.

B.4 The GSLC used with experimental results

An example of the GSLC used on experimental beamforming results is provided below. The experiment was conducted at Brandenburg University of Technology and consisted of an SD7003 airfoil placed in front of circular jet. The circular jet has a radius of 0.1 m and during the experiment the free-stream velocity was set at 50 m/s. The airfoil has a chord length of 0.235 m and the leading edge was placed 0.05 m away from the exit

plane of the jet. The airfoil has a spanwise length of 0.4 m, so that its mounting points are outside of the jet shear layer. For source localisation, a 56 channel microphone array was placed 0.68 m directly above the airfoil. The array was placed so that its centre was 0.55 m downstream of the jet exit plane. More details on the experimental set up can be found in Geyer et al. 2010.

The GSLC was formulated by modelling the shear layer as an axis-symmetric plug flow. Then the shear layer boundary is given by

$$\mathbf{r}(u,v) = u\hat{\mathbf{i}} + r\cos(v)\hat{\mathbf{j}} + r\sin(v)\hat{\mathbf{k}} \tag{B.21}$$

where u is a parameter specifying the stream-wise direction, $r = 0.1$ and v is the angle (in the $y-z$ plane) moving around the periphery of the shear layer. Equations B.11 and B.12 were iteratively solved using Nelder-Mead Simplex Method for each point in the scanning grid.

Conventional cross-spectral beamforming was performed on the data using both no shear layer correction and using the GSLC. Figures B.3a through B.3h compare the beamforming maps with (right column) and without (left column) shear layer correction at select 12^{th} octave band centre frequencies.

As predicted by Padois et al. 2013a, the impact of the shear layer is to move the image downstream. However, unlike a planar shear layer, the downstream movement of the image increases toward the centre of the jet, creating a 'smiley face' appearance. This effect is particularly evident at 8 kHz and 16 kHz (Figures B.3e and B.3g). This makes sense inuitively because toward the centre of the jet, the local distance between the jet periphery and the source increases. Thus sources toward the centre have a higher 'h' value, and consequently move further downstream.

The GSLC successfully accounts for the circular shear layer by moving the source map upstream. The upstream movement is weighted according to the source's distance from the jet centreline. The result is a straight source distribution at the trailing edge of the airfoil.

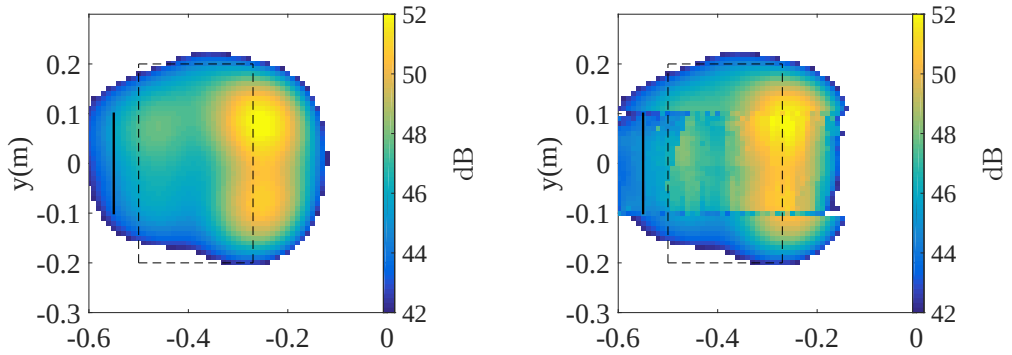

(a) No correction at 2 kHz

(b) GSLC correction at 2 kHz

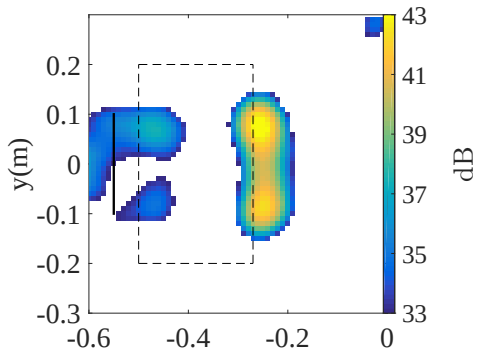

(c) No correction at 4 kHz

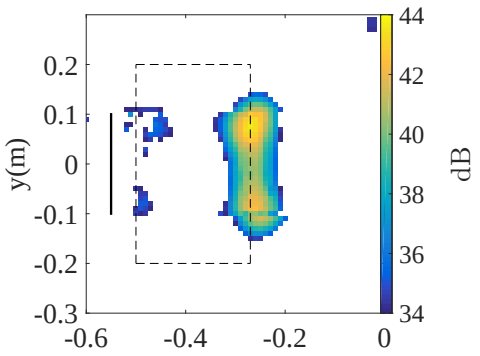

(d) GSLC correction at 4 kHz

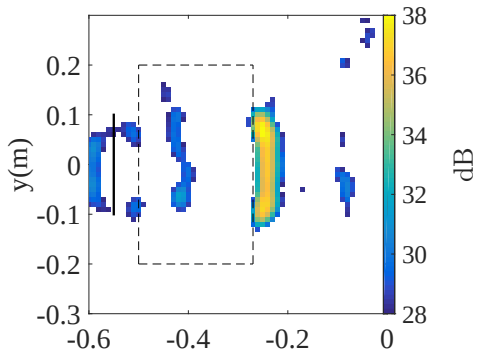

(e) No correction at 8 kHz

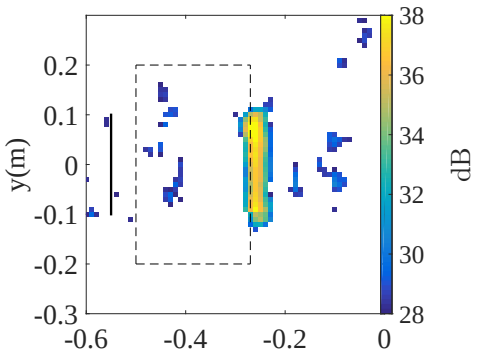

(f) GSLC correction at 8 kHz

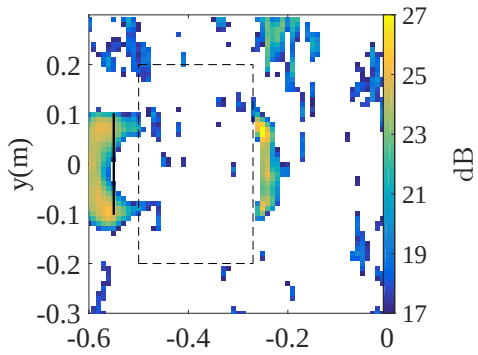

(g) No correction at 16 kHz

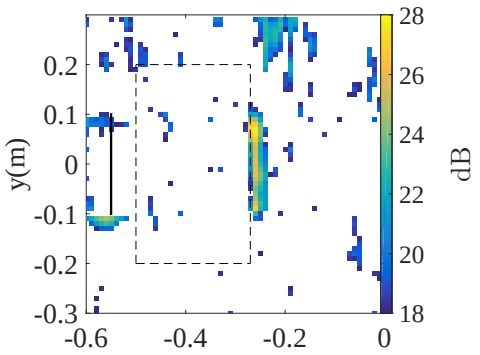

(h) GSLC correction at 16 kHz

Figure B.3: Conventional beamforming on an airfoil placed inside a circular jet flow. Figures a, c, e and f were calculated without using shear layer correction and figures b, d, f and h were calculated using the GSLC. The exit plane of the circular jet lies at $x = -0.55$. The leading edge of the airfoil lies at $x = 0.5\,\mathrm{m}$ and the trailing edge at $x = -0.27\,\mathrm{m}$. The Mach number of the experiment was $M = 0.15$.

B.5 Conclusion

A new method, known as the Generalised Shear Layer Correction (GSLC) method was mathematically developed in this chapter. The method is suitable for use with either three-dimensional beamforming or two-dimensional beamforming where the shear layer forms a non-planar surface. The formulation was mathematically proven to be equivalent to the traditional method of Amiet (Amiet 1975) for a one-dimensional shear layer. The method was then shown to perform well on experimental data.

Appendix C

Three-dimensional beamforming

The work conducted in Chapter 4 allows the extension of two-dimensional beamforming into the third dimension. In particular, the discovery of the 'array gain field' and the properties of steering vector 4 (sv4) mean that accurate three-dimensional source localisation can be performed on *dipole* sources, where directionality of the source map is included into the beamforming algorithm for improved localisation. The work presented here details of a comparison of four different three-dimensional beamforming algorithms using both the top and side-array of the AWT array (see Figure 4.2). The contents of this chapter have been published in Porteous et al. (2015)[1].

C.1 Introduction

In theory, the scanning grid can be either a two-dimensional (2D) planar grid, or a three-dimensional (3D) grid consisting of several parallel planes. This means that localising sound in three-dimensions is theoretically possible given a large enough array. However, in general, planar beamformers have good spatial resolution in the lateral direction (in a plane parallel to the plane of microphones) but poor spatial resolution in the direction normal to the array (Brooks and Humphreys 2005; Sarradj 2012). This makes it difficult to accurately locate sources in a 3D scanning grid unambiguously. Brooks and Humphreys (2005) found that different microphone weighting schemes can marginally improve a planar array's normal spatial resolution. However, the most effective way to improve depth resolution, and therefore perform 3D beamforming, is to use an array that surrounds the source region (a non-planar array) (Padois et al. 2013a). 3D beamforming of experimental aeroacoustic sources has been attempted previously using both planar (Legg and Bradley 2014; Brooks and Humphreys 2005; Geyer et al. 2012) and non-planar arrays (Padois et al. 2013a; Dougherty 2010).

Brooks and Humphreys (2005) used a planar array of microphones to investigate noise from a flap edge and a high-fidelity model of an aircraft main landing gear. The investigation was targeted towards the adaptation of the DAMAS (Brooks and Humphreys 2006) deconvolution technique to improve the 3D localisation capabilities of a planar array. It was found that 3D beamforming without deconvolution suffered from poor longitudinal resolution while 3D deconvolution was found to be very computationally

[1]Portions of this chapter have been reprinted with permission from Porteous, Prime, Valeau, Doolan and Moreau, Journal of Sound and Vibration. Copyright 2015

challenging. Geyer et al. (2012) used a planar array of 56 microphones to investigate the noise generated by the leading edge of an aerofoil placed in a turbulent flow. Conventional beamforming assuming monopole propagation characteristics was applied to a 3D grid with $1\,\mathrm{cm}^3$ spatial resolution. The CLEAN-SC deconvolution method (Sijtsma 2007) was used to deconvolve the results. The planar beamformer was able to localise the noise source generally at the leading edge. However, the main lobe of the source map was highly elongated in a direction normal to the array plane making it difficult to interpret the results.

Padois et al. (2013a) used a non-planar array to beamform an acoustic monopole (fluid injection) and a dipole source (cylinder in cross-flow) in a volumetric scan grid, i.e., a 3D source map. The study used four sub-arrays, each containing 48 microphones arranged in an 8 arm spiral. The four sub-arrays were arranged on each of the four walls of a wind tunnel so that they enclosed the sources. Conventional beamforming and CLEAN-SC deconvolution were used to locate the sources. Like Geyer et al. (2012), the investigation assumed monopole propagation characteristics for both the monopole and dipole sources. The monopole source was located to within 3 cm in a potential scanning volume of $2\,\mathrm{m}^3$ using all three beamforming methods. Conversely, because of the assumption of monopole propagation characteristics, the dipole source was unable to be located adequately with any of the methods.

3D beamforming of aeroacoustic sources evidently presents a significant challenge. It appears that a planar array of microphones, even with optimal microphone weighting schemes and deconvolution, is unsuitable for scanning a 3D grid because of its poor depth resolution. Furthermore, 3D beamforming with planar microphone arrays gives results that are often difficult to interpret. When the array surrounds the source region, as in the study of Padois et al. (2013a), better localisation is achieved. However, the drawback with such a microphone arrangement is the large amount of microphones used (192 in that study). In some situations (for example, small open-jet wind tunnels) there may be limitations on the number of microphones used. Additionally, neither Padois et al. (2013a), Geyer et al. (2012) nor Brooks and Humphreys (2005) have included dipole source directivity characteristics in their beamforming routines, which is essential for when beamforming dipole aeroacoustic sources, such as sources generated by flow over rigid bluff bodies (Howe 1998).

The purpose of this chapter is to investigate several suitable beamforming methods that give accurate 3D beamforming source maps without using a large number of microphones and also accounting for dipole source characteristics. This is achieved by using a novel non-planar array consisting of two mutually perpendicular sub-arrays that partially enclose the source region. The advantage of such an array is a reduced number of microphones and the possibility of studying configurations where the flow is bounded on one side (such as wall-mounted bodies in flow). Although the 3D beamforming techniques are not used for analysis in the subsequent chapters concerning finite cylinders, the development and analysis of such techniques are still the first of their kind.

In this chapter, four potential 3D beamforming algorithms are developed and compared. These four algorithms are herein known as ‘conventional beamforming’ (CB), ‘multiplicative beamforming’ (MB), ‘conventional CLEAN-SC’ (CCS) and ‘multiplicative CLEAN-SC’ (MCS). CB and CCS are extensions of the well-known 2D beamforming rou-

tines (outlined in Chapter 4) to include 3D dipole propagation characteristics. Conversely, MB and MCS are new techniques that are mathematically developed in this chapter. The latter methods rely on the mutual cancellation of spatially incoherent sources between orthogonally aligned microphone arrays to improve the quality of the source map. All four methods are applied to synthetically generated data and compared on the basis of beamwidth (resolution), localisation accuracy and source strength estimation.

C.2 3D beamforming theory

C.2.1 Conventional cross-spectral beamforming (CB) assuming dipole propagation characteristics

Conventional beamforming in 3D has the same mathematical formulation as that for 2D. Here, the array is steered (using Equation 4.1) to points in a 3D volume instead of on a 2D grid.

The choice of steering vector formulation for 3D beamforming is more critical compared with a 2D scan. It was mentioned in Chapter 4 that a trade off exists when comparing sv1, sv2, sv3 and sv4; sv1 and sv4 can guarantee accurate source localisation, but suffer from a spatially bias amplitude estimation. The converse is true for sv2 and sv3. In general, source localisation errors occurs in a direction normal to the array rather than parallel to its face. Hence, sv2 or sv3 are preferred in 2D applications. In 3D, however, correct depthwise localisation is essential, so sv1 or sv4 must be used. A three-dimensional version of the array gain field correction factor outlined in Chapter 4 can be used after the positions of the local maxima are found to correct the amplitude.

In Chapter 4, the transfer vector, $\mathbf{a}(\mathbf{x}, \omega)$, was introduced as that for a monopole source spherically propagating in an anechoic quiescent environment. On the other hand, in aeroacoustics, many flow-induced noise sources have dipolar radiation characteristics because they are caused by the interaction between a rigid surface and the flow (Curle 1955).

When using a planar array, dipolar fields can be seen as mainly monopolar if the array is perpendicular to the dipole axis. In this case, it is sufficient to use classical monopolar beamforming (as it is done usually for an airfoil or a cylinder, for example Sarradj (2012) or the work presented in the main body of this thesis)). However, when using a non-planar array and beamforming in 3D, using a monopole propagation transfer vector may miss the essential nature of the radiation, if it is strongly dipolar, for example in Moreau et al. (2014).

To combat this, Liu et al. (2008) formulated a correction to the transfer function to account for dipole directionality. The formulation reduces to multiplying the transfer function for a monopole source by the cosine of the angle made between the direction of the dipole axis, $\vec{\zeta}$, and the direction from the scanning point to the microphone in question. Therefore, for a dipole source located at x_t, each element of the transfer function $\mathbf{g}(\mathbf{x_t}, \omega)$ is given by

$$g_i(\mathbf{x_t}, \omega) = \frac{e^{-j\omega r_t/c}}{4\pi r_t}\left[\vec{\zeta} \cdot \frac{\mathbf{x_t} - \mathbf{x_i}}{r_t}\right] \tag{C.1}$$

In Equation C.1, ω is the frequency of the sound (in radians per second), c is the speed of sound and $r_t = |\mathbf{x_t} - \mathbf{x_i}|$. The term $\vec{\zeta}$ is a unit vector that is aligned parallel to the dipole axis, that is, a line that passes through the two out of phase monopole sources and form the dipole. Equation C.1 accounts for both the directionality of the propagation of the source (in the square brackets) and the spherical spreading of energy away from the source location assuming a far-field condition (in the denominator).

Figure C.1 illustrates the effect of using a dipole steering vector on a point dipole located at $\mathbf{x_s} = (0, 0, 0)$ at $f = 3\,\text{kHz}$ orientated in the ordinate-direction. In Figure C.1 the dipole source is located in the $z = 0\,\text{m}$ plane and the microphone array is located in the $z = 0.5\,\text{m}$ plane. The maps were obtained by using Equation 4.1 with different steering vectors. Figure C.1a shows the source map acquired using a monopole steering vector. Two lobes above and below the source are apparent, signifying that a dipole source is present but also leading to ambiguity of the its exact location. Figure C.1b shows the source map acquired using a dipole steering vector (Equation C.1, with $\vec{\zeta} = (0, 1, 0)$. Compared with Figure C.1a, the source is now unambiguously located with the maximum in the source map coinciding exactly with the point dipole location, although low level side-lobes exist above and below the source. One limitation of this method is that the dipole axis, $\vec{\zeta}$, must be assumed *a priori*. Incorrect choice of dipole orientation will lead to large phase errors and therefore incorrect source mapping. The impact of searching for an incorrectly orientated dipole is shown in Figure C.1c. Here $\vec{\zeta} = (1, 0, 0)$ and the result is a poor visualisation of the source map, which consists of four side-lobes arranged evenly around the source location. Generally, however, it is possible to infer the dipole orientation from the flow and body orientation.

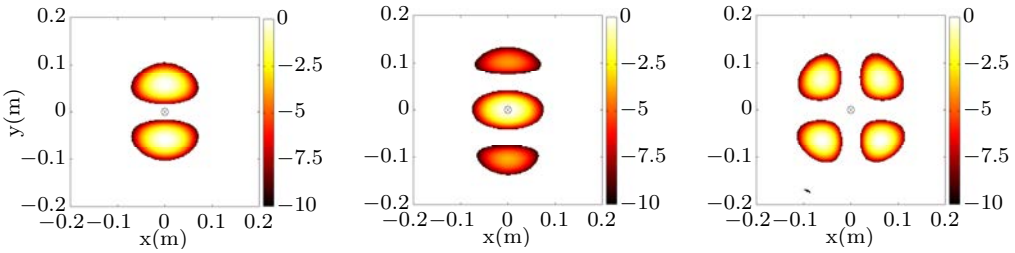

(a) Monopole (b) Dipole, $\vec{\zeta} = (0, 1, 0)$ (c) Dipole, $\vec{\zeta} = (0, 0, 1)$

Figure C.1: (a) Illustration of beamforming a point dipole source at $\mathbf{x_s} = (0, 0, 0)$ at $f = 3\,kHz$ using a monopole transfer vector. (b) Beamforming the same point dipole using a dipole transfer vector with $\vec{\zeta} = (0, 1, 0)$. (c) Beamforming the same point dipole using an incorrect dipole transfer vector with $\vec{\zeta} = (1, 0, 0)$.

C.2.2 Multiplicative cross-spectral beamforming (MB)

The theoretical reasoning behind MB is to utilise the good lateral resolution of one planar beamformer to improve the depth ('normal' or 'longitudinal') resolution of another. Two perpendicular planar beamfomers are arranged around a source and CB is used on both sets of microphones on two sets of overlapping 3D-scanning grids. The resulting 3D source maps are then multiplied together. It is reasoned that points corresponding to source locations will be maxima in both array outputs and should therefore reinforce when multiplied together. Alternatively, the multiplication will not reinforce at positions

where side-lobes and non-source location points occur, leaving a clean 3D source map. This is another reason why it is imperative to use sv4 as the steering vector. The concept is illustrated in Figure C.2.

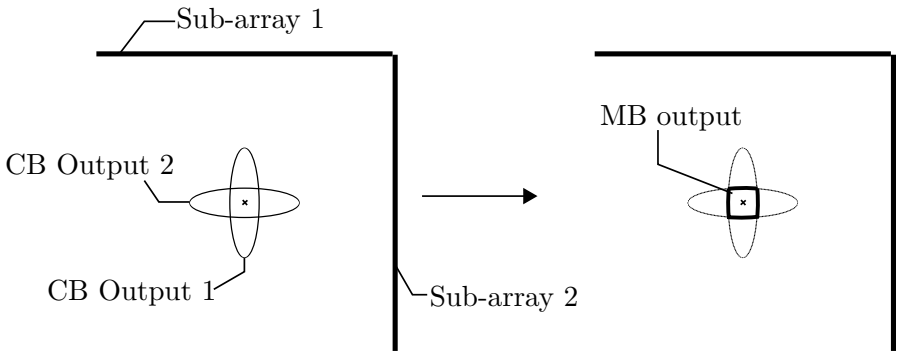

Figure C.2: 2D schematic illustrating the concept of multiplicative beamforming. The CB outputs from each sub-array are multiplied together to create a clean, spatially uniform source map.

One reason why MB may be a preferred method compared with CB is that in real wind-tunnel experiments, the signal measured in perpendicular orientations relative to the source may have poor coherence, resulting in a noisy CSM (Humphreys et al. 1998). Coherence loss was discussed in Chapter 4. Therefore, at higher frequencies, microphones in the outer part of the array may be completely incoherent with one another, reducing the effective aperture of the array (Sijtsma and Stoker 2004). Thus, MB may be a good strategy to maintain satisfactory coherence between signals belonging to smaller sub-arrays, resulting in visualisation of better quality.

Consider a microphone array with M_0 microphones split into two sub-arrays[2] of $M_0/2$ microphones each. We denote S_1 as the set of microphones in the first array and S_2 as the set of microphones in the second array. For convenience, let the microphone indices of the first sub-array be $i = 1...M_0/2$ and the microphone indices of the second sub-array be $i = M_0/2 + 1...M_0$. We then define two $M_0 \times M_0$ diagonal matrices, W_1 and W_2, where the i^{th} diagonal element in each is either a 1 or 0 depending on whether the index lies in S_1 or S_2. That is;

$$W_{ii} = \begin{cases} 1 & i \in \text{sub-array set} \\ 0 & i \notin \text{sub-array set} \end{cases} \tag{C.2}$$

These matrices are analogous to the 'shading' matrices used by Brooks and Humphreys (2006). The beamforming outputs of each microphone sub-array can then be efficiently calculated using the same cross-spectral matrix calculated in Equation 4.1 using all M microphone outputs. The modified version of Equation 4.1 using sv4 is given in Equations (C.3) and (C.4).

$$B_1(\mathbf{x_t},\omega) = \frac{\mathbf{g}(\mathbf{x_t},\omega)^{\mathrm{H}}\mathbf{W_1}\overline{\mathbf{P}(\omega)\mathbf{P}(\omega)^{\mathrm{H}}}W_1\mathbf{g}(\mathbf{x_t},\omega)}{|\mathbf{W_1}\mathbf{g}(\mathbf{x_t},\omega)|^2(M/2)} \tag{C.3}$$

[2] In the following the MB technique is defined for two sub-arrays, but could be easily extended to multiple sub-arrays.

$$B_2(\mathbf{x_t},\omega) = \frac{\mathbf{g}(\mathbf{x_t},\omega)^{\mathrm{H}}\mathbf{W_2}\overline{\mathbf{P}(\omega)\mathbf{P}(\omega)^{\mathrm{H}}}W_2\mathbf{g}(\mathbf{x_t},\omega)}{|\mathbf{W_2}\mathbf{g}(\mathbf{x_t},\omega)|^2(M/2)} \tag{C.4}$$

The final step in MB is to multiply the beamforming outputs of the two sub-arrays together and take the square root of the result to obtain the correct units. That is the final beamforming output at a position $\mathbf{x_t}$ is;

$$B(\mathbf{x_t},\omega) = \sqrt{B_1(\mathbf{x_t},\omega)B_2(\mathbf{x_t},\omega)} \tag{C.5}$$

C.2.3 Three-dimensional deconvolution

CLEAN-SC was chosen as the deconvolution method used for 3D beamforming because of its low computational cost. It was used in two ways; first with CB, denoted 'CCS', and second with MB, denoted 'MCS'. In CCS, the deconvolution is applied to the full array output (Equation 4.1). In MCS, the deconvolution algorithm is applied to the beamforming outputs of the top and side array individually (Equations C.3 and C.4 respectively) and multiplied together. The amplitude correction method for CCS and MCS is the same as for CB and MB: the correction should be applied after performing deconvolution and the resulting locations of local maxima are found.

C.3 Verification of 3D beamforming techniques using synthetic data

The purpose of this section is to numerically verify and compare the performance of the four beamforming methods. In this study, performance is divided into three metrics; resolution, source strength estimation accuracy and source localisation accuracy. To facilitate the comparison, the four beamforming algorithms were used on synthetic (computer generated) data for a case where there is no mean flow. The performance is measured at each frequency.

C.3.1 3D Microphone array

The microphone array used for the anlaysis of the synthetic data mirrored that described in Chapter 4. A schematic of the microphone arrangements used in the analysis of the 3D synthetic data is shown in Figure C.3. Also shown between the two arrays is the scan-grid region used for the analysis of synthetically generated data.

C.3.2 Single point dipole results

A single dipole source ($\vec{\zeta} = (0,0,1)$) was generated first. The dipole was located at $\mathbf{x_s} = (-0.3,0,0)$ and the constant $C(\omega)$ in Equation 4.14 was chosen so that the true source strength was 100 dB/Hz re. 20μPa at a frequency of 3 kHz.

Figure C.4 shows the 3D beamforming maps of the four algorithms applied to the single synthetic dipole case at 3 kHz assuming $\vec{\zeta} = (0,0,1)$. Subfigures of Figure C.4 represent the beamforming map when CB, CCS, MB and MCS are used, respectively. All the maps in Figure C.4 contain isocontours of 0.1, 1, 2, 4, 6 and 10 dB down from

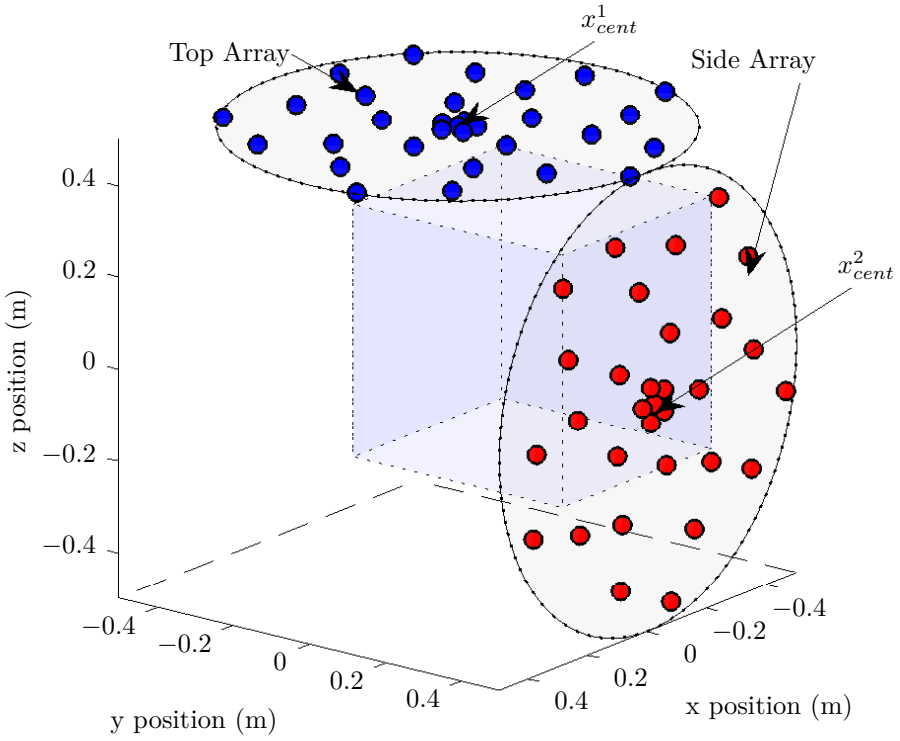

Figure C.3: Schematic showing the locations of the microphones in the array. The array is comprised of two mutually perpendicular sub-arrays, known as the 'top' and 'side' arrays respectively. The top array is located on the $z = 0.5$ plane and the side array is located on the $y = 0.5$ plane. Each sub-array consists of 31 microphones. The 3D cube between the arrays illustrates the scan-grid region used for the analysis of synthetically generated data.

the maximum in the map. On the adjacent orthogonal faces of the maps are projections of the true location of the source in the x-z, z-y and x-y planes denoted with a cross ('x'). Overlaid onto the cross are the projections of the location of the maxima in the aforementioned planes of the beamforming map with a circle ('o'). In all of the source maps, a 3D scanning grid containing 1030301 points in a volume measuring 0.5 m×0.5 m ×0.5 m was used. The grid was therefore a uniform cubic mesh consisting of 5 mm^3 volumes. The CLEAN-SC parameters that were used were a safety factor of 0.99 and a 'clean beamwidth' of $\lambda/4$ for all frequencies.

Figure C.4a shows that conventional 3D beamforming does not locate the single dipole source well and is difficult to interpret. The beamforming maps displays a main lobe in the centre of the map, where the point dipole is located. Additionally, smaller amplitude side-lobes are present above and below the main lobe. As discussed in Section 2.1, the presence of side-lobes is to be expected when using a dipole transfer vector. These side-lobes are merged with the main lobe, creating the appearance of undulations in the source map. The whole map also appears to be skewed or elongated towards the x-z axis,

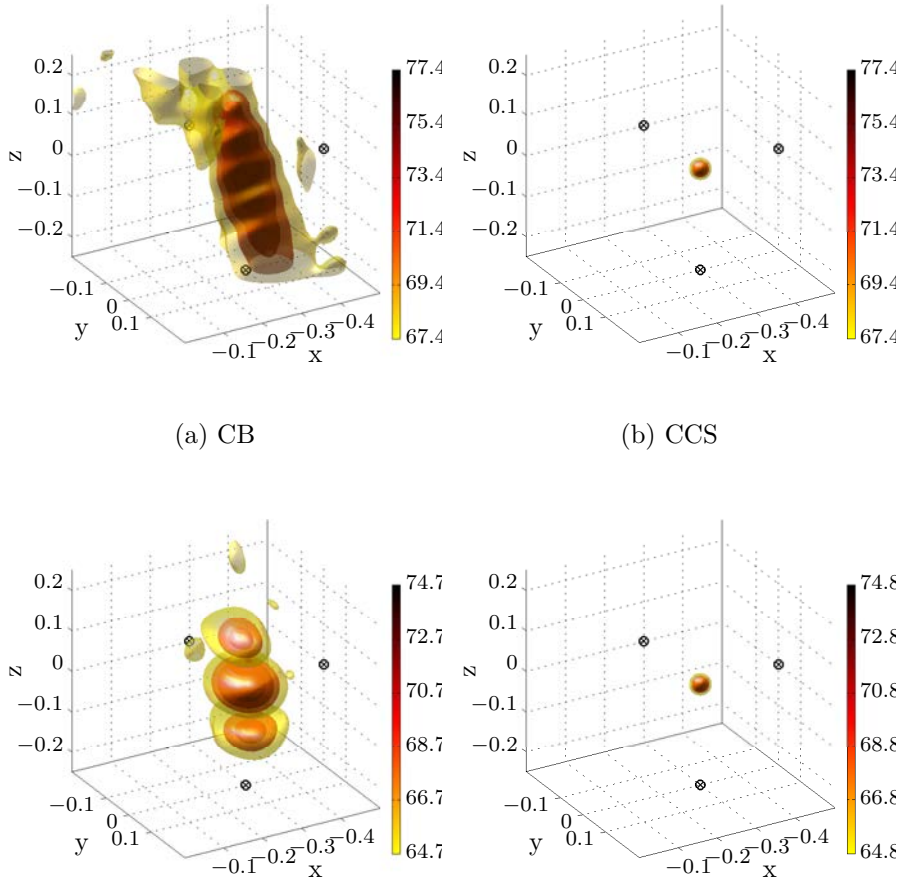

(a) CB (b) CCS

(c) MB (d) MCS

Figure C.4: 3D beamforming sound maps of a synthetic dipole source located at $\mathbf{x_s} = (-0.3, 0, 0)$ with orientation $\vec{\zeta} = (0, 0, 1)$. The maps are taken at a frequency of 3 kHz using CB (a), CCS (b), MB (c) and MCS (d). The colourbar denotes the biased (uncorrected) source strength (in dB/Hz re. 20μPa.s). The symbols 'x' denote the true location of the source and the symbols 'o' denote the estimated location of the source based on the maximum in the source map.

creating a directional bias in the map. The reason for this directional bias is that source maps will always be elongated in the direction in which the least phase information is received. For planar beamformers, this is a direction normal to the array plane, as illustrated in Figure C.2. For the present non-planar beamformer, this direction is towards the geometric centre (the spatial average of the microphone locations) of the array, which happens to be the x-z axis. Deconvolution of the CB map using CLEAN-SC (Figure C.4b) removes the directional bias of the main lobe while simultaneously removing the side-lobes. The output is a uniform sphere located at the position of the dipole source.

MB (Figure C.4c) produces results that are more interpretable compared with CB. As expected large side-lobes along the dipole axis are still present, but these are not merged into the main lobe and are easily distinguishable. Furthermore, the directional bias present in CB is removed with this technique. The main lobe resembles that obtained via CLEAN-SC (although with a much larger diameter). MCS (Figure C.4d) yields similar results compared with CCS. A uniform sphere located at the position of the synthetic

point dipole source is produced.

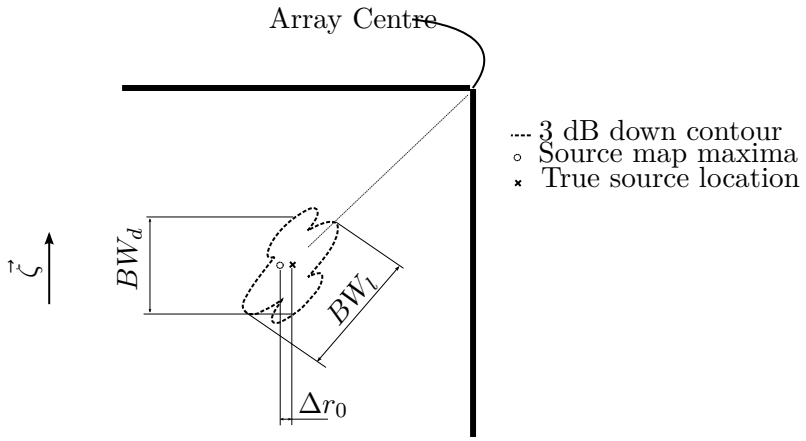

Figure C.5: 2D schematic illustrating the definitions of Δr_0, BW_d and BW_l. Δr_0 is the difference between the maxima in the source map and actual source location, BW_d is the width of the 3 dB down contour in the source direction, $\vec{\zeta}$, and BW_l is the width of the 3 dB down contour in the direction of the array centre.

Table C.1: Comparison of beamforming algorithm performance metrics for a single dipole located at $\mathbf{x_s} = (-0.3, 0, 0)$ at a frequency of 3 kHz..

Method	$\Delta r_0/\lambda$	B_{bias}(dB/Hz)	B_{true} (dB/Hz)	BW_l/λ	BW_d/λ	Processing Time (s)
CB	0	77.4	100.0	1.26	2.10	1.5
MB	0	74.7	100.0	1.01	0.87	1.1
CCS	0	77.4	99.9	0.29	0.31	5.8
MCS	0	74.7	100.2	0.29	0.31	4.8

Table C.1 quantitatively summarises the localisation results. For each method the deviation from the true source location of the maximum in the map is given in column 1. This is calculated as the difference between the location of the maximum in the beamforming map and the true source location, Δr_0. In Table C.1, the bias amplitude denotes the uncorected values, while the true values denote those corrected using the array gain field. The bias and true source strengths are compared in columns 2 and 3. Columns 4 and 5 are the beamwidths at -3 dB down from the source. In this case, two beamwidths are given; BW_l is the 'longitudinal beamwidth' and calculated as the -3 dB down width of the main lobe in the direction from the maximum to the geometric centre of the array (the x-z axis). BW_d is the 'source direction beamwidth' and calculated as the -3 dB down width of the main lobe in the direction of the dipole source axis ($\vec{\zeta}$). The definitions of Δr_0, BW_d and BW_l are illustrated in Figure C.5. The last column compares the computational cost of each method in seconds[3].In Table C.1, all length quantities have been normalised by the wavelength of sound at 3 kHz. Because of the finite size of the mesh, the error in measured beamwidth is approximately 0.09λ.

All four methods accurately localise the dipole source location to within the resolution of the mesh. As can be seen in Figure C.4, the locations of the maxima (represented by circles) lie exactly on the locations of the source (represented by crosses). In terms

[3]All results were computed using MATLAB on a personal computer with a 3.4-GHz Intel Core i7 processor.

of resolution, conventional and MB had similar sized longitudinal beamwidths (BW_l), at 1.26λ and 1.01λ respectively. Conversely, MB had a much smaller source direction beamwidth (BW_d) at 0.87λ, than CB at 2.1λ. Both CCS and MCS had much lower beamwidths of 0.29λ and 0.31λ. These beamwidth are not exactly 0.25λ because of discretisation errors introduced by the finite grid. After correction, all four methods were able able to estimate the true source strength of 100 dB to within ± 0.2 dB. MB and CB methods had comparable computational cost. Deconvolution in both cases caused the running time to increase by approximately 400%. MCS proved 17% faster than CCS.

To evaluate the change in beamformer characteristics with frequency, the statistics presented in Table C.1 were repeated for frequencies ranging from 500 Hz to 5 kHz. Above 5 kHz, the discretisation of the grid causes large errors (relative to the wavelength) in the measured beamwidth. Figure C.6 shows the variation of longitudinal and source direction beamwidth, localisation error and true (corrected) source strength with frequency between the four different methods.

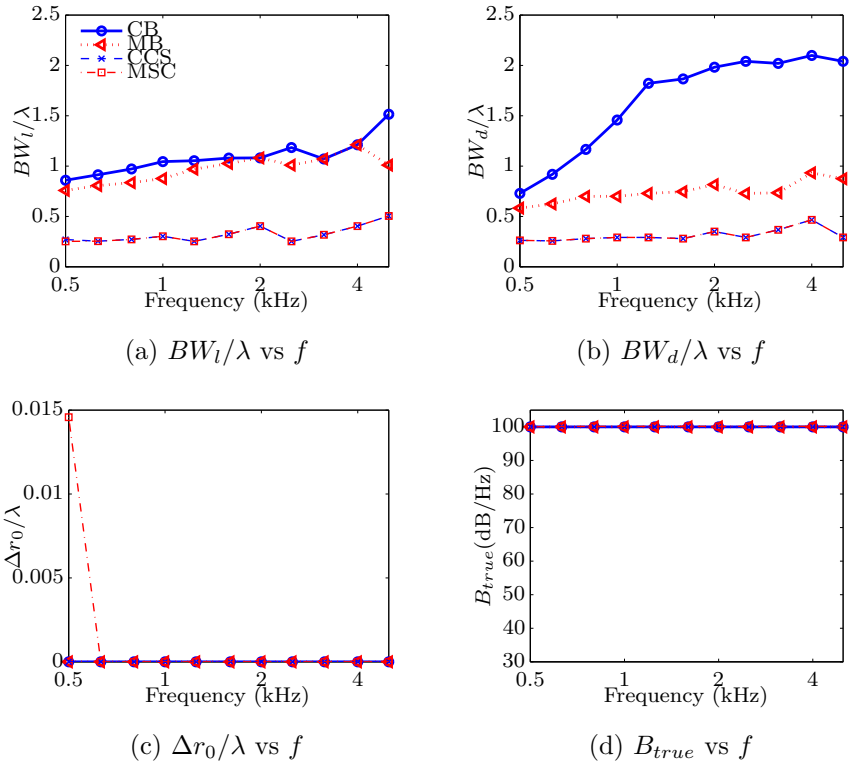

(a) BW_l/λ vs f (b) BW_d/λ vs f

(c) $\Delta r_0/\lambda$ vs f (d) B_{true} vs f

Figure C.6: a) Variation of longitudinal beamwidth, BW_l/λ, with frequency, b) variation of source direction beamwidth, BW_d/λ, with frequency, c) variation of positional error, $\Delta r_0/\lambda$, with frequency and d) variation of corrected strength estimation, B_{true} (in dB/Hz re. 20μPa.s), with frequency for a single synthetic dipole source at $\mathbf{x_s} = (-0.3, 0, 0)$ with orientation $\vec{\zeta} = (0, 0, 1)$.

The longitudinal beamwidth of the four methods is compared in Figure C.6a. CB and MB tend to have longitudinal beamwidths that are similar in magnitude over the entire frequency range. This is approximately one wavelength at all frequencies. Conversely, the beamwidth measured in the assumed source direction (Figure C.6b) shows an improvement when MB is used. For frequencies above 1.5 kHz, CB has a source direction beamwidth that is over 1λ larger than that of MB. This large beamwidth is

primarily caused by poor separation of the main lobe with the side-lobes in the CB algorithm. As seen in Figure C.4, side-lobes tend to merge with the main lobe at -3 dB down from the maximum source strength, increasing the measured beamwidth and thus the spatial ambiguity of the output. The smaller beamwidth of MB is caused because the side-lobes are distinguishable from the main lobe at -3 dB down from the source. This means that a dipole source is identifiable even with the presence of strong side-lobes. Comparatively, both deconvolution techniques have beamwidths that are smaller than both conventional methods. This is to be expected, since the beamwidth is a user defined input parameter in the deconvolution algorithms.

Figure C.6c indicates that there is no theoretical positional error for a single dipole source above 600 Hz for all four methods. Below 600 Hz, the positional error of MCS is 0.015λ at 500 Hz while the error of other methods remain nil. This is because of the smaller aperture of the sub-arrays when using the top and side array individually. When both sub-arrays are used together, as in CB, the aperture of the full array is larger and the amount of phase information received across the array is enough to accurately localise the source down to a frequency of 500 Hz. However, when the two sub-arrays are used individually, as in MB, the top and side sub-array individually only receive a small fraction of the information from the dipole source. That is, they individually have apertures that are not large enough to intercept enough of the outgoing wave front to accurately localise the dipole source. This results in a position error in both the top array and side array that is carried through when CLEAN-SC is applied. Although this effect is relatively minor in the present case consisting of one source, it is important to identify the mechanism through which this error occurs. This is because the same mechanism causes errors at higher frequencies when multiple sources are present (as will be discussed). Interestingly, the positional error remains nil for MB without deconvolution for frequencies down to 500 Hz. It appears that the MB algorithm artificially increases the aperture of the full array for this idealised case so that even at low frequencies, the multiplication of the sub-array beamforming maps results in a peak at the true source location.

Lastly, the corrected source strength lies within ± 0.2 dB from the true source strength of 100 dB for all methods above 500 Hz (see Figure C.6d).

C.3.3 Distributed dipole results

Practical applications of beamforming aeroacoustic sources rarely involve single point dipoles. A situation that better approximates a real aeroacoustic test case is an elongated dipole source, such as a cylinder (Porteous et al. 2014a) or the trailing edge of an aerofoil (Brooks and Humphreys 2003; Moreau et al. 2014). As a test case, this type of source can be approximated in the present section as a line of three spatially incoherent point dipoles. Figure C.7 shows the source map for three incoherent dipoles located at $\mathbf{d_1} = (-0.3, -0.1, 0.0)$, $\mathbf{d_2} = (-0.3, 0.0, 0.0)$ and $\mathbf{d_3} = (-0.3, 0.1, 0.0)$ each with a strength of 100 dB re.20μPa. The map is taken at a frequency of 3 kHz. Multiple incoherent dipole sources are created by separately calculating a synthetic cross-spectral matrix for each point dipole using Equation 4.14 and adding the matrices together. The layout of Figure C.7 is identical to that of Figure C.4. Again, crosses denote the true source locations

projected onto adjacent orthogonal planes while circles denote projections of the positions of the maxima (in this case the top three maxima) of the source map.

The beamforming maps of Figure C.7a show a series of lobes that are at the general location of the simulated dipole sources but are merged together. Additionally, the map is convolved with a number of side-lobes, which makes it difficult to interpret and localise the simulated sources by inspection. Closer analysis reveals that in the beamforming map, local maxima do appear at the location of the sources (as seen by the circles). Therefore, with this information it is possible to locate sources with *a priori* knowledge on their location. However, in all practical situations this is not the case. Indeed, given this map in an experimental situation it would be very difficult to distinguish between a true source and a side-lobe.

Figure C.7c shows that MB is able to localise the source well in the z-x direction, but poorly localises in the y-direction. This is because at this frequency, the lateral beamwidth of the top array is not small enough to capture enough information to separate the individual sources in the y direction. The positional error is slightly larger than that of CB.

CCS (Figure C.7b) significantly improves the dynamic range of the maps and succeeds in separating the sources. Importantly, it allows for localisation of the sources unambiguously from general inspection of the beamforming image. MCS (Figure C.7d) also manages to capture all three sources, but with a bias source amplitude that is 7 dB lower than the values of the other maps. Additionally, an extraneous source is also captured that lies between $\mathbf{d_2}$ and $\mathbf{d_3}$. The results of MCS can be explained by the fact that at low frequencies the side array cannot resolve sources that are behind one another (i.e in the same y-plane) at that wavelength. The longitudinal beamwidth of the side array is large, which leads to a spatial convolution of the source distribution. As a result, CLEAN-SC treats the entire source map as coherent with itself and therefore only resolves one maxima in the computational domain. Furthermore, this maxima appears in an erroneous position, between $\mathbf{d_2}$ and $\mathbf{d_3}$. The top array, however, is able to capture all three-dipoles in their correct positions because its resolution (in the $x-y$ plane) is large. Therefore, when the maps of the side array and top array are multiplied together, mutual cancellation of the maps occur and four maxima's appear in the source maps.

Figure C.8 shows the variation in source localisation and estimated (corrected) source strength of the three dipole sources with frequency from 1 to 10 kHz. In all plots, data is only given for cases where three maxima in the source map were resolved. Where data is absent is therefore indicative of the lower frequency limit (the 'cut-off frequency') of the array for this case.

Compared with Figure C.6, the positional error in estimated maxima for all three-dipole sources (shown in Figure C.6a, c and e) show more variability over the frequencies investigated, although globally the errors remain low, reaching at most a 5^{th} of the wavelength. For $\mathbf{d_1}$, $\mathbf{d_2}$ and $\mathbf{d_3}$, the positional error using all CB, CCS and MCS was nil above 4 kHz. Conversely, for frequencies above 4 kHz, MB had a higher error, particularly when localising $\mathbf{d_1}$. The large error when localising $\mathbf{d_1}$ is primarily due to the inability of the side array to capture phase information at higher frequencies from sources that lie behind one another (on the y-axis), and this effect is enhanced for $\mathbf{d_1}$, which is furthest from the side array plane. Below 4 kHz, all four methods had positional errors up to 0.2λ.

This increase in error is due to the beamwidth of the array becoming larger than the distance between the sources. When this happens, source maxima occur at erroneous positions. As the wavelength of sound is increased further, the cut-off frequency is reached and the beamwidth becomes so large that not all three sources can be resolved. The cutoff frequency is different when using different algorithms. As expected, MB has the highest cut-off frequency at 3 kHz because of the reduced aperture when using the top and side array separately. CB has a slightly lower cut-off frequency at 2.5 kHz. Both deconvolution methods drive the cut-off frequency down to 1.25 and 1 kHz for MCS and CCS respectively.

Figure C.8b,d and f show the estimated strength variation for the three dipole sources. Where three maxima are resolved, CB and MB are able to estimate the strength of the source to within ±2 dB. CCS has good estimation of source strength (±2 dB) for all three sources above 2.5 kHz. Below 2.5 kHz, the strength estimation is less accurate (±12 dB). This is caused by a combination of errors in the calculated position of the source (so the applied correction factor is underestimated) and larger beamwidth at larger wavelengths causing a distorted source map.

Above 2.5 kHz, MCS was unable to estimate the true source strength for any of the sources (with the notable exception of 6.3 kHz for $\mathbf{d_1}$). The estimation by MCS was consistently approximately 12 dB lower than the true maximum. The explanation for this is the same that was discussed when analysing the results of Figure C.7d. Large errors in the estimated strength occur when using multiplicative methods because the multiplication of the two beamforming maps rely on the spatial coherence of the maps generated by the top and side sub-arrays. The main lobes found in the multiplied map will be significantly diminished unless there is no error in the position of the maxima between the two maps. For frequencies above 2.5 kHz, there is evidently a large discrepancy between the position of the maxima between the top and side sub-array maps. This causes an underestimated source strength. However, at 2.5 kHz and below, the strength estimation is better (±2 dB) for $\mathbf{d_2}$ and $\mathbf{d_3}$ but remains poor for $\mathbf{d_1}$. The larger beamwidth of the sub-arrays at lower frequencies means the effect of error in the position of the maxima between sub-array maps is less pronounced. Accordingly, less cancellation occurs between the two source maps for the sources closest to the microphones ($\mathbf{d_2}$ and $\mathbf{d_3}$) and the results are improved. For $\mathbf{d_1}$, the strength remains underestimated by 12 dB because, despite the large beamwidth, the side array map still does not produce a lobe near $\mathbf{d_1}$, meaning multiplicative cancellation still occurs.

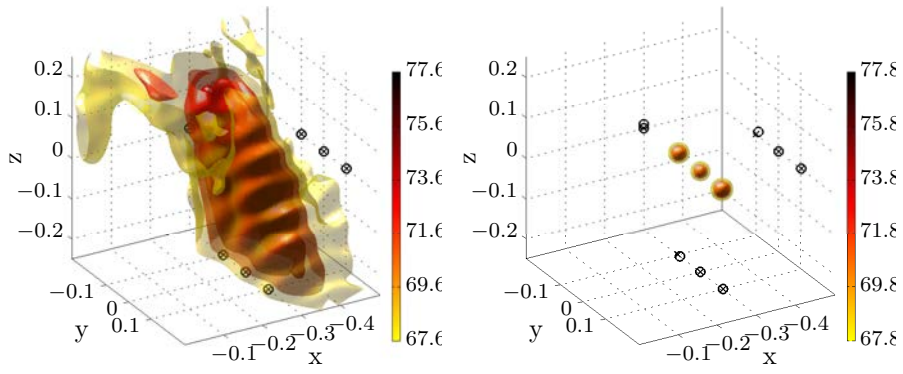

(a) CB

(b) CCS

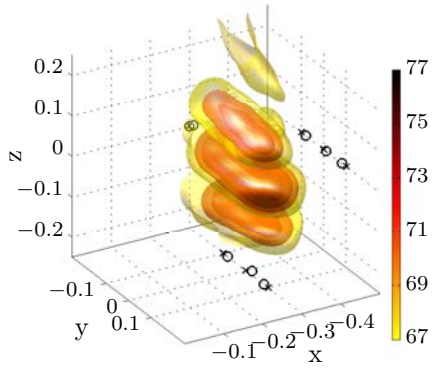

(c) MB

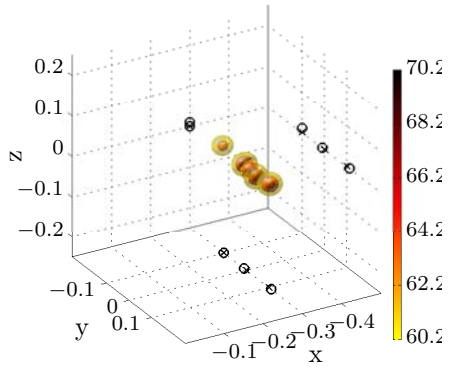

(d) MCS

Figure C.7: 3D beamforming sound maps of three synthetic dipole sources, all with orientation $\vec{\zeta} = (0, 0, 1)$, and located at $\mathbf{d_1} = (-0.3, -0.1, 0)$, $\mathbf{d_2} = (-0.3, 0, 0)$ and $\mathbf{d_3} = (-0.3, 0.1, 0)$. The maps are taken at a frequency of 3 kHz using CB (a), CCS (b), MB (c) and MCS (d). The colourbar denotes the biased (uncorrected) source strength (in dB/Hz re. 20μPa.s). The symbols 'x' denote the true location of the source and the symbols 'o' denote the estimated location of the source based on the maximum in the source map.

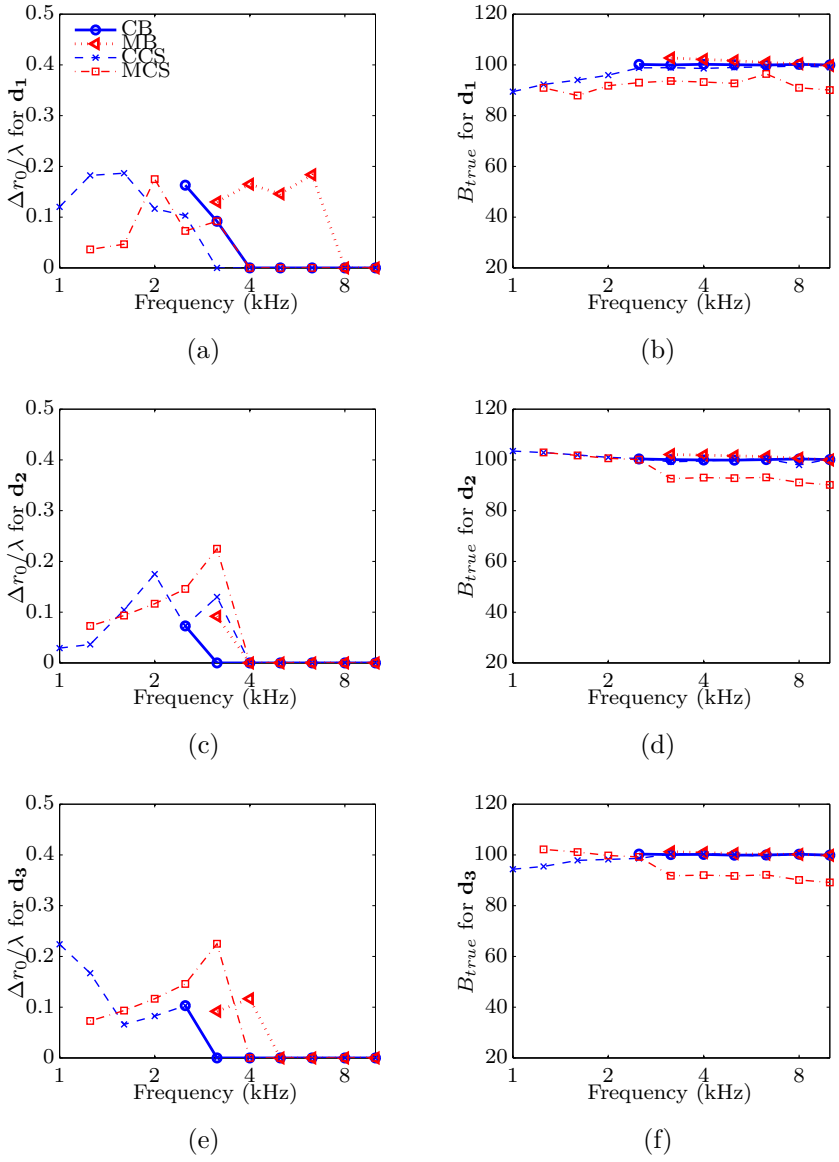

Figure C.8: Variation of positional error, $\Delta r_0/\lambda$ (a,c,e), and B_{true} (in dB/Hz re. 20μPa.s) (b,d,f) with frequency for a three dipole sources, $\mathbf{d_1} = (-0.3, -0.1, 0)$, $\mathbf{d_2} = (-0.3, 0, 0)$ and $\mathbf{d_3} = (-0.3, 0.1, 0)$, all with orientation $\vec{\zeta} = (0, 0, 1)$.

C.4 Conclusion

This chapter has compared four methods for creating 3D beamforming source maps using a non-planar array of microphones. These include CB, MB, CCS deconvolution and MCS deconvolution. CB and CCS are simply 3D extensions of two-dimensional conventional beamforming and deconvolution techniques. MB applies three-dimensional CB to two perpendicular arrays and multiplies the source maps together, with the reasoning that the lateral resolution of one array will improve the depth resolution of another. MCS is similar to MB but applies conventional deconvolution techniques to the source maps before multiplication occurs. The algorithms were formulated for sources that have dipolar radiation propagation characteristics, such as those found by the interaction between airflow and a rigid surface.

The results showed that for an idealised situation in which there was a single point dipole source of radiation, CB did not give results that were easily interpreted. This was because of the presence of side-lobes that were merged with the main lobe, making it impossible to unambiguously localise the source. CCS removed the side-lobes and created a satisfactory source map. Conversely, MB yielded a more interpretable map compared with CB because the side-lobes were distinguishable from the main lobe. MCS also yielded results comparable with CCS. Quantitatively, the true source strength was estimated to within 0.2 dB re. 20μPa (for a 100 dB re. 20μPa source) for all four algorithms by applying a three-dimensional array gain field.

For a line distribution of three incoherent point dipoles, CCS and MCS generally outperformed CB and MB. For frequencies less than 2.5 kHz, CB and MB were not able to resolve all three of the sources. This was due to the beamwidth of the array being larger than the separation between the sources. Alternatively, CCS and MCS were able to distinguish all three sources down to 1 and 1.25 kHz respectively, albeit with source localisation errors that were of the order of 0.2λ. For frequencies above 2.5 kHz, CB and CCS had similar results with the source strengths and source positions estimated well for all three sources using both algorithms. MB similarly performed well at these higher frequencies, however the localisation error for the source furtherest from the array centre was large at 0.2λ. MCS estimated the source positions well but was susceptible to amplitude cancellation, where small positional errors in the source maxima for the two sub-arrays caused the source strength to be severely underestimated by up to 12 dB re. 20μPa .

Performing CCS appears to be the best method for three-dimensional source localisation of aeroacoustic sources using an orthogonal array that partially encloses the source. It does, however, come at increased computational cost (although generally the computational cost is low because of the low number of microphones). MB is a computational cheap alternative, because it separates the side-lobes inherent in dipole beamforming. MB has potential application where a large number of cases need to be analysed in a short amount of time. MCS also gives good results and is less computationally expensive than CCS, but suffers from poor source strength estimation and can yield incorrect source locations at low frequencies if multiple sources are present.